NASA CP-2007

NINTH CONFERENCE ON
SPACE SIMULATION

Sponsored by
Institute of Environmental Sciences
The American Institute of Aeronautics and Astronautics
The American Society for Testing and Materials
The National Aeronautics and Space Administration

Los Angeles, CA April 26–28, 1977

National Aeronautics and Space Administration

FOREWORD

The Goddard Space Flight Center of the National Aeronautics and Space Administration published these proceedings as a NASA Conference Publication for the Ninth Space Simulation Conference. As a co-sponsor, the NASA made these proceedings a permanent record available to those interested in space simulation and to others who may find this technology useful in their field.

The papers presented at this conference provided an international dialogue and a meaningful exchange of advances in the simulation of space environments as well as the evolution of these technological advances into other fields. These papers represent a significant contribution to the understanding of space simulation problems and the utilization of this knowledge by all concerned.

The Goddard Space Flight Center is pleased to cooperate with the Institute of Environmental Sciences, the American Institute of Aeronautics and Astronautics, and the American Society for Testing and Materials in making this important work available to the technical community.

Russell T. Hollingsworth
Engineering Services Division
Goddard Space Flight Center

PREFACE

These Proceedings are the ninth in a series of conferences jointly sponsored by the Institute of Environmental Sciences (IES), American Institute of Aeronautics and Astronautics (AIAA), and the American Society for Testing and Materials (ASTM). The National Bureau of Standards (NBS) was a co-sponsor for the fifth conference in this series and the National Aeronautics and Space Administration (NASA) was a co-sponsor for the sixth through ninth conferences of the series. Proceedings for the fifth conference was published by the National Bureau of Standards, and the sixth through ninth proceedings have been published by the National Aeronautics and Space Administration. Proceedings for this series before the fifth were published by one of the three sponsoring societies given above, that was acting as the host society for the conference. This joint effort of the sponsoring societies, which began in January 1965, has succeeded in the objectives of: reducing the number of overlapping conferences with the resulting economies to the participants and societies; providing a single publication that collects most of the new material in this field in one volume; and, providing the published papers to a larger audience with the joint conference and with wider distribution of the Proceedings to other areas of science and technology. This, the ninth conference, further advanced the last of these objectives and enlarged the audience by meeting in conjunction with the Institute of Environmental Sciences Annual Meeting and Equipment Exposition.

The Technical Committee for this conference was composed of members from all three sponsoring societies and the members are listed on the following pages. The standing technical committees that assisted in the organizing of the program of the conference are:

IES — Space and Solar Radiation Committee
AIAA — Ground Testing and Simulation Committee, and the Life Sciences and Systems
ASTM — Committee E-21.07 Solar Radiation

The three societies have a Permanent Policy Committee, made up of two members from each society to formulate general policy. This Committee recommends the succession for hosting the conferences and reviews the interval between conferences, so enough new material has been developed to warrant another conference. This Policy Committee also reviews the rules and regulations of each society for the conduct of meetings and sees that they are adhered to as much as possible.

The General Committee is appointed for each conference, and is drawn largely from the host society. The conducting of the conference and publishing the proceedings are the responsibility of this Committee. The Committee for the Ninth Conference was greatly aided by the National Aeronautics and Space Administration publication of the Proceedings. The facilities, publicity, outside program, and exhibits committees worked concurrently with the Annual Meeting Committee of the IES.

The Ninth Space Simulation Conference was held in Los Angeles, California at the Marriott Hotel on April 26-28, 1977. These proceedings were published by NASA which co-sponsored this conference, and members of the Technical Program Committee performed the function of editor for the papers presented in sessions which they organized.

John D. Campbell
General Chairman

COMMITTEES FOR
NINTH SPACE SIMULATION CONFERENCE

GENERAL COMMITTEE

General Chairman	–	John D. Campbell, Perkin-Elmer Corp.
Technical Program Chairman	–	Stan Baber, Boeing Aerospace Co.
Publications Chairman	–	Joseph L. Stecher, NASA/GSFC
Facilities Chairman	–	Edward Gulian, Hughes Aircraft
Exhibits Chairman	–	Jack M. Kin, Mattel, Inc.
Registration Chairman	–	Thomas J. Sereno, TRW Systems

TECHNICAL PROGRAM COMMITTEE

Howard Altman	–	CVI
Eugene N. Borson	–	The Aerospace Corporation
George J. Frankel	–	Grumman Aerospace Corporation
Raymond Kruger	–	NASA/GSFC
Douglas McKenney	–	Boeing Aerospace Company
George Mikk	–	Perkin-Elmer Corporation
Charles G. Miller	–	Jet Propulsion Lab
Rod Palmberg	–	Varian Assoc.
Paul Pederson	–	Sci-Med, Inc.
George Wright	–	Sandia Labs

JOINT POLICY COMMITTEE

IES

John D. Campbell	–	Perkin-Elmer Corporation
George J. Frankel	–	Grumman Aerospace Corporation

ASTM

Eugene N. Borson	–	The Aerospace Corporation
Charles Duncan	–	NASA/GSFC

AIAA

Charles G. Miller	–	Jet Propulsion Laboratory
Dwight H. Reilly	–	NASA/LeRC

TABLE OF CONTENTS

SPACECRAFT TESTING

Session Organizer – George Mikk
Perkins-Elmer Corporation

SESSION J-1
TEST DESIGN

Session Co-Chairmen – Jim Norris
TRW

– R. E. "Zeke" King
Hughes Aircraft Company

SESSION J-2
FACILITIES & TEST EQUIPMENT

Session Co-Chairmen – George Mikk
Perkin-Elmer Corporation

– David H. Orbock
Northrop Services

SESSION J-3
SYSTEM & SUBSYSTEM TEST

Session Co-Chairmen – Emil S. J. Wang
McDonnell Douglas Corporation

– Terry L. Hershey
Spectrolab

LIFE SCIENCES

Session Organizer: – George J. Frankel
Grumman Aerospace Corporation

SESSION K-1
MEDICINE & SPACE

Session Co-Chairmen – George J. Frankel
Grumman Aerospace Corporation

– Donald R. Young
NASA Ames Research Center

SESSION K-2
PHYSICAL ENVIRONMENTAL FACTORS

Session Co-Chairmen – Kenneth R. Jackman
Biomedical Engineering Consultant

– Donald R. Young
NASA-Ames Research Center

SESSION K-3
CHEMICAL ENVIRONMENTAL FACTORS

Session Co-Chairmen – Donald R. Young
NASA-Ames Research Center

– Kenneth R. Jackman
Biomedical Engineering Consultant

CONTAMINATION

Session Organizer – Raymond Kruger
NASA-Goddard Space Flight Center

SESSION L-1
SPACECRAFT APPLICATIONS OF CONTAMINATION MONITORS

Session Chairman – E. N. Borson
The Aerospace Corporation

SESSION L-2
MEASUREMENT

Session Chairman – E. N. Borson
The Aerospace Corporation

SESSION L-3
OUTGASSING

Session Chairman – E. N. Borson
The Aerospace Corporation

SESSION M-1
SPACE PHYSICS

Session Organizer and Session Chairman – Charles G. Miller
Jet Propulsion Lab

SESSION M-2

Session Chairman – Charles G. Miller
Jet Propulsion Lab

THERMAL PROTECTION

Session Organizer – G. F. Wright, Jr.
Sandia Laboratories

SESSION N-1
FACILITIES

Session Co-Chairmen – G. F. Wright, Jr.
Sandia Laboratories

– G. J. Hartman
Aerotherm Division-Acurax Corporation

SESSION N-2
TESTING

Session Co-Chairmen – G. F. Wright, Jr.
Sandia Laboratories

– G. J. Hartman
Aerotherm Division-Acurax Corporation

SESSION N-3
ANALYTICAL

Session Co-Chairmen – G. F. Wright, Jr.
Sandia Laboratories

– G. J. Hartman
Aerotherm Division-Acurax Corporation

Paper No. 1

SPACE SHUTTLE TROPOSPHERIC AIR QUALITY ASSESSMENT PROGRAM

Gerald L. Gregory

ABSTRACT

In the Space Shuttle Environmental Statement issued in July 1972, NASA stated that where the possibility of some detrimental environmental impact exists, operational constraints will be imposed to preclude or minimize these impacts. Although the studies preceeding the Environmental Statement showed no evidence of a launch constraint requirement due to air quality effects, NASA began in early 1972 a program to develop and refine the necessary analytical and experimental tools that would be required to implement launch constraints. The overall NASA program considers all phases of Shuttle operations and the tropospheric portion of the program was focused on the launch phase of the Shuttle and the air pollution potential of the exhaust effluents, mainly hydrogen chloride gas and aluminum oxide particulates from the Shuttle propulsion system.

The paper will discuss the program as initiated in 1972, the results obtained during the past 4 years, and the future plans for the program. The program results are covered in some detail with major emphasis on the Launch Vehicle Effluent (LVE) monitoring studies. The LVE studies are a large scale field monitoring program conducted at Kennedy Space Center in conjunction with regularly scheduled Titan III launches. The purpose of the LVE program is to evaluate and refine NASA's ability to predict and forecast the tropospheric air quality modification associated with the lift-off of a large solid propellant launch vehicle. The paper will summarize the current status of NASA's ability in this area and describe the ongoing program planned to continue until Shuttle becomes operational. Although no launch constraints have been identified to date, the author will propose a representative Shuttle operational program suitable for providing the inputs to the launch director should Shuttle launch constraints be imposed due to tropospheric air quality effects.

Paper No. 2

A MATH MODEL FOR THE VENTING PROCESS OF THE SHUTTLE ORBITER PAYLOAD BAY

H. K. F. Ehlers, *Structures & Mechanics Division, NASA-Johnson Space Center, Houston, Texas*

ABSTRACT

A math model has been developed and applied to assess design and operational requirements necessary to meet criteria that depend on proper venting of Shuttle Orbiter compartments during ascent. This model is based on a multi-species transient gas flow model that simulates the pressure variations in a complex system composed of many interconnected compartments. The model uses the method of weighted residuals to solve the set of simultaneous differential equations that govern the dynamic response of such a system containing a number of gas molecule species. The particular advantage of this method is its extreme efficiency because it requires only one-hundredth to one-tenth of the computation time taken by other methods (e.g., Runge-Kutta) for comparable solutions.

The knowledge of the time dependance of the pressure in the various Orbiter compartments is of special interest during ascent, when certain scientific or technical instruments are to be checked out or operated or to assess adequate Orbiter configuration with respect to acceptable differential pressures. Calculations of the pressure vs. time dependencies were performed as part of a parametric sensitivity study to identify the relative importance as well as the most critical of the input variables. The results indicate that the pressure in the payload bay differs only slightly from the outside (atmospheric) pressure during most of the ascent time if the filters are of sufficient conductivity. Therefore selection of the proper type of filter is critical. At a certain point in time however, the gas load inside the bay will start to cause major deviations of the bay pressure from the outside pressure.

Paper No. 3

PRECISION TEMPERATURE GRADIENT MEASUREMENTS ON WINDOW GLASS

George Mikk and Ward Petrie, *Senior Engineers at The Perkin-Elmer Corporation, Optical Technology Division, 100 Wooster Heights Road, Danbury, Connecticut 06810*

ABSTRACT

Surface temperature gradients were measured with miniature thermocouples installed in a 58.5 cm (23-inch) square window. Test measurements at 25 locations were made under vacuum and with the window operating in radiant heat transfer mode. The analysis of thermocouple design and installation is presented along with a lead wire routing scheme to allow for both differential and absolute temperature measurements while using a minimum number of signal feedthru paths through the test chamber wall. Typical test data and operational precautions are presented along with the accuracy analysis for installation effects and measurement effects to support differential temperature measurement precision values of $\pm 0.06^{o}$C RMS ($\pm 0.1^{o}$F RMS).

INTRODUCTION

Typically in design activity, a mathematical model is created of the proposed system, followed by a physical test model, the operation of which, under simulated conditions, is used to verify the accuracy of the mathematical model. The confirmed mathematical model is then used for further detailed design analysis and development.

The subject of this paper is the measurement of surface temperature gradients on a glass window in order to confirm the accuracy of a system mathematical model using such a window. The window, a 25.4 mm thick glass plate, 58.5 cm square, was required to operate in a vacuum environment in a radiative heat transfer mode. The relationship of the plate to this heat flux environment is shown schematically in Figure 1.

The requirements of the test were to instrument a representative plate with temperature sensors, expose the plate to the simulated heat flux environment, and measure the resulting surface temperature differences to a precision of $\pm 0.06^{o}$C or better with the plate operating at a predicted mean temperature level of approximately 21^{o}C.

Various measurement approaches were evaluated with the choice made to use copper-constantan thermocouples made from small diameter wire and operated in a differential mode in order to provide the required precision.

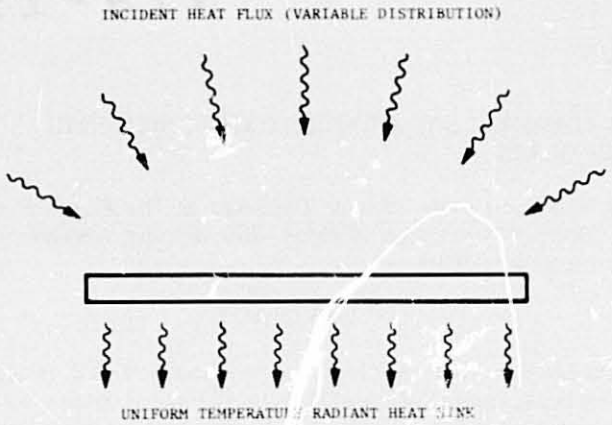

Fig. 1-Heat flux environment relationship

Sensor Analysis

Two installation approaches were considered for this application. The first, and simplest, used a miniature thermocouple attached on the front surface of the window with a patch of adhesive tape; the second employed a miniature thermocouple element inserted into a hole drilled from the back of the glass plate to a point 2.54 mm below the front surface.

Evaluation of these proposed installations was carried out using a steady state thermal analysis computer program available at our facility computer library. This program calculates node temperatures to yield the steady state temperature distribution and also calculates the steady state heat flow between the nodes.

Figure 2 shows the node arrangement used for calculating the patch thermocouple case, and Figure 3 shows the node arrangement for the case with imbedded thermocouples. In all cases of thermocouple installation evaluation, a uniform incident heat flux from a 26.6^{o}C (80^{o}F) blackbody irradiated the front surface of the plate and the rear surface radiated to a blackbody radiant sink at 18.6^{o}C (65^{o}F).

Results of calculations showing surface temperature depression for the case utilizing an adhesive patch to fasten the thermocouple onto the front surface are shown in Figure 4 with the associated nodal temperature map shown in Figure 5, where the temperatures are expressed as amount of temperature depression in ^{o}C. Patch size was varied from 12.7 mm diameter to 25.4 mm diameter to evaluate the radiant energy blockage effects caused by the patch. The surface temperature perturbations range from 0.08^{o}C to 0.12^{o}C, which is in excess of the requirement 0.06^{o}C. These values by themselves could be acceptable if it could be guaranteed that the temperature measurement perturbation at each location would be the same, but questions such as thermal contact between the thermocouple and glass, a variation of which would cause a variation in indicated temperature cannot be fully assessed. These effects are indeterminate depending on thermal contact, lead conduction, and tape patch temperature. For this reason, this approach was discarded, even though it would have been the simplest to implement.

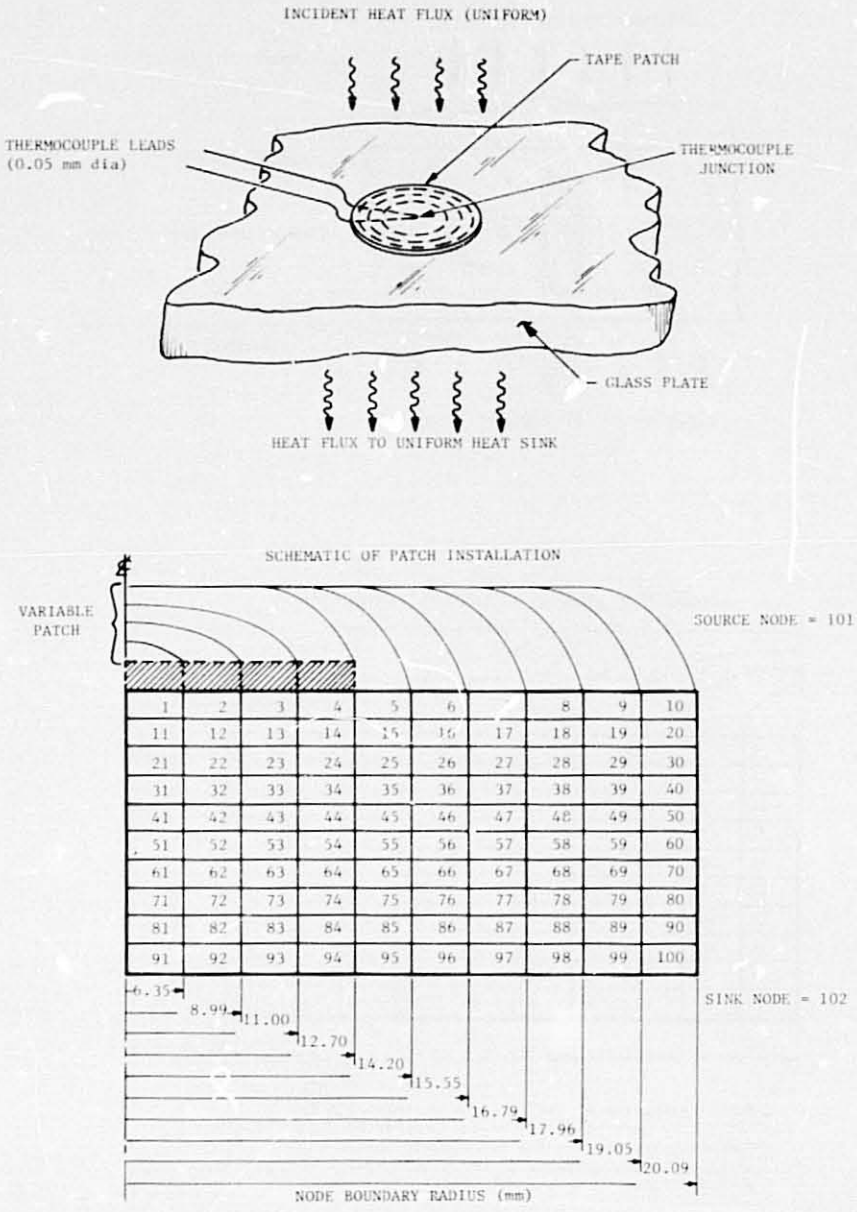

Fig. 2-Node arrangement for computation (Equal area nodes)

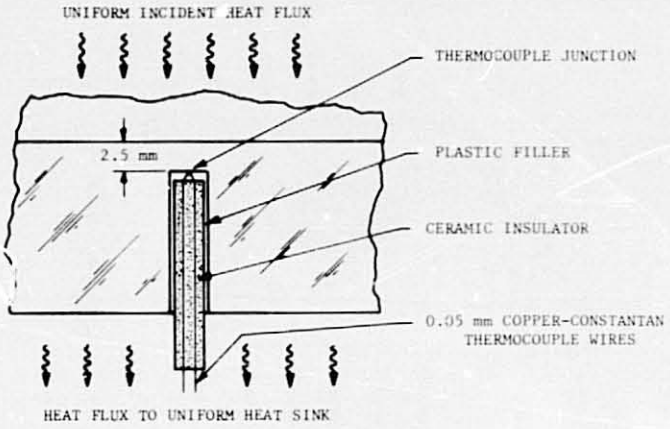

SCHEMATIC OF IMBEDDED THERMOCOUPLE INSTALLATION

1	2	3	4	5	6	7	8	9	10
11	12	13	14	15	16	17	18	19	20
21	22	23	24	25	26	27	28	29	30
31	32	33	34	35	36	37	38	39	40
41	42	43	44	45	46	47	48	49	50
51	52	53	54	55	56	57	58	59	60
61	62	63	64	65	66	67	68	69	70
71	72	73	74	75	76	77	78	79	80
81	82	83	84	85	86	87	88	89	90
91	92	93	94	95	96	97	98	99	100

NODE RADII ARE THE SAME AS FIG. 2

NOTE:
The installation of the imbedded thermocouple is handled by modifying the thermal properties of nodes 11, 21, 31, 41, 51, 61, 71, 81, and 91 to account for the presence of the wire, ceramic and plastic filler.

Fig. 3-Node arrangement for case with imbedded thermocouples

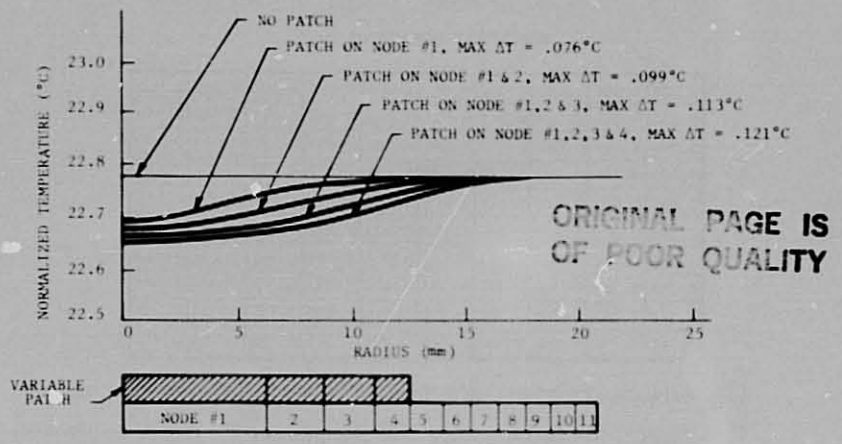

Fig. 4-Surface temperature suppression due to patch

.121	.094	.077	.057	.032	.018	.009	.004	.002	.000
.129	.107	.093	.081	.069	.061	.056	.052	.049	.049
.144	.127	.119	.111	.104	.099	.096	.094	.092	.092
.166	.153	.148	.143	.139	.136	.134	.132	.132	.131
.191	.182	.178	.176	.173	.171	.170	.169	.168	.168
.219	.213	.211	.208	.207	.206	.205	.204	.204	.204
.248	.244	.243	.242	.241	.240	.239	.239	.239	.239
.279	.277	.276	.275	.274	.274	.273	.273	.273	.273
.312	.309	.309	.308	.308	.307	.307	.307	.307	.307
.344	.343	.342	.342	.341	.341	.341	.341	.341	.341

Fig. 5-Nodal temperature map for patch on nodes #1,2,3 & 4
Temperature depression (^{o}C)

The alternate method considered a thermocouple element inserted to just beneath the front surface by means of a hole drilled from the rear surface. This proposed configuration was also analyzed using the computer model to assess its effect on the glass.

The thermocouple set in the bored hole, using a ceramic rod, results in a temperature distribution which is only slightly perturbed. The distribution is somewhat different in that there is a slight depression in temperature at the central nodes near the top of the glass. (See Figure 6.) This condition reverses itself near the bottom of the glass, giving a slight rise in temperature at the bottom. This unusual temperature distribution results from the greater conductance of the ceramic rod/thermocouple wire combination compared to that of the glass itself. The greater conductance path transfers heat away from the top surface more rapidly at the central node depressing its temperature. This greater conductance path also will conduct greater amounts of heat to the central node at the bottom surface, causing its temperature to rise slightly. In both areas, these effects are negligibly small in a practical sense and the temperature distribution closely approximates the temperature distribution of the undisturbed window.

TEMPERATURE DEPRESSION IN °C

0.006	0.004	0.002	0.001	0.001	0.000	0.000	0.000	0.000	0.000
0.054	0.049	0.047	0.045	0.045	0.045	0.044	0.044	0.044	0.044
0.093	0.092	0.091	0.089	0.089	0.088	0.088	0.088	0.088	0.088
0.134	0.134	0.133	0.133	0.132	0.132	0.132	0.132	0.132	0.132
0.177	0.177	0.177	0.176	0.176	0.176	0.176	0.176	0.176	0.176
0.203	0.203	0.203	0.203	0.203	0.203	0.203	0.203	0.203	0.203
0.246	0.246	0.246	0.247	0.247	0.247	0.247	0.247	0.247	0.247
0.306	0.306	0.306	0.307	0.307	0.307	0.307	0.307	0.307	0.307
0.348	0.349	0.349	0.350	0.351	0.351	0.351	0.351	0.351	0.351
0.389	0.391	0.392	0.394	0.394	0.394	0.394	0.395	0.395	0.395

Fig. 6-Nodal temperature map for inserted thermocouple

It is important to note that the thermocouple itself is located at a point approximately 2.54 mm below the surface. Thus, its temperature will be the temperature of the glass 2.54 mm below the surface. For this model, it will differ from the undisturbed temperature by no more than 0.06°C. This may be important for absolute temperature measurements, but should be of little importance to differential measurements where all the sensors will be similarly affected.

On the basis of this analysis, it was determined that a sensor of this type would be the optimum design approach.

Instrumentation Implementation

A sample window was used as the test article. The 2.16 mm diameter thermocouple holes were drilled by an ultrasonic technique using a diamond impregnated core drill, followed by a solid drill to provide a flat bottomed hole.

The sensor design was fabricated using bare 0.05 mm (0.002-inch) diameter copper-constantan thermocouple wire to insure minimum lead conduction effects. A ceramic rod with four axial holes was used to hold the junction in place in the drilled hole. Lead wires from the junction were run through the axial holes. The thermocouple assembly was potted in the hole with Laminar X-500 conformal coating. This technique provided an added benefit because the junction could be easily removed from the hole with a drill bit in a tap handle in the event of sensor failure. A typical installation is shown in Figure 7. A line of nine such sensors was installed in the plate as shown in Figure 8. An additional 16 sensors, not shown in Figure 8, were installed to provide confirmation of temperature stability.

Lead wire hook-up was accomplished in a special manner. It was desired to provide an absolute reading for at least one of the sensor locations. All locations were to be read differentially, either as selected pairs or all referenced to one selected location. To meet both of these aims, a common constantan lead was provided. All junctions were connected to this common run. This common constantan run was then brought out and combined with a reference junction. The copper side of each junction was brought out separately. The scheme is shown in Figure 9. To differentially read any pair of junctions, it is only necessary to read across the copper leads for each junction of the pair. By reading across the copper lead of any junction and the copper lead of the reference junction, an

absolute reading of the junction can be made. Thus, a highly flexible readout capability resulted which enabled the readout of any differential pair desired, and still enabled the absolute temperature of each location to be read.

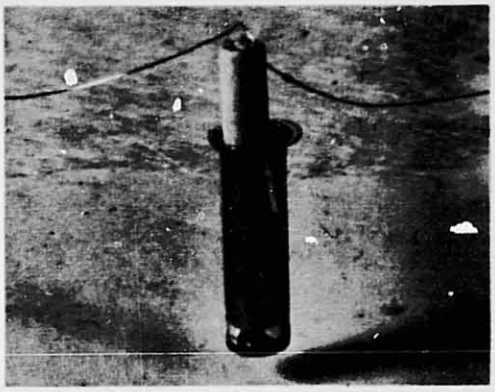

Fig. 7-Thermocouple installation

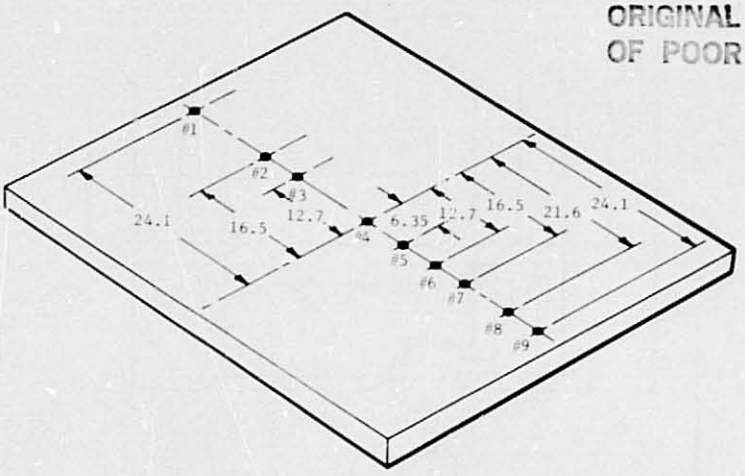

Fig. 8-Thermocouple locations (cm)

The copper leads on the window were routed to an edge area where 14 pin IC chip connectors were mounted. The connectors had been modified by breaking off the pins on one side of the connector. The connectors could now be bonded to the side of the window with the remaining pins extending over the surface, facilitating hook-up of the copper leads. The constantan lead was hooked up to the constantan side of a miniature thermocouple connector which was also bonded to the side of the window.

The copper leg of each junction was routed from the connector interface on the window by way of the copper leg of a copper-constantan harness. DIP component headers were attached to the harness to enable it to interface with IC chip connectors. The mating plug for the constantan lead connector was used to complete the harness interface.

The harnessing was routed to its own penetration through the test chamber where compensated copper-constantan feedthrus were used. From the penetration, the harness was routed to a switch box. Here the switch was wired to provide two readouts, a differential reading of each junction to one of the junctions which serves as a reference, and an absolute reading for each junction including the one used as a reference. The wiring arrangement is shown in Figure 9. At the switch, the constantan leg was wired to a $0^{o}C$ reference junction, providing the absolute readout. The absolute readings were made using a Doric DS 350 digital temperature indicator (DTI). The switching provides readout of the thermocouple junctions as differential pairs with TC #1 as the common or reference junction of the pair for each junction. In this way, differential temperatures could be deduced for any combination of the sensors. Differential readings were made using a Hewlet-Packard 419 DC null volt-ammeter. The switch is wired in such a way that a short across the switch and a short across the connectors on the window can be read. This was done to identify any effects on the readings due to the lead wires or the switches. With the polarity switch in position #1, the absolute temperature of the individual junctions is read. In position #2, the absolute temperature of the common or reference junction is read.

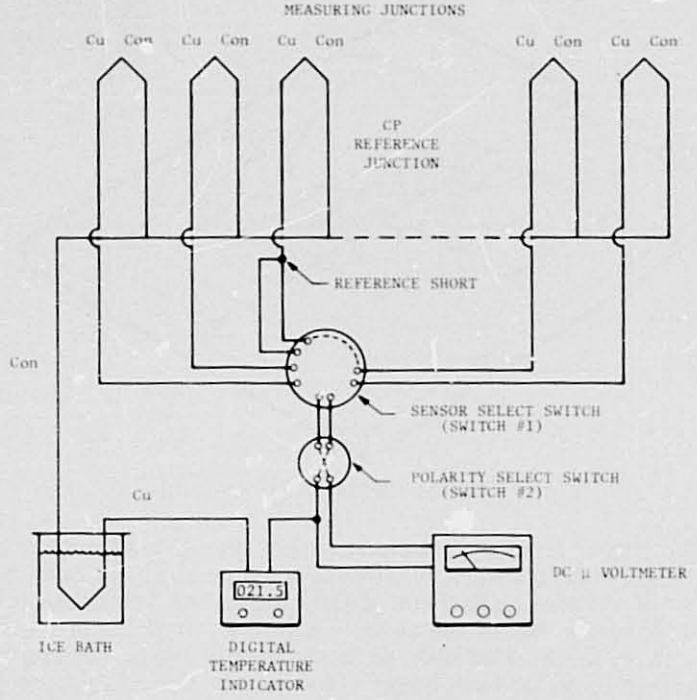

Fig. 9-Wiring arrangement

The accuracy of the absolute temperature data from the window thermocouples is $\pm 0.64^{o}C$ ($\pm 0.46^{o}C$ RMS). Differential measurements are accurate to $\pm 0.06^{o}C$ in magnitude. For values less than $0.56^{o}C$ in magnitude, accuracy is better than $\pm 0.03^{o}C$.

Wire error of $\pm 0.42^{o}C$ is included in absolute temperature. The readout error for the Doric DTI is $\pm 0.19^{o}C$. Reference junction error is $\pm 0.025^{o}C$. The sum of these errors gives $\pm 0.64^{o}C$ ($\pm 0.46^{o}C$ RMS) for absolute temperature measurements. Wire error is not considered in the differential measurements since the junctions were all made from the same batch. The readout error is the accuracy of the Hewlett-Packard voltammeter. The meter's accuracy is $\pm$(2% of range $\pm 0.1\mu v$). For these measurements, the $30\mu v$ and $100\mu v$ ranges were used. The corresponding accuracies are $\pm 0.7\mu v$ and $\pm 2.1\mu v$, respectively. Temperatures are derived by dividing these values by the conversion value of $39.6\mu v/^{o}C$. This gives temperature accuracies of $\pm 0.02^{o}C$ on the $30\mu v$ range and $\pm 0.06^{o}C$ on the $100\mu v$ range.

Test Program

The testing was carried out in a vacuum chamber at vacuum levels better than 10^{-5} torr. Incident radiant energy was provided by a zoned array of quartz IR lamps, which irradiated an intermediate, thin metal shroud which was then the primary test energy source. The test chamber containing the lamp array also incorporates a LN_2 temperature background shroud used as a reference heat sink for the lamp array system.

During temperature measurement system checkout prior to start of the test program, considerable data scatter and absolute temperature level errors were noted. Data and test log review indicated that the problem was related to the LN_2 background shroud cool-down.

A detailed investigation isolated the problem to the chamber penetration consisting of a standard "copper-copper" feedthru which was used in bringing out the lead wires from the window thermocouples, both legs of which were now copper due to the wiring arrangement on the plate for the differential measurements. Investigation revealed that the pins in the feedthru were a nickel alloy similar to constantan and that since the back of the feedthru had a good view of the LN_2 shroud, as the shroud was cooled a temperature differential became established across and through the feedthru. Since copper wires were attached to both sides of the feedthru, different differential thermocouple elements were created at this point in each circuit leg which introduced the scatter noted. Since the constantan leg, which was used for absolute temperature measurement, was routed through a normal constantan pin, the differential in the copper leg caused errors to up to $6^{o}C$ ($10^{o}F$). The solution in this instance was to use a thermocouple grade copper-constantan feedthru, using only the copper pins for the differential thermocouple wires. When this was done, the scatter was eliminated and the absolute temperature level returned to normal.

A vendor search for feedthrus with all pure copper pins has thus far proved negative. Therefore, this problem should be considered any time low level voltage measurements are to be made in a situation where temperature gradients are possible on the feedthrus.

With the resolution of the temperature measurement anomalies, the test program was carried out without further incident and good quality, consistent data was obtained over an extensive program encompassing a range of incident heat flux levels.

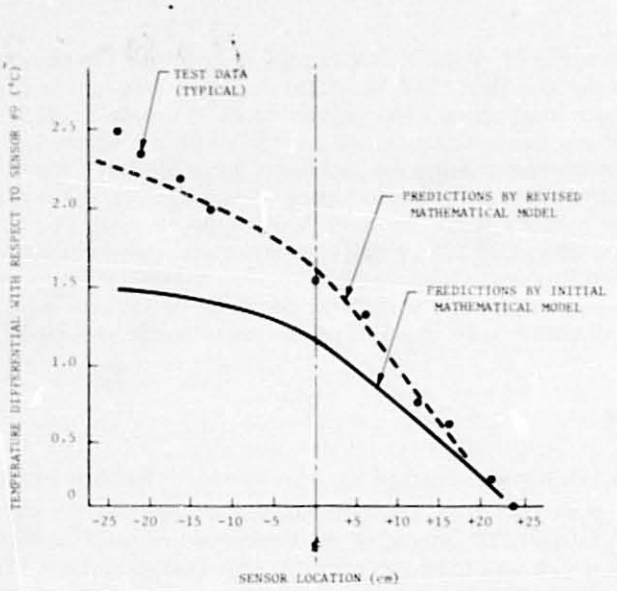

Fig. 10-Summary of test data

The initial predicted temperature response for the window under typical heat flux inputs is shown in Figure 10. When compared to test data, a discrepancy was present. A reevaluation of the mathematical model of the window in its test environment yielded several refinements and modifications in the model, which then provided the expected correlation to verify the model.

Conclusions and Recommendations

Detailed sensor installation analysis, using mathematical modeling, provides effective information on sensor choice, installation effects, test use, and data validity.

Assessment of thermal sensitivity of the total measurement circuit is a must when low level signals in the μv range are being measured. Special care must be given to material compatibility in the case of vacuum chamber feedthrus and associated wiring.

This paper has described a successful test setup using thermocouples to measure temperature gradients in glass with a precision level of $\pm 0.06^{\circ}$C and has highlighted the use of mathematical modeling in the design of sensor installation.

REFERENCES

1. Roeser, W.F., Thermoelectric Thermometry," National Bureau of Standards, NBS Special Publication 300, Vol. 2, pp. 213-232, August 1969.

2. "Manual on The Use of Thermocouples in Temperature Management," American Society for Testing and Materials Publication, STP 470A, pp. 136-154, 1974.

Paper No. 4

DEVELOPMENT OF A FERROMAGNETIC ROTARY VACUUM SEALED SPACECRAFT SPIN FIXTURE

M. B. Levine, *Hughes Aircraft Company, El Segundo, California*

ABSTRACT

The Hughes Aircraft Company Space Simulation Laboratory has conducted a number of successful spacecraft tests on an environmental spin fixture which utilizes a ferrofluidic rotary vacuum seal. The 27cm (10.5 inch) diameter fixture drive shaft supports and spins Hughes Communications Satellites during flight acceptance testing in a thermal vacuum chamber. The drive shaft rotary seal serves to maintain the canned drive system electro-mechanical components at ambient pressure within the space simulator. The ferromagnetic fluid seal was chosen over conventional mechanical sealing devices for its zero-leakage, zero-wear, and minimum friction drag characteristics, as well as its high reliability potential.

INTRODUCTION

A new environmental spin fixture was designed and fabricated by the Hughes Aircraft Company Space Simulation Laboratory for flight acceptance tests of Hughes Communications Satellites. The fixture incorporates a ferromagnetic fluid vacuum shaft seal to sustain an ambient pressure environment within the spin fixture drive housing during thermal vacuum testing in a space chamber. The hermetically sealed drive housing approach was chosen to preclude significant development effort on a non-vacuum compatible direct drive motor and tachometer feedback servo-loop, necessary to meet spin fixture speed stability requirements imposed by spacecraft antenna pointing specifications. The seal is the most critical component in the entire drive housing pressurized system and its low friction drag characteristics help to achieve a fixture speed stability performance level of less than $\pm$.03% speed variation (long and short term).

A description of the spin fixture is provided, along with a summary of seal development problems.

SPACECRAFT DESCRIPTION

The spin fixture was designed to satisfy thermal vacuum acceptance test criteria of two commercial communications satellite programs. Fixture completion was scheduled to support the initial phases of the Intelsat IVA Communications Satellite Program, which consists of a substantial number of flight spacecraft constructed for Intelsat by an international team headed by Hughes Aircraft Company. These spacecraft will be used for global communications coverage. The second program, which started soon after Intelsat, and currently shares fixturing, is the Comstar Program which provides U. S. domestic communications satellite coverage. Both spacecraft families utilize the same basic bus design, with significant differences in their communications systems.

The spacecraft are spin stabilized synchronous orbit vehicles which are maintained on station at the synchronous altitude of 41,300 km (22,300 miles). The basic bus or spinning section contains the solar panel, power distribution, and station keeping propulsion system. The despun electronics section which contains the antenna array and communication equipment is despun by means of a bearing and power transfer assembly (BAPTA) which provides the electro-mechanical interface between the two sections.

FIXTURE DESCRIPTION

The fixture (figures 1 and 5) consists of a drive system module supported by a base frame which transfers the load path to the chamber endbell hardpoints. LN_2 shrouds are incorporated above the fixture base frame to prevent thermal interaction between the spacecraft and the fixture where the fixture structure shadows the chamber or endbell cold walls.

A heat post, which consists of an array of tubular quartz-envelope tungsten filament IR lamps, provides thermal boundary control of the spacecraft rotor. The heat post is oriented parallel to the vertical spin axis at the circumference of the spacecraft and provides an intense thermal energy source which is integrated over the spacecraft as the spacecraft spins past it. A small heat post is mounted under the spacecraft to illuminate the aft thermal barrier.

A spotlight array consisting of a number of quartz-iodide spotlights is mounted above the spacecraft to the chamber hardpoints. This array provides thermal conditioning of the forward sunshield and despun antenna array.

A spoked wheel interface adapter is mounted on the vertically oriented fixture drive shaft to support the spacecraft and provide boundary thermal conditioning at the separation plane. The spoked configuration provides for radiant heat transfer between the spacecraft and the LN_2 cooled fixture shrouds mounted behind the interface adapter. The interface adapter incorporates a shear pin clutch and slip ring cable quick-disconnect. The shear pin clutch provides for a free-wheeling coastdown of the spacecraft in the unlikely event of fixture bearing failure, and the quick-disconnect prevents test cables between the spacecraft and the fixture slipring assembly from wrapping up and damaging the spacecraft in the event the safety clutch is activated.

DRIVE SYSTEM & SHAFT SEAL DESCRIPTION

The concept of a hermetically sealed drive system evolved out of the speed stability requirements imposed by spacecraft antenna pointing criteria. Minimum jitter and wow requirements dictated use of a DC motor and tachometer feedback system (in lieu of an AC motor) with the drive motor mounted directly on the spin fixture drive shaft to preclude instabilities introduced by a coupling or gear train.

Anticipated arcing problems with high power density DC motor brushes in vacuum, indicated the potential for a rigorous development program in this area. As a number of small ferrofluidic seals had been successfully run by the design team, it was decided to enclose the motor/tachometer system and explore the feasibility of developing a large seal for the fixture (structural and dynamic loads as well as geometry constraints required a shaft diameter of approximately 27cm or 10.5 inches) while proceeding with a parallel investigation of conventional mechanical sealing devices. An optimistic response by the ferromagnetic seal manufacturer was evaluated, and design was initiated.

A cross section of the drive system is shown in figure 2. The ferromagnetic seal assembly which consists of upper and lower pole blocks separated by an array of permanent magnets enclosed within a seal housing, is located at the upper surface of the drive system enclosure. Clearance between the pole block I.D. and the drive shaft was held to nominally 0.127mm (.005 inches) radial (.010 inches diametrical) to prevent shaft/seal contact under normal operating conditions while minimizing the ferrofluid gap. This seal gap is a very critical parameter as performance of the seal (ability to maintain zero leakage across a finite pressure differential) is a function of magnetic strength which is inversely proportional to gap width for any specific seal geometry.

The drive shaft is supported by two angular contact roller bearings which are preloaded to provide for differential thermal expansion. The drive motor and tachometer rotors are installed directly on the drive shaft to eliminate speed stability perturbations due to mechanical play in the system.

A slip ring assembly is installed inside the hollow drive shaft to provide the electrical interface between the rotating sections of the spin fixture and spacecraft, and the ground support equipment.

SEAL DIFFERENTIAL PUMPING & DRIVE SYSTEM COOLING

Development testing of the prototype seal assembly indicated an operational performance capability well in excess of 414 kPa (60 psi) differential pressure across the seal, thereby providing a 400% safety margin. However, as the spin fixture delivery schedule precluded adequate development and life testing of the prototype geometry, or cataloging of degradation characteristics of the ferrofluid used, a conservative approach which applied a differential pumping scheme was incorporated into the drive system (figure 3).

The pumping system was designed to provide a dual function:

a. Differentially pump and regulate the seal cavity (between upper and lower pole blocks) to a nominal half-atmosphere.

b. Evacuate the drive housing in the event of a significant leak across the seal.

Guard pumping of the seal cavity to 48 kPa (7 psia) provided additional safety margin by reducing the Δp across each pole block, as well as offering the capability of pumping against any potential nominal real or virtual leak within the seal assembly.

Evacuation of the drive housing would be implemented if a large leak prevented seal cavity vacuum from being maintained by the guard pump. This mode would constitute a test abort condition as it was anticipated that the non-space-qualified motor, tachometer and slip ring components would malfunction fairly rapidly in a vacuum environment, although it was anticipated they would operate during the time required for chamber warmup and abort operations.

A cooling system was provided for circulating filtered ambient air through the drive system, after thermal analysis indicated a potential heating problem if the drive housing were isolated and simply provided with radiation and interface conduction cooling. Air was chosen in lieu of a GN_2 purge to provide the water vapor necessary for motor, tachometer, and slip ring brush lubrication. A centrifugal blower system was

utilized which would maintain a slightly negative pressure within the drive housing for added seal safety, thereby precluding an overpressure potential inherent in a forced air cooling system. Isolation valves and the logic to isolate the housing and shut the blower were provided to allow evacuation of the housing if a large seal leak were to develop. This abort mode logic was initially implemented as an automatic function, however, as confidence in seal reliability increased, the automatic feature was disarmed. Subsequent empirical data obsoleted the need for supplementary cooling, as drive system operating temperatures hardly varied from ambient during either LN_2 cold wall or ambient temperature vacuum test phases, although minimal heating of the drive housing was required during LN_2 cold wall test phases (silicone rubber resistance heater strips bonded to the external surfaces of the housing assembly as shown in figure 6).

SEAL DEVELOPMENT

The ferrofluidic seal is a non-contacting rotary seal which captures magnetic ferrofluid sealant in the gap between the rotary and stationary members. Simple permanent magnets provide the magnetic flux required to retain the fluid which is typically a colloidal suspension of magnetic particles in a low vapor pressure vacuum compatible oil. Figure 4 shows a cross section of the seal assembly, and the details of the geometry of the pole block focussing structure consisting of a series of labrynth type seal stages.

Contact of the shaft and the fragile focussing structure is prevented by stringent runout requirements. However, if large shaft deflections were to occur due to lateral seismic loads, the seal housing would prevent damage to the pole block by laterally restraining the shaft.

An Ester base ferrofluid was originally chosen for its high gauss magnetic saturation capabilities, however, hydrolytic stability characteristics provided the forcing function for a change to a Diester base fluid. Hydroscopic tendencies of the Ester base fluid resulted in an extreme increase of viscosity after the seal had been stored and operated for a period of time in a laboratory ambient environment. Observation of this phenomenon resulted in a series of experiments on the Ester base fluid to determine if the thickening was a result of loss of volatiles due to evaporation, or indeed caused by contact with the water vapor in the air. These experiments proved conclusively that relative humidity and not evaporation was the culprit, with samples exposed to high humidity thickening virtually to the point of solidification.

Subsequent experiments with the Diester base fluid indicated no degradation in either sealing or physical characteristics after significant periods of exposure to high humidity environments,

and the change over to Diester was accomplished post-haste. No observable degradation of viscosity or sealing characteristics has been noted for the Diester exposed to humidity for over a year.

Seal assembly and disassembly procedures are critical due to the high magnetic forces generated by the large complement of permanent magnets and the fragile nature of the pole block focussing structure. A fairly stiff and close tolerance mechanical restraint must be used to maintain concentricity of the shaft to seal interfaces to preclude seal stage damage during assembly operation.

A number of precautionary measures and suggestions are delineated below:

1. Do not expose seal fluids to solvents or lubricants.

2. If seal components or shafts have been in contact with silicone fluids and these fluids have not been completely removed, a slight degradation in sealing potential will occur.

3. Heat in excess of 93°C (200°F) will cause deterioration of the seal fluid.

4. A smooth matte finish is preferred over highly polished or rough surface finishes for the shaft.

5. The stages that comprise the focussing structure are fragile. Extreme caution should be used when assembling the seal so as to not cause damage to these stages.

6. A clean area that is void of ferris particulate matter should be used for assembly and testing.

7. Spare seal fluid should be stored at room temperature in a sealed container preferably away from strong magnetic sources.

8. Field strength of magnets should be established and verified prior to each assembly phase.

9. Seal integrity can be monitored during storage periods by evacuating and isolating the seal cavity and periodically comparing the vacuum gage reading.

10. Ultimate seal pressure capabilities can be empirically determined by cavity pressurization, however, fluid blowout can contaminate equipment unless precautions are taken to contain the effluent.

11. Diester base fluids are superior to Ester base fluids if the fluid surface is exposed to an ambient (relative humidity) environment.

12. Ferrofluid surfaces external to the evacuated cavity can be stored in a dry environment to preclude hydrolytic degradation by bagging with desiccant or a GN_2 purge.

CONCLUSION

The ferrofluidic sealed spin fixture drive has performed successfully during a number of spacecraft thermal vacuum acceptance tests at operational speeds of approximately 60 RPM. Thermal vacuum tests for another program were also successfully conducted at operational speeds of up to 120 RPM with short duration excursions above 300 RPM.

Excellent performance of the fixture drive system relative to speed stability and reliability resulted in a second identical spin fixture drive system being constructed for another program. The only change incorporated in the second system was simplification of the plumbing and controls brought about by deletion of the unnecessary cooling system.

NOTE

This paper is based, in part, on work performed under the sponsorship of the International Telecommunications Satellite Organization (Intelsat). Any views expressed are not necessarily those of Intelsat.

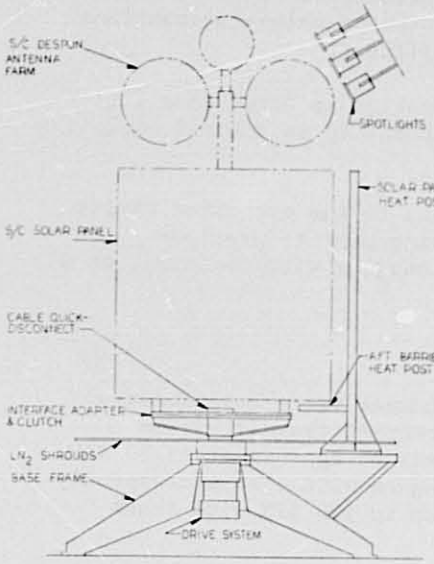

SPIN FIXTURE
FIGURE 1

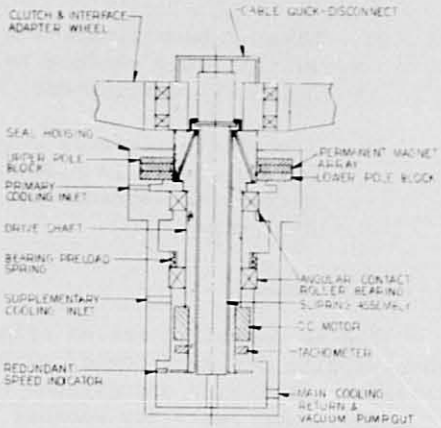

DRIVE SYSTEM
FIGURE 2

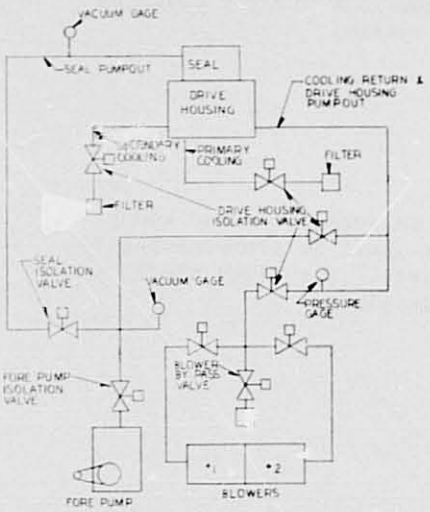

DRIVE SYSTEM VACUUM & COOLING SYSTEM SCHEMATIC
FIGURE 3

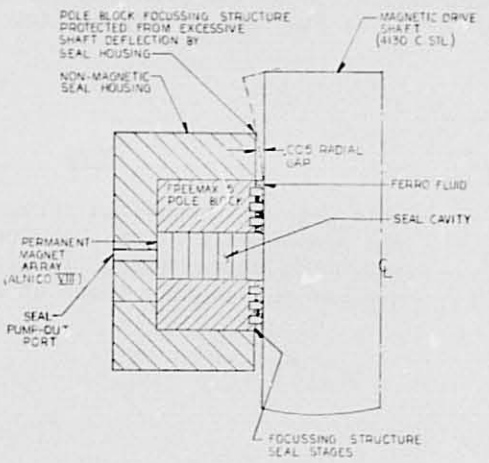

FERROFLUIDIC SEAL INSTALLATION
FIGURE 4

FIG 5.-INTELSAT IV A SPACECRAFT INSTALLED ON THE SPIN FIXTURE

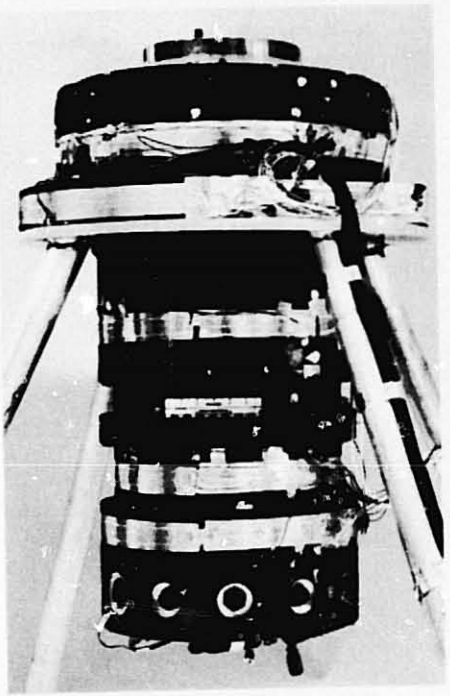

FIG 6.-DRIVE SYSTEM INSTALLED ON A MAINTENANCE STAND

omit

Paper No. 5

SURVIVABILITY TESTING AND ENVIRONMENTAL SIMULATION FOR MATERIALS DEPLOYED AT GEOSYNCHRONOUS ORBIT

V. J. Belanger, A. E. Eagles, *General Electric Company*

ABSTRACT

Synchronous altitude satellites have been observed to exhibit anomalous behavior not noted in sub-synchronous spacecraft. These anomalies have included logic upsets, gradual temperature increases due to degradation of thermal control surfaces, communications, interference and in at least one case, catastrophic power system failure. Studies have been conducted to resolve these anomalies and high correlations were found between anomalous events and high magnetic indices during the hours between midnight and 6 a.m. spacecraft local time.

These correlations indicate the problem is related to some geophysical phenomena that results in electrical discharges in the vicinity of or on spacecraft structural surfaces. It is now generally accepted that this phenomena is the occurrence of a solar magnetic substorm when the spacecraft is in the plasma sheath, a vast region of space extending from the side of the Earth opposite the Sun. This can result in a non-uniform distribution of surface charge on the spacecraft.

In order to study these effects and meet survivability requirements for spacecraft operating in these regions of space, facilities have been developed to simulate the plasma charging environment found at synchronous altitudes. Capabilities and limitations of these facilities are discussed and the effects of basic materials parameters such as surface and bulk resistivity, dielectric constant, dielectric strength, secondary emission and photoemission and the equilibrium state of materials exposed to the environment are also considered. More sophisticated characterizations such as electron bombardment induced conductivity (EBIC) and the related phenomena of secondary emission conductivity (SEC) are also discussed to show how these properties may be used to improve environmental survivability of spacecraft.

Discussions include considerations for the design of future simulation facilities which will improve the reliability of behavior predictions for spacecraft surface materials proposed for application at geo-synchronous orbit.

Paper No. 6

SOLAR PANEL ACCEPTANCE TESTING USING A PULSED SOLAR SIMULATOR

T. L. Hershey, *Project Engineer, Spectrolab (a subsidiary of Hughes Aircraft Co.), Sylmar, California*

ABSTRACT

Utilizing specific parameters as area of an individual cell, number in series and parallel, and established coefficient of current and voltage temperature dependence, a solar array irradiated with one solar constant at AMO and at ambient temperature can be characterized by a current-voltage curve for different intensities, temperatures, and even different configurations. Calibration techniques include: uniformity in area, depth and time, absolute and transfer irradiance standards, dynamic and functional check out procedures. Typical data are given for individual cell (2x2 cm) to complete flat solar array (5x5 feet) with 2660 cells and on cylindrical test items with up to 10,000 cells. The time and energy saving of such testing techniques are emphasized.

1.0 INTRODUCTION

1.1 Purpose of Acceptance Tests

In almost all programs for the fabrication of solar panels or arrays, a final test is desired by the customer prior to delivery. This test can range in complexity from a simple visual examination to a complicated Acceptance Test Plan and Procedure. The purpose of this paper is to discuss a typical program where a visual inspection and electrical performance testing utilizing a pulse solar simulator is included.

1.2 Types of Tests

After the completion of all manufacturing steps in the fabrication of a solar panel, it is then submitted to the Quality Assurance Department for a final visual examination. Prior to this time the panel has undergone production visual inspections and any rework or additional cleaning has already been accomplished. This visual examination, usually under a 10X microscope, may be the final Spectrolab contact with the panel just prior to shipment or it may be the starting point for an exhaustive acceptance test procedure. Table 1 is a typical Acceptance Test Procedure (ATP) test sequence. Items 1 through 5 represent the electrical

ACCEPTANCE LEVEL TES SEQUENCE

1. Visual Inspection
   022186-10

2. Electrical Performance
   022183 Para. 3.8

3. Blocking Diode Reverse Leakage
   022185 Para. 3.9

4. Insulation Resistance
   022185 Para. 3.10

5. Electrical Bonding Test for Shields
   022185 Para 3.12

6. Thermal Cycle Test
   022185 Para. 3.11 8 cycles at +71°C to -141°C

7. Visual Inspection
   022186-10

8. Electrical Performance
   022185 Para. 3.8

9. Blocking Diode Reverse Leakage
   022185 Para. 3.9

10. Insulation Resistance
    022185 Para. 3.10

11. Visual Inspection
    022186-10

12. Electrical Bonding Test for Shields
    022185 Para. 3.12

13. Final Visual Inspection
    022186-10

TABLE I

testing required on this particular type of panel before and after any other environmental testing is accomplished. In some programs there are acoustical, vibration, shock, thermal-vacuum testing, and others in place of the thermal cycle testing required in Step 6 of this example. In such cases where the panel is subjected to the other tests in addition to thermal cycle, the steps 1 through 5 would be repeated between each type of test. Some programs require the interruption of the thermal cycle or thermal vacuum test at specific intervals for the testing of the electrical performance.

Other electrical performance testing is accomplished depending upon the particular electrical configuration of the panel. For example, if there are diodes in the circuit then the protection offered by the diode from leakage and blocking characteristics are measured. If the solar cells are bonded upon an aluminum substrate with a epoxy glass insulation then the isolation of the circuit from the substrate skin is usually a required measurement.

1.3 Theory Of Test

The theory or philosophy of the test is to show that the panel is fabricated in such a manner that under expected operational conditions it will have a high reliability of success for the life of the satellite. In general, all solar panel designs and components have already undergone qualification program and QTP. The acceptance test on each panel is to verify that the individual panel has been manufactured to the required standards to be similar to that of the panel already qualified.

For panels which have physical dimensions giving an area less than a square meter, the handling of the panel presents no major problem and the transporting from one test area to a second and return is not necessarily difficult. But as the size of the panels get much larger the potential for damage from transporting and mounting increases, this also greatly increases the rework and inspection time. The use of a solar simulator which have a larger area of high uniformity and quality corresponding to that of sunlight outside of the earth's sensible atmosphere is difficult to find if a steady state test is contemplated. If, however, a pulse simulator can be used, then the panel is positioned from a point or line source of radiation that during a useable period of time accurately simulates the sun's spectrum and irradiance. The amount of electricity required to operate a pulse simulator versus a steady state simulator is only a small fraction. For a data point every minute; for a pulse simulator this can be a complete IV curve for a panel, circuit or individual cell, the power requirement can be less than 5 kilowatts average with the peak power less than 10 kilowatts. For a steady state solar simulator with an irradiated area of a circle five meters in diameter, the power could be 400 kilowatts just for the lamp system.

A pulse simulator allows the panel to be tested at ambient temperature only. Because of this it is necessary to know the relationship of the electrical output of the solar panels as a function of temperature. The coefficient of current change and voltage change with temperature is known and is inputed into the computer and the IV curve of the desired temperature can be plotted directly by the computer. More is said about this later.

2.0 EQUIPMENT DESCRIPTION

2.1 Solar Simulator

The large area pulsed solar simulator system consists of two major subsystems, the pulse illuminator system and the data acquisition and processing system. Its major components consist of a Pulse Forming Network Assembly and an Illuminator Assembly. Within the PFN assembly is a high voltage power supply and a sophisticated charge sensing device, which determines the exact point at which the energy in the PFN should be discharged. The Illuminator Assembly, or lamp housing, contains the two Xenon flash lamps and the lamp igniter, as well as any auxiliary optics necessary to meet the desired performance levels.

The other major subsystem of this simulator is the data acquisition and processing system. This system synchronized with the operation of the pulsed simulator measures panel I-V performance characteristics, performs an analog to digital conversion on all data, stores the digital information, provides mathematical corrections and prints out uncorrected and/or corrected panel I-V characteristics. Major components of this system include a standard cell, an electronic load, digital data processing equipment, and a digital X-Y plotter. See Figure 1.

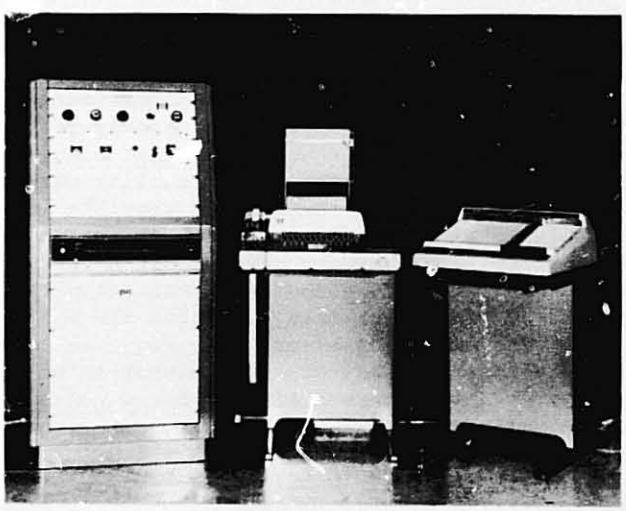

FIGURE 1

2.1.1 Illuminator Assembly

Two FX-47C-6.5 xenon pulse flash tubes are utilized in the illuminator system. They are positioned at the rear of a large light baffle. The primary purpose of this light baffle is to block unused radiation emitted from the flash lamp for personnel protection. The side panel of this baffle assembly is easily removable to provide direct access to the flash lamps.

The illuminator uses 2 E.G. and G. Model No. FX-47C-6.5 xenon lamps connected in series. When pulsed at approximately 2900 A, two of these lamps produce one solar constant over a 17 ft. diameter test plane. In the spectral region between 4000 Å and 10,000 Å, the deviation of the total simulator irradiance from the NRL Johnson curve is typically less than 3%. At 9000 Å, the deviation is greater due to the presence of the xenon emission band. However, in the pulsed mode low pressure xenon lamps radiate much less spectral energy in this region than the steady state high pressure xenon tubes. By increasing lamp current, the spectral curve can be shifted down in the red region and up in the ultra-violet, or vice versa. This flexibility allows a close match to the AMO spectrum without optical filtering. See Figure 2.

2.1.2 Pulse Forming Network Assembly

The pulse forming network is packaged separately. The PFN assembly contains a specially designed high voltage power supply and a charge sense circuit.

The PFN is an 8 mesh delay line especially tailored to match the lamps and produce a light pulse of controlled shape. Eight 240 microfarad capacitors rated at 5 KV are used. A special inductor (wound of #2 AWG solid wire) was designed for this system, which makes it capable of providing a pulse shape that is nearly flat for 1.0 millisecond, the period in which the I-V curve is generated.

The D.C. Power Supply is designed to charge the eight 240 microfarad capacitors in the PFN to 5000 VDC in less than 20 seconds. It consists of a current limited high voltage transformer, a full wave diode bridge and an abort circuit. In the event that either the interlock loop is broken during the PFN charging sequence, or the charge voltage exceeds a predetermined maximum value, the stored energy is dumped harmlessly through the action of a vacuum switch into two 250 ohm, 250 watt resistors in the PFN assembly.

The high voltage transformer has a maximum output short circuit of 1.8 amperes which eliminates the need for a current limiting resistor in the charging loop. Initially about 40 amperes are

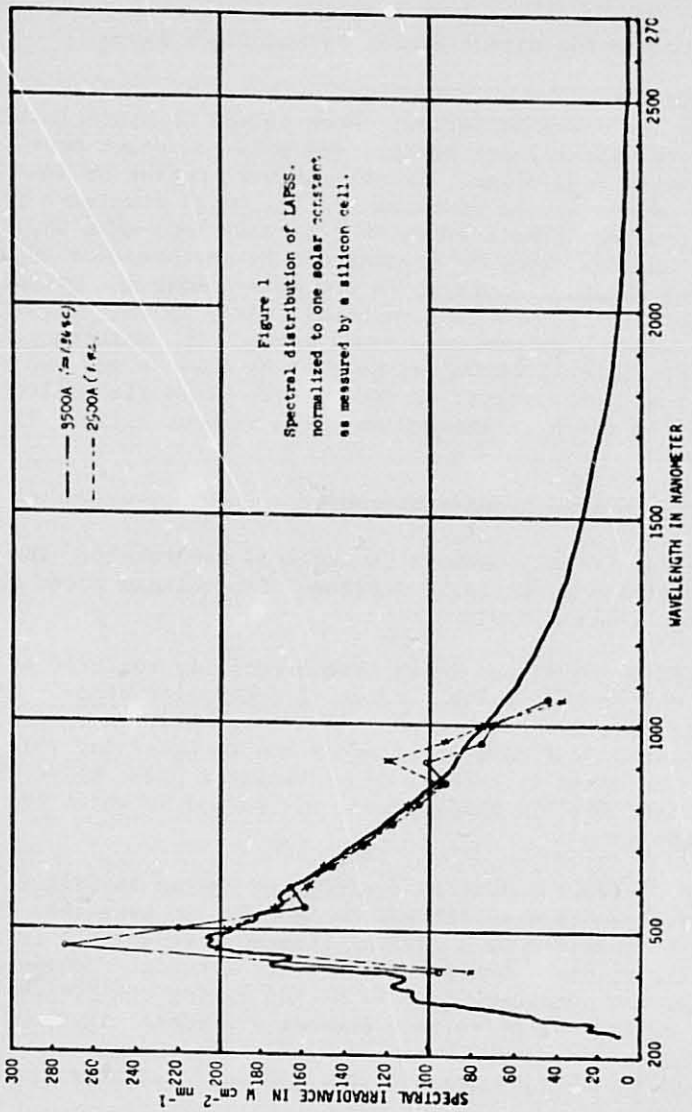

FIGURE 2
SPECTRAL IRRADIANCE VS WAVELENGTH

drawn from a 200 volt single phase AC source at the start of the charge cycle, decreasing rapidly as the voltage rises.

2.1.3 Electronic Load

Solar panel loading during the light pulse from the illuminator is accomplished by the electronic load. The circuitry is similar to a high speed voltage regulated power supply. The solar panel under test represents a load on the power supply and a source of load voltage. As the power supply voltage is varied from zero to full scale value, the I-V characteristic of the solar panel is swept from short circuit current to open circuit voltage. As this occurs, both panel current and panel voltage are monitored.

2.1.4 Data Acquisition and Processing System

After initial system start-up, the solar simulator system is operated from the teletypewriter located at the test console. Test conditions, system constants, raw data, and corrected data are printed out on the test console teletypewriter. The digital plotter can be commanded to plot the corrected I-V curves for visual interpretation.

The computer provides high speed storage as the data is taken and provides the corrections for temperature and light intensity required for all panel tests. In addition, the program provides the timing signals necessary to coordinate system operation and performs a validity check on all incoming data. The program is user oriented, requiring simple commands, e.g. SET (to change parameters such as ambient temperature or standard cell sensitivity) and RUN (to initiate a light pulse).

The keyboard is a standard teletype model 33 teletypewriter. It provides communication with the computer at a rate of 10 characters per second and provides a written record of all tests performed. The program is loaded through the teletype tape reader. Data may be recorded on punched tape as well as printed copy.

The plotter is a Hewlett Packard Model 7200A. Coupled to the teletype, it is activated by commands from the computer and can draw a curve up to 11 x 17 inches with a resolution of 10,000 divisions on each scale.

The system is operated from the Test Console, Figure 1. Initial set-up requires controls located on the front panel of the electronic load. Subsequent operation is controlled entirely via commands typed into the computer.

2.1.5 Control Unit Controls and Indicators

Manually operated controls need be set only once for a given panel type. The voltage and current range switches are set to the lowest (value) compatible with the panel. The Pulse Network Voltage controls the pulse intensity. Once set to produce one solar constant AMO, it need be adjusted only rarely as the lamps age. The Sweep Duration switch allows selection of an optimum number of data points defining the panel curve (the sampling rate being fixed). The Interlock display shows the status of the safety interlock circuit which protects all cabinets having high voltage; depressing the display resets.

As a safety measure, the energy storage capacitor will charge only at the initiation of test sequence. It is not automatically recharged on completion of sequence, eliminating a major potential safety hazard.

2.1.6 Data Reduction

The following system constants must be introduced into the processor memory along with the raw test data so that the necessary mathematical manipulations can be accomplished to correct the data:

1. Electronic load voltage range.
2. Electronic load current range.
3. Ambient test temperature.
4. Selected correction temperature.
5. Current temperature coefficients.
6. Voltage temperature coefficients.
7. Cell area.
8. Number of cells in series.
9. Number of cells in parallel.
10. Calibration constants and zero levels for each of the three data channels.

The ranges are automatically read off the panel controls; the remainder are entered into the program's parameter table as described earlier.

2.2 Solar Panel Description

The solar panel phusical geometry and composition vary from one program to the next. Some panels are only small developmental ones that have only a few solar cells present. Others will have up to 10,000 cells. In many cases the panel will have a curved surface which the solar cells are bonded upon. Figure 3 is an example of 2 cells in parallel and connected 81 in series with a control tap at the 48th cell. Here the cells were mounted upon a

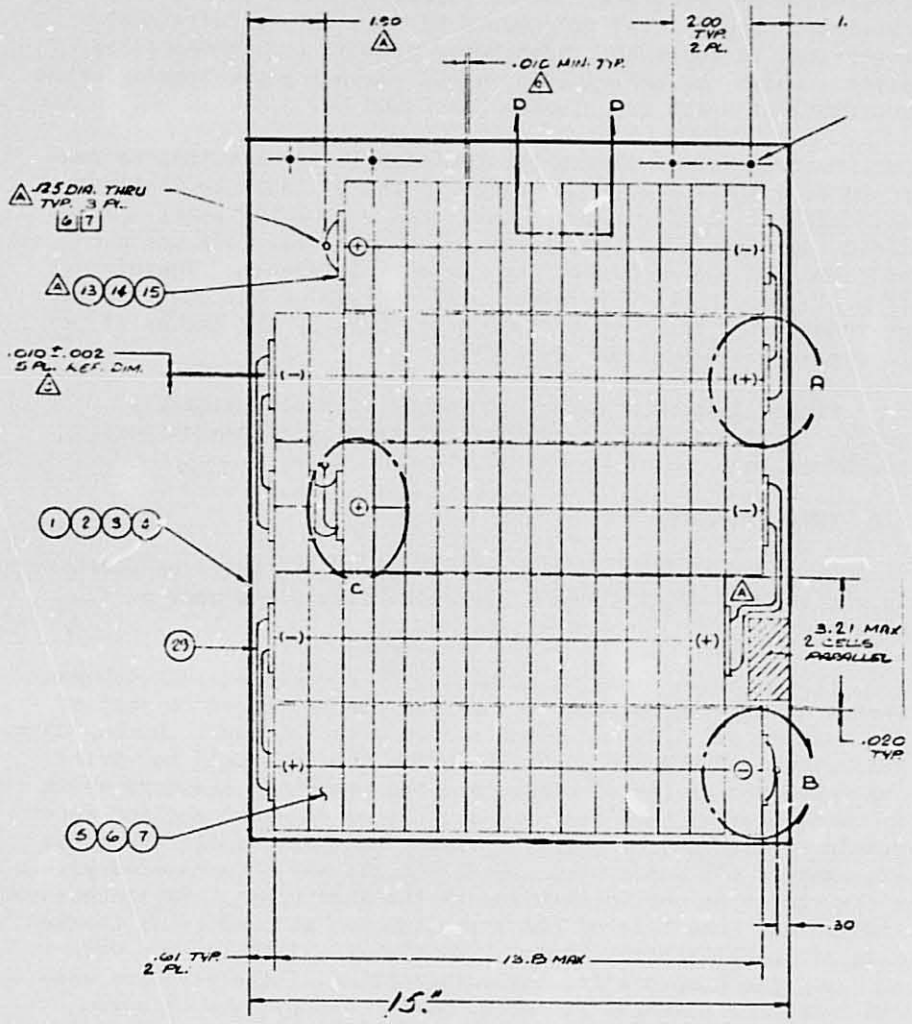

FIGURE 3

TYPICAL SMALL DEVELOPMENT SOLAR PANEL

curved surface with an epoxy-glass insulation beneath the cells. In some programs the cells are mounted on a continuous cylindrical surface. Cylinders up to 7 feet in diameter have been covered with solar cells.

On flat panels the geometrical arrangement of the cells is controlled by cutouts and other forbidden areas dictated by the customer. The general rule would be to localize individual electrical circuits in a particular area or in a geometrical pattern which may optimize potential shadowing problems or other restrictions which are mission generated.

On cylindrical panels the individual circuits must be confined to a particular small angle of the cylinder to minimize the output falloff caused by the curvature of the panel. For a first approximateion the electrical output will fall off proportional to the cosine of the angle of incidence. Therefore, if a single circuit covers up to 10 degrees of the angle of the cylinder, then the output could be reduced by the cosine of 10 degrees or approximately 1.5%.

Figure 4 shows a large flat panel with approximately cells. Figure 5 shows a cylindrical panel with approximately 10,000 cells.

3.0 TEST PROCEDURE

The electrical performance testing of the panel or circuits is not started until three basic calibrations are made on the simulator.

First the calibration simulator is checked against a known standard cell that has an output that can be traced to that of a standard cell flown on a balloon at high altitude. During this calibration of the simulator, both the standard cell to verify the operation of the simulator and the reference standard which is used in every test run, are mounted on the same cooling water supply. This assures that the test conditions of the standards are exactly the same. The standard cells are both mounted within a few inches of one another and in the same plane. The technician insures that the face of the standards are perpendicular to the axis of the simulator. Table 2 is the actual table used when entering the computer for the verification of the standard when the reference standard is serial number #1006. The IV curve that is generated from the running of the standard is then compared to the value specified for that standard. Only if it is within acceptable limits is the calibration of the simulator continued.

Second, the area of the simulators output beam that is going to be used in the actual test being conducted is mapped to determine the lack of uniformity in the test plane or test volume.

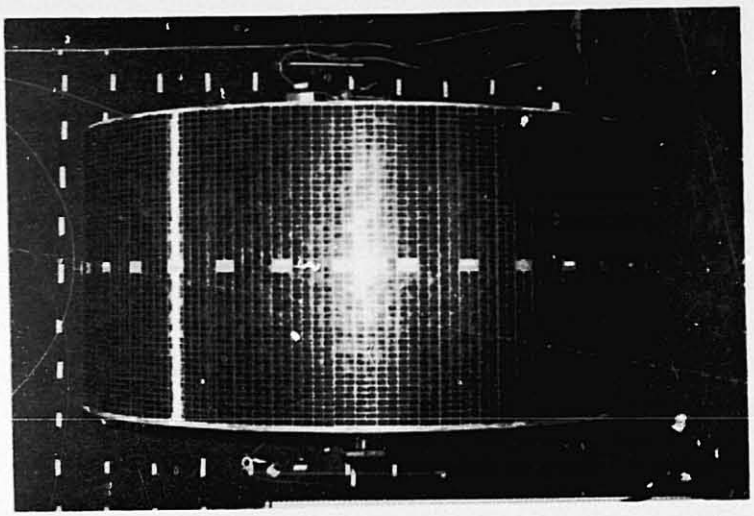

FIGURE 5

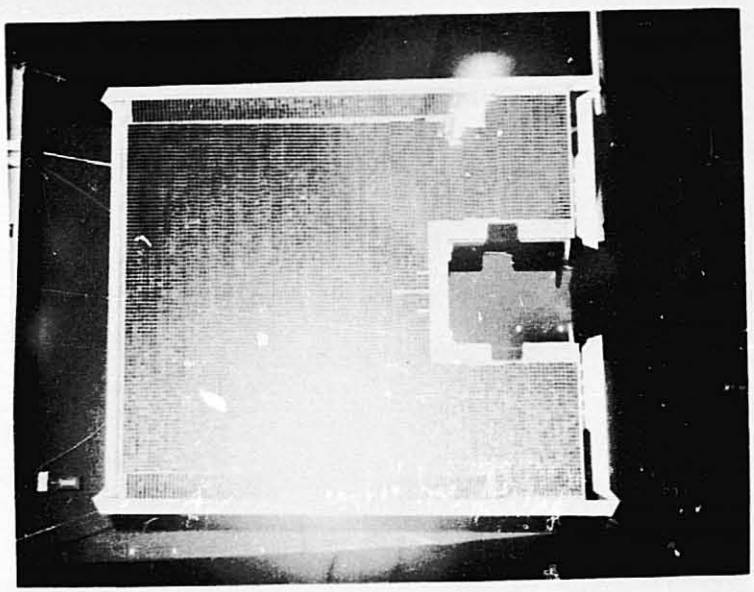

FIGURE 4

PARAMETER TABLE

1	Cell Area	+00190 Sq. Millimeters
2	Cells Parallel	+00001 Cells
3	Cells Series	+00001 Cells
4	Ambient Temp	+00028 Degrees C
5	Standard Temp	+00025 Degrees C
6	I Temp Corr	+00025 Microamps/Sq Cm/Deg C
7	V Temp Corr	-02150 Microvolts/Deg C/Cell
8	AMO Cal Current	+00660 Tenths of Milliamps
9	Sample Count	+00150 Samples
10	Output Count	+00065 Output Values
11	Stand Cell FS I	+01000 Tenths of Milliamps
*12	Stand Cell FS	+01004 A/D Counts
*13	Voltage FS	+01004 A/D Counts
*14	Current FS	+01004 A/D Counts
*15	Stand Cell Zero	+00020 A/D Counts
*16	Voltage Zero	+00019 A/D Counts
*17	Current Zero	+00020 A/D Counts

* Most recent calibration values are to be used if they differ from those specified.

TABLE 2

The size of the panel under test partially determines the total number of test points taken. For large area solar panels a test point usually is taken at one foot intervals or less. The irradiance should not vary by more than 2% over the total test area and the nominal value should be within 2% of the reference standard. Again this is a go/no type test. Figure 6 illustrates a non-uniformity map.

Finally, a dynamic calibration procedure is used to verify that the computer softward does not have some inherent problem caused by an inadvertant change to the program. Here a solar panel with a known output is irradiated by the simulator and the temperature parameters are varied to cause the IV curve to show the temperature dependence under three different conditions. If this and the above two tests are satisfactorily completed, then a solar panel can be tested.

Mounting the panel in the test area, which is a completely blackened room with black drapes and no reflective surfaces, is dependent upon the geometry of the solar panel. Small panels which can be easily supported by either a table, covered with black felt, or supported by wires in the test area. However, the larger panels as shown in Figures 5 and 6 are supported on their own handling fixtures, as in the case of completed cylinders or hemi-cylinders, or from special overhead support hardpoints.

The surface temperature of the solar panel is monitored with thermal sensors taped to the front side of the panel and a digital readout is used with an accuracy of 0.1 degree centigrade. Here the panel is allowed to come to thermal equilibrium with the ambient temperature of the room. The time required to accomplish this depends upon the thermal mass of the solar panel involved. The temperature is monitored until this is reached.

4.0 ELECTRICAL PERFORMANCE

4.1 Types of Output

The standard output of the simulator is an IV curve which starts at the short circuit current and continues until the open circuit voltage is reached. A typical panel has been tested on the pulse simulator to illustrate the typical output. A panel was tested which had four cells in parallel and five cells in series. The panel was fabricated from 2 cm by 2 cm solar cells. The effective surface area was 3.80 square centimeters. Table 3 shows the actual parameters used in the particular test. Note that the panel temperature was at 22 degrees centigrade while the output curve was plotted at 28 degrees centigrade. In Figure 7 the IV curve is drawn for the 22 degree as well as the 28 degree centigrade. This is included to show the effect of the temperature difference. At the particular setting of the table, only

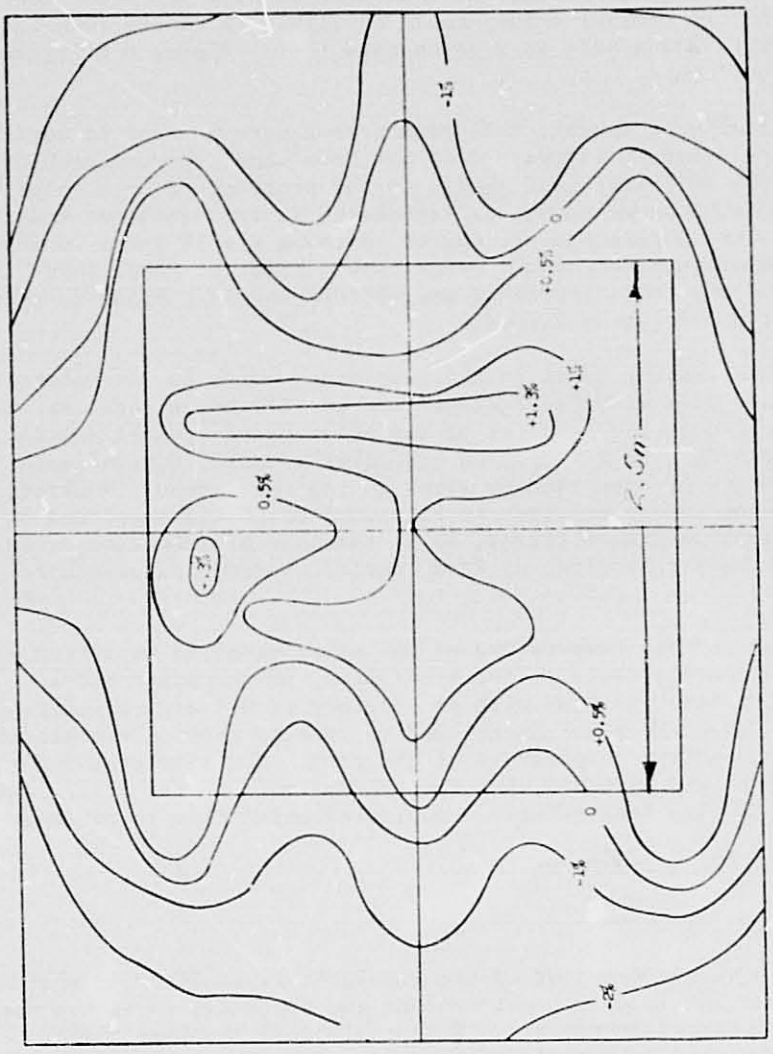

FIGURE 6

MAP OF NON-UNIFORMITY

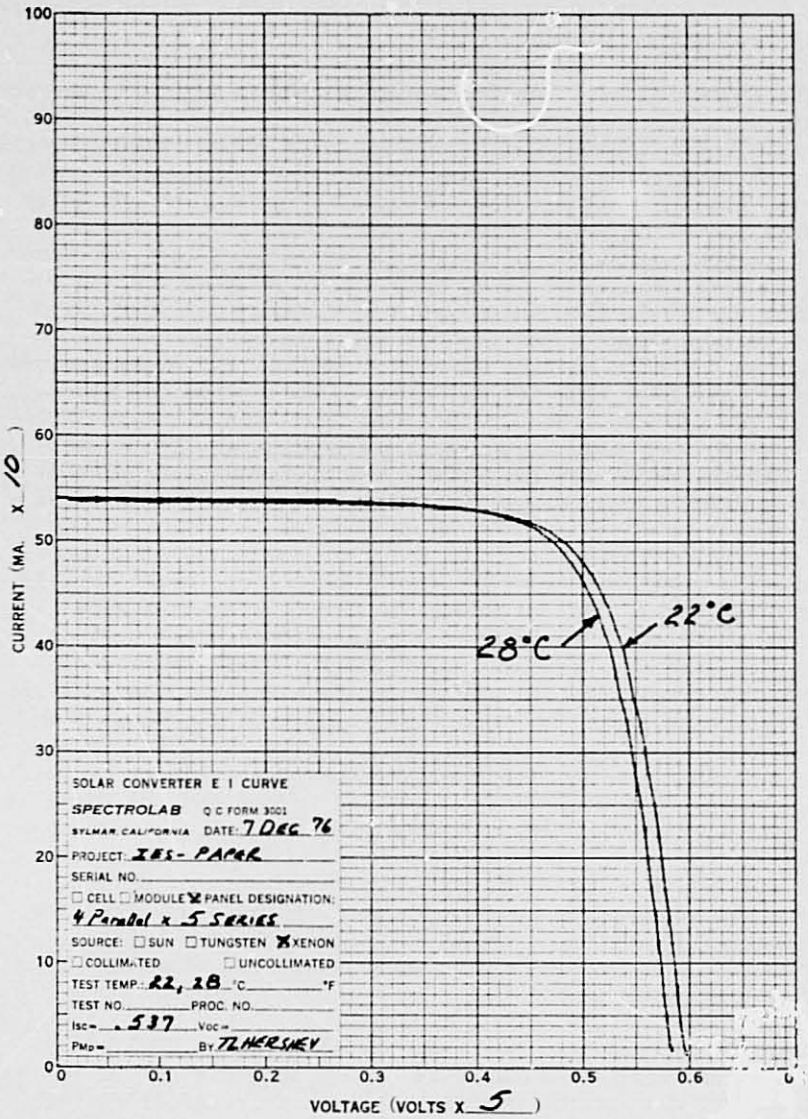

FIGURE 7

SOLAR PANEL IV CURVE

65 data points were requested to be plotted, therefore, the curve did not completely reach the open circuit voltage point. The actual data for each of the points can be printed on the teletype terminal as well as plotted.

The above IV curve was for a simple panel with only one circuit and no additional complications, however, there are panels which have curved surfaces and multicircuits which require special electrical connections. For example, if there are four circuits on a flat panel then the total output of the panel can be given including the diode drop associated with the diodes. Further, if each of the individual circuits (it is assumed they are connected in parallel, which is normal) are to be measured and excluding the diode then there again is little complication. However, most customers desire that the total panel and the individual circuits be plotted and the effect of the diode included. Here the individual circuits are shorted out inside the diode (i.e. on the circuit side of the diode) and then the circuit under test is then tested with only its shorting wire removed. Except for the diode leakage (which has been measured by other test procedure) then the desired individual circuit with diode can be measured.

Another complication arises when the circuit under test is on a curved surface and the curvature causes a considerable variation in depth of field of the pulse simulator as well as the angular effect. Here an analytical technique is used to evaluate the combination of the two effects and a reduced output specification is given for those special circuits. Where complete or hemi-cylindrical arrays are involved, only portions of the cylinder are tested at a time and then the cylinder is rotated. Usually one circuit at a time is tested and the panel or array is analytically summed to determine the output under space conditions. However, where the number of cells in any one projected area element varies greatly due to outputs or circuit irregularities, then the total area is irradiated and then the cylinder rotated through a small angle and repeated until a measure of the output variation can be estimated (knowing it is only an approximation).

Two other techniques are used which are worth mentioning. First, if the output of a panel is needed in the negative voltage region in addition to the positive then it is possible to back bias the array or panel by the use of batteries and pulse the simulator in the usual manner. The general output of the panel can be determined even though the exact voltage may be indeterminant due to the high speed of the data collection on the varying output of the batteries. In general the requirement for extrapolating the short circuit current back in the negative region is defined in such a way that this is acceptable. Secondly, if the panel develops a problem while undergoing test or just a low power problem then an individual circuit can be probed (care

being taken not to shadow the cell or cells under test). If a cell or submodule has a crack or other nonvisible problem many times it can be located with a relative small amount of time in trouble-shooting. Usually the total IV curve is not required in the trouble shooting mode once the general area of the panel has been isolated and then only the short circuit current is required to find the low cell. By masking techniques it is possible to locate which cell in a parallel group of cells in a submoudle is low.

4.2 Parameter Variation

As shown in Table 3 the ambient and standard temperatures can be specified as part of the data input. Here, if the room temperature is 22 degrees centigrade, that should be entered into the computer. However, any temperature can be specified as the standard temperature, i.e., the temperature desired for the output of the data. (The actual temperature of the standard solar cell is controlled by the water bath at 28 degrees centigrade unless changed for some other reason.) The value in the table for the item 8 AMO CAL CURRENT is the short circuit current of a particulat standard cell (S/N 1006) at 28 degrees centigrade.

TABLE 3

1	Cell area	+00380 sq millimeters
2	Cells parallel	+00004 cells
3	Cells series	+00005 cells
4	Ambient temp	+00022 degrees C
5	Standard temp	+00028 degrees C
6	I Temp corr	+00025 microamps/sq cm
7	V Temp corr	-02150 microvolts/deg c/cell
8	AMO cal current	+00660 tenths of milliamps
9	Sample count	+00150 samples
10	Output count	+00065 output values
11	Stand cell FS I	+01000 tenths of milliamps
12	Stand cell FS	+01020 A/D coun
13	Voltage FS	+01020 A/D coun
14	Current FS	+01015 A/D coun
15	Stand cell zero	+00003 A/D coun
16	Voltage zero	+00008 A/D coun
17	Current zero	+00008 A/D coun

Figure 8 illustrates the temperature dependence of the small panel discussed above with 4 cells in parallel and 4 submodules in series. These cells are nominally 2 cm by 2 cm. The items 6 and 7 in the parameter table are the coefficient of temperature dependence of the current and voltage. The voltage dependence in general, over a limited temperature region, is the value in the table. For a specific type of cell and large

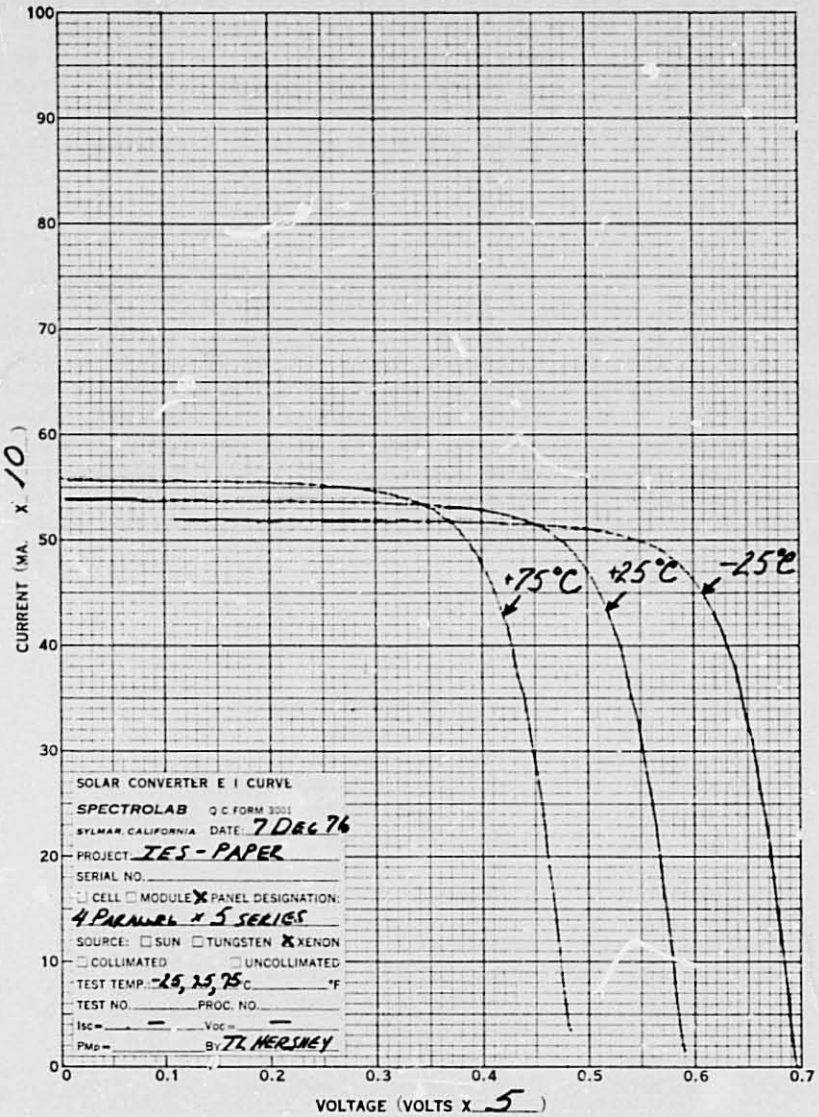

FIGURE 8

IV CURVE SHOWING TEMPERATURE DEPENDENCE

temperature region the actual value should be determined experimentally. The current correction term is area dependent, therefore the item 1 of the table is used to correct for the area of an individual cell. Here again the specific value for a cell should be determined experimentally. In Figure 8 the temperatures were 75, 25 and -25 degrees centigrade. They were used to illustrate the technique only.

Some applications of the simulator require that the irradiance level be varied from an Air Mass Zero (essentially outer-space irradiance with no atmospheric attenuation) to some other value. Figure 9 illustrates the difference in the above panel at 25 degrees centigrade and at two irradiance levels, approximately Air Mass Zero and Air Mass One (AM1 is nominally the irradiance at Sea Level under a given set of conditions).

5.0 SUMMARY

This paper describes a system used in the acceptance testing of large area solar panels or arrays where close spectral match and high uniformity of irradiance is required. The versatility of irradiance, temperature variation have been included. The total amount of electrical energy as well as the operator and technician time required make this a system very attractive for present day use.

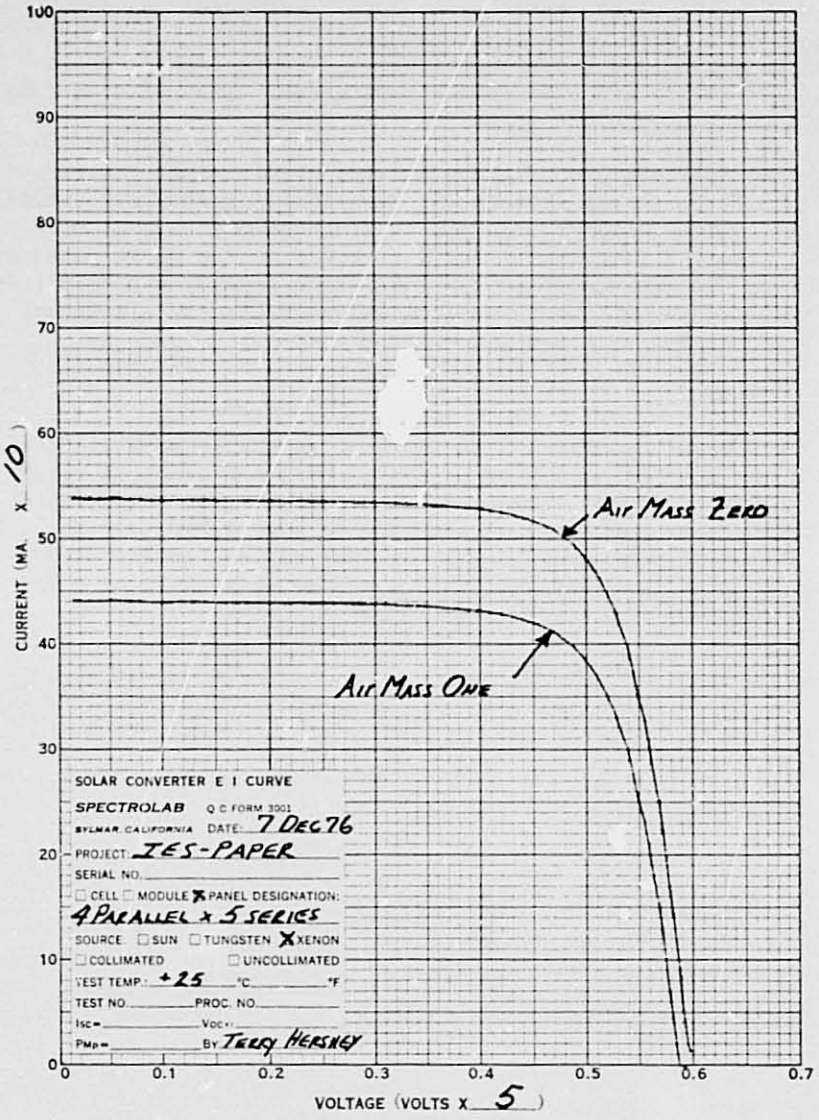

FIGURE 9

IV CURVE SHOWING IRRADIANCE DEPENDENCE

Paper No. 7

LABORATORY FACILITY FOR STUDYING LASER DAMAGE OF SATELLITE MATERIALS

R. J. Schmitt, T. E. Bonham and P. D. Bear, *McDonnell Aircraft Company, St. Louis, Missouri*

ABSTRACT

The development of high energy lasers (HELS) has progressed to the point that the vulnerability of materials to such laser irradiation requires investigation. The heating process due to these lasers causes temporary or permanent thermal effects that can change the thermo-optical properties of irradiated samples. Hence, there has arisen a need to develop and test new materials and components that are not vulnerable to HEL irradiation. This paper describes a laboratory facility designed to permit testing the response of materials to high energy laser radiation.

The HEL testing described in the paper requires uniform irradiance of the test specimen and a means for varying the irradiance in a controlled manner. As the laser beam typically is highly nonuniform, a method is described for producing a uniform intensity beam from an initially nonuniform beam.

A Sylvania model 941 CO_2 electric discharge laser is the laser source for these tests. Intended for use primarily in industrial welding applications, this laser has been designed for reliable operation at relatively high power with little regard to mode purity. The paper describes a tapered parallelepiped beam integrator of square cross-section into which the incident beam is imaged by a zinc selenide lens. Multiple reflections from the highly polished interior walls of the copper integrator cause an overlapping of the input spatial pattern to produce an output beam with nearly uniform cross-sectional intensity. The output is imaged by a series of gold-plated mirrors onto the sample. Beam uniformity of ±10% peak-to-average is readily achieved.

The time variance of the intensity is obtained by controlling the laser discharge current with a programmable microprocessor. Operating open-loop from a real-time power meter, the microprocessor adjusts the laser power to agree point-by-point with pre-programmed levels.

There is a great variety of material types currently requiring vulnerability testing, but a relatively few property measurements can be used to provide nearly complete thermophysical characterization. These properties are temperature, emittance, solar absorptance, far infrared reflectance and transmittance, and material outgassing. The laser exposure is performed while the materials are in a vacuum environment since this duplicates orbital conditions. Moreover, the measurement of properties by which material response is determined is also performed in-situ. This approach satisfies the concern that exposing materials to the air after testing may induce changes in properties that would not occur otherwise. Stable operation of equipment is a prime requirement of this approach because the elapsed time between

pre-test and post-test measurements can be several hours or longer. On the other hand, absolute measurements are not required since changes in properties provide a sufficient characterization. The achievement of these goals is discussed in detail.

The design of the vacuum chamber used in this testing is also discussed. Basically, the chamber is a system with ports around the circumference at two levels. The upper level ports are designed for interfacing the optical measurement apparatus, while the lower level ports are for the laser exposure station, pressure monitoring instrumentation, electrical passthrus, and spares.

Specimen for laser exposure and optical measurement are attached to retaining rings, which in turn are mated to a flat, octagonal carousel. The retaining rings have been designed to permit secure mounting of the samples while maintaining thermal isolation of the sample from the mount. The carousel is mated to a hub that slides on a shaft for vertical motion between the upper and lower levels. The shaft can be rotated to position any sample in any direction. Both rotation and translation are controlled externally by double o-ring sealed arms that pass through a flange at the bottom center of the chamber.

D4

N79-19017

Paper No. 8

COMPUTER ASSISTED THERMAL-VACUUM TESTING

Ward Petrie and George Mikk, *Senior Engineers at the Perkin-Elmer Corporation, Optical Technology Division, 100 Wooster Heights Road, Danbury, Connecticut 06810*

ABSTRACT

In testing complex systems and components under dynamic thermal-vacuum environments, it is desirable to optimize the environment control sequence in order to reduce test duration and cost. Additionally, it is necessary to maintain cognizance of critical trends during the test in order to assure safety of the equipment. This paper describes an approach where a computer is utilized as part of the test control operation in order to achieve these aims. Real time test data is made available to the computer through a time-sharing terminal at appropriate time intervals. A mathematical model of the test article and environmental control equipment is then operated on using the real time data to yield current thermal status, temperature analysis, trend prediction and recommended thermal control setting changes to arrive at the required thermal condition. The program logic flow is developed in relation to facility equipment capabilities, the need to keep a person in the control loop, and the need for real time update of program constants in order to provide successful application on first use. The data acquisition interface and the time-sharing hook-up to an IBM-370 computer is described along with a typical control program and data demonstrating its use.

INTRODUCTION

The objective of thermal-vacuum testing is to expose systems and their components to representative thermal and vacuum environments in order to verify design performance, reliability and proper manufacturing. Typically, this is done by placing the system in a vacuum chamber, outfitted with heat sinks and heat sources. A thermal balance is obtained, controlling the system to the desired temperature levels and distribution defined by predetermined criteria. Test monitoring involves select data reduction, temperature averages of specific areas of the test article, and a visual history of the test progress by plotting of selected temperatures.

Although practical and workable, this type of approach results in variations from test to test and operator to operator. The approach does not provide any firm basis for trend prediction and relies on the operator to accurately anticipate and respond to temperature changes as they occur. Therefore, a method of real time test data analysis and trend prediction was devised to optimize the environmental control sequence and to assure

proper safety of the equipment. The method is based on utilization of a computer and a mathematical thermal model of the test article as a decision tool in controlling the test.

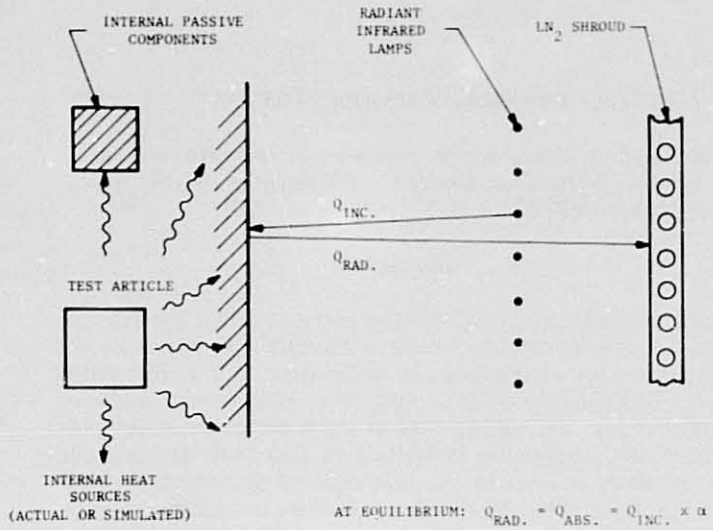

Fig. 1-Typical test setup

A typical test setup is shown schematically in Figure 1. The test is primarily controlled by controlling the incident heat flux on the test article surface from zoned arrays of infrared lamps. The flux level is set to establish a heat balance between energy absorbed by the surface from the lamps and that radiated by the surface to the cold sink, normally a liquid nitrogen cooled shroud, to yield and maintain a predetermined test article surface temperature. Additional heat control zones are employed to simulate internal heat sources and to control other thermal interfaces, such as test mounts and other specialized areas where lamp heat input is not practical.

Typically, servo controls are used to control lamp and heater power supplies, and real time temperature and alarming indicators provide first order test performance information and safety control.

This paper will first discuss the approach for utilizing the computer in the test control process. The program logic flow will then be developed. Finally, sample programs will be discussed for specific test setups to demonstrate the program approach.

DISCUSSION

In order to integrate the computer into the test control loop, it is necessary to first develop an approach which will make this practical and reliable. Among the parameters to consider, the most important are the methods of interfacing to the computer, the data reduction necessary, and a thermal model and its use of the reduced data, including trend analysis/prediction. An additional consideration is the requirement to maintain the capability to revert to simple, operator-based evaluation and control methods in case of computer problems, emergencies such as power failures, or obvious failures of the actual test to respond as predicted by modeling.

Making data available to the computer entails taking data generated by the data system and converting it to a form which is compatible with the computer. Generally, this will require that the data be recorded on some intermediate medium, such as punched paper tape or magnetic tape, since thermal data loggers are generally too slow to input directly to the computer. This will be especially true if the computer is a time-sharing system rather than a dedicated device. The subsequent discussions will be based on interfacing to a time-sharing system.

The introduction of an intermediate data storage medium will, however, make the system near-real time rather than real time in that data would be processed in "batches" at discrete intervals rather than continuously. Thus, the frequency of need to look at temperature progression during the test will dictate the quantity of data points that must be handled for each evaluation and will thus influence the design of the thermal model to be employed.

To be really effective in utilizing the computer, the thermal model should be as simple as possible. This is desirable so that the run time is reasonable. As will be developed later on, the use of the thermal model may require its solution for more than one case in carrying out the trend analysis/prediction. Nevertheless, while simplicity is desirable, it must not be achieved at the expense of maintaining a reasonable degree of faithfulness to the true thermal response of the system. Experience in thermal-vacuum testing indicates that even highly complex test articles can be modeled using simple models of less than 10 nodes. In some cases, thermal modeling may be adequately accomplished by simply utilizing the data in a temperature map, the temperature map itself being the thermal model.

Once a thermal model has been decided on, the information that it generates will dictate how it might be used in analyzing trends and providing predictions. Models that permit computation of temperature changes can realistically provide a basis for predicting where temperatures are likely to go for given boundary conditions. By varying the boundary conditions, it is possible to determine what changes should be made in these boundary conditions for optimum thermal control. In this case, the program can be made truly predictive, providing the operator with a recommendation for changing the environment and showing where the current trends will lead.

If the model is simply a temperature map, then the visual display can be utilized by the operator to evaluate his current status. In conjunction with the maps generated from earlier data, it is possible for the operator to see current trends and deduce where these trends will lead. More reliance is placed on the operator's judgment in this instance, but sufficient data is supplied in a timely fashion to permit him to intelligently make these assessments.

In order to implement the test performance calculations by means of the thermal model, a set of programs for the computer are prepared. These programs are generally grouped into two categories: i.e., the executive program and the performance calculation program. These programs are normally resident in the computer memory during the period that they are needed for test use.

The executive program controls the computer operation. It performs such functions as identifying the storage locations for the input and output data. It also organizes various output data in temporary storage,

making it available in proper sequence to future needs of the program, either for this run or subsequent runs of the program. It will also specify the order of execution of the performance programs. The actual form of this program is determined by the particular operating system used by the computer.

The performance program or programs (often, more than one performance program is executed) would normally be written in a language such as FORTRAN. The thermal model, whether it be the temperature map or true mathematical model, is executed in these programs. Trend data is generated using the model, and if predictions, including instructions to the operator, are to be made, this program is the one which would generate them.

These programs must be prepared so as to provide the operator with the required information in a timely manner. They must further be conceived in such a manner that the operator remains personally aware of what is happening from point to point so that in an emergency, a return to pure operator data evaluation and control action can occur immediately, or in less severe cases, the operator will intervene when it becomes obviously necessary to ignore computer-generated recommendations.

A very definite additional benefit of employing the computer in test control operations in this manner is in the area of test data handling, storage, and future use. Since all data, calculations, and control recommendations can be stored on a medium such as magnetic tape, additional post-test analysis and evaluation can be carried out easily because the data is already available in a form suitable for ready recall and further analysis.

To illustrate an actual implementation of computer use as described above, representative test programs are described.

Illustrative Examples of Representative Test Programs

To demonstrate the use of the computer during a test program, two specific examples will be considered. The first case uses a simple mathematical model to compute changes for given changes in the boundary conditions, i.e., the controlling environment, while the second case uses the temperature map as its thermal model. These examples will demonstrate the range of sophistication that can be achieved using the computer.

Mathematical/Thermal Model in Test Control--To demonstrate the successful use of the simple mathematical model with the computer, a test program involving a test article/test environment control system shown schematically in Figure 2 will be discussed. The objective of this test program is to change the mean temperature of the test article from a start temperature of $+70^{\circ}F$ ($21.1^{\circ}C$) to a stabilized test temperature of approximately $+90^{\circ}F$ ($32.2^{\circ}C$). To carry out such a test efficiently and cost effectively, it must be accomplished in a minimum amount of time.

The thermal model of the test article is simply three nodes coupled to the environment as shown schematically in Figure 2. The three nodes represent key internal elements of the test article, and it will be the stability of these elements that will determine the final stability of the test article. This is a uniform temperature condition that is to be achieved and, therefore, the environmental control surfaces will all be set to the same uniform temperature levels.

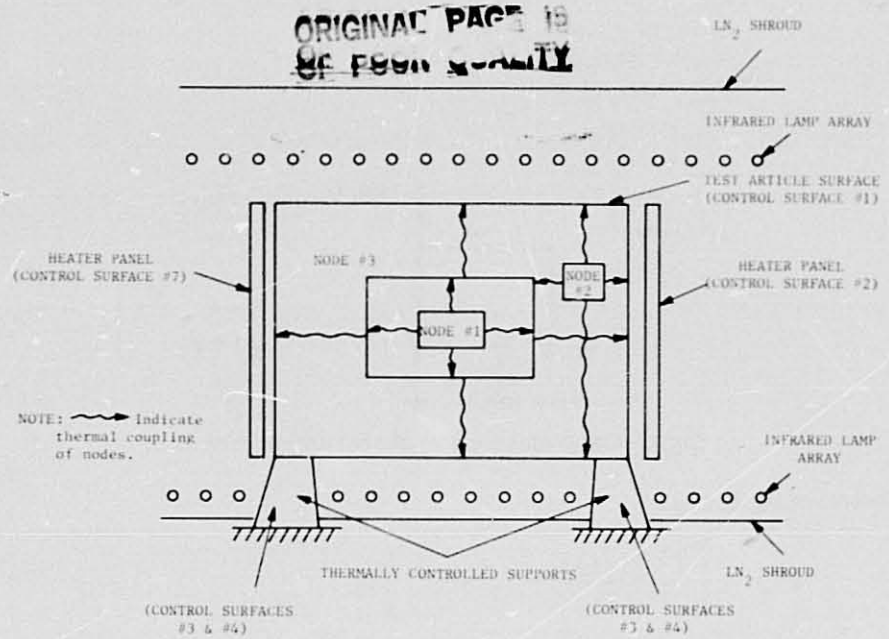

Fig. 2-Mathematical model test setup

Figure 3 shows the electrical analog for this model. The equations covering this model are:

$$m_1 Cp_1 \frac{dT_1}{dt} = \varepsilon\sigma A_1 F_{1-3} (T_3^4 - T_1^4) \quad (1)$$

$$m_2 Cp_2 \frac{dT_2}{dt} = \varepsilon\sigma A_2 F_{2-CS} (T_{CS}^4 - T_2^4) + \varepsilon\sigma A_2 F_{2-3} (T_3^4 - T_2^4) \quad (2)$$

$$m_3 Cp_3 \frac{dT_3}{dt} = \varepsilon\sigma A_3 F_{3-CS} (T_{CS}^4 - T_3^4) + \varepsilon\sigma A_1 F_{1-3} (T_1^4 - T_3^4) + \varepsilon\sigma A_2 F_{2-3} (T_2^4 - T_3^4) \quad (3)$$

where:

m	=	mass of node
Cp	=	specific heat
T	=	temperature
ε	=	emissivity
σ	=	Stefan-Boltzmann Constant
A	=	area
F	=	view factor
dt	=	time increment
dT	=	temperature increment

$R_{1-3} = 1/\varepsilon\sigma A_1 F_{1-3}$

$R_{2-3} = 1/\varepsilon\sigma A_2 F_{2-3}$

$R_{3-CS} = 1/\varepsilon\sigma A_3 F_{3-CS}$

$R_{2-CS} = 1/\varepsilon\sigma A_2 F_{2-CS}$

$C_1 = mCp_1$

$C_2 = mCp_2$

$C_3 = mCp_3$

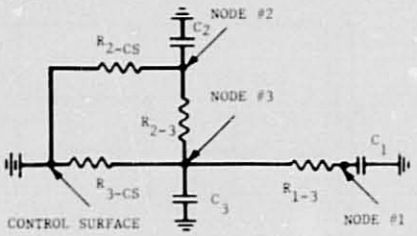

Fig. 3-Electrical analog of thermal model

Rearranging gives:

$$dT_1 = \left[\frac{\varepsilon\sigma A_1 F_{1-3}}{m_1 Cp_1} (T_3^4 - T_1^4) \right] dt \quad (4)$$

$$dT_2 = \left[\frac{\varepsilon\sigma A_2 F_{2-CS}}{m_2 Cp_2} (T_{CS}^4 - T_2^4) + \frac{\varepsilon\sigma A_2 F_{2-3}}{m_2 Cp_2} (T_3^4 - T_2^4) \right] dt \quad (5)$$

$$dT_3 = \left[\frac{\varepsilon\sigma A_3 F_{3-CS}}{m_3 Cp_3} (T_{CS}^4 - T_3^4) + \frac{\varepsilon\sigma A_1 F_{1-3}}{m_3 CP_3} (T_1^4 - T_3^4) + \frac{\varepsilon\sigma A_2 F_{2-3}}{m_3 Cp_3} (T_2^4 - T_3^4) \right] dt \quad (6)$$

This set of equations can now be solved for change in temperature by substituting in present values for the temperatures on the right-hand side. By making the time increments small enough, good approximations can be obtained for this change in temperature. By adding the temperature to the current value, the new temperature for the given time increment is obtained. As a result, predicted temperature-time plots can be generated.

The key to making this model work is to obtain the correct values for the heat transfer coefficients. If there is sufficient knowledge of the test article, these coefficients may be calculated beforehand. However, the simplification involved in this modeling usually will preclude this. Instead, the model will have to generate its own corrections to these coefficients early in the test, based on the temperature history to that point.

Having now obtained the appropriate thermal model, the programs may now be developed. The control program consists of the executive program and the averaging and trend/prediction programs it executes. Figure 4 shows the logic flow of the executive programs for the two samples.

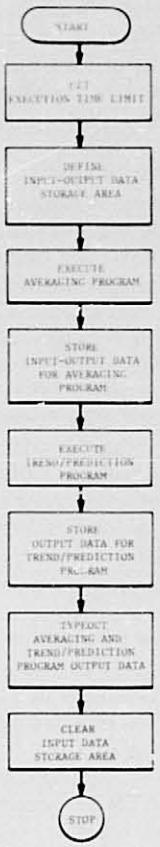

Fig. 4-Executive program logic flow

They are structured so that the data locations for use by the FORTRAN programs are defined prior to execution of the programs. After the data averaging program is run, the input and output data are stored for later transfer to magnetic tape. The trend/prediction program is run and its data is similarly stored. Interspersed throughout the program are a number of data file manipulations which cause the data to be arranged in the proper sequence in data files which will be accessed by subsequent execution of the control program. Note that return of the output data to the terminal is commanded by the executive program.

The data logger which generates the data used in the working programs is a Leeds and Northrup digital data system. It has a capacity for handling 576 channels of data in 24 banks of 24 points each. Individual banks can be selected for readout so that only those banks with the necessary data need be scanned. The data logger records its output on punched paper tape in ASCII code which is compatible with the computer terminal interface. The format of the output data on the paper tape was specially tailored so that it would be compatible with the time-sharing system. This included the use of appropriate character sequences to terminate data

records and the avoidance of characters which would cause unwanted reactions from the computer, e.g., characters such as "@" and "null character" are given special interpretations by the computer and cause unwanted responses from the system ("@" causes erasure of the previous character, and the "null character" causes the computer to ignore all remaining input on the record).

The punched paper tape produced by the data logger is then read into the computer via a time-sharing terminal. In this instance, the terminal was an RCA Teletype with a paper tape reader. This terminal gives a printout of the input data as it is read into the computer.

Additionally, the terminal serves the all-important function as the communications link with the computer. The commands which initiate data input and program execution are given via the terminal keyboard and the program output data is returned via the terminal printout.

The computer system is an IBM 370-158 with a Memorex 1270 time-sharing interface unit. The IBM 370 operating system is the VM/370 CMS. Each user is assigned disk storage on the system. User programs and data files reside on the disk storage. Since this disk storage is limited, permanent data storage is accomplished by transferring all desired data from temporary storage on the disk to permanent storage on magnetic tape. The temporary storage areas can then be reused for new data.

The VM/370 CMS operating system provides the means for program writing, compiling and execution, data file creation and manipulation, and the basic elements for executive programming. In addition, all other aspects of the time-sharing operation are handled via this operating system.

The program input data is shown in Figure 5. This data is input to the computer prior to running the control program. It contains all the temperature data required by the programs. It is loaded into the computer utilizing the input mode of VM/370 CMS operating system. Once it is stored into its assigned location, the FORTRAN program will then be able to access it when the control program is executed.

The program output data is shown in Figure 6. The first grouping of data consists of the temperature averages of the specified control areas and the critical areas of the test article. The next grouping includes the computer-generated instructions for the operator and a prediction of the temperature trends for the next eight hours (assuming that the instructions are followed).

The slope computations use the results of the previous three hours. The sloping is based on a straight line approximation for the curve connecting the data points.

The instructions are based on the execution of the thermal model for values of the environment which are in the range of $\pm 5^{\circ}F$ ($\pm 2.8^{\circ}C$) on either side of the current setting in $0.5^{\circ}F$ ($0.28^{\circ}C$) increments. A weighting system is applied to evaluating the results of holding each of the environmental values for eight hours and scoring its effects on proper trend and the ability of the setting to achieve stability. The environmental setting with the best score is then selected as the proper setting to be given in the instructions to the operator. It is assumed that a uniform environment is the ideal and that all the control areas should be set to the same temperature level. This process is repeated for a total of eight hours with the exception that after the first hour, no further inputs are made to the instructions. This results in the eight hour prediction.

```
THERMAL TEST DATA

TEST CODE  100000

TIME:  237:11:00


01 01  +6.006 V   01 02  +6.933 V   01 03  +7.049 V   01 04  +6.812 V
01 05  +7.045 V   01 06  +6.819 V   01 07  +7.107 V   01 08  +6.930 V
01 09  +6.728 V   01 10  +1.398 V   01 11  +7.604 V   01 12  +5.373 V
01 13  +5.521 V   01 14  +5.376 V   01 15  +5.507 V   01 16  +6.869 V
01 17  +6.727 V   01 18  +6.928 V   01 19  +7.099 V   01 20  +5.117 V
01 21  +5.126 V   01 22  +0.011 V   01 23  +5.006 V   01 24  +6.009 V

02 01  +6.781 V   02 02  +6.853 V   02 03  +6.142 V   02 04  +6.573 V
02 05  +6.739 V   02 06  +6.824 V   02 07  +6.847 V   02 08  +6.769 V
02 09  +6.706 V   02 10  +6.316 V   02 11  +6.930 V   02 12  +6.821 V
02 13  -0.001 V   02 14  -0.002 V   02 15  -0.002 V   02 16  -0.001 V
02 17  +5.378 V   02 18  +5.374 V   02 19  +5.502 V   02 20  +5.520 V
02 21  -3.706 V   02 22  -3.706 V   02 23  -3.706 V   02 24  -3.705 V

08 01 T+239.1 C   08 02 T+239.1 C   08 03 T+239.1 C   08 04 T+239.1 C
08 05 T+239.1 C   08 06 T+239.1 C   08 07 T+239.1 C   08 08 T+239.1 C
08 09 T+239.1 C   08 10 T+239.1 C   08 11 T+239.1 C   08 12 T+239.1 C
08 13  +021.8 C   08 14  +022.3 C   08 15  +019.3 C   08 16  +020.4 C
08 17  +018.2 C   08 18  +016.3 C   08 19  +017.5 C   08 20  +017.0 C
08 21  +017.4 C   08 22  +018.5 C   08 23  +017.5 C   08 24  +019.3 C

09 01  +019.3 C   09 02  +019.3 C   09 03  +019.1 C   09 04 T-016.4 C
09 05  +042.5 C   09 06  +038.4 C   09 07  +020.4 C   09 08  +021.4 C
09 09 T+082.6 C   09 10  +021.4 C   09 11  +026.4 C   09 12  +026.1 C
09 13 T+022.6 C   09 14  +026.9 C   09 15  +026.8 C   09 16  +024.4 C
09 17  +024.4 C   09 18  -000.3 C   09 19 T+046.3 C   09 20  -052.0 C
09 21  +020.5 C   09 22  +000.0 C   09 23  +000.3 C   09 24  +000.3 C

10 01  +021.2 C   10 02  +021.5 C   10 03  +021.1 C   10 04  +021.2 C
10 05  +021.0 C   10 06  +021.2 C   10 07  +020.2 C   10 08  +021.3 C
10 09  +021.4 C   10 10  +021.7 C   10 11  +021.1 C   10 12 T+018.4 C
10 13  +021.3 C   10 14  +021.4 C   10 15  +020.7 C   10 16 T-265.9 C
10 17  +020.3 C   10 18  +020.8 C   10 19  +020.1 C   10 20  +021.3 C
10 21  +021.6 C   10 22  +021.4 C   10 23  +020.9 C   10 24 T+007.8 C

11 01  +021.0 C   11 02  +021.4 C   11 03  +021.1 C   11 04  +020.8 C
11 05  +019.0 C   11 06  +021.3 C   11 07  +020.7 C   11 08  +022.6 C
11 09  +022.7 C   11 10  +023.0 C   11 11  +021.6 C   11 12 T+074.9 C
11 13  +023.6 C   11 14  +023.1 C   11 15  +020.6 C   11 16  +017.6 C
11 17  +013.1 C   11 18  +013.3 C   11 19  +014.2 C   11 20  +018.4 C
11 21  +020.3 C   11 22  +024.1 C   11 23  +024.0 C   11 24  +012.3 C

12 01  +023.1 C   12 02  +019.2 C   12 03  +021.1 C   12 04  +019.3 C
12 05  +020.4 C   12 06  +021.3 C   12 07  +026.1 C   12 08  +016.7 C
12 09  +019.0 C   12 10  +024.6 C   12 11  +021.1 C   12 12  +018.2 C
12 13  +018.5 C   12 14  +021.3 C   12 15  +018.5 C   12 16  +024.1 C
12 17 T+007.1 C   12 18 T+070.6 C   12 19  +018.0 C   12 20  +017.9 C
12 21  +011.3 C   12 22 T-013.8 C   12 23  +017.9 C   12 24  +017.7 C

END OF SCAN

13:33:12 >
```

Fig. 5-Program input data

```
VM/CMS

09:04:00 >tdata
EXECUTION:
IHC002I STOP   1265
EXECUTION:
IHC002I STOP   1265

TEST CODE 10000
TIME: 237:11:00
NODE 1            = 21.1C
NODE 2            = 21.1C
NODE 3            = 20.9C
CONTROL SURFACE 1= 21.4C  HIGH= 23.0C  LOW= 19.0C
CONTROL SURFACE 2= 19.4C  HIGH= 22.3C  LOW= 16.3C
CONTROL SURFACE 3= 20.7C
CONTROL SURFACE 4= 21.1C
CONTROL SURFACE 5= 20.7C
CONTROL SURFACE 6= 20.6
CONTROL SURFACE 7= 22  .3  HIGH= 22.8C  LOW= 21.2C
RJS ARE IN SPEC.


 NODE 1 SLOPE=   0.5 C/24 HRS
 NODE 2 SLOPE=   0.2 C/24 HRS
 NODE 3 SLOPE=   0.2 C/24 HRS
 INSTRUCTIONS:
 CHANGE CONTROL SURFACE 1 -0.3C TO 21.2C
 CHANGE CONTROL SURFACE 2  1.8C TO 21.2C
 CHANGE CONTROL SURFACE 3  0.5C TO 21.2C
 CHANGE CONTROL SURFACE 4  0.1C TO 21.2C
 CHANGE CONTROL SURFACE 5  0.4C TO 21.2C
 CHANGE CONTROL SURFACE 6  0.6C TO 21.2C
 CHANGE CONTROL SURFACE 7 -0.9C TO 21.2C
 PREDICTIONS:
 TEMP F  HR          1     2     3     4     5     6     7     8
 NODE 1            21.1  21.1  21.1  21.1  21.1  21.1  21.1  21.1
 NODE 2            21.1  21.1  21.1  21.1  21.1  21.1  21.1  21.1
 NODE 3            21.0  21.0  21.0  21.0  21.0  21.1  21.1  21.1
 CONTROL SURFACE   21.2  21.2  21.2  21.2  21.2  21.2  21.2  21.2

QUERY DISK
A (191): 120 FILES; 680 REC IN USE, 912 LEFT (of 1592), 43% FULL (6 CYL)
, 3330, R/W
CONWAIT
LOG
CON=  .185H  VIRT=    3.318  CP=   2.56S   ACCESS:  D/T=   581 UR =  101
LOGOFF AT 09:05:09 EST FRIDAY 10/15/76
```

Fig. 6-Mathematical model program data output

To illustrate the effectiveness of this thermal model in practice, consider the test objective which is to change the mean temperature of the test article from +70°F to +90°F (21.1°C to 32.2°C). Figure 7 shows the temperature history for the test. Note that the technique used is to overtemperature the environment by 20°F (11°C) to accelerate the transition. An undercooling of the environment is then used to accelerate the stabilization at 90°F (32.2°C). The transition and stabilization can be accomplished in less than half the time it would ordinarily take if the desired test level, +90°F (32.2°C) were merely set into the environment and the test article was allowed to coast into stability at the new level with only this driving force.

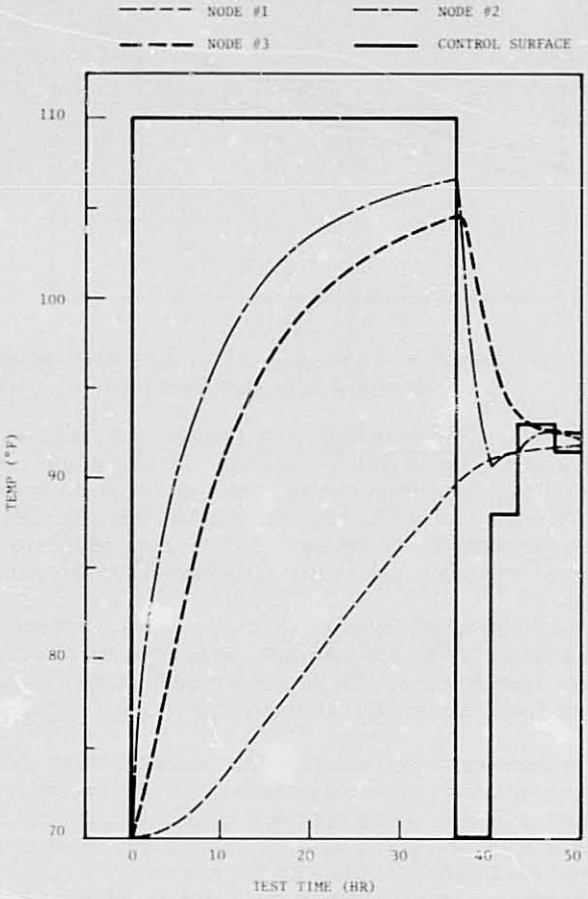

Fig. 7-Temperature history for +70°F to +90°F test

Figure 8 shows comparison of the actual temperature trends early in the transition to that predicted. The agreement here is poor. Correction of the heat transfer coefficients by the program yields a predicted curve that now closely tracks the actual data. With an accurate prediction, the computer can now give accurate instructions to the operator as the transition and stabilization progress.

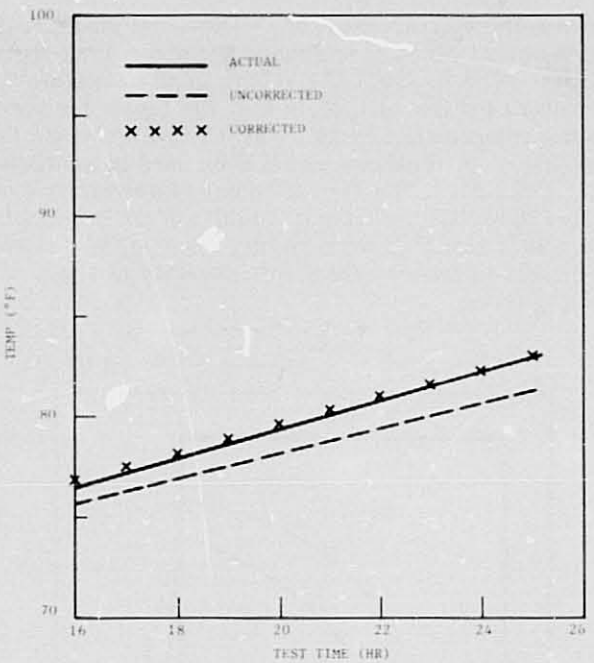

Fig. 8-Comparison of predicted temperature using corrected and uncorrected heat transfer coefficients

Temperature Map as a Thermal Model--A temperature map as a thermal model for computerized test control was successfully employed in the cryogenic testing of a beryllium mirror. The test program is described in detail in Reference 1. Briefly, the objective of this test was to test a beryllium mirror at various temperature levels from 300°K to 150°K in vacuum. Thermal and optical data was obtained after stabilization at the specified levels.

Thermal control of the beryllium mirror was achieved by surrounding the mirror with an 80°K, LN_2 shroud and using a matrix of heater wires to buck the heat transfer from the mirror to the shroud. The heater matrix was divided into five individually controlled zones. See Figure 9 for the test setup.

The temperature map used for the thermal model was based on mapping all the available temperature data from the mirror itself. In instrumenting the mirror, sensor placement was selected so that as complete a map as possible would be given with a reasonable number of sensors. Figure 10 shows the sensor locations on the mirror.

The program output is shown in Figure 11. The first grouping of data is the temperature map. This is followed by the temperature averages of critical areas of the beryllium mirror and of the controlling environment. The final grouping gives the scope of critical areas of the mirror.

Review of this output data allows the operator to see the test progress and to readily evaluate the trends. By comparing the current results with those from previous hours, it is possible to make intelligent evaluation of the current environmental settings and decide on the necessary changes. Also, the slope data gives a ready means for tracking stability.

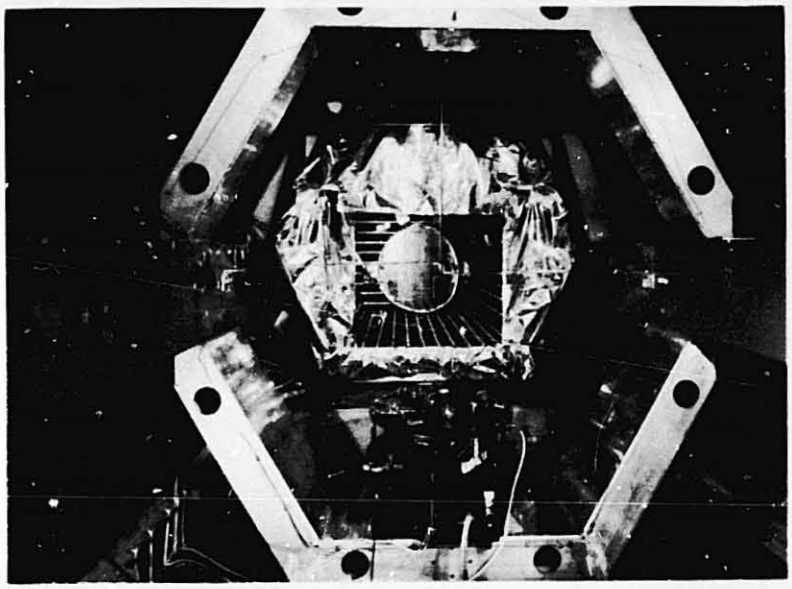

Fig. 9-Beryllium mirror test setup

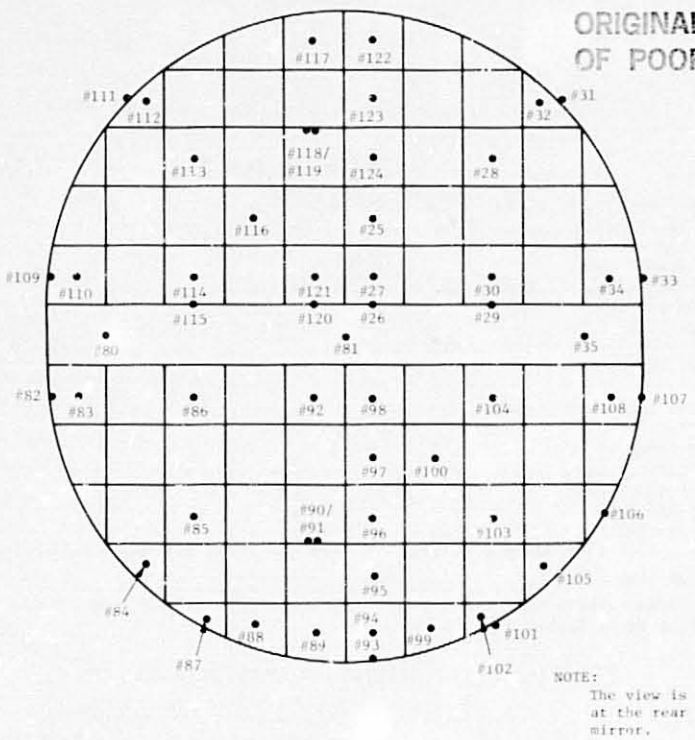

Fig. 10-Thermocouple locations flat beryllium mirror

```
08:38:09 LOAD LDATA (XEQ)
EXECUTION:
TYPE IN CHAMBER PRESSURE
>4.8E-03,
TIME:207:12:87

                                -78.0 -76.8

          -76.8                  -77.1                -77.1

                   -76.7         -78.0        -77.9

                            -78.4 -77.3

 -76.5             -77.0        -76.6 -77.2        -77.7        -76.3

      -76.6                      -76.3              1001.0

 -77.7             -79.0        -77.1 -77.2        -78.7        -76.8

                                 1001.0 -76.6

                   -77.7         -76.8        -77.8

          -77.5                  -79.8                -77.9

                   -76.9                              -77.0
                        -79.4  -77.01001.0 -78.3
MIRROR AVE= -77.5C  HIGH= -76.3C  LOW= 79.8C
TUBE AVE  = -77.2C
VERT GRAD =   1.7C
HORIZ GRAD=   0.8C
SHROUD AVE=-184.8C  INLET=-182.6C  OUTLET=-184.9C
CHAMBER PRESSURE= 0.480E-02
IHC002I STOP  1265
 !!! E(01265) !!!
TYPE IN TEST HOUR
>37
08:40:59 LOAD LDATA1 (XEQ)
EXECUTION:
MIRROR SLOPE= 3.0C
TUBE SLOPE  = 3.0C
IHC002I STOP  1265
 !!! E(01265) !!!
08:41:26 STAT
P (191): 43 FILES; 306 REC IN USE, 486 LEFT (OF 792), 39% FULL (3 CYL).
08:41:26 >LOG
CON=  .176H  VIRT=  .99S  CP=  1.62S  ACCESS:  D/T=  309 UR=   0
LOGOFF AT 08:41:45 EDT SATURDAY 07/26/75
```

Fig. 11-Program output for beryllium mirror

SUMMARY

This paper has described a practical approach which can bring the computer into the thermal-vacuum test control loop, resulting in savings of both time and cost for running such a test. In addition, the use of the computer will tend to reduce variations in the efficient execution of a test from operator to operator and the errors which can accompany this type of testing.

For the future, improvements and expansion of capabilities is possible. This approach can be made even more efficient with an improvement in the computer interface by utilizing magnetic tape and a high speed video terminal in place of the punched paper tape and slower teletype.

The current uses of the computer discussed do not begin to fully utilize the capabilities of the computer. For example, time plots of the type shown in Figure 7 could be routinely generated as part of the data reduction, adding to the operator's bank of data for tracking the progress of the test.

Although not necessary in every application, data reduction and analysis for design purposes is often needed. Usually, this is done after the fact with these necessary results normally appearing days or even weeks after the test is completed. However, by integrating these data reduction and analysis requirements into the test control programs, the complete test results can be available as the test is completed.

The integration of the computer into the thermal-vacuum test control loop is practical and desirable. A significant improvement in the quality of testing has resulted for the applications discussed above and the future will see even greater improvements in the test quality.

REFERENCES

1. Mikk, G., "Cryogenic Testing of a Beryllium Mirror", presented at the SPIE Proceeding, August 1975.

D5

N79-19018

Paper No. 9

OUTER PLANETS PROBE TESTING*

J. A. Smittkamp and M. G. Grote, *McDonnell Douglas Astronautics Company, P.O. Box 516, St. Louis, Missouri 63166*
T. M. Edwards, *NASA, Ames Research Center, Moffett Field, California 94035*

ABSTRACT

An atmospheric entry Probe is being developed by NASA Ames Research Center (ARC) to conduct in situ scientific investigations of the outer planets' atmospheres. A full scale engineering Model of an MDAC-E Probe configuration, designed under NASA Contract NAS 2-7328, was fabricated by NASA ARC. Proof-of-concept test validation of the structural and thermal design is being obtained at NASA ARC. The Model has been successfully tested for shock and dynamic loading and is currently in thermal vacuum testing. It will be subjected to static testing during January 1977.

1.0 INTRODUCTION

PROBE MISSION - The mission of the Probe is to obtain in situ atmospheric measurements of the outer planets in the early 1980's. Missions to Jupiter, Saturn or Uranus are illustrated in Figure 1. Launch is followed by interplanetary cruise when the Probe is attached to the spacecraft bus. Close to the outer planet the Probe is released by the bus and functions autonomously thereafter. The Probe enters the planet's atmosphere on a ballistic trajectory, decelerates in the atmosphere, and during subsonic freefall collects and transmits data about the atmosphere.

PROBE CONFIGURATION - The Probe reference configuration is illustrated in Figure 2. External shape is a spherically blunted conical forebody with a hemispherical afterbody. The Probe weighs about 100 Kg and is 90 cm maximum diameter. Major structural components include: 1) a honeycomb sandwich primary structure aeroshell which has equipment support rings integrally machined with the inboard sandwich facesheet, 2) a honeycomb sandwich shell afterbody, and 3) attach fittings. Major thermal control components include: 1) Radioisotope Heaters, 2) the attach fittings functioning as radiators, and 3) a Multilayer Insulation blanket. During launch the Probe is held in a conical adapter which attaches the spacecraft bus to a cylindrical

*This paper is related to work performed under NASA Contract NAS 2-9027.

adapter of the launch booster.

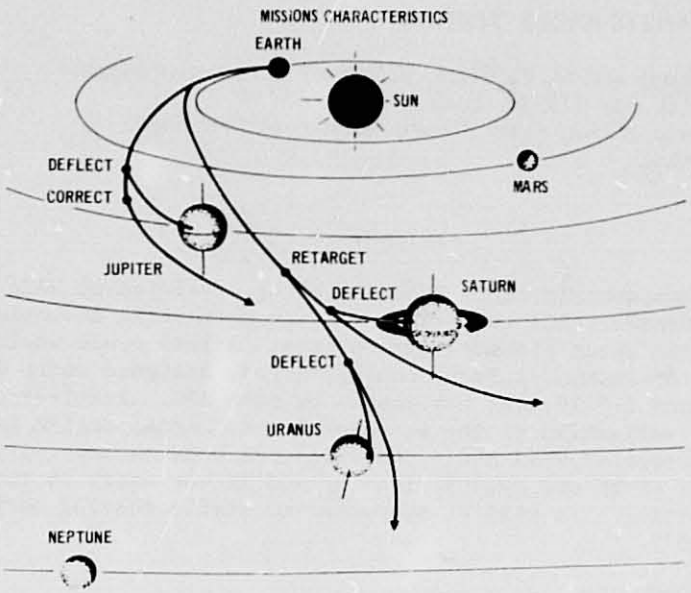

Figure 1 PROBE MISSIONS

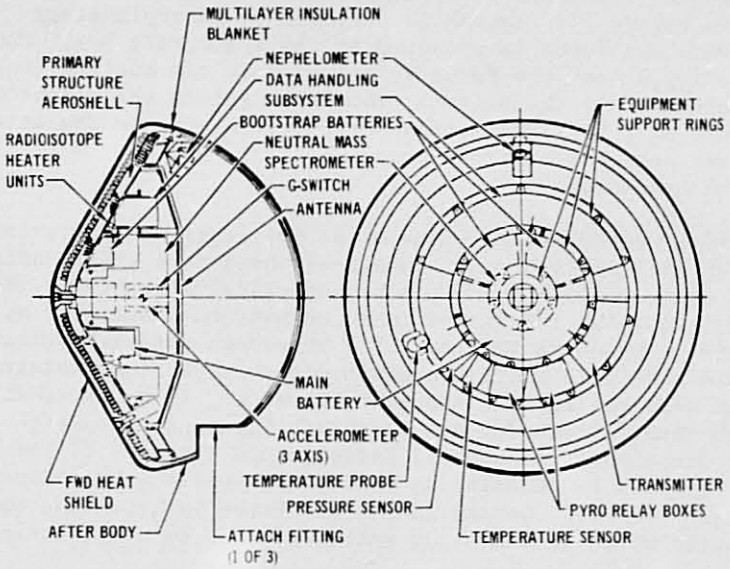

Figure 2 PROBE REFERENCE CONFIGURATION

2.0 TEST PLAN

The test plan was designed to provide a data base which would build confidence in the Probe structural and thermal design. Proof-of-concept tests which utilized a full scale Probe engineering Model as the test Model were planned and maximum use was made of NASA ARC facilities.

Mission events which are critical to the Probe structural and thermal designs were selected for test simulation. The test series and simulated flight event are presented in Figure 3. Four tests were planned; structural tests of shock, vibration, and static loads and a thermal vacuum test. The structural test series was based on a Saturn/Uranus Probe mission with a Titan III launch vehicle. Although the Shuttle is prime launch vehicle, the Titan III was chosen as being representative of launch vehicles. In addition, a Titan adapter, hardware and environments were available for testing. The thermal vacuum tests simulate a mission to any of the outer planets.

TEST	SIMULATED FLIGHT ENVIRONMENT
SHOCK	RELEASE OF PROBE FROM BOOSTER
VIBRATION	LAUNCH VEHICLE BOOST VIBRATIONS BASED ON TITAN IIIE DATA
STATIC	800 g's ATMOSPHERIC ENTRY DECELERATION
THERMAL VACUUM	INTERPLANETARY CRUISE

Figure 3 TEST PLAN SUMMARY

The shock test subjected the Model to shock environment resulting from simulated separation from the launch vehicle.

The vibration test subjected the Model to the dynamic environment of launch.

The static test will simulate quasi-static loading expected during an 800 g_E deceleration during planet atmospheric entry.

The thermal vacuum tests are simulating the deep space interplanetary cruise and the approach cruise portion of a mission.

3.0 TEST MODEL

A full scale engineering Model of the Probe was fabricated by NASA ARC to serve as the test Model. The Model was fabricated per engineering drawings of a MDAC-E Probe designed in a preliminary definition study for NASA-ARC. Completed Model hardware

is illustrated in Figures 4 to 6. An external view of the partially assembled Model resting on a machining fixture is given in Figure 4. The figure shows one of the recessed attach fittings. Figure 5 shows the Multilayer Insulation blanket wrapped around the Model. Simulated equipment was also fabricated and is shown in Figure 6 installed on the equipment support rings of the aeroshell. The simulated equipment approximated the

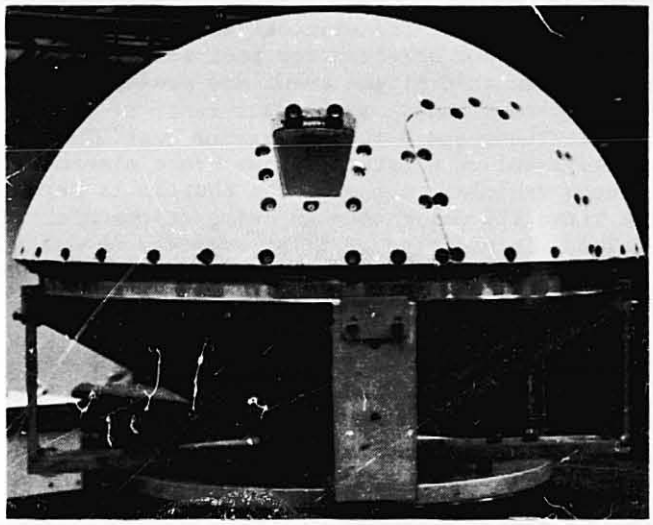

Figure 4 PROBE ENGINEERING MODEL – PARTIALLY ASSEMBLED

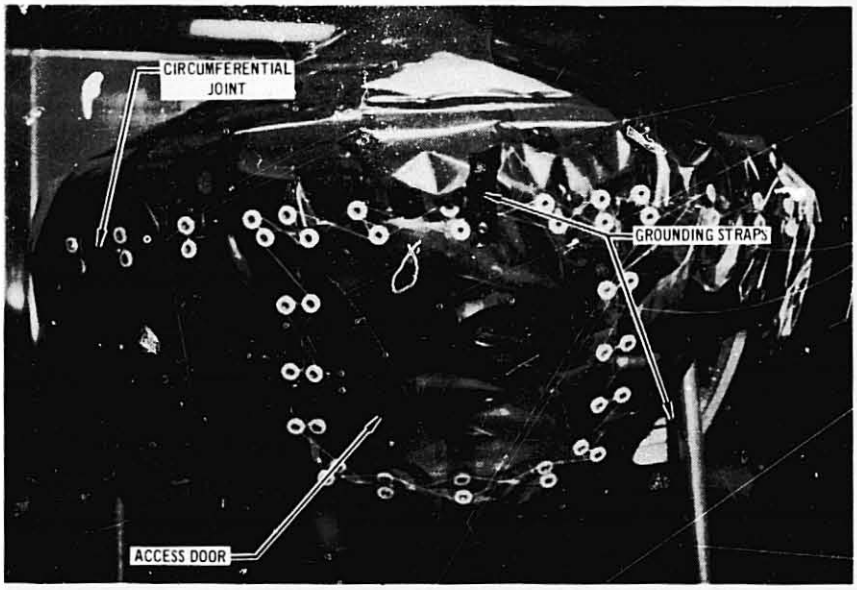

Figure 5 MULTILAYER INSULATION BLANKET

shape, size, weight and attachment pattern of anticipated equipment. Element heaters were installed in the simulated equipment to simulate equipment heat output during thermal vacuum tests. Figure 6 also shows the three attach fittings which connect the Probe to the conical adapter.

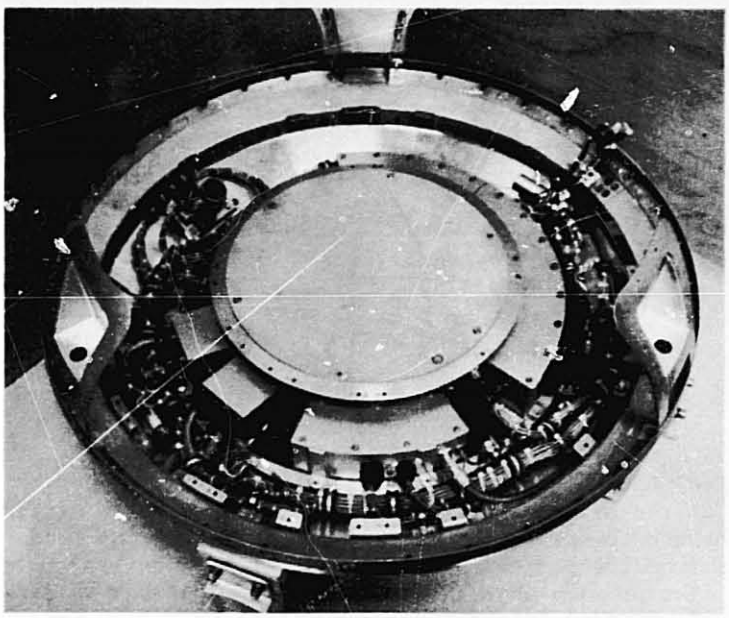

Figure 6 SIMULATED EQUIPMENT IN AEROSHELL

4.0 STRUCTURAL TESTS

CONFIGURATION - The structural subsystem of the Probe is schematically illustrated in Figure 7. The primary structure consists of a honeycomb sandwich aeroshell having a fiberglass outer facesheet and an aluminum inner facesheet. Four equipment support rings are integrally machined with the aluminum facesheet. The aeroshell acts as a decelerator, protects the equipment during 800 g_E's ballistic deceleration and provides continuous support for the forward heat shield. The rings distribute concentrated equipment inertia loads into the aeroshell. Three attach fittings located 120 degrees apart in the afterbody attach the Probe to the conical adapter.

SHOCK TESTS

Stage separation of the Probe and conical adapter from the last stage of the launch vehicle would be accomplished by the release of a V-band clamp ring. The clamp ring disengages when two diagonally opposite preload bolts are cut by pyro actuated bolt cutters. The resulting shock may be critical on the ball

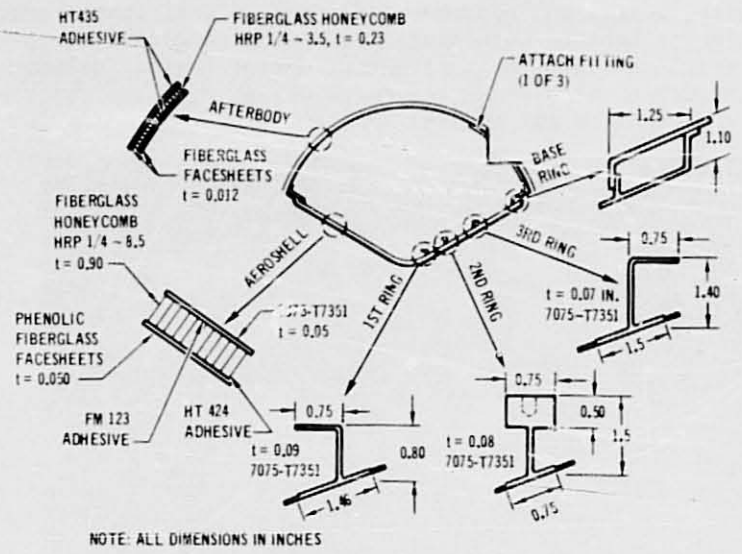

Figure 7 STRUCTURAL CONFIGURATION

lock bolts which attach the Probe to the conical adapter at the attach fittings. (The ball lock bolts utilize pyro generated pressure to self-actuate, allowing the Probe to separate from the conical adapter, and can be sensitive to shock loads.) The primary objective of the shock test was to determine the effect of shock on the operation of the ball lock bolts. Two shock tests were conducted and provided test data for the extreme positions of bolt cutters relative to the ball lock bolts.

The shock test setup is schematically illustrated in Figure 8. The model with simulated equipment was mounted in the conical adapter. This subassembly was then attached to the cylindrical adapter of the Titan III with a V-band clamp ring.

A closeup photograph of the test hardware is shown in Figure 9. The photograph shows the conical adapter, the cylindrical adapter, the V-band clamp ring, one of the pyro actuated bolt cutters and one of the three ball lock bolts. Two 3-axis accelerometers are shown, one directly above the bolt cutter and the other by the ball lock bolt. Also shown are air pressure lines connected to the ball lock bolt. These lines were used to provide air pressure to actuate the bolts in lieu of pyrotechnic pressurization.

The first test was conducted with one of the bolt cutters aligned directly beneath a ball lock bolt as illustrated in Figure 9. The bolt cutters were actuated and the V-band clamp ring disengaged. Accelerations at all of the gages were continuously recorded. After all structural response to the shock had died

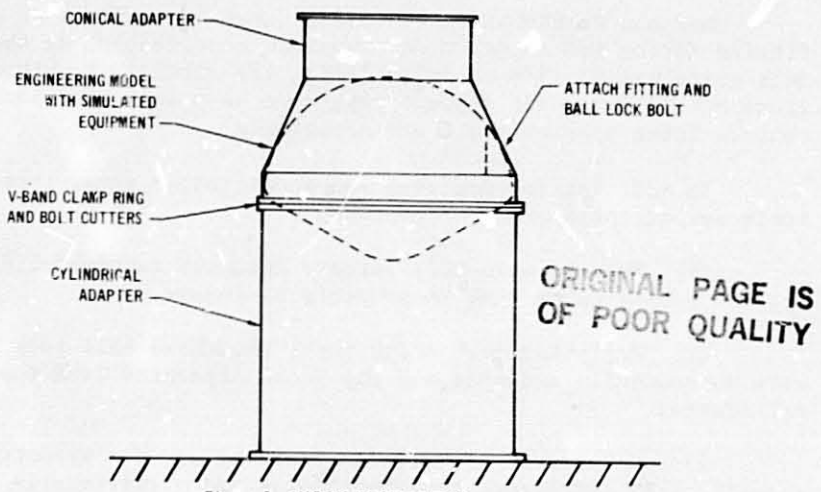

Figure 8 SHOCK TEST SETUP

Figure 9 PHOTOGRAPH OF SHOCK TEST HARDWARE

down, a Model/conical adapter separation test was conducted and the three ball lock bolts operated successfully allowing separation.

The Model and conical adapter were then rotated so that both bolt cutters were 30° from the nearest ball lock bolts and the second test was conducted.

Maximum acceleration of 1920 g's was recorded at an attach fitting during the second test. Maximum acceleration at the ball lock bolts was 800 g's recorded during the first test. Accelerations at the equipment support ring were very small for both tests. These accelerations are acceptable.

In addition to supplying the acceleration data, these tests demonstrated proof-of-concept:

(1) The two pyro bolt cutters actuated successfully allowing the V-band clamp ring to properly disengage.

(2) Following each shock test, the three ball lock bolts were successfully actuated and the Model separated from the conical adapter.

(3) No structural failures occurred and the structure significantly attenuates the shock loads and significantly reduces shock requirements for equipment.

VIBRATION TESTS

The launch dynamic environment may be critical for the attach fittings which transmit launch accelerations and environments to the Probe. The primary objective of the vibration test was to determine the dynamic response of the attach fittings to simulated launch environment. A secondary objective was to obtain qualitative information of the dynamic characteristics of the structural design.

The longitudinal vibration test setup was similar to that for the shock tests except that aircraft bolts were used in lieu of the ball lock bolts and V-band clamp ring pretension bolts. The setup also used a LING A300B shaker table, a head expander to accommodate the large diameter cylindrical adapter and team tables to ensure that only longitudinal (vertical) table motion occurred.

Instrumentation consisted of eight accelerometers attached to the Model to provide qualitative information of structure dynamic characteristics.

A photograph of the longitudinal vibration test setup is shown in Figure 10. From top to bottom are shown the conical adapter, cylindrical adapter, head expander and LING A300B shaker table. One of the team tables to ensure vertical table motion is also shown.

Six vibration tests were conducted; a sinusoidal and a random along each of the Model orthogonal axis. The longitudinal axis was tested first with the setup shown in Figure 10. The shaker table was then rotated to a horizontal position, the

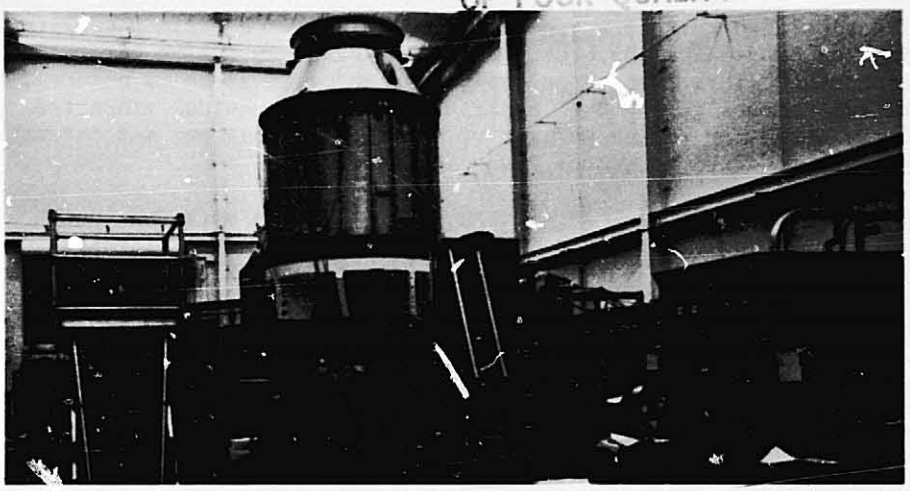

Figure 10 PHOTOGRAPH OF VIBRATION TEST HARDWARE

vertical team tables were removed and vibration tests of the two lateral axes of the Model were conducted. Input environment was controlled at the head expander. The input environments were those given in Figure 11 with one exception. Due to equipment limitations (primarily shaker output capability vs mass of the test specimen and fixtures) the overall level obtained for the longitudinal axis was only 3.16g instead of 8.16g equivalent for random vibration.

The structure appears to have good dynamic characteristics. No major problems were found. The only significant amplifications (greater than 10) of the input environments occurred at

VIBRATION AXIS	SWEEP RATE	FREQUENCY (Hz)	ACCELERATION (g's O-PEAK)
LONGITUDINAL	1 OCTAVE/MIN	5–12	3.0
		12–50	3.0
		50–200	2.25
BOTH LATERAL	1 OCTAVE/MIN	5–10	1.95
		10–22	1.95
		22–200	1.50

SINUSOIDAL TEST VIBRATION SCHEDULE

VIBRATION AXIS	TEST DURATION (MIN. EACH AXIS)	FREQUENCY (Hz)	POWER SPECTRAL DENSITY (PSD) LEVEL (g^2/Hz)
ALL 3 AXIS	4	20–100	0.056 AT 100 Hz INCREASE BY 6 dB PER OCTAVE FROM 20–100 Hz
		100–1000	0.056
		1000–2000	0.056 AT 1000 Hz WITH ROLL OFF OF 12 dB PER OCTAVE FROM 1000-2000 Hz

RANDOM VIBRATION TEST SPECTRUM AND DURATION

Figure 11 VIBRATION TEST LEVELS

the simulated relay box and simulated antenna. A maximum amplification of 34 at 12 Hz occurred at the relay box during lateral sinusoidal vibration and an amplification of 18 at 86 Hz occurred at the antenna during the longitudinal axis sinusoidal vibration. Close attention to the designs of the actual relay box and antenna will be required to reduce these amplifications.

During testing, local structural failures occurred in the afterbody near the cutouts for two of the three attach fittings. The failures were minor and were not detected until all six tests were completed. It is not known which test initiated the failures. One of the failures is shown in the photograph of Figure 12. The afterbody honeycomb sandwich facesheets separated from the core near the core reinforcements. The failures are primarily attributed to the cantilever design of the attach fittings. Modification of the attach fitting design was recommended to provide better load paths.

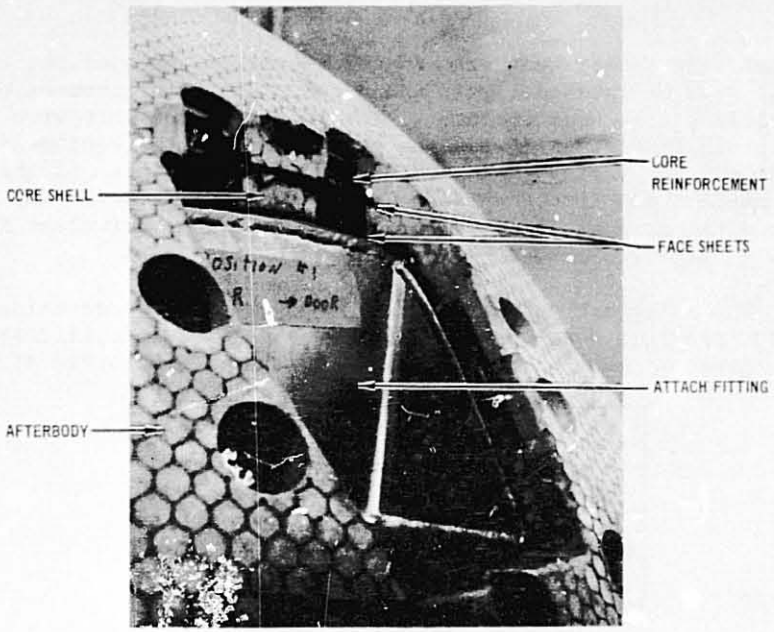

Figure 12 AFTERBODY LOCAL FAILURE - VIBRATION TEST

STATIC TESTS (These tests will be conducted during January 1977)

The aeroshell supports the equipment under 800 g_E's inertia loading balanced by the forebody aerodynamic pressure during planetary entry. Primary objective of the static tests is to determine strength of the aeroshell under this loading.

The static test setup is schematically illustrated in

Figure 13. Only the aeroshell of the Model will be tested and will be mechanically loaded in a specially designed static test fixture as illustrated in Figure 13. A photograph of the partially assembled static test fixture is presented in Figure 14. The fixture was designed and fabricated by NASA ARC and will simulate loading of the aeroshell expected during atmospheric entry deceleration of up to 800 g_E's.

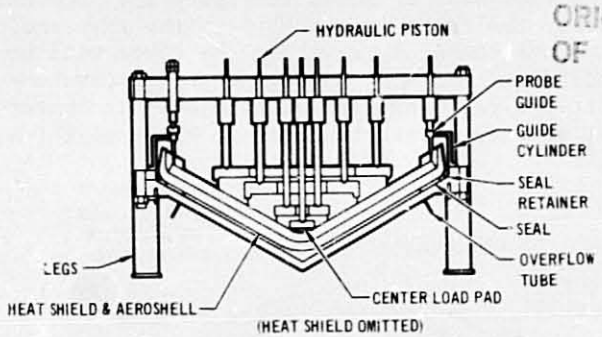

Figure 13 STATIC TEST SETUP

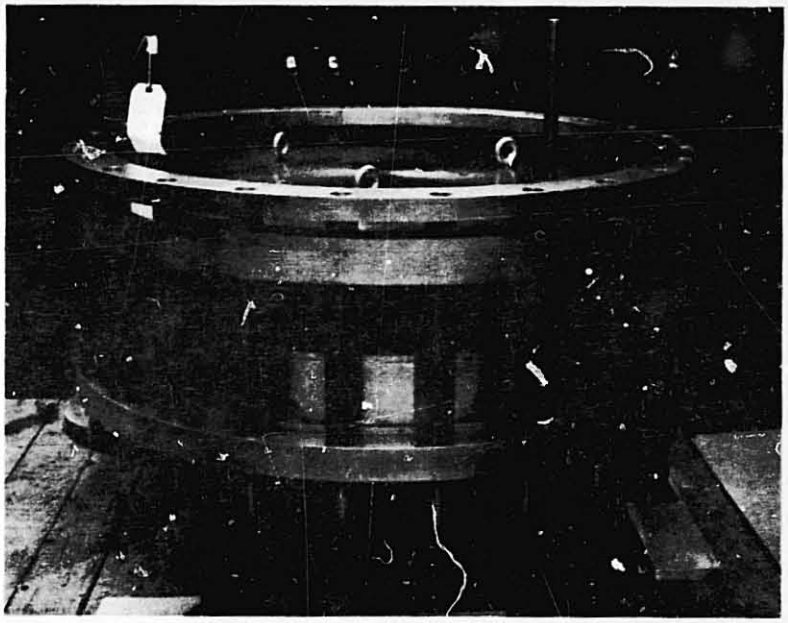

Figure 14 ARC STATIC TEST FIXTURE

The fixture will apply hydrostatic pressure to the forward side of the aeroshell to simulate atmospheric deceleration pressure. Loads to balance the pressure will be applied by hydraulic pistons to the aeroshell equipment support rings to simulate

inertia loads of the equipment. The piston loads will be transmitted to the rings by stiff load distribution plates. Radial deflection isolation of the plates from the rings is provided for.

5.0 THERMAL VACUUM TESTS

CONFIGURATION - The baseline configuration of the Probe thermal control subsystem is shown in Figure 15. During interplanetary cruise, the Probe is attached to the spacecraft's conical adapter and the temperature within the Probe will be controlled between 253°K and 273°K by adjusting the temperature of the attachment fittings via radiators and commandable heaters located on the conical adapter. This temperature range will insure long battery life.

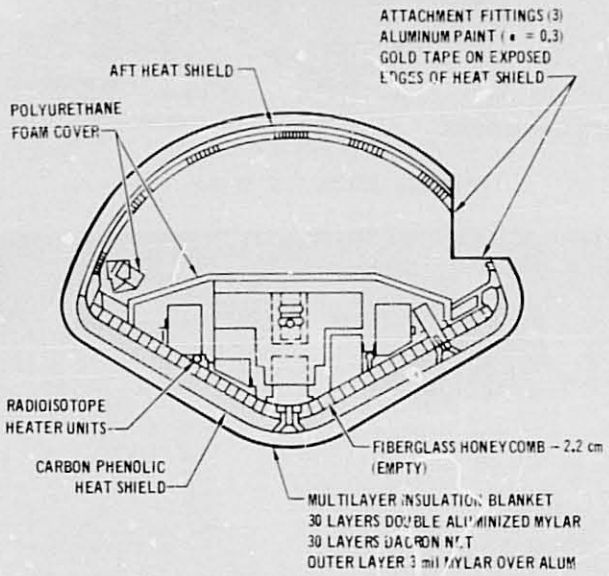

Figure 15 THERMAL CONTROL SUBSYSTEM REFERENCE DESIGN

Depending on the planet, the Probe is separated from the spacecraft between 21 and 56 days prior to entry. During this approach cruise phase, the Probe's internal temperature will be maintained by a balance between the heat loss through the Multilayer Insulation (MLI) blanket and the attachment fittings with the heat generated by the Radioisotope Heating Units (RHU's). Prior to entry, all equipment within the Probe are at essentially the same temperature and will be between 263°K and 283°K. Temperatures higher than 283°K will begin to limit the mission time during the hot atmospheric descent. The minimum activation temperature of the battery is 278°K, but a heater is located on the battery which can be activated prior to entry to raise the battery temperature by as much as 15°K if necessary, thus establishing the 263°K lower limit. The MLI blanket consists of 30

layers of double aluminized mylar and 30 layers of dacron net. The outer layer is a 3 mil mylar over aluminum sheet, and the entire blanket is held together with nylon buttons. There are two joints in the blankets; one around the circumference of the maximum diameter and one around the access door. Figure 5 (Section 3.0) shows the completed blanket installed on the Model. The attach fittings are painted with a low emissivity aluminum paint and the exposed edges of the heat shield near the attach fittings will be covered with low emissivity tape to prevent low temperature exposure on the edge of the heat shield.

TEST PLAN - The purpose of the thermal vacuum test was to verify the passive thermal control concept and to measure the thermal performance characteristics of the Probe Model and the Probe to conical adapter interface. These data will include such items as insulation properties of the flight configured blanket, heat flow paths within the Model and the transient characteristics. The test plan shown in Figure 16 consists of eight runs. The first four runs simulate the approach cruise phase of the flight with the third run being a transient run to simulate the pre-entry power profile as shown in Figure 17. Only the first four runs are addressed in this paper.

RUN NO.	SIMULATION	TYPE	CONDITIONS
1	APPROACH CRUISE	STEADY STATE	RHU = 8 WATTS
2	APPROACH CRUISE	STEADY STATE	RHU = 10 WATTS
3	APPROACH CRUISE	TRANSIENT	PREENTRY POWER PROFILE
4	APPROACH CRUISE	STEADY STATE	RHU = 12 WATTS
5	INTERPLANETARY CRUISE	STEADY STATE	RHU = 10 WATTS ADAPTER TEMP = 294°K
6	INTERPLANETARY CRUISE	STEADY STATE	RHU = 10 WATTS ADAPTER TEMP = 244°K
7	INTERPLANETARY CRUISE	STEADY STATE	RHU = TBD WATTS ADAPTER TEMP = 244°K
8	INTERPLANETARY CRUISE	TRANSIENT	EQUIPMENT CHECKOUT POWER PROFILE

Figure 16 TEST RUN MATRIX

TEST METHODS - Several differences exist between the test configuration and the reference design, Figure 15. The facilities did not have the capability for projecting a simulated solar input of sufficient diameter to cover the Model, and thus solar simulation was not used. Secondly, a higher emissivity aluminum paint (ε = 0.43) was used in place of the Finch type (ε = 0.30) aluminum pain. For the test, the RHU heat dissipation was simulated with heaters installed in typical RHU containers.

To maintain the internal Probe temperatures at specified levels with relatively few RHU's, the Probe must be extensively insulated. This yields a long time constant for the Model which presents problems in reaching steady state conditions within a

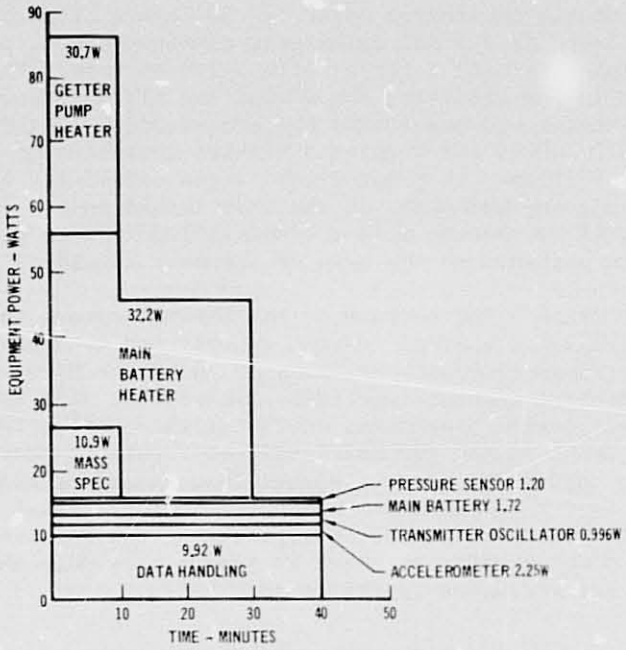

Figure 17 PREENTRY POWER PROFILE

short period of time. Thus, methods were evolved using an analytic simulation to accelerate the attainment of steady state conditions.

The first problem was how and at what level to initialize the Model temperature. The uncertainty in the MLI performance would yield uncertainties in the steady state temperatures. To accelerate the cooldown, all of the heaters are turned off and the Model is allowed to cool until it reaches an estimated value of the steady state temperature (TSS). At this time, the simulated RHU heaters are turned on and the first run is started. To estimate TSS, an existing analytic simulation of the Model was used. The cooldown characteristics of the Model were estimated by running a zero load transient and an eight watt steady state analytic simulation for two values of the MLI conductance that should bracket the performance. For each curve there is a characteristic slope and a corresponding steady state value (TSS) for the initial eight watt case. Thus, the TSS can be estimated from the slope of the cooldown curve, and was calculated as follows:

$$T_{SS8} = 352 - 9.6\ (T_{\tau} - T_{\tau-1\ day}) \qquad (1)$$

where

T_τ = Temperature at present time

$T_{\tau-1\ day}$ = Temperature 1 day earlier

T_{SS8} = Estimated steady state value for 8 watt load

Procedures were also developed to accelerate the run during the course of the run and to derive an applicable steady state criteria. Again, the analytic simulation was used to determine steady state values and expected transient responses during the course of the run. Figure 18 shows a plot of $\frac{dT}{d\tau}$ vs $T - T_{SS}$, and the slope of this curve represents the reciprocal of the time constant of the Model. From this plot the following correlating equation was derived:

$$TSS = T_\tau + 14.2\ (T_\tau - T_{\tau-1\ day}) \qquad (2)$$

The first use of this equation was in establishing the steady state criteria. A change of temperature of 1°K per day will only insure that we are within about 14°K of the final answer and thus a much smaller temperature change must be used as the criteria. To measure these small temperature changes a platinum resistance thermometer (PRT) was included in the instrumentation, and a steady state criteria of 0.1°K change per day was established. During the course of a run, the steady state temperature can also be estimated from Equation (2). To change the temperature, additional heaters can be turned on to raise the temperature, or the simulated RHU heaters can be turned off to accelerate the cooldown.

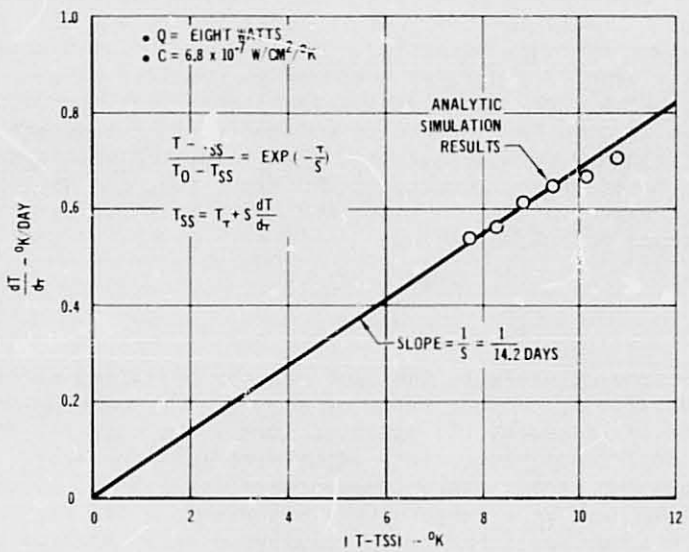

Figure 18 PROBE TIME CONSTANT

To obtain the necessary data, the Model was instrumented with 50 thermocouples (T/C) and one PRT. Each component was instrumented with one or more T/C, and one of the attach fittings was instrumented with six T/C to determine the heat flow paths near the attach fittings. T/C's are also located on the external side of the blanket to help determine insulation properties. A total of 13 heater sets are located within the Model. All of the T/C's and heater wires are brought out in one wire bundle. Since this wire bundle is fairly large (>2 cm dia.) it could be a significant heat leak. To prevent this, the wire bundle was insulated with a MLI wrap and a heater block was located in the bundle about 30 cm from the Model. This heater was tied into a variable voltage controller which was driven by a difference temperature measurement between the heater and the Model. The heater input is varied to maintain a temperature differential of less than $\pm 1°K$, which results in a heat leak of less than 0.1 watt.

TEST RESULTS - The first run was initialized at about 257°K, and the eight watt simulated RHU load was turned on. Figure 19 presents a plot of the bootstrap battery temperature as a function of time. By the middle of day 285, it was apparent that the Model temperature was too low. Using Equation (2) the steady state value was estimated to be 267°K and heaters were turned on to raise the temperature. The temperature initially rose rapidly to a spike and then fell after the heaters were turned off as the localized heating was gradually absorbed into the forward heat shield. Thus, monitoring one of the internal temperature sensors is not a good indication of the finalized temperature, but the total heat input is a good indicator. The resultant temperature rise after the heating spike was about 0.053°K per watt-hr of applied heat. This one temperature level change was all that was necessary to reach stability. The calculated time constant, though, was about 7.0 days as compared to the 14.2 days of Equation (2). With the 7 day time constant, the first test would have taken 23 days to complete if started at room temperature as compared to the 7 days actual test time using the accelerated methods. Based on the results of the first run, the approximate additional watt-hrs (QA) to boost the Model to steady state conditions could be calculated as:

$$QA = \frac{7\ (T_{\tau} - T_{\tau-1})}{0.053} \qquad (3)$$

Figure 20 presents the plot of the bootstrap battery for run No. 2. At the beginning of the run, the temperature was initially raised to the expected level. As with Run No. 1, only one additional temperature adjustment was necessary. Figure 21 presents the steady state temperatures for Run No. 2, and shows that all the equipment temperatures are within a few degrees of each other. Run No. 4 had to be terminated early because of a water cooling failure in the diffusion pump, but the results are

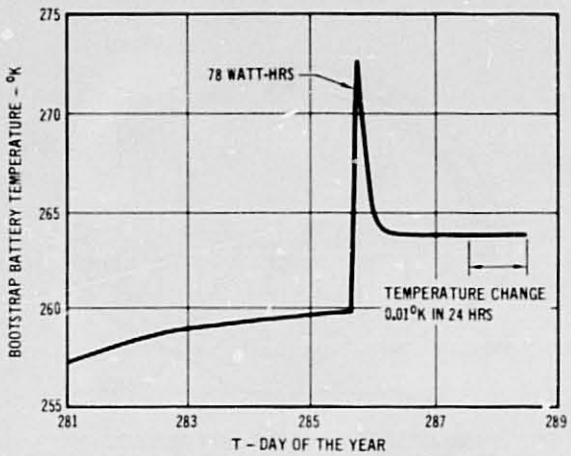

Figure 19 TEST RUN NO. 1 – 8 WATTS

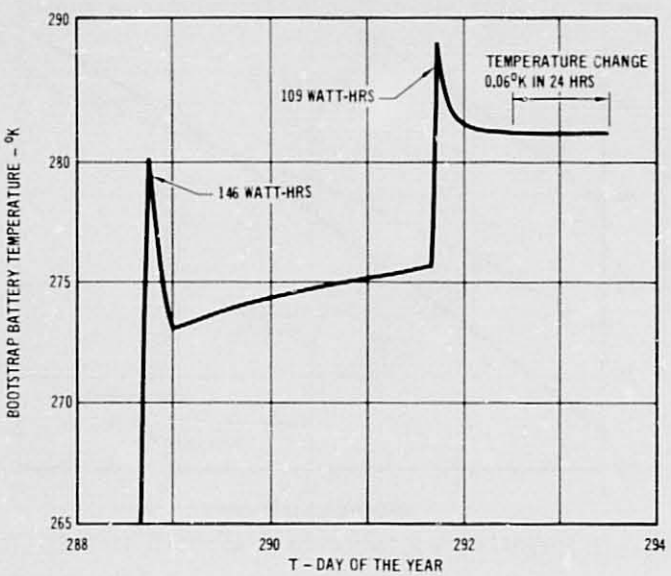

Figure 20 TEST RUN NO. 2 – 10 WATTS

within 2°K of the true steady state results. Figure 22 presents the steady state battery temperature tests results compared to the analytic predictions. Although the temperatures are in the expected range, the slope of the test data is smaller than the analytic prediction. Further analytic work will be necessary to resolve this discrepancy. At the completion of Run No. 2, the pre-entry power profile was run, and the results are presented in Figure 23. As is shown, the battery heater does raise the battery temperature by the required 15°K.

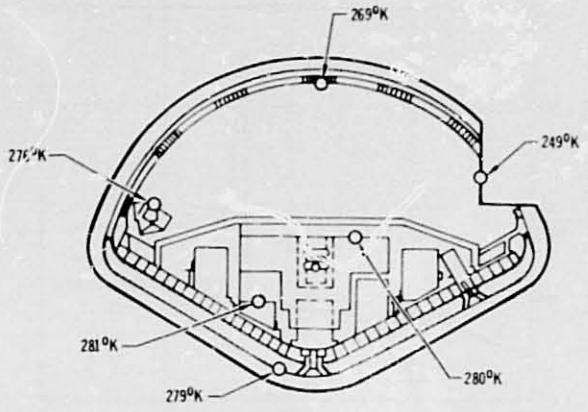

Figure 21 STEADY STATE TEST RESULTS
RUN NO. 2 – 10 WATTS

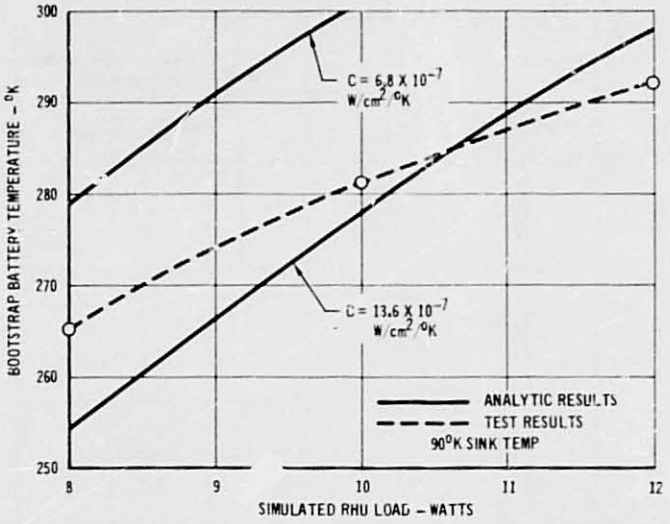

Figure 22 APPROACH CRUISE SIMULATION STEADY STATE TEST RESULTS

TEST CONCLUSIONS - As tested, the Probe Model requires less than nine 1 watt RHU's to maintain the desired 273°K nominal temperature level. Since the simulation did not include solar input and had a higher emissivity paint on the attach fittings than the reference design, the actual requirement will be less. Thus, the concept of controlling the Probe passively with a relatively few number of RHU's has been successfully demonstrated. Further analytic work will be required to correlate the analytic simulation to the test results in order to perform trade studies to determine the final configuration with a high degree of confidence. Although the preliminary correlating Equations (1) and

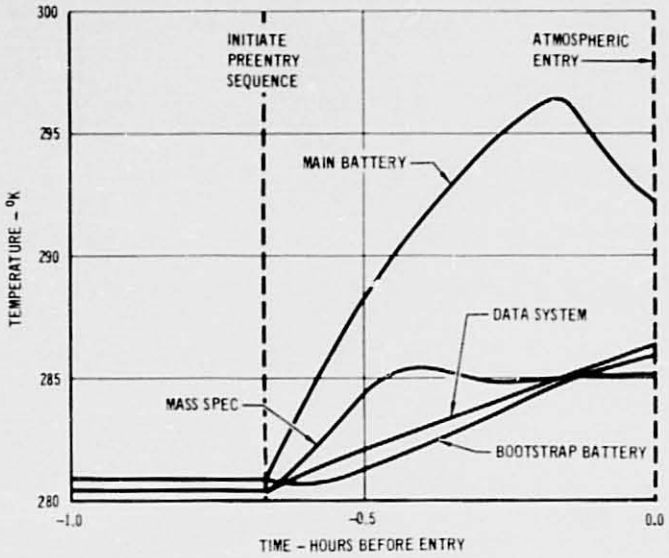

Figure 23 PREENTRY TRANSIENT RUN NO. 3

(2) did not exactly match the actual Model characteristics, the procedures for accelerating the testing did significantly decrease the testing time.

6.0 SUMMARY

Proof-of-concept tests are being conducted on a full scale engineering Model of the Probe. The tests simulate critical conditions expected during the Probe mission. Shock and vibration tests are completed and indicate that the structural concept is basically sound. Thermal vacuum testing successfully demonstrated the passive control concept and verified methods of accelerating the testing. Future static testing will further validate the structural concept.

C-2 N79-19019

Paper No. 10

LIGHTNING TESTS OF THE ORBITER PYROTECHNIC ESCAPE SYSTEM

R. Cohen, *Johnson Space Center, Houston, Texas*
E. H. Schulte, *McDonnell Aircraft Company, St. Louis, Missouri*

ABSTRACT

An Experimental Test Program was undertaken to demonstrate that the Space Shuttle Orbiter Vehicle pyrotechnics actuated Crew Escape System was not subject to failure resulting from a lightning strike in the vicinity of the cockpit. A test sample representing a full-scale portion of the Orbiter Outer Panel was preheated to 325°F and struck with three different current waveforms to simulate the various effects of lightning: 1) 2μ sec risetime, to 180 kA pulse to evaluate fast current rise shock effects, 2) a 205 kA, 100μ sec wide pulse to evaluate full energy shock effects, and 3) a 490 ampere, 370 msec continuing current to evaluate the thermal effects of a lightning strike.

None of the lightning strikes damaged the pyrotechnics altnough some damage occurred to the Thermal Protection System.

These tests, show that the Orbiter outer panel pyrotechnics are adequately protected against damage resulting from a lightning strike.

INTRODUCTION

The Shuttle Transportation System has been designed to reduce the cost of space operations below prior programs. A major factor in implementing this cost reduction involves the high frequency of launches that can be achieved with one Orbiter. Delays in either launch or entry and return to a landing site due to poor weather conditions would negate part of the cost reduction effort. To help preclude such delays, the Shuttle is designed to tolerate the effects of lightning strikes. One element in assuring the success of the design effort has been a test program to confirm that the explosive components utilized in the Shuttle would not be damaged by the direct thermal and shock effects of a lightning strike. To minimize the extent of the test program, the Shuttle was analyzed to determine the explosive components which would be most susceptible to lightning damage. The analysis was based upon factors such as: areas of the Shuttle surface which contain possible lightning attach points (as determined from a prior test program)[1]; relative distance and structural discontinuities between the attach points and explosive component locations; and chemical composition of explosives. This paper describes the test program that was conducted on the Orbiter device which was determined to be most susceptible to the direct lightning effects. These tests were performed by McDonnell Aircraft Company Laboratories, Lightning Simulation and Armament Systems, St. Louis, Mo. in accordance with Reference 2.

Lightning Threat and Test Philosphy

Natural lightning is a complex phenomenon and is further complicated because no two lightning strikes are identical. Therefore, for purposes of testing, analytical and statistical data have been compiled[3,4] in an effort to devise a model which could be used as the basis for performing suitable lightning simulation tests. The "Space Shuttle Program Lightning Protection Criteria Document", JSC-07636, Revision A[2], was based upon just such data, plus the combined knowledge and engineering judgments of many experts in the field of lightning testing and research. The model lightning flash current waveform listed in the JSC-07636 document is shown in Figure 1. It is basically a "worst case" model, i.e., virtually all naturally occurring lightning strikes will be less severe than that detailed in the lightning model. Thus, if a sample successfully passes the "worst case" lightning strike test conditions, a high degree of confidence will be established in that particular design.

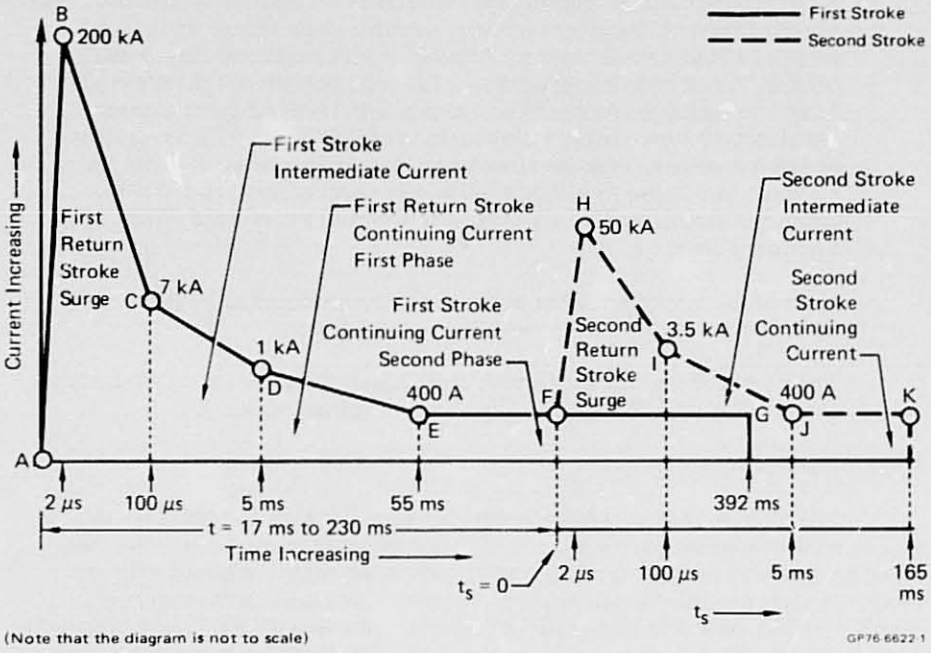

FIGURE 1 – NASA (JSC) LIGHTNING MODEL[2]

The lightning model shown in Figure 1 involves two high-current strokes: the first has a current peak of 200,000 amperes and a current rate of change of 100,000 amperes per microsecond (100 kA/10^{-6}sec); the second stroke is one-fourth the magnitude of the first. The model incorporates intermediate currents persisting for a few milliseconds and a continuing current. The second stroke is not always present in a lightning flash; however, if the second stroke exists, it is known to occur during the time interval from 17 to 230 milliseconds following the first return stroke. This model of the second stroke is for use in swept stroke arc reattachment analysis and was not used for this test. The total charge transferred in the two stroke model is 200 coulombs. Two hundred coulombs are contained in the first stroke when a second stroke is not present in the flash.

Although it is desirable to subject a test sample to the complete model flash in one test current waveform, as shown in Figure 1, only rarely can this be done in the laboratory. Therefore, engineering judgments must be made based upon knowledge of the test sample and lightning parameters as to which portions of the model flash are responsible for the types of damage expected, and then these portions of the waveform are used for testing. For example, the brow of the Orbiter vehicle (the region above the cockpit area) is a primary attach point for a lightning strike (Figure 2). The brow contains pyrotechnics which are a part of the pilot's emergency escape system and the brow is covered with a thermal protection system necessary for re-entry protection of the Orbiter. A lightning strike to the brow therefore poses a multiple threat and one which cannot readily be analyzed mathematically because of the unknown interactions of the various materials when subjected to an intense transient electrical current. The pyrotechnics, mild detonating fuse (MDF), can be de[illegible]d or "dudded" (rendered inoperative) by a severe mechanical shock or by the rapid application of sufficient heat; both conditions may exist in a lightning stroke. In addition, the thermal protection system consists of lightweight brittle ceramic tiles bonded to a fibrous strain isolation pad (SIP) and this protection system may suffer severe damage because of the explosive vaporization of materials subjected to the high current surge. For the test of a system such as this, the unknown effects of the vaporizing and burning of materials should be assessed. Also, during re-entry of the Orbiter vehicle into the earth's atmosphere, the Orbiter metal skin beneath the TPS tiles on the brow may be heated to 161°C (325°F). Therefore, for this test the "worst case" lightning test condition would be the first stroke shown in Figure 1, applied to a preheated panel.

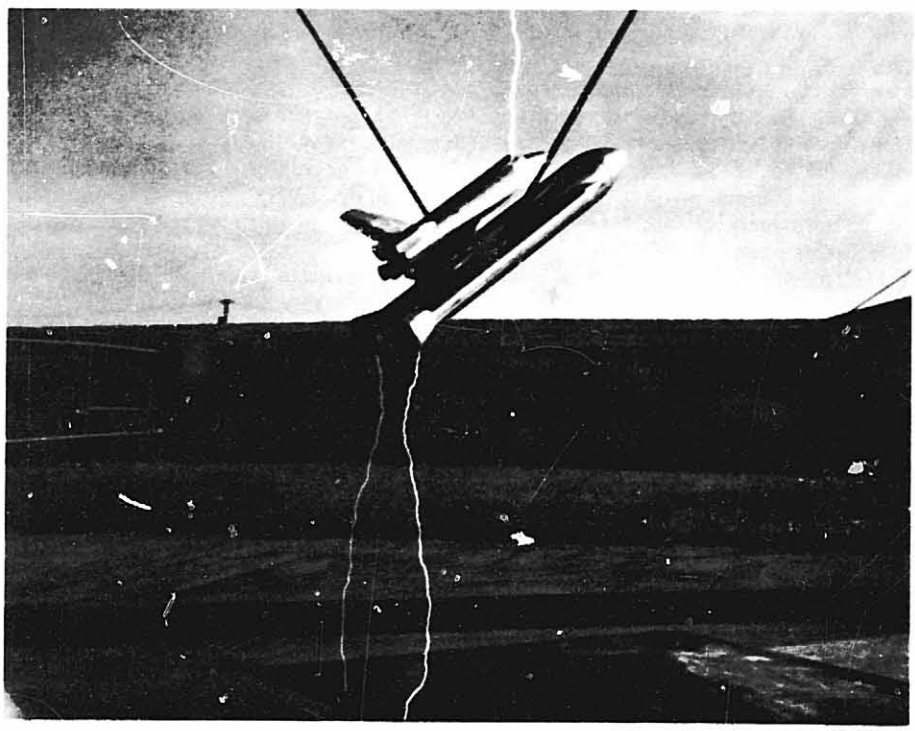

GP76-6622 2

FIGURE 2 – LIGHTNING TEST OF SPACE SHUTTLE MODEL

Referring to Figure 1, the first return current surge (kA) has associated with it a very severe shock phenomenon. For this test the results of this shock were to be evaluated in two parts, one to evaluate the effect of the very fast rise time (100 kA/μsec for 2μsec) and the other to evaluate the effects of the full energy content of the first 100 microseconds of the high-current surge. After the first high-current surge, the principle damage mechanism should be arc heating from the intermediate and continuing currents with the associated burning and eroding of materials. Therefore, for this test, the first stroke intermediate current, the first stroke continuing current first phase, and the continuing current phase were represented by a single constant current level, with the total time (400 milliseconds) consistent with that shown in Figure 1, and the current level selected (500 amperes) so as to deposit the required minimum of 200 coulombs. The possible interaction of effects of the "full energy" return stroke surge and the continuing current was to be obtained by directly coupling the return stroke surge current and the continuing current into one sequentially occurring waveform.

In order to assure "worst case" test conditions, the lightning arc would have to be directed to the area of the test panel directly over the pyro at a point where the metal panel over the pyros was the thinnest. This was accomplished by placing the high-current discharge probe physically close to the test panel, but far enough away to minimize possible interaction with the panel.

Test Specimen

The 45.5 x 61 cm (18 x 24 inch) test sample, designed to simulate a representative full-scale portion of the Orbiter outer panel escape system, is shown in Figures 3 and 4 (topside and underside views). Figure 5 is a sketch of the portion of the panel containing the pyros. For economic reasons a flat plate configuration, rather than the complex curvature of the Orbiter outer panel escape system, was chosen for this test series. The area immediately surrounding the mild detonating fuse (MDF) was the same as the Orbiter configuration, including physical dimensions and material thermal properties. Outlying areas of the panel are first order approximations to the structural configuration of the Orbiter to simulate shock response in the region of the pyro.

The silica Reusable Surface Insulation (RSI) tiles, the Strain Isolation Pad (SIP), the filler bar material between the tiles and the MDF were all supplied by NASA for this test. The tiles had previously been used on another test program and a few micro cracks were noted on a couple of these tiles prior to installation. Upon installation, the cracked areas were located away from the lightning strike locations. The tiles, SIP, and filler bars were installed according to the procedures given in a Rockwell Material Processing Specification for the Orbiter. The Mild Detonating Fuse used for this test was a part of the same lot manufactured by Explosive Technology for Rockwell for installation in the Orbiter flight vehicle. The MDF was bonded in place with Scotchweld 2216 B/A epoxy as installed on the Shuttle vehicle. Two 36-ga iron/constantan thermocouples were installed in the slot with the pyros directly behind the intended strike locations as shown in Figure 5.

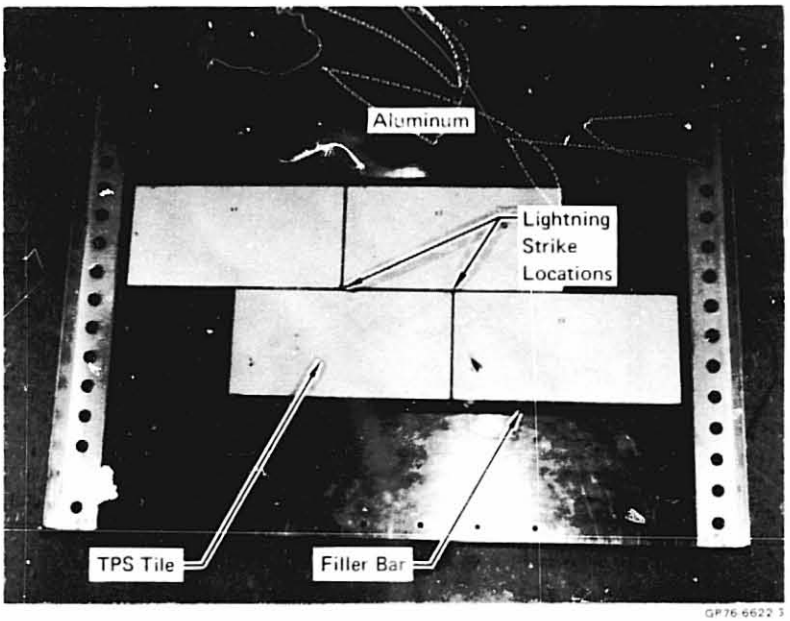

FIGURE 3 – SIMULATED ORBITER OUTER PANEL
Topside View

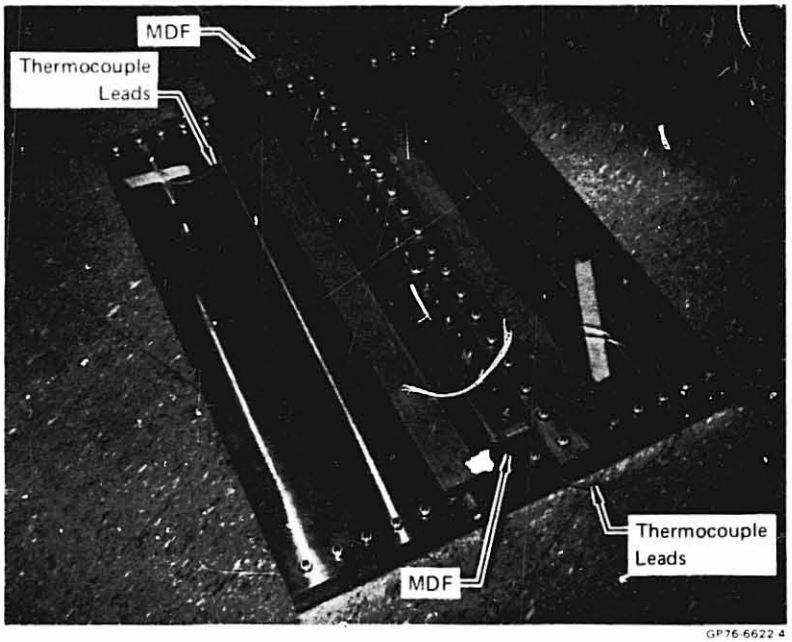

FIGURE 4 – SIMULATED ORBITER OUTER PANEL
Underside View

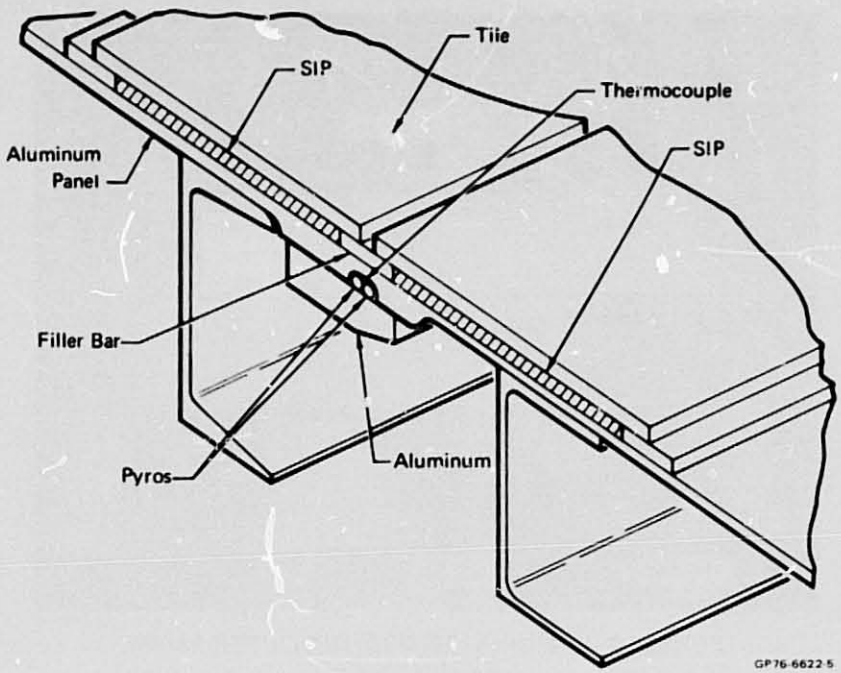

FIGURE 5 – CROSS SECTION OF TEST PANEL PYROTECHNICS INSTALLATION

TEST SETUP

Orbiter Panel

A simplified block diagram of the lightning test setup is given in Figure 6 and an overall view of the test setup is shown in Figure 7. A blast shield enclosed the entire test panel setup, to protect personnel and equipment in the event of detonation occuring during a lightning test. A simplified diagram of the Orbiter panel installation is shown in Figure 8 and the actual installation of the panel for the fast rise-time, high-current test is shown in Figure 9. The high-current output probe was spaced 1/2 inch from the panel immediately above the desired strike point (intersection of the tiles) to insure that the arc would attach at the designated area. The probe was sharpened to a point to minimize the interaction of the probe with the panel. When the fast rise-time, high-current test was conducted, the continuing current supply was disconnected from the circuit shown in Figure 6.

Since it was desired to simulate re-entry heating of the Orbiter panel prior to each lightning strike, a method of heating the test sample was incorporated into the test setup as shown in Figure 9. Several tungsten filament, quartz-iodine linear heat lamps backed by a polished aluminum reflector were used to radiantly heat the test sample. The power to the lamps was manually controlled to obtain an average heating rate of 4.4°C/minute (8°F/minute). Heat losses from the panel were minimized by supporting the panel with fiberglass angles, rather than metal, covering the topside exposed metal surfaces of the panel with blanket thermal insulation, and by using thin stainless foil for electrical contact to the edges of the Orbiter panel.

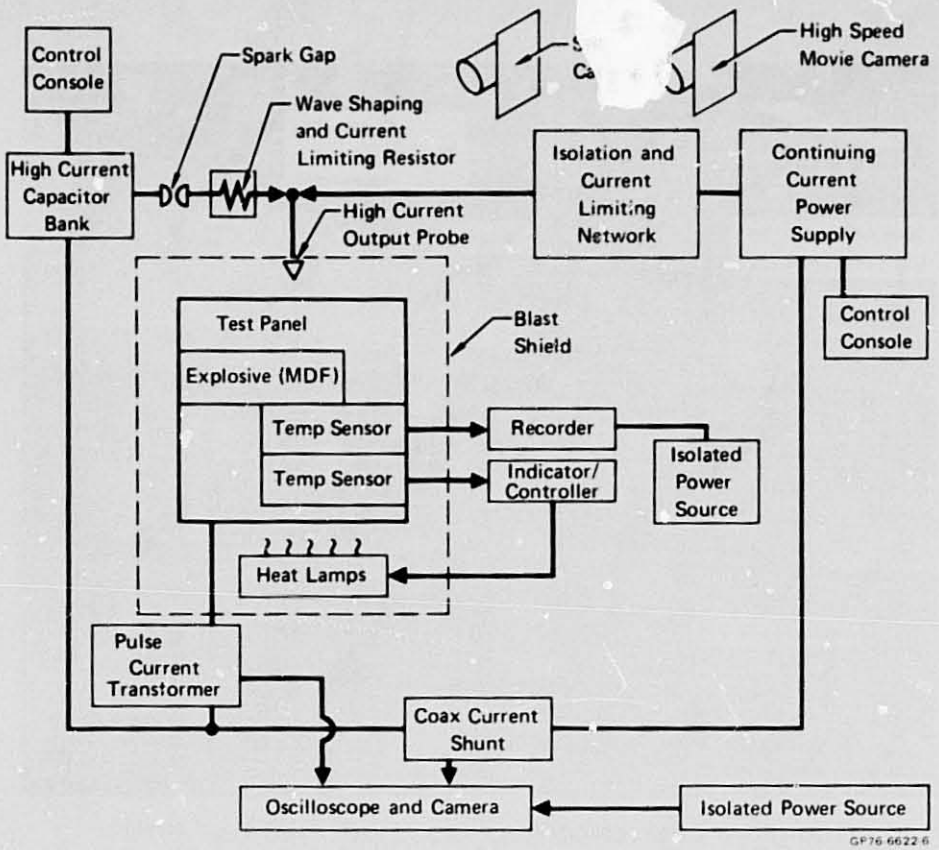

FIGURE 6 – SIMPLIFIED BLOCK DIAGRAM OF LIGHTNING TEST SETUP

For post test evaluation of the pyros, a detonator cap was installed on the ends of the pyros so that both pyros would be detonated simultaneously. Trigger wires at each end of the panel were attached to the MDF and were used to start and stop an electronic counter, thus giving the total elapsed time for the detonation front to propogate between the two fixed points.[5]

Lightning Generators - To provide the fast rise-time, high-current waveform, a 3μf 100 kV capacitor stack capable of attaining 200 kA in 2 μseconds into a low impedance test sample was used. In this configuration the current waveform was a damped sinusoid with the zero cross-over occurring every 4 microseconds.

To provide the 200 kA full-energy current waveform, the MCAIR 600 kilojoule capacitor bank was connected as a 5-stage Marx generator with an output voltage of approximately 110 kV. Waveshaping components were incorporated so that a relatively fast rising, slow decaying waveform was obtained with very little ringing. In this configuration the lightning current was uninterrupted for 100 μseconds.

The continuing current (high coulomb) portion of the lightning waveform was supplied by a 3-phase, 480-volt auto-transformer rectifier power supply adjusted for a current level of slightly less than 500 amps.

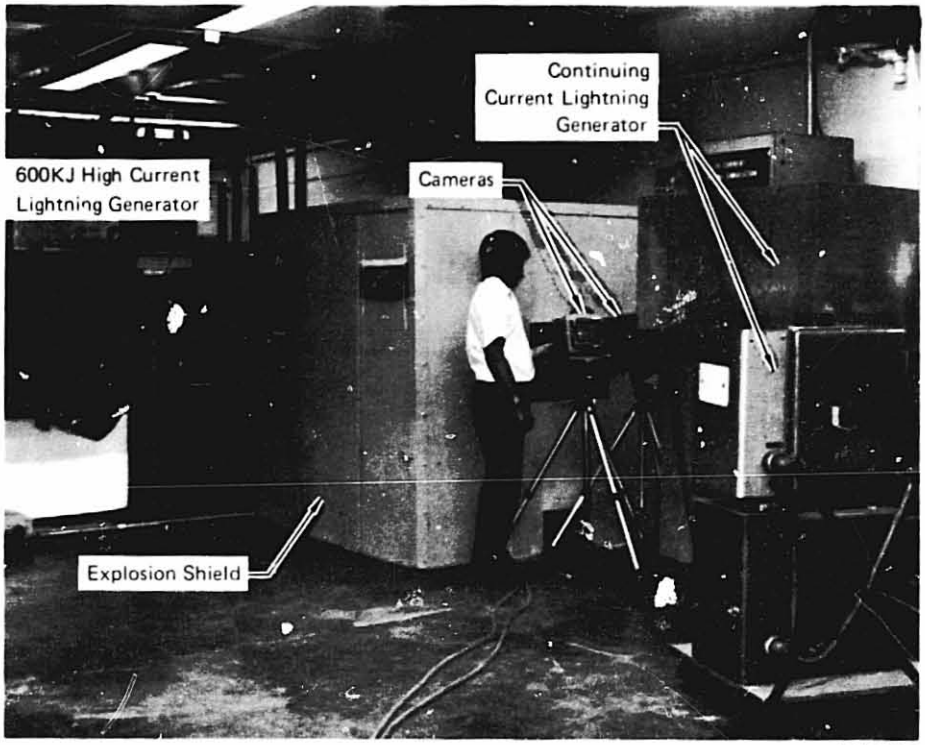

GP76 6622 7

FIGURE 7 – ORBITER OUTER PANEL LIGHTNING TEST SETUP

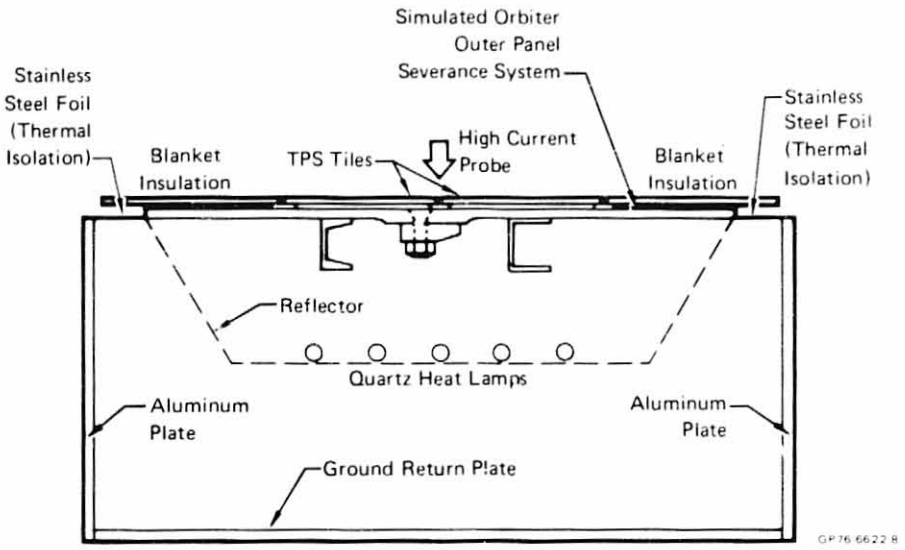

GP76 6622 8

FIGURE 8 – SIMPLIFIED DIAGRAM OF ORBITER PANEL INSTALLATION

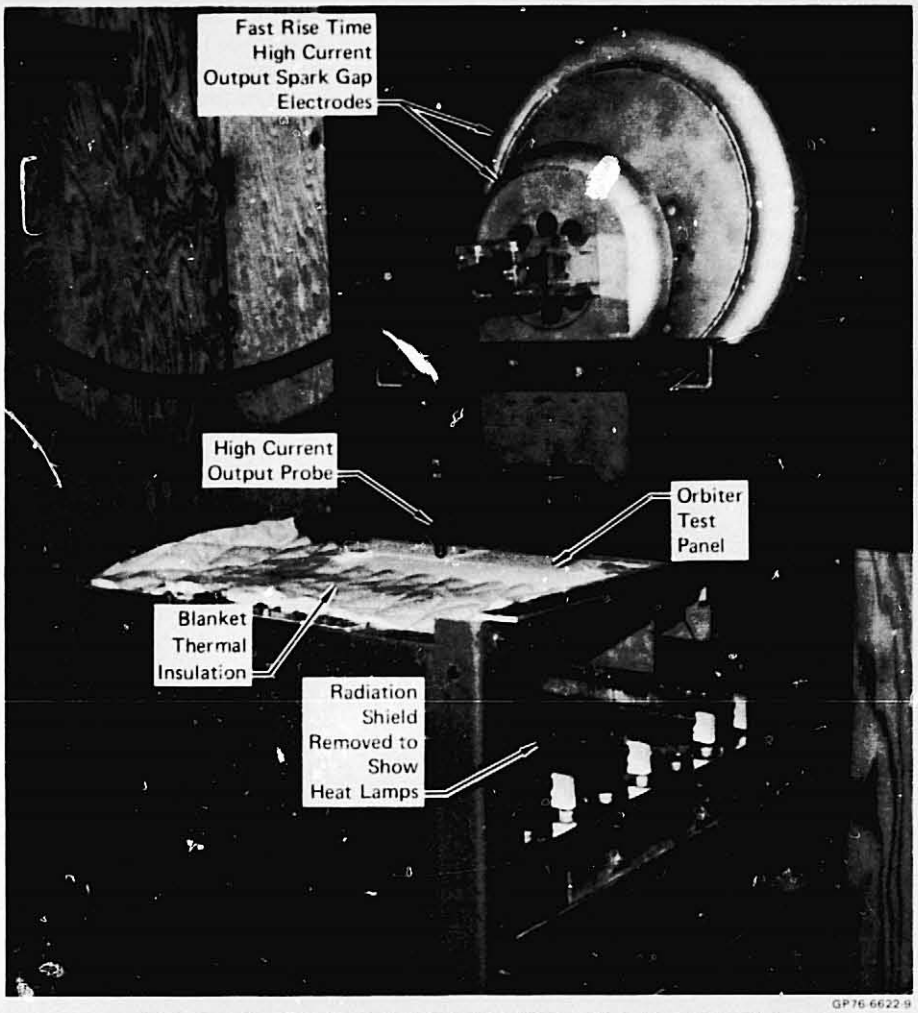

FIGURE 9 – FAST-RISE, HIGH-CURRENT TEST SETUP

Preliminary Test Procedure

(1) Prior to any tests on the simulated Orbiter panel, a piece of filler bar material was subjected to a high-voltage arc to determine its relative dielectric strength and to determine whether a high voltage arc would directly punch thru the filler bar material or flash over the rubber surface to the edge of the material. To determine this, a small high-voltage pulse generator was set up with an output probe to flat plate spacing of 7/16 inch. The voltage output of the generator was then increased in small increments until arc-over occurred. The minimum voltage was 18.2 kV. The filler bar material was then placed on top of the plate and again the voltage pulse was increased until arc-over occurred. The probe-to-plate spacing remained the same.

(2) Prior to the installation of the pyrotechnics in the Orbiter panel, additional preliminary tests were performed to establish final test procedures. The panel was installed in the test fixture and heated to determine the control settings for the heat rate to be used for actual tests. The panel was struck with a fast high-current waveform to verify that accurate and reliable temperature data would be obtained during the actual tests. High-speed movies were also taken to verify camera settings. The Orbiter panel was then removed from the fixture and the pyrotechnics (MDF) were bonded and bolted into the test panel along with the thermocouples.

(3) Before the Orbiter test panel was reinstalled in the test fixture, a dummy plate was installed in the test fixture and struck with the simulated lightning current to verify compliance with the desired waveshape.

TEST RESULTS

Preliminary Tests - The preliminary high-voltage test on the filler bar material showed that the material has a higher dielectric strength than Air because of the RTV coating on the top surface. At a probe to plate spacing of 1.1 cm (7/16 inch), a minimum voltage pulse of 18.2 kV was required to arc the gap. With the filler bar in the gap, the minimum voltage required to arc over was 25 kV. It was also noted that the arc did not directly penetrate the filler bar material but contacted the RTV under the high-voltage probe, tracked across the surface for about 1/2 inch and then punched thru, as seen in Figure 10.

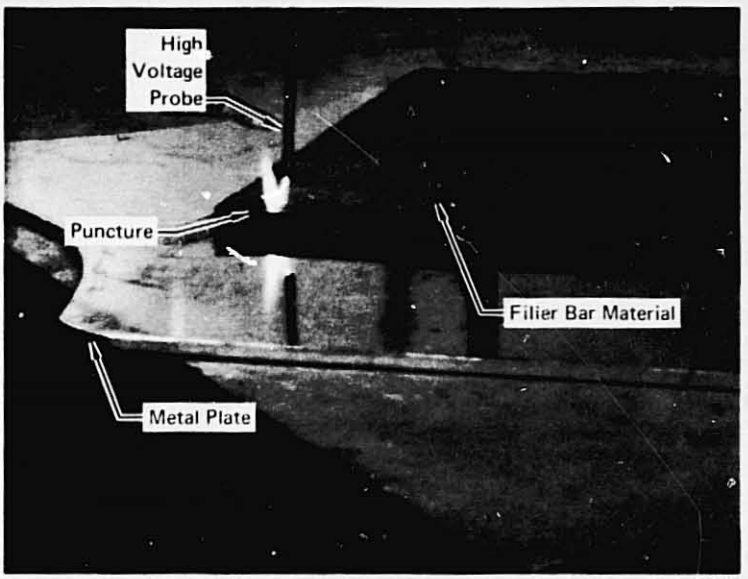

FIGURE 10 – HIGH VOLTAGE FLASH-OVER AND PUNCTURE OF FILLER BAR MATERIAL

Orbiter Panel Lightning Tests - A summary of all the lightning strikes is given in Table I. The panel was struck with the simulated lightning currents while at 325°F. Throughout the lighting tests, the MDF in the panel remained physically undamaged.

TABLE 1 – SUMMARY OF LIGHTNING TESTS ON ORBITER PANEL

Test	Peak Current	Time to Peak Current	I^2t	Charge Transfer	Current Total Time	Max Temp Rise	Notes
Fast Rise Time High Peak Current	180KA	2 μsec	2.3×10^5 A^2 sec.	2.7 Coulomb	≈ 65 μsec	2°F	Arc attachment at edge of filler bar. Damage to SIP and filler bar 3.8 to 4.5 cm (1-1/2 to 1-3/4 in.) dia. Damage to tiles approx 7.6 to 9.5 cm (3 to 3-3/4 in.). Only slight pitting damage to aluminum panel. No visible damage to Pyros.
Full Energy High Peak Current	205KA	25 μsec	1.34×10^6 A^2 sec.	8.2 Coulomb	≈ 260 μsec	14°F	Arc attachment 0.95 cm (3/8 in.) to side of probe in center of filler bar and over to side of intersection of 2 filler bars. Damage to SIP and filler bar 4.5 to 5 cm (1-3/4 to 2 in.) dia. Damage to tiles 9.5 to 10 cm (3-3/4 to 4 in.) dia. No visible damage to Pyros. High speed movie camera failed to function properly.
Continuing Current (High Coulomb)	490 amp Average	≃ 1 msec	9.7×10^4 A^2 sec.	220 Coulomb	470 msec	100°F	Burned 0.63 cm (1/4 in.) dia. hole thru aluminum to epoxy around Pyro. Some RTV continued to burn after cessation of lightning current. No visible damage to Pyros.

GP 76-6622 21

The results of the 2 μsec rise, 180 kA current pulse are shown in Figure 11. Damage to the tiles extends over an area 9.5 cm (1-3/4 inches) in diameter area. The lightning arc did not puncture the RTV used to attach the filler bar to the metal panel as expected; it attached to the metal at the junction of the filler bars and the SIP as shown in Figure 12A. The damage to the metal panel consisted of only slight erosion of the plate over a 0.32 cm (1/8-inch) diameter area. The lightning current waveform is shown in Figure 13. A review of the high-speed movie sequence shows that tile particles are leaving the strike area at an initial velocity approaching the speed of sound. For example, selected frames are shown in Figure 14 and reveal that on the third frame some particles are already 25.4 cm away from the panel. The arc is first seen during frame 1, the exact instant of time of the initiation of the arc during frame 1 is not determinable, therefore the approximate average velocity of the particles during the 2-frame sequence (frame 1 to frame 3) would be 10 inches x 1750 fps ÷ 2 frames = 22.2×10^3 cm/second (8.75×10^3 inches/second).

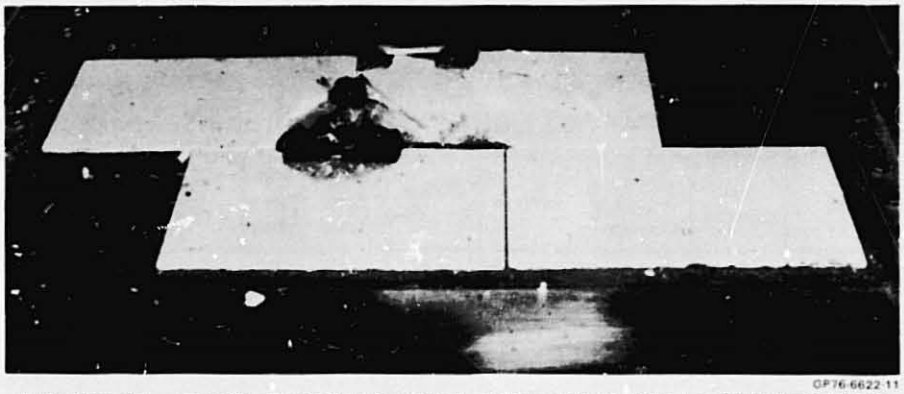

GP76-6622-11

FIGURE 11 – RESULTS OF FAST-RISE, HIGH-CURRENT LIGHTNING TEST

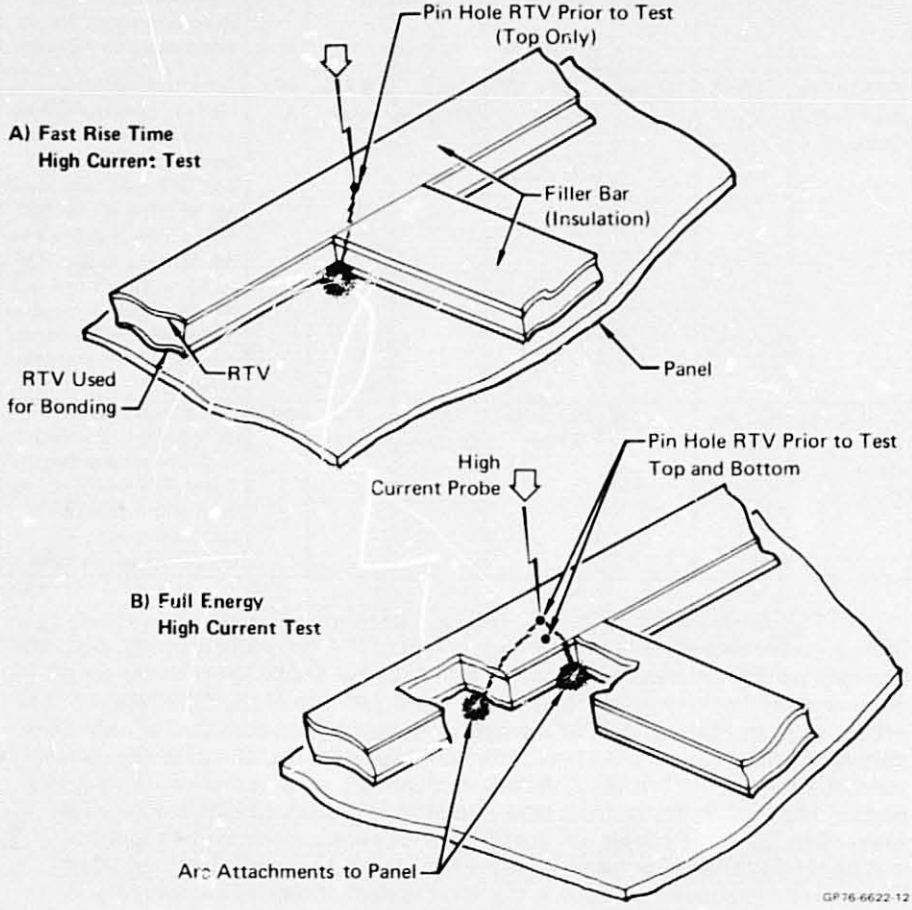

FIGURE 12 – RECONSTRUCTED PROBABLE ARC PATHS TO PANEL DURING HIGH CURRENT SURGE TESTS

Calibration Illustrating
Fast Rise Time (2 μsec)

Vertical: 100kA/Major Division
Horizon: 2 μsec/Major Division

Note: Traces enhanced for clarity.

GP76-6622-13

FIGURE 13 – FAST-RISE TIME, HIGH-CURRENT WAVESHAPE

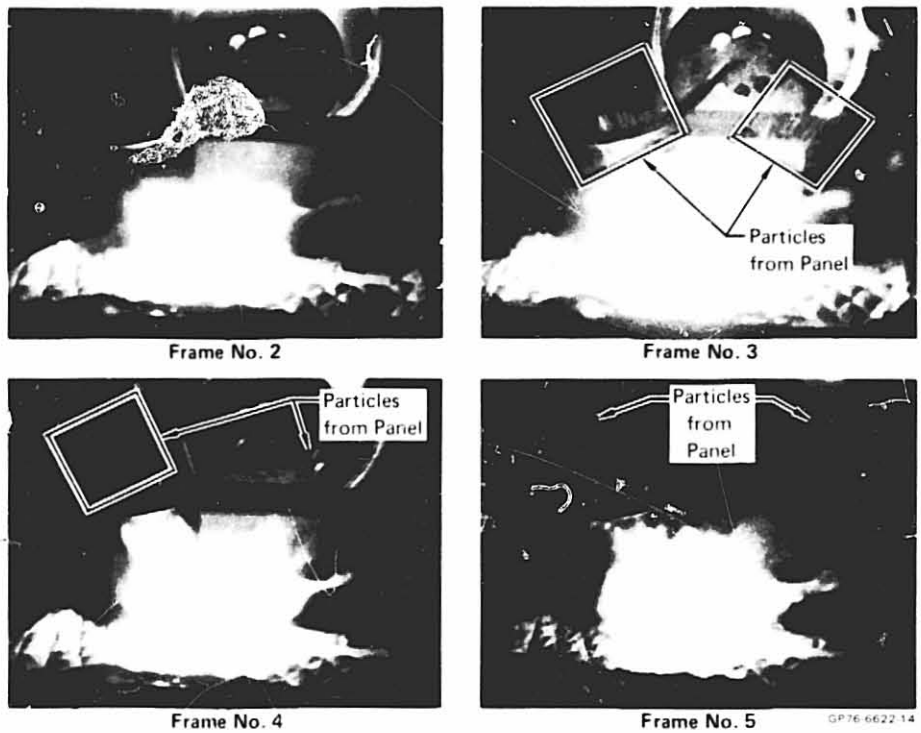

Frame No. 2 Frame No. 3

Frame No. 4 Frame No. 5

GP76-6622-14

FIGURE 14 – SELECTED FRAMES FROM HIGH-SPEED MOVIE OF FAST HIGH-CURRENT STRIKE

Because of the extensive damage to the tiles resulting from the first lightning test, two tiles and associated SIP were replaced prior to the full-energy, high-current lightning test. It should be noted that the NASA supplied tiles had been previously used on an accoustic test and microcracks were observed on the two replacement tiles prior to their installation on the Orbiter panel.

The results of the full-energy, high-current test were similar to those of the 180 kA test except that the extensive damage to the tiles covered an area 10 cm (4 inches) in diameter plus some additional cracking. Damage to the SIP and filler bar was over an area 5 cm (2 inches) in diameter. Although the RTV on top of and under the filler bar was punctured prior to the test, the arc moved to the side approximately 0.95 cm (3/8 inch) before puncturing the RTV and attaching to the metal plate. Although most of the current went thru the aforementioned hole, another arc attachment point was noted at the edge of the filler bar bond line (Figure 12B). The lightning current waveform is shown in Figure 15. For this test, the continuing current was intended to immediately follow the high-current pulse, but it did not. It was therefore necessary to perform a separate high coulomb test. This later test was performed at the same test location without replacing tiles, SIP or filler bar materials (the reasons for doing this are discussed in the next section).

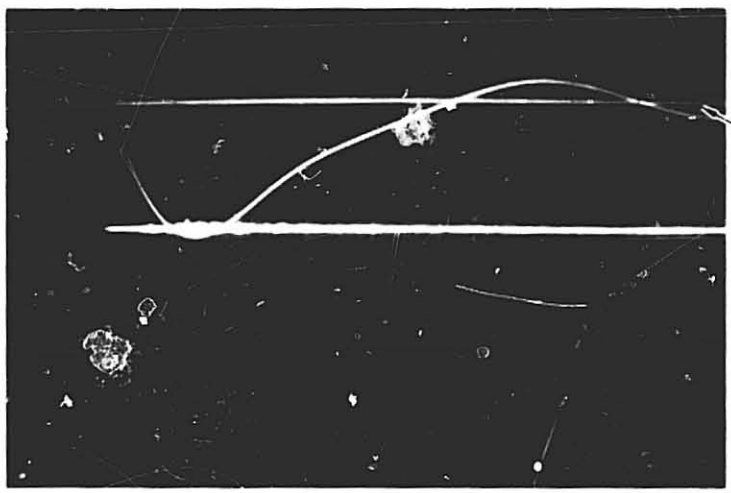

Vertical: 100 kA/Major Division Horizontal: 20 μsec/Major Division

GP76-6622-15

FIGURE 15 – FULL-ENERGY, HIGH-CURRENT WAVESHAPE

The results of the high coulomb (continuing current) test are shown in Figure 16 and the current waveform is shown in Figure 17. For this test the probe was located over the hole previously blown in the RTV used to bond the filler bar to the aluminum panel. After the lightning current ceased, some of the exposed RTV continued to burn for about 20 seconds. Other than this there was no additional damage to the tiles. However, a 0.63 CM (1/4-inch) diameter hole was burned thru the aluminum plate down to the epoxy material surrounding the pyros. The molten aluminum bubbled out of the hole and formed the blister shown in Figure 16 just underneath the output probe. After the aluminum bubble was manually broken and peeled away, the epoxy used to bond the pyros was clearly visible. Some of the epoxy

was then scraped away to reveal the exact location of the pyro as shown in Figure 18. Radiographs of the panel at the burn thru area showed that the thermocouple junction was approximately 0.13 - 0.19 CM (0.050 - 0.075 inch) away from the edge of the hole. Temperatures measured during the various lightning tests are shown in Figure 19 and show that the heat energy input to the pyros was small.

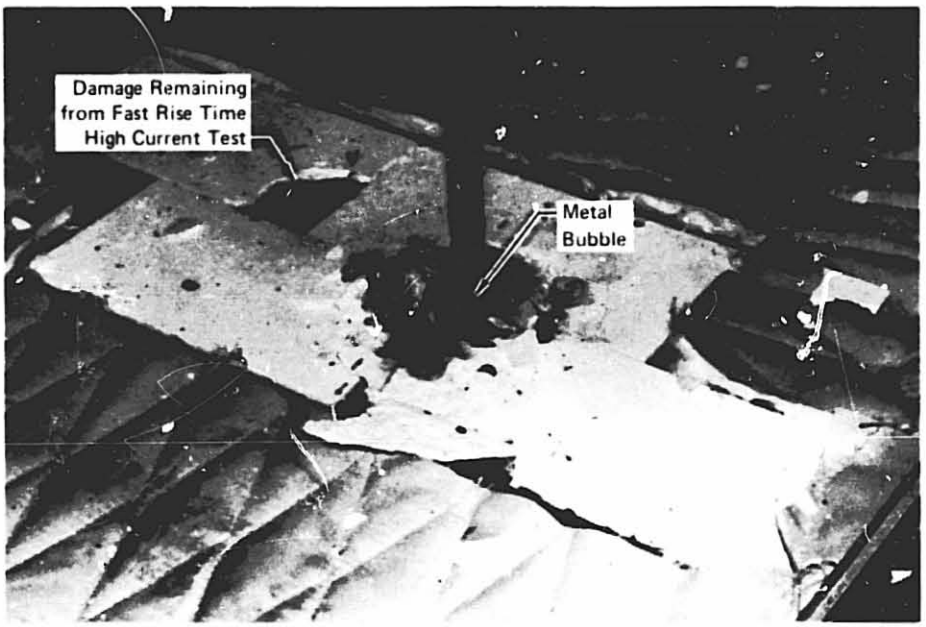

GP76-6622-16

FIGURE 16 – RESULTS OF CONTINUING CURRENT TEST

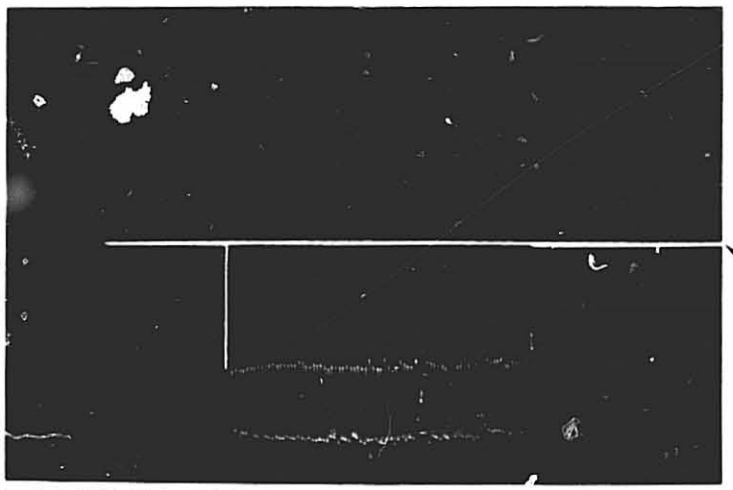

Vertical: 200A/Major Division Horizon: 100ns/Major Division

GP76-6622-17

FIGURE 17 – CONTINUING CURRENT WAVESHAPE

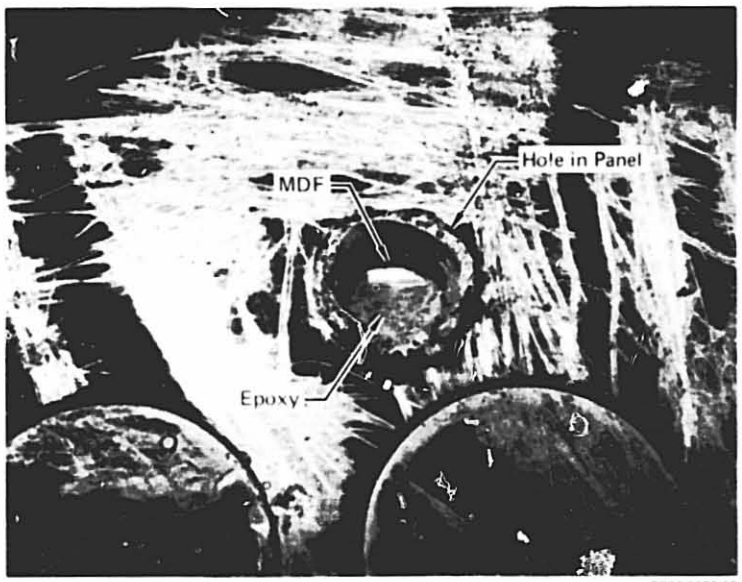

FIGURE 18 – CLOSEUP OF DAMAGE AFTER REMOVAL OF EPOXY TO SHOW MDF

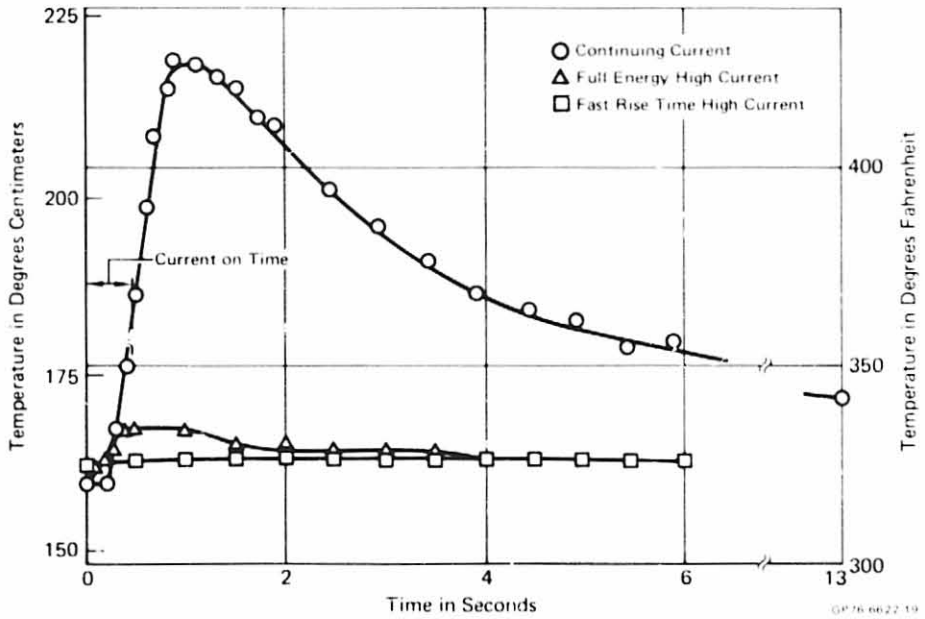

FIGURE 19 – TEMPERATURES AT PYROS DURING SIMULATED LIGHTNING STRIKES

Pyrotechnics Evaluation – After all lightning tests were completed, the MDF's in the panel were connected to a detonator cap and the cap was initiated. The results of this test is shown in Figure 20. The detonation velocity was measured 6,957 meters per second (22,818 ft/sec) which is approximately midpoint of the acceptable limits of 6500-7100 m/sec indicating that the MDF had not been damaged by any of the lightning strikes to the panel.

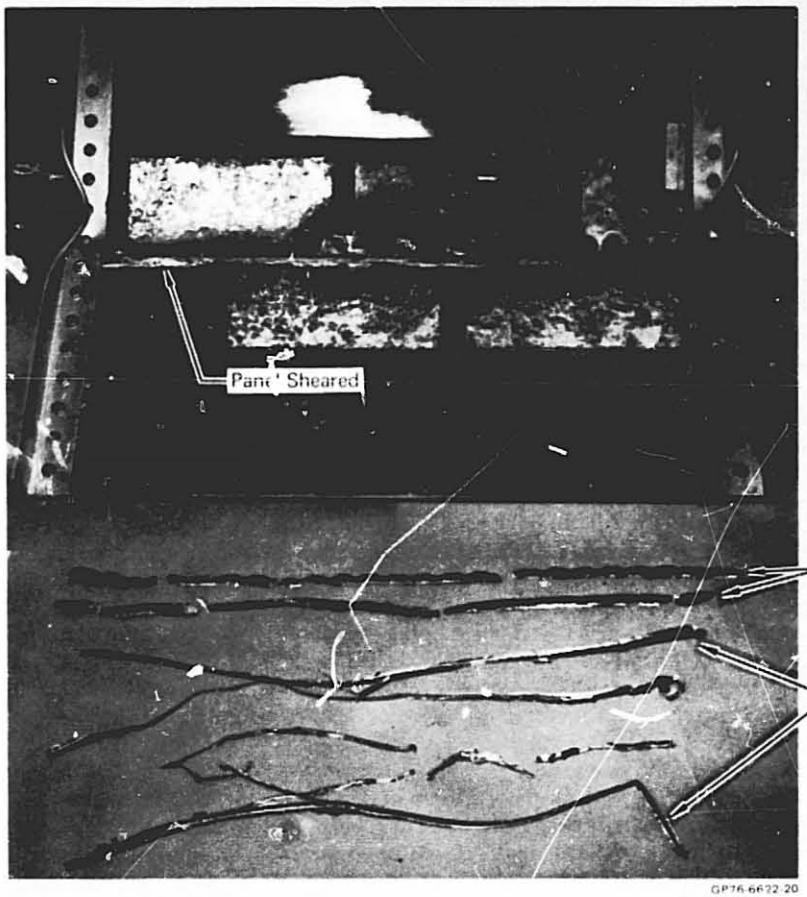

FIGURE 20 – RESULTS OF DETONATION VELOCITY TEST

DISCUSSION OF TEST RESULTS

The fast rise-time 180-kA current pulse produces the initial fast rising shock effects of a natural lightning strike. However, the actual shock effect on the pyros may have been diminished somewhat because the current attach point to the metal panel was diverted to the side of the filler bar and therefore did not attach directly over the pyros as expected. Although the arc may have penetrated the RTV on top of the filler bar as provided by the pin holes, the arc apparently found a path of less

impedance to the 'e of the RTV used to bond the filler bar to the panel rather than penetrating thru it, a phenomenon similar to that previously noted for the smooth RTV on the top of the filler bar.

The continuing current of the NASA lightning waveform model provides the principle heating effect on the panel, and in our test it was intended to immediately follow the high-current pulse without a time lapse between the two; it did not, and therefore a separate continuing current test was required. It is believed that the two tests present a valid overall test and that the tests do still comprise a "worst case" test. The reasoning and noted anomalies are given in the following paragraphs.

The damage to the tiles resulting from the full-energy, high-current test is greater than, but comparable to, the damage resulting from the fast rise-time 180-kA current pulse. The velocity of the materials leaving the scene of the strike is therefore believed to be comparable for the two high-current tests. Thus, the material from the strike area would be blown away 5.8 cm (2.3 inches) from the strike area at the time that the high-current would have decreased to 500 amperes. Under these conditions there should not be any interaction between the continuing current and the particles from the panel and therefore a separate continuing current test should be valid.

After the full energy high-current test, it was noted that there were not one but two arc attachments to the panel. Although the debris from the panel was out of the arc zone at the time the high-current pulse ceased, ionized gases continued to linger for an extended period of time as noted in the photos in Figure 14 (the arc current lasts for less than the time of 1 frame). Therefore, if the continuing current had followed the high-current pulse at that time, then the continuing current would probably have been divided with a percentage going to each attach point, the one directly thru the RTV used to bond the filler bar to the panel, and the other off to the side (at the intersections of the filler bars) over 1.3 cm (1/2 inch) away (see Figure 12B). If this had occurred then the damage would have been much less than that which occurred during the separate continuing current test where the current was introduced into a single attach point. Since the test conditions for this series of tests were intended to be "worst case," it was decided, after consulting with NASA, that the continuing current would be introduced at the hole punched thru the RTV directly over the pyros. The initial high current lightning pulse would have previously removed the tiles and therefore no attempt was made to replace tiles, SIP, or filler bars before the continuing current test.

The voltage in the continuing current power supply is only about 400 volts, therefore, it is not sufficient to throw a 1.3 cm (1/2 inch) spark to a test panel; however, it is more than sufficient to maintain the arc, once it is established. Therefore, to start the arc, a 0.013 cm (0.005 inch) diameter copper wire was placed between the output probe and the desired arc attach point on the test panel (in this case the hole blown in the RTV residue left from bonding the filler bar to the panel). In a fraction of a second after the current starts flowing, the wire vaporizes and becomes a part of the ionized path between the panel and the probe. The vaporization of the wire is rapid but not so fast as to give a significant explosive shock effect which would damage the tiles. Because the arc was confined by the RTV, the heating and melting of the metal panel was confined to a small volume, and resulted in a hole thru the panel. Apparently the heat from the arc and molten metal at the bottom of the hole in the panel caused some gaseous products to be generated from the epoxy over the pyros because a bubble of metal protruded over the RTV and up to the output probe. It appears that this bubble occurred after the arc had ceased because although the bubble touched the probe it was not mechanically attached in any way. After the metal bubble was manually broken away, the interior of the hole in the plate was observed to be relatively smooth and clean with the mid-depth of the hole

being slightly larger in diameter than either the entrance hole near the probe or the exit hole near the epoxy (over the pyros). The epoxy surface was slightly blackened but the damage did not extend any significant depth; estimated to be a couple thousandths of an inch. The epoxy was scraped away to reveal the undamaged sheath of one of the pyros as shown in Figure 18. The epoxy apparently provided a heat barbier between the molten aluminum and the pyros and also provided an electrical barrier keeping the arc from directly attaching to the metal sheath of the MDF. If the epoxy has not been over the MDF, then the pyro may have been "dudded" or possibly even detonated.

The continuing current test produced the heating effects of the continuing portion of the lightning model. The total coulombs transferred to the panel was slightly greater than the 200 specified in the Space Shuttle Lightning Protection Criteria Document, JSC-07636, Revision A, but even under these conditions, the MDF remained undamaged as evidenced by the results of the detonation test.

These tests revealed the significance of a thin layer of RTV in diverting the arc attachment point from one location to another. It, therefore, seems that an extra thick coating of this RTV, applied to the metal plate directly over the pyros (with bare metal to the sides of this rubber strip) could cause the arc to flash to the metal to the side of the pyros. On both sides of the pyros the metal is approximately twice as thick as it is over the MDF; therefore, the only significant damage would be to the tiles.

CONCLUSIONS

From the results of these tests on a simulated Orbiter panel, it is concluded that the Orbiter outer panel escape system is adequate from a lightning point of view so that if a direct lightning strike attached to the Orbiter brow in the vicinity of the MDF pyrotechnics, the pyrotechnics would remain undamaged.

REFERENCES

1 *"Simulated Lightning Test, Shuttle .03 Scale Model," McDonnell Douglas Corporation, Report No. MDC A3155.*

2 *"Space Shuttle Program Lightning Protection Criteria Document," JSC-07636, Revision A, November 4, 1975.*

3 *"Lightning," by M. A. Uman, McGraw Hill, New York, 1969.*

4 *"A Ground-Lightning Environment for Engineering Usage," by N. Cianos and E. T. Pierce, Stanford Research Institute Technical Report 1, SRI Project 1834, August 1972.*

5 *"Standard Operating Procedure for Armament and Explosives Laboratory." Appendix I, "Guidelines for Measurement of Projectile, Detonation and Fragment Velocities." McDonnell Aircraft Company, Report No. A.E.L.10.*

Paper No. 11

TELEMEDICINE; AN EXPANDING NEW SCIENCE ON LAND & SEA

K. R. Jackman, *Biomedical Consultant, La Jolla, California*
Anthony J. Rippo, M.D., G.P., *President, Marine Medical Service Inc., San Diego, California*

ABSTRACT.

Several medical and technical men in San Diego County have long been concerned with the need in many rural communities for a 24-hour day, 7-days a week access to adequate medical care. People isolated from urban areas by travel-times of 40-minutes tend to delay seeking early and effective medical care. The authors have been able to assemble quality technology, within a reasonable budget, which permits narrow-band video-pictures, better known in the 'CB' trade as 'ROBOT' slow-scan television(SSTV), to be transmitted over telephone lines, by micro-wave, through satellite-bounce, or by 'HF' radio. These 'ROBOT' pictures can be accompanied with explanatory 'audio' communication and with diagnostic signals from electronic instruments.
Remarkable progress is being made in San Diego County by physicians, remote clinics, fishing fleets, and deep-sea drilling crews in using 'Audio/Video' and 'SSTV'/ROBOT technology of medical diagnosis and treatment of critically-ill patients many miles away from the medical center. Earlier programs for extending health care have been promising and somewhat effective, but todate they have been much more complicated and costly than the present San Diego trials of 'ROBOT' Telemedicine on land(over telephone lines) and sea(via 'HF' radio).

INTRODUCTION.

'Telemedicine' is the art of applying communication technology through nurse-practioners, paramedics, corpsmen with special training, or even less-trained personnel, in areas of human habitation remote from physicians and hospitals, to provide primary health care, under a physician's guidence, to patients through audio/video communication, for the diagnosis

and management of health problems.

Although recent data from the American Medical Ass'n (AMA) indicate that an increasing number of new physicians are choosing to specialize in 'general' and 'family-practice', at the present rates of population growth, the assurance of access to quality health care at reasonable cost in rural areas is a problem which will be with us into the next century. Meanwhile, the the communication technologies that are being built in to space probes will permit physicians direct aural and video contact with isolated 'physician-extenders' and patients in medically-deprived areas on land and sea, so as to make satisfactory discriminations between serious medical conditions requiring extensive technology and those which do not, and to direct the local treatment of the latter. A wide range of capabilities of the 'physician-extender' in the new art of 'telemedicine' can be tolerated in isolated communities on land or in the crews of ships at sea.

The authors of this first of several reports to the scientific and medical press, on the applications and advancements of 'Telemedicine,' are conscious that the startling technologies that have been developed for the 'Mariner' and 'Apollo' and other space probes can be applied, with negligable changes, to extend physician services into rural areas. In addition to these programs referenced or discussed in the text, the authors wish to acknowledge that C.V.I. Systems of Boulder, Colorado markets equipment which is similar in function to that which we have in operation. This paper is intended to show what had been done locally rather than be a product endorsement.

RECENT AUDIO/VIDEO 'BREAK*THROUGHS' IN HEALTH CARE.

'Telemedicine', although a relatively new art, combining the best efforts of the physician, the engineer, and the scientist, has been quietly practiced over the last four-years in San Diego County by radio(audio-HF) transmissions between a local physician and the working crews of the 'Tuna Fleet' operating around the world, through 'Marine Medical Service, Inc.', a San Diego firm dedicated to providing medical services for fishermen at sea.

To the sucessful 'audio', or verbal instructions by radio(HF) from the physician, it is now possible and practical to add the benefits of 'Slow-scan' pictures (SSTV) of the sick or injured patient. This continuing program, sometimes referred to locally as 'ROBOT 1' after the local manufacturer-- ROBOT Research Inc.,

augments the 'HF'radio instructions in that the physician in his San Diego office or hospital can more accurately diagnose the health problem or critical emergency by 'seeing'the patient, 'look' at the wound, and even 'view' the X-ray film of the injured part before taking action.

Simultaneous with the 'Audio/Video' provision of health-care to fishing fleet crews, there is a program underway in San Diego County whereby small health outposts in rural communities, medically deprived since they are too few in population to support a full-time doctor, can by the 'ROBOT'-method maintain better rural health conditions, Thus these two programs; one on oceans around the world, and the other in 'outpost' clinics in the outer San Diego County areas, can augment each other and learn from each other's problems, successes and failures.

A'ROBOT'LIFELINE TO BETTER MEDICAL CARE.

The objective of the sea and land 'ROBOT' projects in Southern California is to provide the technology, 'hardware', and the 'software' to permit adequate 'Audio/Video' communication between the physicians,on a 24hours/day, seven-days/week basis, and their indivually-trained nurse-practioners or 'physician's-assistants at the rural 'outpost' or on board ship, each of whom are normally a medically-deprived group of people. To these isolated communities can now be added the 30 to 70 men operators on 'off-shore' oil-drilling platforms, or on deep-sea mineral-mining ships operating on remote assignments for long periods of time, in many instances located in distant ocean areas out-of-range of helicopters and CoastGuard airplanes.

The emphasis, within the last several years, of the U.S.Government in extending the NASA/Space technologies, developed in the 1960s and 1970s, to small businesses and industry, gave these authors the hope that, with the typical dynamism of American Industry, someone would put this 'Audio/Video' medical technology together and market an efficient, low-cost health plan for isolated areas. Todate this has not happened to any satisfactory degree. True, there have been several Federal-grants given for primary health and emergency care in isolated communities, but little use has been made of the cheapest and most-dependable method of signal transmission;- the telephone system on land, and 'HF'-radio at sea. More exotic and expensive methods, such as Interactive Television communication have been developed for extension into rural areas with the use of Federal funds, involving micro-wave, satellite

bounce, laser, picture-phone, etc., but little use has been made of the less expensive and generally more dependable method of communicating over long distances which telephone-lines provide in these United States.

'ROBOT-1' will be concerned, first, with the expanded use of telephone lines into 'out-back' rural communities, and from sea 'HF'-stations to physicians' offices and hospitals. Future emphasis, possibly in 'ROBOT-2', on alternate transmission methods of medical information from isolated areas without adequate telephone services, after statistics on costs, practicality, maintainability, and the ease of use have been collected and studied.

Many 'isolated-area' test programs have been , or are now being tried through 'Telemedical' methods into rural areas in the United States. Some examples are the 'STARPACH/ NASA', Indian Health Services on the Papago Reservation, Arizona (by micro-wave); 'NASA'-Simulated Telemedicine Systems, Houston, Texas; 'Apache'; 'NASA'/ Canada CTS, San Antonio, Texas,(Satellite), etc. These projects, where applicable in results to the present San Diego 'remote-health' efforts, will be briefly reviewed in a future paper, to form a background against which these authors can evaluate the San Diego County 'ROBOT' program. This medical evaluation will be made using prototype 'SSTV' Audio/Video equipment for pilot-runs in Southern California rural clinics, in medically-deprived urban areas, on ocean-going San Diego fishing ships, and on isolated 'deep-sea mining'ships and 'oil-drilling rigs' in the Pacific Ocean.

'ROBOT-1' Software and Hardware.

Today's technologies will permit physicians, clinics, and urban hospitals to work effectively with direct 'SSTV'-communication, transmission of photo-electric cardiograms, accurate heart and lung sounds, pictures of eye-grounds, photo-micrographic pictures of laboratory specimens, transmission of photo-fluorograms of fair resolution, pictures of the fundus, lesions, and readings of temperature, blood pressure, and blood flow.

The authors have found in the past few months that all necessary 'hardware' is available locally in San Diego, as 'shelf-items', to combine the necessary 'Audio/Video' phases of 'ROBOT-1' for the benefit of patients in medically-deprived areas on land or sea, that 'SSTV'-Video transmission of rediograms from conventional X-Rays on a 'light-box' over telephone lines or by 'HF'-radio is not only practical(Ref.#3)

but easily diagnosed through a white/black reversal process on both 'ROBOT'-Models #400 and #530 transceivers, and that only minor modifications of 'software' in techniques of camera focussing remains to be 'proofed' with actual longdistance telecommunication 'pilot-runs' to remote clinics or to ships at sea. It is firmly believed by the biomedical consultant member of 'MMS', San Diego, that a new breakthrough in Telemedicine will take place in the next six months by remote patient medical diagnosis from a local San Diego physician's clinic, by combining the proven methods used during the past four-years on 'tuna-seiner' ship-crews medical programs by 'Marine Medical Service Inc.', in San Diego, with the medical needs and selfsupporting potential of doctor-deprived small communities 'out-back'(as we say in Australia.)

There is no doubt that a single institution, such as UCSD in Southern California, with sufficient financial support, could work with aerospace systems technologists and develop the attendant technology. On the other hand, more is necessary than that approach, since now maretime agencies are involved, such as the application of 'ROBOT-1' to deep-sea drilling rigs and mining ships. All 'AUDIO/Video' equipment must be assembled, tested, calibrated, and built into the community structure in a substantial number of areas on land and sea, before it becomes a sensible and accepted form of remote health care.

The authors believe that health care in rural land areas can be much more effective if 'licensed clinics' manned by 'lay' local medical personnel, can be managed and serviced by professional medical agencies and physicians in urban communities. Such 'Rural Clinics' can be licensed as a satellite of the physicians' home offices. The physician in each case is totally responsible for the 'emergency' training and effective use of the 'satellite clinic'(or 'Outpost') lay personnel.

Medical Simplification Needed At 'Outposts'.

In practical rural health care the need at this moment is a quantum jump backward in our technological approach. Most rural communities have electricity and telephone lines. Our health care needs in isolated communities can be 85 to 90% satisfied by something less than full-color 'video'transmissions between rural clinics and urban or suburban medical centers. Black/white 'Video-transmissions of radiograms have proved very sucessful.(Ref.#3)

More important than a mobile clinic, microwave relay station, etc., for the primary care in rural areas may be an 'emergency' installation, like 'ROBOT-1', which is always available at a center-village agency; perhaps at a Fire Station, Sheriff Station, or at a Park Ranger Headquarters for 24-hours each day. Here local 'trained' townspeople can attend the sick or injured, with professional medical advice available through the 'Audio/Video'-link to a distant physician for diagnosis and followup instructions. This 'remote-instruction' system may be of more lasting value to the patient than a mobile medical unit which pulls into town once a week for 'sick-call'

In developing countries around the world, and in some isolated parts in the United States, where the telephone services are absent or undependable in outlying communities, the writers propose to use a modification of 'ROBOT-1' in which some other transmission method, such as 'microwave' or 'satellite-bounce' will be evaluated for economy and then proofed.

Alternates To 'ROBOT-1' System.

As many of our readers probably know, Lockheed Missile and Space Division, at Sunnyvale, California, has a telemedicine-system, called 'STARPAHC', working in the Papajo Indian villages in Southwest Arizona. This project serves over 10,000. people, in 75 villages, in an area of nearly 17,000. square kilometers. This system uses relatively high-level technology, with large capital expenditures. (Ref.#1) Radio Corporation of America, too, has developed equipment modules now being used by the U.S.Navy in several installations to achieve similar communication objectives.(Ref.#5&#6) Too often it appears that whenever NASA technologies are brought to bear on health problems, in urban or rural areas, an attempt is made to apply 'Goldstone technology' and complexities without first considering the capacity of our Nation to meet such expenditures and to provide for such advanced technology support.

'ROBOT'-SSTV differs from more than thirty telemedicine projects outlined by Dr. Sur Wah Chan and Mr. James R. Messick of 'OMERAD', Michigan State University, East Lansing, Michigan. (Ref.#2) in 1975, in that 'Audio/Video' communication is used over telephone lines in the current program in San Diego. The two-way 'hear & see' capability is being applied simultaneously to rural mountain areas and to wide ranging ships. Not one of the Federal Grant programs reviewed in Reference#2 used telephone lines for communication.

Possible 'ROBOT-1' Health Funding.

With today's technologies, the full-range of 'telemedicine' supportive communication in the USA, from rural areas to urban health centers, would require capital expenditures comparable to those involved in building our modern highway systems. Althoug it is possible that the value of such an investment for 'physician extenders' might be argued successfully, the authors question whether this Nation is prepared, this year or for a few years to come, to undertake an investment of this magnitude in rural health services.

Our colleagues at the University of New Mexico were demonstrating over four years ago that physician to 'physician-extender' liaison into isolated and medically-deprived areas can be effectively carried out on a communication level far below that suggested in the preceding paragraph. Given sufficient interest, technical dedication, and a small capital investment, it will be possible within a year to develop and assemble 'low-cost equipment' packages for permanent placement in rural communities, sometimes referred to as medical 'Outposts', in the 'outback' to Australians. These village 'Clinics' will be attended by two or more local inhabitants who have been thoroughly trained by the 'referral physician' in an acute-care hospital or doctor's office, also equipped with similar 'Audio/Video'medical equipment, better known as the 'Medical-Center'. Note-- The foregoing paragraph was drafted three-months prior to this final typing for the 1977 NASA Space Symposium and the prediction of 'one-year' has taken place in a few months by discovering in San Diego a small company, ROBOT Research Inc., which has developed a 'Slow-Scan Television' (SSTV) system for the amateur 'Ham-Radio' market. This fortunate find locally has resulted in the tests of ROBOT-Model#400. (Figures 1 and 2). Plans are now being made to evaluate the new ROBOT-Model#530, a simplified version for use in rural clinics and on tuna-seiner ships.

There is high potential in the use of 'ROBOT-1' programs in present medically-deprived rural areas and for the application of direct service pre-payment financing methods, with formal organizational linkages between such rural primary-care physicians and teaching hospitals. This proposed 'ROBOT-1' system between primary-care physicians and the 'outback' rural towns is immediately suggestive of new forms of successful 'HMOs' for the 1980s.

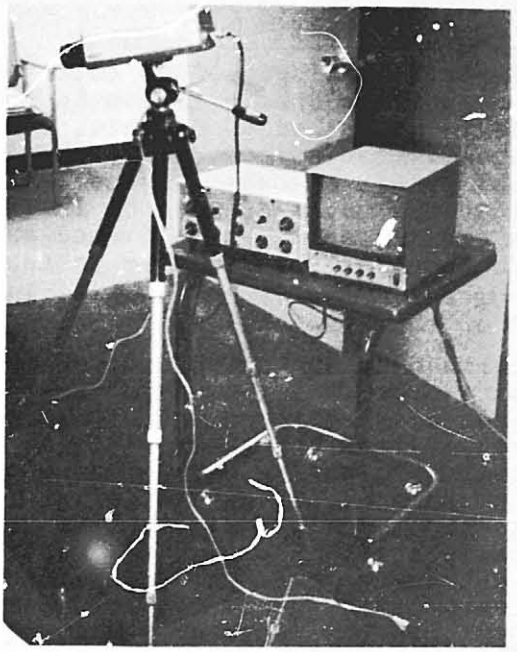

Figure#1. Typical Setup of 'ROBOT-1' System in a Physician's Office.(Model#400.)

Recent Evaluations Of 'ROBOT' Model#400 Systems.

Three-months ago, when the first draft of this paper was prepared on the initial uses of the 'Audio/Video' communication concept to aid rural health situations, few photographs of test results were available, since this 'LifeLine' concept of telemedicine was so new in San Diego County.

The financing of such medical systems in the next few years on the basis of small Federal 'grants' is a short-term solution for a long-term problem. This rural health deprivation problem will not go away without our long-range planning and financial help. The public needs to build financial mechanisms which will support the continued existance of medical-aid systems similar to 'ROBOT-1' across this Nation, and in many medically-deprived developing countries.

A 'consortium' of funding might be desirable. 'HMO' funding for service to the medically-underserved comes readily to mind. Department of Defence funding might be possible inasmuch as the clinical types of equipment likely to be specified in these projects would be of immense utility to the military in battlefield and shipboard applications.

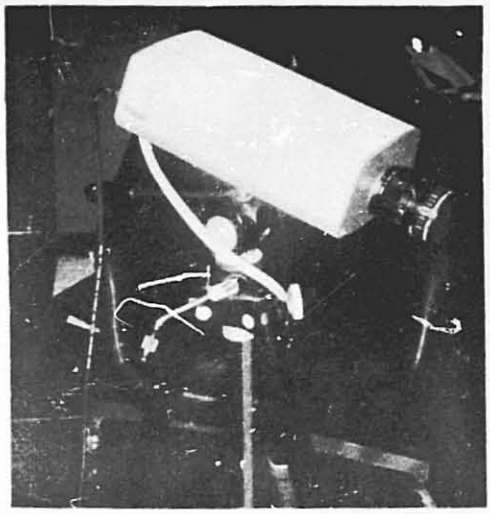

Figure#2. RCA-1000 'SSTV'-Camera, Mounted On A Tripod, And Equipped With A Special 25mm. Lens.

Today, however, with three 'ROBOT' Model#400 systems in use; in the Campo Indian Reservation Clinic (80-mi. South-East of Downtown San Diego), at Dr. Anthony Rippo's medical office in San Diego, and at K.R.Jackman's residence in La Jolla(10-mi.North of San Diego), frequent 'SSTV'-tests have been made over telephone-lines, and recorded with a Minolta Pocket Autopak#270 camera as shown in Figures#1 to #12. Note that the 'ROBOT' Model#400 Scan-Converter has a switch whereby an X-Ray photo might be changed from 'positive' to 'negative' for easier interpretation, as shown in Figures #6 and #7. More engineering specifications on the 'ROBOT' Scan-Converters or Transceivers(on Model 530), shown in Figgures #4 and #5, are available for the reader if requests are directed to the authors.

With four more months elapsing before the Los Angeles presentation on April 26, 1977 by the authors, a color-slide presentation will illustrate the up-to-date test results of newer 'ROBOT' systems, beyond the scope of this paper. 'ROBOT' Model #530 should have been evaluated by that date, both on land and sea.

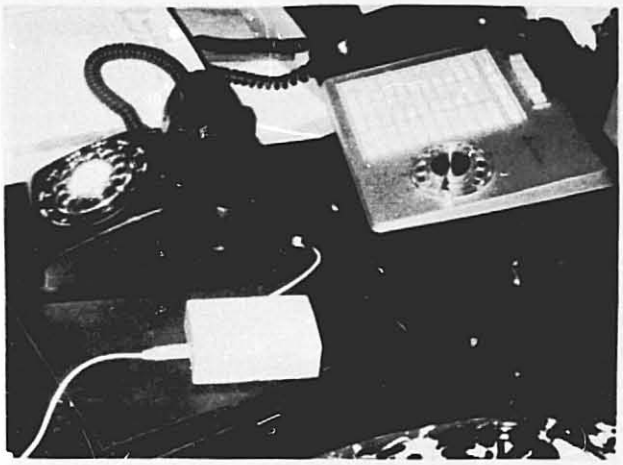

Figure#3. 'SSTV'-Transmission Is Possible Over Telephone Lines Adapted With A Patch Plug.(May be installed on all telephones.)

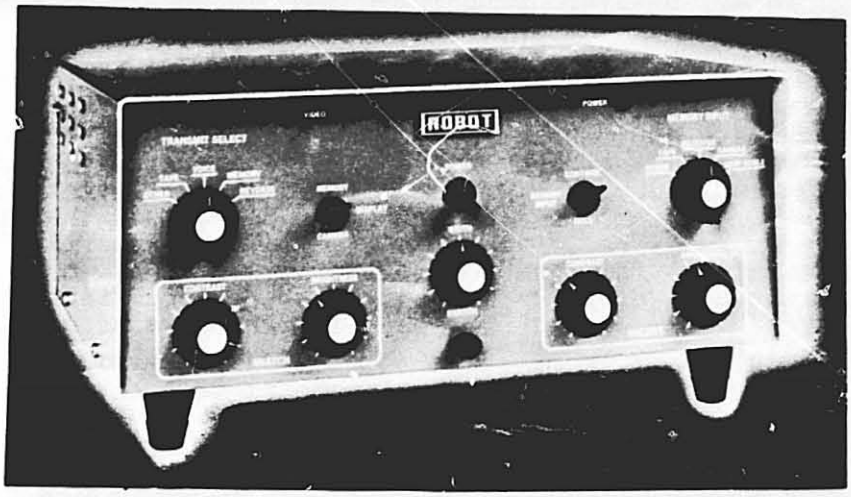

Figure#4. 'ROBOT'-Model#400 Scan-Converter Is Now In Use In San Diego Rural Areas.

Probable 'Futures' For The 'ROBOT-1'Concept.

Looking into the future, say five-years hence, the writers believe that the prestige and backing of academic/medical centers will be necessary in introducing and operating the 'ROBOT-1'system. or a compareble remote area medical program, on a continuing basis.

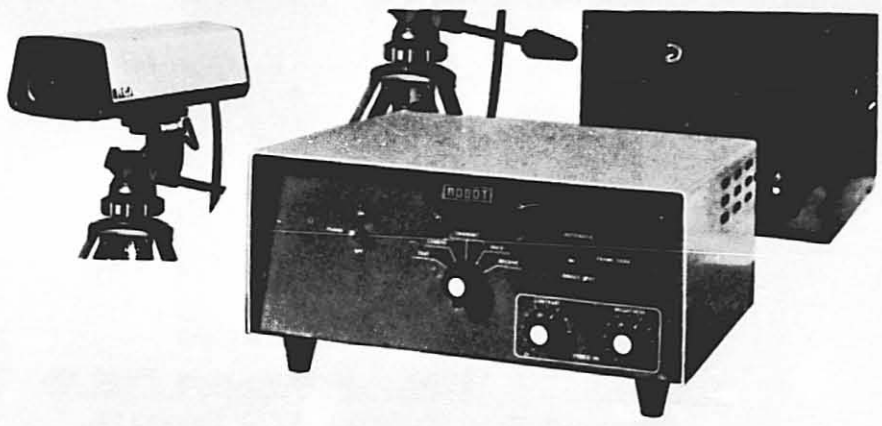

Figure#5. 'ROBOT' Transceiver Model#530 Is Simple To Operate And Will Soon Be Evaluated With Model#400.

Figure#6. 'ROBOT'-#400 System Used To Transmit Bone X-Rays, As A Negative, Between Rooms In A Doctor's Office.

In fact, a 'consortium'of such academic centers in Southern California, with their joint expertise and resources, when combined with independent 'non-profit' research institutions, and with one or more firms with aerospace technology capabilities would add impact and national prestige to this home-grown San Diego 'Audio/ Video' project.

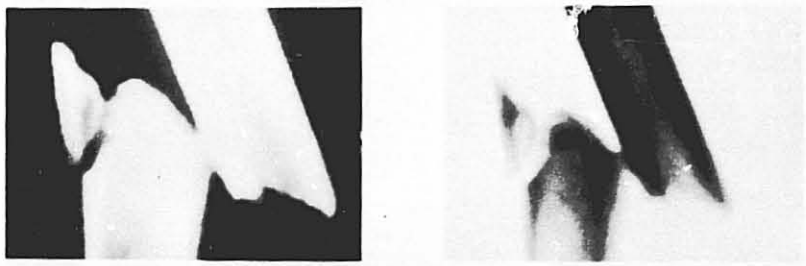

(Positive) (Negative.)

Figure#7. Broken Femur Leg-Bone Displayed On 'CRT'-Monitor. P or N By Switching.

A recent book --"Telemedicine", released in 1975 by eighteen authors, and edited by Dr. Rashid I. Bashshur, PhD, et al.(Ref.#7) defines 'Telemedicine' as the remote practice of medicine via 'interactive communication links'. This book, one of the very few dealing with this new and novel medical approach to better rural health, gives as its ultimate purpose --"to provide an objective analysis of the potential benefits and pitfalls of 'Telemedicine' as an alternate solution to today's pressing problems of health services delivery and as an inevitable trend for the future." With this statement of health experts in mind, would it not be exercising good judgment here in San Diego County where 'ROBOT' SSTV-video is designed and built, to apply this low-cost and effective method of 'physician extender' to medically-deprived areas?

Figure#8. The First Successful 'HF'-Radio Transmissions On 'ROBOT'-Model#400 Were Made On Only 5-Watts, In November 1976, From This Tuna-Seiner In San Diego Harbor.

CONCLUSIONS.

This preliminary introduction to the present and probable extended use of 'Telemedicine' in rural areas of San Diego County, on commercial fishing ships and pleasure yachts around the World, and on deep-sea

drilling rigs and mining ships at remote parts of the Pacific Ocean may be of only passing interest to many readers. However, it will be of vital, life-saving impact to physicians interested in serving patients in many medically-deprived and remote portions of the United States and in most 'developing countries', as well as in medical clinics that must serve large populations, in wide geographical areas.

Figure#9. Radio-Room On A Typical Tuna-Seiner During 'SSTV'-Video Tests On 'ROBOT'#400 To A San Diego Shore Station.

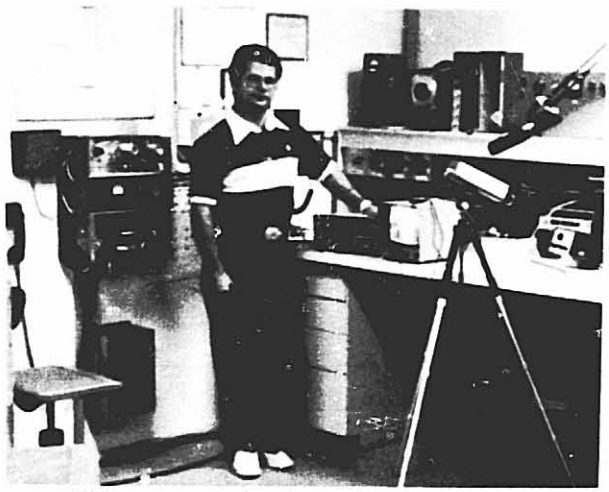

Figure#10. Co-Author Anthony Rippo,MD, Using 'ROBOT'-Model#400 At San Diego Base-Station During 'HF'-Video Reception From A Tuna Seiner At The 'Embarkadero',San Diego.

As indicated at the start of this paper, the term 'Telemedicine is so new and unfamiliar, and its application is so untried on today'smedicalproblems, that it is quite possible that several other economical solutions, than the 'ROBOT-1'approach herein proposed, may eventually prove effective in this age of doctor shortages. However, this 'SSTV'equipment, using telephone lines and 'HF'radio, appears to be the most economical and easiest to install and use.

Figure#11. Monitor Picture Of Clinic Receptionist Transmitted To San Diego Over Telephone-lines From The Campo Indian Reservation Clinic, 80-Miles East.

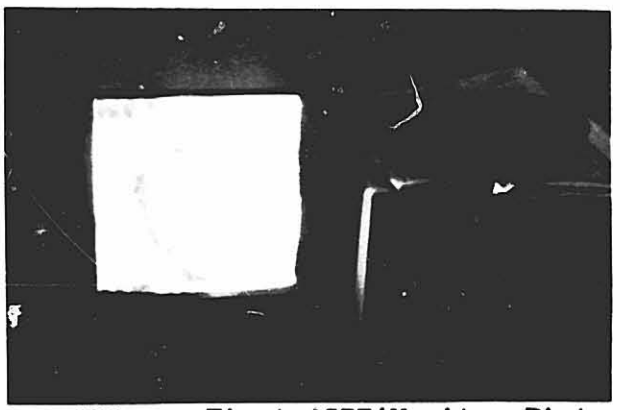

Figure#12. First 'CRT'Monitor Picture Of An Injured Child-Patient Transmitted Over Telephone-lines From Campo Clinic To San Diego.

The authors plan to release several subsequent papers during the next year on the statistical results of the land and sea tests at San Diego, and to review alternate aspects of 'Telemedicine' aid to the patients 'outback' or afloat, It is requested of our readers that any other successful trials in 'physician's extenders' or in the use of Audio/Video means of medical diagnosis and treatment of remote patients, on land or at sea, be brought to the attention of the authors.

****

Biographical References.

Ref.#1. --"Remote Area Health Care Systems," by Lockheed Missile and Space Company Inc., Sunnyvale, California. (1973)

Ref.#2. --"33 Telecommunication Projects in Medical Education and Health Care", by SuiWah Chan, PhD, and James R. Messick, MA, Michigan State University, East Lansing, Michigan. (1975)

Ref.#3. --"Image Communication By Telephone", by Milo M. Webber and Howard F. Corbus, -- Printed in the "Journal of Nuclear Medicine", June 1972. P379-81)

Ref.#4. --"Does Your Local Hospital Need The Medical Technician, Medical Engineer, and the 'ACTION' Professional Volunteer(VPHC)? by K. R. Jackman, Biomedical Engineering Consultant, La Jolla, Calif. Paper given December 6, 1974, at the "Fourth Annual 'Cal-Poly' Measurements Science Conference, San Luis Obispo, California. (17 pages)

Ref.#5. --"Navy Remote Medical Diagnosis System", by Dr. John Silva, PhD, Naval Electronics Laboratory Center, Code#3400, 271 Catalina Blvd., San Diego,Ca. 92152. Paper presented at the San Diego Biomedical Symposium, on February 6, 1976, at the Hilton Inn, San Diego, Calif.

Ref.#6. --"Systems Analysis And Computers In Ambulatory Care", by J. Silva, PhD; D.F.Schaller,MD; W.T.Rasmussen,PhD; and W.C.Giagor,PhD. --Paper given at the "Ambulatory Health Care Symposium", on February 11, 1976, at the Hilton Inn, San Diego, Calif.

Ref.#7. --"Telemedicine", by 18 authors, and edited by Dr. Rashid I. Bashshur,PhD; Patrecia A. Armstrong,BGS; and Dr. Zakhour I. Youssef,PhD.(1975)

Ref.#8. --"Volunteer Medical Engineers Can Aid Physicians and Hospitals In Telemetry Purchases And Tests", by K.R.Jackman, Biomedical Consultant, La Jolla, Calif. Paper presented on October 15, 1974, at the 'ITC/USA/74'Technical Conference and Exhibit.

Ref.#9. --"Teams Of Medical Engineers And Physicians Will Aid Developing Countries", by Kenneth R. Jackman,ME,AE., Biomedical Engineering Consultant.

Paper presented at 'The Jerusalem Conference On Information Technology!(J.C.I.T.)', Computer Committee, The Jerusalem Economic Conference,--"Computer Impact On Developing Countries", at the Panel--"Computer-Aided Medical Screening For Developing Countries", at the Binyanei Ha'ooma Convention Center, Jerusalem, Israel, on August 18, 1971. (36-pages,with 22-pages 'Comments')

Ref.#10. --"Criteria For The Engineer In The Medical Environment", by Kenneth R. Jackman,ME,AE. Published in the "1973 Proceedings",Of the 19th.Annual Technical Meeting, on April 2, 1973, at the Disneyland Hotel, Anaheim, california. (14-pages.)

Ref.#11. -"Remote Medical Diagnosis System", by Terry Mitchell,PH2, in the "San Diego NAVY DISPATCH".

Ref.#12. --"Telemedicine Systems", pamphlet from Lockheed-'LMSC', 1976(Four pages on the Tuskegee Primary Care Network, Tuskegee Institute, Alabama.)

Ref.#13. --"Bionics And Astronautics", by K.R. Jackman,ME,AE, and Dr. Henning E. von Gierke,PhD. Presented at the 'Symposium On BioEngineering' in a 15-paper seminar--"The Future Of Bio-Engineering In Our Daily Lives", at the'15th Annual Technical Meeting and Equipment Exposition', held at the Anaheim Convention Center, Anaheim, Calif., on April 23, 1969.

****

Paper No. 12

EFFECTS OF HYPODYNAMIC SIMULATIONS ON THE SKELETAL SYSTEM OF MONKEYS

D. R. Young and J. W. Tremor, *Ames Research Center, NASA, Moffett Field, California*

ABSTRACT

A research and development program has been undertaken to evaluate the skeletal losses of subhuman primates in hypodynamic environments. The goals of the program are: 1) to uncover the mechanisms by which weightlessness affects the skeletal system, 2) to determine the consequences and reversibility of bone mineral losses, and 3) to acquire a body of data needed to formulate an appropriate countermeasure program for the prevention of skeletal deconditioning. Space flight experiment simulation facilities are under development and will be tested for their capability in supporting certain of the requirements for these investigations.

INTRODUCTION

Losses of bone mineral have been observed in crew members during weightless space flight. Variations in calcium homeostasis were clearest during the 84-day Skylab mission, SL-4 (1). As shown in Figure 1, the urinary calcium excretion was elevated systematically, and there was a maximal loss of 7.9% of mineral content in the os calcis. In contrast, the radius and ulna did not change measurably.

The findings indicate that there is a loss of bone mineral during space flight despite the intake of relatively high levels of dietary calcium and phosphate, and despite physical exercise regimes which are extremely vigorous. Typically, weight-bearing bones appear to be significantly affected, whereas other portions of the skeletal system seem stable. Although the losses have not been of clinical concern, the basis for the alterations has not been explained adequately, and the consequences for passengers and crew members in future long-duration space flight have not been assessed.

Our studies have been directed towards the demonstration of a useful animal model for experimental testing and towards the verification of the underlying mechanisms of action in bone mass loss. Three factors have led us to select the experimental monkey for an animal model. First, there is available a reasonably good caliber of scientific information regarding subhuman primates, e.g., 1) the life support requirements for monkeys have been

defined and systems partially developed, 2) nutrition requirements in support of particular experiments have been delineated, 3) the biochemistry and physiology of the animal is similar to and approaches identity with man, thus facilitating the extrapolation of data between species. Second, flight experience has already been gained through suborbital space flights with squirrel monkeys and chimpanzees, and orbital flights with the chimpanzee and the pigtailed monkey (M. nemestrina). Third, reasonable animal supply sources, and pertinent information on primatology and disease control can be expected through the various national primate research institutes.

The selection of the monkey as an animal model for the calcium research program is further justified by reports which demonstrate a significant bone mass loss in the monkey caused by disuse osteoporosis, and other reports showing general similarities in the calcium metabolism of man and monkeys. For example, total body immobilization of the rhesus monkey (M. mulatta) for 2 months increases bone resorption in the long bones with a resultant loss of cortical bone (2). Immobilization decreased spinal impact tolerance by 33%; the mechanism of the resulting spinal injuries was related to a high incidence of intervertebral disk prolapse in the thoracic and lumbar vertebrae (3). The dynamics of the short-term blood calcium regulation are similar in man and the monkeys, (M. mulatta and M. nemestrina)(4). Calcitonin, a plasma calcium regulatory hormone, also lowers the blood calcium level in adolescent monkeys (M. mulatta and M. fasciculares) (5,6). The average bone formation rate in adolescent rhesus monkeys is 243 mg Ca/day (7), which is substantially similar to that observed in children and is at the lower range of values reported for normal adults (8).

PRIMATE RESTRAINT STUDIES

Procedures and Physiologic Responses

Our experimental approach has been to simulate hypodynamic and hypogravic environments for weight-bearing bones by restraining adult male monkeys (M. nemestrina) in a semirecumbent position according to the technique of Howard et al. (9) for varying periods of time. Figure 2 shows a restraint unit in a typical study of several weeks duration. Figure 3 shows the food (Purina) and water intake during 10 weeks of restraint. During the control phase of testing, the average food intake of seven monkeys was 147 ± 6 g/day/animal, which represents about 530 kcal. During the first 2-3 weeks of restraint, food intake was depressed but then returned to typical normal levels. Mean water consumption during the control period was 787 ± 244 ml/day and declined during restraint. Body weight was reasonably constant during the control phase of testing; variations of 6-12% in body weight were measured during restraint. Changes in the metabolism of body nitrogen and minerals are shown in Table 1, where comparisons of the average daily urinary output are made between restrained animals and body-weight-matched control animals given identical amounts of food and

water over a 10-week period. Urinary excretion in the restrained animals tended to be higher than that of the controls, especially during the last 5-6 weeks of restraint, and the restrained animals were also more variable. Urinary nitrogen and potassium were significantly higher (22%) in restrained animals; phosphorus excretion was increased by a factor of 3.8. Losses of nitrogen and electrolytes were also reported during the Apollo Missions. SL-3, and SL-4 and are associated with body mass loss.

Circulatory changes have also been observed. Therefore, blood volume changes were evaluated during one month of restraint. Blood volume was determined with ^{125}I-labeled albumin (RIHSA) measured in a Volemetron; the hematocrit was also measured. The responses were compared to a well-matched group of control monkeys. Figure 4 shows that the total blood volume decreased 11.7%. The red cell mass by itself decreased 12.0%, which is comparable to the 12% decrease found in SL-3 and the 10% decrease found in Apollo 14 and 17 crew members.

Bone Studies

Further comparison studies were undertaken to evaluate bone mineral losses in the monkey. The bone mineral content at a specific cross section was determined by the photon absorption technique (10) similar to that used to study astronauts. Ten animals were studied during 1 month of restraint. As compared to control animals, the restrained animals lost bone mineral content in the midshaft of the tibia. The mineral content of the distal radius and ulna was unchanged. Table 2 shows the losses in the tibia of the restrained animals. The average 3.5% loss was significant beyond the 5% level of confidence. The data correlate with the results obtained in the Skylab flights. For example, bone mineral decreased 5-7% in the os calcis of one SL-3 (59-1/2-day flight) crewman and two of the SL-4 (84-day flight) crew members.

The bone mineral loss in the experimental monkeys tends to be regional. Figure 5 shows the typical losses in the tibia in a group of three monkeys restrained for 6 months. Relatively large losses of cortical bone are seen mainly in the anterior, proximal tibia. Thus, the losses appear not only to occur in typical weight-bearing bones, but also appear to be in the outermost cortical fibers which would be subject to stress levels during weight bearing.

In a separate series of tests, the carbonate content of the tibia was found to decrease 7%, on the average, during short-term restraint. That reflects losses of the crystalline calcium carbonate-phosphate salts of the bone as well as a change in the total acid-buffering capacity of the body.

Mechanisms of Bone Loss

The balance between the rates of bone formation and bone resorption is a principal relationship which must be affected for a modification of bone mineral content to occur. Prior studies

(11) have shown that skeletal stressing achieved by intermittent or steady compression can produce local and regional bone hypertrophy by stimulating the endosteal and periosteal bone formation rate. Our experience with implantable bone strain gauges (12) indicates stress levels as high as 200 kg in the tibia of active monkeys; those levels are never approached during restraint. Consequently, the reduction of skeletal loading in our studies could have a significant effect on bone homeostasis.

Research efforts have also been focused upon elucidating the biochemical mechanisms which could give rise to bone loss through an increase in resorption rate. Other studies (13) have indicated that bone loss during hypodynamic immobilization is eliminated when the parathormone secreting system is removed, and consequently, that hormone is implicated in the bone loss observed during restraint.

In one experiment, our monkeys were evaluated during the course of 10-24 weeks of restraint. Figure 6 shows the rise in level of serum parathormone as determined by radioimmunoassay. The units shown are relative to a volume of a highly purified parathormone standard. The prerestraint values shown are similar to the normal human range, and the elevated levels are similar to those measured by an identical assay in patients with parathyroid adenoma who demonstrated a hypersecretory response (14).

In another experiment, three animals were observed for 24 weeks. Food intake (Purina) was held relatively constant and approached 180 g/day for each animal. Using the photon absorption technique, bone mineral losses of 4-6% were measured in the midshaft of the tibia. Bone loss was confirmed radiographically, with observation of thinning of the proximal tibial cortex and trabeculae in the calcaneus. Bone formation rate was determined using standard ^{47}Ca kinetics under metabolic balance conditions. The changes in critical calcium metabolism parameters are summarized in Figure 7. Bone formation rate in the control animals was 3.2 - 4.1 mg Ca/kg/day, compared to 7.2 - 13.2 mg Ca/kg/day after 6 months of restraint. Urinary phosphate of the control animals was 12 ± 6 mg/day; it was increased by a factor of 8 in restrained animals. Urinary hydroxyproline of the control animals was 5.2 ± 0.9 mg/day; it was doubled in restrained animals. Urinary calcium was 277 ± 103 mg/day in control animals; it was only modestly elevated, 17%, in restrained animals. The overall calcium turnover rate of the control animals was 377 mg Ca/day and was increased by 53% in restrained animals.

The data are consistent with the hypothesis that parathormone is implicated in hypogravic-hypodynamic bone loss. The increased urinary hydroxyproline and phosphate indicate an increased resorption rate of both the organic matrix and mineral phase of bone, and both are expected to occur with high levels of serum parathormone. Calcium turnover rate is the sum of calcium resorption from bone and intestinal dietary absorption. Dietary absorption, although it remained within normal limits in the restrained animals, was slightly depressed; therefore, the gross turnover rate was probably elevated because of a specific increase

in bone resorption. This provides further indirect evidence favoring the concept of an increased bone resorption rate. The bone formation rate was also increased in the restrained animals. Under clinical conditions of hyperparathyroidism, bone formation and resorption rates are coupled, and both increase during periods of severe bone loss.

The relatively low urinary calcium observed during long-term restraint is not surprising since parathormone itself reduces urinary calcium excretion (15). But, the possibility exists that calcium may be recycled in the body, rather than excreted, and deposited in a variety of tissues. Therefore, our on-going researches, in addition to evaluating specific endocrine involvement in bone loss, and parameters such as serum levels of ionic calcium and alkaline phosphatase, have also included evaluations of intracellular calcium distribution.

Requirements for several newer measurement techniques have been identified. First, it is important to apply a direct measure of bone resorption in our animal model system in order to establish unequivocably the change in that function during restraint. Second, it is desirable to measure skeletal bone mineral and calcium loss with a greater accuracy and convenience than is possible by metabolic balance techniques. Third, it is important to determine the effect of bone loss on the structural integrity of the skeleton.

NEWER EVALUATIONS OF THE SKELETAL SYSTEM

Bone Mineral Content

It has been apparent since the advent of single-photon absorptiometry that a dual-photon approach might be used to measure bone mineral content. The chief advantage of a dual-photon approach is in not having to surround the measured bone in a constant thickness of soft-tissue-equivalent material. In a dual-beam system, the attenuation of the radiation intensity in either air or soft tissue is slight but similar for the two distinct beam energies. On the other hand, absorption in bone is different for photons of different energy levels, and the differences are in proportion to the quantity of mineral present. Therefore, the ratio of the flux of the beam energies can be used to determine bone mineral content.

A prototype system utilizing a high-intensity (1 Ci) source of ^{153}gadolinium has been used to measure both vertebral and total body bone mineral in patients (16). Measurements are made on a modified Ohio-Nuclear whole-body rectilinear scanner. The ^{153}Gd (4 mm bead) is mounted below the scanning table, and a scintillation detector is mounted on the yoke above the subject. The beam size at the body level is less than 1 cm. The source and detector move simultaneously in a raster pattern.

The ^{153}Gd source emits at two energies (44 and 100 keV), and the attenuation is essentially linear when correction is made for the spillover from the higher to the lower energy channel.

Vertebral bone mineral is measured from L4 (lumbar) to T12 (thoracic) with a scan speed of 2.5 mm/sec and with 12.5-mm steps between scans. For measurement of total body mineral, the entire body area is scanned at a speed of 10 mm/sec with step intervals of 25 mm.

The radiation exposure measured by means of thermoluminescent lithium fluoride crystals is 2.1 mrad, with the majority delivered to the skin. The low dose level permits repeated scans without jeopardy to the patient.

The precision of vertebral scans in vivo averages 2.3%; measurement precision of the bone mineral content of vertebral phantoms is 1.7%. The variation of total body mineral content measured in vivo is 1.9%, which approaches the precision obtained in vitro.

We have recently applied the technique to experimental monkeys. Figure 8 shows the positioning of one animal on the scanning table. A scan speed of 2.5 mm/sec was utilized with 10-mm steps between scans. Animals in the 10-12-kg weight range contained 210-265 g of bone calcium. The measurement precision determined in two standards was 2%; that precision was approached in vivo. Consequently, this method could be useful for tracking the time history of skeletal calcium losses.

Bone Resorption Rate

The direct measurement of osteolysis and bone resorption in man has been determined by monitoring ^{48}Ca levels in the blood and urine (17). The procedure is based upon measuring in blood or urine a stable, naturally occurring, calcium tracer, ^{48}Ca, which is liberated from the skeleton through resorptive processes. To implement the studies with our animal model, monkeys are fed standard test diets providing a known and relatively stable daily intake of total calcium. Diets designed for these studies provide 375 mg Ca/day. Typically, dietary calcium is 96.97% ^{40}Ca; that is replaced in the diet by a calcium source which has been depleted of ^{48}Ca, i.e., a source which is 99.91% ^{40}Ca. The natural abundance of ^{48}Ca in the skeleton is 0.18%; during the feeding of diets depleted of ^{48}Ca, the isotope is released from the skeleton, and its abundance in the blood falls as it is excreted in the urine and is only partially replaced by release from bone. The blood level of the naturally occurring isotope, ^{48}Ca, is measured by neutron activation analysis. Aliquot samples are irradiated with a flux of 10^{13} neutrons/cm^2/sec, and the ^{48}Ca is measured as ^{49}Ca, which has a half-life of 8.7 min. Figure 9 demonstrates the nature of the data obtained with monkeys. There is an early exponential decline of ^{48}Ca level in the urine; after 2 weeks, an asymptotic abundance is reached which is the fraction of the total calcium turnover rate derived specifically from bone resorption. From Figure 9 it is inferred that 50% of turnover is derived from skeletal resorption, and therefore, 50% is derived from dietary calcium absorption. Measures of blood level ^{48}Ca provide substantially similar data, but with less precision because of the

low concentrations and relatively small blood samples. The current approaches address themselves to dietary enrichment studies in which monkeys are supplemented with 12 mg ^{48}Ca daily; serum levels increase exponentially to an asymptote; the results are interpreted essentially the same as in the prior approach, and there is a significant improvement in precision.

Bone Bending Rigidity

An experimental technique and the associated apparatus for measuring in vivo the mechanical impedance of the human ulna have been described in detail (18). An electromagnetic shaker is used to apply a steady-state harmonic excitation to the ulna near its midspan, and measurements of the complex driving-point impedance are made. With moderate restraint at the joints, the resistance to rotation is small, and the interosseous space is sufficiently large to avoid significant lateral contact with adjacent bones. At low frequencies, the bones behave as "simply-supported" beams immersed in a viscous fluid. The impedance probe is placed against the skin; with a preload of 600 g, the skin has a significant stiffness, although inconsequential mass. The velocity of the probe produced by a prescribed force yields data from which the bone stiffness can be separated from the skin stiffness with an accuracy of 10%. The absolute impedance of bone is determined for the responses below the first resonance, ~400 Hz. The spring constant k is the product of the impedance and frequency. The average bending stiffness EI is derived from the spring constant. Studies with excised bones tested to fracture in three-point loading show a high correlation, $r = 0.96$, between the bending stiffness and the maximum moment at fracture. Consequently, the parameter EI is a sensitive indicator of changes in the modulus E or in the cross-sectional moment of inertia I which would alter the mechanical integrity of bone.

Figure 10 demonstrates the measurement of impedance in the tibia of a monkey. The probe is placed at the midspan of the tibia. Typical values for the average bending stiffness of the tibia are on the order of 11×10^9 dyne-cm^2. The general approach described above can be applied to assess the effect of local areas of bone demineralization on structural integrity.

The approaches described above and the data base obtained through laboratory experiments indicate that the monkey is a useful test model for the evaluation of certain types of human calcium problems. For that matter, experiments with monkeys may also be a useful adjunct for studies of general metabolic responses, the control of red blood cell mass and plasma volume, and perhaps cardiovascular dynamics in relationship to hypodynamic environments. However, theories and mechanisms concerning the biology of weightlessness can be tested only in a limited fashion in ground-based studies. Eventually, it is necessary to determine that reactions predicted on the basis of simulation experiments do in fact occur in true weightlessness. The design and evaluation of

equipment and holding facilities for future experiments with monkeys thus are critical developmental requirements.

PRIMATE FLIGHT EXPERIMENT SIMULATION AND IMPLEMENTATION

Among the facilities to be developed and used for a variety of space life sciences experiments, three are applicable to the investigations discussed here: a primate holding facility, a primate transporter, and a surgical workbench.

Holding Facility

Primate caging and experimental facilities are currently under development for a spacelab life sciences laboratory simulation. Termed Spacelab Simulation Development III (SMD III), it is scheduled for operation in May 1977. Ames Research Center has the integration and development responsibility for a number of biological experiments, the actual simulation to be conducted at and with the support of Johnson Space Center. The test is to be of 7 days duration.

Two primate cage designs have been completed by Lockheed Missiles and Space Co. (19) and McDonald Douglas Corp. (20). A composite of the two designs is illustrated in Figure 11. Note that the unit is integral with a standard Spacelab rack 105 cm wide, 275 cm high, 72 cm deep at maximum depth.

The primate cage was configured to afford ample living space for an unrestrained 11-14-kg primate and to provide an optimal life support situation. The inside dimensions of the cage are approximately 64 × 64 × 95 cm. Food and water are supplied by a hopper and a lixit valve/reservoir system, respectively. Water dispensed is automatically measured, while food is replaced manually.

Collection of feces is handled by a 6.4-mm mesh screen placed about 15 cm beneath the floor of 6.4-mm rods spaced 38 mm apart. Urine is collected and dried on an underlying phosphoric-acid-impregnated pad. Both incoming and outgoing air is filtered through a 0.5-micron (87% efficient) H.E.P.A. filter. Outgoing air is also filtered through a charcoal bed. The sizing of the waste collection bed permits storage over the mission duration, although ready access allows cleaning and changing if desired. Feces can be readily collected throughout an experiment course.

Fluorescent lighting may be programmed to a required daily regime, while visibility is afforded by the vertical Plexiglass window. Ambient lighting may be controlled by a Velcro-fixed cloth curtain across the window.

Temperature control depends upon spacelab ECS (Environmental Control System) inlet temperatures. The SMD III will provide 16°C air through a ceiling vent located about 2.5 cm from the inlet to the primate holding facility. This air, termed process air, is collected by a blower which provides bleed air to a separate, fan-driven air circulation loop entering the cage from the top and moving linearly down through the cage at the rate of

60 ft^3/min. This cage circulation air with process air is vented from the front bottom of the facility. Temperature is sensed in the process air loop, driving the differential opening or closing of a solenoid actuated valve to control habitat temperature.

Preliminary tests showed that a 12-kg macaque contributes about a 4°C differential, necessitating the inclusion of a resistance heater in the system with air inlet temperatures as low as 16°C.

Transporter

Consideration of constraining mission operations indicated problems in inserting the primate in the holding facility before launch. The approach has been, therefore, to board the monkey in the orbiter a few hours prelaunch, carry it there through the launch phase, and to insert it in the spacelab soon after achievement of orbit. General Electric Co. was contracted to fabricate a primate transporter with this purpose in mind for SMD III. The design was conceived in a prior study (21). It provides a 2-day food and water supply and a self-contained air circulation capability. Since it is to operate in the benign orbiter environment, sophistication of design was minimal. It is illustrated in Figure 12.

The holding facilities and transporters have been designed with appropriate interfaces to facilitate primate transport. When joined to the front of the cage, the doors of transporter and cage are commonly opened, and the ceiling of the transporter is moved down to effect the transfer. To move an unanesthetized animal from the cage, a manually operated squeeze wall mechanism forces the primate into the transporter. An anesthetized animal may be removed by opening the hinged cage front. Access for syringe intramuscular injections is provided by the barred partition in the cage transfer port in conjunction with manipulation of the squeeze wall.

Surgical Workbench

The use of a third facility in SMD III (as well as for flight) is required by this experimentation. A surgical workbench will be used for a number of life sciences functions, e.g., microbiological tasks, sample transfers and measurements, dissections, perfusions, microscope observations, and photography, etc. (22). The design concept is illustrated in Figure 13. Here, as with the primate cage, the double rack is used. It will provide a restraint capability and work space for the anesthetized monkey while blood samples are taken. It also provides a linear airflow and lighting. Contained within a double rack, the working chamber may be extended into the spacelab aisle allowing access through glove ports from both sides. Access for some applications may be directly through the Plexiglass front when it is folded into the top. A downward flowing air current of sufficient velocity across the front insures atmospheric isolation with the front in this

position. A water reservoir and flexible plumbing constitute a wash-down system with waste water collected through the perforated Plexiglass floor by a vacuum/reservoir system; electrical outlets within the chamber service appliances when needed.

Investigations with unrestrained primates, then, will be implemented in spacelab simulations by the use of these three facilities. The following sequence of operations is planned.

Shortly before test start, the monkey will be transferred from the laboratory to the simulated orbiter by transporter. The transporter will, at some time after scheduled orbit, be moved to the spacelab and joined to the holding facility. When transfer has been effected, water consumption and food intake will be monitored, and feces collections will be made on a predetermined schedule. The animal will be anesthetized daily and removed to the surgical workbench where the required treatments and sample taking will be performed. On the last simulation day, by use of the squeeze-wall mechanisms, the animal will be transferred to the transporter for placement in the orbiter while reentry and recovery operations ensue. Postrecovery observations will begin after removal from the orbiter to the ground laboratory.

SUMMARY

Experimental approaches in the development of the monkey as a useful test animal for the evaluation of calcium metabolism have been reviewed. The measurement of total body calcium by photon absorption techniques, the measurement of skeletal resorption rate, and the measurement of bone stiffness have been shown to be feasible and can provide useful information regarding skeletal status. The configuration of developmental primate life support equipment and its application in spacelab simulation programs have been discussed.

ACKNOWLEDGMENT

The contributions of John K. Jackson and Mahmond Yakut of McDonald Douglas Corp., Bruce Maine of Lockheed Missiles and Space Co., Ted Aepli and Roy Smith of General Electric Co., and William E. Berry and Paul X. Callahan of Ames Research Center are gratefully acknowledged in the design of the implementing hardware. The contributions of Chris Cann are acknowledged for some of the physiologic studies.

REFERENCES

1. Whedon, G. D., L. Lutwak, P. Rambaut, M. Whittle, C. Leach, J. Reid, and M. Smith: Effect of weightlessness on mineral metabolism; metabolic studies on Skylab orbital space flights. Calcif. Tiss. Res., 21:423, 1976.
2. Kazarian, L. E., and H. E. Von Gierke: Bone loss as a result of immobilization and chelation. Preliminary results in Macaca mulatta. Clin. Orthoped. and Related Res., 65:67, 1969.

3. Kazarian, L. E., and H. E. Von Gierke: Age and exercise as factors influencing osteoporsis, bone strength and acceleration tolerance. Proc. AGARD Conf., 82:8, 1971.
4. Young, D. R., G. A. Thompson, W. H. Howard, R. R. Adachi, and L. Lutwak: Short-term blood calcium regulation in the monkey. Indian J. Nutr. Dietet., 12:243, 1975.
5. Bell, N. H., R. J. Barrett, and R. Patterson: Effects of porcine thyrocalcitonin on serum calcium, phosphorus and magnesium in the monkey and man. Proc. Soc. Exp. Biol. Med., 123:114, 1966.
6. Raman, A.: The effects of thyrocalcitonin on ionic and total plasma calcium in monkeys. Horm. Metab. Res., 3:48, 1971.
7. Harris, R. S., J. R. Moor, and R. L. Wanner: Calcium metabolism of the normal rhesus monkey. J. Clin. Invest., 40:1766, 1961.
8. Neer, R., M. Berman, L. Fisher, and L. E. Rosenberg: Multicompartmental analysis of calcium kinetics in normal adult males. J. Clin. Invest., 46:1364, 1967.
9. Howard, W. H., J. W. Parcher, and D. R. Young: Primate restraint system for studies of metabolic responses during recumbency. Lab. Anim. Sci., 21:112, 1971.
10. Sorenson, J. A., and J. R. Cameron: A reliable in vivo measurement of bone mineral content. J. Bone Joint Surg., 49-A:481, 1967.
11. Chamay, A., and P. Tschantz: Mechanical influences in bone remodelling. Experimental research on Wolff's Law. J. Biomechan., 5:173, 1972.
12. Young, D. R., W. H. Howard, and D. Orne: In vivo bone strain telemetry in monkeys (M. nemestrina). J. Bioeng., in press.
13. Burkhart, J. M., and J. Jowsey: Parathyroid and thyroid hormones in the development of immobilization osteoporosis. Endocrinology, 81:1053, 1967.
14. Reiss, E.: Analyses and measurements of blood samples. NASA CR-1395, 1969.
15. Agus, F. A., L. B. Gardner, L. H. Beck, and M. Goldberg: Effects of parathyroid hormone on renal tubular reabsorption of calcium, sodium and phosphate. Amer. J. Physiol., 224:1143, 1973.
16. Madsen, M., W. Peppler, and R. B. Mazess: Vertebral and total body bone mineral content by dual photon absorptiometry. Calcif. Tiss. Res., 21:361, 1976.
17. Hansen, J. W., G. S. Gordon, and S. G. Prussin: Direct measurement of osteolysis in man. J. Clin. Invest., 52:304, 1973.
18. Thompson, G. A., D. Orne, and D. R. Young: In vivo determination of mechanical properties of the human ulna by means of mechanical impedance: experimental results and improved mathematical model. Med. Biol. Eng., 14:253, 1976.
19. Conceptual design for a biological specimen holding facility. Final Report, LMSC D056047, Vol. I, Lockheed Missiles and Space Co., Inc., June 1976, Prepared under contract no. NAS8-31491.

20. A conceptual design study of a biological specimen holding facility. Final Report, MDC 66203, Vol. II, McDonnell Douglas Corp., May 1976, Prepared under contract no. NAS8-31490.
21. Biomedical experiments scientific satellite. Preliminary design study, Vol. I, General Electric Co., 1976, Prepared under contract no. NAS2-8896.
22. Callahan, P.: Personal communication.

TABLE 1

Effect of 10 Weeks of Restraint on the Average Daily Urinary Nitrogen, Potassium, and Phosphorus in Monkeys[a]

Test monkeys	Urinary nitrogen, mg/day	Urinary potassium, mg/day	Urinary phosphorus, mg/day
Restrained animals (4)[b]	3389 ± 1337[c]	661 ± 312[d]	82 ± 53[e]
Pair-fed controls (4)	2747 ± 558	540 ± 92	17 ± 30

[a]Values are means ± S.D.
[b]Values in parentheses are numbers of animals.
[c]Significantly different from control animals, $p < 0.01$.
[d]Significantly different from controls, $p < 0.02$.
[e]Significantly different from controls, $p < 0.002$.

TABLE 2

Tibia Mineral Content During One Month of Restraint[a]

Prerestraint	Postrestraint	% Diff
0.61	0.60	-1.64
0.71	0.71	0
0.76	0.74	-2.63
0.80	0.70	-12.50
1.02	0.97	-4.90
0.93	0.95	+2.15
0.84	0.81	-3.56
0.79	0.74	-6.33
1.07	1.03	-3.74
0.99	0.97	-2.02

[a]Values are g/cm; $\bar{x} = -3.50\%$; $t = 2.88$; $p < 0.05$.

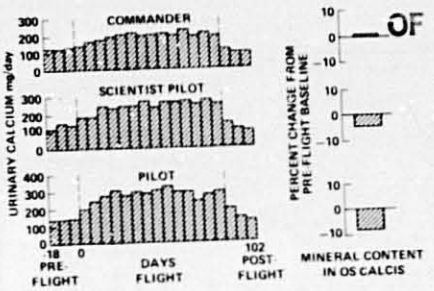

Fig. 1.- Urine calcium and bone mineral loss from os calcis during the 84-day Skylab 4.

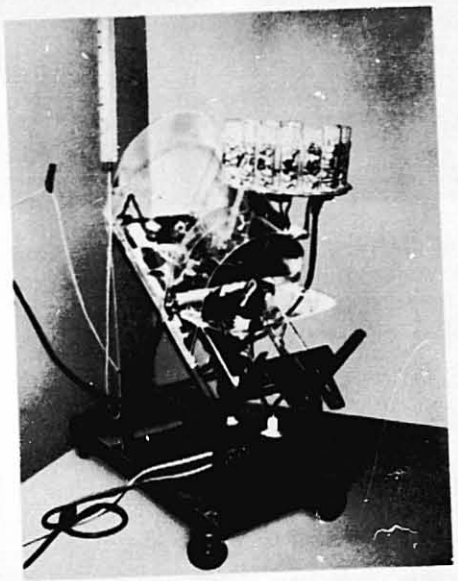

Fig. 2.- Primate restraint unit showing arrangement of equipment and animal as used in these studies. Provisions are for watering and feeding and for the collection and refrigeration of urine samples.

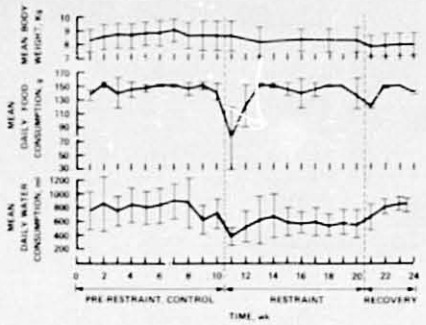

Fig. 3.- Body weight, food consumption, and water intake of seven monkeys during control, restraint, and recovery periods. Values are means ± S.D.

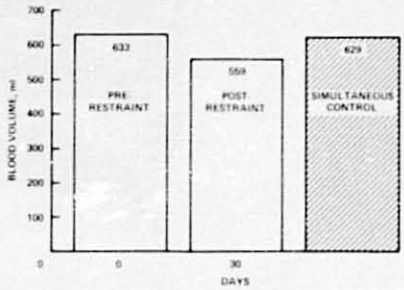

Fig. 4.- Blood volume changes in three restrained monkeys.

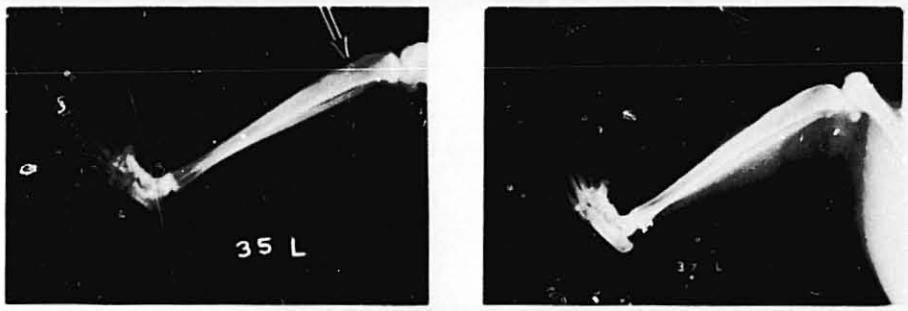

Fig. 5.- Losses of cortical bone in the tibia during restraint. Animal #35 was restrained for 6 months. Significant losses of cortical bone occurred in the proximal-anterior tibia. Animal #37 was a control animal.

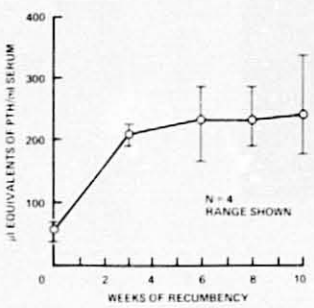

Fig. 6.- Increase in serum level of parathormone during restraint in monkeys.

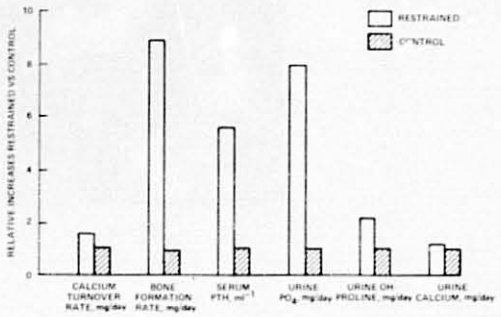

Fig. 7.- Effect of long-term restraint on several calcium metabolism parameters. The relative increase observed in restrained animals is shown on the vertical scale.

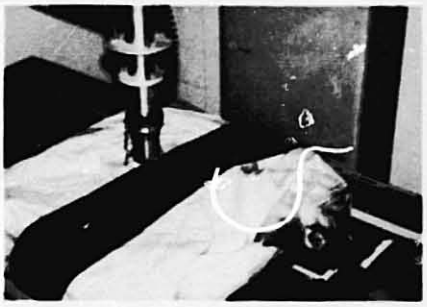

Fig. 8.- Measurement of total skeletal mineral content in the monkey utilizing dual photon absorptiometry are made under anesthesia to avoid motion.

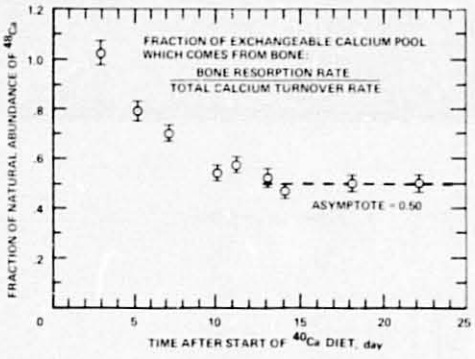

Fig. 9.- Measurement of the fraction of exchangeable calcium arising from bone resorption in the monkey. ^{48}Ca in urine is measured by neutron activation analysis.

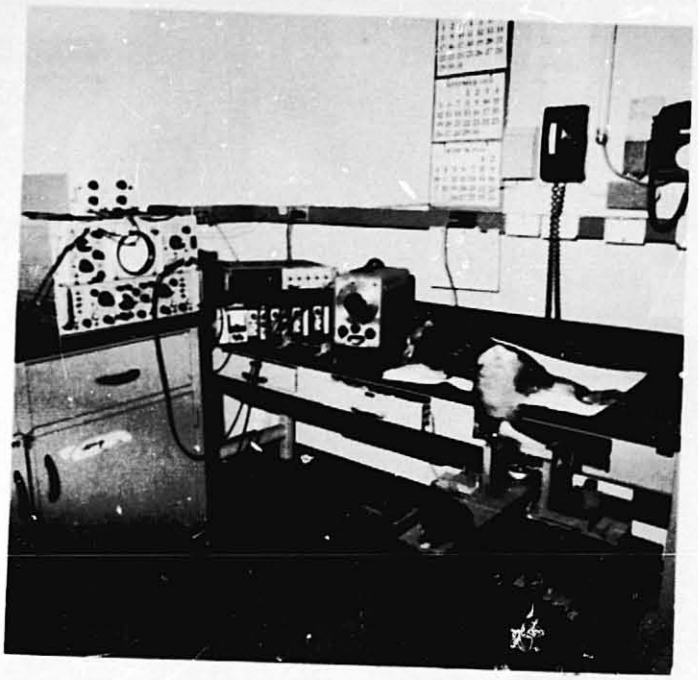

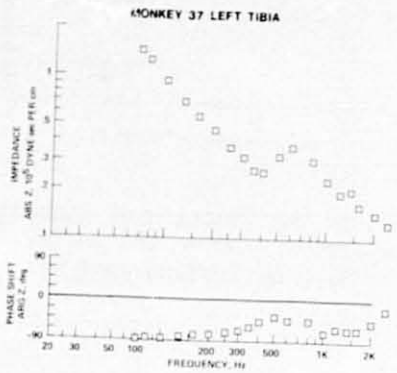

Fig. 10.- In vivo measurement of the impedance of the tibia in a monkey.

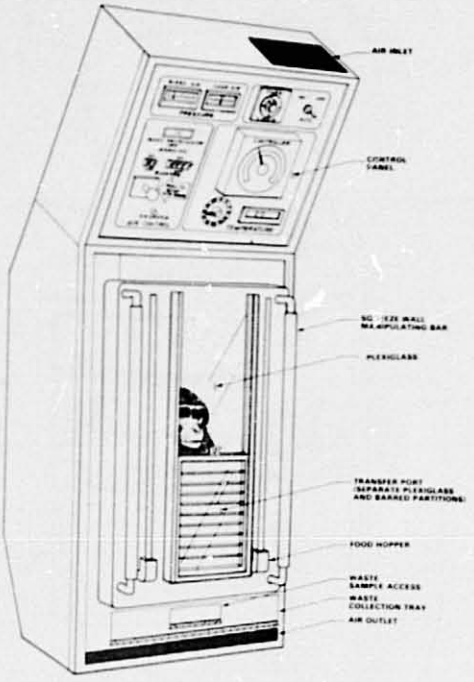

Fig. 11.- Primate holding facility design concept. Control panel is shown in an expanded front view for clarification purposes.

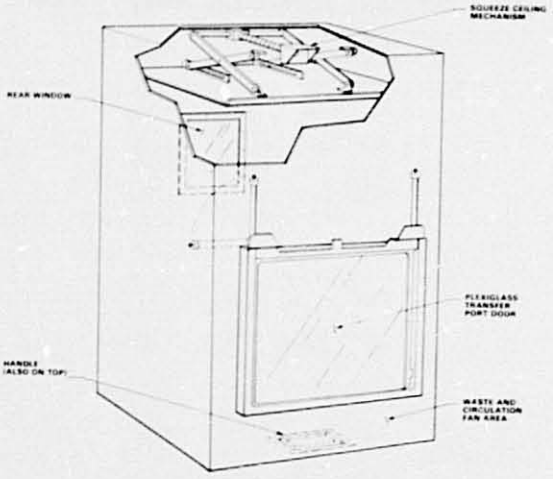

Fig. 12.- Primate transporter design concept.

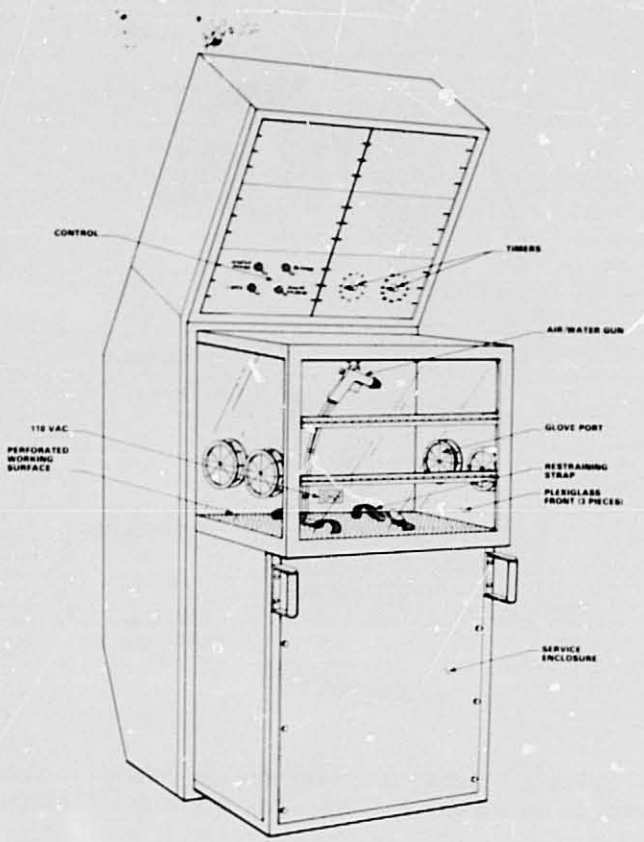

Fig. 13.- Surgical workbench design concept.

Paper No. 13

AIRCRAFT FLIGHT SIMULATION OF SPACELAB EXPERIMENT USING AN IMPLANTED TELEMETRY SYSTEM TO OBTAIN CARDIOVASCULAR DATA FROM THE MONKEY

E. P. McCutcheon, R. Miranda, T. B. Fryer, G. Hodges, B. D. Newsom, and N. Pace, *Ames Research Center, NASA, Moffett Field, California*

ABSTRACT

The utility of a multichannel implantable telemetry system for obtaining cardiovascular data was tested in a monkey with a CV-990 aircraft flight simulation of a space flight experiment. Valuable data were obtained to aid planning and execution of flight experiments using chronically instrumented animals.

INTRODUCTION

The utility of multichannel implantable systems for telemetering cardiovascular variables has been demonstrated in ground-based experiments (1,2). Previous multivariable systems were comparatively large and suitable only for animals weighing at least 20 kg such as large dogs, baboons, or chimpanzees (1,2). Advances in miniaturized, hybrid circuit modules and use of inductively coupled power have made it possible to design a multichannel unit for implantation in monkeys (or dogs) as small as 10 kg. This report describes the evaluation of this type of system in an aircraft flight test simulating a space flight experiment. Basic design features, implantation technique, and initial results are presented. A metabolic experiment performed simultaneously has been reported separately (3,4).

SYSTEM DESCRIPTION

The basic operating principle of the implanted telemetry system is conversion of analog data to a multiplexed, pulse-width-modulated (PWM) format which frequency-modulates (FM) a radio-frequency (RF) transmitter, as described previously (1). The system components placed internally include two pressure transducers, a temperature sensor, and an electrocardiographic (ECG) lead (Figure 1). The transducers are connected to a hermetically sealed mainframe package (6 cm long, 2.4 cm wide, and 1.3 cm thick) containing power converter, signal conditioner, and 88-MHz transmitter with integral transmitting antenna. An attached Silastic-covered coil receives power by inductive coupling from an external coil driven by a 250-kHz oscillator (Figure 1). Total weight of the implanted unit is approximately 40 g. The system

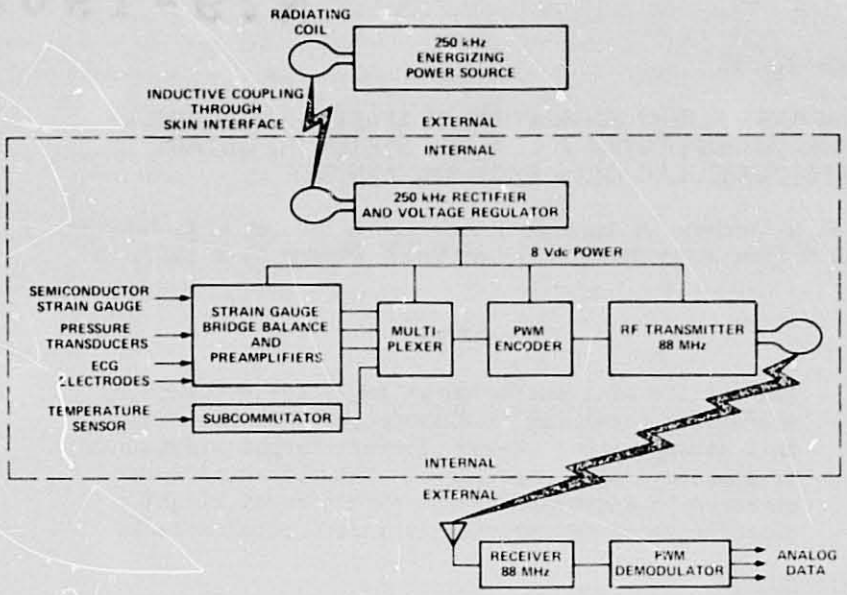

Fig. 1— Inductively powered multichannel telemetry system functional elements

is completed by a receiver and demodulator which convert the PWM signal to the original waveforms.

Transducers and Signal Conditioners

The pressure transducers are bonded semiconductor strain gauges enclosed in a titanium case. One of the transducers is 3.5 mm in diameter, operated as a 500-ohm vertical half bridge. This small size makes it especially suitable for insertion in the descending thoracic aorta. Since long-term zero drift could be a problem with this size transducer, it was a.c. coupled to provide a frequency response of 0.03 to 100 Hz. The second pressure transducer is 4.5 mm in diameter, also a 500-ohm half bridge. It has greater long-term zero stability with a frequency response from d.c. to 100 Hz, and was used for left ventricular pressure measurement. Connecting leads may be any length, but we find 20 cm suitable for monkeys and small dogs.

The single ECG lead consists of a bipolar pair of Silastic-covered, 100-strand, 50-gauge stainless steel wires terminating in 3-mm uninsulated loops. Frequency response at the output is 0.1 to 100 Hz.

Signal conditioning includes bridge completion and balancing for the pressure cells, and amplification of pressure and ECG signals prior to multiplexing. Two additional d.c.-to-100-Hz channels are available if desired.

The sixth channel is subcommutated to provide a total of eight additional subchannels; four of these are active. One is used for temperature, and the other three for system monitoring, although all could be used for physiological data if required. The thermistor temperature sensor is positioned to project approximately 1 cm from the main package in order to detect deep body temperature. The stainless steel case required for thermistor sealing results in a 30-sec time constant. The engineering variables monitored are the unregulated voltage from the internal receiving coil, and the ±3.7-V regulated output from the power supply. After subcommutation, these channels are amplified and multiplexed.

The hybrid signal conditioner modules contain differential amplifiers with adjustable gain to a maximum of 300. Higher gain can be provided for applications with very low-level signals such as EEG. Gains are adjusted to meet the ±1-V range of the multiplexer. The pressure channel gains are 120, and the ECG amplifier gain is 50. Pressure transducer signal conditioning requires approximately 11 mA at 3.7 V, and the remainder, approximately 2 mA.

Multiplexer, Transmitter, and Receiver

Time-division multiplexing of the analog signals is achieved with a low powered CMOS device. This technique converts the polarity and amplitude of the original signal into the width or duration of a pulse (PWM). The basic clock rate for system timing is 10 kHz. Time frames containing eight pulses or "words" are generated at 120 Hz (Figure 2). One of the eight words is a

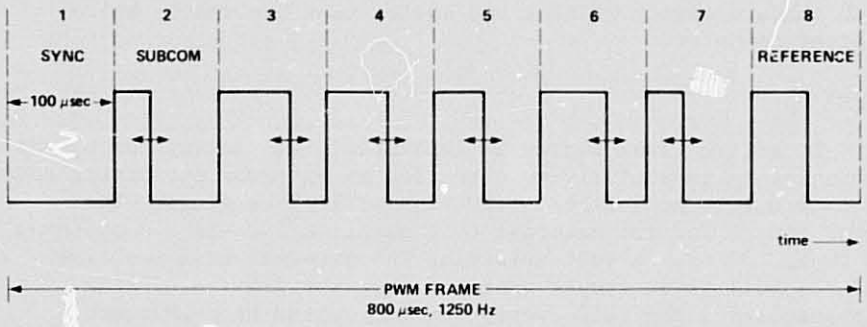

Fig. 2— Pulse width modulation logic of the implanted unit multiplexer

blanked pulse denoting the initiation of the sampling sequence. A second is a system zero reference. The other six words are used for the physiological and system monitoring data. The five high-frequency channels are each sampled at 1250 Hz, providing a signal frequency response of at least 100 Hz. The sixth word samples each of the eight subcommutated channels at 156 Hz, providing a frequency response of at least 15 Hz on each of the eight possible subchannels.

The maximum desired modulation of ±80% alters channel pulse duration ±40 μsec. Signals exceeding the ±1-V multiplexer range will cause overmodulation with saturation and clipping; excessively low level signals will contain noise.

The train of PWM information then frequency-modulates (FM) the 88-108-MHz RF carrier of the transmitter, which broadcasts from the internal loop through the tissue to an external antenna and telemetry receiver. The receiver bandwidth is 500 kHz to provide an acceptable rise time for the PWM signal. The transmitter operates within the maximum allowable field strength of 50 μV/m at 15 m for noncommercial applications. Despite this constraint, the transmitter easily achieves a 5-m range even in a noisy RF environment.

The encoding chain is designed to be independent of minor RF oscillator frequency drift and small variations in signal strength. Since the data are coded into the duration or width of each pulse, a highly linear frequency response in the transmitter and receiver is not required.

Demodulator, Display, and Recording

The received signal is coupled to a demodulator which reverses the encoding process (1,5). The receiver output is clipped and limited in the demodulator to remove effects of amplitude variations. The individual decoded analog waveforms are then displayed on a CRT and processed in a standard manner with onboard direct writing and analog tape recorders, and a digital computer.

Power

No active power source is implanted. All energy for system operation is inductively coupled from an external energizing coil (7 cm o.d.) to an internal receiving coil (5 cm o.d.). The power source for the external coil supplies 250 kHz and operates at 20 V, 150 mA. A vest maintains the external coil position, and the coil power supply operates from the 115-V a.c. line. Alternatively, the coil supply can be powered by rechargeable batteries, with the entire assembly contained in the vest, to obtain data from the unrestrained animal.

The internal coil and power rectifier-regulator combine to provide an 8-V-d.c., 15-mA supply for operation of the internal system components. Total power consumption is approximately 150 mW.

System Accuracy

The primary determinants of accuracy in this system are environmental RF interference, transmitter-receiver distance, percentage channel modulation, nonlinearity, and drift. At 80% modulation, 5-m range, in a relatively noisy environment, noise at the output is less than 0.1% of full scale, nonlinearity 0.25%, and zero gain instability less than 1% for a nominal accuracy of the total system of approximately ±2%, excluding transducer drift. Assessment of transducer stability requires periodic calibration and comparison with a reference standard (Figure 3).

IMPLANTATION

A completed unit ready for implant is shown in Figure 4. The entire unit is placed within the thoracic cavity, using surgical techniques similar to those reported previously (1,2). In our laboratory, the pressure transducers are coated with TDMAC-heparin complex (Polysciences, Inc.) prior to implant to minimize the possibility of thrombus formation. The main unit is stabilized on the rib cage in the intrapleural space deep in the posterior thoracic gutter just above the diaphragm. The internal coil is positioned just cephalad to the main unit in an area where the chest musculature is minimal. Antibiotic coverage is begun the day of surgery and continued 5 to 7 days after surgery.

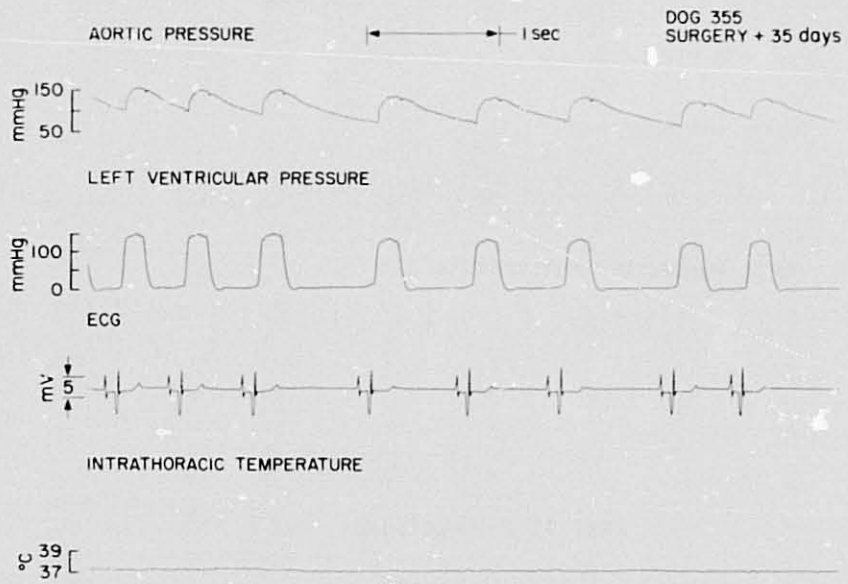

(a)

Fig. 3— Representative data from a 10-kg dog 2 weeks after implantation with comparison waveforms from a manometer-tipped catheter

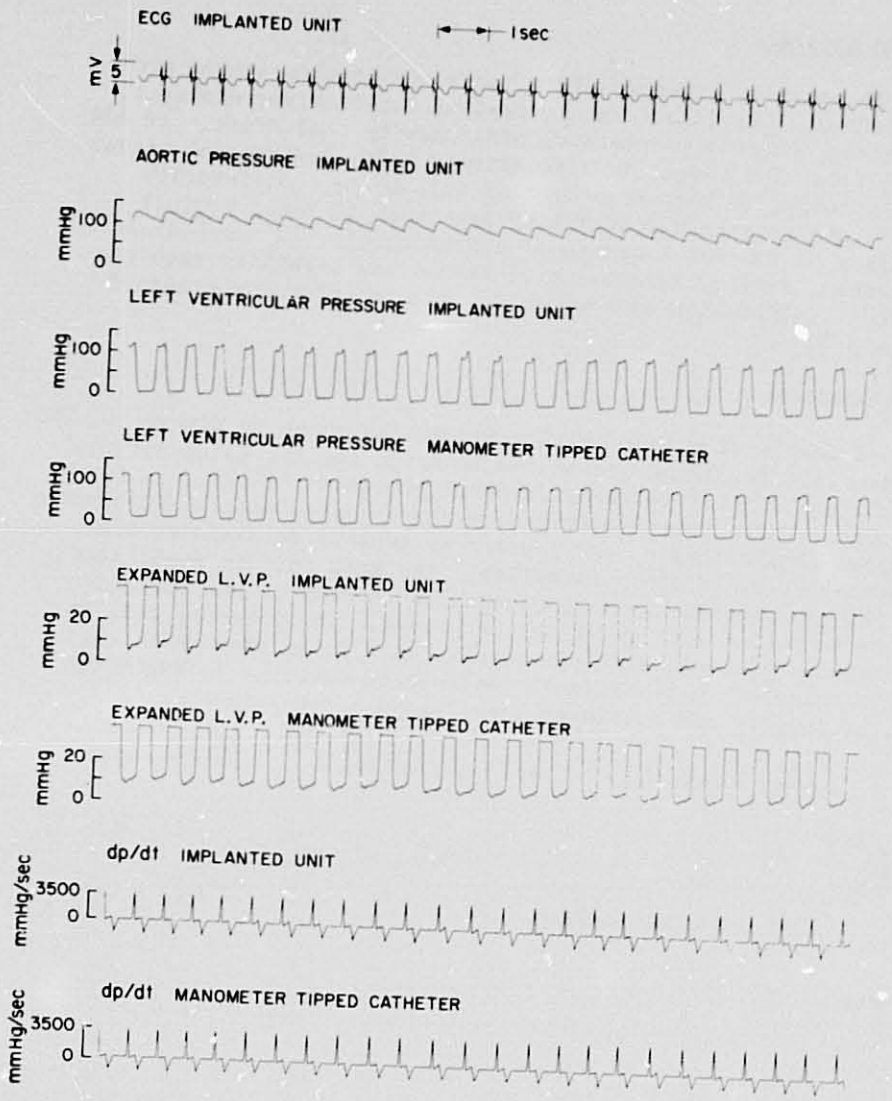

Fig. 3(b)— Concluded

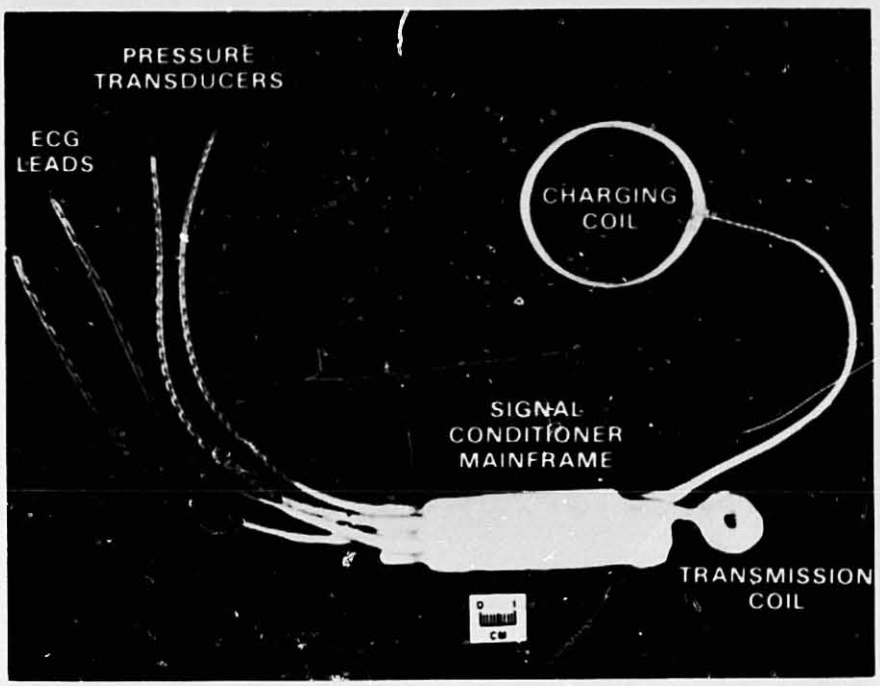

Fig. 4— Multichannel telemetry unit prepared for implantation

RESULTS OF OBSERVATIONS FROM FLIGHT TESTS

To date, units have been implanted in eight monkeys and three dogs. Implant durations with healthy animals have ranged from 64 to 490 days. Durations of full signal output from the units have ranged from 31 to 231 days. The shortened survival times resulted from deliberate sacrifice of the animal to study the effects of the implant and to recover the unit for evaluation, not from long-term or delayed illness caused by the presence of the device.

The postoperative course was generally smooth except for late breakdown of the skin at the incision site in the two flight animals. Detailed hematological and related data on the two *Macaca nemestrina* animals prepared for the flight test are contained in Table 1. These data are representative of the findings from all animals. The most consistent changes were decreased weight, subsequently remaining stable, and anemia, resulting from blood loss during surgery. Progressive recovery and return to normal is apparent. The magnitude and duration of leucocytosis was variable, with little change in three of the rhesus monkeys. X-ray examination has shown a left lower lobe infiltrate which gradually clears. The time to recovery with normal hematology and X-ray findings was 6 to 8 weeks. The tissue

Table 1— History of the Experimental Monkeys
M. nemestrina

Animal no.	Date, 1976	Year acquired	Est. age, yr	Weight, kg	Hct, %	Hgb, g%	RBC, × 10^6	WBC, × 10^3	Plasma protein, g%	BUN, mg%	Comment
603	3/23	1969	15	16	44	15.0	5.5	8.9	7.4		Flight animal
	3/24										Surgery
	3/31			14.25	32	10.5	4.0	13.3	6.9	13	
	4/2				33	11.5	5.5	19.1	7.7		
	4/8				34	9.8	4.8	11.4	7.4		
	4/27			14.5	39	13.4	5.0	11.9	7.8		Begin flights (5/6)
	5/5			14.5							
	5/10			14.4							
	5/17			14.5							
	5/24				38	12.7	5.7	10.6	7.5		End flights (5/21)
	7/26			14.4	47	13.1	6.1	6.9	7.0	13	
	8/9			13.8	42	11.8	6.2	14.9	8.2	15	Healthy, unit working
604	3/31	1974	9	11.8	42	13.0	5.9	6.7	7.2		Backup animal
	4/6										Surgery
	4/15			10.5	(42)[a]	10.6	5.0	21.0	7.9		
	4/27			10.5	32	10.4	4.2	11.6	8.3		
	5/24				34	11.6	5.0	11.6	8.1		
	7/9										Sacrificed

[a]Accuracy questionable.

changes were those expected with thoracic surgery and placement of an implanted device, and the unit is satisfactorily tolerated.

Failure modes of the telemetry system have been variable and of the type likely to occur with any instrumentation inside the body for a long period. In three cases, transducer leads eroded at a tie-down point. Occasionally, internal electronic components have failed. In general, the implant experience indicates the type of improvements needed in future units. Overall, the system operated as designed.

Data have been obtained repeatedly from dogs during treadmill exercise and from awake, chair-restrained monkeys in ground-based tests. In the airborne simulation of a space flight experimental environment, eight flights with over 50 takeoffs and landings were conducted over a 16-day period. The five initial flights were made primarily to check out the onboard recording system. Signals from the implanted unit were always present. For the final week (three flights), the monkey (#603) was fitted with a vest containing the energizing coil and sealed into the pod. Data were obtained and recorded on each of the three flights.

A typical in-flight record is shown in Figure 5, and the effect of lower body negative pressure (LBNP) in Figure 6. The aircraft configuration would not permit the LBNP test in flight, so it was performed with the aircraft on the ground. In-flight heart rates averaged 135 beats/min, and arterial blood pressures averaged 135/90 mm Hg.

Distance between the coplanar external and internal coils could vary about 2.5 to 4 cm, with small degrees of relative motion tolerated without loss of signal. Larger variations in these relationships caused transient signal loss.

During the prolonged period of confinement, the jacket and oscillator supply for the energizing coil within the pod caused skin irritation, and on one occasion, a pressure point over a vertebral process produced a slough of a 2-cm-diam area of skin. This has since cleared without complications.

DISCUSSION

The results indicate that the simulation was successful. The telemetry system operated within the design limits, there were no radiofrequency interference problems, and valuable experience was gained which will aid future planning for flight experiments.

A major improvement for future development of the telemetry system is circuitry with even less power consumption. Decreased power requirements would decrease the amount of energy to be transferred and permit greater latitude in placement of the energizing coil. An increase in the energizing coil size and the power supplied to it is also important, as well as providing a longer cable length so the energizing oscillator can be located outside the pod. These changes are relatively easy to implement.

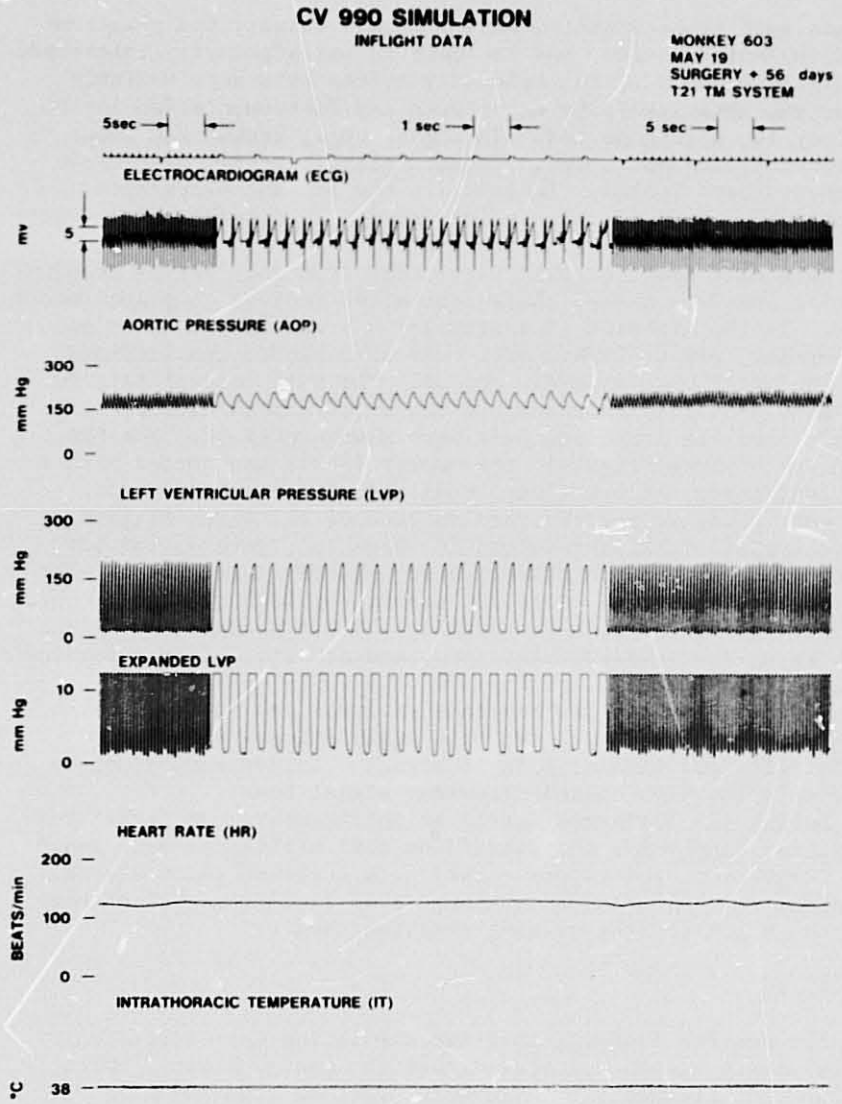

Fig. 5— Typical in-flight data from a 14.5-kg *Macaca nemestrina* confined within the pod (#603)

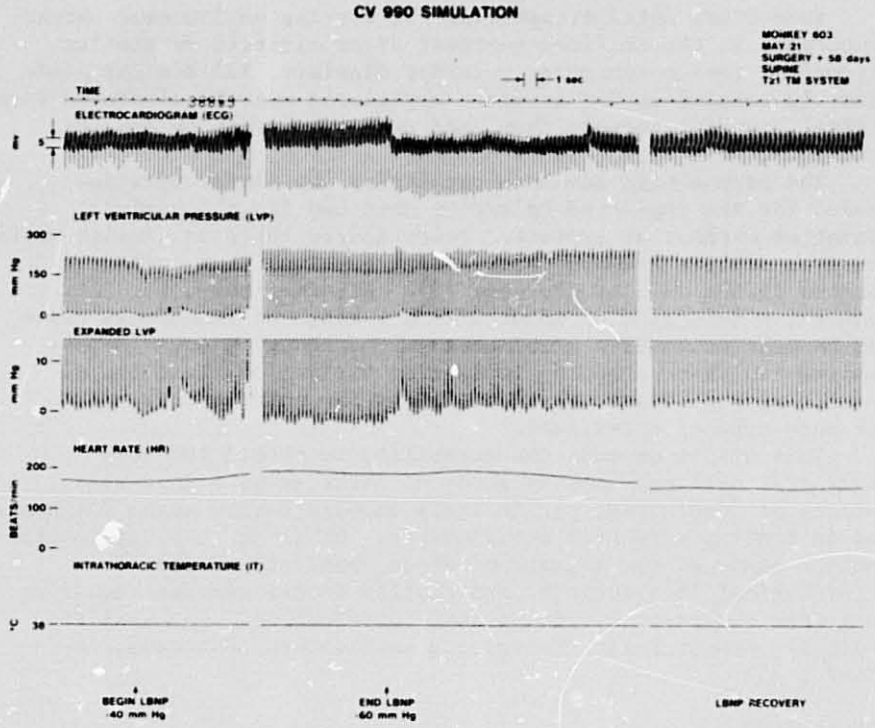

Fig. 6— Changes with lower body negative pressure recorded onboard the aircraft from the pod with the test *Macaca nemestrina* (#603)

Other refinements needed in future units include increased stability of the oscillator frequency with less susceptibility to failure at low power levels, improved transducers with decreased zero drift and longer leads, reinforcement at stress points, and smaller overall size of the implanted electronics package. Frequency stability will reduce the need for receiver tuning and will simplify operation. More stable miniature transducers will remove the need for capacitive coupling and the associated long time constant following power interruption. Smaller overall package size will reduce the extent and duration of the intrathoracic changes.

Monkey skin does not tolerate trauma nearly as well as dog skin. At least 2 months should be allowed for surgical recovery before pod insertion to reduce susceptibility to skin irritation from jackets or other items placed on the animal. Foreign materials over the skin should be minimized, and if used, a protective layer should be provided with extensive padding coupled with careful skin hygiene. An access port must be provided to permit this care. A suitable approach could be the arrangement used in the glove-box or germ-free animal enclosure.

Some other details regarding the working environment should be noted. In the confined quarters of an aircraft or similar situation, device controls, recorder displays, and similar items directly related to the specific experiment must be clustered with minimal distance between them, and such items must be located at a convenient work height.

The technologic advances permitting the miniaturization needed for the implanted telemetry unit and its successful operation without an implanted power source forecast similar units for even smaller animals, with energy received from coils located in the wall of the cage (6). Alternatively, for larger animals, a selection of modules with a range of transducer types can be made available. The necessity of changing experimental designs can then be met by implanting various combinations of modules without requiring a completely new multichannel system for each type of experiment.

This system expands the capability to obtain the more meaningful data provided by study of awake animals in a wide variety of conditions, particularly onboard future space flights and in similar stressful environments. Other obvious applications include study of the effects of drugs, analysis of psychophysiological interactions, and similar investigations requiring long-term observation with minimal interference. The unit is available commercially (Konigsberg Instruments, Pasadena, CA, Model T 21).

CONCLUSIONS

The simulation was useful in demonstrating the following:

1. Cardiovascular instrumentation can be chronically implanted in *Macaca nemestrina* and operated successfully in aircraft flight experiments simulating space flight conditions. Many hours of data were telemetered from all channels of a representative implanted unit on each of eight flights over a 16-day period, thus fully satisfying the basic purpose of the simulation.
2. Improvements are needed to maintain continuous operation of the implanted unit. The proper relative position must be maintained between the internal and external coils. The implanted device was designed to operate in an attended mode with ready access to the animal. The fact that any data could be obtained from a completely enclosed animal even after 5 days without adjustments represents a highly significant achievement. Solutions to the coil positioning problem are a) inclusion of an access port in the pod enclosure, and b) provision of an external energizing coil with a greater field strength over a larger area. The latter approach has been implemented; evaluation is continuing, but current results indicate satisfactory operation.
3. The investigator work space and the data processing capability are important factors in efficient conduct of the experiment and are additional elements requiring careful planning.

4. Postoperative recovery time for macaques after intrathoracic implantation is 6 to 8 weeks, approximately 4 weeks longer than for dogs. The long lead times with chronically instrumented animals must be considered in planning for flight experiments.

5. The knowledge gained from the simulation should permit successful accomplishment of this experiment in a space flight environment.

ACKNOWLEDGMENT

Many people contributed to the successful outcome of this simulation. The pod enclosure, animal insertion and maintenance, and the simultaneous metabolic experiment were provided by A. M. Kodama, R. C. Mains, D. F. Rahlmann, and their assistants at the Environmental Physiology Laboratory, University of California at Berkeley; their efforts are greatly appreciated. For the large number of Ames Research Center personnel whose dedicated work made the test possible, particular thanks are given to S. Kurasaki, J. Connolly, and C. Muehl, as the representatives of this group, and to Mrs. Carol Meaney, who prepared the manuscript.

REFERENCES

1. Fryer, T. B., H. Sandler, W. Freund, E. P. McCutcheon, and E. L. Carlson. A multichannel implantable telemetry system for flow, pressure and ECG measurements. J. Appl. Physiol., 39:318-326, 1975.

2. Sandler, H., H. L. Stone, T. B. Fryer, and R. M. Westbrook. Use of implantable telemetry systems for study of cardiovascular phenomena. Circ. Res., part II, 39:85-100, 1972.

3. Pace, N., D. F. Rahlmann, A. M. Kodama, R. C. Mains, and B. W. Grunbaum. A monkey metabolism pod for space flight weightlessness studies. In Cospar. Life Sciences and Space Research XII, Sneath, P.H.A., ed., Berlin, Akademic-Verlag, 1974, pp. 149-157.

4. Rahlmann, D. F., A. M. Kodama, R. C. Mains, and N. Pace. Results from the EPL monkey-pod flight experiments conducted aboard the NASA/Ames CV-990, May 1976. EPL 76-1, July 1976, p. 137.

5. Fryer, T. B., H. Sandler, and B. Datnow. A multichannel telemetry system. Med. Res. Eng., 8:9-15, 1969.

6. Schuder, J. C. and H. E. Stephenson. Energy transport into the closed chest from a set of very large, mutually orthogonal coils. Commun. Electron., 64:527-534, 1963.

Paper No. 14

NOISE IMPACT ON WILDLIFE: AN ENVIRONMENTAL IMPACT ASSESSMENT

Avi Bender, *Automation Industries, Inc., Vitro Laboratories Division, Silver Spring, Maryland*

ABSTRACT

Various biological effects of noise on animals are discussed and a systematic approach for an impact assessment is developed. Further research is suggested to fully quantify noise impact on the specie and its ecosystem.

INTRODUCTION

The Environmental Impact Statement (EIS), which was born out of the National Environmental Policy Act (NEPA) of 1969, is a basic planning and management document. As such, it should cover all probable environmental impacts associated with a proposed action.

In the past, very little attention has been given to the effects of noise pollution on wildlife. Though seemingly insignificant, closer examination of noise impact on animals reveals possible adverse effects. Noise pollution could conceivably disrupt stable ecosystems and contribute to the extinction of an endangered specie. Due to the complex interaction between organisms, the impact on one specie could affect others, including man.

In an effort to improve management and protection of our natural resources, the NEPA mandated that an EIS be prepared for actions which significantly affect the quality of the human environment. One of the screening criteria put forth by the Environmental Protection Agency (EPA) is the degree to which an action disrupts stable ecosystems, especially when an endangered specie is involved. An increase in the background noise level of natural habitats can interfere with wildlife life patterns. Potential sources of such disturbances are vehicular traffic, construction activities, blasting, and aircraft noise.

There are few documented accounts regarding the effects of noise on wildlife. However, it has been shown through various studies on laboratory animals that they are affected in a manner similar to humans. These effects include auditory, physiological, and behavioral modifications. Laboratory animals have been subjected to acute high level noise inputs (well above 100 dB) in a confined area. Since these laboratory conditions do not accurately represent circumstances in the natural environment, innovative approaches to conducting noise stimuli-response research in the field are needed.

In the preparation of some EISs there have been attempts to evaluate noise impacts on wildlife in situ. The Alaskan Pipeline study included extensive consideration of noise effects based both on field observations and inferences drawn from laboratory data.[1] This was one of the first EIS efforts to focus attention on the gravity of this neglected environmental problem.

Although auditory and physiological reactions were not quantified, the study did assess behavioral modifications (especially avoidance type behavior) associated with responses to various noise inputs.

The following discussion describes various effects of noise on animals. Most of the examples cited describe results obtained with animals under laboratory conditions. A few documented accounts of wildlife impacts are included.

Auditory Effects

Laboratory exposure of mice, dogs, and cats to sound levels from 100-135 dB sound pressure level (SPL) has produced histological changes in the organ of Corti. All animals experienced a threshold shift, some temporary and some permanent.[2] Chinchillas exposed to an octave band of noise centered at 500 Hz with a SPL of 95 dB for a period of 48 to 72 hours developed a threshold shift of 48 dB, with recovery requiring about 5 days.[3] Cats exposed to noise levels of 115 dB SPL for periods of 15 minutes and 8 hours experienced permanent threshold shifts of 5.6 dB and 40.6 dB respectively.[4] In general, the extent of hearing loss depends on the magnitude, frequency, duration, and individual sensitivity of the organism. It is unlikely that wildlife would be subjected to conditions such as those produced in the confines of a laboratory. However, these studies do indicate some of the potential auditory harm intrusive noise may inflict on wildlife.

Physiological Effects

To date, stress has not been quantified for animals in their natural habitats. Adrenal hypertrophy, related to increased background noise, was used as an index of stress in field mice.[5] Stress is associated with certain neural and endocrine activities resulting in increased blood pressure and available glucose. Such physiological reactions are perfectly normal under various circumstances, but prolonged exposure to noise, such as experienced from a snowmobile driven through a wilderness area or from a low flying aircraft, will place an excessive burden on the energy resources of the animal as it attempts to avoid the noise source. Such energy losses by the organism will make it more susceptible to prey or disease, or may even result in death. For example, since the age at which wild sheep attain sexual maturity is dependent on their nutritional state, energy losses as a result of avoidance reactions from low flying aircraft may affect their reproductive process.[1]

Behavioral Modifications

The most apparent results of noise impacts are in the modification of the normal behavioral pattern of the organism. A noise source whose frequency is in the range of the auditory sensitivity of the organism could interfere and mask the communication signals of that specie. Many animals depend on acoustical signals to find their young, mate, establish territorial boundaries, and locate prey. Interference with these acoustical signals can endanger the well being of that organism. Intrusive noise could cause temporary or permanent abandonment of a particular habitat. Some organisms may eventually adapt to new background noise levels, but migration may result in decreased utilization of a habitat in one area and increased use in another area. As

animals are driven away from the noise source, the decrease in available habitat creates greater competition for food and space. In some cases, the result may be a reduced population of a particular specie. In extreme cases, the eventual result can be the elimination of an endangered specie. Aircraft noise, vehicular noise, or sonic booms resulted in condors (endangered specie) abandoning their nests, never to return.[6] The massive hatching failure of sooty terns in Florida was attributed to noise from low flying aircraft.[7] Birds, once disturbed, abandon their nests, leaving their eggs as easy prey for predators.

Ecological Implications

Changes in the homeostasis of individual organisms manifest themselves as changes in the total stability of an ecosystem. Various single specie and ecosystem effects are identified in Table 1. In every ecosystem there is a continuous interaction between organisms and their environment. Pollutional inputs interfere with these interactions and disturb the natural cycle of events.

The remainder of this paper sets forth a systematic approach, illustrated in Figure 1, for assessing the impact of noise from a proposed project. Areas where additional research is required to fully implement the approach are identified.

APPROACH TO ASSESSING NOISE IMPACTS ON WILDLIFE

Step 1: Project Description

Identify noise source(s) and determine magnitude, duration, frequency, and spatial extent. The latter should be represented graphically with noise level contours (isobels); see Step 2. Following is a standard formula for the measurement of noise decay over a given distance:

$$dB = dB_o - 10 \log_{10} \left(\frac{d}{d_o}\right)^2$$

dB = sound level at distance d in decibels
dB_o = sound level at unit distance d_o from source
d = distance between source and receiver (ft)
d_o = unit distance

Note: This model assumes low wind velocity and no muffling effects from surrounding vegetation.[8]

Step 2: Extent of Impact

Define the geographic area affected by the project. Prepare the isobel diagram of Step 1 to the scale of an area map. Overlay the diagram on the map and identify the outermost contour corresponding to the ambient noise level. This outer contour circumscribes the affected area with respect to noise impact. This area represents a potential loss of habitat utilization. An example of a map depicting noise impact is provided in Figure 2.

Table 1. Noise effects on wildlife

SINGLE SPECIE		ECOSYSTEM
AUDITORY	• Complete hearing loss • Threshold shift	Disturbance of natural selection process: * Reduction in number of a specie * Change in the natural patterns of animals * Increased inter and intra specific competition as a result of habitat loss * Reduction in specie diversity * Migration * Loss of endangered specie * Change in predator-prey relationship
PHYSIOLOGICAL	Prolonged stress resulting in: • Metabolic change • Loss of reproductive capacity • Hormonal changes	
BEHAVIORAL	• Masking of acoustic signals • Avoidance type behavior	

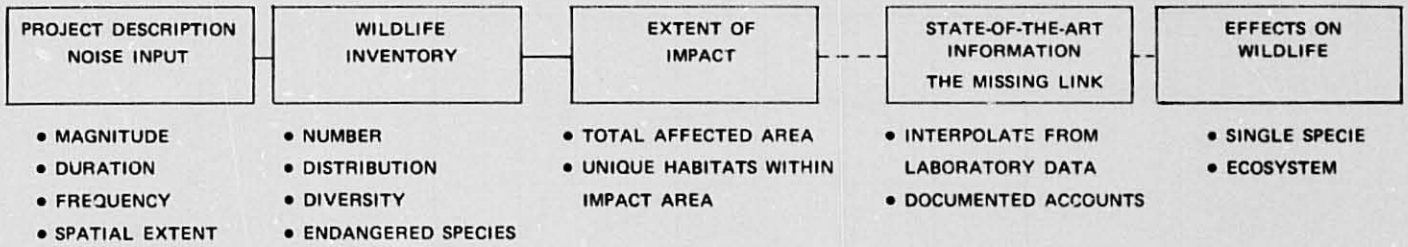

Figure 1. Impact assessment steps

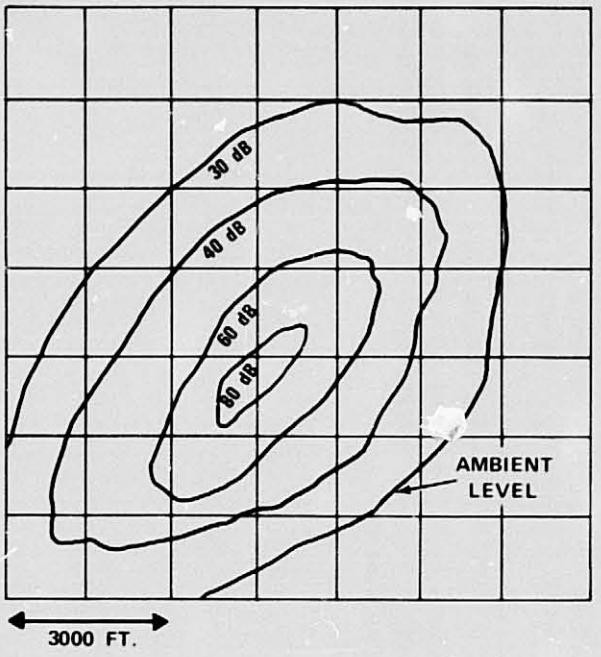

Figure 2. Spacial extent of noise impact

Step 3: Wildlife Inventory

Conduct a survey of the wildlife population in the impacted area defined in Step 2. The survey should include the number and type of animals and their spatial distribution. The techniques for such a survey are well documented.[9] Wildlife populations, unique habitats, and endangered species should be identified on the map with respect to the various noise contours, as shown in Figure 3.

The total area impacted by the noise may be calculated using the graph. Area 1 (A_1) is severely affected, with noise levels 50 dB above ambient. Area 2 (A_2), which has a noise level 30 dB above ambient, contains some endangered species and is also a nesting area.

The wildlife inventory should also relate some of the possible indirect effects on the various trophic levels. Table 2 illustrates a typical predator-prey relationship. The migration of one or more species from the impacted area will create an imbalance in this relationship, resulting in an overabundance or a loss of certain animals. In essence, a functional niche in the affected area may be lost.

Step 4: State-of-the-Art Information on Noise Effects on Wildlife; the "Missing Link"

Assemble data on threshold limit (TL) for noise tolerence for each specie in the affected area. The TL is necessary in making an accurate assessment of probable adverse effects. Unfortunately, data for natural environments are not available. The best we can do currently is to interpolate and infer from studies conducted on laboratory animals.[2] Great care, however, must be taken in the interpolation of such data. As previously indicated, most of the laboratory experiments subjected animals to unusually high noise levels while confined to their cages.

Step 5: Assessment of Noise Effects on Wildlife

Incorporate information obtained in Steps 1 through 4 into an assessment of the various direct and indirect impacts on the wildlife in the project area. Complete appropriate sections of the EIS; e.g., project description, existing environment, probable impacts, and mitigating actions for avoiding adverse impacts on wildlife.

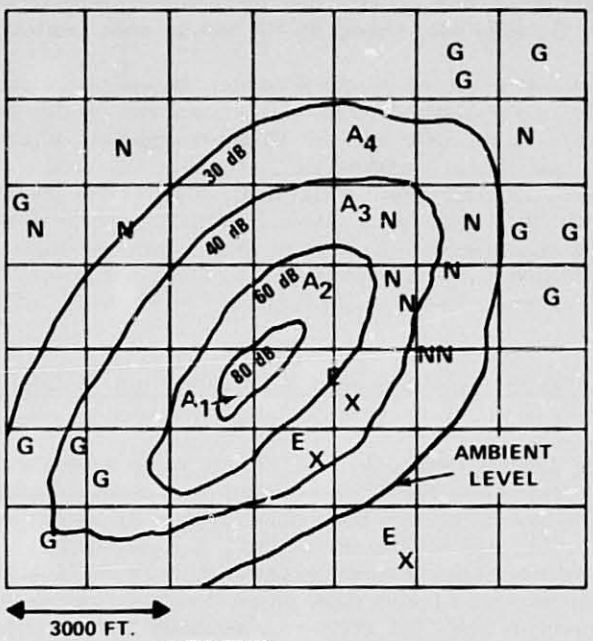

Figure 3. Spatial extent of noise impact on wildlife habitats

Table 2. Predator-prey relationships in impacted area

SPECIE	BOBCAT	RABBIT	RAT	HAWK	RACOON
BOBCAT	0	+	+	0	+
RABBIT	–	0	0	–	–
RAT	–	0	+	–	+
HAWK	0	+	+	0	+
RACOON	–	+	+	0	0

NOTE: SYMBOLS INDICATE RELATIONSHIP OF ANIMAL LISTED IN LEFT HAND COLUMN TO ANIMALS LISTED IN TOP ROW.

LEGEND

+ PREDATOR

– PREY

0 NEUTRAL

SUMMARY

When projects are proposed for pristine or near pristine environments, the EIS should include consideration of noise effects on wildlife. Sufficient attention has not been given to this problem area. This is partly due to the scarcity of data. Further detailed research is needed to clearly define the effects of noise. Each organism hears differently and has varying auditory sensitivities. What may be irritating to one organism may have no apparent effect on another.

A systematic approach for the analysis of a noise impact on a wildlife habitat has been described. The missing information, which impedes the complete and accurate analysis of a given impact, is accurate knowledge of how animals react to various noise levels of varying frequencies. This information is not presently available. The best that can be done at this juncture is to interpolate from laboratory experiments and limited field observations.

Experiments should be performed in the natural habitat of organisms to develop a threshold limit of noise tolerance for wildlife. Conduct of field investigations may eventually be possible using dosimeter type devices and telemetric monitoring to measure the heart rate of animals in response to varying noise intensities. A threshold limit of noise tolerance for different wildlife species may then be determined, based on a correlation between noise input and stress, as indicated by increased heart rate. Noise inputs should attempt to simulate magnitude, duration, and spectral characteristics associated with construction and vehicular noise and other intrusive noise sources associated with man's encroachment into nature.

It is obvious that we can be faced with a problem affecting the quality and well being of our frail ecosystems. In keeping with the spirit of the NEPA, efforts should be made to bring noise effects on wildlife into proper perspective, and then make an effort to resolve them.

REFERENCES

1. The Alaskan Natural Gas Transportation EIS. Alaska Volume, U.S. Dept. of Interior. pages 323-338, March 1976.

2. Memphis State University, Effects of Noise on Wildlife and Other Animals. U.S. Environmental Protection Agency pub., NTIO 300.5, 1971.

3. Benitez, L.D., Eldridge, D.H., and Templer, J.W. Electrophysiological Correlates of Behavioral Temporary Threshold Shifts in Chinchilla. Presented at 80th Meeting of the Acoustical Society of America, Houston, November 1970.

4. Miller, J.D., Watson, C.S., and Covell, W.P. Deafening Effects of Noise on the Cat. Acta Otolaryng. Suppl. 176, 91, 1973.

5. Chesser K.L., Caldwell, R.S., and Harvey, M.J. Effects of Noise on Feral Populations of Mus Musculus. Physiological Zoology, Vol. 48 No. 4, pages 323-325, October 1975.

6. Shaw, E.W. California Condor. Library of Congress Legislative Reference Service, SK351, 1950.

7. Henkin, H. The Death of Birds. Environment 11, 51, 1969.

8. Cross, F.L. Assessing Noise Impact on the Environment. Pollution Engineering, November, 1973.

9. Giles, R.H. Wildlife Management Techniques. Wildlife Society pub., 3rd Ed., 1969.

Paper No. 15

A METHODOLOGY FOR ESTIMATING DOG NOISE IN AN ANIMAL HOUSING FACILITY

S. E. Sierens, M.E., H. A. Ingley, Ph.D., and E. L. Besch, Ph.D.,
University of Florida, Gainesville, Florida 32611

ABSTRACT

A rectangular reverberation chamber was designed, constructed and calibrated for the experimental measurement of the sound power level (acoustic power) of a dog. Calibration of the chamber consisted of comparing the acoustic power measured for a random noise source in the chamber with that for the identical source in a free field environment. Data from dogs indicate that barking noise can be modeled as a square wave pattern with short duration and peak sound power levels in the 500 Hz octave band. A-weighted sound pressure levels of up to 114.7 dBA were absorbed, indicating a potential concern for both animals and man chronically exposed to such environments.

INTRODUCTION

Although noise has been recognized as an important parameter for the research animal bioenvironment (1,2,3), little scientific evidence is available from which exposure levels for animals may be specified (4). Previous recommendations on acceptable noise levels for animals (3) were based on animal exposures to a minimum noise intensity for 40 hours per week. Dog barking appears to be a primary cause of high noise in an animal facility (2,5), but no apparent attempts have been made to quantitate the dog as a noise source or to characterize the dog's sound power levels. Further, little information is available concerning permissible noise exposures of humans in animal facilities or weather existing levels exceeded those specified by OSHA (6). Such information not only would be useful in estimating noise levels but also would allow for appropriate acoustic designs in existing or new facilities. These considerations led to the research reported here.

MATERIALS AND METHODS

Reverberation Chamber

Based on preliminary measurements in a typical animal facility which indicated noise levels associated with barking dogs were predominantly in the frequency range of 250 Hz to 4 KHz, a lower limiting frequency of 250 Hz was selected for the reverberation chamber design (7). The dimensions of the chamber were selected based on two criteria:

1) the interior volume of the chamber should be greater than or equal to $4\lambda^3$, where λ is the corresponding wavelength for the lower limiting frequency (8);

2) the chamber dimensions of length, width, and height should possess ratios of 1.0: 1.259; 1.587, respectively (8).

The chamber (Fig. 1) was constructed of wood with a glazed tile interior wall finish. The glazed tile provided a hard, reflective interior surface necessary to produce a diffuse sound field within the chamber. To further enhance this diffuse quality of the chamber, irregular geometric shapes were constructed on several of the walls. The walls were also splayed so that no two walls were parallel. The final chamber interior surface area (S) was 31.73 m^2 (341.5 ft^2); the volume (V) was found to be 9.82 m^2 (346.8 ft^2).

Chamber Calibration

The schematic (Fig. 2) identifies instrumentation used in chamber calibration. Eight microphone positions were monitored for each of ten speaker locations in the chamber to provide data from which to select an optimum source and microphone position. A noise generator (Bruel and Kjaer, Type 1402), a 100 watt amplifier and a sound driver provided the random noise source. A microphone (General Radio, Type 1560-P6) and magnetic data recorder (General Radio, Type 1525-A) were used to monitor the noise levels in the chamber. All data were analyzed on an audio frequency spectrometer (Bruel and Kjaer, Type 2112) and graphic level recorder (Bruel and Kjaer, Type 2305). The reverberation time (T_{60}) of the chamber was determined for several octave band frequencies.

Reverberation chamber data were compared with data from a free field environment to verify the

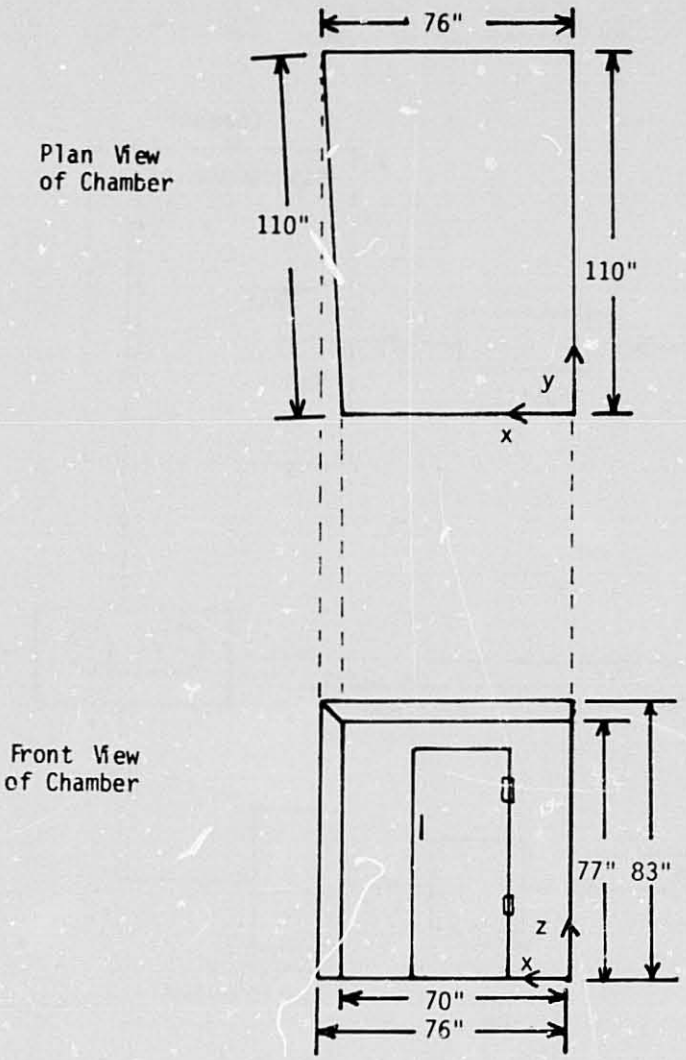

Figure 1. Coordinate System and Reference Axes for Location of Speaker and Microphone Positions, Reverberant Field

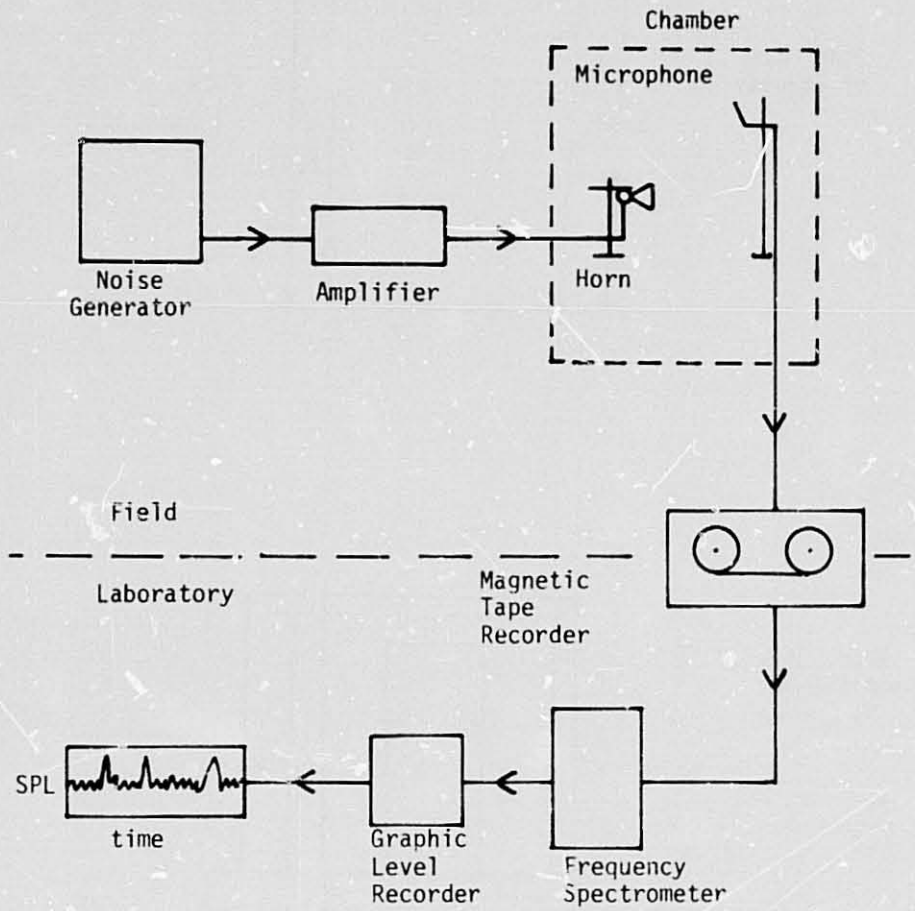

Figure 2. Schematic of Instrumentation Used in Reverberation Time Measurements

reliability of results obtained in the chamber. Although free field measurements usually provide more accurate means of determining sound power levels for a noise source, it is very difficult to use such a field to determine acoustic power levels for laboratory animals.

Animals

A male, adult German Shepherd dog was acclimated to the chamber for a period of 14 days. A microphone was placed in the chamber at the optimum position determined during the calibration runs. The dog was placed in one corner of the chamber which appeared to be a satisfactory location for the sound power level determinations. Dog barks were recorded on magnetic tape for a period of 15 minutes.

From analyses of fifty barks recorded during the test period, peak sound pressure levels, duration times, and rise times were recorded for each bark. Using the sound pressure level and room response data, average sound power levels were calculated for octave bands centered at 250 Hz, 500 Hz, 1 KHz, 2 KHz, 4 KHz, 8 KHz, and 16 KHz.

Calculations

Assuming that the chamber would provide a diffuse sound field, equation (1) was used to determine sound power levels (PWL) for the sound source placed in the room:

$$PWL = \overline{SPL} + 10 \text{ Log } V - 10 \text{ Log } T_{60} + 10 \text{ Log } \left(1 + \frac{S\lambda}{8\lambda}\right) - 13.5 \text{ (dB)} \quad (1)$$

where PWL = sound power level, dB, in frequency band of interest
$\overline{SPL}$ = average sound pressure level (usually from several microphone positions), dB, in frequency band of interest
V = total volume of test room, m^3
T_{60} = reverberation time of test room in frequency band of interest, sec.
S = interior surface area of room, m^2
λ = wavelength of center frequency of test band, m

The volume (V) and interior surface area (S) were determined from the dimensions of the reverberation chamber. The reverberation time (T_{60}) and average

sound pressure level ($\overline{SPL}$) were determined experimentally.

RESULTS

Data (Table 1) from several free field environments compared favorably with data taken in the reverberation chamber utilizing the same sound power source operating at identical power settings. In most comparisons of the free field to reverberant field measurements of sound power levels. the percent error did not exceed 5%.

Data from the barking dog (Table 2) were consistent and reproducible and the range of sound pressure levels in any octave band appeared to be less than 20 dB. The dog appears to have the widest range of sound pressure levels in the lower frequencies with a decreasing range at increasing frequencies. For example, at 1 KHz the range of sound pressure levels was 13 dB (102 to 115) while at 16 KHz the range was 4 dB (68 to 72). The standard deviations in sound pressure level varied from 3.7 dB at 2 KHz to 1.3 dB at 16 KHz. The 95% confidence intervals were extremely small, ranging from 0.4 dB at 16 KHz to 1.0 dB at 2 KHz and 4 KHz, due in part to the large sample size. The sound pressure level in the 500 Hz octave band was within 0.5 dB of the overall sound pressure level (All Pass) indicating that the sound pressure levels in the remaining octave bands contribute little to the total sound level. The A-weighted sound pressure levels measured in the reverberation chamber ranged from 100-119 dBA, with an average A-weighted sound pressure level of 114.7 dBA.

The slope and general pattern of the decay curves (room response) from an interrupted noise source were virtually identical to the slope and pattern of the decay portion of the dog barks. Thus, the barking pattern can be treated as a square wave pattern with a very steep rise time (0.1 second) and a duration of about 0.05 second. These curves - spaced about 1.5 seconds from one another - have peak levels that vary with the octave band (Table 1).

Figure 3 illustrates the sound power level frequency distribution for the dog bark, calculated from equation (1) with appropriate substitutions. Data points of octave bands above 500 Hz appear to be linear with an average slope of minus 10.1 dB per octave. The single exception is at 8 KHz where a

TABLE 1
SUMMARY OF AVERAGE SOUND POWER LEVELS
($\overline{PWL}$) FOR CALIBRATION SOURCE dB

Notation: ○ Sperical Free Field, △ Hemispherical Free Field, Position 2
▽ Hemispherical Free Field, Position 1, □ Reverberant Field

Power Setting (1)

		Octave Band Center Frequency							
	All Pass	A	250	500	1000	2000	4000	8000	16000
○	106.4	106.6	83.2	98.2	101.3	103.2	103.2	87.2	72.0
△	109.6	110.4	80.6	95.0	100.0	106.2	105.0	99.7	77.0
▽	106.4	107.1	77.9	93.9	98.8	102.8	101.4	94.7	73.5
□	108.6	107.7	81.4	97.3	100.8	104.2	100.5	91.9	72.5
$\overline{PWL}$, ○, △, ▽, □	108.7	108.3	81.1	96.1	100.1	104.3	102.2	96.3	74.6
% error	.83	.55	.37	1.25	.69	.09	1.7	4.6	2.8

Power Setting (2)

		Octave Band Center Frequency							
	All Pass	A	250	500	1000	2000	4000	8000	16000
○	117.3	117.7	94.5	108.5	112.3	113.9	107.3	97.5	77.6
△	121.7	122.2	93.2	107.1	112.0	117.7	116.4	110.2	92.9
▽	119.7	120.1	91.9	106.5	112.3	115.5	114.3	107.1	88.6
□	120.6	119.6	94.3	109.0	112.8	115.9	110.2	102.8	82.6
$\overline{PWL}$, ○, △, ▽, □	119.9	120.3	93.4	107.4	112.2	115.9	116.1	107.3	89.6
% error	.58	.58	.96	1.5	.53	0	5.1	4.2	7.8

TABLE 2

MEAN (± SD) SOUND PRESSURE LEVELS ($\overline{SPL}$) FOR THE GERMAN SHEPHERD DOG
(In all instances, 50 barks were analyzed)

			Octave Band Center Frequency, Hz						
	All Pass	A	250	500	1000	2000	4000	8000	16000
SPL, dB	119.3	114.7	96.4	118.8	110.5	100.5	90.2	84.5	69.6
S.D., dB	2.3	2.9	2.5	2.2	2.9	3.7	3.5	2.4	1.3
95% Confidence Interval for the Mean	± 0.6	± 0.8	± 0.7	± 0.6	± 0.8	± 1.0	± 1.0	± 0.7	± 0.4
High	123	119	102	123	115	107	97	90	72
Low	112	100	93	113	102	90	82	79	68

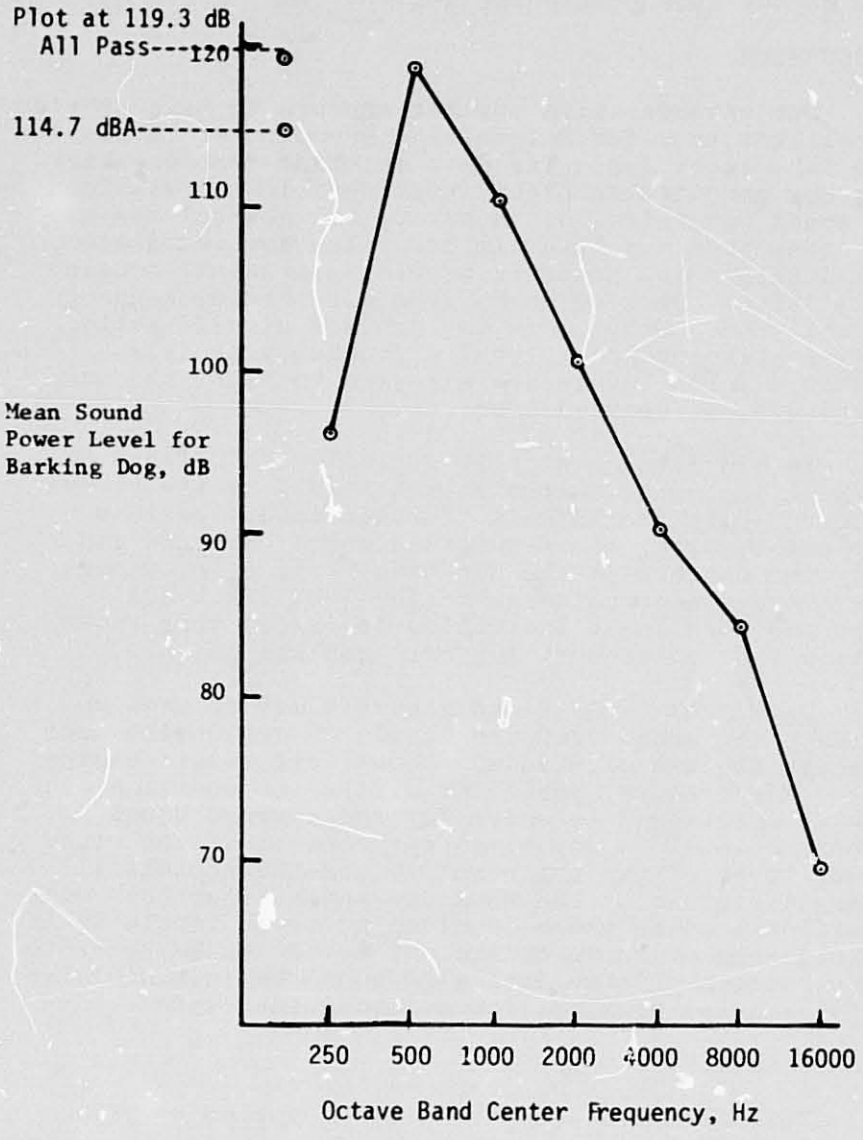

Figure 3. Sound Power Level (PWL) versus Frequency for Dog

slight deviation from the linear decay is noted. From 250 Hz to 500 Hz the rate of increase was about twice the rate of decrease from 500 Hz to 16 KHz, or about 22.7 dB per octave. Analysis of the three 1/3 octave bands in the 500 Hz octave band indicates the the "characteristic frequency" is in the range of 447 to 562 Hz for this particular dog.

DISCUSSION

Our reverberation chamber appears to have provided a reliable tool for determining sound power levels for the laboratory dog. The data obtained from one barking dog resulted in highly reproducible calculations of sound power levels. However, the generalized use of these data may have limited value for immediate applications for acoustic problems in animal housing facilities. Barking noise from more breeds needs to be analyzed. Other dogs may provide significantly different sound power level - frequency profiles, although sound levels are expected to reach the same magnitude as reported here.

In order to completely evaluate the effects of barking dog noise on the animal itself or the humans involved with the animals, further investigations for establishing the A-weighted noise exposure and the time pattern of the dog barks will be necessary. The average A-weighted noise level of 114.7 dBA reported here is an indication in itself that there is a potential concern for both man and animals.

Data from Table 2 and Figure 3 may be used to predict the sound pressure levels in any environment through the use of standard acoustical relationships (8). For example, equations similar to equation (1) may be rearranged to solve for the average sound pressure level in any given environment if the sound power level of the noise source and the acoustical characteristics of the room are known. Further, with additional sound power level data, noise levels in an animal room of known design may be estimated prior to construction. These data also would be invaluable in solving noise problems for existing facilities.

ACKNOWLEDGMENT

This research was partially supported by NIH Grant No. RR 00942.

REFERENCES

1. McPherson, C., Why Be Concerned About the Ventilation Requirements of Experimental Animals, ASHRAE Transactions, Vol. 81, Part 2, pp. 539-541, 1976.

2. Moreland, A.F., Characteristics of the Animal Research Bioenvironment, ASHRAE Transactions, Vol. 81, Part 2, pp. 542-548, 1976.

3. Anthony, A., Criteria for Acoustics in Animal Housing, Laboratory Animal Care 13, pp. 340-350, 1963.

4. The Design and Function of Laboratory Animal Houses, A Laboratory Animal Symposia held in London, 1967, Edited by Hare, R., March 1968.

5. U.S. Department of Health, Education and Welfare, Guide to the Care and Use of Laboratory Animals, DHEW Publication No. (NIH) 74-23, 1974, Bethesda, Maryland.

6. U.S. Department of Labor, Guidelines to the Department of Labor's Occupational Noise Standards for Federal Supply Contract, Office of the Solicitor, Bulletin 334, 1971 (Rev.), Washington, D.C.

7. Sierens, S.E., The Design, Construction, and Calibration of an Acoustical Reverberation Chamber for Measuring Sound Power Levels of Laboratory Animals, Unpublished Master's Thesis, Department of Mechanical Engineering, University of Florida, August, 1976.

8. Beranek, L.L., Noise and Vibration Control, McGraw-Hill Book Company, New York, 1971.

Paper No. 16

THE EFFECT OF 1 TO 5 keV ELECTRONS ON THE REPRODUCTIVE INTEGRITY OF MICROORGANISMS

J. Barengoltz, *Jet Propulsion Laboratory, California Institute of Technology, and* J. Brady, *The Bionetics Corporation*

ABSTRACT

Microorganisms were exposed to a simulated space environment in order to assess the effect of electrons in the energy range 1 to 5 keV on their colony-forming ability. The test system consisted of an electron gun and power supply, a dosimetry subsystem, and a vacuum subsystem. The system was capable of current densities ranging from 0.1 nA/cm^2 to 5 μA/cm^2 on a 25 cm^2 target and an ultimate vacuum of 6 x 10^{-4} N/m^2 (4 x 10^{-6} torr). The results of the experimental program have shown a significant reduction in microbial reproductive integrity.

INTRODUCTION

Planetary quarantine is an international cooperative program concerned with the prevention of the contamination of another planet or satellite of a planet by terrestrial organisms. Such a contamination by an automated spacecraft could yield false positive results from its own life detection instruments and, if the terrestrial microbes grew and spread, would confuse all subsequent studies (Reference 1).

As a part of this program, research is conducted to determine the lethal effect of various natural space environments on microorganisms. In particular the study presented in this paper is directed towards determining the spacecraft-associated microbial burden reduction inherent in a mission history attributable to solar wind electrons.

An electron source system has been constructed to provide exposures to electrons in the energy range 1 to 5 keV in a vacuum. The energy range was selected on the basis of a minimum energy for biological effectiveness (Reference 2) and measurements and models of the energy spectrum (References 3 and 4). Parametric tests in this energy range have been conducted on typical spacecraft microbes at accelerated dose rates (flux) to permit realistic mission doses (fluence) in acceptable test durations. At each energy and dose rate tests with varying doses have been performed and survival curves obtained.

Experimental Apparatus

The Solar Wind Electron Source (SWES) system consists of three subsystems: an electron gun subsystem, a dosimetry subsystem, and a vacuum subsystem (Figures 1 and 2).

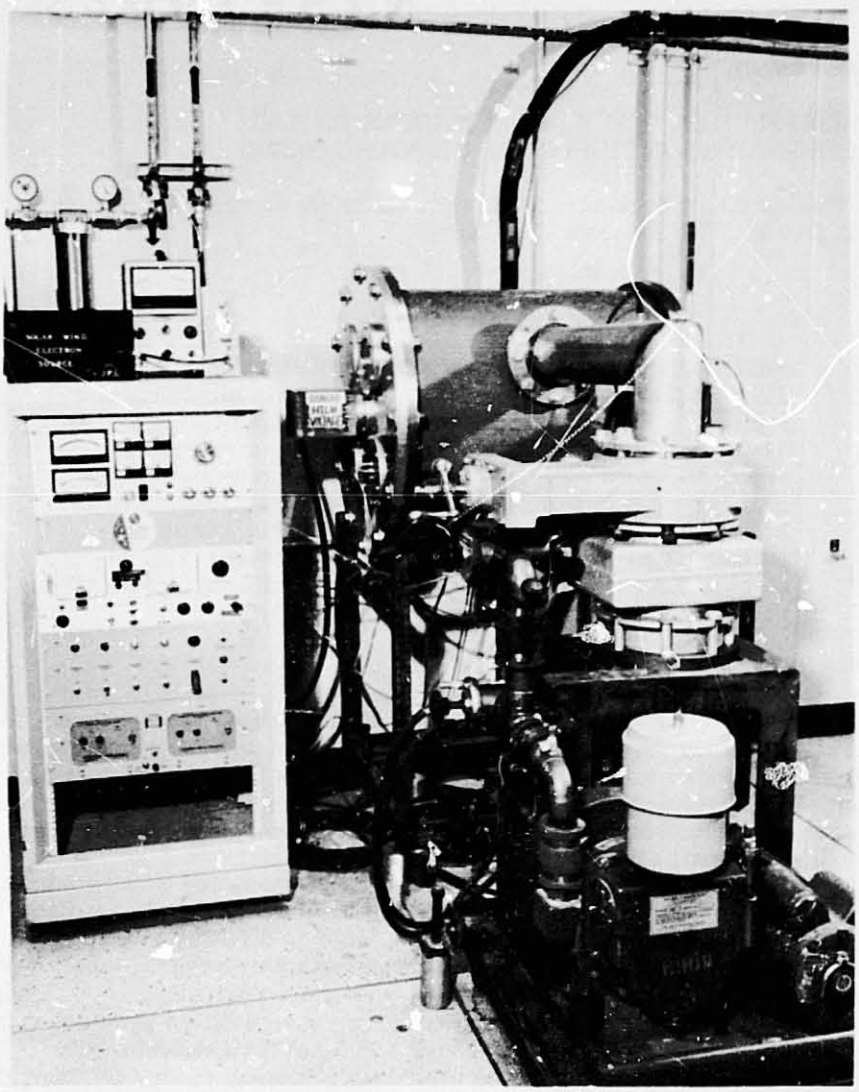

Figure 1. Solar wind electron source, overview of system

The electron gun and its power supply and instrumentation package comprise the electron gun subsystem. The electron gun, visible in the upper right hand corner of Figure 2, may be mounted on the vacuum chamber centerline (as shown) or at one of four off-axis positions. The two-axis gimbal mount permits the beam to be centered in either case. This capability will allow combined environment experiments to be conducted in the future.

The electrons are initially emitted at thermal energies by the "uni-potential high temperature" cathode held at a large negative potential

C-3

Figure 2. Solar wind electron source, interior view showing dosimetry fixture and electron gun

(the accelerating voltage or energy) with respect to the chamber ground. The cathode emission level is adjustable to change the dose rate. The spatial profile of the beam (divergence) is varied by a solid angle electrode. A pre-acceleration element accelerates the electrons to an intermediate energy before they gain the desired total energy in falling to the test fixture (ground). The power supply and instrumentation package (Figure 1) allows adjustment and monitoring of all of the previous parameters, as well as a beam current monitor.

The electron gun subsystem can produce electrons in the energy range of 1 to 5 keV (±5 percent) at current densities variable from 0.1 nA/cm^2 to 5 μA/cm^2. This current density range is equivalent to a flux (dose rate) range of 6 x 10^8 to 3 x 10^{13} e/cm^{2}s. With the present configuration, the subsystem can cover a circular area of 25 cm with a 20 percent overall radial uniformity and a local uniformity (azimuthal) of 10 percent. A straightforward modification of the electron gun by the addition of a pre-acceleration grid and a ground grid provides a much larger radially uniform coverage at the cost of larger inhomogeneities.

The dosimetry subsystem consists of a dosimetry test fixture, a monitor Faraday cup, a Keithley Model 610B electrometer, and the necessary cabling, vacuum feedthroughs, and connectors. The dosimetry test fixture is comprised of an array of four Faraday cups mountable on 10, 20, or 30 cm diameter circles on a phosphor screen plate. These Faraday cups, together with the monitor Faraday cup on the beam axis, provide a direct reading of the incident current density (proportional to flux) at discrete locations. The cup currents are monitored by the electrometer. The phosphor screen glows under electron bombardment to provide a check of local uniformity and overall profile of the beam. It

may be inspected through a vacuum window at the gun end of the chamber (Figures 2 and 3). The use of the dosimetry subsystem is described below.

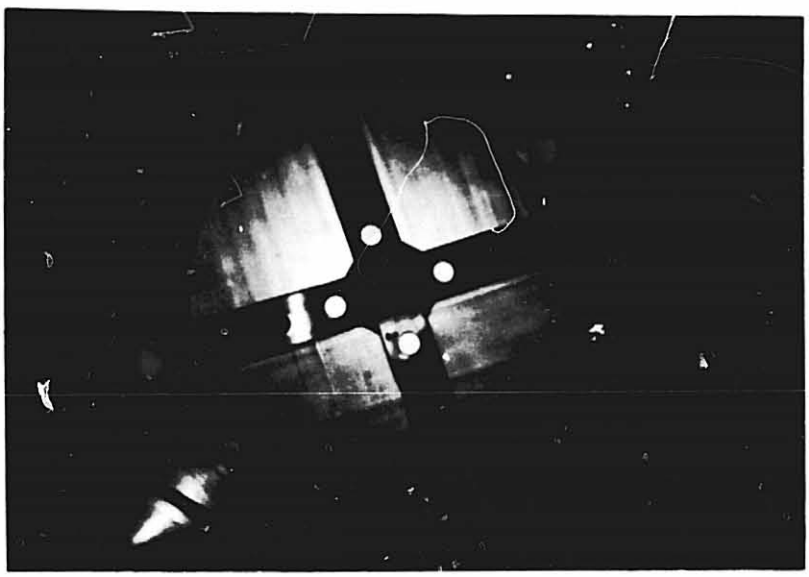

Figure 3. View of dosimetry test fixture through vacuum window with the source in operation

The vacuum subsystem is a 61 cm inner diameter x 70 cm long cylindrical vacuum chamber pumped by a liquid nitrogen trapped 6 in. diffusion pump stand (Figure 1). The subsystem is capable of obtaining a vacuum of 1×10^{-3} N/m^2 (8×10^{-6} torr) from ambient pressure (dry nitrogen) in 1 hour or less. The oil backstreaming, of particular importance to cathode life and beam uniformity, was measured by quartz crystal microbalance techniques over 63 hours of segmented vacuum operation with approximately two hours of gun operation. The deposition rate either exposed to the beam or near the pump inlet was less than 5×10^{-11} g/cm^2 s.

Experimental Procedures

1. Beam Profile and Dosimetry Measurements. The measurements of the beam profile and other dosimetry matters were accomplished with the use of the dosimetry subsystem described above. The dosimetry test fixture was mounted inside the vacuum chamber access door and the cup cables connected (see Figure 2). A complete profile at a particular energy and flux was obtained by consecutive runs with the movable Faraday cups placed on the 10, 20, and 30 cm diameter circles. These runs were normalized for comparative purposes by resetting all controls by the meters and then adjusting the cathode emission precisely with the monitor (center-fixed) Faraday cup.

For the pure culture tests to be discussed, only a single beam mapping run with the movable cups on the 10 cm diameter circle was required. This dosimetry run, which was performed before each experimental run, allowed an optimization of azimuthal symmetry on the circle corresponding to the cultured organism test fixture annulus. When the proper control settings had been noted, the monitor Faraday cup reading to produce the desired flux at the sample annulus was also recorded. During an experimental run, with the dosimetry test fixture replaced by the cultured organism test fixture (Figure 4), the flux was monitored by the monitor Faraday cup. Note that the test fixture has a hole on the beam axis to allow the cup to see the beam. The required fluence was then obtained by timing the duration of the exposure.

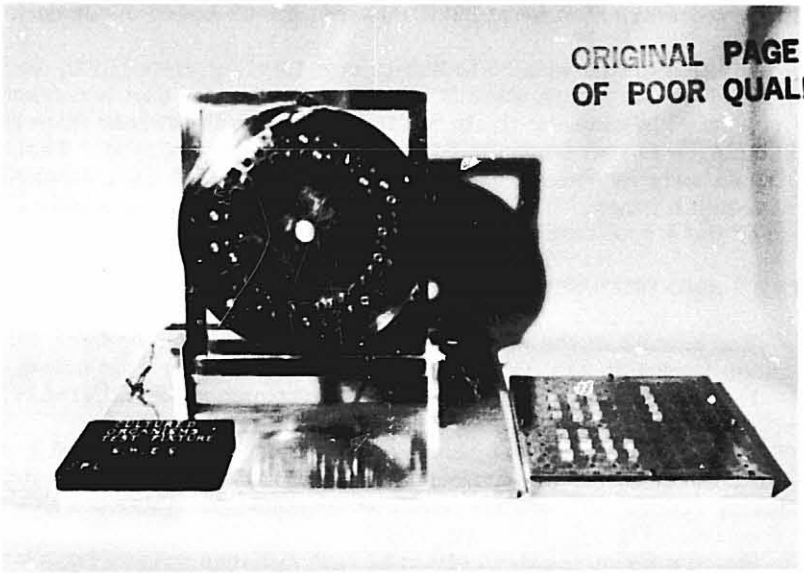

Figure 4. Cultured organism test fixture

2. Microbiology. Pure cultures of MM71 Proof Test Module (PTM) isolates, Bacillus subtilus var. niger (BSN) and Staphylococcus epidermidis (SE) (ATCC-17917) were prepared. Sporeforming organisms were sporulated in the liquid synthetic medium of Lazzarini and Santangelo (Reference 5) modified by the addition of 25 mg of both L-methionine and L-tryptophan to one liter of medium. Mature spores were harvested and washed (7 times with sterile distilled water) by centrifugation (10 min at 9750 relative centrifugal force) with final suspension in distilled water. Nonsporeformers were maintained on Trypticase Soy Agar (TSA; BBL) slants. Lawns were prepared by resuspension of the slant growth in Trypticase Soy Broth (TSB; BBL) and inoculation of TSA plates with the suspension. Plates were incubated at 37°C for 48 hours, and cells harvested (on the day they were to be irradiated) by washing the plates with 20 ml of sterile distilled water. The resulting suspension was washed

with sterile distilled water 4 times by centrifugation (10 min at 9750 relative centrifugal force).

Six sterile aluminum stages were inoculated by micropipette with an amount of each suspension to place about 10^6 microbes on each stage. These stages were allowed to dry in a controlled environment and then mounted on both sides of the test fixture (Figure 4).

After the test exposure, the fixture was assayed in a rapid, consistent manner. Stages were removed from the fixture, placed individually into tubes containing 10 ml of 0.1 percent sterile peptone water, and exposed to ultrasonic treatment (25 kHz for 12 min) in an ultrasonic bath. Upon removal from the bath the tube contents were thoroughly mixed prior to 10-fold serial 1.0 ml dilutions and triplicate 1.0 ml platings of designated dilutions with TSA. The organisms were incubated at 37°C (nonsporeformers) or at 32°C (spores) for 48 hours under dark conditions.

Dilution plates with 30 to 300 colony-forming units (CFU) were enumerated for survivors after the incubation period. Survival fractions were computed by ratioing the bacterial population recovered from the exposed stages to that from the "dark" side stages (controls). These populations were expressed as geometric means. Each experimental run was repeated 4 times. The final survival fractions are arithmetic averages over the 4 replicate runs.

RESULTS AND DISCUSSION

The results of the formal test program are presented graphically in Figures 5 through 12. Certain features of the data may be noted:

1) There is a large variation in the response for different organisms.

2) Isolate No. 5, a micrococcus, is extremely resistant compared to isolate No. 4, a micrococcus, or Staphylococcus epidermidis. This factor causes rather large mean nonsporeformer (MEAN VEG) survival fractions (Figures 6, 8, 10, and 12).

3) An obvious plateau effect at high fluences occurs for survival fractions between 0.001 and 0.01 in the case of BSN and the mean sporeformers and about 0.1 in the case of mean nonsporeformers at all energies.

The plateau effect is tentatively explained by sample clumping and the resultant shielding of individual organisms. It is well known that electrons in the energy range studied cannot penetrate through an organism, e.g., the range of a 5 keV electron in organic material is only 0.57 μm (References 6 and 7). Under this hypothesis, the minimum survival fraction is then interpreted as the fraction of cells which are shielded by at least one other cell. Since the test samples represent an extremely large density ($\sim 10^6$ cm^{-2}) compared to a real surface, this effect would render the present results very conservative.

Isolate No. 5, a micrococcus in a tetrad form, may be an exception in that any cell of the tetrad will typically be shielded by one or more of the others. This self-shielding may explain both the resistance of No. 5 to the radiation and the high plateau survival fraction for the mean nonsporeformers, dominated by the results for No. 5.

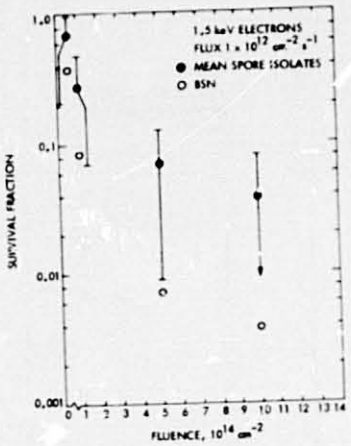

Figure 5. Spore survival at 1.5 keV electron energy

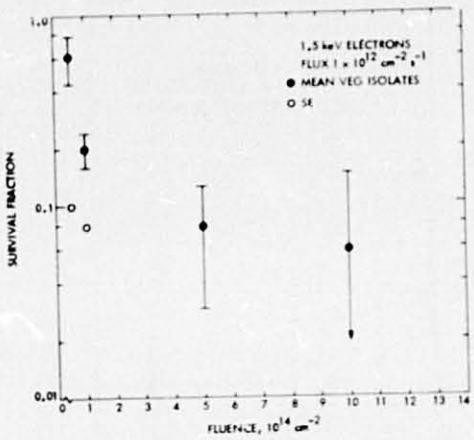

Figure 6. Nonsporeformer survival at 1.5 keV electron energy

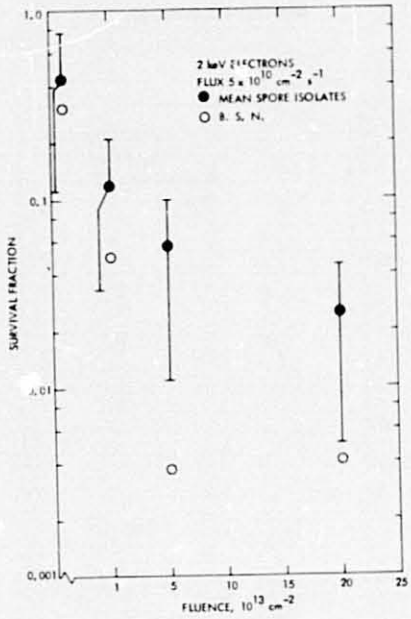

Figure 7. Spore survival at 2.0 keV electron energy

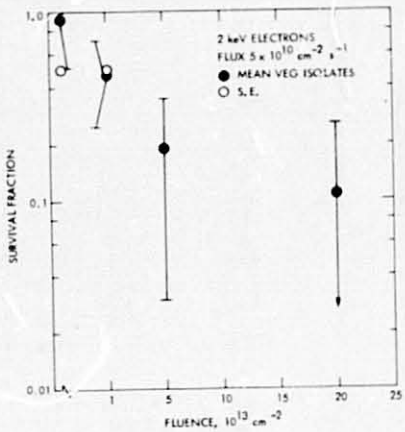

Figure 8. Nonsporeformer survival at 2.0 keV electron energy

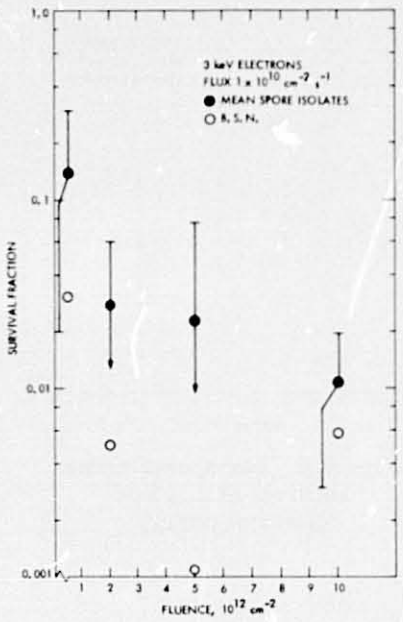

Figure 9. Spore survival at 3.0 keV electron energy

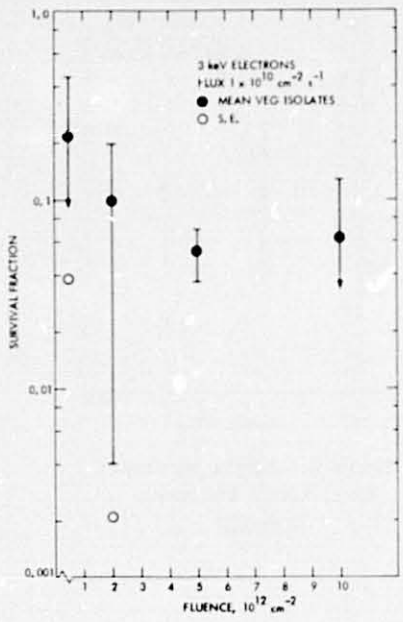

Figure 10. Nonsporeformer survival at 3.0 keV electron energy

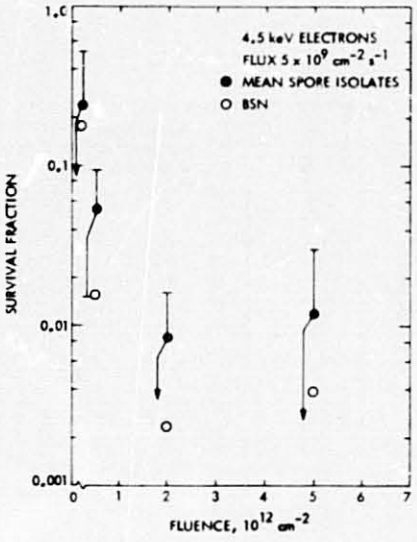

Figure 11. Spore survival at 4.5 keV electron energy

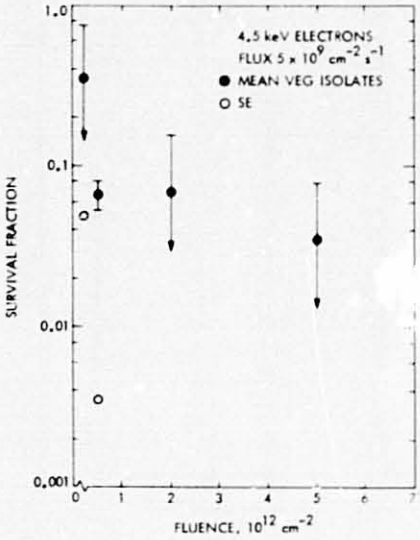

Figure 12. Nonsporeformer survival at 4.5 keV electron energy

The results may also [illegible] marized in terms of the D_{10} values, or the fluence required to pr[illegible]ne order of magnitude reduction in the survival fraction. Calcula[illegible]ues from the linear regression analysis for four fluence values [illegible] given in Figure 13. Because of the plateauing effect the D_{10} values represent over-estimates of the fluence required for the first order of magnitude reduction. Note that D_{10} for B. subtilis as measured by Davis (Reference 2) is considerably smaller than the present results, especially at the higher energies. Davis' values are for the first order of magnitude reduction since she innoculated only 50 microbes on a 1 cm^2 substrate to avoid clumping. A revision of our D_{10} values, to a fit for survival fractions greater than 0.02 only, yields excellent agreement with the published work.

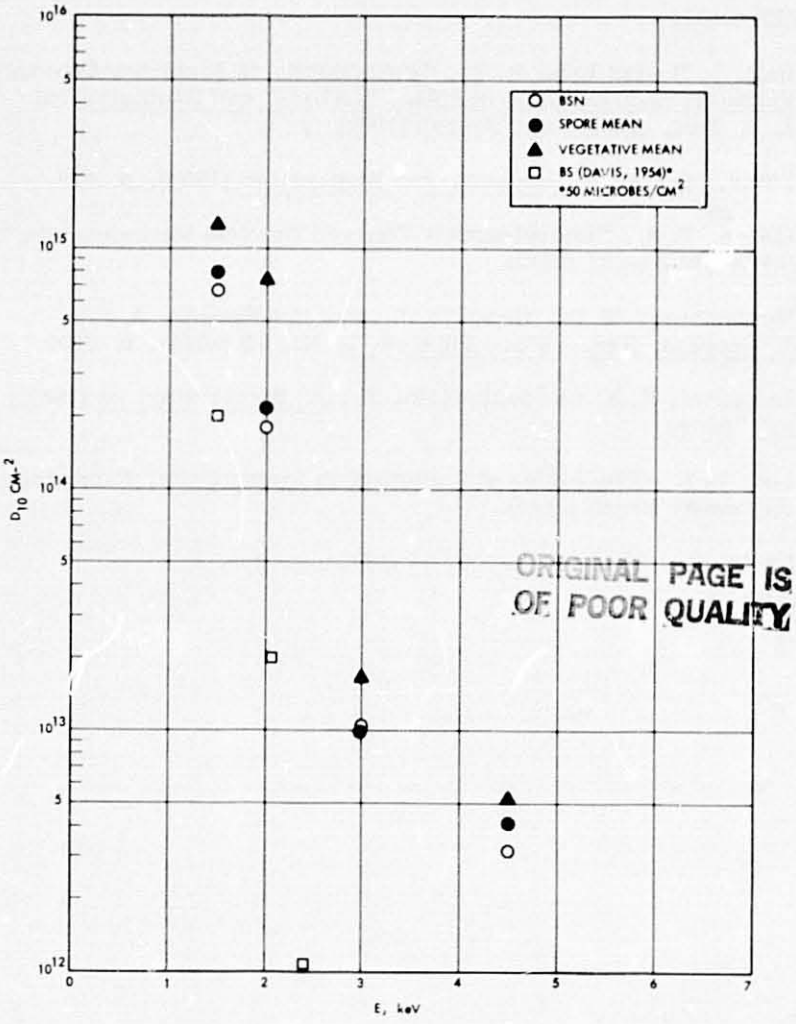

Figure 13. D_{10} values (fluence) as a function of electron energy

ACKNOWLEDGEMENTS

The technical support of A. Ferreira in the construction and operation of the electron source system is deeply appreciated. The authors also wish to thank S. Donovan, J. Farber, G. Simko and S. Yamada for performing the microbiology. The design and fabrication of the electron gun and power supply and the dosimetry fixture by Dr. C. Crawford of Kimball Physics, Inc. is gratefully acknowledged.

This work presents the results of one phase of research carried out at the Jet Propulsion Laboratory, California Institute of Technology, under contract no. NAS 7-100, sponsored by The National Aeronautics and Space Administration.

REFERENCES

1. Hall, L. B. and Lyle, R. G., "Foundations of Planetary Quarantine," Planet ry Quarantine Principles, Methods, and Problems, ed. L. B. Hall, Gordon and Breach (1971), p. 5.

2. Davis, M., Arch. Biochem. and Biophys. 48 (1954), p. 469.

3. Divine, T. N., "Interplanetary Charged Particle Environments," NASA TM 33-637 (1973).

4. Montgomery, M. D., Bame, S. J., and Hundhausen, A. J., J. Geophys. Res., Space Physics 73, No. 15 (1968), p. 4999.

5. Lazzarini, R. A. and Santangelo, E., J. Bacteriology 94 (1967), p. 125.

6. Lea, D. E., The Action of Radiation on Living Cells, Cambridge University Press (1947).

7. Davis, M., Physical Review 94 (1954), p. 243.

Paper No. 17

DEVELOPMENTAL AND HEMOTOLOGICAL RESPONSES TO LOW LEVEL CONTINUOUS EXPOSURE OF NITROGEN DIOXIDE IN MICE

Jarnail Singh, *Stillman College, Tuscaloosa, Alabama*

ABSTRACT

Young healthy mice were continuously exposed to 0ppm, 0.5ppm, 1.0ppm and 5ppm nitrogen dioxide gas for eight weeks. Nitrogen dioxide exposure for eight weeks decreased the average weight of mice, increased the average weight of lungs, heart, and brain and decrease the average weight of liver. Nitrogen dioxide exposure did not have any effects on the WBC and RBC in mice blood but it increased the HCT and HGB in mice blood. Nitrogen dioxide exposure increased the MCV and decreased the MCH and MCHC in mice blood.

Nitrogen dioxide (herein after referred to as NO_2) is a non-explosive, non-flammable colorless gas that most people can smell at concentrations from 1 to 3ppm. Eye and nasal irritation becomes apparent at concentrations of about 13ppm and accidental exposure to concentrations of 150 to 200ppm can be fatal (1). Due to some unknown reasons intermittent exposure, such as for a worker in a factory, is much less harmful than continuous exposure to similar concentrations, such as breathing the city air, for the same total number of hours. Rats given continuous exposure to 5ppm of NO_2 had 18 percent mortality, where as those exposed intermittently to 5ppm and 25ppm for an equivalent number of hours had no mortality (1). The maximum allowed concentration set by the Environmental Protection Agency (EPA) is not more than 0.05ppm of NO_2 in air on an annual basis.

Air pollution by nitrogen dioxide is a potentially important cause of respiratory infection (2-4). Mice continuously exposed to NO_2 covertly developed pulmonary emphysema, bronchial epithelial hypertrophy and persistent lesions (5-6). Investigations have shown that the pathogenesis of the oxidant induced enhancement in suceptibility to infection involves an inhibition in pulmonary antibacteria defense systems due to alveolar macrophage dysfuction (7-9). Most of these studies, however, confine to the adult laboratory animals. Furthermore, almost nothing is known about the effects of low level continuous exposure of nitrogen dioxide on the newly born to adult laboratory animals.

This study was an effort to determine the response of low continuous exposure of nitrogen dioxide on the development and hemotology in mice.

Materials and Methods

Environmental chambers and gas mixtures: Four environmental chambers (one each for 0ppm, 0.5ppm, 1.0ppm and 5.0ppm NO_2) were placed in an air conditioned room in which the average temperature and humidity were 74± 2°F and 54± 2 respectively. The animals were placed in these four chambers for 7 days a week, 24 hours a day for 8 weeks. Each environmental chamber was connected to the gas mixture cylinder on one side and exhaust fan on the other side by means of rubber tubing. Gas mixtures of 0ppm, 0.5ppm, 1.0ppm and 5.0ppm NO_2 were obtained from Matheson Gas Products. The cylinders were fastened with NO_2 regulators and the regulators were fastened with nupro needle valves (micro meter). The valves were connected to the environmental chambers by rubber tubing. The gas flow was set at 200 ml. per minute.

Animals: One litter of 3 day old mice along with the mother was placed in plastic cages with wire covers. Three litters in 3 cages with a total of 25-30 mice were placed in each environmental chambers with gases on all the time except for 5 hours a week. This time was used to clean, change, and sterilize the cages. This was carried out once a week for the first three weeks and twice a week for the second five weeks. The mice were given five minutes of fresh air everyday. The food was a special sterilized commercial product (lab blox) for mice. Tap water was provided in sterilized bottles and like the food was available to the mice at all times. The litters were weaned after the first two weeks of exposure and were separated by sexes. At the end of eight weeks, 20 mice from each chamber were weighed, sacrified and organs removed. These were weighed and blood samples for hemotological studies were collected. Forty four point seven (44.7) lambda blood was transferred to a vial with 10 ml. of isoton in it. The vials were capped and the contents were mixed immediately to avoid any coagulation of blood. These samples were read for White Blood Carpuscles, Red Blood Corpuscles, Hemoglobin, Hematocrit , Mean Corpuscle Hemoglobin, Mean corpuscle volume and Mean Corpuscle Hemoglobin Concentration (herein after referred to as WBC, RBC, HGB, HCT, MCH, MCV and MCHC respectively) on a coulter counter in the local pathalogy laboratory.

Results

Gross Weight Changes: The initial average weight of mice at the

Figure 1 Average weight of mice at the start of the experiment.

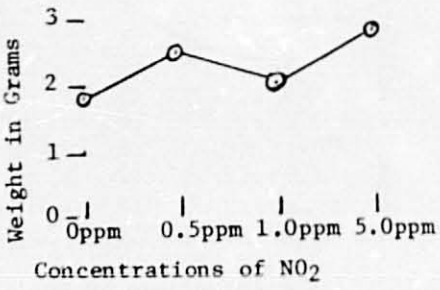

Figure 2 Effects of different concentrations of NO_2 on the average weight change percent of control in mice.

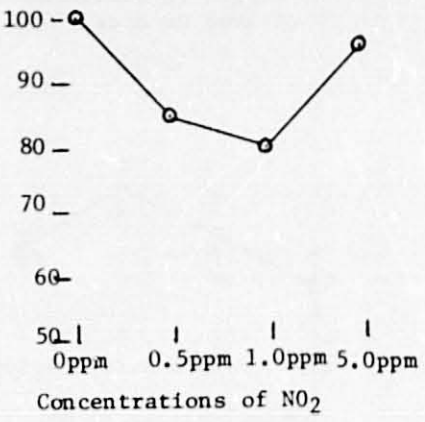

Figure 3 Effects of different concentrations of NO_2 on the average weight (± standard error) of liver in mice.

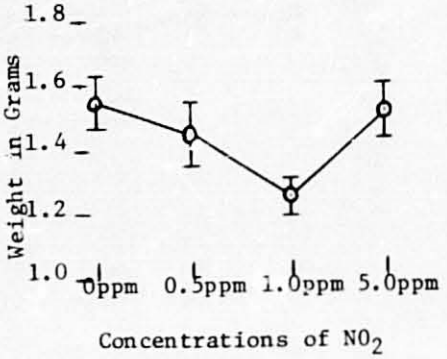

Figure 4 Effects of different concentrations of NO_2 on the average weight (± standard error) of kidney in mice.

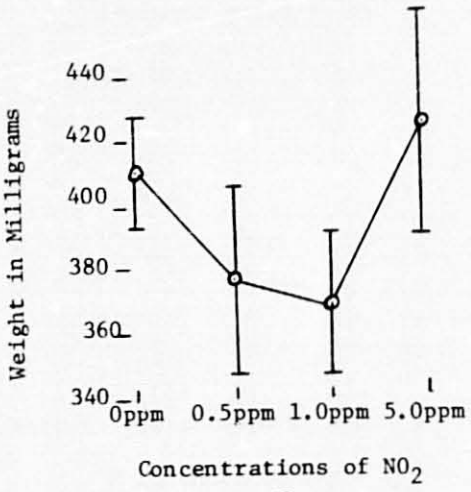

start of the experiment for 0, 0.5, 1.0 and 5.0 ppm NO_2 concentrations were 1.8, 2.5, 2.0 and 2.8 gms respectively (Figure 1). At the end of the experiment mice exposed to 0.5, 1.0 and 5.0ppm

concentrations produced an average weight of 85, 80 and 95
ent of control exposed mice respectively (Figure 2).

e 5 Effects of different
ntrations of NO_2 on the
ge weight (± standard
) of lung in mice.

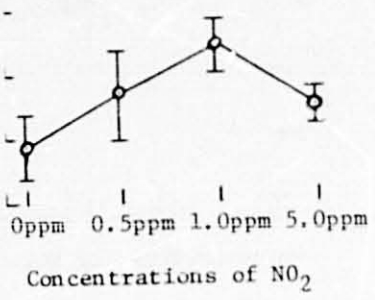

Figure 6 Effects of different concentrations of NO_2 on the average weight (± standard error) of heart in mice.

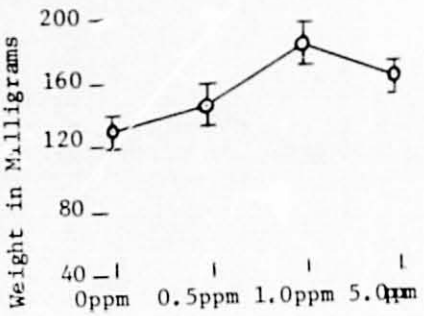

:cts on Vital Organs: Nitrogen dioxide exposure at 1.0ppm
:entration significantly decrease the average weight of liver
ıice as compared with 0,0.5 and 5.0ppm NO_2 exposure in mice
;ure 3). Nitrogen dioxide exposure did not produce any sign-

7 Effects of different
.rations of NO_2 on the
age weight (± standard
r) of Brain in mice.

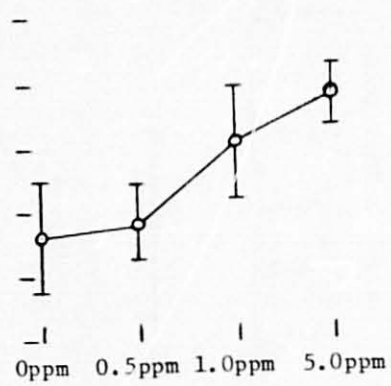

Figure 8 Effects of different concentrations of NO_2 on the average weight (± standard error) of spleen in mice.

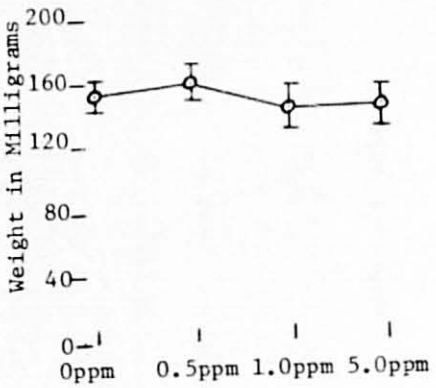

cant changes in the average weight of kidneys (Figure 4) and
een (Figure 8) in mice. One ppm NO_2 exposure significantly

increased the average weight of lungs (Figure 5) in mice as compared with the control exposed mice and 1 and 5ppm NO_2 exposure

Figure 9 Effects of different concentrations of NO_2 on the average RBC count (± standard error) in mice.

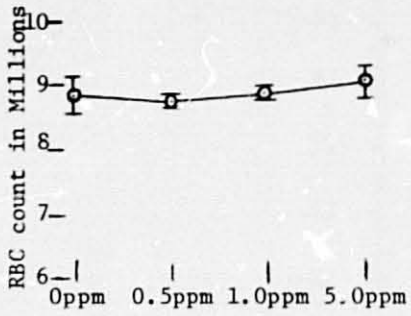

Figure 10 Effects of different concentrations of NO_2 on the average WBC count (± standard error) in mice.

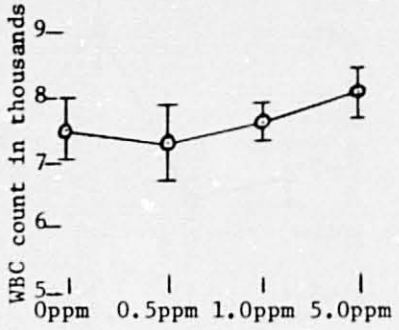

significantly increased the average weight of heart (Figure 6) in mice as compared with control exposed mice. Five ppm NO2 exposure significantly increased the average weight of brain in mice (Figure 7) as compared with the control and 0.5ppm NO_2 exposed mice.

Figure 11 Effects of different concentrations of NO_2 on the average HCT percent (± standard error) in mice.

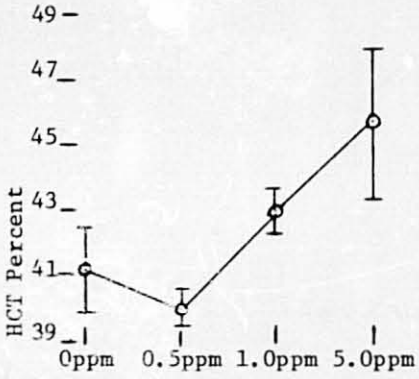

Figure 12 Effects of different concentrations of NO_2 on the average HGB (± standard error) in mice.

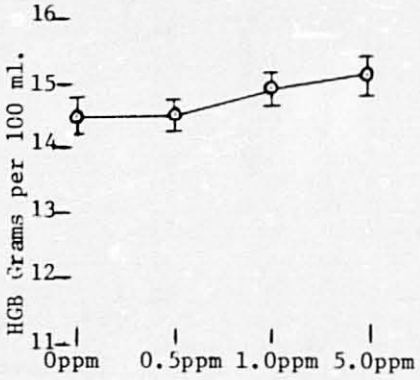

Hemotological Changes: Nitrogen dioxide exposure at different concentrations did not produce any significant changes on the

Figure 13 Effects of different concentrations of NO_2 on the average MCV (± standard error) in mice.

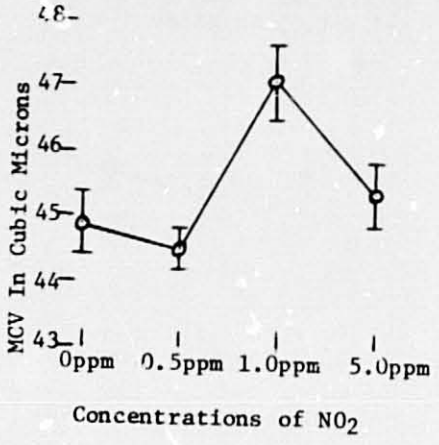

Figure 14 Effects of different concentrations of NO_2 on the average MCH (± standard error) in mice.

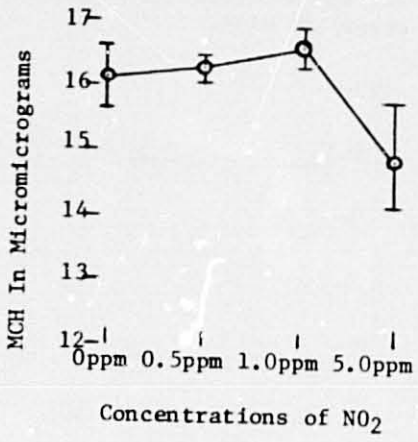

Figure 15 Effects of different concentrations of NO_2 on the average MCHC (± standard error) in mice.

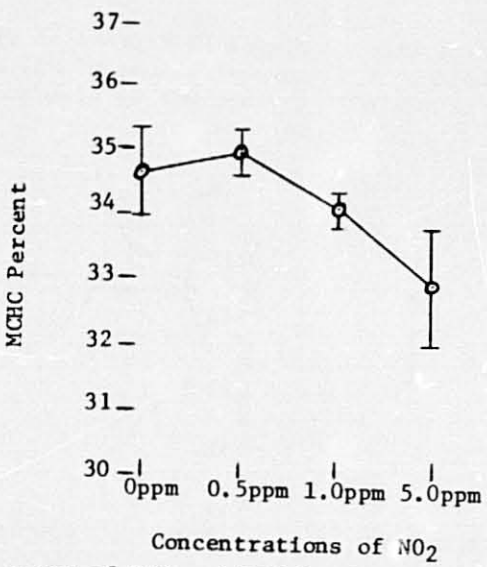

average count of RBC and WBC in the mice blood (Figure 9 and 10). Five ppm NO_2 exposure significantly increased the HCT and HGB in the mice blood (Figure 11 and 12) as compared with the control exposed mice. Mice exposed to 1ppm NO_2 concentration had a

significantly higher amount of MCV as compared with the remaining of the NO_2 concentration exposure (Figure 13) and 5ppm NO_2 exposure significantly reduced the MCH in mice blood as compared with the rest of the NO_2 concentrations (Figure 14). Nitrogen dioxide exposure at 1 and 5ppm concentrations significantly decreased the amount of MCHC in mice as compared with the 0 and 0.5ppm NO_2 exposure (Figure 15).

Comments

It is apparent from the experimental data that nitrogen dioxide exposure decreased the average weight in mice. These findings are in contrast to the earlier investigations (10). Young developing animals have a large metabolism rate than the large ones and as a result are probably more suceptible to NO_2 stress. The increase in the average weight of liver, lungs, heart and brain as a result of NO_2 exposure may be due to an increase of blood volume in these organs (6). Five ppm NO_2 exposure significantly increased the HCT (hematocrit) and HGB (hemoglobin) in mice blood as compared with the control exposed mice. It largely may be due to an adoptive compensatory mechanism in which the organism compensate for the reduced availability of oxygen by increasing the organisms's abilities to extract oxygen from the NO_2 environments. The increase in hematocrit (as a response to stress) is further substantiated by the data, that every increase in the NO_2 concentration exposure increased the total serum proteins in mice (11).

References

1. _____ Chemical Villains: A biology of pollution pp. 120 (1974).
2. Bates, D. V.: Air Pollutants and the human lung. Am. Rev. Respir. Dis. 105: 1-13 (1972).
3. Goldsmith, J. R.: Effects of Air Pollution on Human Health. Air Pollution. New York, Academic Press Inc. 547-615 (1968).
4. Goldstein, E.: Evolution of the role of nitrogen dioxide in the development of respiratory diseases in man. Calif. Med. 115: 21-27 (1971).
5. Freeman, G. and Haydon, G. B.: Emphysema after low level exposure to NO_2. Arch. Environ. Health 8:125-28 (1964).
6. Haydon, G. B., Freeman, G. and Furiosi, N. J.: Covert Pathogenesis of NO_2 Induced Emphysema in Rat. Arch. Environ. Health. 11:776-783 (1965).
7. Purvis, M. R., Miller, S. and Ehrlich, R. J.: Effects of atmospheric pollutants on suceptibility to respiratory infection. Jour. Infec. Dis. 109:238-42 (1961).
8. Ehrlich, R.: Effect of nitrogen dioxide on resistance to respiratory infection. Bacterial. Rev. 30:604-614 (1966).

9. Goldstein, E., Eagle, M.C. and Hoeprich, P.D.: Effect of nitrogen dioxide on Pulmonary bacterial defense mechanism. Arch. Environ. Health 26:202-204 (1973).
10. Freeman, G., Furiosi, N.J. and Haydon, G. B.: Effects of continuous exposure of 0.8ppm NO_2 on respiration of rats. Arch. Environ. Health. 13: 454-456 (1966).
11. Singh, J.: Unpublished data. (1976).

Supported by NIH-MBS
Grant Number 08021

Paper No. 18

ELECTROPHORESIS PATTERN OF SERUM FROM MICE EXPOSED TO DIFFERENT CONCENTRATIONS OF SULFUR DIOXIDE

Jarnail Singh, *Stillman College, Tuscaloosa, Alabama*

ABSTRACT

Three day old mice were continuously exposed to sulphur dioxide concentrations at 0ppm, 0.05ppm, 0.15ppm and 1ppm for eight weeks. At the end of the experiment, blood samples were collected and centrifuged for electrophoresis studies of the serum in 5 percent acrylamide gel. The length of bands of different serum proteins from the SO_2 exposed mice was at a variance as compared with the length of bands from the control exposed mice and alpha-1 band seems to be missing from the serum of SO_2 exposed mice.

Sulphur dioxide (herein after referred to as SO_2) is a non-flammable, none-explosive colorless gas that most people can taste at concentrations from 0.3 to 1ppm in air. At concentrations above 3ppm the gas has a pungent, irritating odour. The current scientific literature indicates that for the most part, the effects of oxides of sulphur on health are related to the irritation of the respiratory system (1-5). Such injury may be temporary or permanent. Laboratory observations of respiratory irritating gases suggest that most individuals will show a response to SO_2 at concentrations of 5ppm. At concentrations of 1 to 2ppm an effect can be detected only in certain sensitive individuals (1) and on occasions, exposure to 5 and 10ppm has produced severe bronchospasm in such person. Exposure of SO_2 at 1 to 15ppm decreased the average weight of body, liver, kidneys, heart, brain and spleen and at the same time increased the RBC (Red Blood Corpuscles), HCT (Hematocrite) and HGB (Hemoglobin) in laboratory mice (6). Since sulphur is an important component of some of the amino acids and proteins, it is reassonable to assume that sulphur in the form of SO_2 may alter the protein pattern in serum. Therefore an experiment was conducted to observe the changes in the electrophoresis pattern of mice as a result of exposure to SO_2 at 0, 0.05, 0.15 and 1.0ppm levels.

Materials and Methods: Exposure of animals sulphur dioxide: Four environmental chambers (one each for 0ppm 0.05ppm, 0.15ppm and 1.0ppm SO_2) were placed in an air conditioned room in which the average temperature and humidity were $74 \pm 2^{o}F$ and 54 ± 2

respectively. One litter of three day old mice along with the mothers was placed in plastic cages with wire covers. Three litters in cages were placed in each environmental chamber with gases on at a flow of 120 ml/minute all the times except for 5 hours a week. This time was used to clean, change and sterilize the cages and chambers. The mice were given 5 minutes of fresh air every day. The food was a special sterile commercial product (lab blox) for mice and like the water was available to mice at all times. The litters were weaned after the first two weeks of exposure and separated by the sexes. At the end of 8 weeks one mice from each chamber was sacrificed and blood samples for serum collected. All specimens of serum were clear and free of hemolysis.

Preparation of the Gel: The electrophoresis gel was prepared with 5 percent acrylamide gel as described by Peacock, Bunting and Queen (7). The gel was prepared before run from the following refrigerated stock solutions: (A) Acrylamide, 20 percent: acrylamide 190 grams, N-N' methylenebisacrylamide 10 grams, dissolved in two litters of water: (B) DMAPN-: (dimethylamino propionitrite) 16 ml diluted to 250 ml; (C) ammonium persulphate: 1.6 percent in water, prepared fresh. To prepare the gel, 40 ml of acrylamide stock (Reagent A), 84 ml of water, 10 ml of DMAPN-buffer (Reagent B) and 16 ml of 10X buffer (described below) were mixed and shaken well and brought to room temperature by running tap water over it. To this 10 ml of ammonium persulphate (Reagent C) was added. The whole mixture was mixed well and poured into the cell just before the run. The 10X buffer contained 110 grams boric acid, 18.6 grams disodium ethylenediamine tetracetate, 216 grams of tris (hydroxymethyl) amino methane and 2 litter of water.

The voltage was applied for 30 minutes before the addition of samples. The serum used was obtained from the mice blood at the end of eight weeks exposure. All the specimens were clear and free of hemolysis. A four place slot former was used. Water at 0-2°C (for colling) was circulated through the cell throughout the run. A potenital difference of 200 volts was applied. The experiment was run for 3 hours. The gel was stained for 1 hour in 1 percent amido black 10 B in 7.5 percent acetic acid and destained overnight in 7.5 percnet acetic acid circulated through at charcoal bath. After destaining was complete, the gel gas photographed with poloroid 70 SX camera.

Results and Comments: The photograph of the electrophoresis pattern of mice serum is shown in the figure. The migration distance of the serum in the gel for 0, 0.05, 0.15 and 1ppm SO_2 exposure was 11.5, 11.3, 11.5 and 11.3 cms. respectively up to the prealbumin line. The serum from control exposed mice seems to have all the characteristics serum proteins e.g. gamma, beta, alpha-2, alpha-1, albumin and prealbumin. These are shown from

top of the figure to the bottom respecti ely. The alpha-2 band in the serum from the control and SO_2 exposed mice is further split into two bands. The most significant observation of the experiment is that alpha-1 band is altogether missing from the serum of 0.05, 0.15 and 1ppm SO_2 exposed mice. The

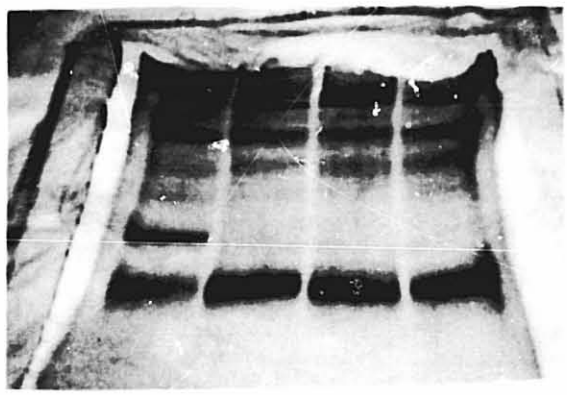

0ppm 0.05ppm 0.15ppm 1.0ppm

Concentrations of SO_2

Photograph of the electrophoresis verticle gel showing the pattern of serum proteins from mice exposed to various concentrations of sulphur dioxide for eight weeks. Serum from 0ppm SO_2 exposed mice show all the serum proteins. Alpha-1 proteins is absent from the serum of 0.05, 0.15 and 1.0ppm SO_2 exposed mice. The distance from the origin to the leading edge of the albumin is 11.5 cms.

deficiency or absence of alpha-1 globulin may be due to the dificiency of alpha-1 antitrypsin as a result of SO_2 stress. Alpha-1 antitrypsin deficiency is also associated with pulmonary diseases like emphysema and hepatic cirrhosis (8).

Work on the effects of SO_2 on the vital organs like lungs is in progress and will be reported in another manuscript.

References

1. Toxicological Effects of sulfur oxides on animals, p. 155. Air Quality criteria for sulfur oxides. U. S. Dept. of HEW Public Health Service. National Air Pollution Control Administration Publication No. AP-50.
2. Amdur, M. O.; The Physiological response of Guinea Pigs to Atmospheric Pollutants. Int. Jour. Air Pollution, Vol., 1, pp. 170-83 (1959).
3. Balchum, O. J.; Dhbick, J. and Menecly, G. R.; Pulmonary resistance and compliance with concurrent radio active sulfur distribution in dogs breathing $S^{35}O_2$. J. App. Physiol. 15, pp 62-66 (1960).
4. Nadel, J. A.; Salem, H. Tamplin, B. and Yokiwa, Y., Mechanism of bronchioconstriction. Arch. Environmental Health 10: pp 75-78 (1965).
5. Amdur, M. O.; Respiratory Absorption data and SO_2 dose reponse curves. Arch. Environ. Health 12: pp 729-32 (1966).
6. Singh, J.; Effects of Sulphur dioxide exposure on the postnatal development and hemotological studies in mice. Proc. Insti. Environ. Sc. pp 147-151 (1976).
7. Peacock, A. C., Bunting, S. L. and Queen, K. G.; Serum protein electrophoresis in acrylamide gel: Patterns from normal human subjects. Science 147: 1451-1453.
8. Dividsohn, I. and Henry, J. B.; Clinical diagnosis by Lab-methods pp 580-81. W. B. Sanders Co. Phla. (1974).

Supported by NIH-MBS Grant
Number 08021.

Paper No. 19

THE EFFECTS OF THE POLLUTANT, SODIUM CYANIDE, ON THE MORPHOLOGY AND PHYSIOLOGY OF OEDOGONIUM CARDIACUM

Elbert Sparks, *Stillman College, Tuscaloosa, Alabama*

ABSTRACT

OEDOGONIUM cardiacum exposed to varying concentrations of sodium cyanide for 15 day periods exhibited both morphological and physiological alterations. Organisms were exposed to the pollutant in concentrations of 1, 10, 25, 50, and 100 parts per million. Exposure period for organisms in each concentration was 15 days. The 15 day period permitted assays of effects caused by the pollutant.

As the concentration of the pollutant increased fragmentation also increased. Exposure also caused organisms to lose chlorophyll. There is a direct proportion of chlorophyll loss to increased pollutant concentrations. This is true for chlorophyll "a" and "b". The third morphological alteration is the incidence of rupture. Cells in the higher concentrations rupture and organelles are lost.

Physiological effects altered by exposure include: reduced oxygen evolution, retardation of sexual and asexual reproduction, retardation of starch production and death. Death occurs when organisms are exposed to high concentrations over the total 15 day period.

INTRODUCTION

Cyanide has a long history of being a poison. (Berry 1976). Many people have heard of cyanide as being the substance used in gas chamber executions. However, many are not aware of the fact that cyanide is a common water pollutant. (Berry 1974). Small quantities of the pollutant occur naturally in water, such as that produced by millipedes as a defense mechanisms against predators. (Berry 1974). Much of the cyanide in industrial use is commercially synthesized. Cyanide consists of carbon and nitrogen atoms joined by a triple bond. The joining of these atoms form the cyanide radical. The compound, referred to as the pollutant. Sodium cyanide is used in this study. Compounds containing the cyanide radical form a group of versatile reagents with many chemical and industrial applications. The cyanide

pollutant enter industrial waste streams from a variety of processing industries such as extracting gold and silver ores, synthetics manufacturing, coal cooking furnaces and electroplating.

The effect of cyanide on the morphology and physiology of the green algae Oedogonium cardiacum may give some indications of the effects on organisms dependent on the algal plant for food and oxygen. The effects could be traced to fish and ultimately man. Early studies indicate that concentrations of cyanide as low as 0.1 ppm in water can kill fish. (Doudoroff 56).

This study will assess the degree to which diseases rather than death will be produced in organisms utilizing the plant as a source of food. In addition, problems will be defined, hypotheses will be established and studies will be designed to assess the effects experienced by food chain organisms.

Materials and Methods

Oedogonium cardiacum, a filamentous freshwater green algae is the organism for study. It consists of several cells - per filament. Each cell has a nucleus and single large chloroplast of irregular net-like shape with many pyrenoids. The basal cell is modified as a holdfast. Growth of the filament occurs as various cells divide-mitotically.

Reproduction occurs both asexually and sexually. Asexual reproduction is by fragmentation or by the production of zoospores. Sexual reproduction is of the oogamous type. A filament may contain a large swollen cell, the oogonium, and small structures resembling zoospores in the antheridium. A sperm (zoospore) from the antheridium swims to the enlarged oogonium and enters through a pore in the wall of this cell and fuse with the single egg contained therein. The diploid zygote germinates producing four haploid zoospores each of which develops into a new filament.

The organism is grown in soil water medium or Bold's basal medium. Sodium cyanide is added to the medium in various concentrations. The control contains only the medium while concentrations of 1 ppm, 10 ppm, 25 ppm, and 100 ppm constituted the experimental groups. ppm dilutions indicate a weight colume ratio of milligrams of sodium cyanide per liter of solution e.g. mg/l.

Each concentration is grown in conical flasks for a period of fifteen (15) days. The growth period is conducted in twelve (12) hour light and dark periods. The light period coincide with the daylight period. The temperature for the growth period is $23^{o}C \pm 2$.

Daily observations are conducted with the light microscope. These observations permit assessment of fragmentation, cellular rupture, formation of reproductive structures and loss of cellular constituents.

Respiration measures are conducted by the use of Warburg apparatus. Each concentration is subjected to five (5) fifteen (15) minute respiratory measures daily for the fifteen (15) day study period.

Chlorophyll extraction techniques enable measures of chlorophyll loss for the fifteen (15) day period. Chlorophyll "a", "b" and total chlorophyll is measured by the spectrophotometer. Calculations based on spectrophotometric readings provide data indicating the amount of chlorophyll loss during the fifteen (15) day period.

Chromatographic assays are employed to determine the presence of carbohydrates produced and stored in the filaments at the end of the experimentation period. Carbohydrates are extracted and subjected to paper chromatography for analysis of the carbohydrates.

Discussion

Oedogonium c is grown in either soil water medium or Bold's basal medium containing sodium cyanide in concentrations of 0 ppm, 1 ppm, 10 ppm, 50 ppm, and 100 ppm for a period of fifteen (15) days. The growth period consists of twelve (12) hour dark and twelve (12) hour light periods. The temperature for the growth period is 23°C $\pm$ 2 degrees centrigrade. Daily observations with the light microscope indicates that as the concentrations of pollutant increased fragmentation of the filaments increased. Observations indicate that 1% of the filaments in the control (ppm) showed some fragmentation while 6% of the filaments fragmented in 100 ppm concentration. Figure One (1) indicates the percentage of fragmentation in the concentrations studied. Cell fregments occurred in all concentrations. However, the frequency of fragments increased with the increase of the pollutant. Fragmentation includes breaking of single cells of filaments, breaking of filaments, or abnormal twisting of cells causing the walls to rupture and break. The incidence of fragmentation is more apparent in the cells with the greatest exposure.

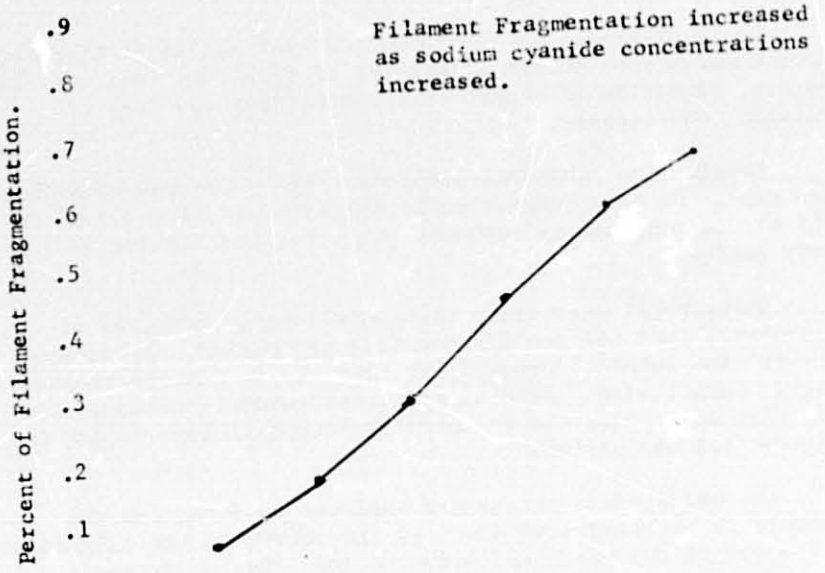

Fig. I- Filament Fragmentation

In addition to filament fragmentation the number of cells void of protoplast increased as the concentrations increased. Few cells in the control (0 ppm) flask are void of cellular constituents. However, an increase in cells without protoplasts were visible in concentrations of 50 ppm and 100 ppm.

Reproductive structures developing on filaments in the control were numerous. Both oogonia and antheridia are visible in the control. Sexual reproduction is apparent in the appearance of antherida and oogonia on filaments. Antheridia are indicated by short walls formed in the cell producing sperm cells. The number of cross walls increase as maturation of the antheridium takes place.

Also reproduction can be noted by the appearance of the oogonium. Increases in the reproduction structures indicate a tendency for increase in off spring.

As concentrations increase the number of oogonia and antheridia decreased. 8 % of the filaments in the control contained an antheridia or oogonia. In some instances filaments contained both antheridium and an oogonium. As the concentrations increased the incidence of reproductive structures decreased. The 100 ppm concentration showed 1% of the filaments with reproductive

structures.

As sodium cyanide concentrations are increased reproductive structures on filaments decrease

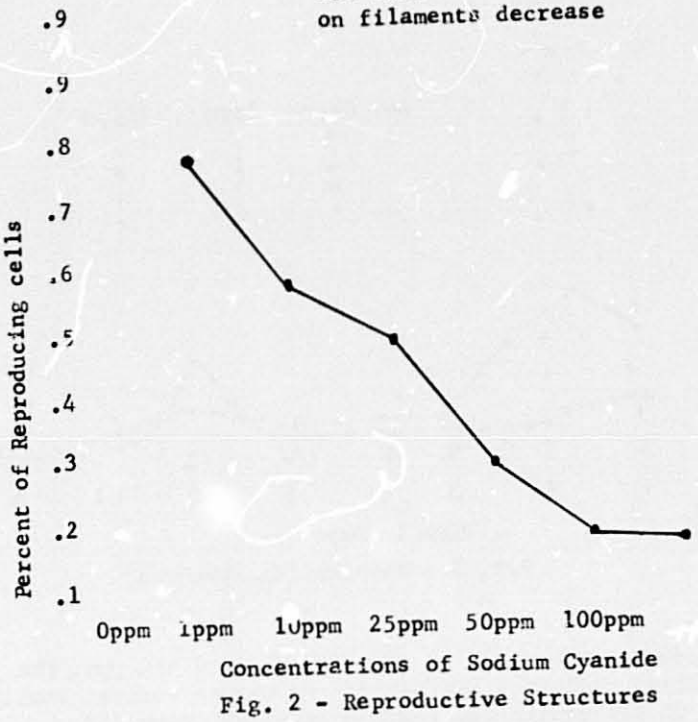

Fig. 2 - Reproductive Structures

The percentage of reproductive structures decreased from 8 % to 1 % in concentrations of 0 ppm to 100 ppm.

Respiration of oxygen evolution is a measure of the physiological activities of the cells. Measures were conducted for five (5) fifteen (15) minute periods per day. The measures are averaged to provide a measure of the oxygen evolved for that day. The fifteen (15) day measures for 0 to 100 ppm are recorded in Figure 3. The data indicate that the control organisms were producing six (6) micro liters of oxygen on the tenth (10) day and the 1 ppm and the 10 ppm had ceased to evolve any measurable amounts of oxygen on the tenth (10) day.

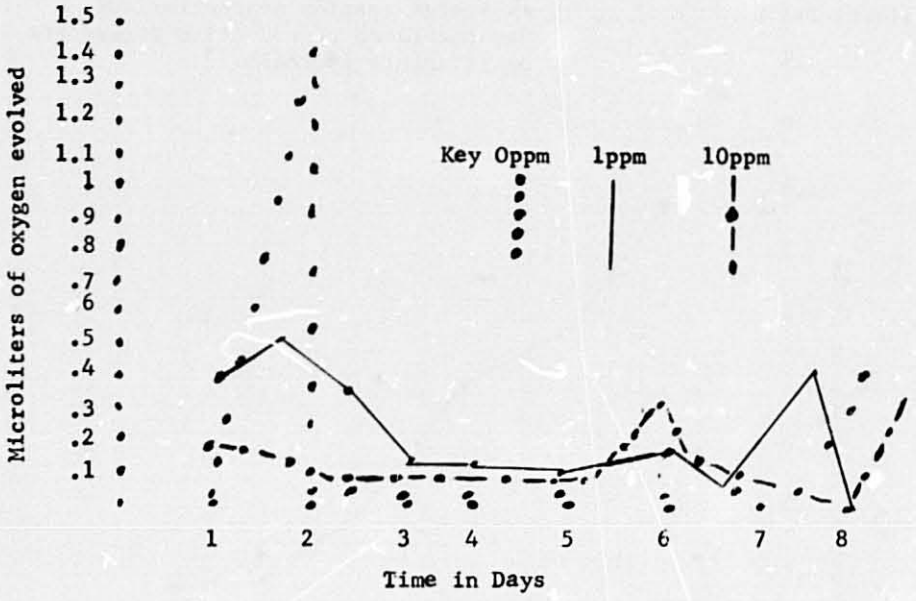

Fig. 3 - Respiration Measures

Figure 4 contains data for 25 ppm, 50 ppm, and 100 ppm. The 50 ppm concentration indicates practically no oxygen evolved about nine (9) days. On the nineth and tenth days almost five (5) microliters of oxygen are evolved. This measure is not indicative of the 25 ppm and 100 ppm. Oxygen is produced on two (2) days and then decreases through the tenth (10) days measures.

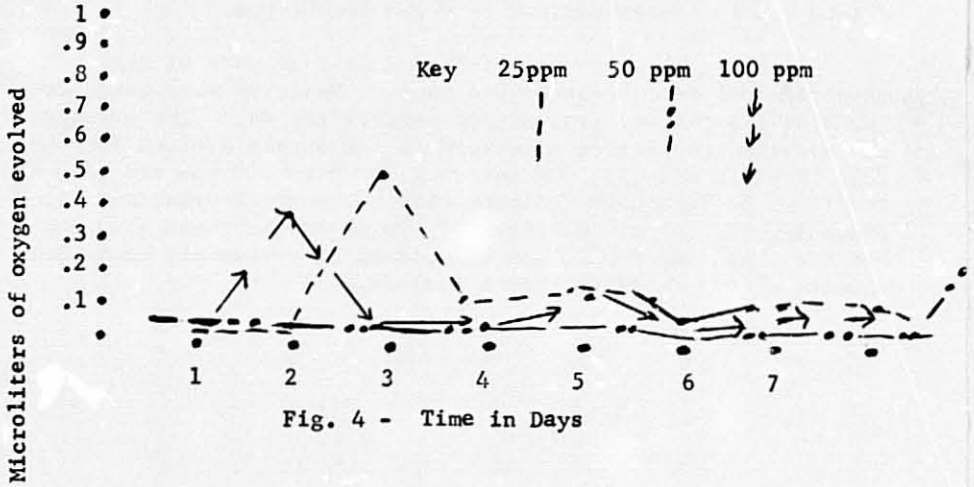

Fig. 4 - Time in Days

The data indicate that oxygen production decreases as the concentrations of the pollutant increase.

Chlorophyll is extracted at the close of ten (10) day study period. The extraction procedure provides data for chlorophyll "a" and "b" and total chlorophyll. The measure does not indicate the amount of chlorophyll lost per day. The measure is the amount lost over ten (10) day study period. Visible observations indicate that chlorophyll is lost to some degree. The control organisms are quite green while the organisms in the 100ppm concentration are a white to milky white color. Indicating chlorophyll has been lost during the experimentation period.

The chlorophyll is extracted and measures are made using the B & L spectrophotometer. Calculations show that the control organisms contain .4 mg of chlorophyll "a" per gram of tissue, .5 mg of chlorophyll "b" per gram of tissue, and 8 mg of total chlorophyll per gram of tissue. Organisms in the 100ppm lost 1.6 mg of chlorophyll "a" per gram of tissue, 1.9 mg of chlorophyll "b" per gram of tissue and 2.1 mg total chlorophyll per gram of tissue. Figure 5 include calculations for each concentration for the study period.

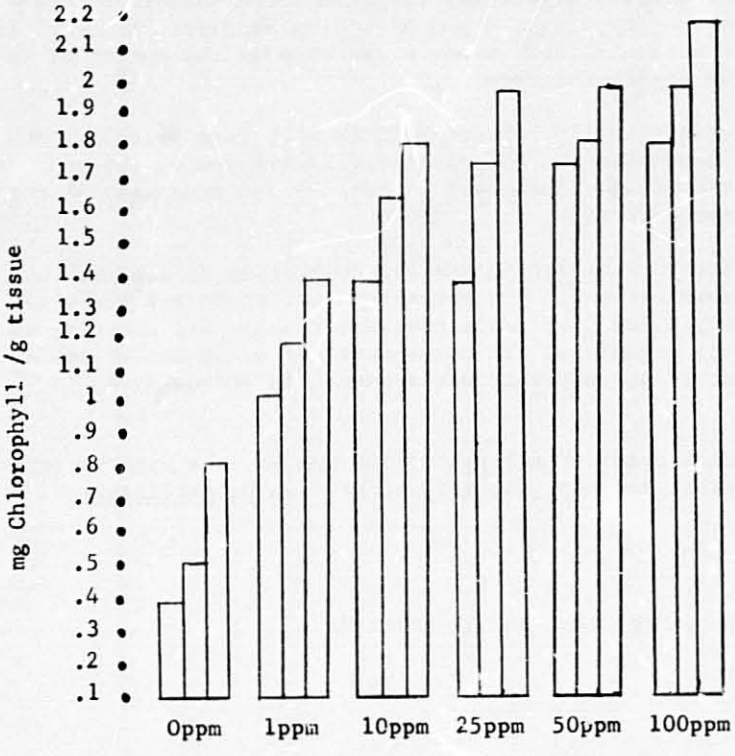

Fig. 5 - Chlorophyll Loss

Spectrophometric measures are based on the percentage transmittance. Therefore, the higher the bar graph the smaller the amount of chlorophyll present. As a result more chlorophyll was lost from the organisms exposed to higher concentrations of sodium cyanide. Chlorophyll extraction did not occur until the study was completed. However, visible observations on a daily basis indicated that the 100 ppm concentration organisms were void of much of their chlorophyll two (2) to three (3) days before the other concentrations.

Findings

O. cardiacum exposed to sodium cyanide concentrations of 0 ppm, 1 ppm, 10 ppm, 50 ppm, and 100 ppm for fifteen (15) days showed a variety of morphological and physiological changes. Morphological changes that occurred include an increase in the number of cells fragmenting as the concentration of the pollutant is increased. Along with increased fragmentation, a larger number of cells rupture and all cytoplasmic material and organelles are lost. Rupturing increases as the pollutant concentration decreases.

Reproductive structures occur in large numbers in the growth medium containing 0 ppm of sodium cyanide. However, increase in concentration causes a decrease in the number of reproductive structures forming.

Physiologically, chlorophyll is lost from organisms exposed to concentration of pollutants from 1 ppm to 100 ppm. largest amount of chlorophyll is lost by the organisms in the 100 ppm concentration.

Carbohydrates are in smaller quantities as measured by paper chromatography. The extraction procedure and analysis technique yielded only small traces carbonhydrate material in the control organisms. In concentrations of 10 to 100 ppm no assessment of carbohydrate was apparent in chromatographis analysis

Sodium cyanide in 1 ppm to 100 ppm cause a wide variety of morphological and physiological effects on O. cardiacum.

Supported by NIH Grant No. RR-08021-04

BIBLIOGRAPHY

Berry, James W., David Osgood and Philip A. St. John. 1974. CHEMICAL VILLAINS - A BIOLOGY OF POLLUTION. C. V. Mobsy Co., Atlanta, Ga.

Clark, John M., 1964. EXPERIMENTAL BIOCHEMISTRY. W. H. Freeman.

Coss, Ronald A., and Jermy D. Pickett - Heaps, 1974. THE EFFECTS OF ISOPROPGL N-PHENYI CARBAMATE ON THE GRFEN ALGAE OEDOGONIUM CARDIACUM. J. Cell Biology. 63: 84.

Dodge, J. D., 1973. THE FINE STRUCTURE OF ALGAE CELLS. Academic Press, London and New York.

Doudoroff, P., 1956. SOME EXPERIMENTS ON THE TOXICITY OF COMPLEX CYANIDE TO FISH. 28: 1020.

Ennis, W. B., Jr. 1948. SOME CYTOLOGICAL EFFECTS OF O-ISOPROYL N - PHENYL CARBAMATE UPON AVENA. Am. J. Bot.

Johnson, U. G., and A. Cronquist. 1968. FINE STRUCTURE OF CELL DIVISION IN CHLAMYDOMONAS REINHARDI. J. Cell Biol. 38: 403 - 425.

Leedale, G. F., 1970. PHYLOGENETIC ASPECTS OF NUCLEAR CYTOLOGY IN ALGAE. Ann. N.Y. Academy of Sci., 175: 429-453.

Pickett - Heaps, J.D., K.L. McDonald and D. H. Tippit. 1975. CELL DIVISION IN THE PENNATE DIATOM DIATOMA.

Round, F. E., 1973. THE BIOLOGY OF THE ALGAE. St. Martins Press New York.

Smith, A. D., S. Duckett and A. H. Waters, 1963. NEUROPATHOLOGICAL CHANGES IN CHRONIC CYANIDE INTOXICATION. 200: 179-181.

Wilber, Charles G., 1969. THE BIOLOGICAL ASPECTS OF WATER POLLUTION. Charles Thomas Publisher, Springfield, Ill. 181 - 184.

D16

N79-19029

Paper No. 20

QUARTZ CRYSTAL MICROBALANCE (QCM) MONITOR OF CONTAMINATION FOR LES-8/9

John T. Lynch, *MIT, Lincoln Laboratory, Lexington, MA*

ABSTRACT

A Quartz Crystal Microbalance (QCM) was used to monitor condensable contamination during the launching of two Lincoln Laboratory Experimental Satellites--LES-8 and LES-9. The QCM was installed on the dispenser truss and measured contamination by means of a frequency shift of a quartz crystal oscillator. By using a special crystal cut and a second reference quartz crystal, the sensor had extreme sensitivity and remarkable temperature independence. A 1-Hz frequency shift, which corresponds to 3.5×10^{-9} g/cm^2, was resolved by the flight instrumentation.

A Titan III-C launched LES-8/9 into orbit on 14 March 1976. From time of ignition to injection into orbit, the QCM functioned as anticipated. An enormous change in QCM frequency (1062 Hz, corresponding to 3.7 µg/cm^2) occurred at the time of the firing of the retro-rockets which separate the spent Stage II. A significant but much smaller change occurred during the 200-second period following payload fairing jettison.

INTRODUCTION

Lincoln Laboratory designed and built two satellites, LES-8/9, which were launched into synchronous orbit from the Eastern Test Range at Cape Canaveral, Florida on 14 March 1976. Careful examination and control of contamination were exercised during the fabrication, testing, and launching of the satellites. A wide variety of techniques were used to monitor contamination during these various phases including monitors which measured accumulated contamination from liftoff through injection into synchronous orbit. This paper describes the technique used and the results obtained in monitoring contamination during the launching of the satellites.

The launch contamination monitor was a Quartz Crystal Microbalance (QCM) which was installed on the dispenser truss of the satellites. The QCM measured contamination by means of a frequency shift of a quartz crystal oscillator which occurs when the crystal mass increases as a result of contamination loading. The device is extremely sensitive, 1 Hz corresponding to 3.5×10^{-9} g/cm^2. This sensitivity is achieved by using a special crystal cut which produces small temperature dependence and by using a second reference quartz crystal the signal from which, when mixed with the signal from the sensing crystal, gives a beat frequency remarkably independent of temperature and power supply fluctuations.

Analog signals proportional to the QCM beat frequency were read out by the launch vehicle (Titan III-C) telemetry system. The telemetry signals were recorded at various ground stations and processed subsequently to give QCM frequency as a function of time. The QCM frequency was measured once every two seconds. It is therefore possible to associate contamination buildup with specific events during the launch sequence.

SYSTEM CONSIDERATIONS

The Quartz Crystal Microbalance (QCM) responds to contamination which couples to the thickness-shear oscillation in the crystal. This coupling is strong for thin films or residues whose thickness is very small relative to the crystal thickness. The coupling is weak for large particulate contamination, i.e., dust.

Outgassed contaminants are called volatile condensable materials (VCM). An example of the contamination process is the evaporation of low-molecular-weight material (i.e., volatile) from a painted surface which is hot as a result of solar illumination. The low-molecular-weight material then condenses on a cooler surface which may be shaded from the sun.

The sensitivity requirement for the QCM contamination monitor is that mass densities which are a fraction of 0.1 µg/cm^2 be measurable. It was therefore determined that uncertainties in the QCM frequency should be less than ±3 Hz. The QCM readout and telemetry had a precision of 1 Hz, which permits fine-scale measurements of temperature-induced variations, etc. To give physical meaning to these numbers the mass density of various thin films and a droplet type of contamination have been calculated in Table I.

Because the external satellite surfaces are near the Payload Fairing (PLF), the QCM had to be placed near the PLF at the same height as the satellites.

The dispenser truss was therefore ideally suited. The most probable sources of contamination were retro-rocket exhaust products and ablation products from the retro-rocket impingement pads on Stage II. Figure 1 shows the placement of the QCM relative to LES-8/9 and the upper stages of the Titan III-C. The QCM is directly in line with one of three retro-rockets. Figure 2 which details the payload region more clearly shows the dispenser truss mounting arrangement. The QCM is pointed at an angle of 25^{o} from the vertical so that it has a direct view of the retro-plume and still has some sensitivity to contamination coming directly into the payload region from the side.

TABLE I

Mass Density of Films of Stearic Acid

$CH_3 (CH_2)_{10} COCH$ and of Water H_2O

Thickness	Mass Density	QCM Frequency
Stearic Acid		
2.1 nm (monolayer)	0.18 $\mu g/cm^2$	51 Hz
100 nm smooth film	8.5 $\mu g/cm^2$	2430 Hz
Water		
0.4 nm (monolayer)	0.04 $\mu g/cm^2$	11 Hz
1 μm radius half-spherical droplets covering 1.0% of surface	0.66 $\mu g/cm^2$	189 Hz

INSTRUMENTATION

The QCM flown on the LES-8/9 dispenser truss was procured from Faraday Laboratories, La Jolla, California. The QCM was of a design similar to that used on the NASA OGO-6 satellite (Ref. 1, 2). The sensor consists of two quartz crystals each of which resonates at approximately 10 MHz. The sensing crystal is displaced in frequency approximately 1 kHz below the reference crystal. The output of a mixer circuit provides a beat frequency which increases when the sensing crystal is contaminated.

The QCM is a modification of a single-crystal device commonly used to measure the thickness of vacuum-deposited thin films. The AT cut of the crystal has a minimum temperature coefficient with frequency and is used for all thickness monitors. The

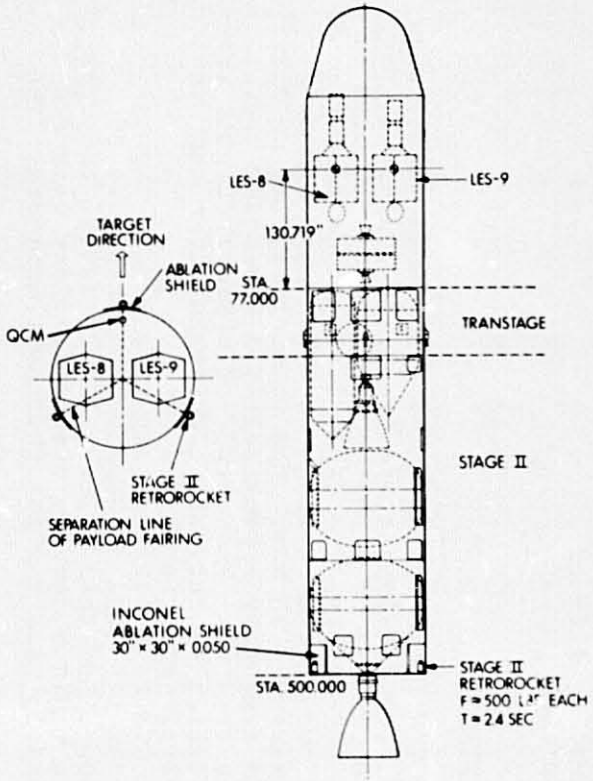

UPPER STAGES OF TITAN III-C FOR P74-1 MISSION

FIGURE 1

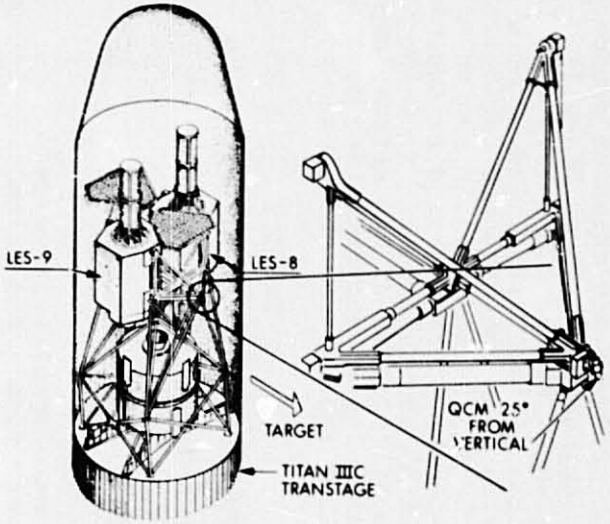

QCM LOCATION ON DISPENSER

FIGURE 2

contamination sensor achieves immunity to power supply fluctuations and further immunity to temperature changes by using two crystals selected by careful measurement to have nearly identical temperature vs. frequency characteristics.

A photograph of the QCM in various stages of disassembly is shown in Fig. 3. The QCM has the feature that the crystal head is removable and replaceable. Shown in the figure are:

1. assembled unit (head plus oscillator electronics),
2. unit with head removed, and
3. head disassembled (crystal visible).

A diagram of the sensor body and head is shown in Fig. 4.

EXPERIMENTAL RESULTS

The QCM functioned as expected from installation to satellite separation, which marked the end of the experiment. Readings made prior to launch indicate negligible changes in frequency (less than ±2 Hz) during this period. From launch vehicle ignition until payload separation some seven hours later, launch vehicle telemetry was recorded during specific "telemetry windows". Digital QCM data have been received and reduced for those available time periods of interest.

A plot of the QCM frequency vs. time for the entire launch is shown in Fig. 5. This plot is linear in frequency change (hence, linear in contamination). Note the gaps in the time axis so that the full 24,000 seconds could be displayed as well as the critical first 600 seconds. An enormous amount of contamination was measured at the time of the retro-rocket firing. The change was 1062Hz, or 3.7×10^{-6} gm/cm^2 or 3.4 mg/ft^2. Another significant change, although minor by comparison to the retro-rocket contamination occurred during the time interval following PLF jettison. Other time periods for which data are available show small frequency changes, generally less than ±10 Hz (±3.5×10^{-8} gm/cm^2). The temperature of the sensor head was about 31°C (88°F) at the time of ignition and dropped only 1°C during the following 7-hour period.

A plot of the QCM frequency vs. time for the first 300 seconds following ignition (part of telemetry window I) is shown in Fig. 6. A greatly expanded frequency axis is used to see better the minor frequency changes.

A plot of the QCM frequency vs. time for the interval from PLF jettison to a time just prior to the

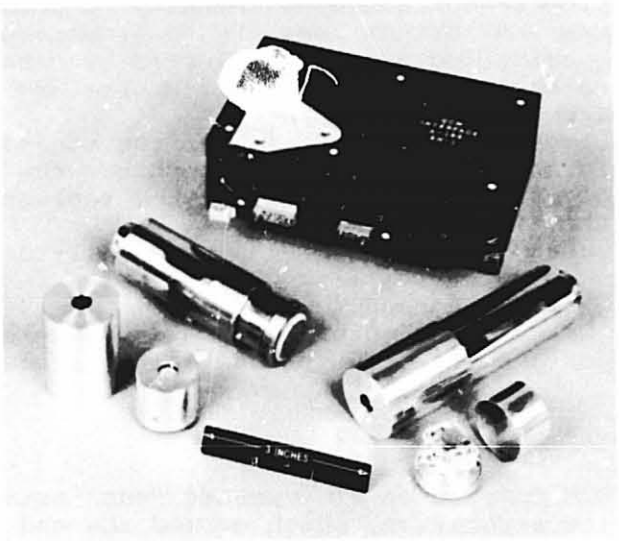

PHOTOGRAPH OF QCM IN VARIOUS STAGES OF DISASSEMBLY
FIGURE 3

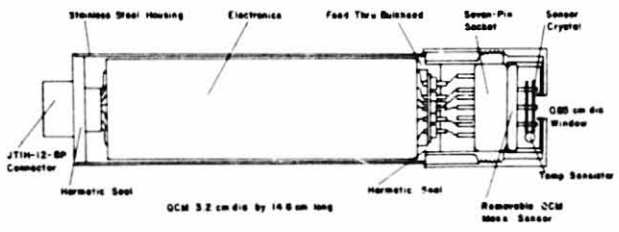

DIAGRAM OF QCM
FIGURE 4

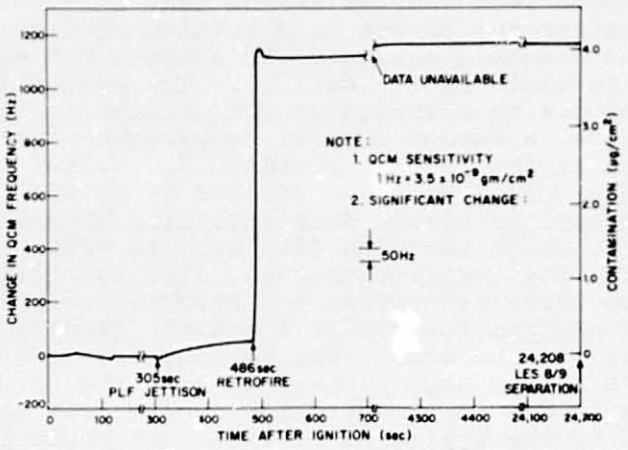

QCM FREQUENCY VS. TIME FOR ENTIRE LAUNCH
FIGURE 5

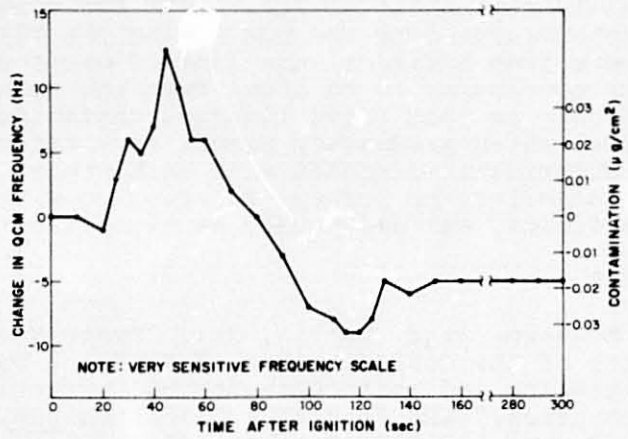

QCM FREQUENCY VS. TIME: IGNITION TO PLF JETTISON
FIGURE 6

firing of the Stage-II retro-rockets is shown in Fig. 7. The linear frequency and time axes were selected to display clearly the gradual 65 Hz change which occurs over the 200 second time interval. The contamination may be due to molecular scattering of satellite desorbed molecules by ambient gas molecules in the low earth orbit (Ref. 3). The change in QCM frequency due to a change in QCM package temperature or a change in sensor crystal temperature due to a change in radiative background (e.g., $\sim 350^{\circ}$ PLF to $\sim 0^{\circ}$K deep space) has been bounded by ±1 Hz.

The next available data following Window 1 is Window IV, which includes 4210 sec. to 4658 sec. after ignition. The QCM frequency vs. time is plotted for this time interval in Fig. 8. Also indicated is the last QCM reading for Window I and the reading for Window XI (24,000 sec). The reading from 24,030 sec. to 24,208 sec. change by only ±1 Hz. The 35 Hz increase in QCM frequency which occurs from the end of Window I to the beginning of Window IV could be due to parking orbit contamination or could be due to heating of the sensing crystal relative to the reference crystal as a result of direct solar illumination.

CONCLUSION

The QCM had little opportunity to be contaminated by direct line-of-sight sources. The two contamination events measured by the QCM during the Titan III-C launch were from indirect, non-line-of-sight sources. The major conclusion to be drawn from the measurements reported here is that these indirect contamination mechanisms, which presumably result from interaction of the contaminant molecules with each other, with ambient molecules, or perhaps interaction with static electric fields, can definitely be significant.

REFERENCES

1. D. McKeown, W. E. Conlin, Jr., "Space Measurements of the Contamination of Surfaces by OGO-6 Outgassing and Their Cleaning by Sputtering and Desorption," NBS Special Publication 336, Paper No. 7, pp. 113-127, October 1970.

2. D. McKeown and R. S. Dummer "Gas-Surface Energy Transfer Experiment for OGO-F," IEEE. Trans. on Geoscience Electronics, Vol. GE-7, No. 2, pp. 98-106April 1969.

3. R. L. Harvey, "Spacecraft Self-Contamination by Molecular Outgassing," Technical Note 1975-1, Lincoln Laboratory, M.I.T. (31 March 1975).

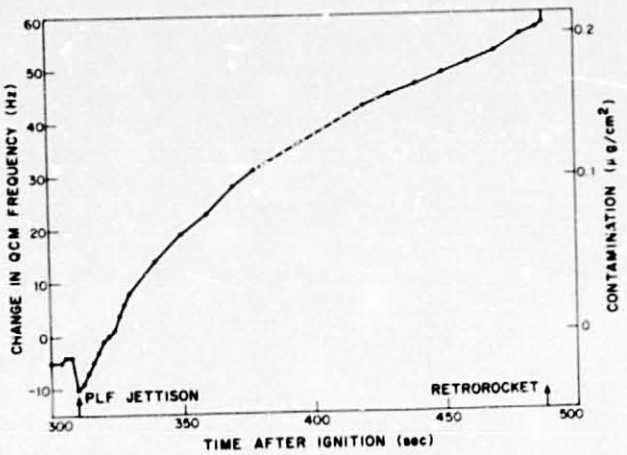

QCM FREQUENCY VS. TIME: PLF JETTISON TO STAGE II RETRO

FIGURE 7

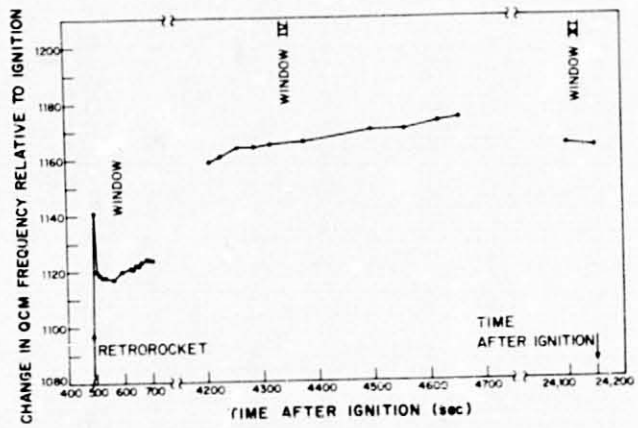

QCM FREQUENCY VS. TIME FOR WINDOW IV, XI, AND END OF I

FIGURE 8

Paper No. 21

ESTIMATION OF OUTGASSING FROM AN EXPENDED APOGEE MOTOR AND ITS EFFECTS ON SPACECRAFT SURFACES

John J. Scialdone, John F. Rogers, and Raymond Kruger,
Goddard Space Flight Center, Greenbelt, Maryland

ABSTRACT

An experimental and theoretical investigation has been carried out to evaluate the degradation of the solar cells and other sensitive surfaces of a spacecraft, resulting from the molecular outgassing of an expended solid propellant apogee motor. The motor, following its burnout, is retained by the spacecraft and is a source of gases and particulates which will be released mainly by the unburned propellant-to-casing insulation. The deployment of the solar array within a few minutes after the motor burn results in the interception and reflection to the surfaces of the spacecraft of the molecular outgassing and particulates. Various methods, based on some experimental data, have been used to analytically assess the magnitude of the outgassing from the engine. The results of this investigation indicate that during the 2 minutes' exposure of the solar cells to the motor outgassing, the deposit of the fraction of outgassing with low volatility on the cells will be about 6×10^{-7} g/cm^2 or about 43 Å for a material density of 1.4 g/cm^3. This is predicted on the array deployment occurring 8 minutes after motor burnout when the motor is at an average temperature of about 473 K (200°C). A solar cell degradation of less than 1 percent is predicted for this accumulation. The accretion of the same material for an indefinite time on the silver-coated Teflon insulation of the hydrazine tanks has been estimated at 5×10^{-8} g/cm^2 (3.6 Å). This thickness, according to tests, should cause no significant change in the α/ϵ of the insulation. The hydrazine tanks are exposed to a higher flux of contaminants than any other sensitive location of the spacecraft. Contaminant deposits on other spacecraft surfaces are, therefore, less than 3.6 Å and they should not be degrading.

INTRODUCTION

An experimental and theoretical investigation has been carried out to assess the probable contamination and degradation of the solar array cells and other sensitive surfaces of a spacecraft. The contamination may be produced by molecular outgassing of the spacecraft apogee motor.

A solid propellant motor is retained by the spacecraft following its firing which lasts 45 seconds and produces an impulse of about 1862 N·s (420 lb·s). The motor is a source of gases and particulates which are released mainly by the unburned propellant-to-casing insulation. The deployment of the solar array, within a few minutes after the motor burn, results in the interception and reflection toward the spacecraft surfaces of the molecular and particulate products. During a portion of the deployment sequence, a period of about 2 minutes, the solar cells surfaces of the array are exposed to the contaminant flux. After this, the other side of the array receives and reflects the contaminant toward the spacecraft. The relative position of the motor, solar paddles, and instruments on the spacecraft main body are shown in Figure 1.

The investigation is discussed in two parts: one covering an assessment of the magnitude of the contaminant deposits on the solar cells and the metal-coated Teflon insulation of the hydrazine tanks; the other, an evaluation of the effect of those deposits on the optical/thermal properties of those surfaces.

The deposit assessment portion of this report includes experimental data on the motor insulation obtained from micro-volatile condensable mass (VCM) tests, thermogravimetric tests (TG), and quartz crystal microbalance (QCM) measurements. The data are analyzed and used to generate an estimate of the magnitude of the outgassing from the motor as a function of time. These rates and other experimental data on the outgassing properties, plus view factor data, are used to estimate the deposits on the surface of interest.

EXPERIMENTAL DATA

Temperatures of the Insulation Material

Qualification tests of the solid propellant motor (Reference 1) indicate that the dome region of the titanium motor case approaches a temperature of about 523 K (250°C), at approximately 280 seconds after motor ignition. A maximum temperature of about 723 K (450°C) is measured near the nozzle 80 seconds after ignition. Many different temperatures are recorded at various locations of the case. Figure 2 shows the average temperature of the motor as a function of time. The maximum average temperature is indicated to be 506 K (233°C)

followed by a rapid drop to approximately 423 K - 413 K (150 - 140°C) in about 10 minutes.

The calculations have been based on a motor insulation temperature of 473 K (200°C) at the time of the array deployment followed by a decay of 25 K every 10 minutes. The insulation between the case and the propellant, which remains in the engine following the burn, is taken to be the source of molecular outgassing and particulates.

Insulation Material

This material is an asbestos-filled vulcanized isoprene rubber protected with other materials according to its location in the motor. The surface adjacent to the propellant is covered with an epoxy resin and carbon black in a plasticizer. The surface in contact with stagnant hot gas is coated with Teflon tape, and in another engine location, this surface is covered with a woven polypropylene industrial cloth. These sections, about equal in weight, have thicknesses between 0.5 and 1.5 mm and are cured at 355 K (82°C) for 1 hour and at 380 K (107°C) for 2 hours at a pressure of 5.5×10^5 Pa (80 psig). The total weight at installation is about 8.6 kg (19 lb). It was estimated that about 5.9 kg (13 lb) of insulation remains in the motor after firing. This is based on measured expended mass and measured nozzle erosion.

Samples of the three sections described above and of charred insulation materials taken from an engine fired at atmospheric pressure were tested in the micro-VCM test apparatus. The results of the tests, which consist of exposing the samples to a temperature of 398 K (125°C) for 24 hours and measuring the percentage total mass loss (TML) and the collected volatile condensable mass (CVCM) on a 298 K (25°C) plate, are listed in Table 1. The samples which were prepared by Thiokol Corporation for these tests have been identified by their physical appearance.

The TML's varied from 1.38 to 5.89 percent and the CVCM from 0.16 to 1.54 percent. The larger quantities were obtained for samples which had an adhesive for the bonding of the insulation to the titanium case (the samples had a commercial aluminum foil to simulate the titanium). An average of the TML results is 3.2 percent and the CVCM is about 0.64 percent. The charred material produced a 2.22-percent TML and a 0.73-percent CVCM. The basic insulation produced a 2.4-percent TML and about a 0.3-percent CVCM.

Thermogravimetric tests of the basic insulation material were also performed. The samples were heated as rapidly as possible, under vacuum, to temperatures of 398 K, 473 K, and 523 K (125°C, 200°C, and 250°C). These temperatures were then maintained for the remainder of the tests. The weight loss of the samples was measured continuously for the 24-hours duration of the test. The results are shown in

Table 1
Micro-CVCM Test Results

Material Physical Appearance	TML Percent	CVCM Percent
One Black Surface, Other Green with Adhesive, ~1.5mm Thick	3.67	0.88
One Black Surface, Other Teflon, ~1.0mm Thick	1.38	0.25
One Cloth Surface, Other Green with Adhesive, ~1.0mm Thick	5.89	1.54
Basic Insulation, Green	2.40	0.30
Charred Material from Fired Motor	2.22	0.73
Charred "Asbestos-like" Material from Fired Motor	3.68	0.16

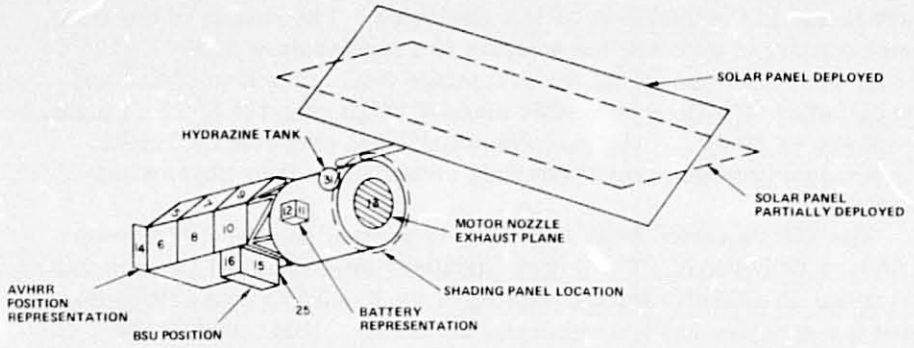

SOLAR PANEL NODES ARE 1, 2, 3, 4, 17, 18, 19, and 20 NUMBER ASSIGNMENTS VARY ACCORDING TO ORIENTATION

VIEW FACTORS (10^{-8} cm^{-2}) MULTIPLIERS

NODE	5	6	7	8	9	10	11	14	15	16	25	31	SOLAR PANEL
NO SHADE	3.73	1.25	4.99	1.69	6.91	2.33	31.19	20.15	29.33	3.01	4.35	54.34	1068
6½-INCH DIAMETER SHADE	3.65	1.20	4.93	1.60	6.74	2.17	15.11	19.78	20.29	2.45	2.79	23.90	1068
12-INCH DIAMETER SHADE	3.55	1.12	4.65	1.48	6.19	1.98	6.00	15.58	13.49	1.92	1.88	1.98	1068

Fig. 1—View factor nodal configuration of spacecraft

Figures 3a, 3b, 3c, and 3d. The 71.2-mg sample lost about 2 mg while at room temperature and during the 10 minutes needed to reach 473 K (200°C) (Figures 3a and 3b). At 473 K (200°C) (see Figure 3c), it lost 1.8 mg in about 1.2 hours. This loss was followed by an additional loss of 0.98 mg until that portion of the test was terminated. The total loss for the 24 hours is therefore about 6.7 percent and the long-term fraction of this may be between 1.37 and 3.9 percent. Figure 3d shows the change in weight as the material was heated (at a constant rate) above 473 K (200°C).

Figure 4 shows the accretion rates of the outgassing from a sample of the insulation held at a temperature of 473 K to 523 K (200 to 250°C) for about 4 hours as measured by two QCM's, one held at 211 K (-62°C) and the other at 296 K (+23°C). The QCM's had the same field-of-view of the source. The insulation was heated on its rear side to about 523 K (250°C) while the side facing the QCM's was 473 K (200°C). After an initially increasing rate of deposit, reaching a maximum of 440 Hz/min for the 211 K (-62°C) QCM and 170 Hz/min for the 296 K (+23°C) QCM, obtained within 8 minutes from the start, these rates decayed as shown. The rate as measured by the 296 K (+23°C) QCM dropped more rapidly than the other, indicating a depletion of the material accreting at that temperature. The total accumulation on the 211 K (-62°C) QCM was, using a sensitivity of 4.45×10^{-9} g/cm^2 Hz and taking the density of the material as 1.4 g/cm^3, 1.9×10^{-5} g/cm^2, and on the 296 K (+23°C) QCM, 4.3×10^{-6} g/cm^2, giving a ratio of about 4.4. The test, which was intended to provide a deposit of contaminant for measurement of optical degradation, was not repeated at different temperatures.

The evaporation rates at different surface temperatures, from 253 K to 300 K (-20°C to +27°C), of the material which had been deposited on the QCM at 211 K (-62°C), are shown on semilog paper in Figure 5. The rates measured for a period of 30 minutes for each temperature appear to have the same slope, indicating the material being evaporated at the various temperatures had the same properties.

On the other hand, the material component deposited on the 296 K (+23°C) QCM left this surface quite slowly as shown by the normalized curve of Figure 6. The curve covers a period of about 14 hours during which the QCM recorded continuously the mass available on its crystal.

ANALYSIS

Outgassing Components Characterization

The insulation material left in the motor following burnout has been estimated at 5.9 kg (13 lb). At the time of deployment, its temperature is about 473 K (200°C). In outgassing tests conducted at this temperature, material was deposited on a 211 K (-62°C) and a 296 K (+23°C) QCM surface as shown in Figure 4. Heating the 211 K (-62°C) surface to various

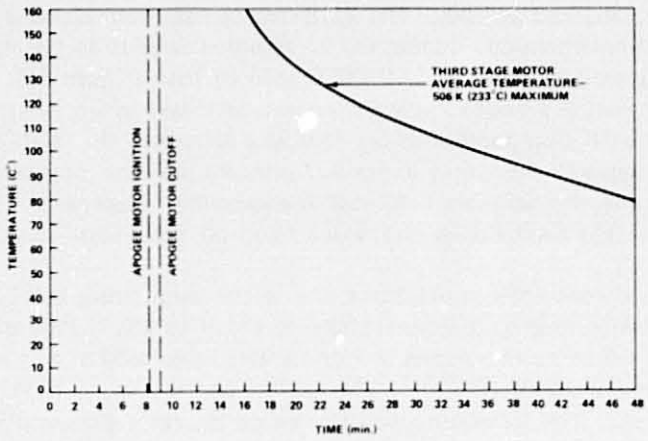

Fig. 2—Temperature history during launch

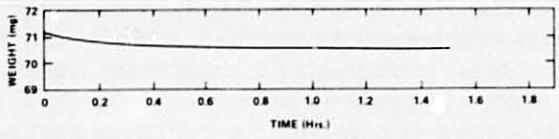

Fig. 3a—Weight loss at room temperature

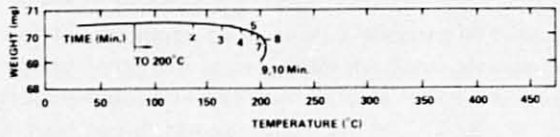

Fig. 3b—Weight loss with temperature increase to 200°C

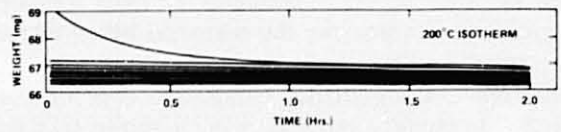

Fig. 3c—Weight loss versus time—sample at 200°C

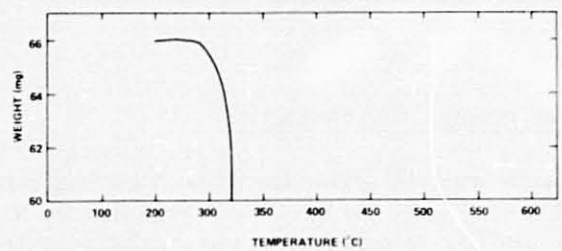

Fig. 3d—Weight change versus increase in temperature

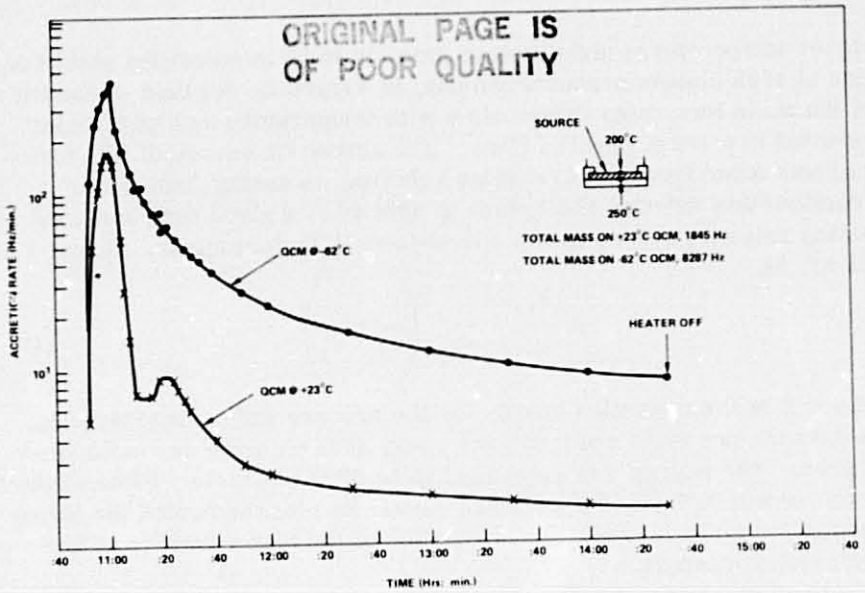

Fig. 4—Rates of deposit versus time on QCM's at -62°C and +23°C

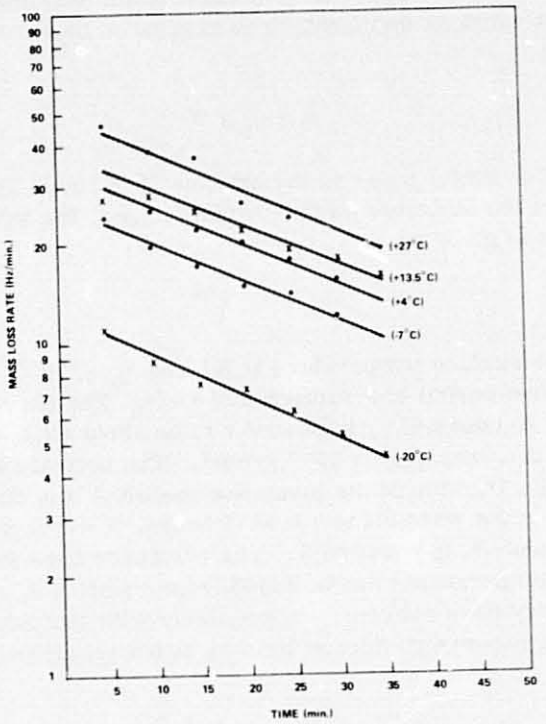

Fig. 5—Mass loss rates versus time at different temperatures of the material collected on the -62°C QCM

higher temperatures and allowing time (40 to 50 minutes) for stabilization at each plateau produced the data in Figure 5. A graph of the log of the mass loss rates versus time with temperature as a parameter resulted in a set of parallel lines. The activation energy of this material was found from the Arrhenius relation, assuming first-order reaction; this relation (Reference 2) applied at a given time and comparing rates w_1 and w_2 at two corresponding temperatures, T_1 and T_2 (in K), is:

$$\ln \frac{w_1}{w_2} = \frac{E}{R} \left(\frac{1}{T_2} - \frac{1}{T_1} \right) \tag{1}$$

where E is the activation energy for the process under consideration in calories per mole and R the gas constant in calories per mole per degree. The energy was calculated to be 5990 cal/mole. Plots of the rates versus 1/T yielded a straight line. Its slope indicated the above energy for mass loss and a confirmation of the high volatility of this material component.

In contrast, the smaller fraction of the insulation deposited on the 296 K (+23°C) surface desorbs very slowly from a surface at 295.5 K (+22.5°C) as shown in Figure 6. The depletion of this material from the surface at constant temperature is expressed by the relation (Reference 2),

$$m = m_o e^{-t/\tau} \tag{2}$$

where m_o is the initial mass on the surface, t is time, and τ is the residence time of the molecule on that surface, i.e., the time needed for $m = m_o/e$. It is given by

$$\tau = \tau_o e^{E/RT} \tag{3}$$

where T is the surface temperature in K, and $\tau_o \simeq 10^{-13}$ s is the average oscillation period of a surface molecule. The curve of Figure 6, when fitted to equation 2, indicated τ to be about 62.5 hours. The initial mass, m_o, was 4.28×10^{-6} g/cm^2. The activation energy for this low volatile fraction of the insulation material was then found to be E = 24.7 kcal/mole when using τ = 62.5 hours, T = 295.5 K, and R = 1.98 cal/mole K in equation 3. The residence time for this material at other temperatures can be found from equation 3, assuming that the above energy does not change appreciably with temperature. A direct relation between residence time τ_2 at temperature T_2 and τ_1 at T_1 is

$$\tau_2 = \tau_o \left(\frac{\tau_1}{\tau_o} \right)^{T_1/T_2} \tag{4}$$

where τ_o is the constant given previously. Using this expression, the time for the initial mass of deposit to become 1/e was calculated to be 16 days at 283 K (+10°C), 471 days at 263 K (-10°C), and as indicated from the test, 62.5 hours at 295.5 K (22.5°C). It is apparent that this fraction of the outgassing is of major concern for the contamination. It will remain for a long time on the surfaces on which it deposits. During this stay, it can be polymerized by radiation and may remain permanently on the surfaces. It has been estimated from the considerations which follow that its fraction of the outgassing is about 1.4 percent, corresponding to about 82 g of the total 5.9 kg of material remaining in the engine at burnout. These considerations form the basis for this estimate. The CVCM at 398 K (125°C) for the charred material is 0.73 percent and the average for all materials configurations is 0.64 percent. If these results are modified by the 0.54 view factor of the collector plate to the exit flow port of the VCM apparatus (Reference 3), the actual condensables on the 298 K (25°C) collector are 1.2 to 1.35 percent of the sample. The TG test at 473 K (200°C) showed a long-term mass loss which corresponds to 1.37 percent of the total.

Outgassing Flow from the Motor

The TG test of the sample at 473 K (200°C) showed that an initial exponentially decaying mass loss occurred from the time 473 K (200°C) was obtained and that a condition of a small, quasi-steady mass loss was reached. That mass loss was L = 1.8 mg obtained in a period of Δt = 1.2 hours. The sample mass when 473 K (200°C) was reached was the initial mass, W_o = 71.2 mg less the losses, W_t = 1.2 mg, to get to the temperature and the loss, W_r = 0.8 mg, at room temperature. The flow rate from the motor at 473 K (200°C) can be estimated applying these test results to the VCM fraction, 1.4 percent, of the total mass of the insulation remaining after burnout, W_i = 5.9 kg, as follows:

$$\dot{m} = \frac{L}{\Delta t} \frac{[CVCM \cdot W_i]}{[W_o - (W_t + W_r)]} = 1.77 \text{ g/hr} = 2.96 \times 10^{-2} \text{ g/min} \qquad (5)$$

An alternate estimate can be obtained from the initial, maximum rate of insulation depositing on the 211 K (-62°C) QCM. This rate, $\Delta f/\Delta t$ = 440 Hz/min as shown in Figure 4, must be modified to get the rate of outgassing at the sample source. The parameters for this modification are: the view factor between source and QCM, $F = 1.07 \times 10^{-4}$, for the test arrangement; the area A_c = 0.317 cm^2 of the QCM crystal detecting surface; the area of the insulation sample A_s = 20.26 cm^2; the density ρc = 2.7 g/cm^3 of the quartz crystal and ρ = 1.4 g/cm^3, the experimentally measured density of the material. The rate of outgassing per unit area, ϕ, for the material at 473 K (200°C) is then:

$$\phi = \frac{A_c}{A_s F}\left(\frac{\Delta f}{\Delta t}\right)\left(\frac{\mu}{\rho_c}\right) \quad k = 2.5 \times 10^{-6}\ g/cm^2/s = 1.5 \times 10^{-4}\ g/cm^2/min \quad (6)$$

where $k = 4.45 \times 10^{-9}$ g/cm^2 -Hz is the mass constant for the 10 MHz QCM. For a steady-state pressure-controlled outgassing, the flux inside the motor is constant and the flow from the motor which has a throat area A = 55 cm^2 is

$$\dot{m} = \phi A = 8.25 \times 10^{-7}\ g/min$$

The rate $\dot{m} = 2.96 \times 10^{-2}$ g/min, obtained from the TG test, is 3.7 times larger than this and it has been used as a measure of the motor flow rate when the insulation is at 473 K (200°C). One can also obtain the flow at 473 K (200°C) starting from the data at 495.5 K (22.5°C) in Figure 6. In fact, the initial rate at 295.5 K (22.5°C), which is 1.14×10^{-9} g/cm^2/min when modified with the residence times (62.5 hours) at 295.5 K (22.5°C) and 8.12×10^{-6} hours at 473 K (200°C), indicates a rate of 8.75×10^{-3} g/cm^2/min and a corresponding flow of 4.85×10^{-1} g/min. This flow is about 16 times higher than the one being used. However, the TG value was used because of its direct determination from a test at 473 K (200°C) and in view of the many assumptions needed in the large extrapolation from 295.5 K (22.5°C) to 473 K (200°C).

The change in outgassing rate, due to the decreasing temperature of the insulation with time, has been estimated using the activation energy derived previously, under the assumption that it is valid at those temperatures. Equation 2, differentiated with respect to time, gives the rate as a function of time with the temperature as a parameter. The ratio of the initial rates for the same material at temperatures T_1 and T_2 is

$$\frac{\dot{m}_1}{\dot{m}_2} = \frac{\tau_2}{\tau_1} = \exp\frac{E}{R}\left(\frac{1}{T_2} - \frac{1}{T_1}\right) = \tau_0 \frac{\left(\frac{\tau_1}{\tau_0}\right)^{T_1/T_2}}{\tau_1} \quad (7)$$

where the various forms of the equations are in accordance to equations 3 and 4. The rates versus temperature, based on E = 24.7 kcal/mole and calculated using this relationship, are shown in Figure 7.

Contaminant Deposit on Solar Cells and Hydrazine Tanks

The contaminant accretion rate ($\Delta M/\Delta t$, where ΔM is the difference in mass over the time period Δt) on a spacecraft surface of temperature T = C, is the product of the flow from the motor, times the view factor

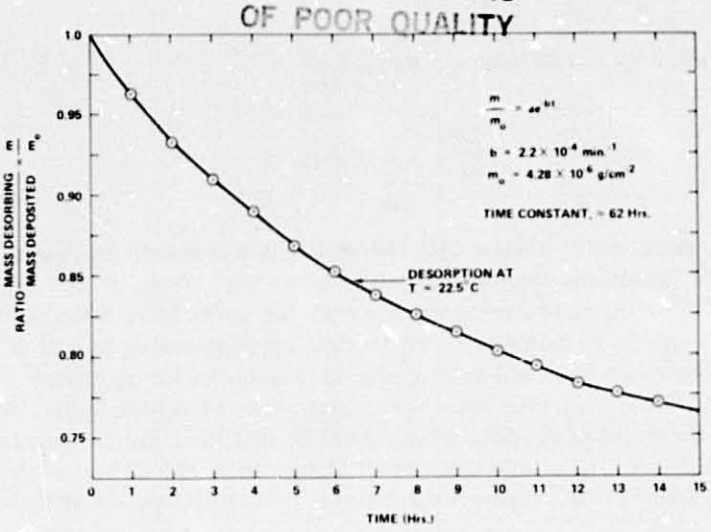

Fig. 6—Mass desorbing from a QCM at 22.5°C versus time

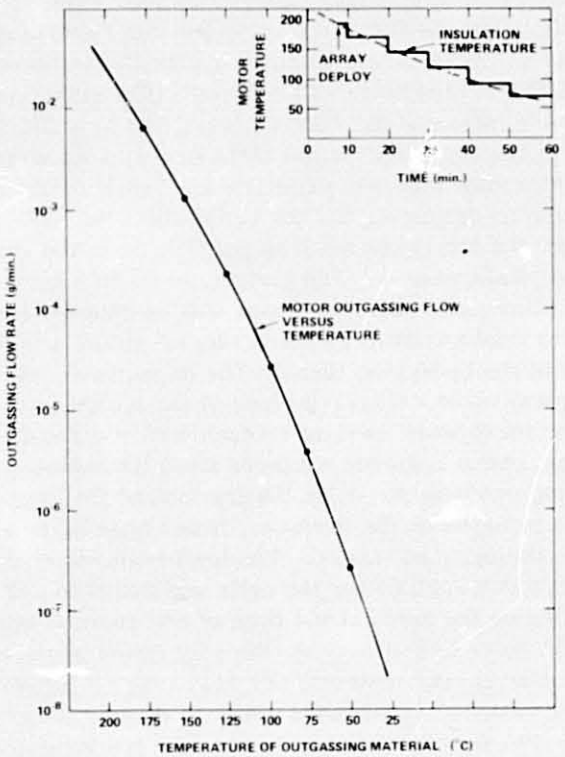

Fig. 7—Outgassing rates versus motor temperatures

ψ and a sticking coefficient σ, so that

$$\left.\frac{\Delta M}{\Delta t}\right|_{T=C} = \dot{m}(t)\,\psi\sigma \qquad (8)$$

The rate, $\dot{m}(t)$, varies with the motor temperature as shown in Figure 7. Since the temperature decreases with time, $\dot{m}$ is a function of time. For the calculation made here, the rates have been assumed to change every 10 minutes by an amount corresponding to a 25 K drop. The rates have not been reduced to account for material depletion. This is a conservative assumption, also justifiable, on account of the relatively short time (about 80 minutes) for the insulation material to acquire a temperature of about 298 K (25°C) and a corresponding outgassing rate several orders of magnitudes lower than that at 473 K (200°C).

The view factor multiplier, ψ (cm^{-2}), as defined here, expresses the fraction of the total material from the motor which impinges on a unit area of the spacecraft surface under consideration. The view factor multipliers for the numbered surfaces are indicated in the tabulation in Figure 1. View factor multipliers for the same surfaces, but modified by different diameters of proposed baffle rings around the motor, have been indicated for comparison. These baffle rings were suggested as a possible modification if the deposits were found to be too large. These view factor multipliers are based on the sources being diffuse and on averaging for the array rotation. The conventional view factors for the total area viewing the flow from the engine were calculated using Reference 4. The factor, $\psi = 1.06 \times 10^{-5}$ cm^{-2} applies to the solar cells surface, which will be exposed for 2 minutes during the array deployment. The next largest value, $\psi = 5.4 \quad 10^{-7}$ cm^{-2}, applies to the hydrazine tanks. The deposits on the tanks will be the largest for any other critical surface of the spacecraft. Therefore, calculations for these were used as a conservative estimate of contamination on other, more removed surfaces from the motor.

The sticking coefficient, σ, is the fraction of the impinging contaminant which remains on the surface. It has been taken as unity for the deposits on the cells and tanks. The temperatures of these are estimated to be 243 K (-30°C) for the cells and 273 K to 263 K (0 to -10°C) for the insulation on the tanks at the time of and several hours after deployment. At these temperatures, the stay times of the molecules of this high activation energy material are very long (471 days at 263 K (-10°C)) and the rates of evaporation are less than 10^{-12} $g/cm^{-2}/min^{-1}$. Therefore, the 100-percent sticking is not only conservative, but is based on justifiable grounds. However, for reasons of conservatism, it was assumed that 10 percent of the total contaminant would reach the

tanks during the 2 minutes of solar array deployment. After these 2 minutes, the solar array is fully deployed and the opposite side of the cells, which now views the spacecraft, is taken as a 100-percent diffuse reflector.

The deposit, ΔM, on the surface for a time, Δt, while the temperature is constant, is

$$\Delta M = \sigma \psi [\dot{m} \Delta t]_{T=C} \tag{9}$$

The total deposit, M, will be the summation of these elemental deposits at constant temperatures, i.e.,

$$M = \sum \Delta M = \sum \sigma \psi [\dot{m} \Delta t]_{T=C} \tag{10}$$

The rates and deposits on the solar cells and tank insulation have been calculated using these expressions. Table 2 shows a sample of the calculations and Figure 8 the deposits on the cells and insulation as a function of deployment time. For a deployment 8 minutes after motor burnout, which is probably the earliest deployment, the deposit on the cells is calculated at 6.2×10^{-7} g/cm^2 and on the tanks at 4.6×10^{-8} g/cm^2. These masses correspond to thicknesses of about 43 Å and 3.5 Å when the measured material density of 1.4 g/cm^3 is used. The deposits decrease by a half decade or more for every 10 minutes' delay in deployment.

CONTAMINANT-INDUCED SURFACE DEGRADATION

Test Set-Up and Instruments

The test for the measurement of surface degradation was run in a liquid nitrogen-shrouded vacuum chamber at a pressure of 5×10^{-6} torr. The layout of the thermal test samples in the X-25L solar simulator beam is shown in Figure 9. A QCM was positioned in the beam and another located outside the beam. The contaminant source was located beneath the quartz entrance window with its normal towards the sample plane. A radiometer for monitoring the output of the solar simulator was located externally to the vacuum chamber. A specially built system for recording QCM data and for thermally controlling the QCM was used for this test. The QCM's (which were the commercially available Celesco Model 700) were mounted inside a separate liquid nitrogen-cooled shroud. Their temperatures can be maintained at any desired temperature above 90 K by balancing the electrical power into a resistance heater on the QCM holder against the heat loss to the shroud. The sensing heads of these QCM's contain a demountable crystal assembly, a mixer/oscillator circuit, a stainless steel base in which these components are mounted, and a stainless steel cover for the crystal

Deposits on Solar Cells and Hydrazine Tank Insulation
for Array Deployment 8 Minutes after Burn and 2 Minutes of Solar Cells Exposure

Time from Motor Shutdown	Source Temperature	Outgassing of Motor	Solar Cells		Hydrazine Tank	
			Impinging Rates	Deposits	Impinging Rates	Deposits
min	°C	g/min	g/min/cm^2	g/cm^2	g/min/cm^2	g/cm^2
0 - 8	-	-	-	-	*	-
8 - 10	200	2.96×10^{-2}	3.16×10^{-7}	6.32×10^{-7}	1.60×10^{-9}	3.20×10^{-9}
10 - 20	175	6.34×10^{-3}	-	-	3.44×10^{-9}	3.44×10^{-8}
20 - 30	150	1.26×10^{-3}	-	-	6.84×10^{-10}	6.84×10^{-9}
30 - 40	125	2.11×10^{-4}	-	-	1.16×10^{-10}	1.16×10^{-9}
40 - 50	100	2.53×10^{-5}	-	-	1.37×10^{-11}	1.37×10^{-10}
50 - 60	75	4.22×10^{-6}	-	-	2.29×10^{-12}	2.29×10^{-11}
60 - 70	50	2.11×10^{-7}	-	-	1.14×10^{-13}	1.14×10^{-12}
70 - 80	25	9.51×10^{-9}	-	-	5.16×10^{-15}	5.16×10^{-14}
80 - 90	~25	$<9.51 \times 10^{-9}$	-	-	$<5.16 \times 10^{-15}$	$<5.16 \times 10^{-14}$
				$\Sigma = 6.32 \times 10^{-7}$ (43 Å)†		$\Sigma = 4.56 \times 10^{-8}$ (3.5 Å)†

Notes:

*Assumes 10 percent reflection from array.

†Contaminant density 1.4 g/cm^3.

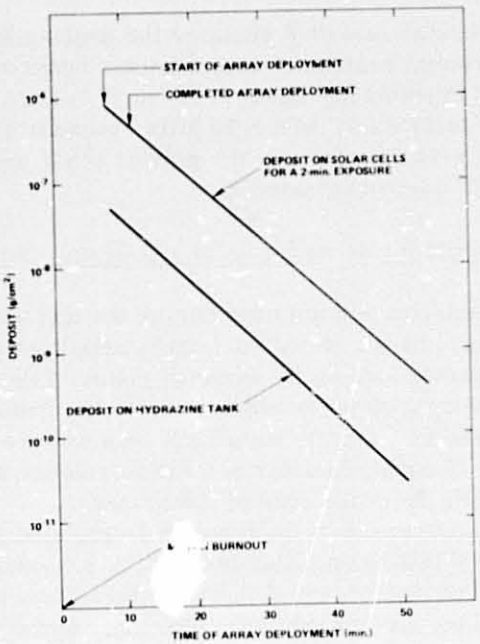

Fig. 8—Material deposit on solar cells and hydrazine tanks as a function of solar array deployment

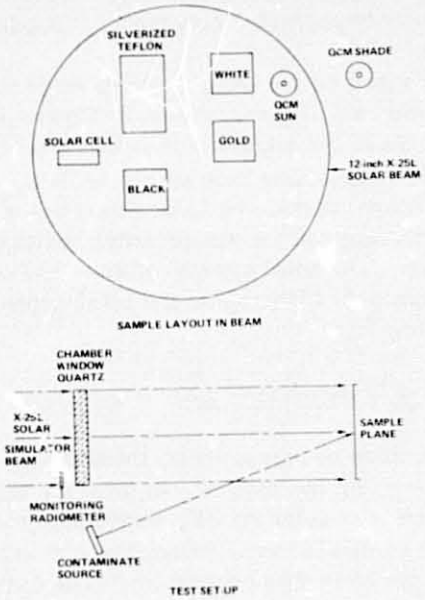

Fig. 9—Layout of thermal test samples in X-25L solar simulator beam

assembly. The crystal assembly contains the sensing and reference crystals and a platinum resistance thermometer between the two crystals. The AT-cut crystals are about 1.27 cm (0.5 inch) in diameter and 0.0152 cm (0.006 inch) thick, with a 10 MHz resonant frequency. The electrodes, serving as the contaminant deposit area, are aluminum with a 0.635-cm (0.25-inch) diameter.

The Deposit of Contaminants on the QCM and Sample Surfaces

The motor insulation sample used during the test was sandwiched between two 10-cm x 10-cm (4-inch x 4-inch) aluminum plates with a 5-cm (2-inch) diameter hole on the forward plate. Two 50 W heaters were bonded on the rear panel in order to drive the temperature of the source to 523 K (250°C). One thermocouple was centered on the insulation in the 5-cm (2-inch) diameter hole while another was located about 2.5 cm (1 inch) from the edge of the holder.

The physical appearance of the forward facing side of the insulation remained unchanged before and after the test, i.e., a relatively shiny black. The major change occurred in the material bonded between the aluminum foil backing and the rubber insulation. Initially, the material beneath the aluminum foil was shiny green and relatively flexible. At the test completion, this layer of material had become brittle and changed to a dull black. Heating schedules of the source had been intended to produce deposits corresponding to about 10^3, 5×10^3, and 1×10^4 Hz on the QCM. It was not possible, however, to produce deposits greater than about 4400 Hz.

The accretion rates on the QCM's which were aligned to face the source and were held at 213 K are shown in Figure 10. It was necessary to continuously increase the contaminant source temperature in order to achieve a reasonable deposition rate on the QCM's. Durin , the last maximum source temperature, the QCM accretion rate decreased rapidly even with increasing source temperature indicating depletion of outgassing products. The total amount of time the contaminant source was above 273 K was 9-3/4 hours and the total deposition on the QCM was 4.05×10^{-5} g/cm^2.

Test Technique for α/ϵ Determination

The thermal method to measure the integrated absorptance, α, and thermal emittance, ϵ, by the rate of temperature change during heating with the X-25L solar simulator on/off, was employed. The radiant intensity of the solar simulator was continuously monitored by a radiometer during the heat-up phase of this procedure. The data reduction procedure was essentially that documented in Reference 5.

RESULTS

The silverized Teflon sample was black on the reverse side and edges and the data presented is for this configuration. Figure 11 shows the degradation of the sample α and ϵ versus mass loading as indicated by the QCM. The sample ϵ was degraded at all three mass loadings, whereas the α was not significantly perturbed until after 2.1×10^{-5} g/cm^2 was deposited. The resultant α/ϵ ratio, which is also given in Table 3, is thus driven by the decreasing ϵ values. The visual appearance of the sample after the final contaminant loading was "hazy" and fringes could be seen when the Sun gun was rotated with respect to the sample. A reflectance measurement was made (using a Beckman DK-2A recording spectrophotometer) before and after (2.1×10^{-5} g/cm^2) on the sample with the results given in Figure 12. No data are given beyond 600 nm as there was no significant change in the reflectance. The spectral region below 400 nm displayed the most significant decrease in reflectance due to the contaminant film.

The white sample α and ϵ values exhibited the same trend as the silverized Teflon as shown in Table 3.

The evaporated gold sample α changed at all of the three levels of contaminant mass loading. The ϵ for gold could not be determined because black stripes, which were included to prevent excessive temperatures which would result with an all gold sample, dominate the thermal ϵ characteristic of the sample.

The solar cell output as a function of mass loading is given in Figure 13. The solar cell was at 248 K (-25°C) during the contaminant loading periods with the X-25L solar simulator on. The ratio of solar cell output to solar simulator monitoring radiometer is plotted to account for any fluctuations which occur in the X-25L simulator. The data are a composite of two separate mass loadings with the cell being cleaned between runs. With the QCM mass loading above 3.4×10^{-6} g/cm^2, the solar cell indicated no further decrease in output, even at the maximum loading of 3.0×10^{-5} g/cm^2. The reason for this characteristic is not known.

CONCLUSIONS

A deposit of 6.2×10^{-7} g/cm^2 on the solar cells corresponding to a thickness of about 43 Å which was calculated for the earliest solar array deployment, will not affect to a detectable degree, the performance of the solar cells. In fact, according to the degradation tests, a deposit, an order of magnitude higher than that calculated, produces a 4-percent degradation in cells' performance.

Similarly, the accretion of about 5×10^{-8} g/cm^2 (3 to 4 Å) on the silver-coated Teflon insulation of the hydrazine tank, is too small to

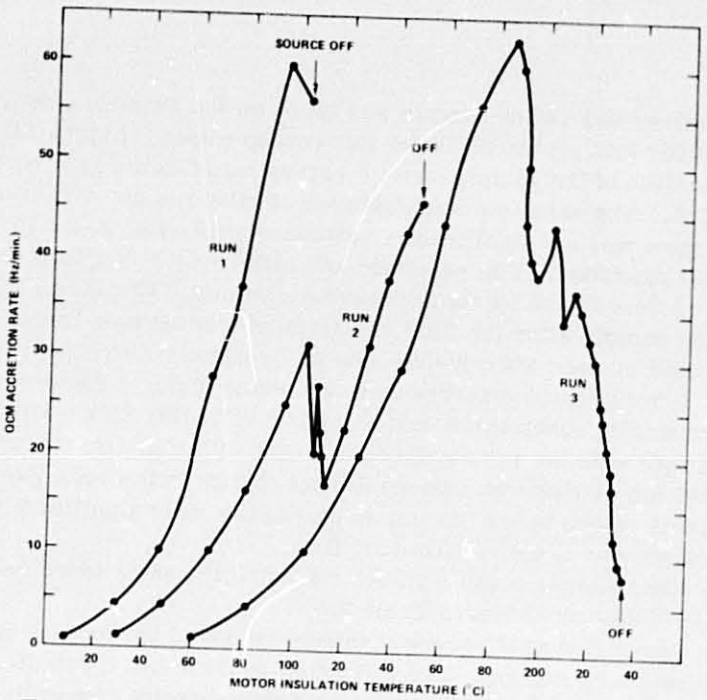

Fig. 10—QCM accretion rate versus motor insulation temperature

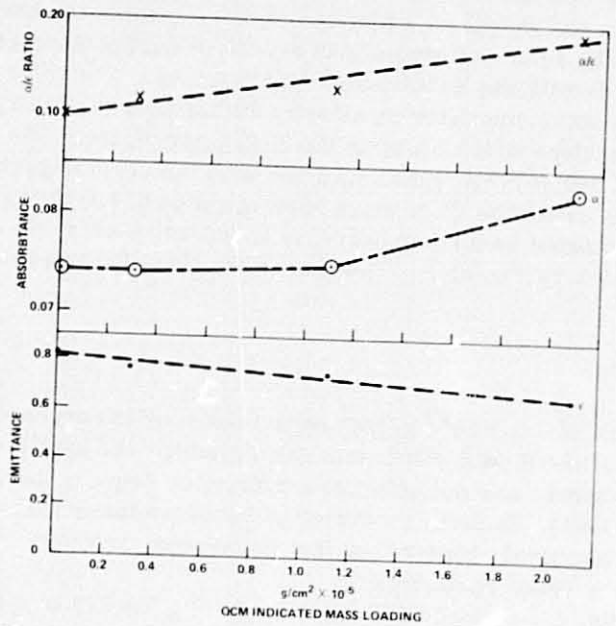

Fig. 11—Silverized Teflon absorptance and emittance versus contaminant mass

Table 3
Absorptance and Emittance
versus
QCM Indicated Mass Loading

QCM Indicated Mass Loading g/cm^2	White				Silverized Teflon (Black on Reverse Side)*				Gold (Black Stripes on Reverse Side)*		
	α	ϵ	α/ϵ	Temp.† °C	α	ϵ	α/ϵ	Temp.† °C	α	ϵ	Temp.† °C
Clean	0.14	0.90	0.16	-54.7	0.074	0.82	0.10	-74	0.21	0.47	-6.8
3.0×10^{-6}	0.14	0.86	0.16	-52.5	0.074	0.77	0.12	-72	0.24	0.47	+3.3
1.1×10^{-5}	0.14	0.79	0.18	-48	0.075	0.74	0.13	-70	0.26	0.47	+8.7
2.1×10^{-5}	0.16	0.70	0.23	-36	0.67	0.67	0.20	-62	-	-	-

Notes:

*Black treatment used for temperature control.

†Temperature at stabilization with Sun on.

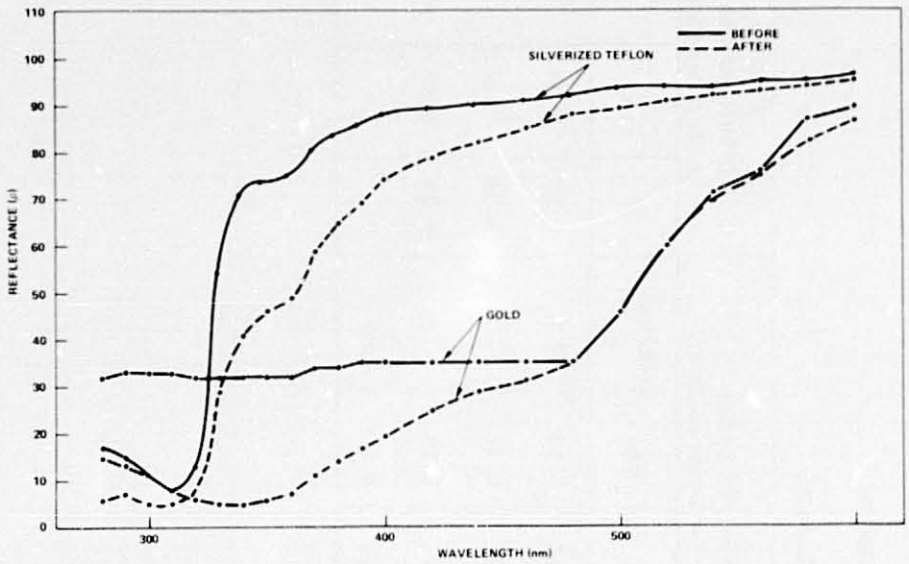

Fig. 12—Reflectance change of silverized Teflon and gold

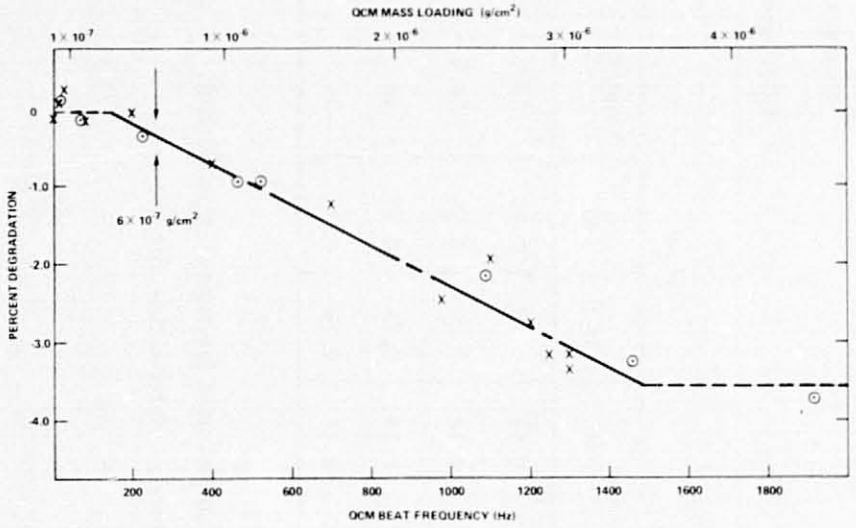

Fig. 13—Solar cell versus QCM mass loading

cause sensible change in the α/ϵ properties of the surface. The degradation test showed an α/ϵ change from 0.10 to 0.12 when a film of 3×10^{-6} g/cm^2, about 220 Å thick, was added to the clean surface. Degradation data as a function of mass deposits have been provided for the above surfaces, and for a white surface and a gold surface.

In conclusion, these degradation tests indicate that the calculated deposits would have to be one or two orders of magnitude higher to produce sensible effects on the thermal optical properties of the surfaces on which they will deposit. On the other hand, no estimate was possible on the size distribution, quantities, and velocities of particulates ejected by the motor 8 minutes after its firing, without actual engine firing and statistical measurements. If a number of particulates deposited on surfaces, they would be centers of scattering. Those orbiting for a time with the spacecraft would be sporadic sources of interference with radiation observations.

ACKNOWLEDGMENTS

The authors thank T. J. Jarrell and A. C. Darrah for computing the view factors, R. Marriott for the VCM data, F. C. Gross for the TG data, B. Paxson and A. R. Winker for the test set-up and operations, and E. Kunz of Thiokol Corporation for providing motor samples and related data.

REFERENCES

1. Brooksbank, R. M., "Qualification Test of a Thiokol TE-M-364-15 Rocket Motor at Simulated Altitude Conditions, "AEDC-TR-74-27. Rev., May 1974.

2. Santeler, D. J., Holkeboer, D. H., Jones, D. W., and Pagano F., "Vacuum Technology and Space Simulation," NASA SP-105, pp. 184-198.

3. Scialdone, J. J., "An Equivalent Energy for the Outgassing of Space Materials," NASA TN-8294, August 1976.

4. Jackson, C. E., Jr. and Puccinelli, E. F., "Viewfactor Computer Program (VIEW)," NASA Tech Brief B-75-10032, April 1975.

5. "Measurement of Thermal Radiation Properties of Solids," Richmond, J. C., ed., NASA SP-31, pp. 89-90.

Paper No. 22

THE RESPONSE OF A QUARTZ CRYSTAL MICROBALANCE TO A LIQUID DEPOSIT

A. P. M. Glassford, *Lockheed Palo Alto Research Laboratories, Palo Alto, California*

ABSTRACT

Theory has been developed for predicting the loss of response of a QCM to a liquid deposit due to viscous effects in the deposit. The loss of response is expressed by a response factor, equal to the response of the QCM to a liquid film divided by its response to a solid film of the same mass per unit area. The theory assumes a droplet-type deposit morphology, and considers the influence of droplet distribution parameters. Experiments have been conducted to examine the validity of the theory, using DC 704 silicone oil as the subject deposit material. Experiments were made in two series - one with constant deposit mass and variable temperature, the other with variable deposit mass and constant temperature. Satisfactory agreement with the theory was found. Interpretation of the data using the theory has enabled information on droplet area coverage and number density to be deduced.

INTRODUCTION

The quartz crystal microbalance (QCM) has been used in the aerospace industry for several years to monitor the build-up of condensed contaminant deposits on spacecraft surfaces in both simulation and flight situations. Also, the QCM is being used increasingly in basic research on contamination-related phenomena and its accuracy and behavior in this application have consequently been subject to critical analysis. One of the areas of concern is the response of the QCM to liquid deposits, as opposed to solid deposits. Because the dynamic coupling of a liquid deposit to the crystal surface is less than one hundred per cent, the sensitivity of the QCM, measured in frequency change per unit added mass per unit area, is reduced. This is a significant problem in the aerospace contamination measurement application because many of the species outgassed from common materials, e.g. RTV silicone adhesives and potting compounds, as well as common diffusion pump oils exist as very low vapor pressure liquids at near ambient temperatures. It is therefore desirable to develop a technique for predicting the response of the QCM to liquid deposits quantitatively.

When a liquid deposit is oscillated in shear by the QCM measuring crystal only the liquid layer in immediate contact

with the crystal moves with the same velocity as the crystal surface. Liquid layers some distance from the surface can move only in response to a shear stress in the liquid, which requires a velocity gradient to be established. The presence of a velocity gradient means that the average deposit velocity during oscillation will always be less than that of the crystal surface. It has been shown elsewhere[1][2] that the frequency change of the QCM produced by an added mass is a function of its kinetic energy. Since a solid deposit moves throughout with the same velocity as the crystal surface, the change in frequency produced by an added liquid mass will always be less than that produced by an added solid mass of the same magnitude.

A further reduction in QCM response is produced by the tendency of liquid deposits to occur as a distribution of droplets. The formation of a droplet from an equivalent mass uniformly distributed over the same base area will increase the mean distance from the deposit mass to the crystal surface. Since the velocity of the liquid deposit decreases with distance from the crystal surface the formation of droplets will decrease the average velocity of the deposit, and hence further reduce the magnitude of the induced frequency change. The response will also be affected by the droplet size and number per unit area. For a given deposited mass per unit area the response of a system of a large number of small size droplets will be greater than that of a few large size droplets, because of the greater average distance of the deposit from crystal surface in the latter case. Also, the measured mass per unit area will vary with the number of droplets per unit area for a given droplet size.

The approach taken in this paper to estimate the magnitude of these effects is to determine the velocity profile of the oscillating liquid deposit, and then to derive the QCM response using the Rayleigh energy method for harmonically oscillating systems. The problem is addressed theoretically in three stages. First, the effect of viscosity is determined for a uniform liquid deposit. Second, the effect of droplet geometry is derived. Third, the effect of droplet size and distribution is investigated. A limited experimental program was then conducted to assess the validity of the derived theory.

QCM Response

The sensitivity of a QCM, S, is defined as the relationship between the added solid mass per unit area, $(\Delta m/A)_s$, and the resulting change in frequency, Δf_s. Hence for a solid mass

$$\Delta f_s = S_s \times (\Delta m/A)_s \qquad (1)$$

This paper is not concerned with the absolute sensitivity of the QCM to liquid deposits, but with the relative loss of sensitivity if the deposit is liquid rather than solid. This can

be expressed by a "response factor", F, defined as the frequency change, induced by a liquid deposit Δf_ℓ, divided by the frequency changed induced by a solid deposit of the same mass per unit area. Hence, for liquid films the relationship equivalent to (1) is

$$\Delta f_\ell = S_\ell x \, (\Delta m/A)_\ell \tag{2}$$

and, for $(\Delta m/A)_s = (\Delta m/A)_\ell$

$$F = S_\ell / S_s = \Delta f_\ell / \Delta f_s \tag{3}$$

F can be derived using the same Rayleigh energy method for undamped harmonically oscillating systems as was used successfully[1] [2] to derive the absolute sensitivity, S. In this method the total kinetic energy, T, and potential energy, V, of the system are expressed in terms of the displacements, u_i, in each degree of freedom, as follows

$$T = \tfrac{1}{2}a\left(\dot{u}_1^2 + \dot{u}_2^2 \ldots\ldots \dot{u}_n^2\right) \tag{4}$$

$$V = \tfrac{1}{2}c\left(u_1^2 + u_2^2 \ldots\ldots u_n^2\right) \tag{5}$$

The frequency of the system, f, is then given by

$$f^2 = c/a \tag{6}$$

For small perturbations of the system, such as the addition of mass to the QCM crystal, equation (6) can be rewritten

$$(f + \Delta f)^2 = (c + \Delta c)/(a + \Delta a) \tag{7}$$

The surface of a crystal oscillating in thickness shear is an antinode, so mass added there does not affect the potential energy of the system, making Δc zero. Ignoring squares of small quantities, equation (7) can be rewritten as

$$\Delta f/f = -\Delta a/a \tag{8}$$

Equation (8) can be written for solid and liquid deposits. Noting that f and a are independent of the phase of the deposit, the following expression is obtained for F from (3) and (8).

$$F = \Delta a_\ell / \Delta a_s \tag{9}$$

The response factor is thus determined from the ratio of kinetic energy coefficients of the liquid and solid deposits. These coefficients are determined from an equation similar to (4). The oscillating crystal and deposit is a single degree of freedom system, so the velocity of the system can be represented by the velocity at a single location. The logical location to select in this context is the crystal surface. In general,

oscillation velocity and deposit density can vary across the crystal and these variations can be represented by a distribution function.[2] The effect of non-uniform distribution functions is to introduce a multiplicative constant into the expression for T and hence a. Since the present analysis is concerned with comparing equivalent situations this constant would appear in both denominator and numerator of the right-hand side of equation (9), making F independent of the distribution functions. In this paper the distribution functions are thus assumed equal to unity to minimize algebraic complexity of intermediate expressions in the following derivations. A general expression for the kinetic energy of a deposit, ΔT, can then be written in terms of a uniform crystal surface velocity, $v_o \sin 2\pi ft$

$$\Delta T = \tfrac{1}{2}\Delta a (v_o \sin 2\pi ft)^2 \qquad (10)$$

The problem is now to obtain expressions for the kinetic energies of the liquid and solid deposits. This is done by integrating the kinetic energy throughout the deposit, for which the velocity distribution in the deposit must be known. The solid has the same velocity throughout, equal to that of the oscillating crystal surface. The velocity in the liquid deposit will vary through the thickness and must be determined by viscous theory.

VELOCITY DISTRIBUTION IN THE DEPOSIT

Uniform Film Deposit

Figure 1a shows the model for the oscillatory motion of a uniform liquid film. The fluid motion in the film is described by the Navier-Stokes equations. For the present case there are no pressure gradients or body forces, and flow takes place only in the y-direction. The Navier-Stokes equations thus reduce to:

$$\frac{\partial v}{\partial t} = \frac{\mu}{\rho} \cdot \frac{\partial^2 v}{\partial x^2} \qquad (11)$$

This equation is to be solved for the boundary conditions:

$x = 0,\ v = v_o \sin 2\pi ft$ (crystal surface velocity)

$x = x_m,\ \frac{\partial v}{\partial x} = 0$ (zero shear stress at outer boundary)

Equation (11) and the above boundary conditions are whol analagous to the heat conduction problem of a parallel sided

infinite slab with harmonically varying temperature at one surface with the other surface insulated. Carslaw and Jaeger give the following solution to this problem[3], translated here into momentum transfer terms.

$$B = \left| \frac{\cosh k(x_m - x)(1+i)}{\cosh kx_m(1+i)} \right| \tag{12}$$

$$\phi = \arg\left(\frac{\cosh k(x_m - x)(1+i)}{\cosh kx_m(1+i)} \right) \tag{13}$$

$$k = \left(\frac{2\pi f \rho}{2\mu} \right)^{\frac{1}{2}} \tag{14}$$

$$v/v_o = B \sin(2\pi ft + \phi) \tag{15}$$

B is the amplitude of the oscillation at a distance x from the crystal surface while ϕ is the phase angle by which the displacement at this location trails that at the crystal surface. Numerical values of B and ϕ are given in Figure 2 as functions of kx_m and x/x_m. Equation (12) can be expanded as follows:

$$v/v_o = B\cos\phi \sin 2\pi ft + B\sin\phi \cos 2\pi ft \tag{16}$$

The velocity of the liquid thus consists of a component $B\cos\phi \sin(2\pi ft)$ in phase with the crystal motion which contributes to the inertial energy of the system, and a component $B\sin\phi\cos(2\pi ft)$ 90 degrees behind the crystal motion which contributes to the damping of the crystal motion. Although damping is not included in the Rayleigh theory, its effect will be negligible for small deposit thicknesses, since $\sin\phi \sim 0$. At larger thicknesses, however, its effect may increase to significant proportions, as noted in the Discussion.

Droplet Deposit

Figure 1b shows the model of the motion of the oscillating liquid droplet. If surface tension forces are ignored, the motion is described by equation (11), but the boundary conditions are now:

$$v = v_o \sin 2\pi ft \text{ at } x = 0,$$

and

$$\frac{\partial v_t}{\partial n} = 0 \text{ at all points on the droplet surface}$$

where v_t is the tangential velocity on the droplet surface, and n is the coordinate normal to the surface. The solution to

equation (11) with the above boundary conditions will be much more complex than for the uniform film, because the variable droplet geometry requires the introduction of more descriptive parameters. A solution to this problem has not been located in the literature, and hence for the present purposes the velocity distribution in a droplet of height x_m will be assumed to be the same as that in a uniform film of thickness x_m. In fact, the actual velocity at a given distance from the crystal surface should be higher in the droplet than in the uniform film, because the effect of area reduction with distance in the droplet will be to reduce the velocity gradient needed to exchange momentum with the outer levels of the droplet. The loss of QCM response calculated using the uniform film velocity profile will therefore be greater than the actual loss.

DETERMINATION OF THE RESPONSE FACTOR

It was noted earlier that the loss of sensitivity of the QCM to a liquid deposit is due to three effects which act together but which are conceptually separable: viscous effects, droplet formation, and droplet distribution. In the interest of clarity of presentation, these three effects are considered one at a time in the following analysis. F is derived in turn for the uniform liquid film, individual liquid droplets and then distributed liquid droplets.

In the theoretical analysis, F is shown to be primarily a function of the distance of the deposit from the QCM surface, while the primary data output from the QCM is mass per unit area. To connect the theory with experimental data, the concept of nominal deposit thickness, ℓ_n, is used. ℓ_n is defined as the deposit mass per unit area divided by the density. Further, it was shown in the viscous flow analysis above that distance from the QCM surface to points in the deposit can be non-dimensionalized by multiplying them by k, equation (14). The theoretical expressions for F are thus developed as functions of $k\ell_n$. The following paragraphs present the derivation of the kinetic energy of the various deposits, ΔT. Finally, in order to simplify the algebra, ΔT is derived per unit area, permitting the crystal area to be eliminated from the integrations.

Uniform Film Deposit

For the uniform solid deposit the velocity throughout is equal to that of the crystal surface. The kinetic energy per unit crystal surface area, ΔT_{su} is given by

$$\Delta T_{su} = \tfrac{1}{2}\rho \int_o^{x_m} (v_o \sin 2\pi ft)^2 \, dx \qquad (17)$$

$$= \tfrac{1}{2}\rho \; x_m \; (v_o \sin 2\pi ft)^2$$

By comparison with equation (10), the kinetic energy coefficient per unit area, Δa_{su}, is given by

$$\Delta a_{su} = \rho x_m \tag{18}$$

The kinetic energy of the uniform liquid deposit, $\Delta T_{\ell u}$ will be a function of the component of the local velocity in phase with the inertia forces, $v_o B \cos\phi \sin 2\pi ft$.

$$\begin{aligned} \Delta T_{\ell u} &= \tfrac{1}{2}\rho \int_o^{x_m} (v_o \cos\phi \sin 2\pi ft)^2 \, dx \\ &= \tfrac{1}{2}\rho \int_o^{x_m} (B \cos\phi)^2 \cdot dx \, (v_o \sin 2\pi ft)^2 \end{aligned} \tag{19}$$

By comparison with equation (10)

$$\Delta a_{\ell u} = \rho \int_o^{x_m} (B \cos \phi)^2 \, dx \tag{20}$$

From equations (9), (18) and (20) the response factor for a uniform film, F_u, is thus

$$\begin{aligned} F_u &= \int_o^{x_m} (B \cos \phi)^2 \, dx / x_m \\ &= \int_o^1 (B \cos \phi)^2 \, d(x/x_m) \end{aligned} \tag{21}$$

F_u has been computed from equations (12), (13) and (21) for various values of kx_m, and is plotted in Figure 3 as a function of $k\ell_{nu}$, noting that for a uniform film ℓ_{nu} is equal to x_m. The shape of the curve represents a transition from the very small response loss for small deposits ($k\ell_{nu} < 0.2$) to the asymptotic response of a quasi-infinite film ($k\ell_{nu} > 1.6$) which is almost totally confined to the region near the crystal and is thus independent of nominal thickness. Also plotted in Figure 3 is the product $F_u \cdot k\ell_{nu}$, which is proportional to the actual QCM output. The rising of this QCM output function to a maximum, followed by a steady decline is the most commonly encountered practical manifestation of QCM viscous effects.

Single Droplets

Whereas the geometry of a uniform film can be characterized by a single dimension, several geometric parameters are necessary for the specification of condensed droplets. Since

the purpose of this paper is to demonstrate the credibility of the analysis rather than perform an analysis of droplet geometry some simplifying assumptions are made. The droplet is assumed to have the form of a spherical cap with contact angle θ_c and height x_m. Relationships between area, volume and x_m and θ_c are derived in the Appendix.

For a solid droplet of volume V_d and base area A_d the kinetic energy per unit base area, ΔT_{sd}, is given by

$$\Delta T_{sd} = \tfrac{1}{2}\rho \int_o^{x_m} A(x)\,(v_o \sin 2\pi ft)^2\,dx/A_d$$

$$= \tfrac{1}{2}\rho\,(V_d/A_d)\,(v_o \sin 2\pi ft)^2 \qquad (22)$$

Hence, from (A6), (A9) and (10),

$$\Delta a_{sd} = \rho\,\frac{x_m}{3}\left(\frac{2 - \cos\theta_c\,(2+\sin^2\theta_c)}{(1-\cos\theta_c)\sin^2\theta_c}\right) \qquad (23)$$

For a liquid droplet of the same dimensions, the kinetic energy per unit base area, $\Delta T_{\ell d}$, is (assuming that the velocity profile is given by equation (15))

$$\Delta T_{\ell d} = \tfrac{1}{2}\rho\int_o^{x_m} A(x)\cdot(v_o B\cos\phi \sin 2\pi ft)^2 dx/A_d$$

$$= \tfrac{1}{2}\rho\int_o^{x_m} A(x)/A_d)\,(B\cos\phi)^2\,dx\cdot(v_o \sin 2\pi ft)^2 \qquad (24)$$

From equations (10), and (24)

$$\Delta a_{\ell d} = \rho\int_o^{x_m} (A(x)/A_d)\,(B\cos\phi)^2\,dx \qquad (25)$$

Hence from equations (9), (23) and (25)

$$F_d = \frac{3\sin^2\theta_c\,(1-\cos\theta_c)}{(2-\cos\theta_c(2+\sin^2\theta_c))}\int_o^1 (A(x)/A_d)(B\cos\theta)^2 d(x/x_m) \qquad (26)$$

In order to evaluate F_d for the purposes of illustration of the effect of droplet and/or comparison with the experimental data of the next section, it is necessary to know the value of θ_c. θ_c depends on several parameters, such as temperature and

surface condition, and data relevant to the present situation are not available. However, photomicrographs made by the author of similar deposits showed contact angles near 30^o, and it can be shown by evaluating equations (A5) and (A6) that the function $A(x)/A_d$ varies little for $10^o < \theta_c < 50^o$. So that the derived equations may be evaluated a value of θ_c equal to 30^o has thus been assumed. F_d has been computed from equation (26) for various values of kx_m using θ_c equal to 30^o, and equations (12), (13), (A5) and (A6). The nominal deposit thickness of the droplet, ℓ_{nd} relative to its own base area, A_d is given by

$$\ell_{nd} = V_d/A_d = 0.512\, x_m \qquad (27)$$

where V_d and A_d are given by equations (A12) and (A11). F_d is plotted versus $k\ell_{nd}$ in Figure 4. While the relationship is qualitatively similar to that for the uniform film, the effect of configuring a liquid deposit as a droplet is shown to be a further decrease in the response of the QCM for a given nominal thickness.

Distribution of Droplets

A real liquid deposit will consist of a distribution of droplets of various sizes and spacings. The effect of droplet spacing will be to cause the deposit mass per unit area of QCM crystal - the quantity sensed by the QCM - to be lower than the mass per unit droplet base area. Assuming all droplets to be the same size, the nominal deposit thickness for the distributed droplets, ℓ_{ndd}, is related to the nominal thickness of the droplet referred to its base area, ℓ_{nd}, by an area coverage factor, α_A:

$$\ell_{ndd} = \alpha_A \times \ell_{nd} \qquad (28)$$

where

$$\alpha_A = \frac{\text{area covered by droplets}}{\text{total QCM area}} = A_d N_d \qquad (29)$$

The response factor, F_{dd}, is a function only of droplet geometry, not the distribution, and thus is given by equation (26) as a function of kx_m. However, the computed value of F_{dd} is now plotted versus $k\ell_{ndd}$, given as follows (from equations (27) and (28)).

$$k\ell_{ndd} = \alpha_A \times 0.512\, kx_m \qquad (30)$$

Figure 4 shows a family of curves of F_{dd} versus $k\ell_{ndd}$ for various values of α_A. In practice α_A has a maximum value of

$\pi/4$ cos 30 or 0.907, corresponding to a close packed hexagonal distribution. Another significant value of α_A is 0.785, for a close packed square distribution. The QCM response is seen to fall with decreasing area coverage.

PRACTICAL APPLICATION OF THE THEORY

The single fundamental output from a QCM with an added mass is change of frequency. A solid, evenly distributed deposit can be characterized by a single parameter-mass per unit area - and the QCM sensitivity is constant. Hence, a single frequency change data point can be translated into an added mass. However, unless the deposit mass is small enough for F to be near to unity, a liquid deposit requires several parameters to be determined, such as droplet shape and size and area distribution, and liquid viscosity. Hence several data points are required for determination of the deposit parameters, which precludes direct unequivocal measurement of the mass of a particular liquid deposit. The most appropriate use of the theory appears to be in the analysis of processes made up of a series of data points from which the various parameters can be deduced. Two situations of this type occur quite frequently in practice. In one situation a QCM with a deposit on its surface is warmed up with no loss or rearrangement of deposit. In this situation k varies, while the geometric parameters ℓ_{ndd}, A_d, V_d, and α_A remain constant. Thus the response factor F_{dd} varies with $k\ell_{ndd}$ at constant α_A, and the QCM response during warm-up should follow one of the constant α_A characteristics of Figure 4. In the other situation the QCM is held at constant temperature while the accumulation or loss of deposit is measured, in which case k is constant, while the geometric parameters vary. It is suggested that during condensation a liquid droplet deposit builds up by growth of the individual droplets at constant distribution density, N_d, until adjacent droplets touch and coalesce, thereby reducing N_d and increasing the spacing between droplets. Growth resumes at constant N_d until coalescing occurs again. In practice, the droplets will have a distribution of sizes and spacings, so a succession of discrete steps in N_d are unlikely. A more likely process is growth at constant N_d from an initial condition of relatively widely and randomly spaced nucleation centers, until the droplets begin to coalesce, whereafter N_d adjusts continuously downwards while the deposit maintains a more or less close packed arrangement. Characteristic paths can be derived for this postulated process as follows. Equations (28) and (29) can be combined to give

$$k\ell_{ndd} = A_d \cdot N_d \cdot k\ell_{nd} \tag{31}$$

For θ_c equal to 30°, noting (27), (31) and (A6)

$$k\ell_{ndd} = 167\,(N_d/k^2)\cdot(k\ell_{nd})^3 \qquad (32)$$

The relationship between F_{dd} and $k\ell_{ndd}$ for isothermal growth at constant N_d/k^2 is found by determining F_{dd} for a given $k\ell_{nd}$ from equations (26) and (27), and $k\ell_{ndd}$ from equation (32) for constant values of N_d/k^2. These constant N_d/k^2 characteristics are shown in Figure 4. According to the suggested mechanism growth will occur along one or more lines of constant N_d/k^2 until a close packed situation occurs, at which point N_d will decrease and growth will continue along another line, constant N_d/k^2.

EXPERIMENTAL INVESTIGATIONS

The validity and usefulness of the theory presented above was examined by a series of experiments using Dow Corning DC 704 silicone oil on a Celesco Model 700 quartz crystal microbalance. Noting the remarks in the previous section, two types of experiments were conducted. In the first type the response of constant temperature QCM to a steadily increasing deposit was measured. In the second type a deposit was formed on the QCM and then its response was measured as a function of temperature.

Apparatus

The apparatus is shown schematically in Figure 5. The QCM can be maintained at any desired temperature above 77°K by balancing the electric power into a resistance heater wound. on the holder against heat lost through a thermal link between holder and shroud. Also mounted within the shroud but shielded from the QCM by a cooled partition is a pot containing DC 704. The pot temperature can be maintained at any temperature above 77°K by balancing electrical heater power against a thermal l. The pot has an orifice whose axis lies along the line between pot and QCM permitting a flux of DC 704 molecules to be directed at the QCM sensing crystal through a hole in the partition, which can be closed by a remotely controlled shutter. The whole apparatus is mounted in a glass bell jar, evacuatable to pressures below about 2×10^{-7} torr.

Viscosity of DC 704

In order to determine k for an experimental situation, the relationship between the viscosity of the subject liquid must be known as a function of temperature. Figure 6 shows kinematic viscosity versus temperature obtained from the Dow Corning Company.[4] DC 704 is a phenyl-methyl siloxane, a high molecular weight silicone oil related to the general family of polydimethyl siloxanes, which have been shown to exhibit non-Newtonian flow behavior at high shear rates.[5] The shear

rates experienced by a liquid deposit on a oscillating QCM can be quite high, and could conceivably reach the order of magnitude required for non-Newtonian behavior to occur. The possibility of this situation being reached in the present experiments is covered in the Discussion.

QCM Response Data

In the first series of tests the QCM was held at constant temperature while its surface was exposed to a constant flux of DC 704 molecules. The test was begun with the QCM surface clean. The shutter was then opened and the QCM output recorded as a function of time. Data interpretation was based on the assumption that after the initial adsorption and nucleation processes were completed, the condensation rate could be assumed to be constant. This constant actual condensation rate was determined from the initial indicated condensation rate, since the response factor for small nominal thicknesses is essentially unity. The actual mass per unit area on the QCM at later times in the deposition was then calculated from the assumed constant condensation rate and the time since the beginning of exposure. The accuracy of this linear extrapolation was confirmed by interrupting the flux and cooling the QCM at the conclusion of the test in order to regain full response of the deposit by solidification. The agreement between this final measurement and the magnitude predicted by the linear extrapolation was surprisingly good -- always better than five percent, and usually no worse than one percent. The response factor was calculated as a function of deposit thickness by dividing the indicated mass per unit area by the calculated mass per unit area for the same instant of time. The nominal thickness was found from the calculated mass per unit area and the density, while k was found for the test temperature from equation (14) and Figure 6. Data from four experiments of this type, performed for QCM temperatures of 27°C, 37°C, and 51°C, are plotted in Figures 7 and 8. The experiment at 37°C was repeated for two net condensation rates -- 0.61×10^{-8} and 1.22×10^{-8} gms/cm^2/sec. The data for 27°C and 51°C were obtained for net condensation rates of 1.53×10^{-8} and 1.72×10^{-8} gms/cm^2/sec, respectively. The data for 27°C and 37°C appear to follow the scenario proposed in the previous section. For the early stages of growth ($k\ell_n < 0.25$) the data appear to follow roughly two N_d/k^2 characteristics, with a transition near $k\ell_n \sim 0.1$. For $0.25 < k\ell_n < 0.5$ the process occurs along a more or less close-packed characteristic. The departure of the data from the theoretical close packed characteristics for $k\ell_n > 0.5$ is probably due to the increasing significance of effects neglected in the present analysis, and is covered in the Discussion. The number of droplets per unit area in these deposits can be estimated by fitting theoretical constant N_d/k^2 curves to the data for $0.05 < k\ell_n < 0.25$, using equation (31) or Figure 4.

At 37°C, for which k is 11687 cm^{-1}, the data can be fitted by N_d/k^2 equal to about 0.045, making N_d of the order of $6x10^6$ cm^{-2}. At 27°C, for which k is 9474 cm^{-1}, N_d/k^2 equal to 0.04 is a reasonable fit, making N_d about $4x10^6$ cm^{-2}. Use of these values for N_d at 51°C, where k is equal to 14980 cm^{-1} indicates that corresponding values of N_d/k^2 at 51°C should be in the range of about 0.03 to 0.02. Constant N_d/k^2 curves for these values have been drawn on Figure 8, showing that 51°C data do fall in this range, even though the shape of the data is inconclusive.

These values of N_d can be compared with the photomicrographs of Shapiro and Hanyok[6], which show DC 704 deposits on various surfaces. These photomicrographs show number densities in the range of $5x10^5$ to $1x10^6$ cm^{-2} for deposits on a mirror surface, which, because of its smoothness would be expected to have somewhat fewer nucleation sites than the QCM surface.

In the second series of tests deposits of different magnitudes were condensed on the QCM and their response measured as a function of temperature. The true mass per unit area of each deposit was found by cooling the QCM below the solidification temperature, which was near -35°C. The response at other temperatures was determined by heating or cooling the QCM through a series of equilibrium temperatures. This technique is limited to temperatures below the region in which re-evaporation rate of the DC 704 became significant, which was about 20°C. The response factor at a given temperature was calculated from the mass per unit area indicated by the QCM at that temperature divided by the true mass per unit area. The nominal thickness was found from the actual mass per unit area divided by the density. k was variable in these tests and was calculated from equation (14) and Figure 6. The data for several experiments with different nominal thicknesses are shown in Figure 9. The maximum value of $k\ell_n$ reached in each test was determined by either the attainment of a temperature at which the re-evaporation rate became significant (about 20°C) or an abrupt loss of output occurred, the possible cause of which is suggested in the Discussion. It was noted in the previous section that the deposit geometry should remain constant during these tests, in which case the data should follow the constant α_A characteristics of Figure 4. The data do indeed follow the same general pattern as the theoretical curves, although they appear to show a slightly faster decline at high values of $k\ell_n$. However, the data for the $5.12x10^{-5}$ cm deposit shows the same inflection point near $k\ell_n$ of 0.4 as predicted by theory, this being the only set of data in which the inflection point was observed.

The slightly different shape of the data curves from the constant α_A curves of Figure 4 is thought to be due to temperature dependent effects ignored in the theory, for example, droplet shape or constant angle. It was first thought that the

discrepancy might have depended on the temperature at which the deposit was formed. A deposit formed on a cold QCM may have a continuous film morphology, which breaks down into droplets as heating occurs. To investigate this possibility several experiments were made with a 6.54×10^{-5} cm film thickness. In one experiment the deposit was formed cold (-45°C) and the data were acquired during heating. In a second experiment an equivalent deposit was formed near 20°C and data were obtained during cooling, then by reheating and recooling. The data from these two series of tests shown in Figure 9 are virtually indistinguishable.

It was concluded from these data that a transition from continuous film to droplet geometry, or any other irreversible geometric change does not occur in the temperature range studied, even if the deposit is formed in the solid phase. This means that the surface mobility of DC 704 at -45°C is sufficient to produce a morphology similar to that obtained for liquid phase deposition.

The deposit nominal thicknesses used in these tests was quite high, so that sufficiently large values of $k\ell_n$ could be reached. It is possible that the thicknesses were high enough to cause the deposit morphology to begin to differ from the distributed, even sized droplet pattern assumed with apparent success for smaller nominal deposit thicknesses. This possibility was assessed using the following relationship, which can be derived from equations (27), (29), (30), and (A6).

$$\alpha_a = 5.5 \cdot \ell_{ndd}^{2/3} \cdot N_d^{1/3} \qquad (33)$$

The data for ℓ_{ndd} equal to 1.75×10^{-5} cm can be fitted quite well by the theoretical curve for α_A equal to 0.6, Figure 4. Insertion of these numbers in equation (33) gives N_d equal to 4.2×10^6 - 2 cm which is in good agreement with the earlier data, and tends to confirm the validity of the model for this nominal thickness. The data for 5.12×10^{-5} cm for $k\ell_{ndd} < 0.25$ can be fitted by α_A equal to about 0.8, while for $k\ell_{ndd} > 0.25$ a better fit is obtained for α_A equal to 0.70. These α_A values correspond to N_d values of 1.2×10^6 -2 cm and 8.0×10^5 -2 cm, respectively, and also suggest that at this thickness the deposit is approaching a close packed situation. The data for the 6.54×10^{-5} cm deposit at $k\ell_{ndd} < 0.3$ can only be fitted by α_A equal to unity, which is impossible for a droplet deposit, for which α_A cannot exceed 0.91. This seems to indicate that a transition to a more film-like morphology is occurring at these higher nominal thicknesses, which is to be expected.

DISCUSSION

The intent of this paper was to demonstrate that the variable response of the QCM to liqui deposits can be explained almost totally by viscous effects coupled with a droplet type deposit morphology. It is apparent from the agreement obtained between the theory and the experiments that this has been satisfactorily achieved. Good qualitative and quantitative agreement was obtained up to non-dimensional nominal thicknesses of about 0.5. Above this value a very rapid fall off in response was experienced in all tests where this $k\ell_n$ value was reached. Detail analysis of the experimental data in this region revealed a discontinuity in the second differential of F versus $k\ell_n$, indicating a change of controlling phenomenon. It is suggested that this could be due to the onset of non-Newtonian effects in the silicone oil, or a change in the modal response of the oscillating crystal under the higher damping forces which will arise with heavier deposits. The oscillation amplitude of the crystal is of the order of 50Å,[7] so that for a deposit of nominal thickness of 1000 Å on a 10MHz crystal the shear rate is of the order of $(10^7 x 2 x 50)/1000$ or 10^6 sec^{-1}. This is well within the range in which silicone fluids can show a sharp loss of apparent viscosity. However, a detailed analysis of the velocity profile in the deposit, plus viscosity data for DC 704 at high shear rates would be needed to investigate this point further. Assessment of the possibility of modal changes is beyond the scope of this work.

Although the quantitative agreement between the theory and the data appears to be quite good, it should be re-emphasized that several major assumptions were made. These were:

(1) Use of the uniform film velocity profile for the liquid droplet.
(2) Assumption of spherical-cap droplet shape and uniform droplet size distribution.
(3) Neglection of damping effects in the Rayleigh frequency perturbation analysis.
(4) Exclusion of all other possible surface forces except viscous drag from the analysis.
(5) To permit reduction of the data the viscosity data obtained from Dow Corning were arbitrarily extrapolated from about -12°C to about -35°C.

It is logical to suppose that refinements of the analysis in these areas would produce better agreement with the experiment.

It was noted in the text that it is not possible to use the theory to interpret isolated data points because of the many parameters involved. Instead the utility of the theory will probably be to generate insight into condensation and revaporation processes. Interpretation of the data presented in this paper has generated credible values for area coverage and

number density for the droplet and has suggested that the spherical cap shape assumption may be acceptable. Further work in which some of the neglected effects are included in the analysis, coupled with more careful, systematic experimental measurements may well prove to be a fruitful source of data on contamination deposit morphology.

NOMENCLATURE

A_d	Droplet base area
a, Δa	Rayleigh kinetic energy coefficient
B	Oscillation velocity magnitude
c, Δc	Rayleigh potential energy coefficients
F	QCM response factor
f	QCM frequency
k	$(2\pi f\rho/2\mu)^{\frac{1}{2}}$
ℓ_n	Deposit nominal thickness
$(\Delta m/A)$	Deposit mass per unit area
N_d	Number of droplets per unit area
r	Solid radius of spherical cap droplet
S	QCM sensitivity
T	Rayleigh total kinetic energy
u	Rayleigh displacement coordinate
V	Rayleigh total potential energy
V_d	Droplet volume
v	Local velocity in deposit
v_o	Maximum crystal surface velocity
x	Distance between QCM surface and a point in the deposit
x_m	Distance between QCM surface and the most distant point in the deposit
α_A	Fraction of QCM surface covered by droplets
ϕ	Phase angle of motion in the deposit
θ_c	Droplet contact angle
μ/ρ	Kinematic viscosity of the deposit
ρ	Deposit density

Subscripts:

l	droplet
dd	distributed droplet
ℓ	liquid
n	nominal
s	solid
u	uniform

REFERENCES

1. Stockbridge, C.D., "Resonant Frequency Versus Mass Added to Quartz Crystals," Vacuum Microbalance Techniques, Vol. 5, 1966, Plenum Press, N.Y., K. Behrndt, pp. 193-206.

2. Glassford, A.P.M., "Analysis of the Accuracy of a Quartz Crystal Microbalance," Paper No. 76-438, AIAA 11th Thermophysics Conference, San Diego, California, July 1976.

3. Carslaw, H.S., and Jaeger, J.C., "Conduction of Heat in Solids," Oxford University Press, 2nd Edition, 1959, Chapter III, Section 3.6.

4. Private Communication from A.J. DeSapio, Dow Corning Company, Sept. 1975.

5. Lee, C. L., Polmanteer, K. E., and King, E.G., "Flow Behavior of Narrow Distribution Polydimethyl Siloxane," Journal of Polymer Science; Part A2, Vol. 3 (1970) pp. 1909-1916.

6. Shapiro, H., and Hanyok, J., "Monomolecular Contamination of Optical Surfaces," Vacuum, Vol. 18, No. 11, (1968), pp. 587-592.

7. Stockbridge, C.D., "Effect of Gas Pressure on Quartz Crystal Microbalances," Vacuum Microbalance Techniques, Vol. 5, 1966, K. Behrndt ed., pp. 147-178.

APPENDIX

The principal geometric parameters of the spherical cap droplet are indicated in Figure 10. Other parameters may be derived as follows:

Droplet height, x:

$$x = r(\cos\theta - \cos\theta_c) \tag{A1}$$

$$x_m = r(1 - \cos\theta_c) \tag{A2}$$

Hence
$$x = x_m(\cos\theta - \cos\theta_c)/(1 - \cos\theta_c) \tag{A3}$$

Droplet cross-sectional area, A(x):

$$A(x) = \pi(r\sin\theta)^2 \tag{A4}$$

Obtaining r^2 from A2 and $\sin^2\theta$ from A3

$$A(x) = \frac{\pi x_m^2}{(1 - \cos\theta_c)^2}\left[1 - \left((x/x_m)(1-\cos\theta_c) + \cos\theta_c\right)^2\right] \tag{A5}$$

Base area, A_d (= A(x) at $x/x_m = 0$):

$$A_d = \frac{\pi x_m^2 \sin^2\theta_c}{(1 - \cos\theta_c)^2} \tag{A6}$$

Volume, V_d:

$$V_d = \int_o^{x_m} A(x) \cdot dx \tag{A7}$$

Substituting A4 in A7

$$V_d = \frac{\pi r^3}{3} \left[2 - \cos\theta_c (2 + \sin^2\theta_c) \right] \tag{A8}$$

Substituting A2 in A8

$$V_d = \frac{\pi x_m^3}{3} \left[\frac{2 - \cos\theta_c (2 + \sin^2\theta_c)}{(1 - \cos\theta_c)^3} \right] \tag{A9}$$

For θ_c equal to 30^o the following relationships follow from A5, A6 and A9.

$$A(x) = 175\, x_m^2 \left[1 - (0.134(x/x_m) + 0.886)^2 \right] \tag{A10}$$

$$A_d = 43.8 x_m^2 \tag{A11}$$

$$V_d = 22.4\, x_m^3 \tag{A12}$$

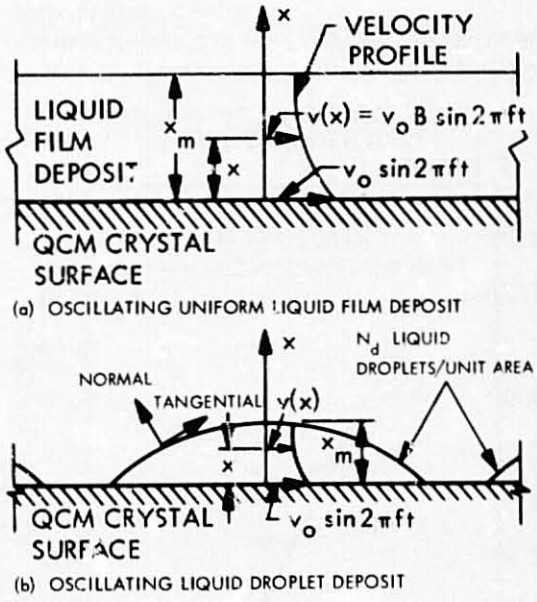

Figure 1. Schematic of Uniform and Droplet Liquid Deposits.

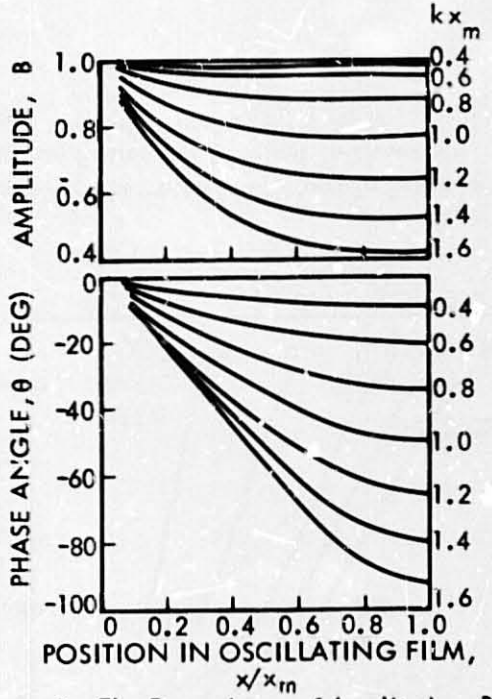

Figure 2. The Dependence of Amplitude, B, and Phase Angle θ, on Position in the Liquid Film, x/x_m and Non-Dimensional Thickness, kx_m, for an Oscillating Liquid Film.

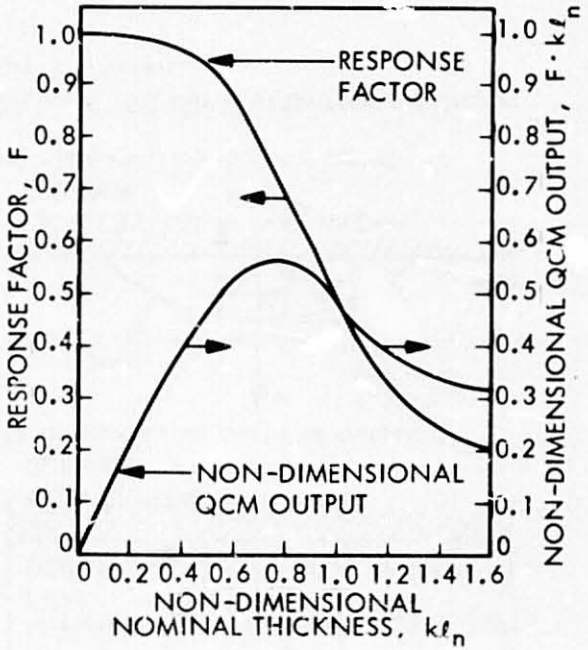

Figure 3. Theoretical Response Factor and QCM Output Versus Deposit Thickness for Uniform Film Liquid Deposit.

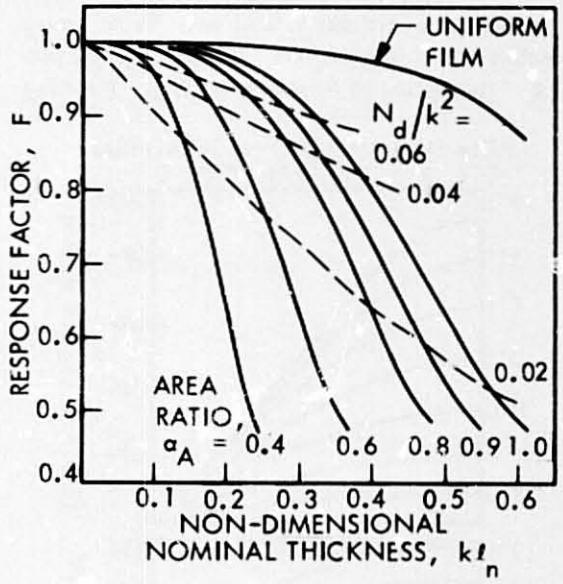

Figure 4. Theoretical Relationship Between Response Factor and Nominal Thickness for Liquid Droplet Deposits ($\theta_c = 30^o$).

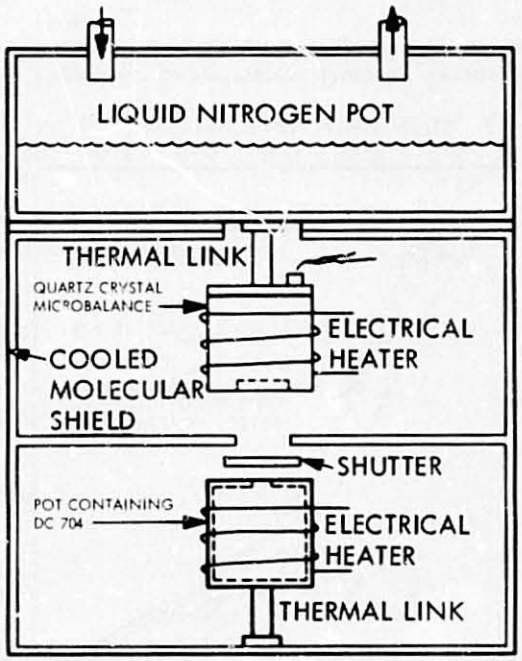

Figure 5. Experimental Apparatus.

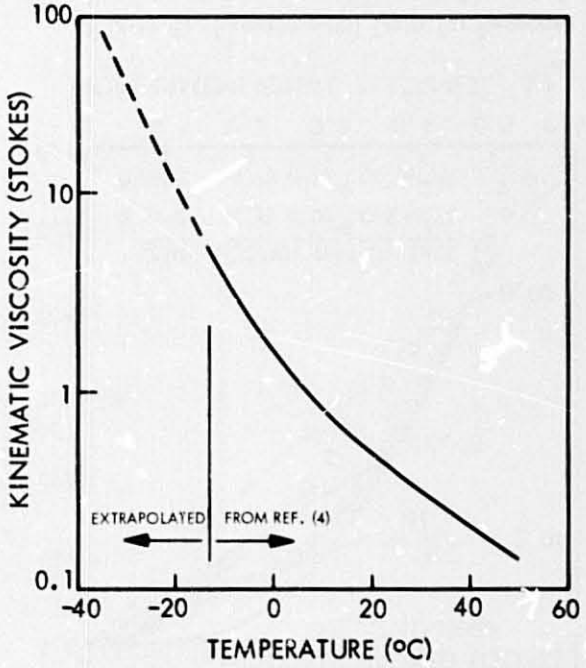

Figure 6. Viscosity of DC 704 Silicone Oil

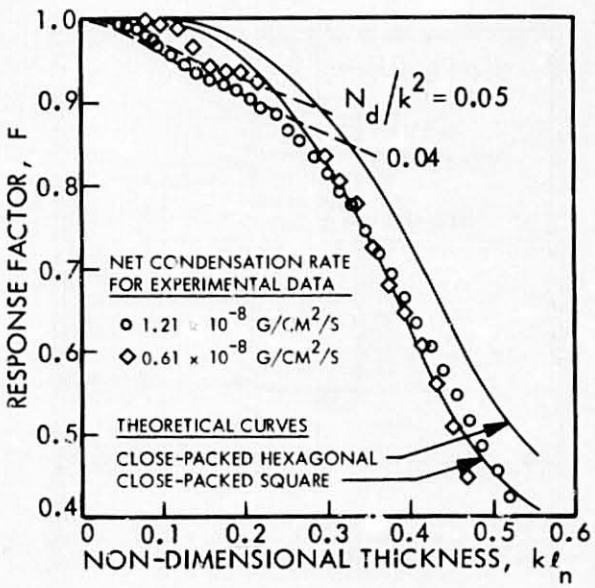

Figure 7. Experimental Data for Response Factor as a Function of Deposit Magnitude at 37°C.

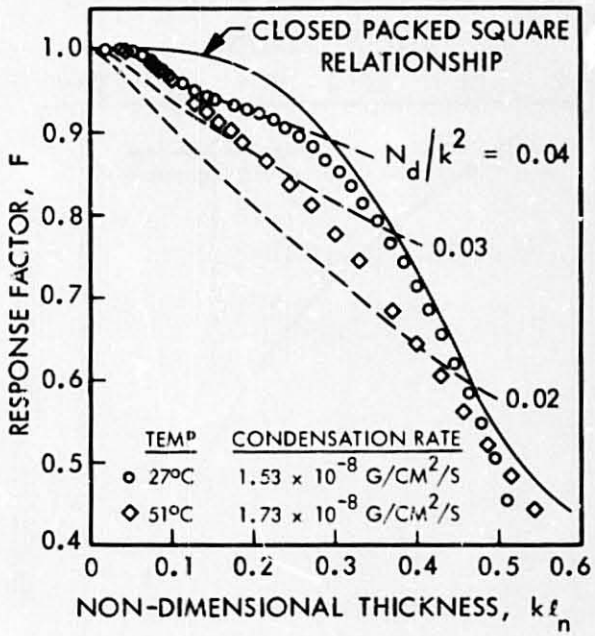

Figure 8. Experimental Data for Response Factor as a Function of Deposit Magnitude at 27°C and 51°C.

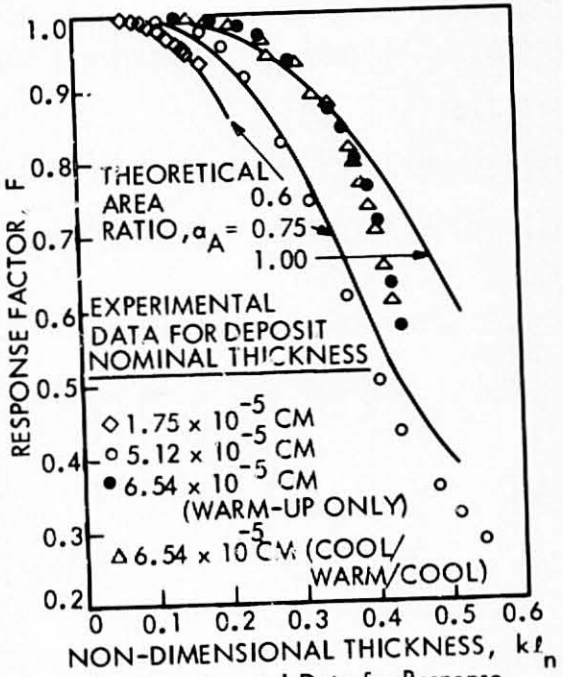

Figure 9. Experimental Data for Response Factor as a Function of $k\ell_n$ for Three Values of Nominal Thickness.

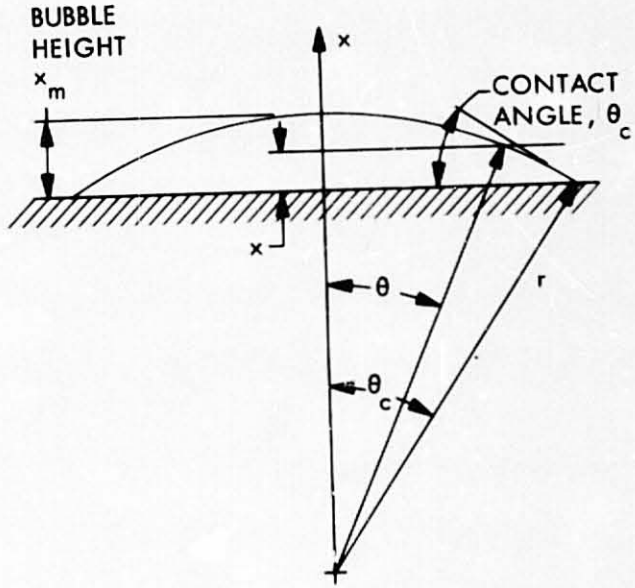

Figure 10. Major Dimensions of a Spherical Cap Droplet on a Surface.

D19

Paper No. 23

AIRBORNE PARTICLE MONITORING BY ELECTROSTATIC PRECIPITATION

J. C. Robinson, *I. T. Stoneback, Ernest F. Fullam, Inc., Schenectady, New York*

ABSTRACT

For qualitative analysis of atmospheric particulates by microscopy, the sampling device should preserve the particles in the state existing at the moment of capture. A collector is described that uses electrostatic precipitation to capture and disperse specimens on various substrates for direct insertion into microscopes. Sampling runs in various atmospheres are described. Micrographs are presented to show particle morphology and distribution on the substrates. Chemical identification by x-ray energy probe and electron diffraction is illustrated.

Qualitative analysis of airborne particles smaller than five microns requires careful collection and definition of the object of interest. The smaller the particle, the more physical forces act upon it to obscure its individuality. Such particles group and regroup constantly, making precise definition of a "particle" difficult in air pollution matters.

Analysis of abatement equipment performance must deal with this difficulty. Unfortunately, contemporary sampling systems often add to the confusion, whereby, particles collected for analysis do not necessarily represent a true "sample" of the atmosphere under study.

For this reason, the device described below was developed so that a sample could be extracted and deposited onto a substrate that could then be inserted directly into a microscope. Subsequent physical alterations, often a result of the transfer from collection device through intermediate steps, are eliminated. All particles are preserved in the size and shape prevailing at the sampling location at the instant of capture.

Description

Collection substrates can be standard microscope

slides, carbon planchets, or film coated specimen grids. Substrates are inserted between two electrodes. A high voltage source is energized to create an electrical field between the electrodes. Airborne particles moving thru the field receive a charge and are attracted to and dispersed on the oppositely charged collecting surface. The surfaces are then ready for examination and analysis in the electron or light microscope without further preparation.

Control parameters include operating mode, air flow, and electrostatic field. Two optional modes of operation are provided. In the continuous mode, the electrostatic field is energized continuously as air is drawn over the collecting surface. In the pulsing mode, an air sample is drawn in, the flow is stopped, and the field is energized. Timing cams provide a selection of on-off intervals. The number of cycle repeats or the length of a continuous run are controlled by a time clock. Air flow is regulated by the blower speed; the maximum flow being approximately 85 liters per minute. Field energy is regulated by changing the electrode gap.

The instrument is powered by a 12 volt acid-gel rechargeable battery for which a plug-in 110 volt recharger is provided. High voltage is generated by a power source with a maximum output of 5000 volts. The high voltage circuit is securely insulated from the surrounding equipment, however, the total power output is only 500 milliwatts.

An internal light is provided for viewing the electrode adjustment and the specimen deposition. A rotatable 90° elbow is provided to direct the air intake and control variations caused by surrounding air movement.

A secondary collection system is included to provide a simultaneous quantitative record of the total particulates in the atmosphere being sampled by the precipitator. Air is drawn thru a pre-weighed Millipore filter secured in a cassette which can be closed and transferred to a laboratory for postweighing without risk of contamination.

Performance Evaluation

Verification that the test specimens include representatives of all particles in a sampled atmosphere requires that the identity of all particulates in that atmosphere be known. This is never the case in investigative sampling. Although verification can be accomplished by laboratory controlled runs using known inputs, the experiments must include a sufficiently

wide range of materials and environmental conditions to satisfy all situations.

As an alternative to such an extensive program, sampling runs were made under various circumstances to show the capabilities of the equipment.

Run No. 36: The atmosphere was sampled on an autumn day in a semi-rural area where vegetation and earth dust particles predominate. The collector was at ground level with the intake port pointed downwind. Wind velocity was five mph and temperature was 10° C.

The collection surface was a microscope slide glass and the gap between the glass and the upper electrode was a 3.5 mm. The duration of the run was 60 minutes in the pulsing mode. Particle distribution over a three mm^2 area is shown in Figure 1.

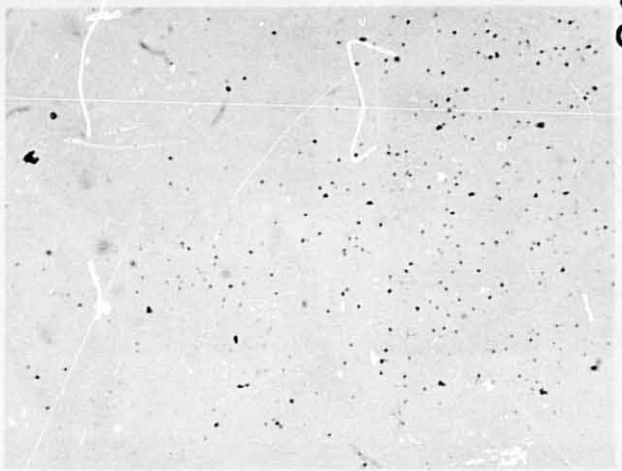

Figure 1

Run No. 34: The location of the collector was at ground level on the shoulder of an asphalt, two lane road carrying continuous car and truck traffic. The intake port pointed across the road. There was no wind and the temperature was 20° C.

The collection surface was a pyrolytic graphite planchet and the gap between the planchet and the upper electrode was 4.7 mm. The duration of the run was 115 minutes in pulsing mode.

Particles collected are shown in scanning electron micrographs Figures 2 and 3. As would be expected, the particles are predominately organic (petroleum hydrocarbons and vegetation) and include many metallic

particles, eg. aluminum, iron, magnesium.

The x-ray energy probe read-out that identifies chemical elements is shown in Figure 4. The peaks, reading from the left, identify magnesium, aluminum, silicon, sulfur, chlorine, potassium, calcium, titanium and iron. All of these elements are in the single soil particle on the left in Figure 3, the major element being silicon.

Figure 2

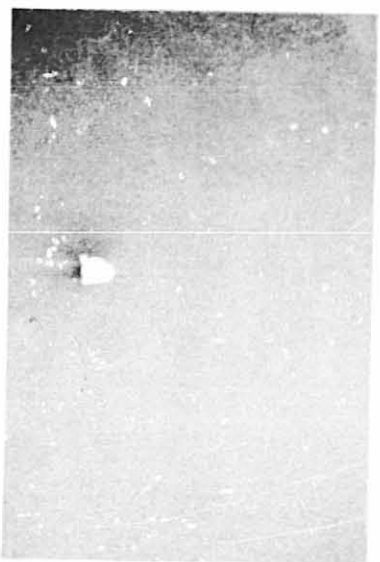

Figure 3

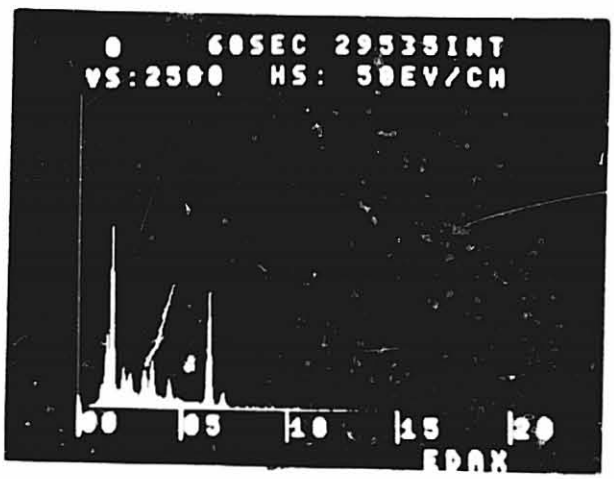

Figure 4

Run No. 35: The collector was placed two feet away from an automobile exhaust pipe expelling wet vapor from a warm engine (1968 Chevrolet 307). The collection surface was a pyrolytic graphite planchet and the electrode gap was 2.7 mm. Duration of the run was 2 minutes in pulsing mode.

Particles collected are shown in SEM micrographs, Figures 5 and 6. The large sphere in Figure 5 is a hydrocarbon particle encasing a lead particle. The irregular shaped particles in Figure 6 are calcium sulfate.

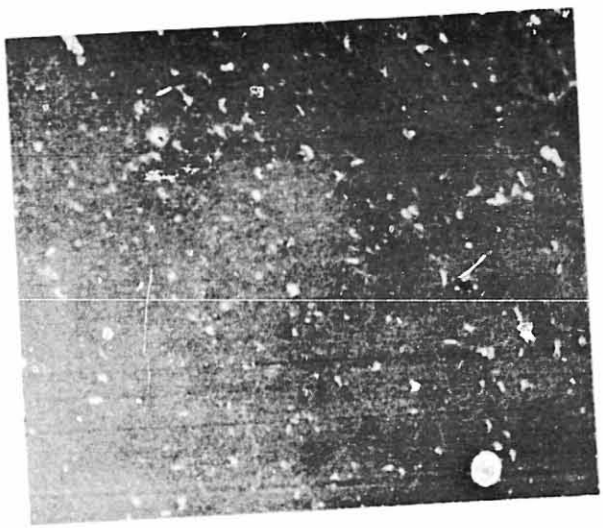

Figure 5

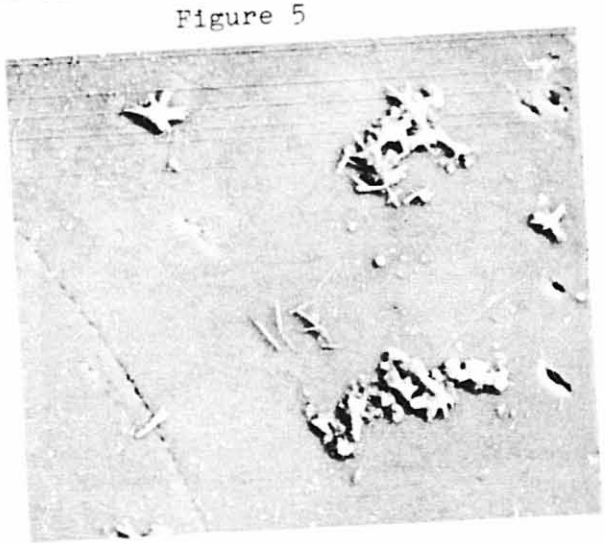

Figure 6

Run No. 38: In this case, smoke from burning magnesium was directed into the collector intake in a laboratory controlled experiment. The collection surfaces were formvar film covered grids which were subsequently examined on a transmission electron microscope. The electrode gap was 2.5 mm. Two runs were made of 2 minutes duration, one with continuous and one with pulsing mode. Distribution results are compared in Figure 7 and 8 respectively. They are not significantly different.

Figure 7

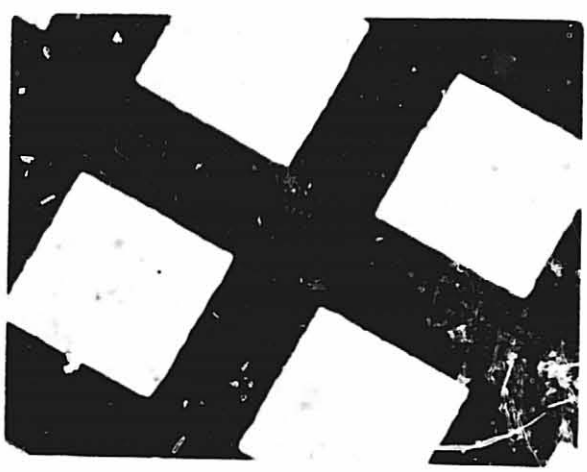

Figure 8

Figure 9 is a transmission electron micrograph illustrating the size range of the particles dispersed.

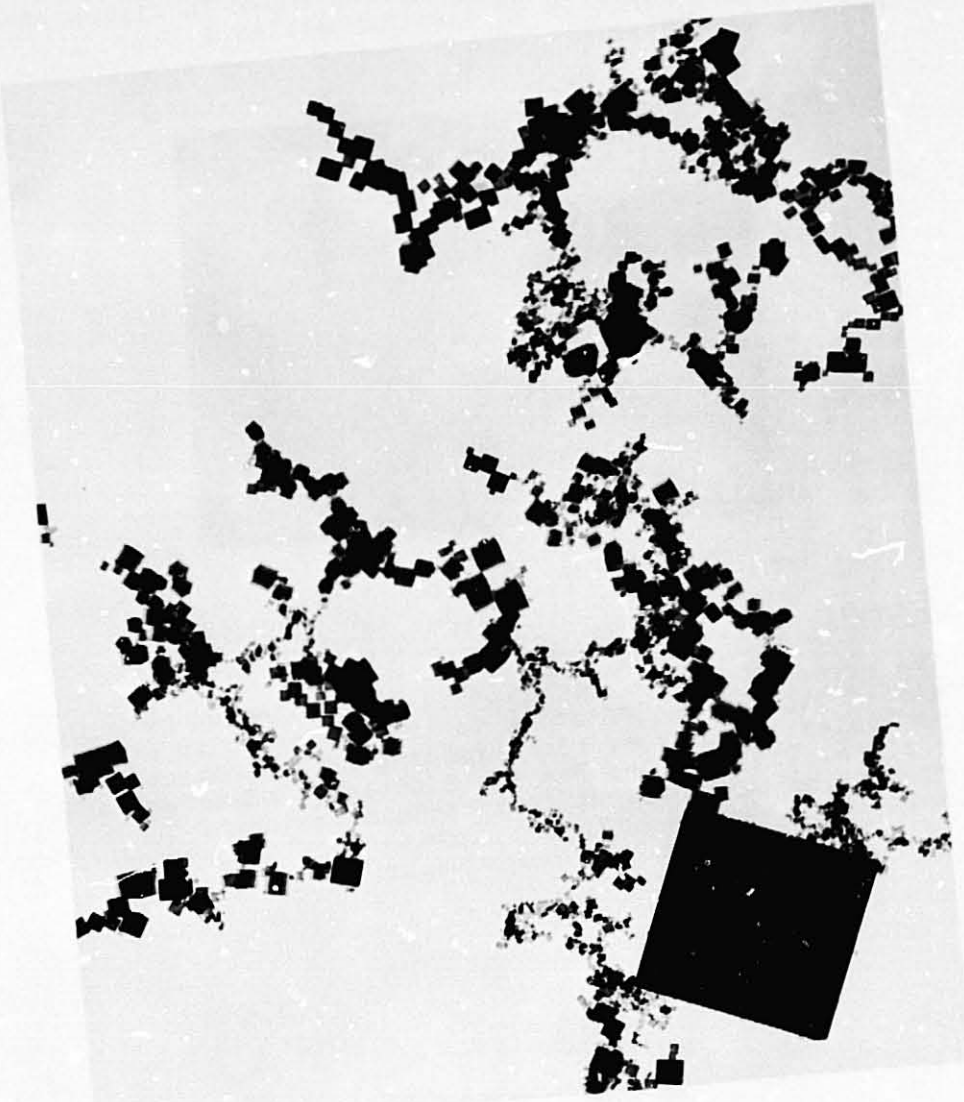

Figure 9

Run No. 39: Collection was made in the same location as Run No. 34 on formvar covered grids for examination by a transmission electron microscope. The inorganic chemical compounds collected were identified by electron diffraction. The pattern shown in Figure 10 identifies a particle of aluminum silicate ($Al\ Si_2\ O_3\ (OH)_2$).

Figure 10

SUMMARY

The principle advantage of particle collection by electrostatic precipitation is the preservation of particles in the condition existing at the moment of capture. This device has the additional advantage of dispersing particles directly onto a choice of collecting surfaces thereby enabling optional selection of the microscope equipment to be used.

C-4

References

Cadle, R. D., Particle Size Theory and Industrial Applications, National Center for Atmospheric Research, p. 2 (1965).

Green, H. L., Lane, W. R., Particulate Clouds: Dusts, Smokes and Mists, VanNostrand, Chapter 5 (1957).

Husar, R. B., "Recent Developments in In Situ Size Spectrum Measurement of Submicron Aerosols", Instrumentation for Monitoring Air Quality, ASTM Special Technical Publication 555, p. 157 (1974).

Orr, C., Dallavalle, J. M., Fine Particle Measurement, MacMillan, p. 96 (1959).

Settig, Marshall, Pollution Detection and Monitoring Handbook, Noyes Data Corp., (1974).

Paper No. 24

THE ROLE OF LIGHT MICROSCOPY IN AEROSPACE ANALYTICAL LABORATORIES

E. R. Crutcher, *Boeing Aerospace Company, Seattle, Washington*

ABSTRACT

Light microscopy has greatly reduced analytical flow time and added new dimensions to laboratory capability. Aerospace Analytical Laboratories are often confronted with problems involving contamination, wear, or material inhomogeneity at levels that would not concern other industries. The detection of potential problems and the solution of those that develop necessitate the most sensitive and selective applications of sophisticated analytical techniques and instrumentation. Cost and often more important, time effective analyses that optimize a diverse laboratory's capabilities must be used. This inevitably involves light microscopy, no other single instrument is as versatile a starting point for solving Aerospace contamination problems. The microscope can characterize and often identify the cause of a problem in 5-15 minutes with confirmatory tests generally requiring less than one hour. When an identification cannot be made the characterization indicates which instruments in the laboratory can most efficiently identify the source of a problem with the aid of the microscopic data. Assemblage analysis, the identification of the percentage contribution of multiple contamination sources, is impracticle if not impossible using any other instrument or combination of instruments. Light microscopy has made and will continue to make a very significant contribution to the analytical capabilities of Aerospace Laboratories.

INTRODUCTION

The microscope does much more than magnify. It is a sophisticated optical instrument capable of working with very small samples and characterizing them by the effects their electron distributions have on the visible electromagnetic

spectrum. Electron orbital energy, spatial distribution, density, and electron freedom all result in optical effects measurable with the microscope. An experienced microscopist can identify a large number of compounds by these observed effects. Those not identified can be characterized for future identification. These effects are so sensitive that careful measurement of them in known materials can detect spatial or crystal faults, molecular weight changes, internal stress, degree of crystallinity, trace impurities and other conditions which alter electron configurations. All of this can be done nondestructively and within a relatively short period of time.

Even with the most modern laboratory wet chemical techniques involving the use of the microscope can be important. As few as 1000 atoms of an element can be detected using microscopic wet chemical methods. Microcrystal tests are among the most widely used techniques for the qualitative identification of organic functional groups. These tests are based on the characterization of the crystalline products from the reaction of an unknown and a known, specific, reagent. If the form or progress of a chemical reaction is of interest the microscope offers a method of approach not offered by any other instrument. Solubility studies, thermal phase transformations, rates of change and other physiochemical properties of compounds can be studied to great advantage microscopically.

Many industrial, as well as natural materials, have characteristic morphologies. Common biologicals, pollens, spores, diatoms, insect parts, hair, plant parts, plant ash (tobacco), and other materials are sometimes encountered in contamination samples. The recognition of them with some knowledge of their natural history can often help solve a contamination problem. Industrial artifacts from production, as well as the products themselves, often have important microscopic morphologies. The application of the microscope to metallurgy, ceramics, and microelectronics are examples of the importance of morphologies to products. Industrial artifacts as contaminates also exhibit helpful diagnostic morphologies. Wear particulate in a hydraulic system has a shape characteristic of the type of wear that produced it. The recognition of that shape can help identify the type and extent of wear. Airborne industrial artifacts such as paint spheres, metal grinding or cutting residue, weld residue, tire wear, etc., can help indicate the origin of contaminates in a controlled environment. These materials within a part can indicate a control or a cleaning problem during assembly.

Figure #1 is a graphic representation of some of the techniques in Light Microscopy. Most of these techniques are applicable to common Aerospace contamination problems. The theory and mechanics of using these techniques is much to large a task to be covered in this paper but the bibliography at the end will hopefully be of value to those interested in pursuing analytical microscopy. The purpose of this paper is to point out the added capabilities as well as the cost effectiveness that resulted from our increased utilization of the light microscope.

EQUIPMENT AND SETTING

The Light Microscopy Laboratory, also known as the Particle Identification Laboratory, is part of a much larger laboratory complex. Instruments available in the general laboratory include:

Liquid Chromatograph	Gas Chromatograph
GC/Mass Spectrograph	Scanning Electron Microscope
Emission Spectrograph	Transmitting Electron Microscope
Fourier Transform Spectroscopy I.R.	Electron Microprobe
Standard I.R. Spectrograph	Energy Dispersive X-ray
X-ray Diffraction Laboratory	Fast Neutron Activation
Differential Scanning Calorimetry	Atomic Absorption
Thermal Gravimetric Analysis	General Wet Chemistry Lab
	General Physical Test Lab
	Differential Thermal Analysis

The microscopy laboratory has a Bausch & Lomb and a Nikon Zoom Stereomicroscope, a Nikon Apophot Research Microscope, a Nikon LKE Research Microscope with a Mettler hotstage, a Carl Zeiss Episcopic Brightfield/Darkfield Research Microscope, two laminar flow benches, a large centrifuge, sedimentation and density gradient equipment, and various other support equipment for sample collection and preparation. The research microscopes have polarized light, phase contrast, and numerous interference technique capabilities as well as a wide range of illumination systems. A 2000 slide standards cabinet is an additional piece of equipment very important to light microscopy. The Microscopy Laboratory consists of two rooms: one 19 x 14 feet and one 7-1/2 x 13 feet. The Laboratory is located in the 2-01 Building of the Boeing Aerospace Plant II complex in South Seattle.

OPTICAL MICROSCOPY Optical Crystallography Photometry Interference Microscopy Dispersion Staining	CHEMICAL MICROSCOPY Hot or Cold Stage Microscopy Microcrystal Tests Ultramicro Analysis Environmental Cell Microscopy
MORPHOLOGICAL MICROSCOPY Optical Metallographics Biological Microscopy Wear Analysis Counting Analysis	SUPPORT TECHNIQUES Sample Preparation Particle Manipulation Density Analysis Sedimentation Analysis

FIGURE #1

The Field of Light Microscopy as Used in This Paper Includes the Body of Techniques Seen Above.

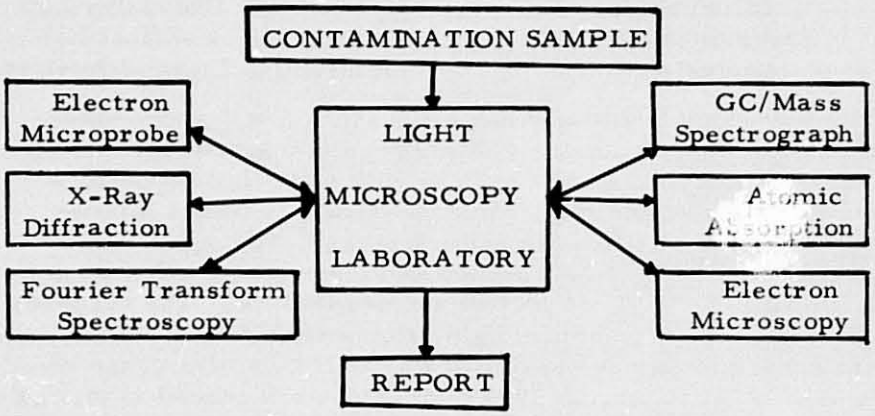

FIGURE #2

Flow Chart for the Analysis of a Contamination Sample.

APPLICATIO.

Three hy[illegible]etical case histories are presented here. They are based on actual case histories but developed to emphasize general techniques in contamination identification rather than specific results. The first is a typical hydraulic sample sequence, the second is a corrosion problem, and finally an airborne contaminate problem. Essentially these sample[illegible] follow the same flow diagram as represented in Figure #2.

PROBLEM 1 - Hydraulic Oil Particulate Contaminatio[illegible]

One hundred milliliters of a MIL 5606 hydraulic oil were filtered through a cellulose ester membrane filter and the particulate was counted per ARP 589. The oil failed to meet the required particulate cleanliness level and was brought to the Light Microscopy Laboratory for evaluation. Oil remaining in the sample bottle was poured into graduated, clean, capped centrifuge tubes and centifuged. The clean oil was then poured into a clean sample bottle for later analysis as required. The particulate in the bottom of the tube was washed with clean kerosene and centrifuged twice more. A final wash was made with chlorobenzene and the particulate was entered into a density gradient tube. The filter used in the particle count was examined using a stereoscopic microscope for particle distribution and an estimate was made of the sample complexity, type of material, and quantity of each type. A clean cork bore, #8, was selected and a portion of the filter was punched out to be cleared and mounted. The filter was cleared using a 1:1:1 solution of hexane, 1,2 dichloroethane, and dioxane. This was then mounted in a permanent mounting media and covered with a coverglass. This sample was then examined under transmitted polarized light, brightfield illumination and oblique top light.

Common natural or industrial minerals were tentatively identified and their locations on the slide recorded. Morphologically identifiable materials such as biologicals, tooling residue, wear metal, or industrial artifacts were recorded along with their position. The density gradient column had equilibrated by this time and the particulate was removed by density to confirm the quantitative estimates and the identification of common materials. Wear metals were mounted for electron microprobe analysis to identify the alloy type wearing and crystalline materials requiring identification were mounted for X-ray diffraction or microprobe analysis depending on size. Elapsed time to this point was one hour. Generally 15-30 compounds have been identified or charac-

terized by this time and an assemblage analysis has been completed indicating a rough percentage distribution of particle types from system wear, airborne fallout, and industrial activities. Within another few hours, depending on the number of particles requiring additional analysis, the alloy types experiencing wear will be identified. In another 48 hours, X-ray data will identify the few remaining compounds.

A typical turn around time for a sample of this type is two to three hours with one or two wear metal alloy types identified. Total manhours expended, 4-6 hours including the typed report. The filter, particulate, and mounted slide are retained for future reference by program with new standards prepared as necessary. If a large number of samples are being examined from one program the analysis time can often be reduced to under one hour.

PROBLEM 2 - Corrosion

A magnesium part fabricated by a subcontractor was received in an airtight, clean, sealed drum. Upon opening the drum, water and oil was found and the part exhibited some corrosion. The part was photographed to document it's condition, then a small sample of the corrosion product was collected, as was a sample of the oil and water. The part was resealed after drying in a clean barrel with excess desiccant. The samples were delivered to the Light Microscopy Laboratory for evaluation. Two questions were asked of the laboratory: (1) What caused the corrosion? and (2) Is the corrosion product stable in its new environment? Paint chips, and other materials were found on initial examination as well as different colored corrosion materials. The corrosion material varied from a waxy to a hard tough substance. Under crossed polarized light most of the material was demonstrated to be isotropic (cubic or amorphous), or microcrystalline (crystals a micrometer or less in greatest dimension). The two main types of corrosion material were mounted for X-ray diffraction and electron microprobe analysis. The results from X-ray diffraction were inconclusive, no apparent crystallinity was indicated even in the material identified as microcrystalline by microscopic examination. Electron microprobe analysis identified carbon, magnesium, cadmium, potassium, iron, zinc, with traces of chlorine and sulfur in the microcrystalline material and magnesium, zinc, sodium, oxygen, sulfur, and chlorine in the other particle. The microcrystalline material charred in the electron beam, the other particle did not. Under the microscope an acetone extraction was made. The microcrystalline material was leached by the acetone and the evaporite was collected on the

tip of a fine tungsten needle. The needle with the sample was entered into the direc probe of the mass spectrograph for analysis of the organic material. With the microscopic identification of chemically altered paint films and the analysis of the oil found in the barrel a cause for the corrosion could be hypothesized. The water and oil was of a type that could have come from an unfiltered machine shop compressed airline. During shipping the trolley that held the part rubbed through some of the paint on the inside of the barrel exposing the metal to corrosion. Water vapor began setting up a galvanic attack between the magnesium part and a cadmium coated washer used on it. This initial corrosion product complexed with iron and zinc from the barrel and organics from the paint and the oil. The material as it then existed was somewhat unstable as indicated by the X-ray and mass spec. data. Stored in a dry environment with excess desiccant any additional corrosion possible would be negligible compared to that which had already occurred, though the corrosion product may change. Total hours charged: 10; turn around: 72.

PROBLEM 3 - Airborne Contamination

A class 200,000 particle/cubic foot room failed to meet that criteria. A volumetric sample collected on a cellulose ester membrane filter was brought to the Light Microscopy Laboratory. The filter was examined using the stereomicroscope and then cleared using the same technique mentioned earlier with the hydraulic oil example. This NO SMOKING area had a recirculating air system but cigarette ash was identified in the sample. The sample was also found to contain a large amount of opaque black particulate. Some of the black particulate was in the form of shiny spheres with very low density. The area surrounding the room was surveyed to characterize external sources of particulate. The blower for the air system was located outside the room about 20 feet above the floor on a wall that had no entrance into the controlled area. Below the blower and about 15 feet west was a copy station with Zerox and IBM copiers. These machines were in almost constant use with a line of people awaiting their turn. Many of the people were smoking cigarettes. A volumetric sample from that station exhibited a similar distribution of particulate types indicating this area as the major source of particulate. The melting point of the toner, as well as its appearance and density, matched that of the black spheres found in the controlled environment room. An examination of the air duct above indicated that during a recent overhaul of the blower

a taped joint in the duct had been broken and not repaired. Outside air was being drawn in through this crack in the duct and was causing the area to fail. The duct was repaired and the problem disappeared. Total hours charged: six including the report; turn around time: four hours.

The prior three examples demonstrate the relationship between the light microscope and other instruments available for use in the general laboratory complex. The majority of the work done in the microscopy laboratory does not require additional instrumental analysis. The identification of a diatomaceous sludge in the bottom of a cooling water reservoir pinpoints the source and suggest the solution to a rapid increase in suspended solid loads. A density separation followed by a magnetic separation of the dense material and a hardness separation of the light material determines whether the black oil suspended particulate coming from a joint is metal wear, rubber gasket wear, graphite lubricant, or molydisulfide lubricant. These last two examples required five minutes each from receipt of the sample to verbal communication of results. No other method of analysis is capable of that speed or sufficiently versatile to identify all five of the materials represented. It is this versatility that results in many thousands of dollars of cost avoidance and cost savings each year.

DISCUSSION:

On sight a mounted particle under the objective of a polarized light microscope exhibits the following characteristics:

Color	Homogeneity	Refractive Index Relative to the Mountant
Shape	Types of Inclusions	
Cleavage	Crystallinity	Size
Fracture Type	Luster	Relative Light Absorption

With a little more work the crystal type can be identified, as well as its index of refraction in given directions, its dispersion, density, solubilities, melting point, elemental composition, etc. The sample can then be quantified by count of each particle type, by area, or by volume and density. All of this can be done using microscopic techniques but for a few materials other instrumental techniques may be quicker. The effective use of the light microscope is the result of balancing its capabilities with those of available instruments. Many materials are sufficiently distinct to be identified by those features which are quickly recognizable by a trained microscopist. For those that are not so quickly

identified or that require further characterization it is important to balance microscopic and instrumental time with cost effectiveness. With the results of a quick microscopic overview an analytical approach for a specific particle type is often obvious. It is this quick overview by a trained microscopist that results in the greatly enhanced analytical efficiency.

Prior to our increased utilization of the microscope many problems resolved within minutes microscopically required many hours, even days using other methods. If a serious problem was encountered samples were sent to every instrument, tying up instruments and personnel for extended periods of time, often in an attempt to analyze materials not suitable to that piece of equipment. Light microscopy has resulted in a considerable improvement over the old approach.

Light microscopy as a general analytical tool is not taught on any educational level in this country with few exceptions (the training offered by McCrone Research Institute, 2820 S. Michigan Ave., Chicago, Ill. 60616, is one of the most notable exceptions). Most universities offer courses on the application of the microscope to biological sciences, geological sciences, etc., but none on the microscope itself as an analytical instrument. At Boeing we are now actively documenting, training and implementing microanalytical techniques for routine use. In this way we expect to have a broad base of experienced personnel within the Company and a thorough documentation of applicable techniques.

CONCLUSION:

The versatility of the microscope and the available non-instrumental techniques of micro and ultramicro analysis can supplement any laboratory responsible for the testing of a wide variety of materials. This is particularly true of Aerospace contamination problems. The greater utilization of light microscopy, with its related techniques and improvements in instrumental interfacing has resulted in decreased analytical flow time and significantly increased data collection.

BIBLIOGRAPHY:

General

Benedetti-Pichler, A. A., Identification of Materials via Physical Properties, Chemical Tests, and Microscopy, Springer-Verlay, New York, New York, 1965.

Bloss, F. Donald, An Introduction to the Methods of Optical Crystallography, Holt, Rinehart, and Winston, New York, New York, 1961.

Burrells, W., Industrial Microscopy in Practice, Fountain Press, London, 1961.

Cherkasov, Yu A., "Application of 'Focal Screening' Measurements of Indices of Refraction by the Immersion Method", Trans. by Ivan Mittin, International Geological Review, Vol. #2, pp 218-23?, 1960. (Dispersion Staining Techniques)

Fulton, Charles C., Modern Microcrystal Tests for Drugs, Wiley-Interscience, New York, New York, 1969.

Heyn, A.N.J., Fiber Microscopy, Interscience Publishers Inc., New York, New York, 1954.

Hutchison, Charles S., Laboratory Handbook of Petrographic Techniques, Wiley-Interscience, New York, New York, 1974.

Insley, Herbert and Van Derck Frechette, Microscopy of Ceramics and Cements Including Glasses, Slags, and Foundry Sands, Academic Press Inc., New York, New York, 1955.

Jones, E.J., "Practical Aspects of Counting Asbestos on the Millipore "π"MC", The Microscope, Vol. #23, pp 93-101, 1975. (Filter Clearing Technique)

Kapp, Ronald O., How to Know Pollen and Spores, Wm. C. Brown Company Publishers, Dubuque, Iowa, 1969.

Leigh-Dugmore, C.H., Microscopy of Rubber, W. Heffer and Sons Ltd., Cambridge, England, 1961.

McCrone, Walter C. and John Gustav Delley, The Particle Atlas, 2nd Edition, Ann Arbor Science Publishers, Inc., Ann Arbor, Michigan, 1973.

Needham, G.H., The Practical Use of the Microscope Including Photomicrography, Thomas, Springfield, Illinois, 1958.

Oster, Gerald and Masahide Yamamoto, "Density Gradient Techniques", Chemical Reviews, Vol. 63, No. 3, pp 251-268, June, 1963.

Scott, Douglas, William W. Seifert and Vernon C. Westcott, "The Particles of Wear", Scientific American, Vol. 230, No. 5, pp 88-97, May, 1974.

Winchell, Alexander Newton, The Microscopic Characters of Artificial Inorganic Solid Substances or Artificial Minerals, John Wiley and Sons, Inc., New York, New York, 1931.

Paper No. 25

KINETICS DATA FOR DIFFUSION OF OUTGAS SPECIES FROM RTV 560

C. K. Liu and A. P. M. Glassford, *Lockheed Palo Alto Research Laboratories, Palo Alto, California*

ABSTRACT

A detailed analytical and experimental study has been made of the outgassing behavior of RTV 560 silicone rubber. The four outgas species which predominate in the temperature range of 285 K to 425 K have been separately identified. The initial concentration of these species in the parent material and their bulk volatilities have been determined. The diffusion coefficients and activation energy for diffusion of the two major species have been deduced from outgassing rate data. It is shown that using these data in a diffusion theory model, the outgassing rates of these major species can be predicted for arbitrary geometry and any temperature within the range studied.

INTRODUCTION

To assess the possibility of contamination of critical spacecraft surfaces by condensation of outgas products from structural materials, it is necessary to have access to a data base for the outgassing behavior of these materials. In principle, this data base may take two forms. In the most common form, outgassing rates are measured experimentally for materials and components in the specific configurations and thermal environments which they will have and experience in practice. This type of data is cost effective and meaningful for given specific applications, but cannot be applied reliably to situations with different geometries and temperatures, for which additional measurements would be needed. A more fundamental approach is to identify the basic physical processes controlling the outgassing phenomenon, the physical relationships and equations representing these processes, and the basic physical properties of outgas species and parent material which relate to the controlling processes. When the basic physical properties have been measured experimentally, they can be used in conjunction with appropriate analytical solutions of the physical equations to predict outgassing rate for any desired combination of geometry and temperature history. This approach generates a universally applicable data base, and is clearly more suited to the assessment of contamination threats at the design stage. However, although the fundamental physical processes controlling outgassing are well understood qualitatively, it has not been possible in practice to obtain the necessary fundamental

physical properties. This is due in part to the difficulty of describing practical outgassing situations, where several species may be released simultaneously from a parent material by more than one mechanism – bulk diffusion, surface desorption, etc. It is also partly due to the lack of apparatus and experimental techniques sufficiently sensitive to generate data with enough resolution to permit separation of the various coexisting species and processes, and hence obtain fundamental property data.

This paper describes measurements in which some fundamental outgassing-related properties were obtained for RTV 560 silicone rubber, which is used extensively in the Shuttle Orbiter's Thermal Protection System. RTV 560 is prepared by mixing the uncured silicone with a catalyst. The principal outgas species from the cured material originate as by-products from the curing process and are therefore initially distributed evenly throughout the bulk material. Outgassing in vacuum occurs by diffusion of these products through the bulk material to the free surface, whence they evaporate. In this case, the outgas situation can be adequately described and modeled by diffusion theory, while the data needed to support the model are therefore the diffusion properties of each species.

To measure the outgassing rate with the sensitivity needed to resolve these diffusion properties, an apparatus based on the use of the quartz crystal microbalance (QCM) was developed. Basically, this apparatus achieves the desired resolution capability by in situ measurement of the outgassing rate directly by condensation of outgassed molecular flux on a cooled QCM surface, rather than by the less sensitive method of measuring a weight change of a few percent or less in the parent material before and after each test.

The validity of the data was tested by using it to predict outgassing of RTV 560 samples of widely differing geometry and temperature

APPROACH

Diffusion Model

The phenomenon of transient diffusion of molecules of one species through a solid of different composition can be expressed by Fick's Second Law.

$$\frac{\partial C}{\partial t} = -D \nabla^2 C \qquad (1)$$

where C is the concentration of the diffusing species in the medium, in mass per unit volume, and D is the diffusion coefficient. D is highly temperature dependent and is commonly expressed by the following relationship,

$$D = D_o \exp(-E_d/RT) \qquad (2)$$

where E_d is the activation energy for diffusion and D_o is a constant. For diffusion in polymers, D can also be concentration dependent

(Ref. 1). However, this dependence should be negligible for the dilute concentrations that apply in the outgassing situation. Also, E_d may vary with temperature, but prior knowledge of this dependence is not necessary to the present analysis, which is based on isothermal conditions.

Equation (1) can be solved for any selected boundary conditions to determine the concentration distribution as a function of location and time. Many of these solutions are given by Crank (Ref. 2). For the case of outgassing from RTV 560 or similarly prepared polymer, the initial concentration, C_o, of the outgas species in the material is uniform. When the material is exposed to the vacuum environment, the concentration of these species at the free surfaces is reduced to a very low value by evaporation. If the internal diffusive flow resistance is high compared with the effective surface evaporation "flow resistance," then it can be assumed that the outgas species concentration is zero at the free surface. In practice, a material cannot be instantaneously exposed to the vacuum environment, since a minimum of several minutes are required to evacuate the test chamber to low pressure. However, this period is very short compared with the total exposure time for tests lasting periods of days, and hence the pressure reduction can be considered to be essentially instantaneous. The boundary conditions to the diffusion equation applicable to the outgassing situation are thus

$$\text{at } t = O,\ C\,(\text{throughout}) = C_o$$

$$\text{at } t > O,\ C\,(\text{free surface}) = O$$

For most practical outgassing situations and in the tests reported in this paper, the diffusive flow is approximately one dimensional in rectangular coordinates. This situation is shown in Figure 1 for flow from both sides of an infinite slab of thickness, L. Since there is a no-flow boundary at $x = L/2$, this model also applies to outgassing from one side of a slab of width $L/2$ whose other side is sealed. For this case, Eq. (1) becomes

$$\frac{\partial C}{\partial t} = -D\,\frac{\partial^2 C}{\partial x^2} \tag{3}$$

while the boundary conditions are

$$C\,(x, O) = C_o$$

$$C\,(O, t) = C\,(L, t) = O$$

The solution to Eq. (3) with these boundary conditions (Ref. 3) is

$$C(x,t) = \frac{4C_o}{\pi} \sum_{m=O}^{\infty} \frac{1}{2m+1} \cdot \sin \frac{(2m+1)\pi x}{L} \exp\left[- \frac{D(2m+1)^2 \pi^2 t}{L^2} \right] \quad (4)$$

The outgassing rate, $\dot{Q}$, in mass per unit area per unit time leaving the free surface is equal to the concentration gradient at the surface multiplied by the diffusion coefficient,

$$\dot{Q} = D \left| \left(\frac{\partial C}{\partial x} \right)_{x=O,\,L} \right| \quad (5)$$

From Eqs. (4) and (5),

$$\dot{Q} = \frac{4DC_o}{L} \cdot \sum_{m=O}^{\infty} \exp\left(\frac{-D(2m+1)^2 \pi^2 t}{L^2} \right) \quad (6)$$

$$\frac{\dot{Q}L}{DC_o} = 4 \sum_{m=O}^{\infty} \exp\left(\frac{-D(2m+1)^2 \pi^2 t}{L^2} \right) \quad (7)$$

The nondimensional outgassing rate, $\dot{Q}L/DC_o$, is plotted versus nondimensional time, Dt/L^2 in Figure 2. From the log-log plot it can be seen that $(\dot{Q}L/DC_o)$ varies as $(Dt/L^2)^{-1/2}$ for times less than $0.03\ L^2/D$. From the log-linear plot, it is seen that for times greater than $0.06\ L^2/D$, $(\dot{Q}L/DC_o)$ varies exponentially with time. This is due to the fact that all terms in Eq. (7) for $m \geq 1$ become negligible by comparison with that for $m = 0$. Therefore, Eq. (6) can be re-written as

$$\dot{Q} = \frac{4DC_o}{L} \exp\left[- \left(\frac{D\pi^2}{L^2} \right) t \right], \quad t > \frac{0.06\ L^2}{D} \quad (8)$$

Hence, if experimental isothermal (i.e., constant D) outgassing data for times greater than $0.06\ L^2/D$ are plotted versus time on a log-linear plot, a straight line of slope $(-D\pi^2/L^2)$ and intercept $(4DC_o/L)$ should be obtained, from which D and C_o can be calculated.

Species Identification

For the case of outgassing from polymers, there will be in general, several species diffusing through the parent material simultaneously.

An essential feature of the experimental apparatus required to determine D and C_o is therefore a means to identify each outgas species. In the present work the means used was to measure the bulk evaporation rates of the different species. The experiment to perform this measurement will be described in Species Identification Experiments. The relevant theory is based on a modified Langmuir equation,

$$\frac{\dot{m}_e}{A} = \alpha_e P_v \sqrt{\frac{M}{2\pi RT}} \tag{9}$$

Here $(\dot{m}_e/A)$ is the measured evaporation rate per unit area, P_v is the vapor pressure of the species, M is its molecular weight, and T is the temperature. α_e is an empirical evaporation coefficient, less than or equal to unity, which accounts for nonideal behavior at high evaporation rates, less than total surface coverage, etc. The vapor pressure of most substances can be approximated by an equation with the following form

$$\ln P_v = B_1 - H_L/RT \tag{10}$$

where H_L is the latent heat of vaporization and B_1 is a constant. Combining Eqs. (9) and (10) gives

$$\ln \frac{\dot{m}_e}{A} \sqrt{T} = B_2 - H_L/RT \tag{11}$$

where

$$B_2 = B_1 + \ln \left(\alpha_e \sqrt{\frac{M}{2\pi R}} \right) \tag{12}$$

Hence, if the evaporation rate of an outgas species is measured as a function of temperature, a plot of $\ln (\dot{m}_e/A \cdot \sqrt{T})$ versus 1/T should be linear with a slope of $(-H_L/R)$ and intercept of B_2. In general, different outgas species have different values of B_2 and H_L, and will therefore have unique and distinguishable reevaporation characteristics.

THE THERMAL ANALYSIS APPARATUS

Apparatus Description

Experimental outgassing rate measurements were made by using the Thermal Analysis Apparatus (TAA), shown in Figure 3. The principal components of the TAA are a sample pot, a collector QCM, and a system of shrouds, all of which are thermally grounded to a liquid nitrogen reservoir. The sample pot is a cylindrical container with a small orifice in one end. The base of the sample pot contains an electrical resistance heater and a platinum resistance thermometer. By balancing the heat input to the sample pot against the heat leak along the sample pot support strut to the cooled shielding structure, the pot temperature can be controlled to any temperature above ~100 K. A collector QCM is positioned along the normal line-of-sight of the sample pot orifice.

This QCM is normally allowed to cool to about 90 K, at which temperature all significant outgas species impinging on its surface will be condensed. The QCM views the sample pot orifice through a shuttered hole in the shielding structure, permitting the impinging flux to be interrupted when appropriate. Both QCM and sample pot are completely surrounded by the cooled shrouding to reduce the background outgassing rate to undetectably low levels.

The QCM is mounted in an aluminum holder with an electric resistance heater. Its temperature can be controlled to any temperature between about 90 K and 420 K by balancing electrical heat input against heat leakage along its support struts to the liquid nitrogen reservoir. The QCM is a Celesco Model 700 unit, which contains a built-in platinum resistance thermometer. The accuracy of this QCM has been established in a previous work (Ref. 4).

The material sample being tested is held within the sample pot in a holder configured to produce one-dimensional diffusive flow during outgassing. Sample preparation and holder geometry will be described in Sample Preparation.

Experimental Procedure

The general experimental procedure used in the TAA was as follows:

(1) After weighing and installing the sample and holder in the sample pot, the apparatus was assembled, the bell jar was replaced, and the system evacuated. About 5 minutes after the beginning of evacuation, the pressure was low enough to switch to the diffusion pump and to fill the liquid nitrogen pot. The final pressure was below 2×10^{-7} torr, measured outside the cold shroud.

(2) Thermal equilibrium was attained in the second phase of the tests. The QCM cooled down to near 90 K in about 1 hour. The sample pot was either heated electrically or allowed to cool to reach the particular test temperature selected. This took from 1/2 to 2 hours, depending upon the required temperature difference from ambient.

(3) The outgassing rate was measured by opening the shutter and collecting the outgas flux on the QCM. The QCM reading was recorded as a function of time. The measurement began as soon as the system pressure fell below about 10^{-5} torr. However, not all of the impinging flux would condense on the QCM until it was quite cold, and since the QCM output is temperature dependent, the data were difficult to resolve until thermal equilibrium was approached. However, steady state measurements with equilibrated QCM and isothermal sample could be obtained within about 1 hour of beginning the evacuation.

(4) When the QCM had accumulated a substantial deposit, or at any other arbitrarily specified time, the shutter was closed and the QCM heated slowly, while the reevaporation rate of the collected outgassing species was recorded as the crystal cleaned up.

(5) Experiments were terminated when the outgassing rate data had become linear on a log-linear rate versus time plot. This usually took 1 to 7 days. The apparatus was then warmed up, let back to atmosphere with laboratory air, and the sample removed and reweighed.

Data Reduction Procedure

The measured data were QCM frequency outputs; time since initiation of an experiment; sample pot and QCM temperatures; and sample initial and final weight, measured at 1-atmosphere pressure. Reduction of all of these data except QCM frequency is straightforward. The deposit mass per unit area on the QCM crystal is equal to the frequency shift from the clean condition multiplied by the QCM sensitivity constant, 4.43×10^{-9} gms/cm^2/Hz. The mass collection rate per unit area on the QCM was obtained from the deposit mass per unit area versus time data. The total mass flow rate through the sample pot orifice, $\dot{m}_o$, is related to the QCM mass collection rate per unit area, $(\dot{m}/A)_q$, as follows

$$\frac{\dot{m}_o}{\pi r^2} = \left(\frac{\dot{m}}{A}\right)_q \times 0.98 \qquad (13)$$

where r is the distance from the sample pot orifice to the QCM crystal surface and the factor 0.98 is an empirical factor allowing for the fact that the flux distribution from the orifice is not a pure cosine function because of the finite thickness of the orifice. This factor was determined by scanning the flux distribution from a similar orifice in an earlier experiment. The outgassing rate from the sample in the pot is equal to $\dot{m}_o$ divided by the exposed sample area.

For the case of evaporation of the deposit from the QCM surface during warmup, the measured rate of deposit mass loss is less than the true evaporation rate due to the finite flow resistance of the aperture in the QCM casing. The true evaporation rate is equal to the measured rate divided by 0.805 (Ref. 4).

OUTGASSING EXPERIMENTS

Sample Preparation

Material Preparation – The material selected for the outgassing tests was RTV 560, a two-component room temperature vulcanizing (RTV) silicone rubber produced by the General Electric Company (Ref. 5). RTV 560 is a methyl-phenyl compound which will be used extensively as an adhesive in the Space Shuttle Orbiter Thermal Protection System. This material was prepared in the laboratory in 40-gram batches. Two drops of dibutyl tin dilaurate catalyst were used for 40 grams of silicone which, according to the manufacturers data, corresponds to 0.1% by weight. The low catalyst percentage was selected for these tests to extend the curing time and give entrapped air more time to escape. Although the size of a drop is not a standardized quantity, this procedure gave approximately the same curing time as predicted by the manufacturer as well as good batch-to-batch data agreement.

Sample Holder – The basic type of sample holder used is shown in Figure 4a. It is made from stainless steel in the form of a flat disk,

2.85-cm diameter, and 0.51-cm thick, with a cylindrical recess of 2.29-cm diameter and 0.25-cm deep. The recess was totally or partially filled with RTV 560, which was then cured in place, forming a disk-like sample. The holder geometry constrains the outgassing flow to be one-dimensional, perpendicular to the free surface of the sample. (In this case, L is equal to twice the sample thickness, since outgassing takes place from only one side of the sample.) The sample holder dimensions were selected in accordance with two criteria. The total amount of material had to be adequate to provide a measurable deposit mass flux at the QCM surface, but could not be so high as to exceed the capacity of the QCM. Also, since D and C_o are extracted from outgassing data for evacuation times greater than $0.06\ L^2/D$, L had to be small enough to prevent this minimum time from being excessive. Since neither D nor the outgassing rates were known in advance, these dimensions had to be estimated. However, the dimensions given proved to be adequate for most of the sample temperature range investigated.

A second type of holder, shown in Figure 4b, was used in later experiments in which the object was to investigate the validity of the diffusion theory and the generated data when applied to the outgassing of RTV 560 at large L. These holders were made from stainless steel tubing of 0.48- to 0.88-cm inside diameter and had an effective L of the order of 2.1 to 2.4 cm. (In this case, L is equal to the holder length, since outgassing takes place from both ends.) As with the disk-type holders, the sample was cured in place.

Sample Storage – It was noted during the early experiments that the proportion of the most volatile of the outgas species decreased noticeably with time if the samples were stored at room temperature before vacuum exposure. To reduce this effect, later samples were stored in a refrigerator between the end of curing and the beginning of vacuum testing.

Species Identification Experiments

Before attempting to measure D and C_o for each outgas species, it was necessary to establish a technique for identifying them individually. In the present work this was done by means of their evaporation characteristics, as was described earlier. A preliminary series of tests was conducted in which a sample of RTV 560 was heated until a significant deposit had accumulated on the cooled QCM. After interrupting the impinging flux, the QCM was heated slowly and the QCM output was measured as a function of temperature. Typical warmup data are presented in Figure 5, showing the successive evaporation of three different species. The evaporation rate, $\dot{m}_e/A$, can be calculated as a function of temperature, T, from the rate of change of the QCM output during warmup. When these rates are plotted as $\ln(\dot{m}_e/A \cdot \sqrt{T})$ versus $1/T$, several distinct linear characteristics are obtained, each corresponding to a separate outgas species as discussed in Approach. For the temperature range of 10°C to 150°C, four species were found and referred to as M_1, M_2, M_3, and M_4, in order of increasing

volatility. The characteristics in Figures 5 and 6 were reproducible from test to test, and served as a reliable means for identifying the proportions of each species collected on the QCM at any point in the later isothermal outgassing tests.

According to Eq. (11), it should be possible to deduce the latent heat of the various species from the slopes of the respective reevaporation characteristics. However, these characteristics are plotted from apparent reevaporation rate data, as indicated by the QCM. It is known that the response of the QCM to liquid deposits is less than 100% and becomes less as the temperature increases due to the decrease of viscosity in the liquid deposit (Ref. 6). The indicated loss of QCM output for evaporating liquid deposits will therefore be due partly to actual evaporation, and partly to loss of QCM sensitivity. During many of the QCM warmup experiments, a sudden increase in the apparent evaporation rate was frequently observed, which always occurred at the same temperature for a given outgas species. This discontinuity was interpreted as being due to a loss of QCM response as the deposit changed phase from solid to liquid. The outgas species property data that can be reliably extracted from the QCM warmup measurements are thus heat of sublimation for the solid phase, and the melting point of each species. These are shown in Table 1. For the portion of the warmup curve of each species at temperatures above its melting point, the apparent evaporation rates will be erroneously high, making the slopes of the data meaningless. However, the fractional loss of QCM response due to viscous effects is a function of viscosity and true deposit mass per unit area (Ref. 6). In most of the tests, the QCM warmup measurements were begun with about the same mass on the crystal (approximately 8×10^{-5} g/cm^2). Since both viscosity and evaporation rates are functions of temperature, the indicated evaporation rates for the condensed species in the liquid phase were reproducible from test to test, permitting warmup data to be used for species identification. It is noted that this is a fortuitous situation, permitting positive species identification to be made in a specific apparatus. However, comparison of data for liquid phase evaporation from different workers should be made with extreme caution. Further development of QCM thermogravimetric technique is needed in this area.

Table 1. OUTGAS SPECIES OF RTV 560

Outgas Species	Melting Point (K)	Heat of Sublimation (K cal/g-mol)	Initial Concentration (g/cm^3)	Activation Energy for Diffusion (K cal/g-mol)
M_1	205	5.22 (200 K)	0.0084 (± 50%)	
M_2	275	13.7 (260 K)	0.0456 (± 10%)	7.91
M_3	319	8.62 (312 K)	0.0146 (± 10%)	8.49
M_4	367	21.4 (362 K)	0.0056 (± 50%)	

Isothermal Outgassing Tests

Test Program – A series of experiments was conducted in which the isothermal outgassing rates of RTV 560 samples was measured as a function of time. The tests and conditions are listed in Table 2. The primary object of these tests was to generate data from which $D(T)$ and C_o could be deduced for each species. Most of the tests were conducted according to the general procedure described in Experimental Procedure. The exceptions are that in Tests 5, 6, and 7, the QCM was maintained at higher temperatures in order to collect only the less volatile species. The major portion of the diffusion coefficient data was obtained from Tests 3 through 8. Tests 4L, 9, and 10 were conducted primarily as part of the model verification, see Discussion. Test 8R was a repeat of Test 8 with a longer orifice to QCM line-of-sight distance, r, in which the $1/r^2$ relationship assumed in the data reduction was successfully verified. (All tests were conducted at $r = 10.09$ cm except Tests 8, 9, and 10 where $r = 7.17$ cm.)

Although four species were identified in the overall test program, the major portion of the observed outgassing rate, and hence the derived diffusion coefficient data, related to species M_2 and M_3. Species M_1 is quite volatile and difficult to study without making special sample holders with very long diffusion paths and/or storing in a refrigerator before the test, so as to delay the outgassing process sufficiently for it to be studied. In practical applications where the cured RTV 560 is stored at room temperature, M_1 will outgas completely in a very short time and will not pose a problem. Since its volatility is high, it is also less likely to condense on a critical surface. Hence, no concerted attempt was made to study the diffusion of M_1 in detail. M_4 was encountered only at the higher end of the temperature range studied, and data obtained were not sufficient for determination of D as a function of temperature. However, there is every reason to believe that extension of the test program to higher temperatures would enable M_4 to be characterized in a manner similar to M_2 and M_3.

Data Analysis – The isothermal outgassing rate versus time data for all tests were basically similar in form. As a typical example, data for Test 8 is shown in Figure 7. In Test 8, species M_2 predominated in the early stages, while M_3 predominated at later times. The slope of the linear portion of the M_3 data at these later times is quite clear and D_3 can be determined with confidence. At early times, however, the slope of the linear portion of the M_2 data is less obvious and difficult to interpret. Hence, in those tests where more than one species was found, usually only the later portion of the curves was used to obtain slope data. By plotting the isothermal outgassing data from the tests of Table 1 in the manner of Figure 7, it was possible to obtain D for species M_2 and M_3 for a number of temperatures. Noting Eq. (2), these data for D_2 and D_3 have been plotted in Figure 8 in the form $\ln D$ versus 1/temperature. Linear relationships are obtained for both species which can be fitted by the following equations.

$$D_2 = 0.03324 \exp(-7910/RT) \qquad (14)$$

Table 2. RTV-560 OUTGAS TEST SUMMARY

Test No.	Sample Temperature (K)	QCM Temperature (K)	Diffusion Length (L, cm)	Sample Weight (gms)	Total Weight Loss (%)	Test Duration (hr)	Outgas Species Observed	Diffusion Coefficient (D, cm^2/S)
1	408.0	1[illegible]	0.50	1.4728	2.66	28	M_2, M_3	$D_2 = 1.47 \times 10^{-6}$
2	305.5	100	0.47	1.3817	1.53	147	M_2	$D_2 = 7.58 \times 10^{-8}$
3	343.5	100.	0.47	1.3711	2.34	121	M_2, M_3	$D_2 = 3.12 \times 10^{-7}$ $D_3 = 2.65 \times 10^{-8}$
4	383.0	100	0.40	1.1744	3.01	101	M_2, M_3	$D_2 = 1.01 \times 10^{-6}$ $D_3 = 7.94 \times 10^{-8}$
5	422.0	264	0.38	1.1394	3.64	52	M_2, M_3, M_4	$D_2 = 2.94 \times 10^{-6}$ $D_3 = 2.76 \times 10^{-7}$
6	423.0	300	0.58	1.6651	3.[illegible]6	26	M_3, M_4	
7	423.0	340	0.52	1.5533	3.23	32	M_4	$D_4 = 9.30 \times 10^{-7}$
4L	383.0	100	2.42	0.6308	2.08	127	M_2, M_3	$D_2 = 1.05 \times 10^{-6}$
8	398.0	100	0.25	0.7473	2.88	25	M_2, M_3	$D_2 = 1.58 \times 10^{-6}$ $D_3 = 1.30 \times 10^{-7}$
8R	398.0	100	0.22	0.6588	3.17	49	M_1, M_2, M_3	$D_1 = 9.0 \times 10^{-6}$ $D_2 = 1.33 \times 10^{-6}$ $D_3 = 1.18 \times 10^{-7}$
9	298.0	90	2.07	1.7809	0.49	96	M_1, M_2	$D_1 = 3.24 \times 10^{-6}$
10	284.5	90	2.05	1.7559	0.26	71	M_1, M_2	$D_1 = 3.03 \times 10^{-6}$

$$D_3 = 0.006316 \exp(-8490/RT) \quad (15)$$

The activation energies for diffusion, E_d, for M_2 and M_3 are thus 7910 and 8490 cal/mol, respectively.

In principle, C_o can be obtained from the intercept of the linear portion of the $\ln C$ versus time curve, as noted in the section on Diffusion Model. However, a systematic error is present in this intercept when drawn from experimental data, due to the finite time required to evacuate the apparatus and to heat the sample to equilibrium test temperature. These effects tend to displace the experimental data in Figure 7 to the right, which, in turn, leads to a larger apparent value for the intercept. This displacement can be partially corrected for, but some error is inevitable. Furthermore, small random errors in determining the slope are magnified into large random errors in intercept reading because of the logarithmic nature of the ordinate. The net effect of these influences is to attach relatively large uncertainty bounds to the C_o value deduced from the intercept.

The value of C_o can also be estimated from weight loss measurements, since for relatively long evacuation periods C_o will be only slightly higher than the total mass loss. In the present apparatus, the weight loss measurements were made ex situ, in which the raising of the local pressure to 1 atmosphere introduced an unknown error. Also, when more than one species are being outgassed, it is difficult to resolve the relative amounts of each species.

The value of C_o can also be calculated from the total amount collected on the QCM during an experiment, while the relative proportions of each species can be found from QCM warmup data of the type shown in Figure 5. Since the QCM measurements were made in situ, they are inherently more reliable than the ex situ weighings. However, the loss of QCM response when the deposit melts and the fact that more than one QCM warmup had to be made per test introduces new sources of uncertainty.

The most satisfactory method for obtaining reliable and consistent values of C_o was by selecting the values which gave the best correlation between experiment and theory for all tests. This was possible only for species M_2 and M_3 because of the lack of sufficient detailed experimental data for M_1 and M_4. The theoretical predictions were made as described in the following section. The values for C_{o2} and C_{o3}, selected by this method and estimated to be accurate to $\pm$ 10%, are given in Table 1. Values of C_{o1} and C_{o4} estimated to a lower degree of certainty using the intercept and mass loss approaches are also given in Table 1.

These C_o data can be compared with Total Mass Loss (TML) and Volatile Condensible Material (VCM) data obtained from SRI-type tests for samples outgassed at 125°C for 24 hours. For RTV 560 with regular curing, Ref. 7 gives a TML of 0.0253 gms/gm. The Total Mass Available (TMA) for outgassing at 125°C is equal to the sum of the C_o's (excluding C_{o4}, since no measurable amount of M_4 was outgassed at 125°C), divided by the density of RTV 560 of 1.42 gms/cm^3. This gives a TMA of 0.0483 gms/gm for the four components detected. The [illegible]

should always be less than the TMA, although it should tend toward it for long evacuation periods. The TMA and TML from these two sources are therefore of the same order and do have the correct relationship. Further comparison of these data would require more knowledge of the sample size, preparation technique, and temperature history for which the TML data were obtained. Reference 7 also gives the VCM at 298 K to be 0.0055 gms/gm. This would correspond to M_3 alone, M_1 and M_2 being excessively volatile at 298 K. For M_3 alone the TMA is 0.0103 gms/gm which is significantly higher than the VCM. However, this is to be expected, since M_3 diffuses more slowly from the sample than M_1 and M_2, and hence a lower fraction has outgassed in the 24-hour VCM test period.

Verification of the Data

With the data generated for D_2, D_3, C_{o2}, and C_{o3}, it is possible to predict the outgassing rates of M_2 and M_3 for an RTV 560 specimen of any geometry and temperature. Also, since M_2 and M_3 are the only significant species for the major part of the temperature range studied, the total outgassing rate, $\dot{Q}_T$, should be essentially equal to the sum of the rates for M_2 and M_3 i.e., $(\dot{Q}_2 + \dot{Q}_3)$. To assess the accuracy with which the measured total outgassing rate could be predicted by $(\dot{Q}_2 + \dot{Q}_3)$, a comparison between measured and predicted data was made for four cases.

The measured data from Tests 4, 4L, 9, and 10 were used in the comparison. Tests 4 and 4L were both conducted at 383 K, but the flow path was about six times larger in Test 4L than in Test 4. These two tests, therefore, determine the effect of variable flow path length. Tests 9 and 10 were conducted for samples of length similar to Test 4L, but at temperatures of 298 K and 284.5 K. These two tests plus Test 4L reflect the effect of temperature variation over the range studied.

Since in each of these four cases the flow was one-dimensional, the outgassing rates for M_2 and M_3 can be calculated from Eq. (6), using diffusion coefficient data from Eqs. (14) and (15), and initial concentration data given in Table 1. It was assumed that diffusion of the two species proceeds independently, so the total outgassing rate is equal to the algebraic sum of the component rates. This calculation was made by computer for each of the temperature and length combinations corresponding to Tests 4, 4L, 9, and 10 given in Table 2.

The total outgassing rate data for Tests 4L and 4 and the predictions of $(\dot{Q}_2 + \dot{Q}_3)$ for these tests are shown in Figure 9. It can be seen that the prediction agrees with the data to better than 10%. The predicted rates for $\dot{Q}_2$ and $\dot{Q}_3$ are also shown separately in Figure 9. For Test 4, most of M_2 has been removed by 30 hours, after which the outgas species is almost totally M_3. With the increased diffusion path length of Test 4L, the main outgas species remains M_2 for the entire duration of the experiment.

Figure 10 shows the total outgassing rate data and the predicted $(\dot{Q}_2 + \dot{Q}_3)$ rates for Tests 9 and 10, at 298 K and 284.5 K, respectively. The agreement is not quite as good as at 383 K, but is still of the acceptable order of 10%. Since the agreement is better at 284.5 K than at

298 K, it is concluded that there is no systematic temperature dependent error, which in turn, means that the expressions for D_2 and D_3 in Eqs. (14) and (15) are accurate over the temperature range studied. The disagreement appears to be random, and is probably due to sample-to-sample variations in C_{o2} and C_{o3}.

DISCUSSION

Within the range of temperature and geometric parameters studied, the goal of obtaining diffusion property data for the major outgas components of RTV 560 has been achieved. The validity of the data and the diffusion theory model has been verified in the parameter ranges studied by comparison of theoretical prediction and experimental data for several specific combinations, temperature, and geometry. In addition, the diffusion data generated and the technique of QCM thermogravimetry used to separate the different outgas species gives information on their relative volatility, which is often more useful than the outgassing data itself. For example, the data indicate that species M_2 from RTV 560 will not condense on a 298 K surface with the normal level of impingement rates and hence, a detailed knowledge of the outgassing rate of M_2 is not necessary if the surface of interest is at 298 K or higher.

Although the conclusions drawn from the present experiments must necessarily be confined to the parameter range studied, the analytical and experimental approach can be extended to a much broader parameter range for RTV 560, and also to many other polymeric materials in which the outgas products are originally bulk-distributed. Because of the greater amount of information provided by these experiments than by the usual engineering tests, the time and expenditure required for their performance is somewhat higher. Hence, it would be quite costly to generate diffusion data for the very large number of polymeric materials used in the aerospace industry. The most cost-effective use of the described techniques is to perform detailed outgassing analyses of those materials which constitute the most significant and/or commonly encountered outgassing sources, in terms of total amount of base material per spacecraft, percentage of outgassable material, and frequency of use on space vehicles. The detailed data would also be of great help in justifying or eliminating the need to high-cost, aerospace-grade materials in place of low-cost, commercial-grade materials.

In addition to the overall results of the experiments, two significant intermediate conclusions implicit in the final result should be emphasized individually.

First, the outgas products from RTV 560 consist of a small number of distinct species, whose properties and concentrations are reproducible between sample batches. Although no detailed study was made of the effect of catalyst percentage, it was observed by the authors in earlier tests on RTV 560 that increasing the catalyst percentage to 0.5% increased the initial concentrations of the outgas species, but did not alter their properties.

Second, the technique of using QCM thermogravimetry to differentiate between outgas species worked well. Since the QCM is the basic contamination sensor used in the aerospace industry, extension of its overall capability in contamination analysis is highly desirable.

However, although the volatility data obtained with a specific QCM in a specific application were repeatable, the absolute accuracy of the measured re-evaporation rate data generated is subject to error if the deposit is liquid, because of the degradation of QCM response in this case. Also, since the evaporation rate is highly temperature dependent, errors in measuring the true temperature of the evaporating deposit could complicate correlation of data from different experiments. Finally, the measured apparent evaporation rate of a real deposit expressed on a per unit substrate area basis may be less than the bulk evaporation rate, because it may be distributed in islands or droplets, instead of a uniform film. The area coverage factor then becomes another experimental parameter which can vary from application to application. In view of these factors, further development of QCM thermogravimetry is required to improve its quantitative capability.

ACKNOWLEDGMENTS

This work was performed as part of an Independent Research Program at the Lockheed Palo Alto Research Laboratory.

REFERENCES

1. Smith, T. G., "Review of Diffusion in Polymer Penetrant Systems," University of Maryland, NASA Contract No. NGR20-002-053, Sep 1968, p. 105

2. Crank, J., The Mathematics of Diffusion, Oxford University Press, London (1956)

3. Barrer, R. M., Diffusion in and Through Solids, Cambridge University Press, 1951

4. Glassford, A.P.M., "An Analysis of the Accuracy of a Commercial Quartz Crystal Balance," Paper No. 76-438, 11th AIAA-Thermophysics Conference, San Diego, Jul 1976

5. General Electric Company, Technical Data Book, S-35

6. Glassford, A.P.M., "The Response of a Quartz Crystal Microbalance to a Liquid Deposit," to be presented at 9th IES-AIAA-ASTM-NASA Space Simulation Conference, Los Angeles, Apr 1977

7. Campbell, W. A., Marriott, R. S., and Park, J. J., "A Compilation of Outgassing Data for Spacecraft Materials," NASA TN D-7362, NASA/Goddard Space Flight Center, Sep 1975

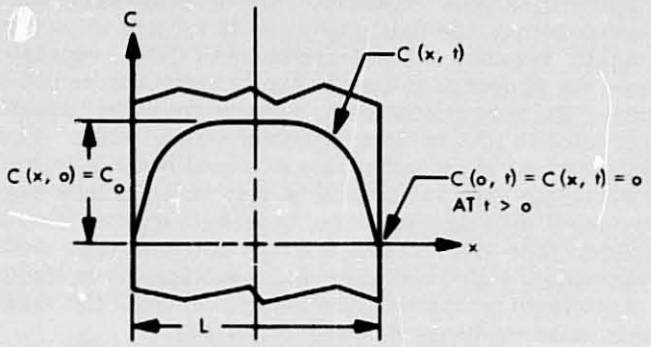

Fig. 1 Bulk Diffusion Model

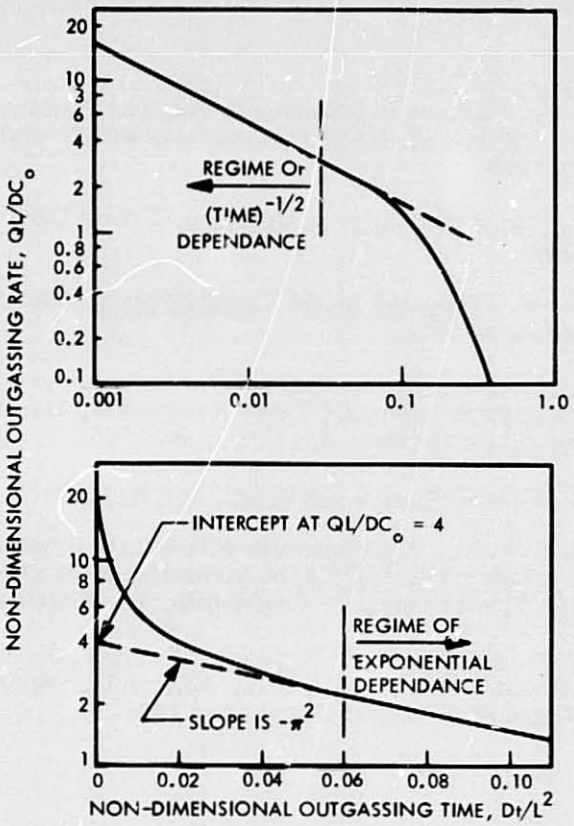

Fig. 2 Nondimensional Outgassing Rate

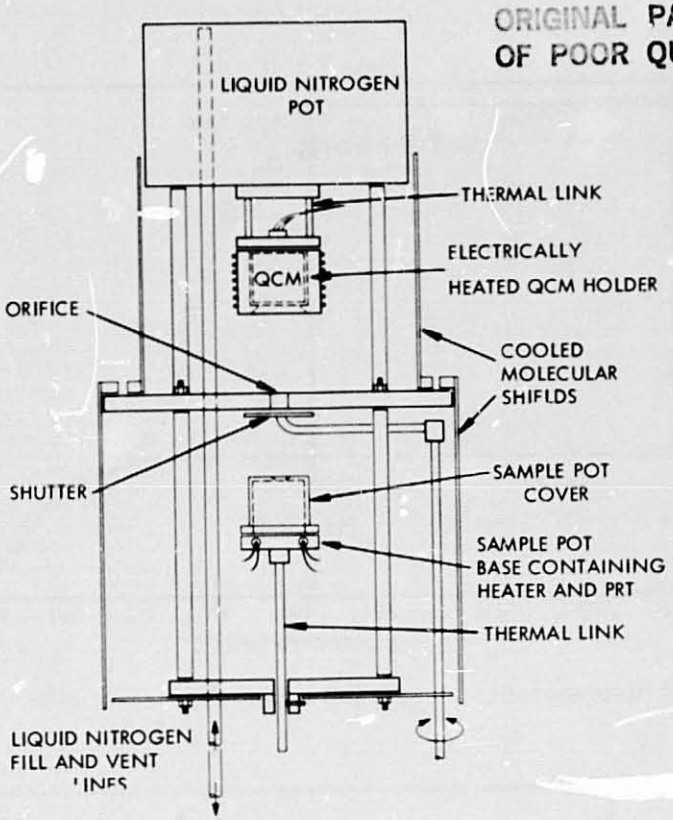

Fig. 3 Thermal Analysis Apparatus

(a)

FLAT PLATE – 2.86 CM DIA., 0.51 CM THICK WITH RECESS OF 2.29 CM DIA., 0.25 CM DEPTH

(b)

	THIN CYLINDER	THICK CYLINDER
LENGTH, (CM)	2.10	2.41
O.D., (CM)	0.96	0.63
I.D., (CM)	0.88	0.48

Fig. 4 One-Dimensional Sample Holders

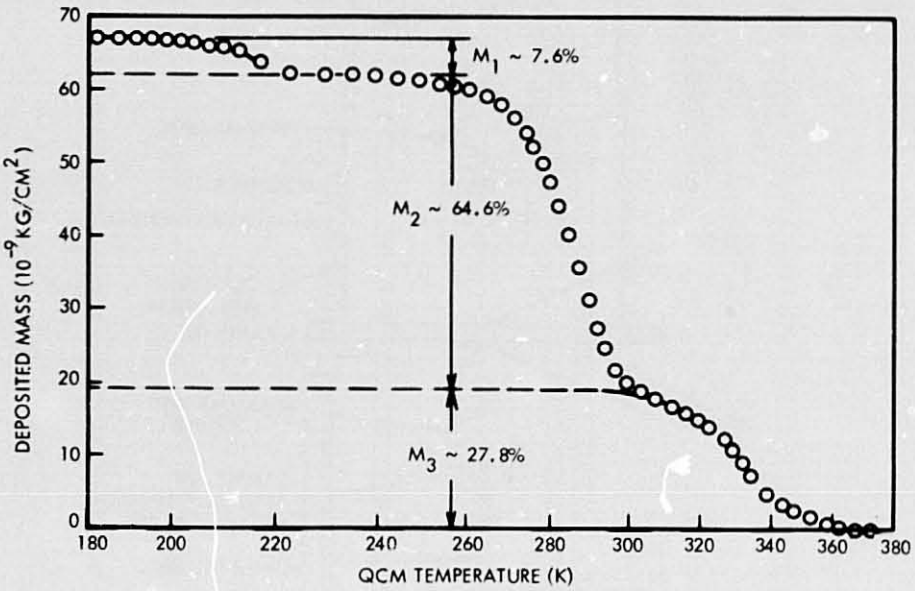

Fig. 5 Reevaporation of RTV 560 Outgas Deposit on QCM - Test 8R

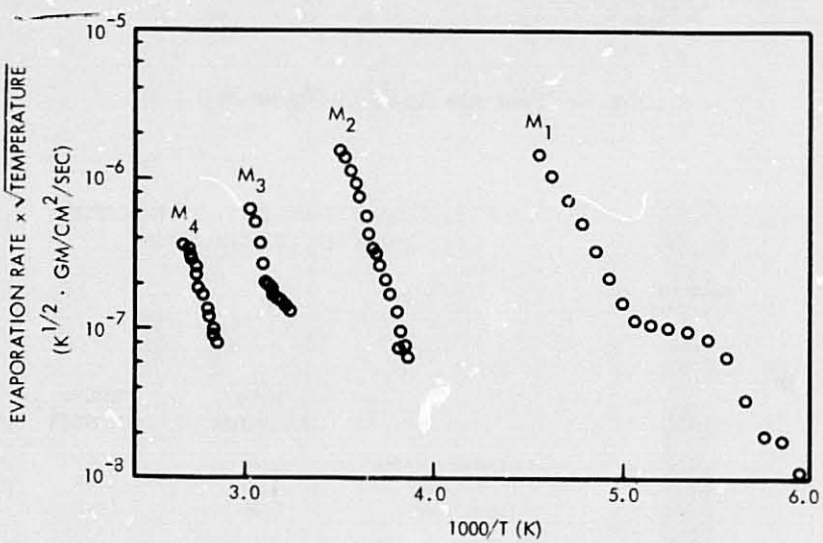

Fig. 6 Evaporation Rate of RTV 560 Outgas Species From the Collector QCM

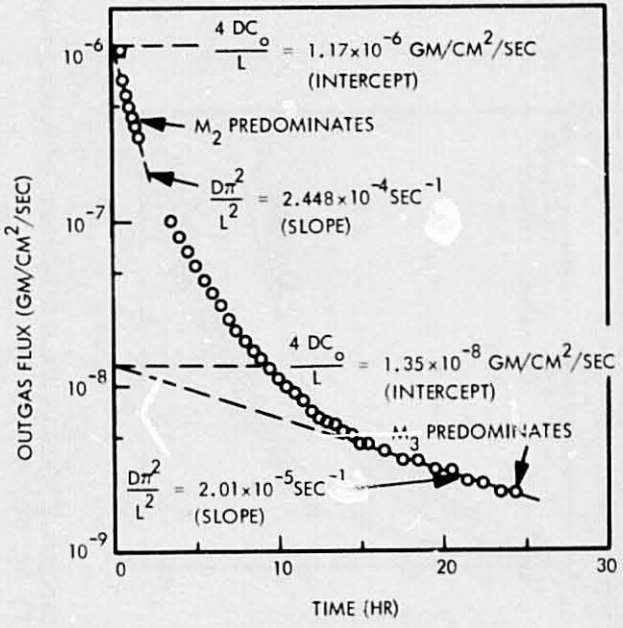

Fig. 7 Determination of D and C_o From Typical Outgassing Data – Test 8 Sample Temperature = 398 K, Diffusion Length = 0.25 cm

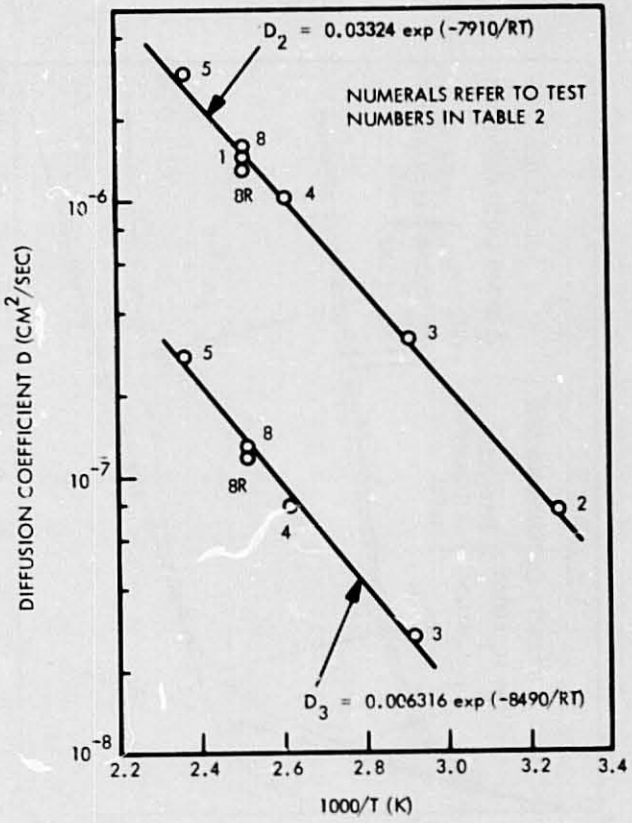

Fig 8 Diffusion Coefficient of RTV 560 Outgas Species

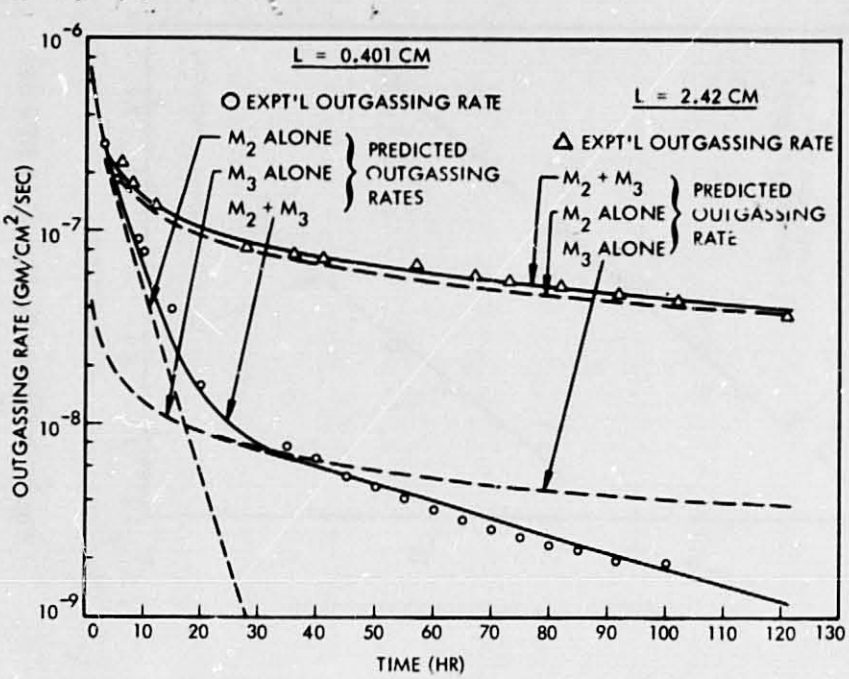

Fig. 9 Comparison of Measured and Predicted RTV 560 Outgas Rate and Relative Amounts of M_2 and M_3 at 383 K for Two Diffusive Flow Path Lengths

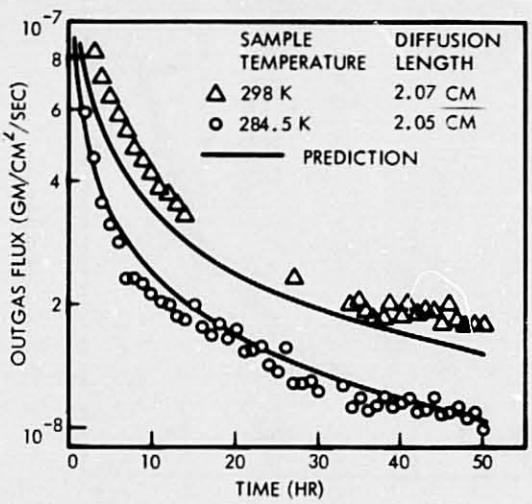

Fig. 10 Comparison of Measured and Predicted Outgassing Rate of RTV 560 at 298 K and 284.5 K

Paper No. 26

EUROPEAN TESTS ON MATERIALS OUTGASSING

A. Zwaal, *Product Assurance Division, ESTEC, Noordwijk, Holland*

ABSTRACT

With a view to international co-ordination of spacecraft materials, a number of European firms and institutes have performed outgassing tests on identical materials at 125°C in high vacuum. This paper presents the outgassing data obtained with the different types of equipment and discusses both the results and the critical parameters.

INTRODUCTION

The aim of the tests was to facilitate the interpretation of outgassing data from different sources, and to improve both the test methods and the verification of outgassing specifications.

The Micro-VCM Test {1} has been generally accepted as a screening test for materials for spacecraft application. Over 2000 different materials have been tested according to this method, which is specified in ESA/PSS-09/QRM-02T {2}, and ASTM's E-21 Committee is currently preparing a similar specification.

Earlier tests {3} by ESTEC (equipment under contract at INTA, Madrid), Goddard Space Flight Center (GSFC) and Jet Propulsion Laboratory (JPL) with similar micro-VCM equipment according to the original JPL design {1} highlighted a number of discrepancies in the results obtained at the three locations.

Not all of the discrepancies could be explained, and some were probably caused by inhomogeneities in the materials and by the test methods, and probably not by the equipment. There were therefore a number of reasons for performing further outgassing tests with different equipment such as micro-VCM, macro-VCM and vacuum balance.

PARTICIPATING INSTITUTES, EQUIPMENT TYPES AND MATERIALS TESTED

The institutes taking part in the test series and the equipment they used are listed in Table 1.

Seven materials were tested, as listed in Table 2. Items 1 and 2 were supplied by CNES, and the remainder by ESTEC.

Sample size

(a) The three paint samples had been prepared on Al foil (4,4mg/cm^2) for all institutes except DFVLR, who received their samples on a metal disc of 1 cm diameter (items 1-2-5).
(b) The bulky samples had been cut into smaller pieces(2.5mm cube) at ESTEC before despatch to the participants (items 2-4-6).
- DFVLR samples (items 3-4-6) had been prepared on metal discs of 1 cm diameter.
- ESTEC 2 tests were performed on 20 x 20 x 4 mm^3 blocks for items 3-4-6.
- The CNES samples (items 3-4-6) had been prepared as discs of 30 mm diameter and about 2.5 mm thick.

(c) Rilsan BMNO had a granular structure and the 2.5 mm cubes were tested as received.

TEST PARAMETERS

Tests were conducted on the same data for the two micro-VCM systems and the CNES macro-VCM system. The vacuum-balance tests were undertaken over a period of about two weeks, starting on the same date as the above tests. Except for the MBB tests which were conducted about eight months later.

The test procedure specified in ESA/PSS-09/QRM-02T was followed as closely as the equipment allowed.

The main test variables from above specification, temperature, time and humidity are recorded in Figure 1:

- The materials samples had been conditioned for a minimum of 24 h at 20° $\pm$ 1°C and 65% relative humidity.
- The material samples were weighed just before the test under atmospheric conditions (W_{oa}) or under vacuum (W_{ov}) for the vacuum balance system.
- After pumpdown to 10^{-5} torr, the sample compartment was raised to +125° $\pm$ 1°C.
- The sample heaters were turned off 24 h after 125°C had been reached and dry nitrogen or inert gas was introduced into the vacuum system at 100-200 torr
- At the moment when the sample temperature had falled to 50°C, further dry nitrogen was admitted up to atmospheric pressure.
- After unloading from the system and after a further cooling down period in a dessicator (about 30 minutes),the samples were

Institute System	Heating-up cooling-down times (h)	Pumping speed $L.S^{-1}$ N_2-20°C	Condensors
ESTEC-1 Micro-VCM	½/2	1.5	2 x chrome, ø 31 mm 1 x NaCl. ø 25 mm
INTA Micro-VCM	¼/2	1.5	3 x NaCl, ø 25 mm
CNES Macro-VCM	1½	3.0	2 x quartz, ø 30 mm
MBB 'Macro-VCM' Vacuum Balance	-	60	1 x aluminium, ø 70 mm
DFVLR Vacuum Balance	½/high-frequency heating	-	NO
ESTEC-2 Vacuum Balance	2-3/1 (dummy sample)	25	NO
DERTS Vacuum Balance	-	-	NO
SNIAS Vacuum Balance	-	-	NO

TABLE 1

TABLE 2

No.	Trade name	Manufacturer	Chemical nature	Preparation method
1	PSG-120	Pyrolac	White silicone paint	On Al foil,4,4mg/cm^2
2	PSE-109	Pyrolac	Black epoxy paint	On Al foil,4,4mg/cm^2
3	Silicoset-105	ICI	silicone potting	0.6% CRA - RT cure
4	BSL-203	Ciba	epoxy adhesive	100p/A, 14p/B - RT
5	Chemglaze Z-306	Hughson	Black polyurethane paint	On Al foil, 4,4mg/cm^2
6	Araldite AV-134B/HY994	Ciba	epoxy adhesive	100p/134, 40p/994 22h/RT + 2h/60°C
7	Rilsan BMNO	Aquit. Org.	polyamide 11 grains	A,R.

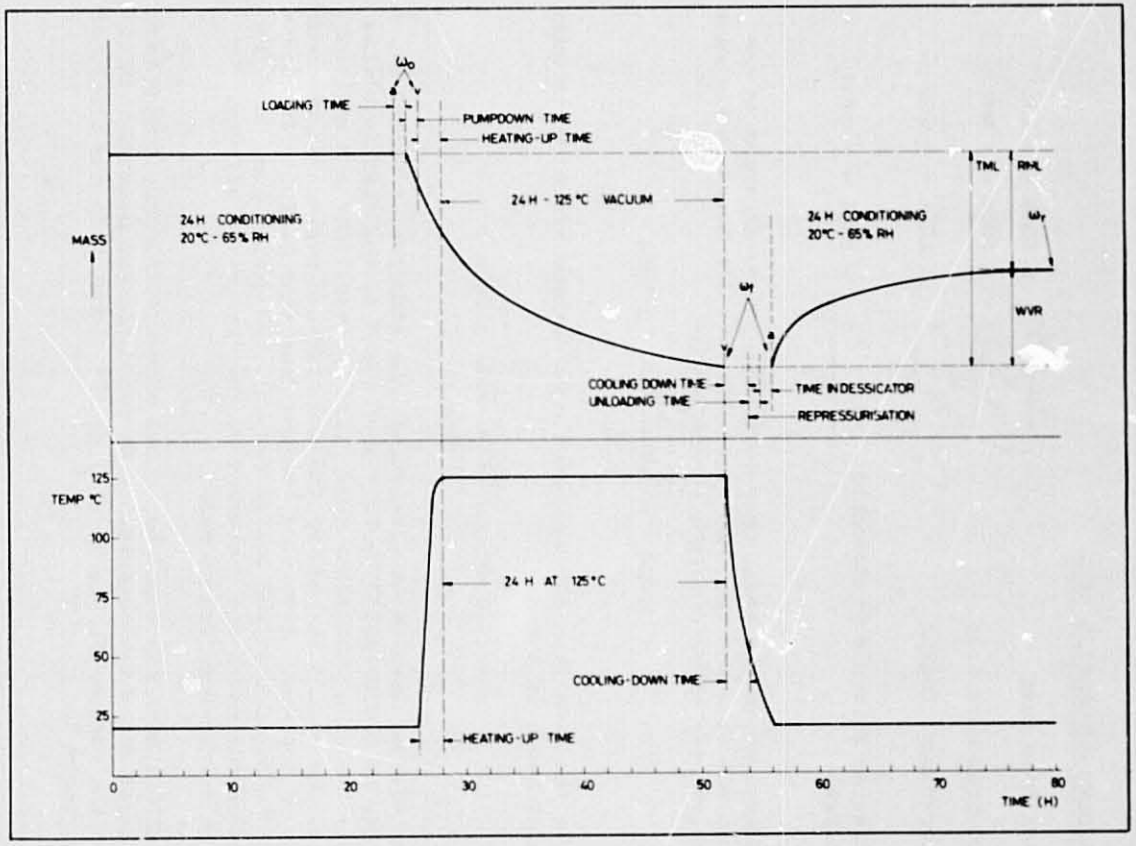

Figure 1.

weighed (W_{fa}).
- For the vacuum-balance systems, the sample mass after the tests was determined in vacuum (W_{fv}).
- The samples were re-exposed to 20° ± 1°C and 65% relative humidity for 24 h and then re-weighed (W_r).
- The collectors which were maintained at 25° ± 1°C during the test were weighed just before the test (W_c) and just after (W_c') both times under atmospheric conditions.

MEASURED OUTGASSING DATA

Total Mass Loss	$\frac{W_o - W_f}{W_o} \times 100\% = \%\ TML$
Recovered Mass Loss	$\frac{W_o - W_r}{W_o} \times 100\% = \%\ RML$
Water-Vapour Regain	$\frac{W_r - W_f}{W_o} \times 100\% = \%\ WVR$
Collected Volatile Condensable Material	$\frac{W_c - W_c'}{W_o} \times 100\% = \%\ CVCM$

Differences in the total-mass-loss data can be expected as the micro-VCM data and the CMES macro-VCM data are based on the mass measurements under atmospheric conditions

$$\%\ TML' = \frac{W_{oa} - W_{fa}}{W_{oa}} \times 100\%$$

While the data from the vacuum-balance methods are based on mass measurements in vacuum.

$$\%\ TML = \frac{W_{ov} - W_{fv}}{W_{ov}} \times 100\%$$

Both methods involve uncertainties: the atmospheric method has a number of uncontrolled periods ar the end of the test involving cool-down time, unloading time, time in dessicator and weighing time; the vacuum method has the uncontrolled periods at the beginning of the test, involving loading time (the humidity is difficult to control in the vacuum system), and during pump down the mass measurements are disturbed by the 'byoyancy' effects, for which corrections can be made.

At ESTEC, both the atmospheric and vacuum total-mass losses were measured for three materials with two different balances. In this case the vacuum TML was about 5 to 10% higher than the atmospheric TML (Table 3).

TABLE 3

Materials	Atmospheric TML %	Vacuum TML %
(5) Chemglaze Z-306	1.51	1.62
(6) Araldite AV 134	2.01	2.10
(7) Rilsan BMNO	1.29	1.43

RESULTS

Table 4 gives the measured data: % TML, % RML, % WVR and % CVCM (respectively columns 3, 6, 9 and 12) for the seven materials tested by the eight participating institutes. ESTEC 1, INTA, CNES and DFVLR conducted their measurements in triplicate or duplicate (see column 15) and the calculated 1 σ error

$$\{1\ \sigma = \sqrt{(\bar{x} - x)^2 / n' - 1}\}$$

is given in columns 4, 7, 10 and 13. Columns 5, 8, 11 and 14 give the ratios of measured values to the average value for all participants.

INTERPRETATION OF RESULTS

Total Mass Loss (TML)

Table 5 gives the ration $TML/TML_{average}$ noted in column 5 of Table 4 in another way. The low TML value for PSG-120 by ESTEC-1 was verified in a second test on a 710 mg sample. The obtained data TML = 0.72%. RML = 0.69% and CVCM = 0.09% were quite close to the earlier ones, the lower CVCM percentages might be explained by the creeping of the silicone products condensed on the collector.

The correlation between the ESTEC-1, INTA and CNES (all having systems based on the same design for routine tests) results is quite good, factors 1.01, 1.01 and 1.03 with 1 σ values respectively 0.12, 0.15 and 0.12.

The MBB average value ($TML/TML_{average}$) is high (1.14) mainly because of the two bulky epoxies BSL-203 and AV-134 (values 1.46 and 1.42). A high initial water sorption by these two materials might explain the high values but, on the contrary, the water vapour regain (WVR) after the test was about half of the average WVR (see table 7). In this case, we should not forget that the MBB tests were made eight months later than the others, so that ageing of the materials might be a factor.

The DFVLR average value of 0.57 is certainly too low, the low outgassing data being caused by a lower sample temperature, as will be explained below.

TABLE 4

Results of European outgassing tests, 1 March 1975

1	2	3	4	5	6	7	8	9	10	11	12	13	14	15	16	17
	Material	Institute	%TML	± 1 σ	TML / TML$_{max}$	%RML	± 1 σ	RML / RML$_{max}$	%WVR	± 1 σ	WVP / WVP$_{max}$	%CVCM	± 1 σ	CVCM / CVCM$_{max}$	no.	SAMPLES mg	SAMPLES mg/cm^2
1	PSG-120 white silicone paint	ESTEC 1	0.73	0.03	0.88	0.71	0.01	0.84	0.03	< 0.01	0.75	0.130	0.01	0.75	3	242	23
		INTA	0.96	0.02	1.16	0.92	0.02	1.09	0.04	< 0.01	1.00	0.200	0.03	1.16	3	235	23
		CNES	1.02	0.01	1.23	1.02	0.02	1.20	0.00		0.00	0.152	0.03	0.88	2	332	23
		MBB	0.78		0.94	0.73		0.86	0.05		1.25	0.210		1.21	1		23
		DFVLR	0.54	0.01	0.65										2	24	23
		ESTEC 2															
		DERTS	0.95		1.15	0.87		1.02	0.06		2.00				1	252	23
		SNIAS	0.86		1.04										1	306	23
	Average values		0.83			0.85			0.04			0.173					
2	PSE-106 black epoxy paint	ESTEC 1	5.48	0.02	0.94	4.52	0.03	0.85	0.06	0.01	1.16	0.065	0.01	0.22	3	258	8.6
		INTA	5.55	0.13	0.95	4.57	0.13	0.86	0.75	< 0.01	0.91	0.105	0.01	0.35	3	170	8.6
		CNES	5.59	0.20	0.95	5.31	0.23	0.99	0.27	0.02	0.33	0.402	0.1*	1.35	3	255	8.6
		MBB	5.81		0.99	4.81		0.90	1.00		1.21	0.620		2.06	1		
		DFVLR	4.22	0.26	0.72										2	8	4.9
		ESTEC 2															
		DERTS	6.65		1.13	5.50		1.03	1.15		1.39				1	195	8.6
		SNIAS	5.85		1.00										1	310	8.6
	Average values		5.65			5.34			0.83			0.299					
3	Silicone 105 silicone rubber	ESTEC 1	2.44	0.06	1.16	2.62	0.01	1.11	0.03	< 0.01	0.62	0.392	0.05	0.46	3	230	40
		INTA	2.57	0.06	1.23	2.53	0.07	1.08	0.04	< 0.01	0.83	0.262	0.05	0.66	3	203	40
		CNES	2.44	0.18	1.07	2.44	0.16	1.04	0.00		0.00	0.455	0.02	1.15	2	325	110
		MBB	2.60		1.14	2.56		1.09	0.04		0.83	0.49		1.23	1		
		DFVLR	1.23	0.01	0.55										2	142	142
		ESTEC 2	2.15		0.94	2.10		0.89	0.05		1.03				1	1694	166
		DERTS	2.00		0.88	1.87		0.79	0.13		2.69				1	294	
		SNIAS	2.60		1.14										1	710	130
	$\bar{x}$ range values		2.28			2.35			0.05			0.397					
4	RSL 203 epoxy	ESTEC 1	1.15	0.03	1.10	0.64	0.04	0.82	0.33	0.06	1.02	0.042	0.03	2.33	3	31	40
		INTA	1.11	0.03	1.06	0.63	0.01	0.81	0.46	0.04	1.28	0.029	< 0.01	1.16	3	202	40
		CNES	0.90	0.10	0.86	0.83	0.10	1.06	0.07	0.01	0.19	0.001	0.001	0.06	3	2660	166
		MBB	1.32		1.46	1.34		1.71	0.19		0.50	0.005		0.00	1		
		DFVLR	0.50	0.02	0.48										2	177	177
		ESTEC 2	1.07		1.03	0.70		0.89	0.37		1.02				1	1765	165
		DERTS	1.12	0.12	1.07	0.55	0.02	0.70	0	0.15	1.58				2	801	
		SNIAS	0.97		0.93										1	711	133
	Average values		1.04			0.79			0.26			0.018					
5	Chemglaze Z-306 black polyurethane paint	ESTEC 1	1.37	0.04	0.97	0.43	0.03	0.81	0.04	0.02	0.90	0.054	0.02	0.53	3	148	3.5
		INTA	1.15	0.14	0.82	0.58	0.12	1.16	0.05	0.04	0.54	0.113	0.04	1.11	3	114	7.5
		CNES	1.41	0.25	1.00	1.24	0.22	2.48	0.17	0.04	0.16	0.121	0.04	1.19	2	306	3.5
		MBB	1.62		1.15	0.48		0.96	1.14		1.09	0.120		1.18	1		3.5
		DFVLR	0.90		0.64										1	10	10
		ESTEC 2	1.62		1.15	0.23		0.46	1.39		1.32				1	258	3.5
		DERTS	2.27	0.47	1.61	0.10	0.15	0.06	2.08	0.33	1.98				2	134	3.5
		SNIAS	0.92		0.65										1	710	3.5
	Average values		1.41			0.50			1.05			0.102					
6	Araldite AV134B HY994 epoxy	ESTEC 1	2.58	0.05	1.13	1.93	0.05	0.85	0.66	0.01	1.57	0.064	0.01	0.61	3	225	40
		INTA	2.55	0.06	1.12	2.12	0.07	0.94	0.43	0.02	1.02	0.072	0.02	0.69	3	203	40
		CNES	2.44	0.29	1.07	2.36	0.30	1.04	0.08	0.01	0.19	0.182	0.03	1.74	2	1830	259
		MBB	3.23		1.42	2.39		1.32	0.25		0.60	0.190		0.96	1		
		DFVLR	0.51	0.03	0.22										2	154	154
		ESTEC 2	2.10		0.92	1.96		0.87	0.14		0.33				1	1696	157
		DERTS	3.21		1.41	2.23		0.99	0.94		2.33				1	305	
		SNIAS	1.94		0.72										1	710	91
	Average values		2.28			2.26			0.42			0.105					
7	Rilsan BMNO polyamide grains	ESTEC 1	0.93	0.01	0.89	0.66	0.01	0.83	0.27	< 0.01	1.03	0.052	0.01	0.91	3	195	40
		INTA	0.99	0.04	0.94	0.69	0.03	0.86	0.20	< 0.01	0.76	0.017	0.01	0.30	3	196	40
		CNES	1.06	0.06	1.01	0.94	0.07	1.18	0.12	0.01	0.46	0.110	0.02	1.93	3	1940	1.5
		MBB	0.95		0.91	0.59		0.74	0.17		1.41	0.05		0.87	1		40
		DFVLR	0.78	0.01	0.74										2	305	40
		ESTEC 2	1.43		1.36	1.15		2.44	0.28		1.07				1	609	40
		DERTS	1.06		1.04	0.76		0.94	0.11		1.29				1	302	40
		SNIAS	1.27		1.21										1	719	40
	Average values		1.05			0.82			0.26			0.057					

A metal disc of 10 mm diameter, on which the material was prepared was heated by means of an HF coil outside the vacuum system; the sample was surrounded by liquid nitrogen-cooled walls, the temperature of the metal disc was controlled by a thermocouple on a dummy metal disc situated close to the sample disc. Corrections for the forces, caused by the HF heating on the metal disc hanging from the vacuum microbalance were taken into account.

Between the metal disc and the front of the material sample there is a temperature difference which depends on the nature of the thermal contact with the metal disc, on the thermal conductivity and thickness of the material, and on its emissivity. An approximate calculation by DFVLR showed a 10^{o} temperature difference for 3 mm-thick samples.

Typically, for samples of 140 to 180 mg, the three materials SIL-105, BSL-203 and AV-134 with thicknesses of 2 - 3 mm gave the lowest $TML/TML_{average}$ values in Table 5 (respectively 0.55, 0,48 and 0.22). The three paint samples PSG-120, PSE-109 and Z-306 (resp. 24,8 and 10 mg) gave very similar (to each other) but still low values (resp. 0.65, 0.72 and 0.64). Best correlation with other data was obtained for Rilsan, which might be explained by the cavity sample holder which was used instead of the metal disc because of the granular structure of Rilsan. The reproducibility of the DFVLR tests is quite good.

The ESTEC-2 (vacuum-balance system) values do not differ significantly from other values, which is interesting because samples 3, 4 and 6 were 20 x 20 x 4 mm^3 blocks; hence the size of these three samples did not seem to be critical.

The DERTS average value ($TML/TML_{average}$) of 1.23 is high mainly because of high water sorption by samples 2, 5 and 6, with corresponding ratios, 1.48, 1.61 and 1.41. The water sorption correlation can easily be seen by comparing the $TML/TML_{average}$ values with WVR_a in the last column of Table 5.

Recovered Mass Loss (RML)

Table 6 gives the $RML/RML_{average}$ values from column 8 in Table 4 in an alternative form.

The RML values should be independent of conditioning parameters as long as such pre- and post-conditioning parameters as humidity, temperature and time are the same. In other words, the influence of sorbed water (=WVR) should be cancelled out in the RML data. From the fact that the RML data are not as selfconsistent as the TML data, we can conclude that either conditioning or other parameters (e.g. test temperature) caused the poorer correlation.

As the post-conditioning differed widely for all participants (which fact will be explained in Section 6.3 from the widely

TABLE 6

$RML/RML_{average}$

Material \ Institute	ESTEC 1	INTA	CNES	MBB	DFVLR	ESTEC 2	DERTS	SNIAS	WVR_a %
1 PSG-120	0.84	1.08	1.20	0.86	-	-	1.02	-	0.04
2 PSE-109	0.85	0.86	0.99	0.90	-	-	1.40	-	0.83
3 SIL-105	1.11	1.08	1.04	1.09	-	0.89	0.79	-	0.05
4 BSL-203	0.82	0.83	1.06	1.71	-	0.89	0.70	-	0.36
5 Z-306	0.86	1.16	2.48	0.96	-	0.46	0.06	-	1.05
6 AV-134	0.85	0.94	1.04	1.32	-	0.87	0.99	-	0.42
7 Rilsan	0.83	0.86	1.18	0.74	-	1.44	0.94	-	0.26
Average value	0.88	0.97	1.28	1.08	-	0.91	0.84	-	
1 σ $\pm$	0.10	0.13	0.53	0.33	-	0.35	0.41	-	

TABLE 5 $TML/TML_{average}$

Material \ Institute	ESTEC-1	INTA	CNES	MBB	DFVLR	ESTEC-2	DERTS	SNIAS	WVR_a %
1 PSG-120	0.88	1.16	1.23	0.94	0.65	-	1.14	1.04	0.04
2 PSE-109	0.94	0.91	0.95	0.99	0.72	-	1.48	1.00	0.83
3 SIL-105	1.16	1.13	1.07	1.14	0.55	0.94	0.88	1.14	0.05
4 BSL-203	1.10	1.06	0.86	1.46	0.48	1.03	1.07	0.93	0.36
5 Z-306	0.97	0.82	1.00	1.15	0.64	1.15	1.61	0.65	1.05
6 AV-134	1.13	1.12	1.07	1.42	0.22	0.92	1.41	0.72	0.42
7 Rilsan	0.89	0.84	1.01	0.91	0.74	1.36	1.04	1.21	0.26
Average value	1.01	1.01	1.03	1.14	0.57	1.08	1.23	0.96	
1 σ $\pm$	0.12	0.15	0.12	0.22	0.18	0.18	0.27	0.21	

differing WVR data), we cannot assume that the pre-conditioning was the same for all participants, and hence no further conclusions can be withdrawn from the data.

Ignoring the Chemglaze Z-306 paint (≈ 74% of the total mass loss is due to water) in the CNES data, we obtain an average value of 1.09 ± 0.08 instead of 1.28 ± 0.53 and for DERTS 0.97 ± 0.24 instead of 0.84 ± 0.41.

As with the TML data, the RML data for BSL-203 and AV-134 are high in the MBB results.

Ignoring SIL-105, the ESTEC-1 average value becomes 0.84 ± 0.02, indicating a very low 1 σ value.

Water Vapour Regain (WVR)

Table 7 gives the $WVR/WVR_{average}$ values in an alternative form to Table 4 (column 11), except for the non-water-sensitive silicones. The water-vapour regain (WVR) measured by CNES is only 27% of the average water-vapour regain, and the DERTS values are 71% higher. These high DERTS values also caused a high total mass loss (Table 5), which means that the pre-conditioning caused the high water sorption. The low WVR data recorded by CNES cannot be traced in the TML data (Table 5), which means that the pre-conditioning was probably much better than the post-conditioning.

Comparison of ESTEC-1 TML data with data from other institutes

The two micro-VCM systems (ESTEC-1 and INTA) gave a good correlation for five of the seven materials (1.03 ± 0.02); the value of 1.19 for the Z-306 paint could be explained by a 30% higher water sorption in the ESTEC sample. The low value of 0.76 for PSG-120 could not be explained, as already mentioned before.

Collected Volatile Condensible Materials (CVCM)

Table 9 shows the $CVCM/CVCM_{average}$ ratio from column 14 of Table 4.

The average value is only taken for six materials. The results for BSL-203 have not been included because of their lowness (0.018%).

The correlation in the CVCM data is very poor, especially for the materials PSE-109, AV-134 and Rilsan. The low 1 σ values for the CVCM measurements (see column 13 of Table 4) might indicate a better correlation. The ESTEC micro-VCM condensors are two chromium-plated aluminium discs (33 mm ø) and one sodium-chloride disc (25 mm ø). No noticeable difference in CVCM was observed with the two different condensor types.

The INTA system had only three sodium-chloride discs, while the CNES macro-VCM system had a quartz disc of 30 mm diameter as condensors. The MBB macro-VCM system with a vacuum balance had an

TABLE 7 $WVR/WVR_{average}$

Material \ Institute	ESTEC-1	INTA	CNES	MBB	DFVLR	ESTEC-2	DERTS	SNIAS	WVR_a %
2 PSE-109	1.16	0.91	0.33	1.21	-	-	1.39	-	0.83
4 BSL-203	1.42	1.23	0.19	0.50	-	1.02	1.58	-	0.36
5 Z-306	0.90	0.54	0.16	1.09	-	1.32	1.98	-	1.05
6 AV-134	1.57	1.02	0.19	0.60	-	0.33	2.33	-	0.42
7 Rilsan	1.03	0.76	0.46	1.41	-	1.07	1.26	-	0.26
Average value	1.22	0.90	0.27	0.96	-	0.94	1.71	-	
1 σ ±	0.28	0.28	0.19	0.39	-	0.43	0.44	-	

TABLE 8 Comparison of ESTEC-1 TML results with those from other institutes.

Material \ Institute	ESTEC/ INTA	ESTEC/ CNES	ESTEC/ MBB	ESTEC/ DFVLR	ESTEC/ ESTEC-2	ESTEC/ DERTS	SNIAS
1 PSG-120	0.76	0.72	0.94	1.35	-	0.77	0.85
2 PSE-109	1.03	0.99	0.94	1.30	-	0.63	0.94
3 SIL-105	1.03	1.08	0.91	2.11	1.23	1.32	1.02
4 BSL-203	1.04	1.28	0.76	2.30	1.07	1.03	1.19
5 Z-306	1.19	0.97	0.85	1.52	0.85	0.60	1.49
6 AV-134	1.01	1.06	0.80	5.05	1.23	0.80	1.57
7 Rilsan	1.06	0.88	0.98	1.19	0.65	0.85	0.73
Average value	1.02	1.00	0.88	2.11	1.01	0.86	1.11
1 σ ±	0.13	0.17	0.08	1.36	0.25	0.25	0.32

TABLE 9 $CVCM/CVCM_{average}$

Institute / Material	ESTEC	INTA	CNES	MBB	$CVCM_{average}$ %
1 PSG-120	0.75	1.16	0.88	1.21	0.173
2 PSE-109	0.22	0.35	1.35	2.08	0.298
3 SIL-105	0.99	0.66	1.15	1.21	0.397
4 BSL-203	2.33	1.61	0.06	0.00	0.018
5 Z-306	0.53	1.11	1.19	1.18	0.102
6 AV-134	0.61	0.69	1.74	0.96	0.105
7 Rilsan	0.91	0.30	1.92	0.87	0.057
Average (BSL-203	0.67	0.71	1.37	1.25	
$1\sigma\pm$ not included)	0.28	0.36	0.39	0.43	

TABLE 11 1σ values for TML in percent of TML

Institute / Material	ESTEC	INTA	CNES	DFVLR
1 PSG-120	4.1	2.1	1.0	1.9
2 PSE-109	0.4	2.4	3.6	6.2
3 SIL-105	0.0	2.3	6.6	0.8
4 BSL-203	4.3	2.7	11.1	4.0
5 Z-306	2.9	12.2	17.7	-
6 AV-134	1.2	2.3	11.9	5.9
7 Rilsan	1.1	4.5	5.7	1.3
Average	2.0	4.1	8.2	3.4

aluminium plate of 70 mm diameter as condensor. The interpretation of the CVCM data cannot lead to any form of conclusion as to which parameter or parameters caused the discrepancies.

The most critical parameters in this case are:

(i) Sample temperature: thermal degradation increases by more than 15% per degree increase in sample temperatures.
(ii) Sticking coefficient of condensor material: perhaps not such a critical parameter as several hundred monolayers of condensed material shield the original material.
(iii) Geometry of sample compartment and condensor arrangement.
(iv) Condensor temperature.

In the case of poor thermal conductivity condensors like NaCl and quartz, one can expect a temperature difference across the condensor. Re-evaporation of condensed materials, with a vapour pressure of some 2 x 10^{-7} torr at 25°C, might show enormous differences in CVCM values when the condensor temperature varied by only 1°C.

Accuracy of Measurements

Table 10 gives the sum of the 1 σ values for TML, RML and CVCM (from columns 4, 7 and 13 of table 4)

TABLE 10

Sum of 1 σ values

	TML	RML	CVCM	
ESTEC-1	0,18	0.18	0.14	7 materials and 3 samples
INTA	0.48	0.45	0.17	7 materials and 3 samples
CNES	1.07	1.07	0.20	7 materials and 2 samples
DFVLR	0.34	-	-	6 materials and 2 samples

In practice there is no difference between the 1 σ values for TML and RML, which is surprising in that the influence of sorbed water is, in principle, cancelled out in the RML, so that more accurate RML data were expected.

Table 11 gives the 1 σ values for TML in percent TML for the four participants who tested two or three samples of the same material. The largest errors in the INTA and CNES results are due to the Z-306 paint, for which about 74% of the total mass loss is caused by water.
From Table 12 can be concluded that:-
The 1σ values for the TML data seem to be more or less independent of the height of the TML, which implies that 1 σ errors of about 0.13% can normally be expected. The bold figures differ from the average TML values by more than 0.20%.

TABLE 12

Total Mass Loss (%TML) figures from the micro- and macro-VCM tests at INTA, ESTEC and CNES.

Material / Institute	PSG-120	PSE-109	SIL-105	BSL-203	Z-306	AV-134	Rilsan
ESTEC	0.72	5.49	2.64	1.10	1.37	2.60	0.93
	0.72	5.50	2.64	1.16	1.34	2.54	0.92
	0.76	5.47	2.65	1.19	1.41	2.60	0.93
INTA	0.94	5.42	2.57	1.07	1.30	2.48	0.91
	0.98	**5.18**	2.64	1.13	**1.03**	2.59	0.85
	0.95	5.38	2.51	1.13	1.11	2.58	0.89
CNES	1.01	5.52	**2.33**	0.90	1.23	**2.75**	1.01
	1.03	**5.81**	2.55	1.00	**1.58**	**2.17**	1.10
	-	5.42	-	**0.81**	-	2.41	-
$TML_{average}$	0.89	5.47	2.57	1.05	1.30	2.52	0.94
$1\ \sigma$	0.13	0.16	0.11	0.13	0.17	0.16	0.08

The acceptable 1 σ values on outgassing results (test are carried out in triplicate) from the micro-VCM test as being fixed in specification ESA/PSS-09/QRM-02T issue 2 are:

(a) $\pm$ 0.05 for TML and RML data up to 0,50% and $\pm \frac{1}{10}$ of the data is excess of 0.50%.
(b) $\pm$ 0.03 for CVCM data up to 0.15% and $\pm$ 1/5 of the data in excess of 0.15%.

The ESTEC and INTA micro-VCM data are within above 1 σ values except for the TML figure on Z-306 from INTA. Also the TML figures on the materials BSL-203, Z-306 and AV-134 from CNES are not within the above limits.

The overall accuracy on TML data around 1.0% is within 15% for the micro-VCM systems.

The overall accuracy on CVCM data around 0.10% is poor, approximately a factor of 2, which figure is high as the present acceptance criteria for spacecraft materials selection are micro-CVCM outgassing figures of TML $\leq$ 1.0% and CVCM $\leq$ 0.10%.

CONCLUSION

Total Mass Loss data of reasonable accuracy can be obtained on organic materials with the micro-VCM, macro-VCM and vacuum-balance systems as long as sample conditioning and test temperature are within the limits as specified in ESA/PSS-09/QRM-02T.

Also special attention should be paid to the test procedures as low water sorption time constants of materials (e.g. down to about 5 minutes for polyurethane paints) may influence the outgassing figures significantly.

The low accuracy of the CVCM data obtained with the micro-VCM and macro-VCM systems, of which systems most of the critical parameters have been fixed within narrow limits, indicate that prediction of spacecraft contamination based on measurements of outgassing rates and condensation rates will be of a much lower accuracy as most of the "contamination critical" spacecraft parameters cannot be predicted very accurately.

Further investigation on outgassing and condensation phenomena as well as on the absolute calibration of outgassing systems seems to be worthwhile in order to find out what the critical parameters are and how critical they are.

PROPOSED IMPROVEMENTS

(i) Better pre- and post-conditioning of samples
(ii) Closer working to specification ESA/PSS-09/QRM-02T, issue 2
(iii) Use of blank condensors to verify the cleanliness of the system
(iv) If possible, closer temperature tolerances; 125 $\pm$ 0.2°C as sample temperature and 25 $\pm$ 0.2°C as condensor temperature
(v) Investigation of the use of a pure material as a standard for equipment calibration.

ACKNOWLEDGEMENTS

All participants who contributed to the tests themselves, and those who attended the discussions of the results at the meeting of 16 January 1976 at DFVLR,Porz-Wahn, are thanked for their inputs.

REFERENCES

1. Whittick, J.S. & Murace, R.F., Polymers for spacecraft applications, SRI project ASD-5046, Stanford Research Institute, September 1967 (NASA CR-89557).

2. A screening method employing a thermal vacuum for the selection of materials to be used in space, ESA/PSS-09/QRM-02T.

3. Park, J.J.,Marriot, R.S., Campbell, W.A. and Staugaitis, C.L., Outgassing tests in support of a proposed ASTM specification, NASA SP-336, pp. 437-448.

Paper No. 27

HIGH CURRENT LIGHTNING TEST OF SPACE SHUTTLE EXTERNAL TANK LIGHTNING PROTECTION SYSTEM*

E. Mumme, *Martin Marietta Corp., New Orleans, Louisiana*
A. Anderson, *Martin Marietta Corp., New Orleans, Louisiana*
E. Schulte, *McDonnell Aircraft Co., St. Louis, Missouri*

ABSTRACT

During lift-off, the Shuttle launch vehicle (External Tank, Solid Rocket Boosters and Orbiter) may be subjected to a lightning strike. This paper describes tests of Martin Marietta's proposed lightning protection method for the External Tank and development materials which were subjected to simulated lightning strikes. Results showed that certain of the high resistance paint strips performed remarkably well in diverting the 50 kA lightning strikes over the CPR 421 Thermal Protection System.

INTRODUCTION

It has long been recognized that lightning is a real threat to aircraft, and although one normally thinks of spacecraft as operating outside of the earth's atmosphere, they must, however, traverse the lightning environment which may extend to 15,000 meters (50,000 feet).

Kennedy Space Center, one of the launch sites for Shuttle, is equipped with extensive and sophisticated arrays of lightning detection and monitoring equipment, but even so, they cannot predict or prevent all possible lightning strikes to launched vehicles. Although assurances can be given that a lightning strike probably will not occur during launch, based upon "blue sky" atmospheric conditions, other circumstances may not always permit the delays imposed by the "blue sky" restriction. Therefore, some protective measures must be incorporated in the complete Space Shuttle system to insure survivability. Because of the complicated outer surfaces of the Shuttle System, tests must be performed to demonstrate the adequacy of the protective measures.

The Space Shuttle in the launch configuration consists of three major systems: the Orbiter, the External Fuel Tank (ET), and the Solid Rocket Boosters (SRB's). In this configuration, if a lightning strike should occur, it is most likely to strike the nose of the ET as shown in Figure 1. To complicate matters, The Shuttle ET contains cryogenics (liquid hydrogen and liquid oxygen) and must therefore be thermally insulated to prevent excessive loss of cryogens due to heat input from the external environment. Good thermal insulators generally do not possess much mechanical strength and because they are extremely poor electrical conductors, they cannot be expected to conduct lightning current safely. As a result, a lightning strike to an area protected by one of these types of materials may cause severe damage to the insulation system. Therefore, the design of such a system is complicated by the lightning threat and the materials and installation costs for protective measures.

*Sponsored by National Aeronautics and Space Administration, Marshall Space Flight Center, Alabama; Contract No. NAS 8-30300

GP76-6623-1

FIGURE 1 – LIGHTNING ATTACHMENT TEST OF SHUTTLE MODEL[1]

This paper describes the design approach taken by Martin Marietta Corporation for lightning protection of the Shuttle External Tank. The paper also describes the test panels manufactured by Martin Marietta for lightning tests to verify the design concept and adequacy of conductive materials. The actual lightning tests were conducted at the McDonnell Aircraft Company's Lightning Simulation Laboratory located in St. Louis, Missouri. The test set-up and test results are detailed herein. The lightning tests were conducted in accordance with Reference 2.

Lightning Threat

Natural lightning is a complicated phenomena and has been extensively studied and statistically summarized by noted authorities such as Uman[3] and Cianos and Pierce[4]. For testing purposes, the lightning environment is generally simplified, based upon the various statistical studies plus the combined knowledge

and engineering judgment of many experts in the field of lightning theory and simulation. The effects of lightning are considered as being either direct or indirect effects. The direct effects are those which are normally associated with observable physical damage and the indirect effects are those normally associated with the more subtle aspects of lightning effects such as the induced electrical transients on wiring. For this presentation, we are concerned with the direct effects of lightning.

For direct effects testing, the NASA idealized lightning model waveform shown in Figure 2 was used. The magnitudes of the various components of this waveform are considered to be those found in a severe lightning strike and not often found in nature. However, each component has relevance toward producing the various damage mechanisms found in a real lightning strike. For additional information, the reader is referred to the References listed.

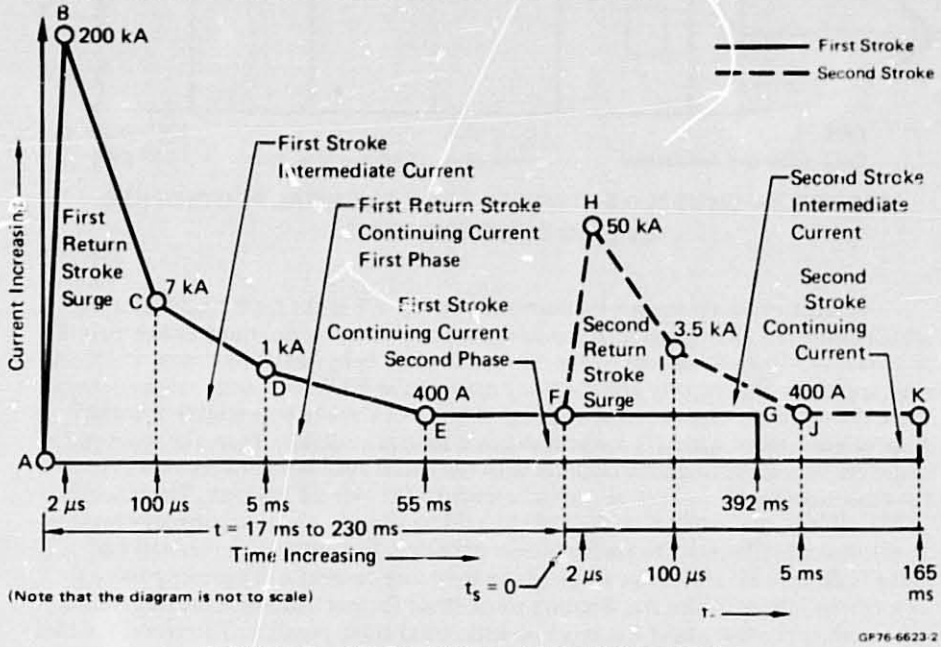

FIGURE 2 – NASA (JSC) LIGHTNING MODEL

In the launch configuration for the Space Shuttle, the lightning rod on the nose of the ET is the most likely attachment point for lightning and any portions aft of this area are considered to be in a lightning swept stroke region and are therefore subject to a lightning restrike. The lightning test conditions for a primary (most likely) attach point are those of the first stroke shown in Figure 2 and the restrike test conditions are those of the second stroke shown in this figure. Either of the test conditions can inflict severe damage to a spacecraft system or to a conventional aircraft if it is not adequately protected. In particular, the thermal protection system (TPS) used on the Shuttle ET (see Figure 3) is vulnerable to lightning. If the lightning should puncture the TPS, a hole several inches in diameter may be blown in the TPS, thus exposing the cold bare metal of the tank. A small hole in the TPS itself may be tolerable but aerodynamic forces during ascent may cause larger portions to be torn away. In addition, the direct lightning arc attachment to the metal skin may cause a hole to be burned thru the tank wall.

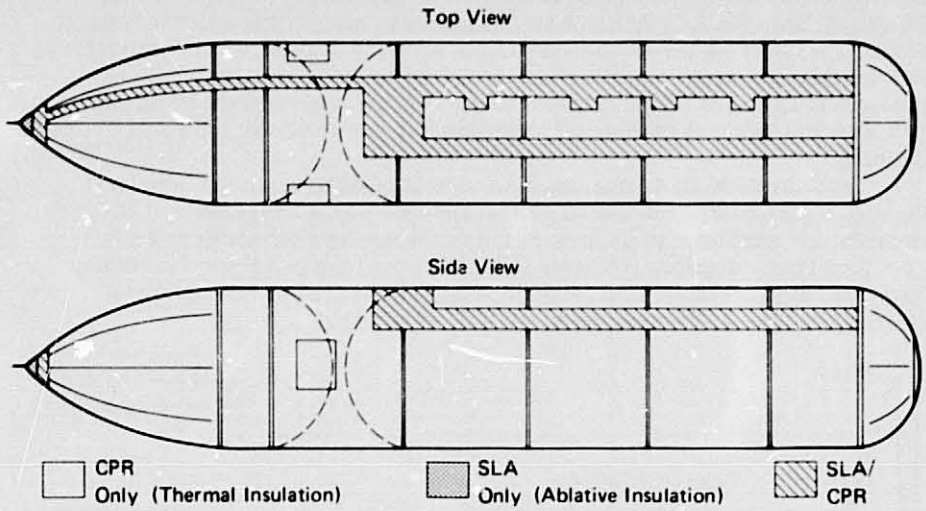

FIGURE 3 – SHUTTLE EXTERNAL TANK THERMAL PROTECTION SYSTEM CONFIGURATION

GP76-6623-3

As mentioned above, the lightning rod on the ET is the most likely lightning attach point and the areas aft of the nose may also become lightning attach points as shown in Figure 4 because of the "swept stroke" behavior of lightning. Lightning may approach and initially attach to the nose of the ET from a wide range of angles. Once the main arc channel is established, it will not deviate appreciably from this path unless a more desirable lower resistance path is available. Thus, the spacecraft could fly thru a lightning arc channel with the result that it will sweep rearward on the tank with probably several reattachments to the side of the tank. The velocity of the vehicle, the external surface of the vehicle and the air flow boundary layer conditions all influence the reattachment behavior. In addition, the second fast rising high peak return stroke surge of the lightning current will probably force a new reattachment of the arc. Because all of these factors can influence test results, it is desirable to test under the most realistic conditions possible. Therefore for this test series, the complete second stroke current waveform shown in Figure 2 was used and the arc was blown by a 10 feet/second airstream to conservatively simulate the early movement of the launch vehicle. When the nose clears the protection system of the launch pad, the vehicle will actually be moving at 19.5 meters per second (64 feet/second). At this low velocity, the lightning arc would not be blown very far and thus the simulation would impose a "worst case" test condition regarding the possibility of burn-thru of the metal tank wall if the arc would attach directly to the skin.

Protection System Theory

When lightning strikes a conductive surface on a moving vehicle, the strike may sweep across the surface. The resulting surface damage will be distributed over the path length and should be relatively minor in a given spot. However, if lightning strikes an insulated surface overlaying a conductive substrate, the strike

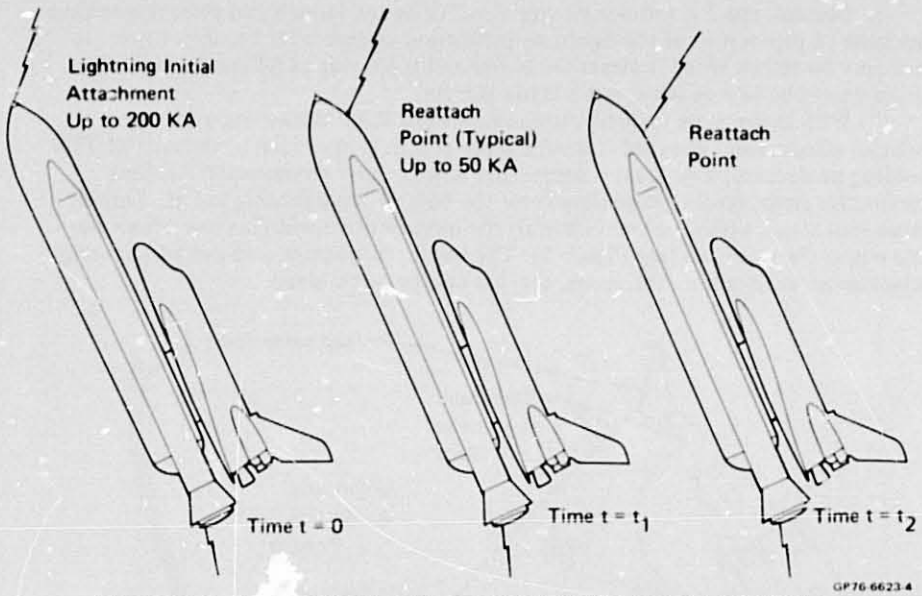

FIGURE 4 – ILLUSTRATION OF LIGHTNING ARC BEHAVIOR (SWEPT STROKE) ON MOVING VEHICLE

may penetrate the insulation and attach to the underlying metal. The lightning strike cannot readily sweep over the surface, and thus confined, can cause more extensive damage.

On the External Tank, the thermal protection system (TPS) insulator is used to maintain a low temperature on structural members. The strain characteristic of metal is greater at low temperatures and falls off quite rapidly at elevated temperatures. Consequently, from both thermal and structural considerations, the integrity of the TPS has to be preserved.

Considering the direct lightning effects of lightning confined by TPS and the thermal/structural effects when TPS is removed in divots by lightning, it becomes paramount that the TPS be protected from lightning! Theoretically, it should be possible to protect an insulated surface from lightning by covering it with a conductive layer. If the conductive layer is in the form of a narrow strip, it would have to be grounded to structure at intervals so that neither the resistive voltage drop nor the inductive drop (the inductance of the layer L times the restrike rise time, di/dt) would not exceed the voltage breakdown of the insulating material at any point along the strip.

The TPS system on the External Tank is extensive (see Figure 3) and from inception, the design has included conductive strips over the forward nose (ogive) area of TPS. Aluminum foil of an undefined thickness was originally proposed. This concept was soon abandoned when consideration was given to the possible impingement of the aluminum upon the underbelly TPS tiles of the Orbiter, thus damaging the tiles and possibly jeopardizing reentry.

With weight, manufacturing cost, and other considerations in mind, the overall lightning protection concept on the ET was re-examined.

First, except for the lightning rod, the ET is not required to be designed to take the full return stroke (200 kA), see Figures 2 and 4, but only the restrike (50 kA).

Second, the ET will not be struck while on the launch pad since it is within the cone of protection of the lightning protection system of the launch tower. It will only be struck when it clears the tower and is moving at 64 feet/second. The strike would be to a moving, not a static vehicle!

With these more realistic requirements (50 KA restrike and a moving vehicle) efforts were directed toward a more practical approach to the area of TPS needing protection. The general protection scheme now recommended is four conductive strips (paint) extending from the base of the lightning rod aft. One of these four strips would be connected to the oxygen pressurization line where the line enters the nose cap (see Figure 5). The width, frequency, and method of strip attachment to structure, thickness, etc. has still to be resolved.

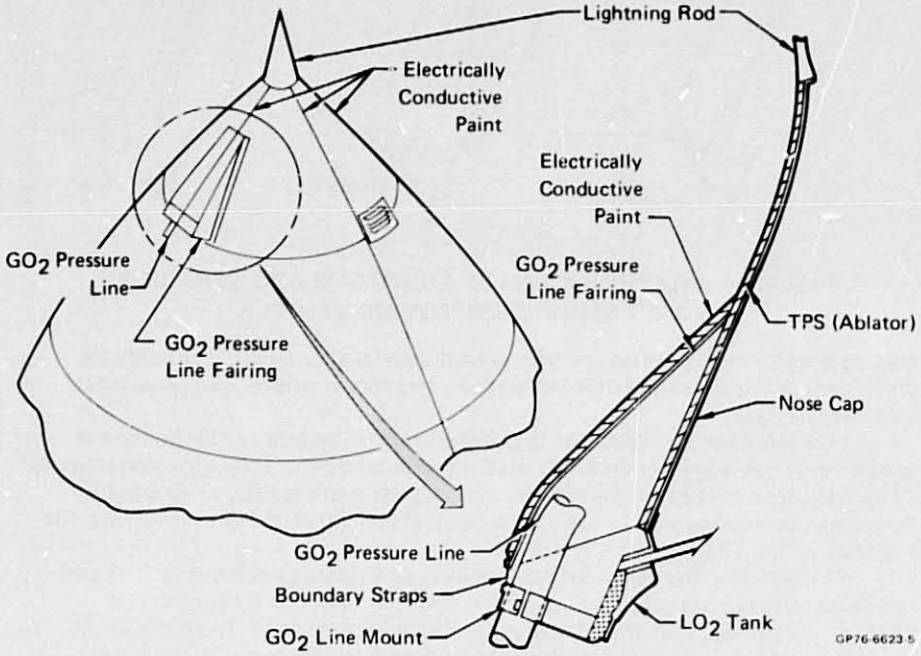

FIGURE 5 – LIGHTNING PROTECTION SYSTEM FOR SHUTTLE EXTERNAL TANKS

Test Panel Design and Construction

Resistivity, adhesion, and TPS compatibility tests were conducted by Martin Marietta Corporation on a number of materials. These tests resulted in narrowing the field to four candidate coatings: one low-resistance silver-filled (Electrodag 504), two intermediate-resistance carbon or graphite-filled (Electrodag 501 and Eccocoat SEC), and one high-resistance carbon-filled (Dynalog 305). Both Electrodag 504 and 501 use a MEK solvent while Eccocoat SEC and Dynalog 305 use water as a solvent.

Fourteen panels were supplied by Martin Marietta Corporation for lightning tests at McDonnell Aircraft Lightning Laboratory and are described in Table 1. Each panel consisted of an .20 cm thick (.080 inch) slightly curved aluminum plate 83 x 111 cm (36 inches by 44 inches) covered with approximately 2.5 to 3.7 cm (1 to 1.5 inches) of Thermal Protection System (TPS) sprayed-on foam (CPR 421) covered in its entirety with FRL seal coat. A strip of electrically conductive paint approximately 10 cm (4 inches) wide was sprayed the length of the panel over the centerline of the foam and contacted the metal substrate at both ends.

TABLE 1 – LIGHTNING TEST PANELS

Conductive Strip			
Martin Marietta Part Number	**Thickness**	**Color**	**Type**
079#1	0.025 cm (10 mil)	Black	Eccocoat SEC
079#2	0.025 cm	Black	Eccocoat SEC
080#1	0.025 cm	Black	Dynaloy 305
080#2	0.025 cm	Black	Dynaloy 305
089#1	0.025 cm	Black	Electrodag 501
089#2	0.025 cm	Black	Electrodag 501
090#1	0.0051 cm (2 mil)	Silver	Electrodag 504
090#2	0.0051 cm	Silver	Electrodag 504
099#1	0.051 cm (20 mil)	Black	Eccocoat SEC
099#2	0.051 cm	Black	Eccocoat SEC
100#1	0.051 cm	Black	Dynaloy 305
100#2	0.051 cm	Black	Dynaloy 305
109#1	0.051 cm	Black	Electrodag 501
109#2	0.051 cm	Black	Electrodag 501

GP76 6623 13

Lightni..g Test Setup

The lightning test setup provided a means of generating the pertinent test conditions which were discussed in the lightning threat section, as well as the necessary instrumentation for verifying compliance of the various parameters. The test setup provided for a high-current arc to be struck to the test panel and for the arc to be blown by a 3 meter per second (10 feet/second) windstream. A simplified block diagram of the test setup is shown in Figure 6 and a view of the test setup is shown in Figure 7. The various portions of the test setup are further described in the following paragraphs.

The 3 meters per second wind velocity was provided by a motor driven centrifugal blower. The high velocity flow normally produced by this type blower was greatly attenuated and smoothed by a stilling chamber equipped with high density screens. The output from the stilling chamber was then ducted over the strike region on the panel. The duct was constructed of non-metallic materials (plexiglas and fiberglass with nylon screws) so as not to influence arc behavior. The test panel itself acted as the floor of the wind tunnel. The air velocity was measured at many points throughout the duct and beyond and found to be very uniform.

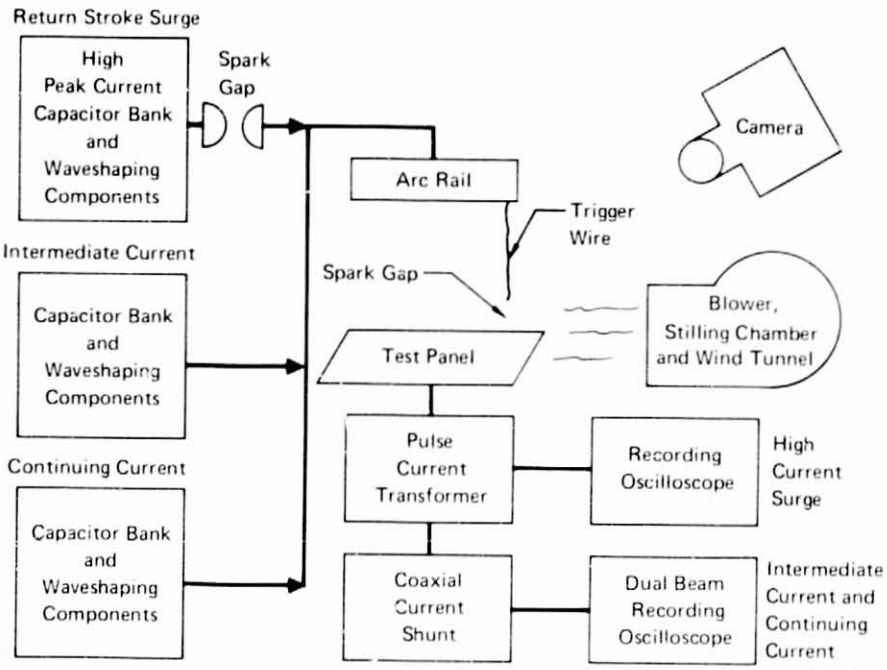

FIGURE 6 – TEST SETUP – SIMPLIFIED BLOCK DIAGRAM

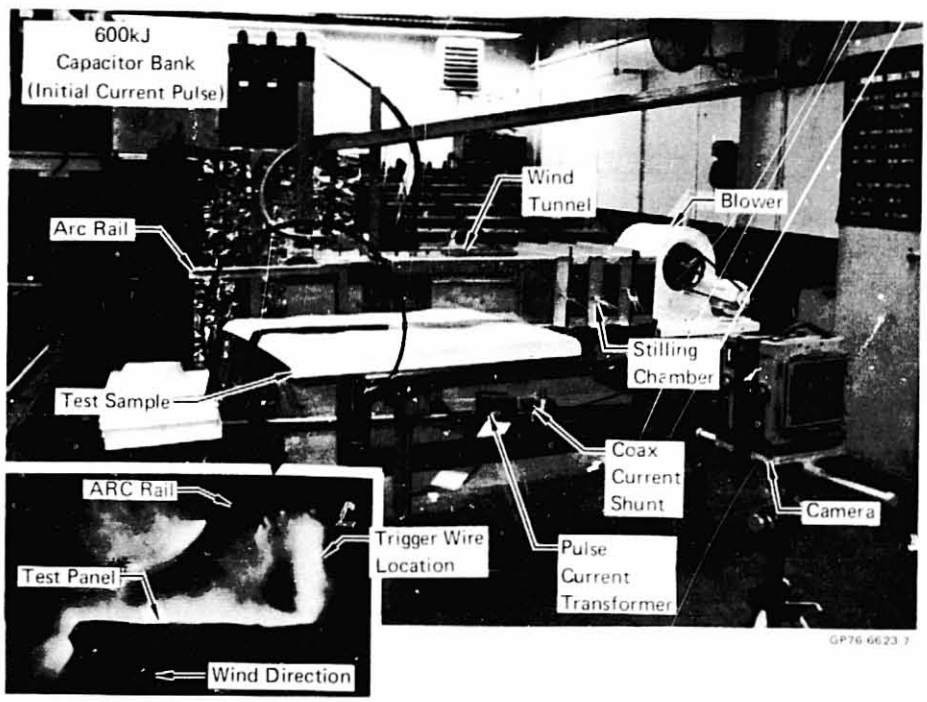

FIGURE 7 – LIGHTNING TEST SETUP

The test panel was placed at the exit of the stilling chamber but isolated from it by a 10 cm wide piece of fiberglass so as to keep the metal of the test panel isolated from the stilling chamber. The lower edges of the plexiglas on the sides of the tunnel were allowed to rest directly on the TPS of the test panel. The test panel was electrically grounded at the metal tab at the end of the panel. The overhead rail electrode which allowed the arc channel to move with the air stream was mounted 8 inches above the test panel as shown in Figure 7.

Referring to the second return stroke portion of the waveform shown in Figure 2, it is difficult to realize the large differences in both time and amplitude of the various portions of the waveform because neither axis is drawn to scale. To provide the complete second return stroke current requires either one large versatile lightning generator or multiple generators connected together to provide a continuous waveform. This test requirement had never been imposed prior to this test. In fact, the original MCAIR 600 kJ lightning generator was upgraded to a 1 MJ capacity to meet this test requirement. The return stroke surge was provided by the 600 kJ capacitor bank and waveshaping components and the output voltage for this portion was approximately 75 kV. The return stroke intermediate current and return stroke continuing current were supplied by 90 kJ and 390 kJ capacitor banks respectively, along with their associated isolation and waveshaping components. The 90 kJ and 390 kJ banks were operated at approximately 11 kV so that a 25 cm (10 inch) arc length could readily be maintained. An overall view showing the relationship of the test setup to the various capacitor banks is shown in Figure 8.

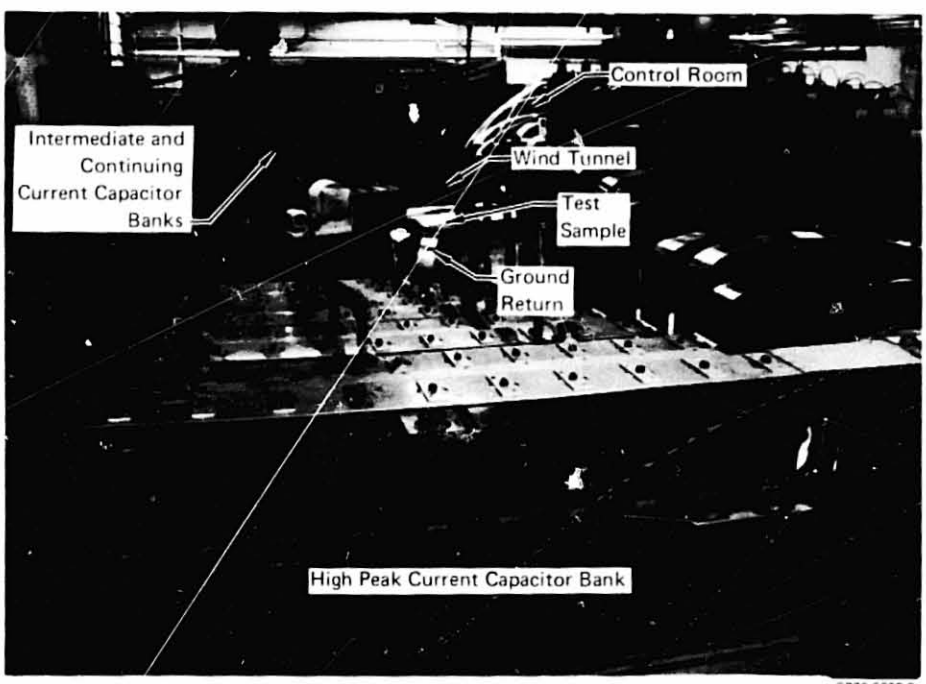

FIGURE 8 – OVERALL VIEW OF TEST SETUP

The output from the 1 MJ lightning generator was connected to the arc rail above the test panel as shown in Figure 7. A 0.32 gage copper wire was attached to the arc rail at the wind tunnel exit and extended to within 2.5 cm (1 inch) of the paint strip on the test panel as shown in Figure 9. A nylon cord was used to maintain the position of the lower portion of the wire when the blower was on and prior to the initiation of the lightning strike. The arc initiator wire was used to insure arc attachment to the paint near the central portion of the panel. When the arc is initiated, the wire immediately vaporizes to form the continuation of the arc from the overhead rail to the test panel. The arc is then blown by the windstream away from the tunnel exit as the various capacitor banks continue to dump thru the arc path to the test panel. By terminating the trigger wire above the panel, the arc channel at the surface of the panel is less likely to be affected by metal vapor ions, leading to a more realistic swept strike behavior. Initially the panels were positioned under the trigger wire so that the shortest electrical path thru the paint to the substrate was upstream (inside the wind tunnel). But because of damage occurring inside the wind tunnel which may affect test results, succeeding tests were conducted with the shortest electrical distance outside the wind tunnel.

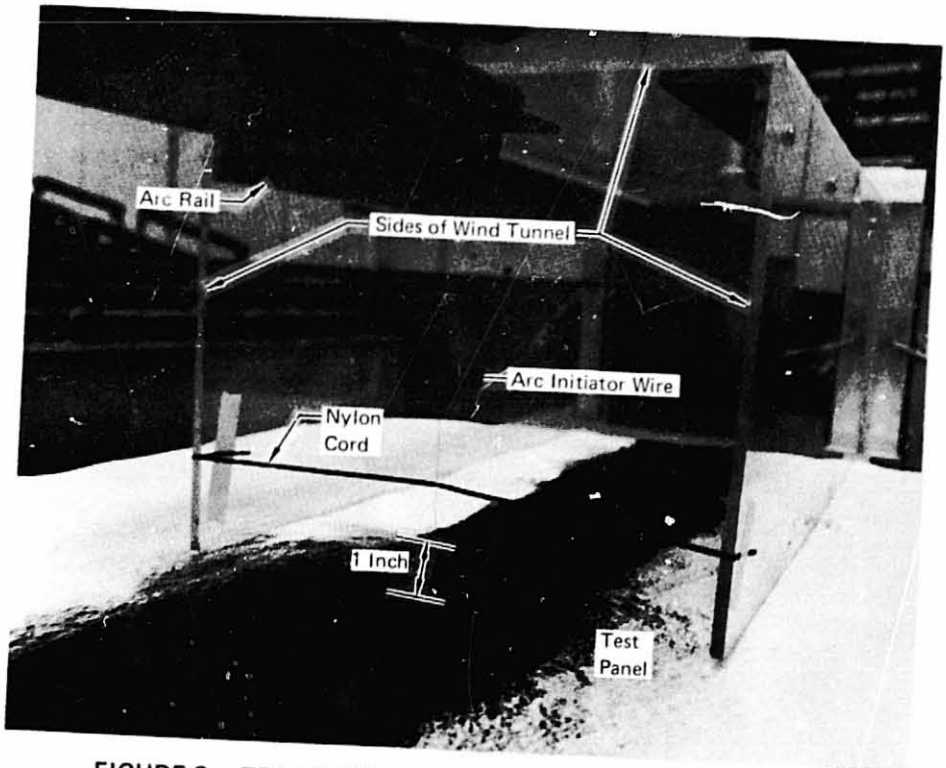

FIGURE 9 – TEST PANEL INSTALLATION IN WIND TUNNEL
(Prior to Test)

Because the various portions of the complete lightning current waveform vary widely in both magnitude and time, several different instruments were required to accurately record all phases. In addition, all instrumentation was electrically isolated to prevent erroneous readings because of ground loops. The return stroke surge current was measured using a Pearson wide band pulse current transformer and monitored on a Tektronix 485 oscilliscope. The intermediate current and continuing current portions of the lightning waveform were measured using a T&M Research Company coaxial current shunt. These two portions were recorded on the two different sweeps of a dual beam Tektronix 555 Oscilloscope. Each beam was separately driven with different vertical amplitudes and time bases. All three time bases were triggered simulataneously. A comparison of the NASA simplified idealized 2nd return stroke waveform and the various portions of the actual typical test waveform are shown in Figure 10. It should be noted that the idealized model waveform is not to scale either vertically or horizontally whereas the oscilloscope waveforms are linear on both axes. Close examination of the intermediate current and continuing current oscilloscope waveforms reveals the corresponding points on the two traces.

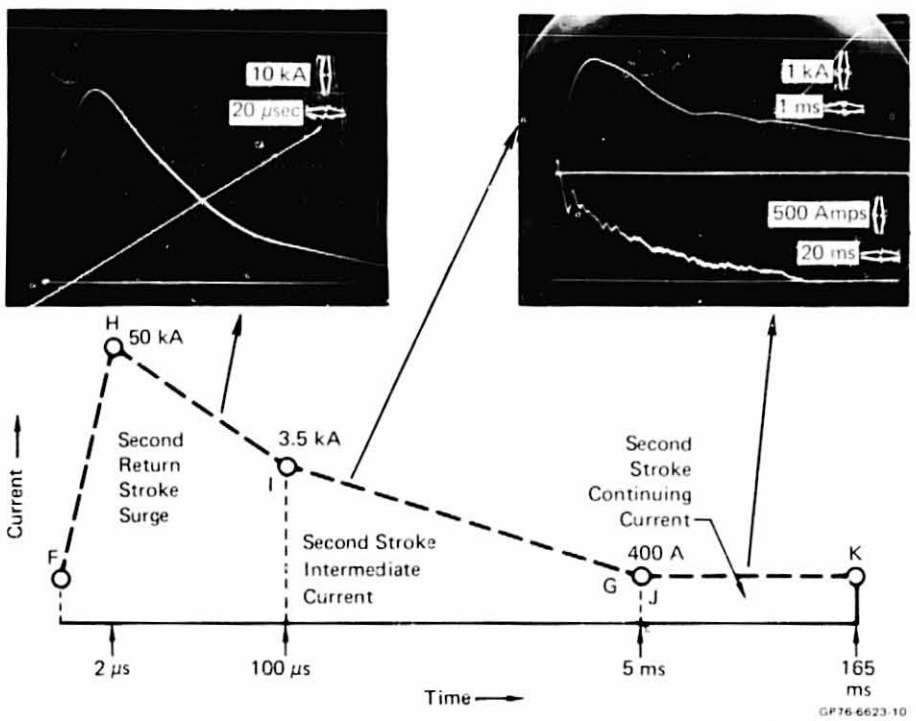

FIGURE 10 – COMPARISON OF NASA WAVEFORM AND ACTUAL TEST WAVEFORM

Still cameras equipped with filters were used to photograph the arc on Polaroid film. The optical filters greatly attenuated the arc brillance, allowing good optical definition of the main arc movement, but it masked out lower luminance activity. The cameras were opened prior to the test and remained open during the entire test. The tests were also visually monitored.

Test Procedure

In general, each test panel was mounted in the test setup and subjected to the lightning current shown in Figure 10 unless noted otherwise in the Test Results. Photos and current waveforms were taken during the strikes. Some panels were struck more than once to note damage progression.

Test Results and Discussion

Each of the panels was subjected to the lightning current waveform shown in Figure 10. Note that both amplitude and time scales are non-linear in this figure. The results of these simulated lightning strikes are tabulated in Table 2 and photos of all tests panels were taken. A typical tested panel is shown in Figure 11. Damage to this panel after several repeated strikes is shown in Figure 12. In general, the panels having relatively low electrical resistance paint were tested sucessfully, whereas those having a high resistance received only a portion or none of the intended lightning current. The eletrical resistance of the conductive strips typically increased as a result of the lightning strike; some panels only showed slight increases in resistance whereas the very low resistance paints increased more than three orders of magnitude. On some panels, the reasons for the increase was obviously erosion or cracking in the conductive paint, but on other panels, the reasons were not readily apparent.

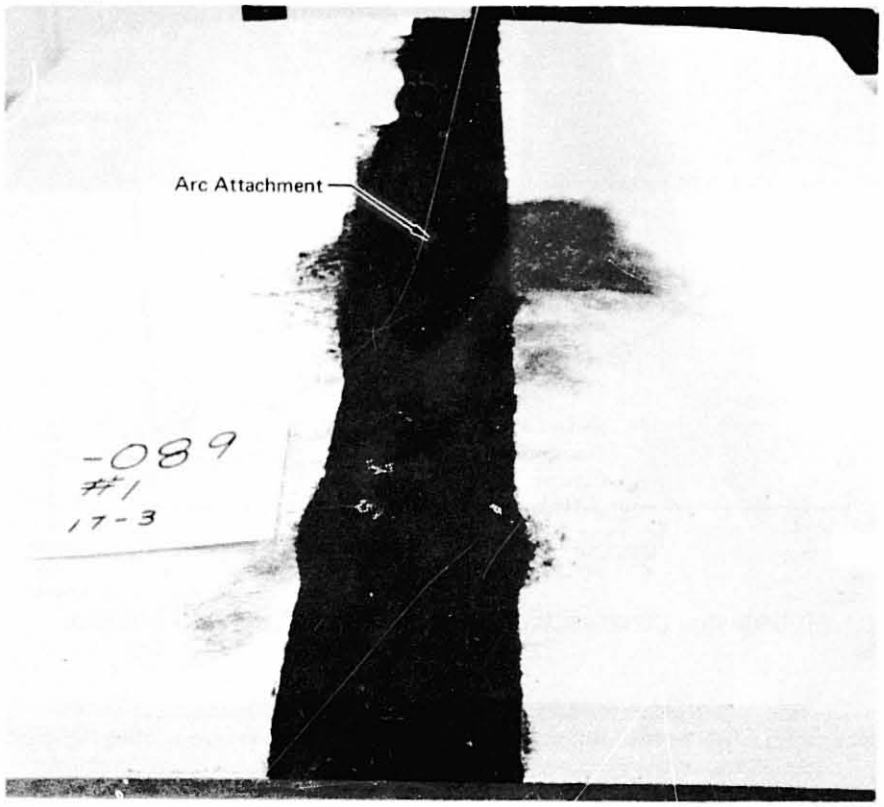

GP76-6623-11

FIGURE 11 – PANEL 089 AFTER FIRST LIGHTNING TEST

TABLE 2 – TEST RESULTS

Panel #	Res Before	Res After	Notes:
090 #2	0.32Ω	33kΩ	Discolored paint, removed quarter size hole or paint and CPR 421 at strike point; removed paint and CPR 421 at edge of panel inside wind tunnel; conductive path severed at opposite end of panel. (Shortest electrical path inside wind tunnel).
079 #1	135Ω	19Ω	No damage at strike point; track visible in paint. Removed paint and CPR 421 at edge of panel inside wind tunnel. Conductive path severed at opposite end of panel (cracked at CPR 421 seam). (Shortest electrical path inside wind tunnel.)
099 #1	60Ω	178Ω	No damage at strike point; some cracking in paint at CPR 421 seams at downwind end of panel; some aluminum burned away at paint attachment to aluminum.
080 #1	25.2kΩ	35.4kΩ	Small amount of current into panel; burned 2.5 cm (1") off end of trigger wire. Slight burn marks at end of panel; no other visible damage.
080 #1	35.4kΩ	35.4kΩ	No current to panel; trigger wire 1.3 cm off panel – no damage. Camera lens opening increased
089 #1	204Ω	220Ω	Prefired while charging capacitor banks. Trigger wire 1.3 cm off panel. No visible damage; visible arc path in paint.
089 #2	194Ω	210Ω	No damage to conductive paint or CPR 421. Some aluminum burned at downwind end at paint/ aluminum interface.
109 #1	82Ω	85.6Ω	No damage to conductive paint or CPR 421 Aluminum panel edge burned.
109 #2	91.4Ω	95.3Ω	No damage to conductive paint or CPR 421. Aluminum burned at edge of paint/aluminum interface.
079 #2	140Ω	174Ω	No damage at initiation point. Dime size chips of paint removed 25 cm aft of strike at edge of paint. Cracking in paint at edge of panel. Aluminum panel burned in several places at or near paint/aluminum interface.
090 #1	0.26Ω	Open	Quarter sized divot of paint and CPR 421 removed at strike point. Paint discolor in both directions from strike. Aluminum burned at downwind end at paint/aluminum interface.

GP76-6623-14

TABLE 2 – TEST RESULTS (Cont)

Panel #	Res. Before	Res. After	Notes:
080 #2	22kΩ	28.4kΩ	Only small amount of current into panel no visible damage to panel. Burned 2.5 cm off end of trigger wire.
100 #1	5.7kΩ	5.7kΩ	Would not fire to test panel. Trigger wire intact.
100 #1	5.7kΩ	8.55kΩ	Decreased trigger wire gap to 1.3 cm off panel. Two explosive sounds approx. 1/2 second apart. Flame burned briefly at trailing edge of panel. No damage to panel at strike; cracks and burned paint at edge of panel. Several burned aluminum spots at end of panel.
100 #2	6.2kΩ	11kΩ	Some current into panel but not enough to melt trigger wire. No damage at strike Arc tracks and some charring at end of panel.
079 #2	171Ω	251Ω	Second test of this panel. Paint and CPR 421 coming loose at strike point. Several square inches of paint and CRP 421 removed aft of strike; cracking and peeling of paint at trailing edge.
089 #1	220Ω	232Ω	Second test on this panel. Dime size divot removed few inches from strike point, additional cracking halfway to trailing edge; paint chipping and cracking at trailing edge of CPR 421. Panel generally still good.
089 #1	232Ω	256Ω	Third test on this panel. Additional cracking and material removal at same locations as observed on previous shot. Panel still appears in reasonable shape.
089 #1	256Ω	457Ω	Fourth test on this panel. 7.6 cm (3") diameter hole blown in CPR 421 and 0.48 cm (3/16") diameter hole melted thru aluminum. This hole is approximately 10 cm aft of strike point. See Figure 12.
099 #2	55.4Ω	2.8kΩ	No damage at strike point or along top of panel. Crack in paint at top forward edge of panel upwind end. Crack in paint at trailing edge at junction of two layers of CPR 421.

GP76-6623-15

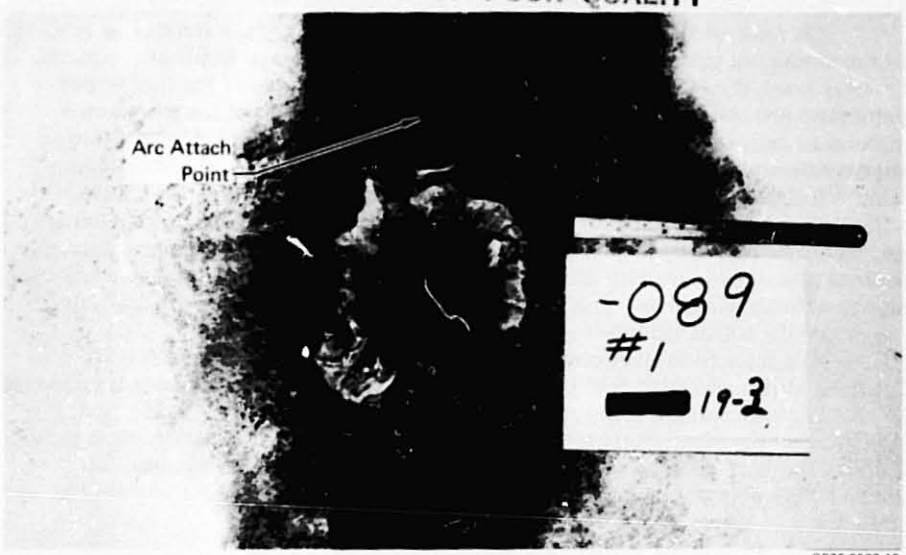

GP76-6623-12

FIGURE 12 – PANEL 089 AFTER FOURTH LIGHTNING TEST

In general, it appears that the Electrodag 501 and Eccocoat SEC painted panels survived the lightning strikes the best. The low resistance silver-filled paint (Electrodag 504) performed less effectively than the moderate resistance paints because more of the current was carried by the paint rather than the ionized air channel above the paint. Consequently, the paint strip essentially exploded causing some damage to the surface of the TPS.

As a result of these tests, it appears that the initial current into the various paint strips locally heats a conductive path in the paint to the vaporization point and then the majority of the lightning current is conducted in the ionized gases above the paint. This condition is verified because the magnitude of the lightning current was relatively independent of the electrical resistance of the paint up to a certain value. The lightning current would not establish an ionized path in the panels utilizing the high resistance paints, i.e., the initial current into the test panel was limited by the high resistance of the paint and the available output voltage. For example, Panel 080 No. 1 had an initial resistance of 25KΩ, thus the maximum initial current into the paint would be limited to approximately 75 kV/25KΩ = 3 amperes. Apparently three amperes were not sufficient to vaporize the paint. However, it should be noted that the high resistance paints appear to be more easily degraded by current flow as evidenced on some tests; the current into the paint strip, although not sufficient to vaporize very thin (32 ga) copper wire, caused a large resistance change. The conclusion that most of the lightning current is conducted in the ionized gases above the paint is also indicated by the fact that Panels 090 No. 2 and 079 No. 1 suffered severe damage only in the confined areas at the end of the panel inside of and butted to the wind tunnel. The explosive pressures in the gases probably caused the damage to occur to the TPS.

On most of the panels which appeared to test properly, a burning or eroding of the aluminum substrate occurred at the trailing edge (down wind) of the panel. In some cases, the burning occurred some distance to the side of the conductive paint strip attachment to the aluminum substrate. Inspection of the still photos appears to indicate the arc on the upper rail probably was not moving at the wind tunnel velocity 3 meters per second as is commonly seen in similar tests at higher wind velocities. Photographs similar to that shown in Figure 7 indicate that in addition to the many secondary attachments along the path length that a final arc appears to be established from the arc rail to the trailing edge of the panel thru the ionized plasma produced by the exploding paints rather than the original arc moving slowly with the air stream. This cannot be verified at this time because high-speed movies of the actual arc travel were not taken.

The tests reveal that certain of the tested paints would survive several lightning strikes provided that the attachment to the aluminum substrate is improved so that explosive pressures are not allowed to occur in these areas. In addition, it is obvious that the most severe test of the paint system is the high peak current pulse and not the later continuing current. Therefore, if a portion of the continuing current were diverted, the difference in the results of the test would probably be negligible.

Conclusions and Recommendations

Based upon the results of these tests, it is concluded that 10 cm (4 inch) wide, 0.25 or 0.51 cm (10 or 20 mil) thick coatings of Eccocoat SEC or Electrodag 501 could be used as lightning diverters over CPR 421 Thermal Protection System (TPS) material providing that adequate techniques for the attachment of the paints to a substrate material can be demonstrated.

It is recommended that additional design and testing be accomplished to determine the maximum allowable distance between attachment points (grounding points) and the method of attachment to the substrate. This test essentially demonstrated the capacity of the conductive strip to conduct the high-current pulse without damaging the TPS. Additional tests and/or analyses are needed to evaluate the stress on the TPS resulting from inductive and resistive voltage drops along realistic lengths of diverter strips.

REFERENCES

[1] *"Simulated Lightning Test, Shuttle .03 Scale Model", McDonnell Douglas Corporation, Report No. MDC A4155*

[2] *"Space Shuttle Program Lightning Protection Criteria Document," JSC-07636, Revision A, November 4, 1975.*

[3] *"Lightning", by M. A. Uman, McGraw Hill, New York, 1969.*

[4] *"A Ground-Lightning Environment for Engineering Usage", by N. Cianos and E.T. Pierce, Stanford Research Institute Technical Report 1, SRI Project 1834, August 1972.*

P24

N79-19037

Paper No. 28

THE PHYSICS OF GRIDDED AND CONDUCTIVE COATED DIELECTRICS FOR SPACECRAFT

E. C. Okress, Dr., *Consultant, The Plaza 6H, The Parkway at 18th St., Philadelphia, Pennsylvania 19103*

ABSTRACT

Theoretical aspects of electrostatic control and design of gridded and conductive film bonded polymers, for spacecraft Thermo-optical control blankets are considered. Brief commentaries relative to the salient features of the primarily developed facility for and characterization of said polymers is also considered.

INTRODUCTION

Absence of electrically conducting grid or transparent semi-conducting coating on typical spacecraft dielectrics (e.g., polymers such as Teflon and Kapton, which are utilized for the outermost dielectric of Thermo-optical control blankets, etc.), limits the electron irradiated dielectric's rate of relieving charge (e.g., by secondary electron emission, photo-electron emission, surface and volume leakage currents and charge spreading) before ultimately step-wise transition to electric and thermal breakdown occur, or as soon as the charging rate exceeds the charge dissipation rate so that the resulting normal and tangential electric potentials attain the electric breakdown potential or total voltage in the medium.

Charge leakage mechanisms of solid dielectrics are enhanced by induced conductivities, due to electron bombardment (EBC), spreading potential (tangential edge electric field of charge layer) and normal electric field. In the case of highly porous or fiber cloth and even compact dielectrics, all comprising micropores, charge leakage mechanisms also include, in the first two cases, field enhanced internal secondary electron emission, (provided the corresponding yield is greater than unity at low electron energy), leading to self-sustained micropore electron emission under certain conditions (aside from impact ionization) [1]. In the case of compact dielectrics, electron avalanche in the micropores and Malter emission from their apertures and/or electron avalanche in the conductron band by impact ionization occur. At 30nA/cm^2/sec., charging rate, the magnitude of the residing charge and said charge dissipation mechanisms of the dielectric must be such that electric breakdown threshold voltage is not attained.

For transparent semi-conducting coating on said typical dielectrics, this means substantially less than $10^{12}\ \Omega$cm or more specifically the order of $10^{9}\ \Omega$cm and preferrably less resistivity is required. The coating thickness (resistance) and volume resistivity must satisfy the required discharge current capacity, without undue heating, and still satisfy tolerable requirements of the spacecraft Thermo-optical control blanket, etc.

For electrical conducting grids on said typical dielectrics, the pitch must be such that not only must the residing charge be properly subdivided, to limit the charge accumulation and hence energy of a possible electric or thermal breakdown discharge, but more preferrably the grid pitch should be so related to the propagation velocity of the electron avalanche, originating at the center of a window pane of the grid, such that step-wise transition to electric or thermal breakdown is aborted. The cross-section of the filaments of the grid must be adequate to avoid electric breakdown and satisfy the conduction current capacity of the grid, without undue heating, and limit optical screening by the grid so as still satisfy the requirements of the spacecraft's Thermooptical control blanket, etc.

Degradative electron irradiation etching reveals various micron size structures attributed to processing and molecular orientation of the polymer film (e.g., etched parallel stretch lines occur in one-way stretched polymer films, while lamellate brick-wall, not grid, structures occur in two-way stretched polymer film). The etched regions are characterized by treeing discharges. Said etching increases the surface energy of the polymer by breaking bonds at the surface layer (i.e., of a few microns depth). The degree of increased surface energy, by said means, is not comparable with that afforded by alternate gaseous (e.g., oxygen) discharge (e.g., $61° \pm 7°$ to $31° \pm 4°$ contact angle), which functions by displacing atoms of one kind by those of another to a significant degree (e.g., an atom of one kind per several atoms of another) at the surface layer. The intensity of said etching increases with exposure time to the electron irradiation, since the dependence of moles of absorbed molecules takes time to diffuse into the polymer. Apparently large (micron-size) regular structure, composed of long period spatially ordered volumes (500-1000 Å.D) of highly ordered molecular groups with rheological mobility, representing distribution of strain due to fabrication stresses, is built into anisotropically stretched polymer film. Correlation of physical properties (e.g., % elongation tenacity, tear, modulus etc.) with said structural size of brick pattern is apparently indicated, especially in the size range of 1 to 100u.

REDUCED CHARGE CHARACTERISTICS OF DIELECTRICS & SEMI-CONDUCTORS

A threshold criterion for charge storage and leakage as a function of the resistivity of a dielectric may be defined. Surface resistivity is usually a dominant factor, and it may be modified as the situation may warrant. The residual charge on the surface of a dielectric may be limited, aside from secondary electron and photoelectric emissions, by electric [3] or thermal [3] discharges in ambient residual gas, due to normal outgassing, especially from electron and/or ion bombardment heating, and/or by ionization irradiation and in vacuum by microthermionic and field emissions, spreading potential [4] and total voltage [5].

Reduced charge, σ/ε', defined by the ratio of charge density, σ, to (real) dielectric constant, ε', becomes invariant, at and in excess of a specific resistivity, ρ. However, in the event that the resistivity is such that said reduced charge is markedly reduced, the charging is also reduced, due to leakage. The threshold criterion of charge storage and charge leakage asserts itself at and below about $\rho = 10^{12}\Omega$cm. It is a step function of reduced charge, σ/ε', versus resistivity, ρ, [6]. The resulting resistivity demarcation, between dielectrics and semi-conductors, may serve as a threshold criterion for significant charge leakage or charge storage. Exceptions do occur, the most conspicuous of which is vinyl polymer of methyl-methocrylate (i.e., Perspex or Plexiglass or Lucite), having a resistivity $\rho \simeq 10^{15}\Omega$cm, but which nevertheless affords relatively negligible charging! Residual charge on the dielectric of resistivity $\rho >> 10^{12}\Omega$cm, is independent of the dielectric resistivity whenever, normally, limited in ambient residual gas electric discharges, as previously mentioned.

The field just outside a localized charge on the surface of an dielectric tends to zero as the dielectric constant, ε', approaches infinity, in contrast to that of a metal's $4\pi\sigma$, since the charge distribution, for a dielectric is impossible for a metal. In the case of a semi-conductor, if the residual lifetime of a charge is short relative to the relaxation time for redistribution of charge, then the semi-conductor will act like an insulator; otherwise, if the residual lifetime is sufficiently long, for a stable configuration of charge formation, then that semi-conductor will act as a metal, provided that the size of the material is not comparable with the thickness of the surface skin or layer within which the charge is accommodated. In other words, the cardinal parameter which characterizes an insulator is the time or relaxation time-constant, for charge transfer, $\tau = \varepsilon'/\sigma_c$ sec., where ε denotes the permittivity of the dielectric (i.e., $\varepsilon = \varepsilon'\varepsilon_o$, F/m, where ε', denotes the real dielectric constant or real permittivity or simply dielectric constant and $\varepsilon_o = 8.85 \times 10^{-12}$, F/m denotes the permittivity of space) and σ_c denotes the electric conductivity, mho/m. The effect of the (real) dielectric

constant, ε', of a dielectric in reducing the electric field, E, just outside the charged surface with charge density, σ, is illustrated by the relation, $E = 2\pi\sigma[2/(1 + \varepsilon')]$.

Whenever the magnitude of the localized charge densities become such that the normal component of electric field to the surface becomes sufficient to evoke field emission (i.e., 10^6 to 10^7 V/cm), then at the edges of the charged area, the electric field parallel to the surface, becomes of comparable magnitude. Such tangential electric fields create enhanced dielectric surface conductivity, thus permitting the charge to rapidly spread over much larger areas, so as to promote stability against electric or thermal discharge, before stray ion incidence; I.e., the spreading of the surface charge leaves an overall surface density smaller than that required for electric or thermal discharge, before stray ion incidence. The spreading of the surface charge leaves an overall surface density smaller than that required for electric or thermal discharge, by a factor denoted by the ratio of the original charged area, prior to said electric field induced conductivity, to the final spreading charged area attained.

The decay of surface charge on dielectrics is determined by the electron (or hole) conduction in the dielectrics. The degree of retention of surface charge on dielectric surface is a function of its carrier mobilities, such that decreasing the temperature means decreasing the carrier mobilities and hence increasing ability of charge retentation. Hence, low temperatures means extremely low carrier mobility and hence high resistivity of dielectrics [6]. Furthermore, the heating of most organic, in contrast to inorganic, polymer dielectrics, even in vacuum, may cause surface oxidation and hence significant change of its properties (e.g., surface resistivity, electric strength, etc.).

Surface charges reside in various energy levels, some of which render charge mobility, while others do not. Unavailability of an occupation level induces the charge to create its own level by decending into its self-generated potential well, due to its own image in the dielectric surface. A charged dielectric, in principle, ceases to be a dielectric insulator. When electrons enter a dielectric, its electron traps become charged such that their resulting potential energy barriers stop further electrons from entering the conduction band, thus accounting for the high resistivity of dielectric insulators. Absence of freely or loosely bound mobile electrons in dielectrics is also attributed to their transparency.

CONSIDERATIONS PERTINENT TO CHARGE CONTROL WITH CONDUCTIVE COATING AND GRID BONDED POLYMERS

The quiet time ambient environment is characterized by essentially low density (e.g., ~1/cm^3), low temperature (e.g., ~10^4°K) hydrogen plasma. During geomagnetic substorms, the said spacecraft environment plasma at synchronous altitude depends substantially on local and universal time variations, during the midnight to dawn sector. The low energy plasma component decreases by 1 to 2 orders of magnitude and a hot plasma (e.g., T_e ~ 10 keV, T_p ~ 2-6 T_e of ambient density of 1/cm^3) surrounds the spacecraft, with rapid time varying parameters. Although a portion of the trapped hot (e.g., >1 MeV) environment electrons occur at synchronous altitudes, these irradiations (e.g., ~10^6 electrons/cm^2/sec - omnidirectional) apparently do not contribute significantly to the spacecraft charging problem.

Since, during severe charging events, the incident ion or proton current may be a significant portion of the incident electron current (e.g., ~10% [7]), the proton induced secondary current, I_{ps}, is therefore significant and ought not be ignored, since the proton (exterior) scattering electron emission yield, $\delta_{ps}(E) > \delta_s(E)$, between 10 to 20 keV, at which incident electron and proton irradiations are maxima. During quiet synchronous altitude sunlit environment, the secondary electron current, $I_{see} << I_{pe}$. However, during severe charging events (substorms) $I_{see} \approx I_{pe}$, due to the primary electron irradiation current rising by about two orders of magnitude.

Whenever the spacecraft is in the said (hot) plasma environment, its potential is a function of whether its photoemissive yield (i.e., in sunlight) is significant. If so, the said potential is substantially controlled by the I_{pe} and I_{pE} relationship and thus significantly reduced, though of significant residual (negative) magnitude [7] (e.g., hectovolts). Without the (hot) plasma environment, I_{pE} dominates, if the photoemission yield is significant, and the resulting potential accrues from I_{pE} ~ 0. Without sunlight or with insignificant photoemission yield, the spacecraft charges negatively until its potential (e.g., > -10 kV) significantly reduces I_{pe}. This potential should be distinguished from that of the sticking potential, V_s, of the dielectric surface, subjected to electron (and ion or proton) irradiation from the plasma. At about 1 keV, the secondary electron emission yield, δ_{see}, and the stopping power, dE/dx, are comparable, i.e., δ_{see} ~ dE/dx and dE/dx ~ ℓn E/E. So, δ_{see} is put in the approximate energy-independent form [8]: δ_{see}/dE/dx, which typically vary between ~0.015 to ~0.025 1/MeV-cm^2/g.

The coupling of insulated surfaces, in close proximity to the external environment is via the net charge on these surfaces rather than the differential charge. An inhomogeneous potential distribution surrounds the spacecraft, due to differential

charging. This follows from the fact that the spacecraft surfaces comprise a variety of materials with various electrical characteristics. Hence; dominant local current variations prevail and the various components of the spacecraft accumulate charge at various rates causing large voltages. Such differentially charged components in close proximity establish large electric fields and can lead to electric breakdown, externally and internally, whether in darkness or in sunlit shadows on the spacecraft. Such electrostatic discharge phenomena besides causing EMI, also degrades the spacecraft dielectrics, by tracking, causing carbonization of polymers and so altering their thermo-optical properties and so disturbing the thermal balance of the spacecraft. Even in sunlight, the dielectrics of the spacecraft beyond the terminator can accumulate large [7] negative potentials, provided that the charging time is small relative to the rotation period of the spacecraft.

Besides the differential charged components, as causes of electric discharges, there are the internal dielectric causes, for while charge deposition in dielectrics charges them, energy deposition causes ionization, inducing either: (1) transient conductivity (e.g., bombardment induced conductivity (BIC), which is electronic (EBC) and/or ionic; or (2) dielectric deterioration, due to the Thomas effect [9], for significant secondary electron emission and/or photoemission coefficients, with electron and/or ion or proton and/or photon irradiation of the dielectric. The transient conductivity relaxes the otherwise charge accumulation, due to irradiation of the dielectrics.

Electron penetration depth in polymers may be derived from analytical approximations or from tables [10]. In any event, this is of the order of 1/10 mil in typical polymers of spacecraft's thermo-optical control blankets (e.g., Kapton) at about 10 kV energy, in contrast to mils thickness of these dielectrics. In contrast, proton penetration may be derived by integration of the stopping power, which data are available [11]. For the said energy, the proton penetration is less than that for the electron.

Dielectric degradation of typical organic, in contrast to inorganic, polymers, utilized for the spacecraft's thermo-optical control blankets, are due essentially to:

1. Charge particle (e.g., electron, proton, etc.) and electromagnetic irradiation etching and aging; and

2. Electrostatic vacuum and residual gaseous discharge phenomena.

The former (i.e. #1) has already been commented upon in this text's INTRODUCTION. The latter, to be commented upon, causes carbonization and blackening of the organic polymer's surfaces, which disturbs the spacecraft's thermo-optical control.

TRANSPARENT SEMICONDUCTING COATING BONDED TO SOLID (OUTERMOST SHEET) DIELECTRIC, OF SPACECRAFT THERMO-OPTICAL CONTROL BLANKETS, ETC.

To mitigate the high resistivity (>> 10^{12} Ωcm) of typical solid sheet dielectrics (e.g., Kapton, Teflon), utilized for the outermost sheet of spacecraft thermo-optical control blankets, etc., transparent semiconducting coating may be bonded to the surface of such dielectrics, thus affording:

1. Complete coverage of sufficiently low resistivity (<< 10^{9} Ωcm) and sufficiently high current capacity coating, bonded to said high resistivity dielectric, in order to dissipate to grounding terminals, the residing charge, due to the incident electron irradiation, even in the event that the secondary electron and/or photo-electric yields of the said coating are negligible.

2. Negligible optical screening or shielding, due to absence of opaque metallic grid, described elsewhere in this text.

Specifically binary anion - deficient oxides (e.g., In_2O_3, SnO_2) are optically required, for transparent semiconductor coatings on high resistivity dielectric polymer substrates, for charge control, since their bond gap (~3.5 eV) yields transparent (visible spectrum) coatings, for the outermost dielectric of spacecraft thermo-optic control blankets. The degree of doping controls the transparency beyond the absorption edge of the high transparent region, which decreases with decreasing resistivity of the semiconductor coating.

However, said semiconductors are chemically relatively unstable (i.e., readily oxidized (or reduced) since the free energies of oxide formation for SnO_2 and In_2O_3 at 500°K are -114 and -123 kcal/mole, respectively [12]. Furthermore, the host oxides are very hydroscopic (e.g., In_2O_3 decomposes partially into $In(OH)_3$ at <150°C, which in turn decomposes to InOOH at 200°C, all of higher resistivities than the simple oxide. In the presence of moisture, single phase In_2O_3 prevails at 375°C only [13]. Also SnO_2 forms readily hydrates of SnO and SnO_2 [14], all at higher resistivities than the simple oxide, of which the most stable is $SnO_2 \cdot H_2O$ [15] of higher resistivity than the simple oxide. Relative to temperature stability, Sn doped In_2O_3 coating by e.g., chemical vapor deposition [16,17] or vacuum evaporation [16,17] (as indicated for plastic or polymer substrates on account of temperature considerations) is satisfactory, as is the hardness, which is a function of the SnO_2 content. The composition of the transparent binary oxides (e.g., SnO_2: In_2O_3), for relatively low temperature deposition required on a polymer (e.g., Kapton, Teflon) substrate, results in a relatively amorphous

structure, which is not at all as critical in every chemical respect, including the effect of the substrate on which the coatings are deposited, even though the said polymer substrates provide more pollution of copious mobile ions, than even glasses, which otherwise would diffuse into the transparent semiconductor binary oxides and inadvertently interstitially and/or substitutionally dope them at the normally much higher deposition temperature. Whether a dopant is effective normally as a source of charge carriers in a structured binary transparent semiconductor, depends upon whether its ionic size is sufficiently small, for a substitutional site, regardless of whether compound formation or solid solution prevails. Dopants are selected empirically since equilibrium phase diagrams for many binary anion-deficient oxides are not available [18]. Even in the ideal case, mixing equations for complex permittivities are much more difficult to solve in the equilibrium state, let alone for the nonequilibrium (reaction) state. Even in the equilibrium state, the results are already so complex that only qualitative properties accrue and these are of questionable practical merit even qualitatively, let alone as a quantitative guide, although some generalities do accrue [19,20]. Hence, resort to empirical mixing techniques prevail [16,21]. Nonstoichiometric In_2O_3 and SnO_2 semiconductors, due to oxygen vacancies, are relatively unstable without doping for donor or acceptor states. In the case of In_2O_3, the Sn atom dopant is utilized, which displaces the In atoms in the lattice to yield free electrons to the conduction band, on account of their greater valence. The optimum doping is much lower for higher deposition temperature (of the substrate) than for lower deposition temperature, though other factors of the deposition kinetics, determine the ratio of active to inactive dopant sites, created oxygen vacancies, etc. The optimum doping for sputtered oxides (and for reactive sputtering of In-Sn alloy) is about 20 mole % Sn in the binary oxide, SnO_2: In_2O_3, transparent semiconductor. The optimum doping for chemical vapor deposition is less than that, for the former deposition processes [16].

The surface resistivity of 20 mole % SnO_2: In_2O_3 coatings [21] (e.g., 1000 Å thick) vary typically between >2 and >10 KΩ/□, for <10 to >30 mole % SnO_2: In_2O_3. The corresponding volume resistivity varies between 600 μΩcm, to >3500 μΩcm, as deposited, for ~1000 Å to >2000 Å coating thickness. For thicker coating, the surface resistivity decreases radically, approaching an asymptote e.g., of the order of <50 Ω/□ as deposited [21] at and beyond 2000 Å thickness. The radical variation of surface and bulk resistivity with said coating thicknesses from ~1000 Å to > 2000 Å is practically inconsequencial, with respect to charging control considerations and even Joule heating considerations, since these resistivities are so much lower than the derived maximum of $<10^9$ Ωcm, as discussed elsewhere in this text. Consequences of an electrical double layer, implied by Coehn's law [22] at the boundary, between said transparent semiconducting coating bonded to said typical polymers, has not been considered

in this text, neither has it been referred to in the literature.

For any semiconductor, if the residual lifetime of charge is short relative to the relaxation time for redistribution of charge, then the semiconductor will act like an insulator; otherwise, if the residual lifetime is sufficiently long, for a stable configuration of charge formation, then that semiconductor will act as a metal, provided that the size of the material is not comparable with the thickness of the surface layer within which the charge is accommodated. In other words, the cardinal parameter which characterizes an insulator is the time constant or relaxation time constant, $\tau = \varepsilon/\sigma_{cc}$ sec, for charge transfer, where ε denotes the permittivity of the dielectric (i.e., $\varepsilon = \varepsilon'\varepsilon_o$, F/m, where ε' denotes the real dielectric constant or real permittivity or simply dielectric constant, $\varepsilon_o = 8.85 \times 10^{-12}$ F/m, denotes the permittivity of space, and σ denotes the electric conductivity, mho/m. The initial requirement to satisfy the resistivity of a dielectric for charge control is based on determining the ratio of reduced charge, σ/ε'm, for the candidate dielectrics [23]. Reduced charge storage for candidate dielectrics denotes the initiation of charge leakage, whenever this ratio exceeds unity.

Since said polymer dielectrics exceed the threshold of 10^{12} Ωcm, by a significant margin, charge storage on the surface will be limited by electric discharge in any residual gas, (e.g., during spacecraft outgasing by induced ionization from incident radiation)or by enhanced surface conduction by electron irradiation (EBC), or by spreading potential (i.e., tangential electric field at the edge of a charge path), which may approach in magnitude that of the normal electric field of the residing charge to abort step-wise transition to electric and/or thermal breakdown.

Therefore, resistivities of polymer substrates (e.g., Kapton, Teflon) have to be shunted to the degree that the exit charge (rates) and the charge leakage (rates) equate to the incident charge (rate), without encountering electric or thermal breakdown, V_c, as represented by the following equality:

$$I_{pe} + I_{pp} + I_{re} = -(I_{pE} + I_{see} + I_{ps} + I_{sl} + I_{vl})$$

where I_{pe} denotes the primary electron current, due to the plasma environment of the spacecraft;

I_{pp} denotes the primary ion or proton current, due to the plasma environment of the spacecraft;

I_{pE} denotes the exterior photoelectron current;

I_{re} denotes the redistributed electron current or incident electron backscatter current;

I_{see} denotes the secondary electron emission current;

I_{ps} denotes the proton exterior scattering electron current (i.e., due to I_{pp});

I_{sl} denotes the surface dielectric leakage current;

I_{vl} denotes the volume dielectric leakage current.

From the foregoing considerations, the foregoing equality may be satisfied without encountering step-wise transition to electric and thermal breakdown, due to differential charged surface components as well as within the polymers themselves, subject to environmental life test.

Pertinent data relative to the experimental aspect of transparent semiconductor coatings bonded to typical polymer substrates designed for spacecraft thermo-optical control blankets, etc., was presented elsewhere [24]

The foregoing current equality may be simulated in the laboratory to the degree warranted. For reasons to be briefly commented upon in the last section of this text, the said simulation is limited to currents, I_{pe}, I_{re}, I_{see}, I_{sl}, I_{vl}. Hence, an electron flood beam bombards said target polymer specimen in a vacuum chamber, as illustrated.

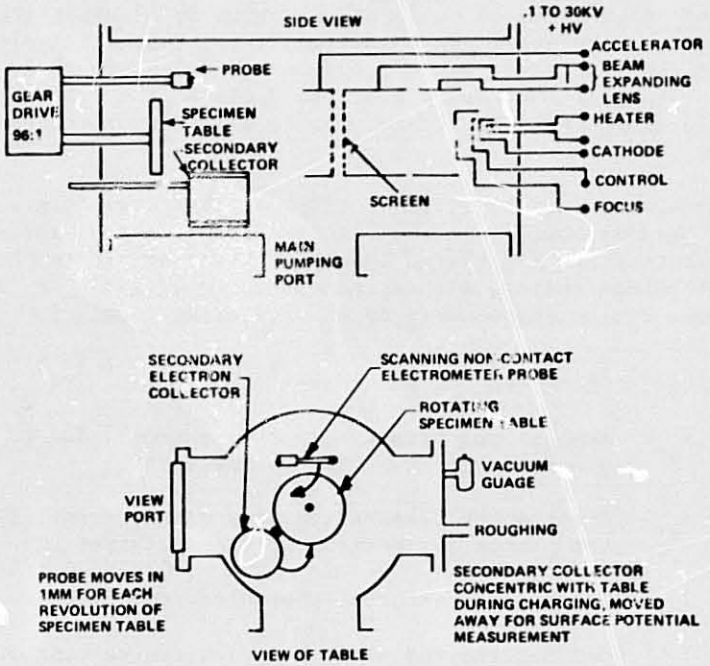

METALLIC GRID BONDED TO SOLID (OUTERMOST SHEET) DIELECTRIC OF SPACECRAFT THERMO-OPTICAL CONTROL BLANKETS

To mitigate to a substantial degree the deleterious effects of the high resistivity ($>10^{12}\ \Omega$cm) typical solid sheet dielectrics (e.g. Kapton, Teflon) which are utilized for the outer layer of spacecraft thermo-optical control blankets, an electrically conductive grid may be bonded to the outermost surface of such dielectrics so as to:

1. Subdivide the dielectric surface into proper and identical pane area. Thereby, the residing charge, due to electron irradiation, and hence associated potential energy available for step-wise transition to electric and/or thermal breakdown, along the surface (i.e., tracking) and/or through the dielectric, is limited so as tominimize or avoid failure of the dielectric.

2. Ensure that the pitch of the grid is so related to the propagation velocity of an electron avalanche, originating on a pane so that step-wise transition to electric and/or thermal breakdown along and/or through the dielectric is aborted. The cross-section of the filaments of the grid must be of adequate current capacity to avoid undue heating, as well as maintain structural integrity of the grid and afford sufficient total pane area for required thermo-optical control. Bonding of an electrically conducting grid, onto the typical outermost sheet polymer (e.g., Kapton, Teflon) of spacecraft thermal control blankets, requires consideration of:

    1. Induced conductivities accruing from simulated electron irradiation (i.e., 0 to ~30 keV energy and ~30 nA/cm^2, flux) experienced by spacecraft, at synchronous orbit or altitude, from the enveloping plasma during the midnight to dawn sectors' geomagnetic substorm environment comprise:

        1.1 Bombardment induced conductivity (BIC).

            1.1.1 Electron bombardment induced conductivity (EBC).

        1.2 Photo-induced conductivity (PC), only during sunlet periods.

        1.3 Normal electric field induced conductivity - the Rasch-Hinrichsen Relation.

1. Cont'd

1.4 Malter avalanche interstice conductivity (MAC)

1.5 Spreading potential induced conductivity.

2. Dielectric deterioration, due to the:

2.1 Internal (surface layer) deterioration, due to the Thomas Effect [9], for significant secondary electron emission and/or photo-emission yields on electron and/or proton and/or photon irradiation of said polymers.

2.2 External surface dielectric deterioration, due to tracking phenomena

2.3 Volume dielectric deterioration, due to:

2.3.1 Treeing, coring, etc. in contaminated polymers, due to discharges in microscopic voids, cracks, fibers, pits, etc., resulting in carbonization thereof.

2.3.2 Ultra-violet and/or soft x-rays and charged particle bombardment erosion and chemical processes and products (e.g. ozone, nitric acid) of residual ionized gases.

Evaluation of the various cited induced conductivities, with respect to the said polymers, indicates that the spreading potential is of predominant influence in determining the grid geometry, for the adverse conditions of negligible secondary electron (and/or photoelectric) yield(s), as well as localized circular surface or spot charge on the dielectric, which may have a metal substrate.

The normal and tangential components of the electrostatic potential, due to said spot charge on the dielectric may be derived from classical considerations, [25] using series expansions by the method of images. Results of the necessary numerical integrations for this case of the potential (Green) function for the circular spot charge on the dielectric, on a metal substrate, are available [26]. The essential features of the results of said numerical integrations are:

1. The tangential component of the electric field, E_{11}, (i.e., corresponding to the spreading potential referred to previously), at the edge of the spot charge can become substantial. In fact, it can become

Cont'd
not only of substantial absolute magnitude but comparable to that of the perpendicular component, which is maximum over the center of the spot charge and nearly negligible at the edge of the spot.

2. The electrostatic field is more concentrated near the center of the spot charge and spreads out toward the edge and beyond.

3. Outside the charge spot, where the electrostatic field returns to the backplate, the field is much less, for the charge spot.

4. The negative electrostatic field outside the charge spot is nearly negligible.

5. The electrostatic fields are relatively independent of the dielectric thickness, sufficiently removed from the edge of the charge spot. Near the edge of the charge spot the electrostatic field intensity increases, as the dielectric thickness decreases. For equal charge densities, the electrostatic field near the edge is nearly independent of dielectric thickness, for equal charge density difference; and the electrostatic field, far from the edge of the spot charge, is nearly independent of dielectric thickness, for equal voltage.

The cardinal consideration relates to the tangential electrostatic field, E_{11}, to the dielectric at the edge of the spot charge. That is, at the rim of the spot charge, the parallel electric field component, comparable in magnitude to that of the normal electrostatic field component, $E_{\perp}$, not only enhances the surface conductivity [27, 28] of the dielectric, but permits the charge spot to spread out rapidly (e.g., ten times its original spot diameter) and thereby tends to restore stability against otherwise electric discharge, before arrival of any stray ion. Thereby, a dielectric surface may be charged completely, to grounding terminations, if any, or eventually lead to electric and/or thermal breakdown, for continued charging by incident electron irradiation. Whenever, the dielectric surface is limited by electric discharge, well after the induced surface conduction has equalized the charge distribution, that which is left is an overall surface charge density, less than that for corona breakdown, by a factor determined by the ratio of charging area to total area. A local charge spot or area on a dielectric is more stable than a larger area with the same surface density. Surface charge, with many qualifications, may be limited to the order of 3 keV/

cm^2 by electric discharge in a residual gas, however, attenuated. For a minute (e.g., $<\overline{mm}^2$) spot charge on a dielectric, the limit of the area of the electric field for cumulative ionization, which may occur, increases the electric breakdown, so that higher charge densities will be stable. Still higher charge densities will be supported for brief periods, until a stray ion initiates an electric discharge, limited only by field emission, due to the normal electric field of such higher charge densities when charge spreading ensues. For the maximum normal component of the electric field of 30 kV, a comparable tangential electric field engenders a charge spot rim expansion at a radial tangential velocity $v = 5.93 \times 10^5 (E_{11})^{\frac{1}{2}} = 3.25 \times 10^6$ m/s. The distance covered, $S_d = vt$, where

$$t = (1/5.93 \times 10^5) \int_{y=0}^{y=s} dy \, (E_{yo} + yF)^{\frac{1}{2}} \text{ and } F = E_{11}/s, \text{ V/cm},$$

is equated to the step-wise transition to electric breakdown, t_{SWTB}, threshold of between 10^{-8} to $>10^{-9}$ sec. Hence, the radial distance, S_d, transversed by the rim of the spot charge amounts to 0.325 cm. Hence, the pitch, $p = S_d 2^{\frac{1}{2}}/2$, of a square net or array varies between ~3/32" + ~1", respectively, in vacuum, $<10^{-3}$ T. and ~1" at pd = 4T. mm residual air (spacecraft outgassing). The governing criteria, for the grid filament geometry and cross section are the critical or electric breakdown field or potential or voltage at the grid filaments and the grid or mesh currents to the grounding terminations. Application of the Kilpatrick [29] (empirical) criterion, for vacuum breakdown; the Peek [30] (empirical) critierion and Felsenthal-Proud [31] criterion, for gaseous breakdown; and the Parr-Scarisbrick [32] tracking criterion are considerered elsewhere, [33] for the electrically conductive grid bonded to said typical polymers.

The determined grid parameters bonded to said typical polymers with or without metallic substrate are summarized in the accompanying table:

t_{SWTB}	S_d	p
10^{-9} sec (min.)	0.325 cm	0.229 cm
10^{-8} sec (nominal)	3.25 cm	2.28 cm

Parameter	Vacuum ($<10^{-3}$ T.)	Residual Air (pd=4Tmm)
Lattice Pitch	3/32" to 1"	to 1"
Filament Size	>2 to <10 mils D.	12.6 mils D.
Dielectric Tk.	>3.5 to $<15^+$ mils	1 to <3.5 mils

These results denote order of magnitude anticipated.

The foregoing considerations assume that:

1. The bonding, between the electrically conducting grid and the dielectric is continuous; and that the

2. The grid filaments are continuous (no gaps) and are free of asperity;

Otherwise, the inception of surface discharges may ensue at the gaps and asperities. This prospect is particularly serious in sufficient ambient residual gas $>>10^{-3}$T. (e.g., due to outgassing). Furthermore, require absence of

3. scratches, pits, inclusions (e.g., gas filled voids, fibers, and impurities), on the surface and in the dielectrics (polymers), as they are sources of treeing, coring, tracking, and internal discharges, leading to dielectric deterioration and failure. In the case of voids, for example, some speculative parameters may be illustrated:

Applied electric stress	Permitted air* NTP filled spherical cavities	Permitted discharge magnitude	Probability of potentially dangerous tubular cavities
2 kV/mm.	< 1 mm.	~ 30pC	negligible
4 kV/mm.	< 0.1 mm.	< 0.05 pC	low
>4 kV/mm.	< 0.1 mm.	< 0.05 pC	high

* For lower pressure, discharges occur sonner.

The experimental results of the foregoing grid bonded polymers, for electrostatic discharge control, are presented elsewhere [34].

There is another parameter which may affect the pitch of the lattice or grid pitch, if it is not small relative to the electron Debye length $(\lambda_D)_e = (kT_e/4\ n_e e^2)^{1/2} = 6.9\ (T_e/n_e)^{1/2}$cm. Where ions and electrons are not in thermal equilibrium, the ion Debye length $(\lambda_D)_i$ is slightly different than $(\lambda_D)_e$:

Height, Km. =	100	150	200	400
$(\lambda_D)_e$ cm. =	0.3	0.4	0.5	0.4
$(\lambda_D)_i$ cm. =	0.3	0.3	0.4	0.3

Where t_e, T_e n_e, e denote the Boltzmann's constant, electron temperature, electron concentration and electron charge, respectively.

BRIEF COMMENTARIES RELATIVE TO THE FACILITY FOR AND CHARACTERIZATION OF POLYMERS

The electron irradiated polymer specimen's characterization includes: I. Its VOLTAGE-CURRENT CHARACTERISTICS, comprising dependent variables, (1) surface and volume charging-discharging currents, (2) D.C. (and pulsed) secondary electron emission (SEE) current(s), and (3) the uniform or average primary electron beam current and if desired the former dependent variables (i.e., 1 and 2) normalized with respect to the latter (i.e., 3) , as a function of independent variable, primary electron beam energy or voltage. The SEE collector and backplate potentials, specimen temperature and ambient gas pressure are parameters, with negligible photoelectron current and primary electron beam interception currents or the latter dependent-variable-corrected; II. ELECTROSTATIC DISCHARGE (ESD) PHENOMENOLOGY; and the III. ELECTROSTATIC POTENTIAL OR CHARGE DISTRIBUTION over the electron irradiated specimen's surface. These characterizations are determinable with the aid of the SS-ESD Facility, which essentially comprises a vacuum chamber with flood gun and specimen diagnostic instrumentation and power supplies. The vacuum chamber size is sufficient with large access ports for mounting, dismantling and adjusting spacecraft materials for characterization with electron beam irradiation. A component of the vacuum chamber is the electron flood gun, providing electron irradiation simulation of the space vehicle environment.

Said SS-ESD facility presently does not provide ion or proton irradiation. Although, Knott, et al. [35] have shown that proton irradiation does not significantly affect spacecraft charging periods, about 10%[7] of the incident electron current is attributed to protons. The latter's generated secondary current cannot be ignored. The reason for this assertion is simply because its yield is greater than that for the electrons in the vicinity of 10-20 KEV DC, where the incident electron and photon fluxes are maximum. The resulting difference in yield, enables the photon generated secondary current to be comparable to the electron generated secondary current.

The design of the said flood gun includes an electrostatic, three-element cylindrical lens with a parallel plane grid accelerator section, to assure uniform beam expansion and required electron energy at the spacecraft material in the restricted space of the chamber. Furthermore, control grids may be modulated to simulate the required electron energy and current density and distribution and provide pulsed secondary electron emission yield measurement capability. A wide range of adjustment in electron flux density and energy of the beam is available (e.g., 0 to 30 KVC and 30n A/cm^2 at the spacecraft material on the diagnostic table referred to).

The design of the specimen diagnostic table yields versatility, for the measurement of various electrical properties of spacecraft materials. It consists of an electrically isolated rotatable table for securing spacecraft materials up to about five inches in

diameter. The charging currents flowing along the surface and/or through the specimen may be monitored. A non-contact surface potential probe may be mounted on a movable arm, which is connected through a gear box to the rotating table. The gear ratio is such that for every rotation of the table the probe arm is advanced in millimeter steps, allowing the probe to track the surface of the sample, similar to that of a tone arm which tracks a record on a phonograph. This motion is driven by a DC reversible electric motor, which may be coupled to a resistance commutator for driving one axis of an X-Y recorder. A Monroe model 144 "Isoprobe" electrostatic voltmeter requires their #1009 probe. This is a feed-back electrostatic probe, which has high resolution and is relatively independent of probe-to-surface distance within its operating range. The required electronics incorporates a phase-lock loop amplifier, for the reduction of spurious pick-up and noise. During the electron irradiation, of the sample under test, said probe may be swung completely out of the way so no part of it will shadow the sample, during electron beam irradiation.

A secondary electron emission collector (cylinder) is also part of the diagnostic table assembly. This may be swung in place around the sample during the charging phase. It is used to monitor electrons leaving the surface of the sample. By pulsing the flood gun's electron beam, secondary electron emission yield measurement capability of dielectrics is provided.

Other salient features of the SS-EDS facility include a large viewing port for photographing samples during electron beam irradiation and for observation of electrostatic effects.

The applications of the author's foregoing designed and primarily developed SS-ESD facility, for characterizations of spacecraft materials was presented elsewhere [24], [33], [37]

APOLOGY

Allotted space and time precluded incorporation of the following two of the originally submitted abstract topics, i.e.; 1. Theory of polymer electron irradiation effects and aging, aside from the brief comments made elsewhere [24]; and 2. Theory of D.C. voltage-exponential current threshold characteristic conduction, transversely and longitudinally, between close and loose packed dielectric cylinders (e.g., silica fiber fabric, for which experimental transverse (exponential) electrical resistance data already exists [1,2]).

REFERENCES

[1] W. Viehmann reported (private communication) the earliest transverse D.C. conductivity measurements of silica cloth, used for spacecraft thermo-optical control blankets, by means of a vacuum diode, which he refers to as a "Contactless Method in Vacuo" [2]. His measurements show an exponential characteristic in anode current density as a function of anode voltage at the order of 140 V and a maximum equilibrium charge and associated potential of the order of 180 V. He speculated that this phenomenon for silica fabric "could be due to (internal) secondary electron generation and/or "hole" conduction through the fabric."

[2] W. Viehmann, C. M. Shai and E. L. Sanford. Abstract IV-8, #1555, "Investigation of Conductive Thermal Control Coatings by a Contactless Method in Vacuo." Session IV, Materials Development, Oct. 28, 1976, at The Spacecraft Charging Technology Conference, 27-29 Oct. 1976, U.S. Air Force Academy, Colorado. Proceedings pending.

[3] J. J. O'Dwyer, The Theory of Electrical Conduction and Breakdown in Solid Dielectrics, Ch. 6 and 7, (Clarendon, 1973).

[4] W. R. Harper, Contact and Frictional Electrification, e.g., p. 19, (Oxford, 1967). The mathematical aspect of spreading potential is deferred to Section 5 of this text.

[5] J. G. Trump and R. J. Van deGraff, Jour. Appl. Physics, 18, #3, 327- March 1947.

[6] G. S. Rose, S. G. Ward, Brit. J. Appl. Phys. 8 121-, March '57. D. K. Davies, p.29-,Proc. Static Electrification Conf., May'67. Inst. Phys. Physical Soc. (London, England 1967).

[7] S. E. DeForest, J. Geophys. Res. 79, 651- 1972.

[8] E. A. Burke, J. A. Wall, A. R. Frederickson, IEEE Trans. Nuc. Sci. NS17, 193- 1970.

[9] A. M. Thomas, J. Instn. Elect. Engrs., Pt. II, 91, 549- 1944. Bombarding electrons are trapped at the penetration depth (e.g., to 1/10 mil at 10 kV for Kapton) of the dielectric. When sufficient proton deposition on the surface of the dielectric occurs (or sufficient photoemission or secondary electron emission occurs), these $\pm$ charges cannot be neutralized. This situation may result in sufficiently high electric fields in the dielectric between them reaching intrinsic breakdown strength and hence surface erosion. The Thomas Effect may be mitigated by decreasing the dielectric resistivity, $\rho << 10^{12}\ \Omega$ cm, to at least the electron penetration depth. Further development in ref. [36].

[10] E.g., D.C. Shreve and J.S. Lonergan, Electron Transport and Space Shielding Handbook, NASA CR-SAI 71-559-LJ, 1971.

[11] E.g., T.W. Armstrong and K.C. Chandler, Nuc. Instr. Meth., 113, 313- 1973.

[12] T. B. Reed, Free Energy of Formation of Binary Compounds, (M.I.T. 1971).

[13] R. Roy and M. W. Shafer, J. Phys. Chem. 58, 372- 1954.

[14] R. W. Weast, Ed., Handbook of Chemistry and Physics, 47th Ed. (Chemical Rubber, 1967).

[15] H. F. Mark, J. J. McKetta, Jr., D. F. Othmer, Eds., Encyclopedia of Chemical Technology, 20, 317- (Interscience, 1969).

[16] Various deposition techniques are discussed in the literature e.g., J. L. Vossen, "Transparent Conducting Films," in Physics of Thin Films, G. Haas and R. W. Hoffman; Eds. Vol. 9 (Academic, 1976).

[17] E. Ritter, "Transparent Conductive Coatings", pp. 181 to 200 in Progress in Electro-Optics, E. Camatini, Ed. (Plenum, 1973).

[18] E. M. Levine, C. R. Robbins, and H. F. McMurdie, Phase Diagrams for Ceramists, 1969 Supplement, (American Ceramic Society, 1969).

[19] G. P. DeLoor, Thesis, Leiden, 1956.

[20] R. Mecke and H. Schill, Z. Elektrochem. 57, 270- 1953.

[21] J. L. Vossen, R.C.A. Review 32, 289- June 1971.

[22] L. B. Loeb, Static Electrification, (Springer-Verlag, 1958).

[23] See section entitled "Reduced Charge Characteristic of Dielectrics and Semiconductors," in this text.

[24] L. Amore, A. Eagles, and E. Okress, Paper IV-5, #1435, "Development and Testing of Spacecraft Polymer Materials for Electrostatic Discharge Control," Oct. 28, 1976, Session IV. Materials Development. Spacecraft Charging Technology Conference, 27-28 Oct. 1976, U.S. Air Force Academy, Colorado. Proceedings pending.

[25] W. R. Smythe, Static and Dynamic Electricity, pp. 67-69, 72-76, 182-184, (McGraw-Hill, 1939).

[26] H. E. J. Newgebauer, "Electrostatic Fields of Xerographic Images," in Xerography and Related Processes, J. H. Dessauer and H. E. Clark, Eds. (Focal, 1965).

[27] J. M. Stevels, "The Electrical Properties of Glass," p. 355, Eq. 3.9, in Handbook Der Physik, S. Flügge, Ed., Vol. XX, (Springer-Verlag, 1957).

[28] J. P. Suchet, Electrical Conduction in Solid Materials, Ch. 5, (Pergamon, 1975).

[29] W. D. Kilpatrick, Rev. Scient. Instrum. 28, 824- 1957.

[30] F. W. Peek, Jr., Dielectric Phenomena in High Voltage Engineering, (McGraw-Hill, 1929).

[31] P. Felsenthal and J. M. Proud, Phys. Rev. Jl, 139, 1796- 1965.

[32] D. Parr and R. M. Scarisbrick, Proc. Instn. Elect. Engrs., 112, 1625- 1965.

[33] Reports of Contracts F33615-76-C-5258; F33615-76-C-5075 and F33615-75-C-5267. Available at: Department of the Air Force, Air Force Materials Laboratory (AFSC), Wright - Patterson Air Force Base, Dayton, Ohio, 45433.

[34] Loc. cit. Reference [24] in section entitled "Transparent Semiconducting Coating Bonded to Solid (Outermost Sheet) Dielectric, of Spacecraft Thermal Control Blankets, etc.," of this text.

[35] E. Knott, et al., Planet. Space Sci., 20, #8, 1137- 1972.

[36] A. Meulenberg, Jr., "Evidence For a New Discharge Mechanism For Dielectrics In a Plasma", paper 5A 70, American Geophysical Union, June 16-19, 1975, Washington, D.C.

[37] V.J. Belanger, A.E. Eagles, E.C. Okress, "ESD Environmental Testing facility For Satellite Materials Developed at Geosynchronous Orbit", 9th. Space Simulation Conference, April 26-28, 1977 Los Angeles, California.

D25

N79-19038

Paper No. 29

CANCELLATION OF RESIDUAL SPACECRAFT ACCELERATIONS FOR ZERO-G SPACE PHYSICS EXPERIMENTS

James B. Stephens, *Jet Propulsion Laboratory, California Institute of Technology, Pasadena, California*

ABSTRACT

The Drop Dynamics Module houses an acoustic positioning system which counteracts the effects of small accelerations of a spacecraft and thus allows long-term study of free-floating materials such as liquid drops. The acoustic positioning system provides an acoustic "well" in the center of the experiment chamber. Data collection is by cinematographic photography. The module subsystems are discussed in this paper.

I. INTRODUCTION

The Drop Dynamics Module (DDM) is a Spacelab-compatible acoustic positioning and control system for conducting drop dynamics and physics experiments in the nearly weightless environment of space. The use of acoustics for levitating and manipulating materials counteracts perturbing effects caused by small accelerations of the spacecraft. The system consists basically of a chamber, a drop injector subsystem, an acoustic positioning subsystem, a control subsystem, and a data collection subsystem. The principal means of data collection is by cinematographic cameras. A drop of a selected liquid is positioned in the center of the chamber by forces created by acoustic standing waves. By varying the phase and amplitude of the acoustic waves, the drop can be spun or oscillated up to fission. The module is designed to perform its experiments unattended, except for startup and shutdown events and other unique events requiring the attention of the Spacelab payload specialist.

The major module subsystems are presented in the following discussion.

II. MODULE SUBSYSTEMS

Figure 1 is a functional block diagram of the module, while Figure 2 is an artist's concept of the module in place on Spacelab. The Spacelab-borne subsystems of the module include the acoustic chamber, control electronics, and imaging and data acquisition. The ground-based subsystems include the

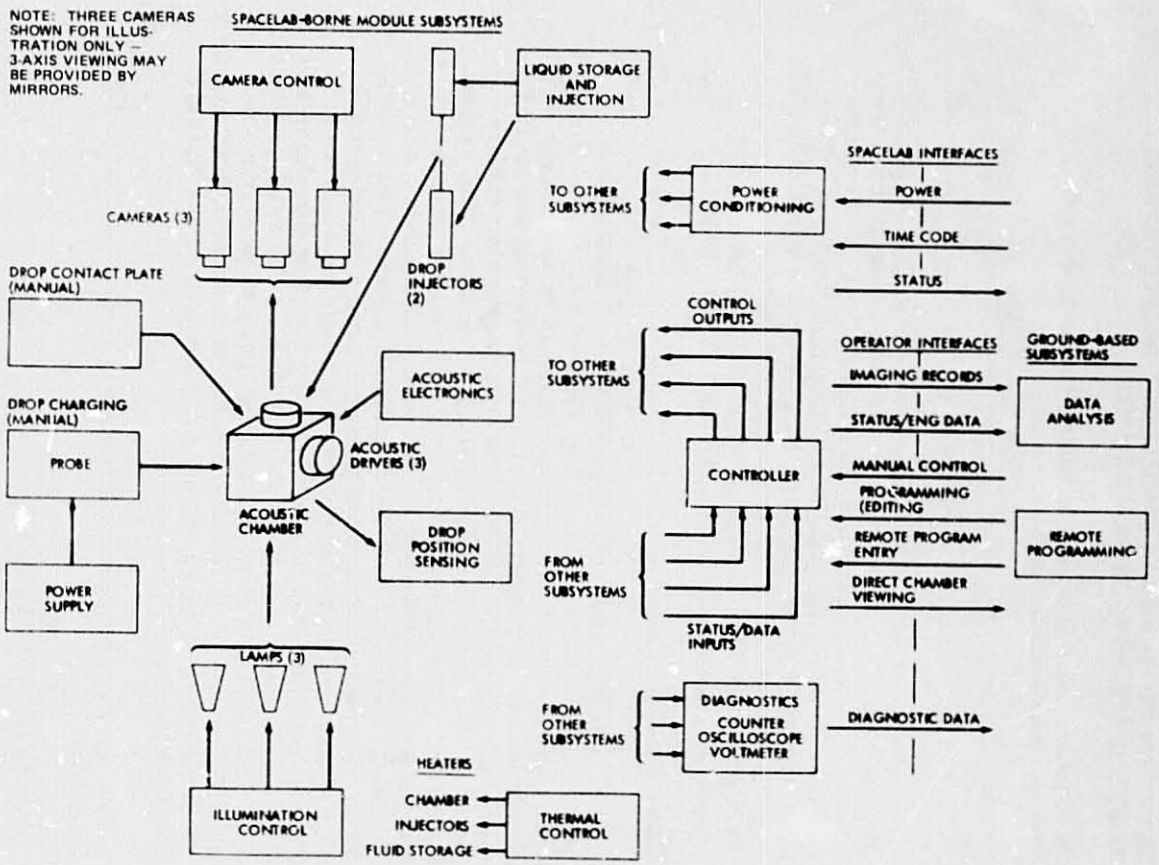

Fig. 1—Drop dynamics module functional block diagram

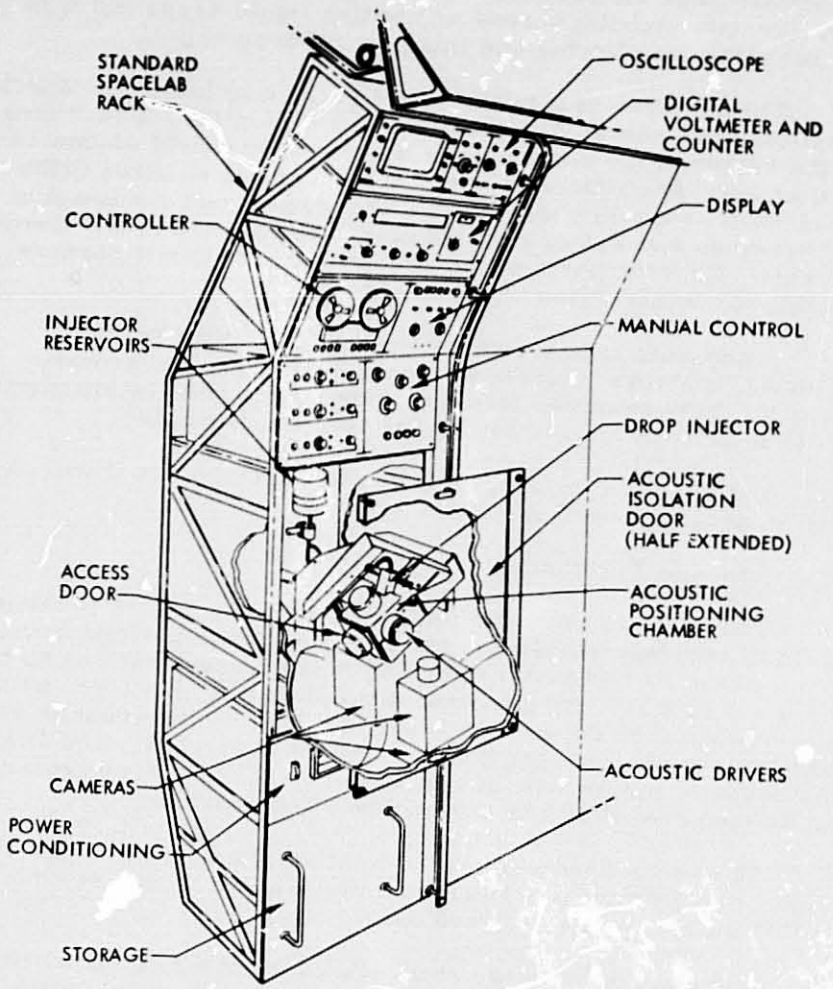

Fig. 2—Spacelab rack subsystem (possible implementation)

necessary hardware and software for generation of automatic sequence programs and for data analysis from the imaging and other data records.

A. Acoustic Chamber

The acoustic chamber is center stage for the experiment activities: it is the resonant cavity which provides the necessary acoustic standing waves to position liquid drops and it is the backdrop for viewing and imaging the drop action.

The chamber is a thick-walled (1.27 cm) lucite rectangular parallelepiped unit (i.d. approximately 15.2 x 15.2 x 16.9 cm). At the center of the chamber the imaging clear field of view is 12 x 12 cm. Acoustic driver ports are located on three orthogonal walls; the other three walls are transparent for imaging and viewing, and one of these is hinged for access to the chamber interior. Injector ports at the center of two opposite corners provide for introduction of the liquid drop.

A separate frame acts as a mount structure for the cameras, mirrors, lights, sensors, injecters, and acoustic drivers. This chamber frame is mounted on retractable support slides to provide access for adjustment and servicing.

The chamber mockup is shown in Figure 3, as it will be used in zero-g aboard KC-135 aircraft.

B. Acoustic Positioning

The DDM will provide sufficient acoustic forces to initially position and maintain the center of a 2.5 cm drop within 3.0 cm of the center of the chamber during module accelerations up to 10^{-2}g. For a 2.5-cm diameter drop of water, this force will be approximately 80 dynes. At 300°K and 1 atm, the acoustic resonant frequencies of these drivers will be 1141, 1141, and 1027 Hz. The acoustic forces will be controlled so that the drop centers (as defined above) within 1.0 minute after injection.

The acoustic power level, relative phase, modulation frequency, modulation amplitude and modulation phase are controlled independently for each axis.

Introduction of phase shift will cause the X-Y signal to rotate about the "Z", or long axis of the chamber, while the torque is controlled by varying either the amplitude or phase. The nominal maximum drop rotation rate will be 12 rad/sec for a 2.5-cm drop, with a controllable angular acceleration of up to 1.0 rad/sec^2. The minimum rate of change of acceleration will be 0.01 rad/sec^3, and the minimum rise time for the torque on the drop will be 0.1 sec. For a 2.5-cm diameter water drop,

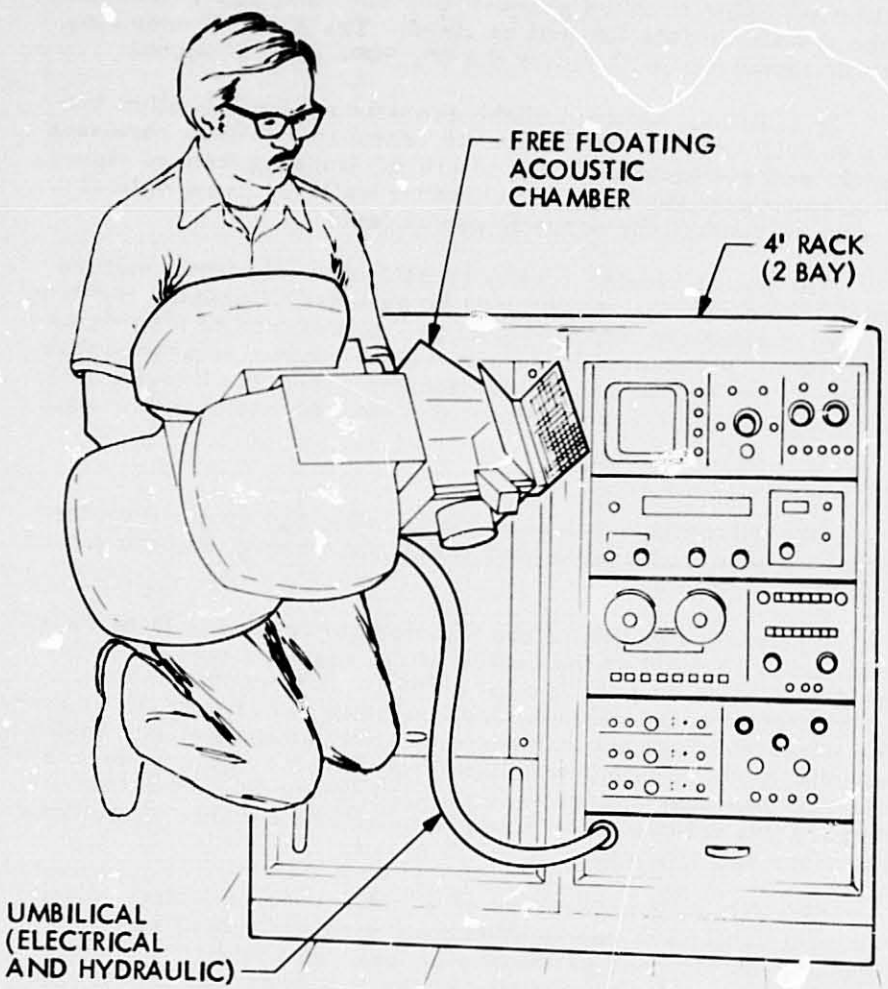

Fig. 3—KC-135 rack subsystem (possible implementation)

the maximum acceleration of 1.0 rad/sec^2 will correspond to a torque of 5.1 dyne-cm.

Modulation of the acoustic signal amplitude alone will cause an oscillation force to be applied to the drop in any or all of the three chamber axes. The nominal drop oscillation stimulus frequencies will be in the range of 0 to 100 Hz, with controllable increase or decrease at a maximum rate of change of 1 Hz/sec. The oscillation signal (acoustic amplitude modulation) will be available in three phases: 0°, 90°, and 180°. The phase of the Z-axis modulation will be fixed. The X and Y axes may each be modulated with either the 0°, 90°, or 180° signal.

In addition, removal of the acoustic power will allow the drop to drift undisturbed within the chamber. A drop centering system will maintain the drop within the imaging field of view and prevent collision with the chamber walls by using optical sensors to control the acoustic power level.

The power levels, sensor location and other parameters of the drop centering system will be selected to prevent the drop from contacting the chamber wall in the presence of a 10^{-2}g acceleration. The centering forces will be limited to assure that the drop does not fission unintentionally within the imaging field of view even if this results in a collision with the chamber wall.

C. Fluid Management

Apart from acoustically manipulating the drop within the chamber, provisions have been made for storing, injecting, and charging the fluids.

The main function of the injector subsystem is to place a drop (up to 10 cm^3) at the center of the chamber with as little residual motion as possible, at a rate of 0.1 - 1.0 cm^3/sec. After injection, the residual drop velocity is 0.5 cm/sec or less. The subsystem can accommodate any nonflammable, non-toxic, reasonably chemically inert liquid which has a vapor pressure of less than one atmosphere at the maximum module operating temperature (55°C). The subsystem will be capable of multiple injections and retrievals of liquid drops

Six different reservoirs of liquid will be provided. Each reservoir will have two flexible plastic tubes (tygon) attached, each with an attached probe (the probes resemble long blunt hypodermic needles). The tips of the injectors will be changed every time the liquid is changed. The injecter mechanisms drive the probes into the center of the chamber where the liquid is released. Once the drop is formed, the probes are abruptly withdrawn from the chamber, leaving the drop in the center.

After injection the drop may be electrically charged or discharged by inserting the charging probe so that it penetrates the drop. The voltage can be manually adjusted, the drop charged, and the probe withdrawn.

The drop may be electrostatically charged to ±1000 volts. The drop charging voltage will be controllable to ±1V up to 100V, and ±5V up to 1000V. The charging mechanism will also be capable of discharging the drop to within 10V of the chamber wall potential. Provision will be made for maintaining the entire interior surface of the chamber at module ground potential during charged drop experiments. This will require the chamber interior to be coated with a conductive material, so that the entire surface is one conducting surface.

D. Viewing and Imaging

The chamber interior can be viewed directly by the operator through the transparent walls. With the chamber in its normal operating position, the entire chamber interior is visible. The direct viewing provision will allow the module operator to operate module controls comfortably while viewing the chamber interior.

For direct viewing, the DDM will provide steady (non-pulsed) illumination of the chamber interior. The intensity and direction of illumination will be sufficient so that a clear (undyed) water drop may be clearly seen against the chamber background, with an apparent drop brightness of at least 200 ft-Lamberts.

The principal means of data collection during the experiments is by three 16 mm cinematographic cameras mounted on three mutually orthogonal sites of the acoustic chamber. Included in the field of view of each camera is an alphanumeric film annotation display and a reseau pattern or grid for geometric calibration of the cameras to an accuracy of 0.02 cm. One camera images the chamber center directly, while the other two image it via mirrors.

The cameras will have a focal length of 25 mm, aperture of f/8, and depth of field 16.09 cm for two views and 17.78 cm for the third view. Practically any high-speed color or black-and-white film is usable.

Imaging will be accomplished so that the size and shape of the drop may be determined to ±0.02 cm. The minimum resolution in the object plane will be 20 cycles/cm (line pair/cm)(When using color film, the imaging resolution requirements are reduced.) Images will be recorded at rates up to 200 per second for each of the three views.

The imaging sample rate (frame rate) will be stable to within ±0.1 frame/sec, and the images of each of the three axes will be synchronized to within ±0.0005 sec of each other and of the module clock.

The illumination subsystem utilizes three strobe lights which are mounted around the acoustic driver ports to illuminate the drop from any of the three orthographic sides opposite the camera imaging ports; i.e., the drop can be front, back or side lit. The light can be diffused or filtered by a coating applied to the chamber wall as desired.

E. Control and Sequencing

The module may be controlled manually by the operator, completely automatically, or in some combination of these modes.

The module basic control functions will be controlled through software programs generated either by the DDM or at remote locations (away from the module). To facilitate remote programming, the program language and memory medium will be compatible with commonly used general purpose computers. The program memory will be non-volatile for the expected duration of a Spacelab mission.

The DDM will provide subroutine capability for programming short, frequently used sequences. Typical sequences which could be stored in subroutines will include the basic rotation and oscillation experiment sequences described in Ref. 1. There will be no limit on the size and number of subroutines other than that imposed by total controller memory capacity. The purpose of the subroutines will be to simplify programming and to allow manual commanding of simple operations. Subroutines will be stored in read-only memories (ROMS) or similar storage media. Subroutines may be accessed either manually or under software control.

F. Data Analysis

The ground-based portion of the DDM will provide support for the reduction and analysis of DDM imaging records and engineering and status data records. The objective of the data analysis will be to convert raw DDM data to a form usable by the science users. Prior to analysis of imaging records, high-quality copies will be made for storage and distribution to users. In general, data analysis will consist of:

1) Formatting and tabulating all module engineering and status data and correlating it to the imaging records

2) Mathematical characterization of drop profiles as a function of time, acoustic power, phase, and modulation frequency

3. Derivation from (2) of drop oscillation resonant frequencies (particularly the fundamental), rotation rates, damping constants, drop radii, and line shapes.

The imaging records will be analyzed by digitizing the coordinates of at least 32 points on the drop profile for a selected set of images (see Ref. 1). In addition the location of tracer particles, if any, will be digitized.

The digitizing of imaging records may be accomplished manually with the assistance of a light table, or automatically. The digital imaging records will be on magnetic tape in a format compatible with standard general-purpose computers.

The DDM will provide software for analysis of the module data records and the digitized imaging records. This software will be written in a commonly used language (such as Fortran).

III. CONCLUSIONS

The design of the module meets the requirements of the baseline experiment proposed by JPL; however, modifications may be made as needed to accommodate other experiments, providing funding is available. The baseline experiments on rotation and oscillation of liquid drops are precursors to future experiments in which the oscillation of rotating drops will be studied. The experiments are also precursors to ones in which the drops are electrically charged, electrically conducting, dielectric, non-Newtonian, or superfluid; and where external fields are applied (electric, magnetic, electromagnetic, acoustic, or thermal). In addition, it is envisaged that multiple drop experiments will be performed in which the interactions of free drops can be observed. These and other studies in basic physics will be greatly aided by the capabilities of the Drop Dynamics Module.

REFERENCES

1. Wang, T. G., Elleman, D. D., and Saffren, M. M., JPL Drop Dynamics Experiment, JPL Document 701-224, 30 July 1975.

2. Drop Dynamics Module Project Plan, JPL Document 701-221, 16 July 1976.

omit

Paper No. 30

UNIQUE TEST FACILITY FOR EVALUATION OF MHD ELECTRODE AND INSULATOR MATERIALS

I. M. Grinberg, R. G. Luce, and A. A. Boiarski, *Battelle's Columbus Laboratories, Columbus, Ohio*

ABSTRACT

The development of central-station, open-cycle, coal-fired MHD power generators depends to a great extent on the ability of the critical electrode and insulator components to perform satisfactorily. The unique performance requirements for the materials must be considered in terms of the long-duration physical, thermal, chemical, and electrical environments in which reliable generator operation must be maintained. Development of electrode and insulator materials requires their evaluation in an environment that closely simulates expected central-station channel operational conditions in order to adequately relate the effects of long-time material exposure with those of high-temperature, seed, coal-slag, and electrical current transfer on critical material properties. Such screening evaluations are difficult to conduct economically under well-characterized controlled conditions in an operational MHD generator. This paper describes a unique MHD test facility which is capable of providing a simulated MHD environment over a broad range of gas temperature, pressure, fuel, electric field, and combustion gas conditions and is well suited for the conduct of materials evaluations.

The test facility utilizes a hybrid electric arc-heated combustion-driven gas supply. The use of electric arc-heated gas in conjunction with combustion-driven flow is shown to provide the flexibility required to independently assess relative effects of the important gas side properties on material performance. It is also shown that the important MHD channel parameters can be independently controlled without application of a magnetic field with application of an applied voltage to provide the desired current density in electrode materials.

A brief description of each of the components and operational envelope of the overall system is given in terms of the attainable simulated test channel conditions. Conditions achieved in tests recently conducted to evaluate electrode materials used in the UC2 MHD facility are shown. Also included is a brief description of diagnostics used to characterize the gas environment.

D2C

N79-19039

Paper No. 31

APPLICATION OF AN ELECTRON BEAM FACILITY FOR HEAT TRANSFER MEASUREMENTS IN CAPILLARY TUBES

A. R. Lunde and Ted Kramer, *Boeing Aerospace Company, Seattle, Washington*

ABSTRACT

A unique method has been developed for the determination of heat transfer coefficients for water flowing through capillary tubes using a rastered electron beam heater. Heat flux levels of 150 and 500 watts/cm^2 were provided on the top surface of four square tubes. Temperature gradient along the tube length and mass flow rates versus pressure drop were measured.

INTRODUCTION

The objective of this investigation was to provide the information necessary to design a convectively cooled foil window for a high power electron beam gun. A total of three test specimens were fabricated and tested. Testing was performed in the vacuum chamber of an electron beam facility. This facility was developed to provide a capability for vacuum testing materials and heat transfer systems which are exposed to high heat fluxes. The heat flux characteristics of this facility are shown in Figure 1. It can be seen that the range of test conditions extends from approximately 150 w/cm^2 on a 103 cm^2 area to over 10,000 w/cm^2 on an area of 1.5 cm^2.

The test facility is described herein. Descriptions of test articles and test setup are presented and details of heat flux calibration are given. Typical pressure drop and heat transfer results are reported and the results of burnout testing are shown.

ELECTRON BEAM HEATER

The Alloyd manufactured Electron Beam Heater, shown in Figure 2, consists of the electron gun, 15 KW cathode power supply, a 45 cm diameter by 75 cm vacuum chamber, and a 1500 liter/sec. diffusion pumping system. The electron gun is magnetically focused and deflected, and employs bias cup grid control of beam current. An accelerating anode effectively makes operation of the gun

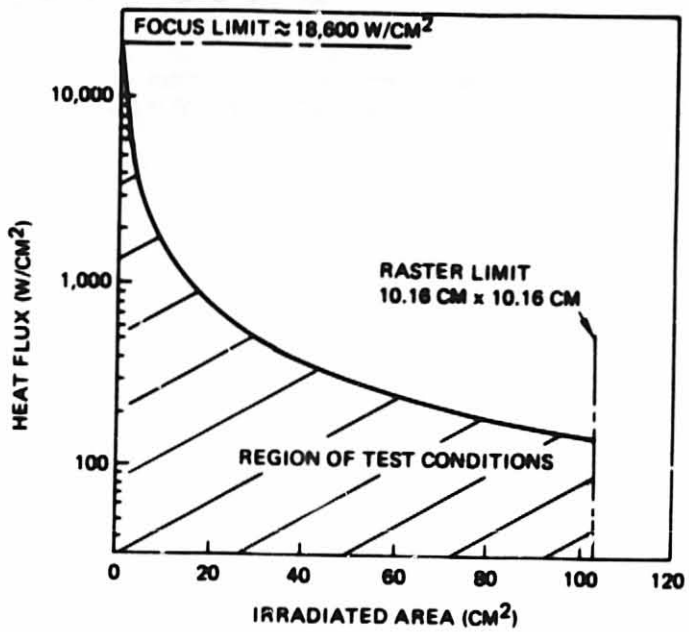

FIGURE 1 TEST CONDITION RANGE

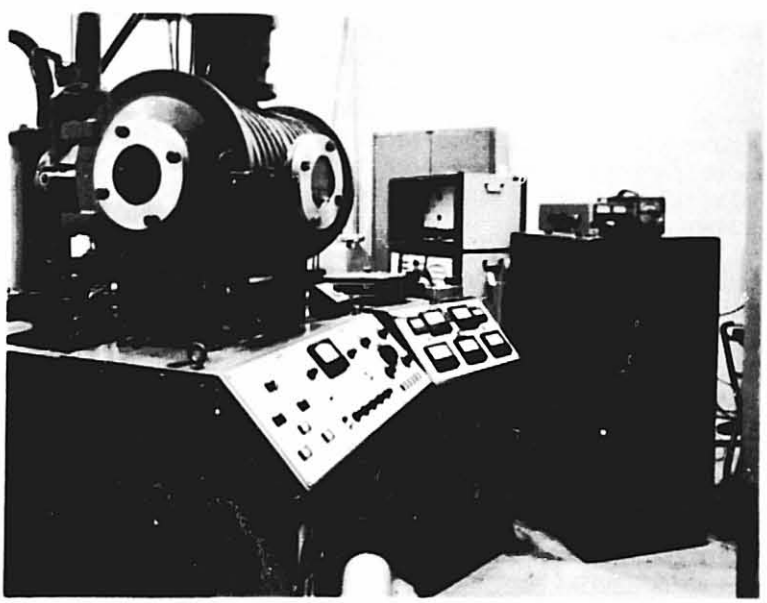

FIGURE 2 E-BEAM TEST FACILITY

independent of target geometry, spacing, and materials. The anode is connected to the system ground, thus focusing operation of the cathode and bias cup structures at high negative potentials. The tantalum ribbon filament cathode is directly heated by 20 to 30 amperes of current from a filament transformer.

The cathode power is provided unfiltered from a three-phase, full wave selenium rectifier bank and three-phase high voltage transformer. Power to the high voltage transformer is varied by a motor driven, three-phase variable auto-transformer connected to the 480 volt line. The auto-transformer drive motor is actuated in either direction by pushbuttons on the control panel.

A symmetrical two-axis stator-wound deflection coil was fabricated and fastened to a mount on the end of the original focus and deflection assembly. Deflection rates up to 120 kilocycles per second were verified. Two identical triangle-wave-form oscillators, power supply, and direct coupled driver amplifiers were designed and built with sweep rates from 10 cps to 100,000 cps. The dynamic deflection system is used for rectangular uniform raster production.

The vacuum system, employing an NRS-HS-6-1500 six inch diffusion pump and a Welch 1397 mechanical pump, is semi-automatic in operation, requiring only pushbutton actuation of all pumps and valves. Interlocks are provided to reduce probability of damage. Pump-down time starting with a hot diffusion pump is approximately 10 minutes.

TEST ARTICLE

A total of three test specimens were fabricated and tested. Each specimen consisted of four parallel water-cooled tubes. The tubes were square in cross section, measuring 0.0635 cm by 0.0635 cm outside dimensions with 0.00889 cm wall thickness. Tube material was 7075 T6 aluminum. The tubes terminated in manifolds instrumented with pressure taps. Tube span between manifolds was approximately 25 cm. The manifolds were supported on a common rigid plate with a support rib located beneath the tubes. The tubes were bonded to phenolic spacer blocks which were, in turn, bonded to the rib to provide dimensional stability during cyclic heating and cooling. Figure 3 shows specimens 1 and 2 which were identical in configuration. The coolant tubes were mounted side by side in these two specimens. The third test specimen was identical to the first two except the coolant tubes were spaced 0.23 cm between centerlines and a 1 mil aluminum foil was bonded with Mithra 200 epoxy to the top surface of the tubes. Figure 4 shows the foil configuration and tube arrangement of the third test specimen.

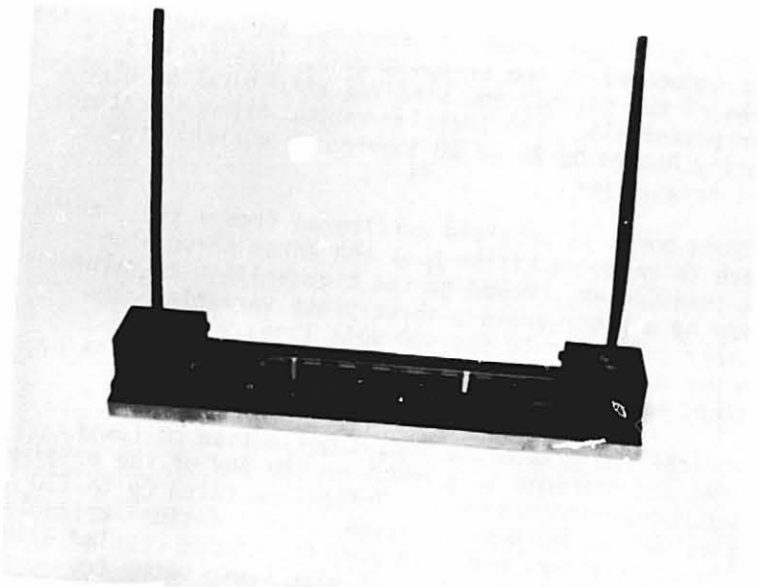

FIGURE 3 TEST SPECIMEN 1 & 2 CONFIGURATION

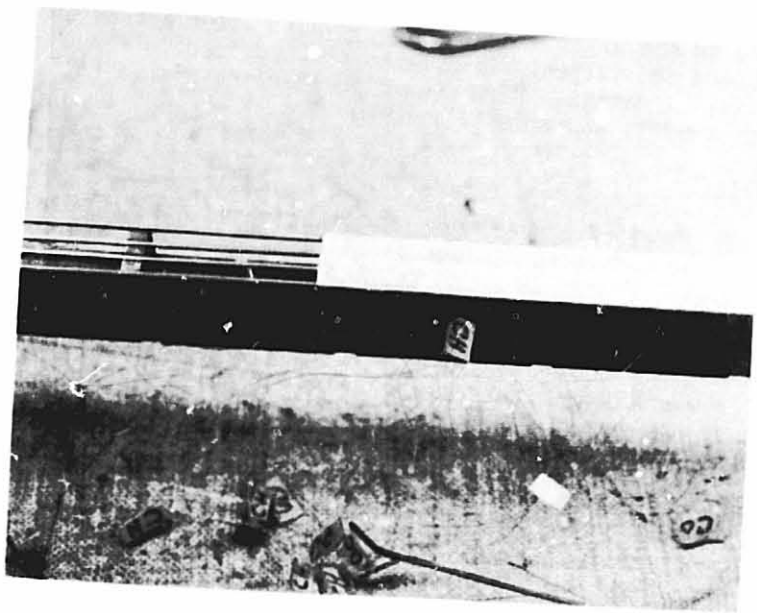

FIGURE 4 TEST SPECIMEN 3

Thermocouples of butt-welded 0.00508 cm chromel-constantan wire were bonded to the underside of the tubes at 2.5 cm increments along the length of the test section. Thermocouples were also bonded to the underside of the foil at a number of axial stations midway between the tubes of specimen three. Additional thermocouples were located on the water lines serving the inlet and outlet manifolds of all test specimens.

TEST CONFIGURATION

The test article was mounted in the vacuum chamber as shown in Figure 5. Water cooled shield plates were aligned along the length of the square tubes to shield the thermocouple leads. A reference calorimeter (Hy-Cal Model C-1312) was mounted adjacent to the test tubes within one of the shield plates. This allowed electron beam flux level to be established prior to irradiating the test tubes. Once irradiance level was established, the electron beam was rastered on to the test tubes for a specific time and then back to the reference calorimeter.

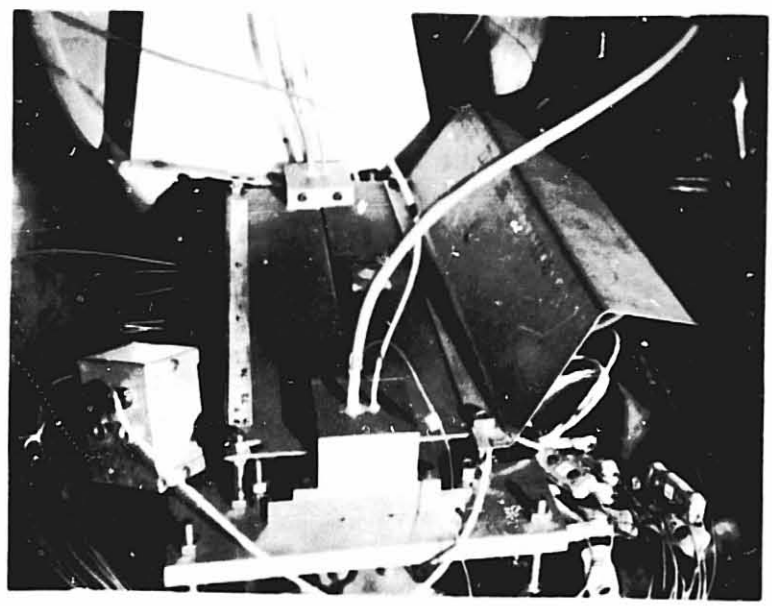

FIGURE 5 TEST ARTICLE MOUNTED IN CHAMBER

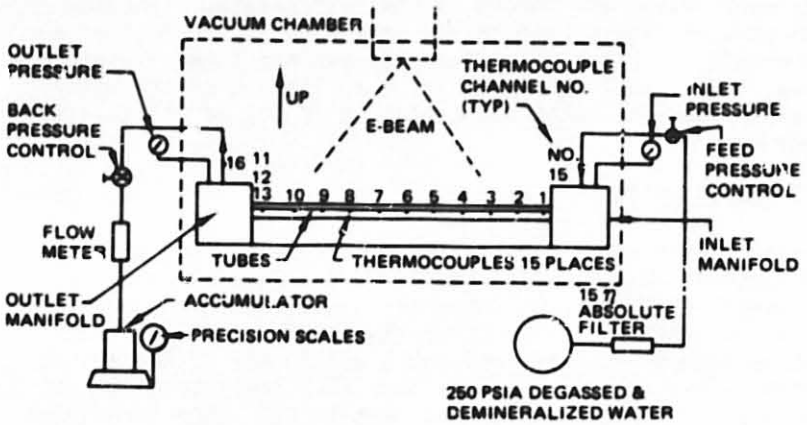

FIGURE 6 TEST SETUP SCHEMATIC

A schematic diagram of the test setup is shown in Figure 6. The test fluid was degassed, demineralized water. Flow rate was controlled by a valve ahead of the test specimen. A downstream valve was used to hold exit pressure to 4.65 atm. Pressure gauges connected to the inlet and outlet manifolds provided a rough reading of pressure drop and were used to set the inlet control valve. An electronic differential pressure transducer was connected across the manifold pressure tap lines for accurate pressure drop measurement.

Thermocouple voltage and pressure transducer signal were recorded continuously on magnetic tape. In addition, selected thermocouple signals and pressure drop were recorded on pen recorders to provide visual information required to monitor the experiment.

CALIBRATION PROCEDURE

Water flow rate versus pressure drop across the test specimen was determined prior to exposure to the electron beam. This was accomplished by starting with the maximum water pressure and maintaining a constant back pressure. The water flow rate passing through the test specimen was maintained for a given time, accumulated in a beaker and weighed. The supply pressure was then reduced for another set of conditions. This was continued down to a supply and back pressure difference of 3.45×10^{4} Kg/m-sec^{2}.

Electron beam irradiance level and uniformity were measured prior to each test. This was accomplished by removing the test specimen and replacing it with a calibration assembly consisting of a Hy-Cal Model C-1312 S/N 36008 water cooled calorimeter mounted on a translating mechanism. Calorimeter response sensitivity was 0.0112 mv/(w/cm^2).

The calibration assembly was designed so that the translating calorimeter could be moved along the test specimen axis. Care was taken to ensure that the elevation and coordinates of the calorimeter and test specimen were identical. At the beginning of each calibration, the calorimeter was centered at midspan. The chamber was pumped down and the electron beam established and shaped to give a line source approximately 0.60 cm wide by 12.7 cm long. Heater power was set to provide the desired midspan flux level. The calorimeter was then moved to a series of selected positions along the line source axis and the output recorded to establish the centerline beam irradiance levels. The calorimeter was repositioned at midspan and the electron beam line source offset 0.127 cm to the right and the measuring process repeated. This procedure was then repeated with the electron beam offset 0.127 cm to the left At the completion of calibration the beam was rastered over to the reference calorimeter and its output recorded. The scanner assembly was then removed and the test specimen installed.

Figure 7 shows a typical set of irradiance scans. The centerline profile is seen to be relatively uniform along the scan axis; however, the profile for the 0.127 cm left-offset increases from left to right while the 0.127 right-offset profile decreases. This phenomenon was caused by the electron beam line source being slightly skewed relative to the direction of travel of the calorimeter. Since the scan axis and test section axis were coincident, the line source was skewed relative to the test section axis by an identical amount.

Analysis of heat transfer test results required a knowledge of the local flux intensity levels over the entire 0.40 cm wide by 12.7 cm long line source. The electron flux scans shown in Figure 7 were used to provide this information. It was assumed that the flux intensity in a plane perpendicular to the line source was normally distributed about the source axis as shown in Figure 8. Local offset of the line source axis and calorimeter centerline is L and the skew angle is θ. Electron flux intensity q was assumed to be a function of x, the distance from the line source centerline.

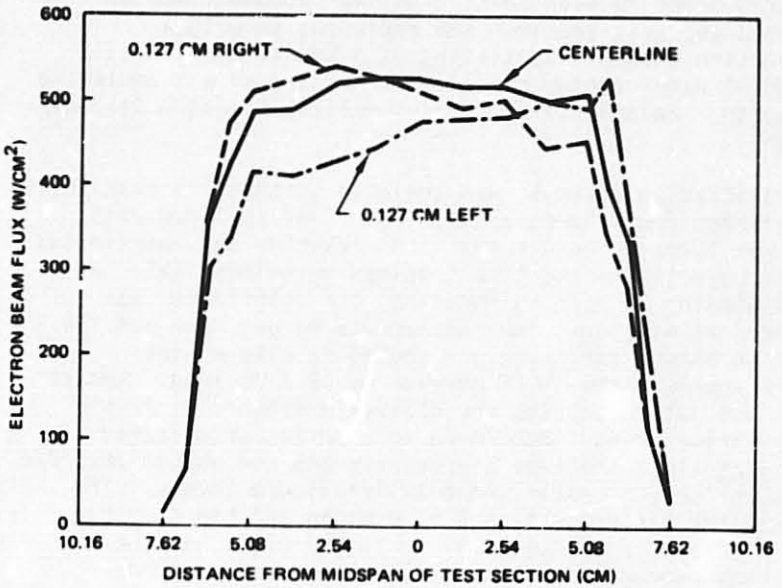

FIGURE 7 MEASURED FLUX ALONG TEST SECTION

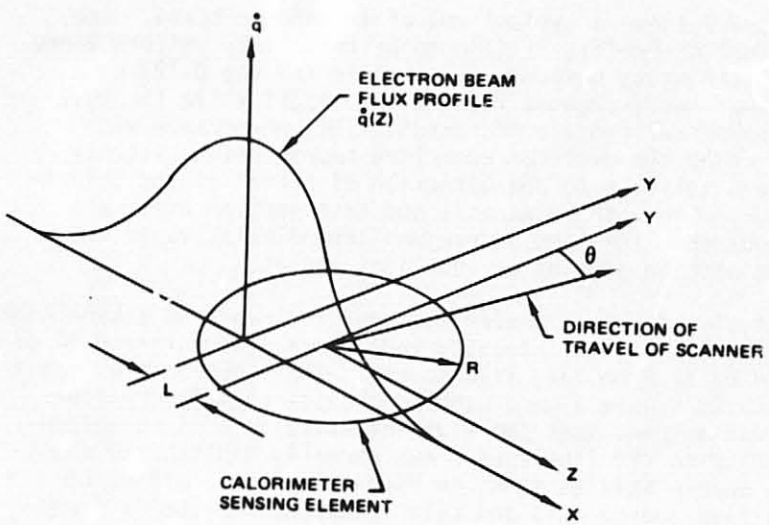

FIGURE 8 CALORIMETER & E-BEAM COORDINATES

The total amount of power Q incident on the 0.254 cm diameter calorimeter sensor was expressed as

$$Q = \int_{-R}^{R} \int_{-y}^{y} q(x)\,dy\,dz \qquad (1)$$

where R = sensor radius

z,y = cartesian coordinates with origin at center of calorimeter sensor

Integrating in the y direction and introducing the relationship between radial location on the sensor and the cartesian coordinates z and y gave

$$= 2 \int_{-R}^{R} q(x) \sqrt{r^2 - z^2}\; dz \qquad (2)$$

where $y = R^2 - z^2$

Since z and x were related by the expression

$$z = x + L \qquad (3)$$

and q was assumed to be normally distributed, the expression for power incident on the calorimeter sensor became

$$Q = 2a \int_{-(R+L)}^{R-L} e^{-bx^2} \sqrt{R^2 - (X+L)^2}\; dx \qquad (4)$$

For the case in which the beam was offset to the right by 0.127 cm, the expression for power delivered to the sensor was

$$Q' = 2a \int_{-(R+L+0.127)}^{(R-L-0.127)} e^{-bx^2} \; R^2-(x+L+0.127)^2 \; dx \qquad (5)$$

A similar expression was written for the case in which the beam was offset 0.127 cm to the left. This expression along with equations 4 and 5 represented three simultaneous equations which were solved for the unknowns a, b, and L.

Total incident power Q on the calorimeter sensor was calculated from electron beam flux scan data using the expression

$$Q = \pi R^2 q_m$$

where q_m = electron flux indicated by calorimeter

Figure 9 shows a typical calculated flux profile at one axial station. Measured data are spotted on the chart for comparison.

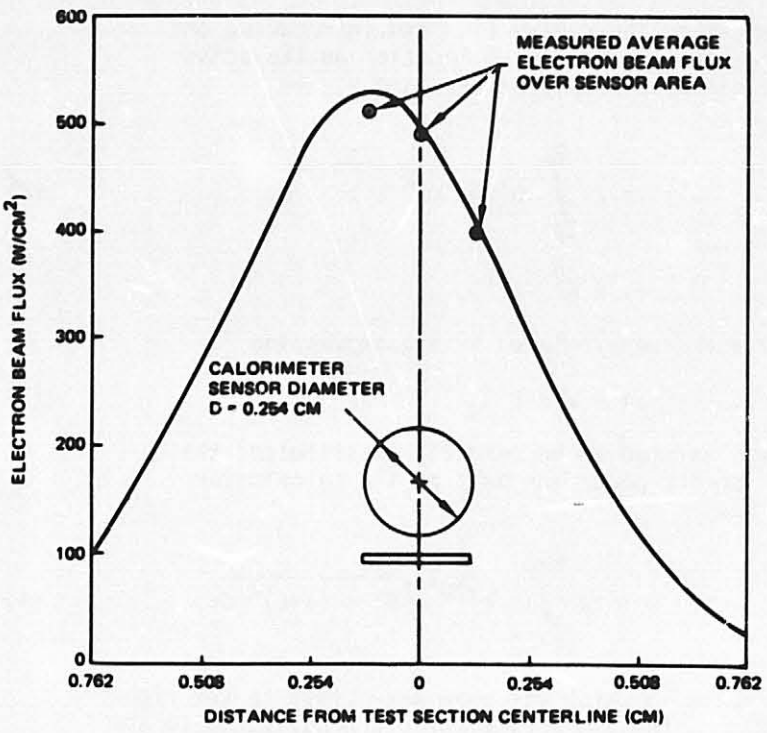

FIGURE 9 CALCULATED FLUX PROFILE

TEST PROCEDURE

The test chamber was pumped down and the electron-beam turned on to the reference calorimeter. The flux level was established as determined during calibration. The maximum water flow rate was established through the test

specimen and the temperature data acquisition initiated. Then, at a determined time, the electron beam was rastered over to the test specimen for a specific time interval and back to the reference calorimeter. The flow rate was decreased and the same procedure followed. Temperature, time, pressure difference, and water flow rate were recorded for a series of ranges of differential pressure from 3.45×10^4 Kg/m-sec^2 to 68.9×10^4 Kg/m-sec^2.

TEST RESULTS

Figure 10 shows measured mass flow rate as a function of friction pressure drop between the inlet and outlet manifolds of the test specimen. Friction pressure drop was calculated by subtracting dynamic loss from measured total pressure drop between manifolds. The tube entrance region loss was approximately 3% of the total pressure differential.

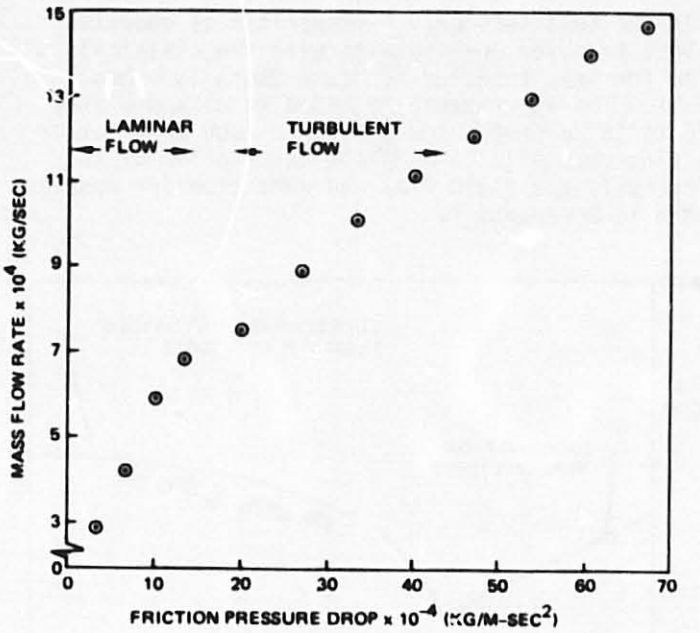

FIGURE 10 MASS FLOW RATE MEASUREMENTS

Typical measured wall temperatures along the tubes are shown in Figure 11. Electron beam flux level was 250 w/cm^2 for these results. Average convective heat transfer coefficients were calculated from measured tube wall temperatures with the aid of a computer routine which analyzed the combined convection/conduction heat

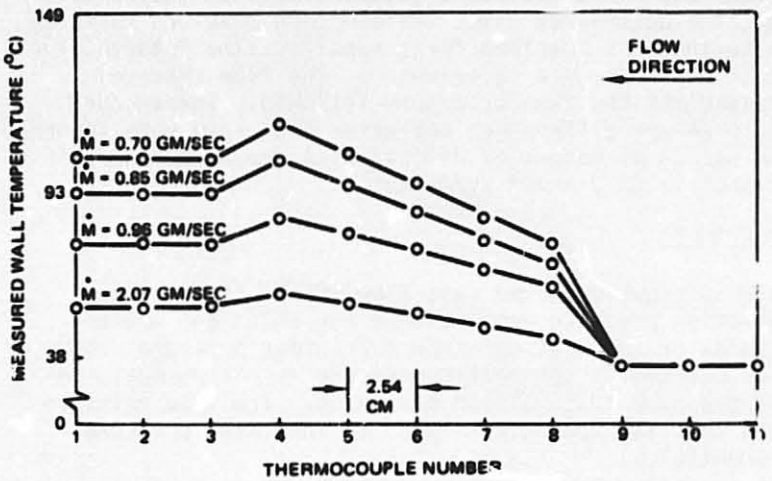

FIGURE 11 MEASURED TUBE WALL TEMPERATURES

transfer in the test section. A comparison of computed log-mean heat transfer coefficients with the classical correlation for heat transfer in round ducts is shown in Figure 12. The experimentally based results are seen to fall 10 to 16 percent below the round tube correlation for large flow channels. A complete description of the computer analysis and fluid flow and heat transfer results is presented in Reference 1.

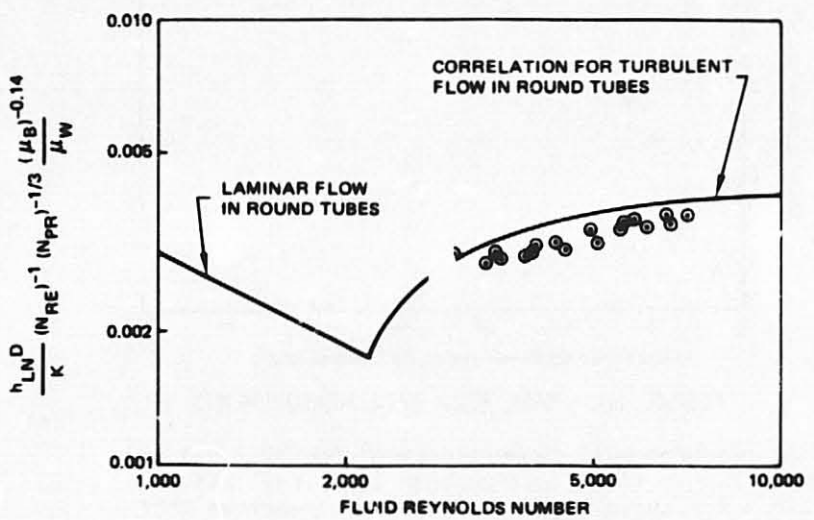

FIGURE 12 COMPARISON OF EXPERIMENTAL LOG-MEAN HEAT TRANSFER COEFFICIENTS WITH THE CLASSICAL CORRELATION

Testing was extended to burnout for all three specimens. Figure 13 shows tube burnout which occurred at a flow rate of 0.521 gm/sec. and a pressure drop of 6.9×10^4 Kg/m-sec^2. Electron beam flux at burnout was 204 w/cm^2. Failure was due to formation of vapor bubbles along the heated wall which drastically reduced the local convective heat transfer coefficient.

Figure 14 shows the results of foil burnout on specimen 3 which occurred at an electron flux of 150 w/cm^2. Failure was caused by low thermal conductance across the bond joint between foil and tubes. It was found that bond thickness could not be controlled with sufficient accuracy during application of the foil to the tubes so that a thickness limit of less than 0.00254 cm could not be maintained. In addition, it was not possible to test the bond joint for voids which would have contributed to its apparent high thermal resistance.

COMMENTS

The thermal bond between foil and coolant tubes represents the greatest resistance to heat flow in an electron beam foil window. Adhesive bonding does not provide sufficient joint conductance to support a foil heat deposition rate of 150 w/cm^2.

CONCLUSIONS

The electron beam facility utilizing a rastered electron beam heater is a flexible tool for vacuum testing materials and high heat flux cooling systems. Potential applications for this facility include testing space materials and components subjected to simulated laser heating, simulation of heating in radioisotope heat sources, and simulation of heating in rocket chambers and electronic components such as field effect transistors and RF generators.

Uniform heating can be achieved with the rastered electron beam. The heat flux field can be mapped with a water-cooled calorimeter.

Small thin-wall tubes are capable of supporting heat fluxes in excess of 500 w/cm^2 at moderate coolant pressure drops. Coolant flow rates must be maintained high enough that maximum tube wall temperature does not exceed the local saturation pressure of the coolant.

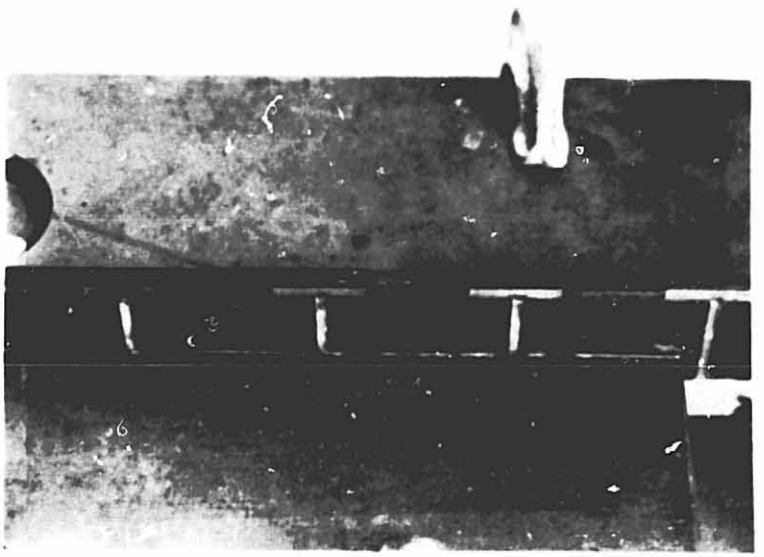

FIGURE 13 TUBE BURNOUT - SPECIMEN 1

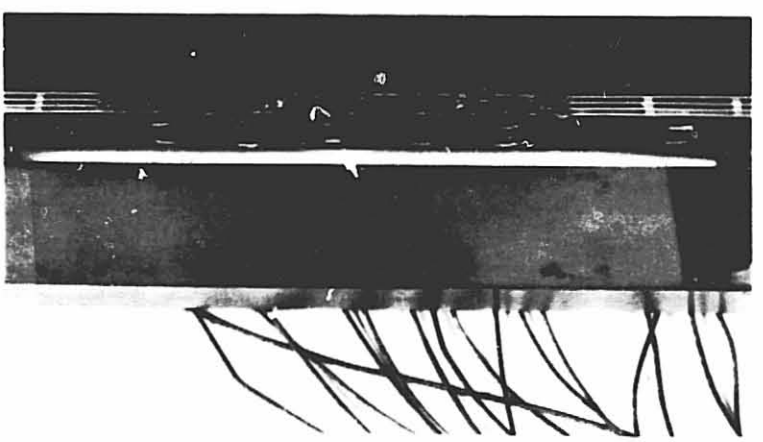

FIGURE 14 RESULTS OF FOIL BURNOUT

REFERENCES

1) Kramer, T. J., "Fluid Flow and Convective Heat Transfer in Square Capillary Ducts Subjected to Nonuniform High Heat Flux", ASME Paper No. 76-WA/HT-29, 1976.

D27

N79-19040

Paper No. 32

ABLATIVE PERFORMANCE OF CARBON-CARBON NOSETIPS IN SIMULATED RE-ENTRY ENVIRONMENTS

D. E. Nestler, *General Electric Company, Re-Entry and Environmental Systems Division, Philadelphia, Pennsylvania*

ABSTRACT

A summary is presented of ablation performance data for carbon-carbon nosetip models obtained over a range of pressures from 10 to 168 atm. Two classes of tests are reviewed: (1) steady state, in which a constant environment is imposed on the model, and (2) ramp, in which the pressure is increased from 10 to 80 atmospheres to simulate re-entry pressure history.

Steady state recession rates which differ by a factor of two for a given material over the pressure range tested are shown to be compatible with the JANAF thermochemical theory for graphite, provided that an augmentation of turbulent heating due to surface roughness is introduced.

Ramp tests are used to deduce the pressure at which boundary layer transition occurs, from photographic observation of gouging due to turbulent heating. Different camera views, as well as post-test evaluation, show that boundary layer transition on 3-D carbon-carbon is not uniform; transition occurs earlier at 45 degrees between the orthogonal weave axes.

Comparison of arc test parameters with typical re-entry vehicle parameters is included, to assess the adequacy of the test simulation. Based on this comparison, recommendations are made for facility developments which would yield improved simulation capability for re-entry vehicle nosetip ablative performance.

INTRODUCTION

Three-dimensional weaves of carbon-carbon are prime contenders for nosetips of future re-entry vehicles. The 3-D carbon-carbon material can provide ablative performance comparable to that of graphite, but with superior mechanical properties.

It has become current practice to test advanced carbon-carbon nosetip materials in high pressure arcs to determine their relative ablative performance prior to flight-testing selected candidate materials. Two types of tests are commonly conducted: (1) steady state, in which a constant environment is imposed on the model, and (2) ramp, in which the pressure is steadily increased by advancing the model towards the nozzle exit.

The objective of this paper is to present the results of evaluations of selected arc test data of carbon-carbon nosetip models, including an assessment of the adequacy of the test simulation.

NOMENCLATURE

B	dimensionless blowing parameter; $B' = \frac{\dot{m}}{C_h}$
C_h	heat transfer coefficient for actual surface
C_{h_o}	heat transfer coefficient for smooth surface
E	Euler number; $E = \frac{S\ dU_e}{U_e\ dS}$
H_{CL}	centerline enthalpy of arc flow
H_s	enthalpy of solid particles being mechanically removed from ablating surcace.
H_w	wall enthalpy
K	surface roughness
$\dot{m}_m$	thermomechanical mass loss rate
$\dot{m}_{TC}$	thermochemical mass loss rate
Pr	Prandtl number
p	local static pressure
p_s	stagnation pressure
$\dot{q}_c$	convective heat flux
$\dot{q}_{RR}$	reradiative heat flux
$\dot{q}_T$	turbulent convective heat flux
Re^*	local sonic point unit length Reynolds number; $Re^* = \rho_e\ U_e/\mu_e$
S	wetted surface length measured from stagnation point
$\dot{S}$	steady state recession rate
T_e	static temperature at edge of boundary layer
T_w	wall temperature
Tu	turbulence level
U_e	velocity at edge of boundary layer
β	cone half angle
ϵ_T	compressibility correction in turbulent heat flux relation
μ_e	absolute viscosity at edge of boundary layer
ρ_e	density at edge of boundary layer
θ	momentum thickness of boundary layer

STEADY STATE TESTS

The two facilities most frequently used for steady state tests are the 50-megawatt arc of the Air Force Flight Dynamics Laboratory and the HIP facility of the MacDonnell-Douglas Research Laboratory. In the 50-megawatt arc, initially spherical-nose models sharpen to a biconic shape (Figure 1A) with a quasi-steady state turbulent recession rate. In the HIP facility, the models are initially biconic, and retain their turbulent shape during exposure (Figure 1B). Nominal test conditions for steady state tests in these facilities are given below:

FACILITY	PRESSURE (ATM)	ENTHALPY (kj/kg)	ENTHALPY (btu/lb)	MODEL DIAM. (cm)	MODEL DIAM. (in.)
50 MW Arc	80	11600	5000	1.27	0.50
HIP	124	6914	3000	0.762	0.30
HIP	168	8027	3800	0.762	0.30

The enthalpy values quoted are flow centerline values which are inferred from calorimeter heat flux measurements as required to match theory, and tacitly assume no heat transfer augmentation due to free stream turbulence in the arc flow.

Centerline recession history corresponding to Figure 1A is shown in Figure 2. Average recession rates are determined from such plots for the quasi-steady or equilibrium ablated shape.

Recession rates for identical carbon-carbon models were correlated empirically with test conditions for a range of pressure from 80 to 168 atmospheres (Figure 3). The correlating parameter employs exponents of 0.8 and 0.2 on stagnation pressure and model diameter, respectively, since these exponents appear in simple turbulent boundary layer heat flux theory.

It is relatively straightforward to show qualitatively by means of the graphite thermochemical response models that an increase in the value of H_{CL} or p_s from one steady state run to another will cause an increase in steady state recession rate $\dot{S}$. The derivation of an explicit proportionality expression relating $\dot{S}$ to H_{CL} and p_s is not straightforward, however, due to the complex variation of the mass loss rate parameter B with pressure and wall temperature (Figure 4).

In the 50 MW or HIP high pressure arc environments, the heat flux is so high that the surface temperature is driven into the sublimation regime. In a steady state test, T_w is determined by the steady state energy balance:

$$0 = \dot{q}_c - \dot{q}_{RR} - \dot{m}_{TC}H_w - \dot{m}_m H_s$$

FIGURE 1. TYPICAL SHAPE CHANGE HISTORIES

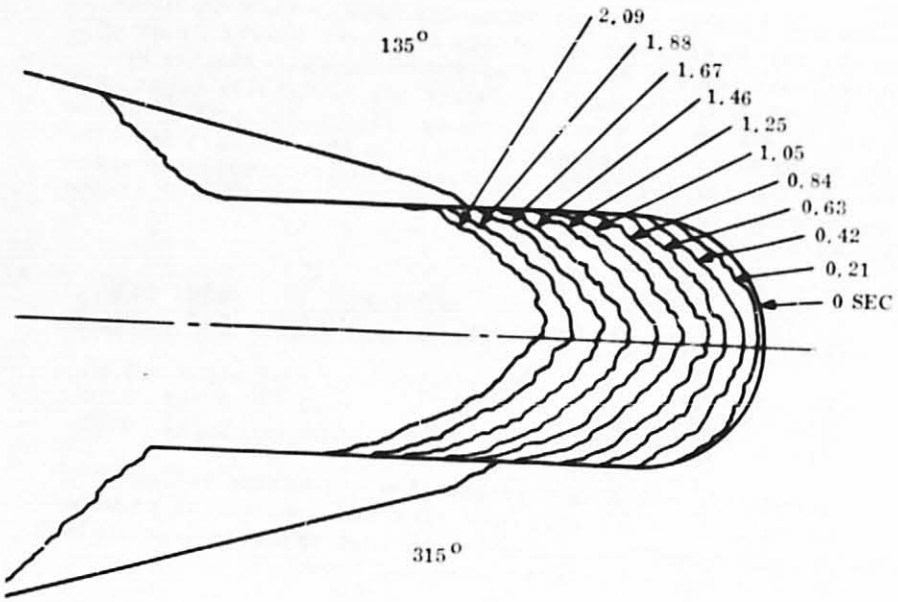

A. 50 MW Arc - 80 Atm.

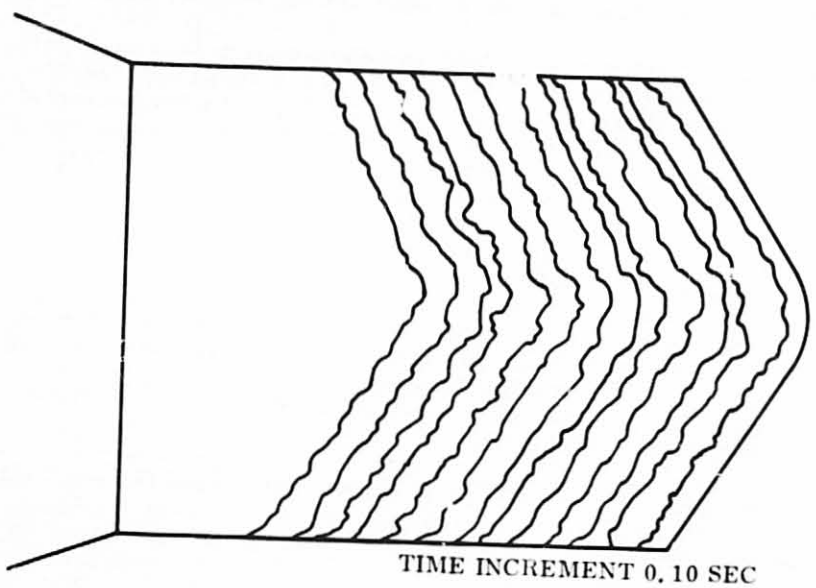

B. MIP - 124 Atm.

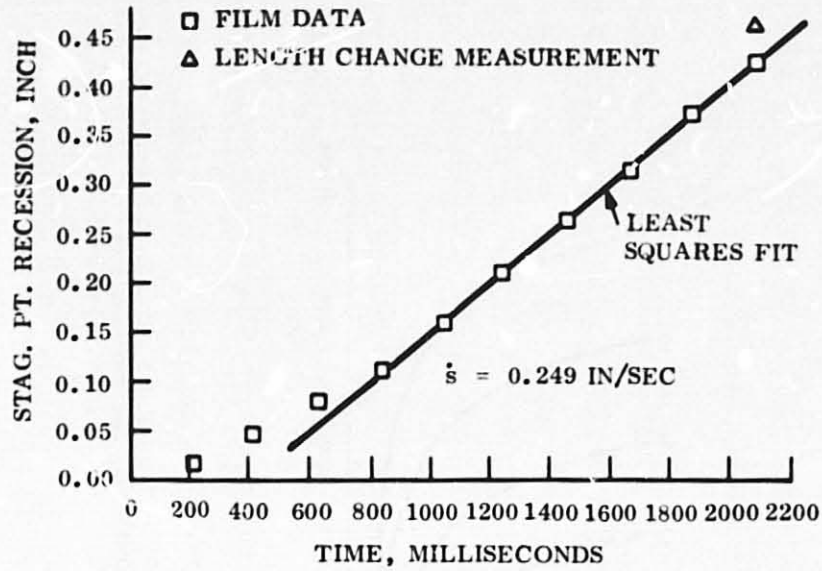

FIGURE 2. Typical Recession Rate Determination (50 MW Test)

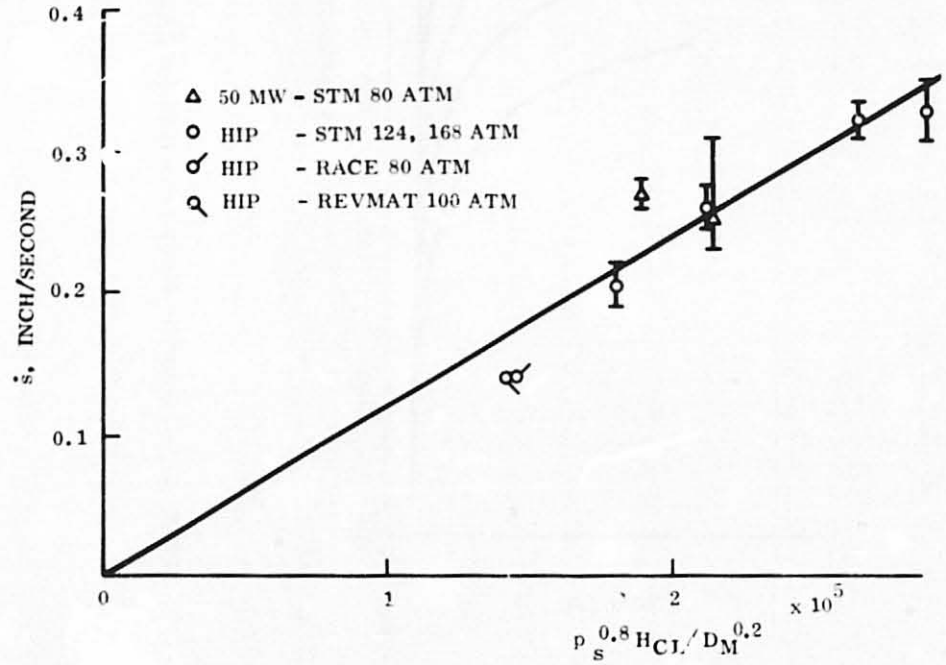

FIGURE 3. CORRELATION OF STEADY STATE RECESSION RATE

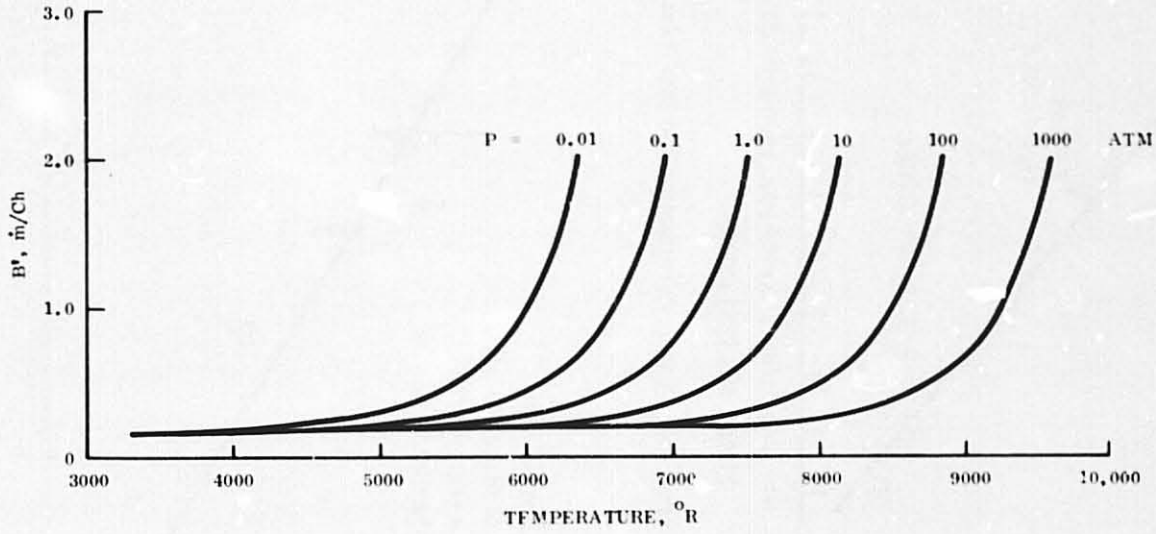

FIGURE 4. Graphite Mass Loss Rate for JANAF (Aerotherm) Thermochemistry

Neglecting thermomechanical mass loss rate $\dot{m}_M$, Eq. (1) may be written as:

$$\dot{q}_c = \dot{q}_{RR} + \dot{m}H_w \qquad (2)$$

or:

$$C_h\ (H_{CL} - H_w) = \dot{q}_{RR}(T_w) + \dot{m}H_w \qquad (3)$$

in which:

$$H_w = f\ (B', p) \qquad (4)$$

as shown in Figure (5).

A comparison of steady state recession rates measured at different facilities and test conditions can be obtained by using the steady state energy balance (Eq. 3) to determine the convective heating rate which must have existed to have produced the measured mass loss rate. This convective heating rate can then be compared with the theoretical value predicted for the given test conditions. If the inferred experimental heating rate exceeds the theoretical value, the degree of augmented heating due to surface roughness can be computed.

Since a quasi-steady shape change is achieved during the steady state tests, the axial recession is equal at all locations on the model surface. Due to difficulties in defining the effective nose radius of the sharpened equilibrium shapes, it is more convenient to work with turbulent heating to the conical region of the model, rather than with laminar stagnation point heating. The theoretical smooth surface turbulent heating transfer coefficient C_{h_o} for a cone is predicted by the Eckert reference enthalpy relation:

$$C_{h_o} = \frac{\dot{q}_T}{H_R - H_W} = \frac{.0348}{Pr^{2/3}} (\rho_e U_e)^{0.8} \left(\frac{\mu_e}{S}\right)^{0.2} \epsilon_T \qquad (5)$$

The mass loss rate on the conical region is determined by:

$$\dot{m} = \rho\, \dot{S}\, \sin\beta \qquad (6)$$

in which $\dot{S}$ is the measured <u>axial</u> recession rate, and β is the cone half-angle. The re-radiation heat flux $\dot{q}_{RR}$ is computed from the measured surface temperature. Eq. (3) is now used to solve for C_h by iteration, using Figure 5 to determine H_w and Figure 4 to determine B'. Comparison of C_h and C_{h_o} yields the augmented heating ratio C_h/C_{h_o}.

The analysis procedure described above was applied to the 124 and 168 atm HIP test conditions, and the 80 atm 50 MW arc test condition, for ablation tests of 3-D carbon-carbon. Local properties needed in evaluating Eq. (5) were determined by isen-

tropic expansion from centerline stagnation conditions to local pressure appropriate to the quasi-steady cone angle for each condition.* The test conditions selected for the 50 MW arc are representative average values of many runs, while specific runs were selected for HIP tests. The test conditions and calculated values of C_{h_o}, C_h, and C_h/C_{h_o} are shown in the following table.

	MEASURED						CALCULATED		
Facility	p_s atm	H_{CL} kj/kg	H_{CL} btu/lb	$\dot{S}$ cm/sec	β deg	T_w °K	C_{h_o}	C_h	C_h/C_{h_o}
50 MW	80	11600	5000	.635	45	4000	3.15	4.40	1.4
HIP	124	6914	2980	.508	57	4167	4.56	6.40	1.4
HIP	168	8027	3460	.787	57	4167	5.86	8.80	1.5

It is seen that a consistent degree of augmented heating is inferred from the measured recession rates and wall temperatures for the three different test conditions.

The values of C_h/C_{h_o} computed above should be regarded as first approximations, due to the inherent uncertainties in test conditions. The effects of relaxing some of the assumptions made in the analysis are summarized below.

Assumption	Effect of Relaxing Assumption
• No thermomechanical loss	Finite thermomechanical loss yields lower C_h/C_{h_o}
• "Standard" H_{CL}	Lower H_{CL} yields higher C_h/C_{h_o} e.g., H_{CL} = 8180 kj/kg (3500 btu/lb) yields C_h/C_{h_o} = 1.9 instead of 1.4 for 50 MW arc.

RAMP TESTS

The ramp test technique has become a standard test procedure in the 50 MW arc, and has also been used at the HIP facility. Typical determination of transition pressure is shown in Figure 6. By using three cameras, transition can be observed on 6 rays for each model, as inferred from the onset of gouges in the profile.

The results of simply averaging the recorded transition pressure according to camera view are shown below for two test series.

*A mass balance calculation showed that the boundary layer on the cone surface is fed by a small central core (.061 cm radius for HIP at 168 atm, .112 cm for 50 MW arc at 80 atm), such that centerline stagnation conditions are a reasonable approximation.

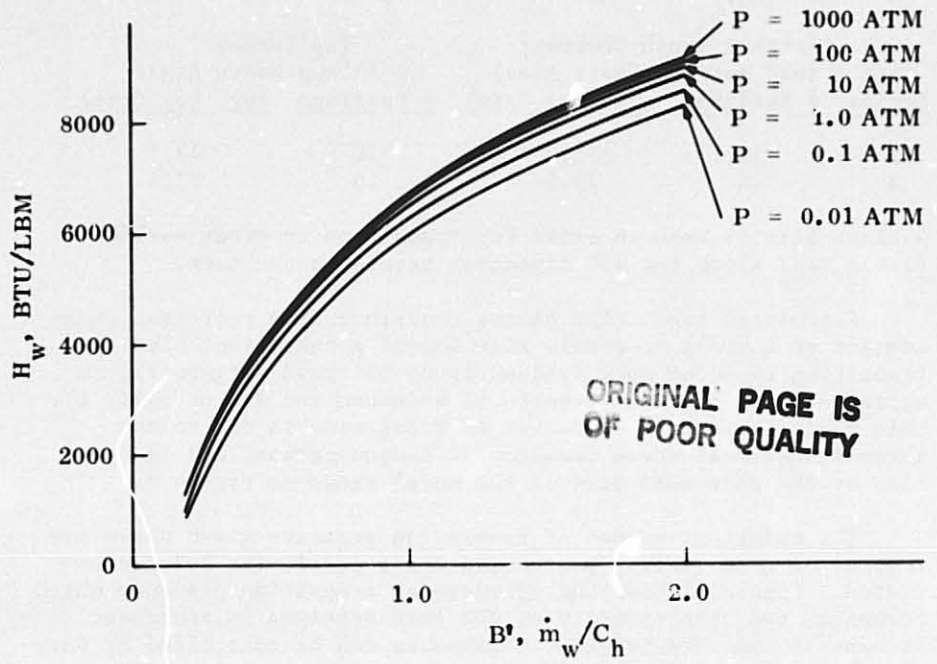

FIGURE 5. H_W vs. B' for JANAF (Aerotherm) Thermochemist

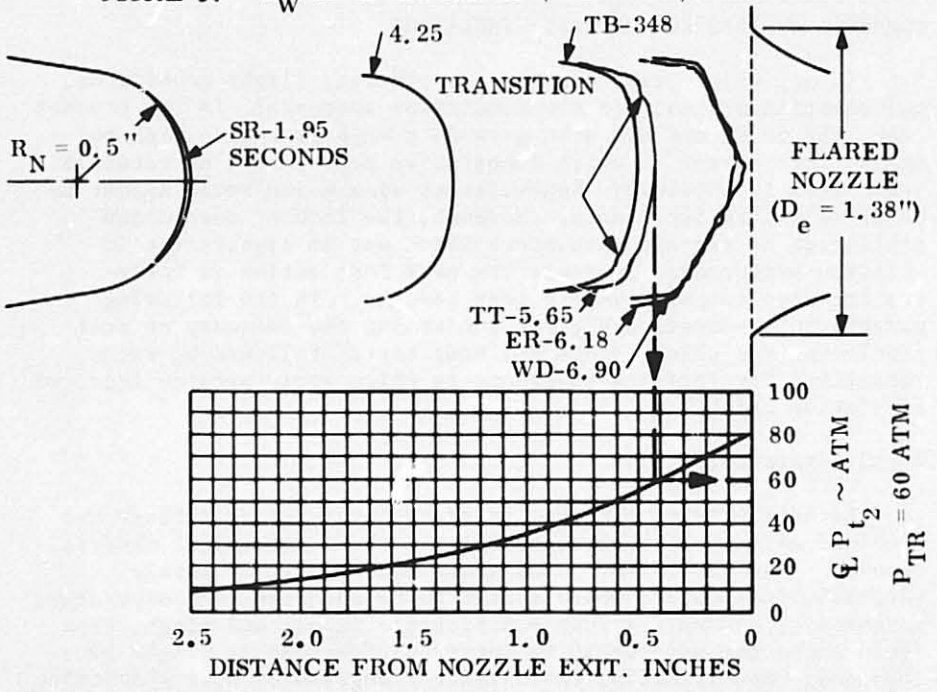

FIGURE 6. TYPICAL DETERMINATION OF TRANSITION PRESSURE

Test Series	North & South Cameras (45° Between Weave Axes) # Readings	Avg. P_{TR} (atm)	Top Camera (Along Weave Axes) # Readings	Avg. P_{TR} (atm)
A	38	71.6	20	77.7
B	24	73.5	10	77.4

A clear bias is seen to exist for transition to occur earlier (lower P_{TR}) along the 45° direction between weave axes.

A study of transition gouges occurence from post-test examination of a group of models also showed a consistent bias for transition to occur more frequently on 45° rays (Figure 7), in agreement with previous results of Heinonen and Jumper (Ref. 1). This non-axisymmetric character of transition is due to the three-dimensional weave geometry of carbon-carbon, and is typified by the post-test view of the model shown in Figure 8.

The numerical values of transition pressure given above are typical of good quality processing for a particular 3-D carbon-carbon. Figure 9 shows the decrease in transition pressure which occurs as the open porosity of the test specimen is increased. It appears that the transition pressure can be controlled by varying the open porosity of the material.

COMMENTS ON ADEQUACY OF TEST SIMULATION

In any ground test designed to simulate flight conditions, the question arises: is the simulation adequate? In the present case, the 50 MW and HIP arcs provide a high pressure, high enthalpy environment in which comparative performance of material candidates is obtained; hence, exact simulation would appear to be of secondary importance. However, the lack of one-to-one similitude in certain parameters which may be significant in ablation performance suggests the need for caution in interpreting even comparative arc test results. In the following paragraphs, comments are given concerning the adequacy of test simulation for steady state and ramp tests, followed by recommendations for facility developments which would provide improved simulation capability.

Steady State Simulation

Recession rates obtained in steady state tests reflect the combined effects of thermochemical and thermomechanical material removal. The simulation of ablative performance of purely thermochemical nature would appear to be adequate for comparative assessment; however, a subtle difference in arc and flight flow field character may result in larger differences in flight performance. Specifically, the different degrees of nose sharpening associated with different surface roughness has little effect on turbulent forecone heating in a low supersonic environment such

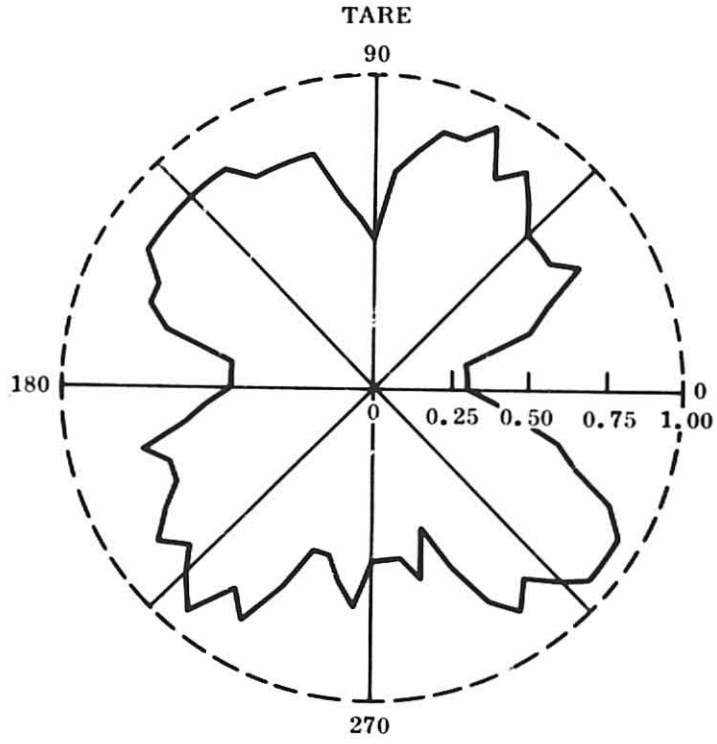

FIGURE 7. FREQUENCY OF TRANSITION VS. CLOCK ANGLE
13 MODELS

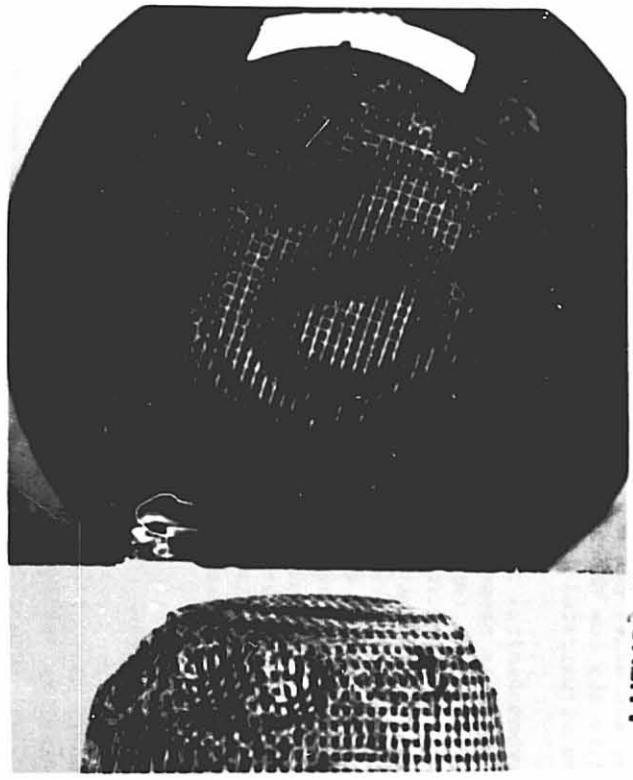

FIGURE 8. POST-TEST PHOTOGRAPH OF 50 MW ARC
RAMP TEST MODEL

as that of the arcs, but has a large effect in hypersonic re-entry due to the bow shock curvature-streamline swallowing phenomenon illustrated in Figure 10.

Thermomechanical contribution to recession rate at a given test condition is properly simulated only if the full scale nosetip is tested. The test models in the arcs are smaller than flight nosetips, particularly for the HIP facility where pressure is more representative of re-entry. Local dynamic pressure along the biconic turbulent ablated shape will be lower in arc tests than in re-entry, for common stagnation pressure, due to flow field effects (supersonic vs. hypersonic freestream Mach number). Thus, pressure gradient forces (dp/ds) will be larger in arc tests than in re-entry; while dynamic pressure and shear forces will be smaller. Hence, differences in recession rate between two materials may be obtained in arc tests which will not occur in flight.

Transition Simulation

Boundary layer transition on a nosetip may be effected by the following variables:

K/θ	relative roughness
T_w/T_e	wall-to-stream temperature ratio
B'	dimensionless blowing parameter
E	dimensionless pressure gradient parameter (Euler number)
Tu	turbulence level

Comparison of arc and flight environments is given below.

	Typical Re-entry	50 MW Arc (80 atm)
P_s (atm)	80 - 150	80
H_{CL} (kj/kg)	9280 - 18560	11600
(btu/lb)	4000 - 8000	5000
$(K/\theta)_{K=.0025\ cm\ (1\ mil)}$	3 to 8	3.0
T_w/T_e	0.6 to 1.3	0.7
$Re^*/ft \times 10^6$	5 to 20	8.0
B'	0.2 to 0.5	0.4
E	Arc higher than re-entry due to radial gradients in approach flow	
Tu	Arc higher than clear-air re-entry	

It is seen that reasonably good simulation of several parameters which affect transition is achieved by the arc test conditions, except for E and Tu. Also, an indirect influence of pressure and enthalpy on roughness height of the ablating surface may have significance, since the arc values are on the low

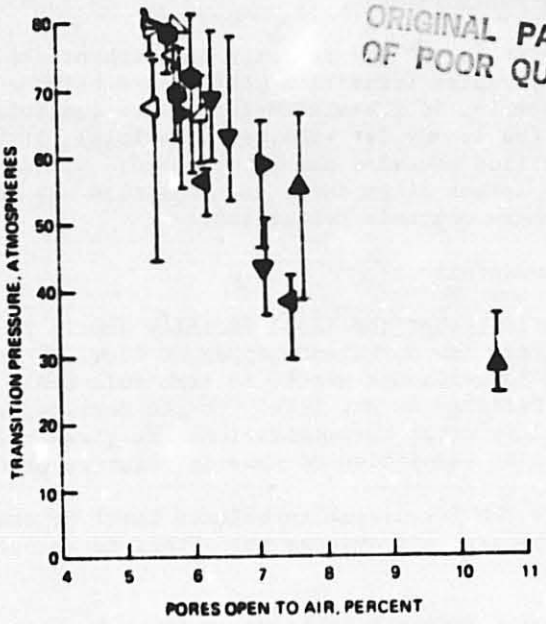

FIGURE 9. TRANSITION PRESSURE VS. OPEN AIR POROSITY

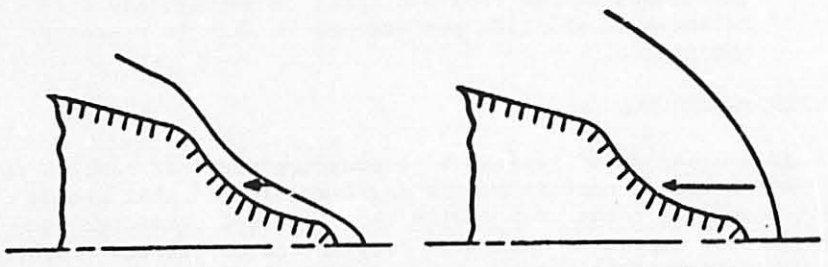

Re-entry

Arc

FIGURE 10. ARC SIMULATION DEFICIENCY OF OBLIQUE SHOCK STREAMLINE SWALLOWING

end of the re-entry values.

Differences in arc and re-entry environment can result in different comparative transition performance between two materials. For example, if freestream turbulence controls transition in arc tests (as it may for smoother materials), little difference in transition pressure may be observed; yet during clear air re-entry, larger differences in transition may result because surface roughness controls transition.

Facility Recommendations

It is obvious that the ideal facility should provide high enthalpy, uniform low turbulence approach flow, hypersonic Mach number, and a large enough nozzle to test full scale nosetips. Since such a facility is not likely in the foreseeable future, more practical specific recommendations are given below for improved arc test simulation of nosetip ablative performance.

- Reduce the freestream turbulence level by use of a stilling chamber, and observe the affect on transition pressure.

- Provide a moderate increase in pressure-enthalpy-nozzle diameter (model size) similitude, such that variation in test model diameter could be accomplished at a given test condition.

- Provide a thorough calibration of the arc, including measurement of radial and axial gradients of flow properties. This information would permit application of nose shape change computer codes to extrapolate differences in ablation performance in arcs to re-entry conditions.

CONCLUDING REMARKS

An evaluation of typical high pressure arc test results for 3-D carbon-carbon nosetip models has demonstrated that steady state recession rates over a wide range of test pressures show a consistent degree of augmented heating due to surface roughness. The non-axisymmetric nature of boundary layer transition has been quantified. The test simulation has been assessed to be reasonably adequate, with the exception of thermomechanical contribution to ablation, and arc freestream turbulence effects on transition.

REFERENCES

1. Heinonen, E.W., and Jumper, G.Y., Jr., "A Method for the Evaluation of Damage on the Surface of Carbon-Carbon Ablation Samples", Proc. of Eighth Conf. on Space Simulation, NASA SP-379, Nov., 1975.

D28

N79-19041

Paper No.

HIGH TEMPERATURE STRAIN GAGE EVALUATION

Jose I. Gonzalez, *Martin Marietta Corporation, Orlando, Florida*

ABSTRACT

The structural thermal test of an advanced ramjet missile section required strain measurements as high as 922°K (1200°F). Since there is relatively little experience in the use of strain gages above the 700-755°K (800-900°F) level, a program was initiated to select and evaluate the best available gage.

Candidate gages suitable for measurements up to 922°K (1200°F) were selected. This involved the determination of their operating characteristics, availability, cost, installation aspects, etc. Gages selected were the AILTECH SG-425 (weldable), the BLH type HT 212 (free filament), and the Bean type BPTH-08-600 WD-120 wire dual filament gage.

The evaluation involved the following tests: strain as a function of load at room temperature and apparent strain as a function of temperature.

Based on results of evaluation, the AILTECH (weldable) gage was selected. The choice was based on: 1) total apparent strain of AILTECH is about 10 percent of test strain while that of next best gage is of the same order of magnitude as test strain. In addition, the total apparent strain resulting with the AILTECH is less than the data scatter of the next best gage, 2) moisture sealant on filament gages requires refurbishing after being subjected to temperatures on the order of 700°K (800°F), and 3) AILTECH is comparatively simpler to install.

I. INTRODUCTION

The structural thermal test of an advanced ramjet missile section requires temperature and strain measurements as high as

---

The author wishes to acknowledge the contributions rendered by James Luksa in test planning, implementation, and data assessment, and that of Thomas R. Meyer in conducting the tests.

922°K (1200°F). Although temperature measurement techniques have been well established for testing in the 922°K (1200°F) there is relatively little experience in the use of strain gages above the 700-755°K (800-900°F) range. While there are numerous gages available, their accuracy, application techniques, and costs vary greatly. In view of this, a program was initiated to select and evaluate the best available gage(s) for the above test.

This paper discusses the evaluation of the candidate gages and the selection of the AILTECH weldable gage.

II. DISCUSSION

A. Candidate Gages

One of the initial requirements of the program was the selection of strain gages suitable for measurements up to 922°K (1200°F). This involved the determination of their operating characteristics, calibration/correlation data, cost, installation aspects, etc. Table I summarizes gages which were considered prior to selection. Some of the criteria which were used in screening and selecting a suitable gage were as follows:

1. Gage must be capable of withstanding temperatures up to 922°K (1200°F) for short periods of time without marked deterioration due to oxidation, moisture or temperature.

2. Gage must be capable of withstanding repeated transient cycles.

3. Gage must be capable of accommodating large thermal stress, including that generated within the gage itself.

4. Gage must be resistant to corrosion.

5. Gage installation should be comparatively simple and require little or no refurbishment.

Three gages were selected for further evaluation based on accuracy, cost, and prior usage history. The gages which were selected were the AILTECH type SG-425-09A-10 weldable gage, the BLH type HT 212-4A/4B free filament gage, and the Bean type BPTH-08-600 WD-120 wire-dual filament gage. Details for each of these are available in vendor catalogs, References 1, 2, and 3, respectively.

TABLE I

High Temperature Strain Gage Selection Chart

Manufacturer	Type	Temperature Limit Error			State of the Art	Remarks
		5 Percent	10 Percent	20 Percent		
BLH Electronic, Inc.	FMW9-50-12		644°K (700°F)	922°K (1200°F)	Available	Weldable bond. Physical size too large for our requirements.
	FMWFB9-50-12		811°K (1003°F)	922°K (1200°F)	Available	
	HT-212-4A/4B	589 K (600°F)	811°K (1000°F)	922°K (1200°F)	Available	Ceramic and flame spray bond. High temperature capabilities. Has been used with success. Selected for evaluation.
William T. Bean, Inc.	BPTH-08-600WD-120	589°K (600°F)	700°K (800°F)	922°K (1200°F)	Available	Ceramic and flame spray bond. High temperature capabilities. Has been used with success. Selected for evaluation.
HITEC Corp.	HFP-12-125-S/W		811°K (1000°F)	1366°K (2000°F)	Available (New)	Ceramic and flame spray bond. High temperature capabilities. Recommended for dynamic testing.
AILTECH, Inc.	SG-425-09A-10	644°K (700°F)	783°K (950°F)	922°K (1200°F)	Available	Weldable bond. Physical size is large but acceptable. High temperature capabilities. Selected for evaluation.
Hughes Aircraft Co.	CSG-201	922°K (1200°F)	1089°K (1500°F)	1228°K (1750°F)	Available/ Development	Capacitance type gage. Weldable bond. Excellent high temperature capabilities. Cost of gage and necessary readout equipment prohibitive.
Boeing Aerospace Company	CS-20-100	922°K (1200°F)	1089°K (1500°F)		Available/ Development	Capacitance type gage. Weldable bond. Excellent high temperature capabilities. Cost prohibitive.

The AILTECH gages were purchased with a magnesium oxide (MgO) insulated integral stainless steel jacketed copper lead-wire 3.048m (10 feet long). The strain element is a platinum tungsten alloy. These gages were temperature compensated for Inconel 718 (we provided vendor with sample of material) over a range of temperatures from room to 922°K (1200°F). The BLH gages have free-filament wire grids and the strain sensing element is a nickel-chormel alloy. The HT-212 gage does not have temperature compensation. Chromel alumel thermocouples come installed in the -4B series while the -4A series does not have thermocouples. The Bean gage grid consists of a stabilized dual platinum filament. The BPTH series is temperature compensated over the range from room temperature to 811°K (1000°F).

The total (thermal and mechanical) strain range for the missile test section is on the order of 1 1/2 percent, 0.015 mm/mm (0.015 in/in). In view of this, ceramic cement gage installations were eliminated since this bonding method is not effective above 1/2 percent mechanical strain, 0.005 mm/mm (0.005 in/in). This affected both of the above filament gage candidates and required that these gages be applied with a flame spray technique.

B. Test Specimen

All gages were mounted on tensile coupons fabricated of Inconel 718 1.78 mm (0.07 inch) thick as shown in Figure 1. The choice of tensile coupon was made to ascertain that we had a constant stress distribution applied over a well defined cross sectional area where gages could be installed. A 1.78 mm (0.07 inch) thickness was used because it is representative of the thinnest wall of the missile test section (Figure 2). This wall thickness is the most likely to be affected by gage application (particularly the weldables). An added feature of this thin wall is that it minimizes undesirable temperature gradients across wall thickness. The coupon was designed to be compatible with the Instron Universal Testing machine. The coupons were heat treated to the same specifications as the missile test section structure.

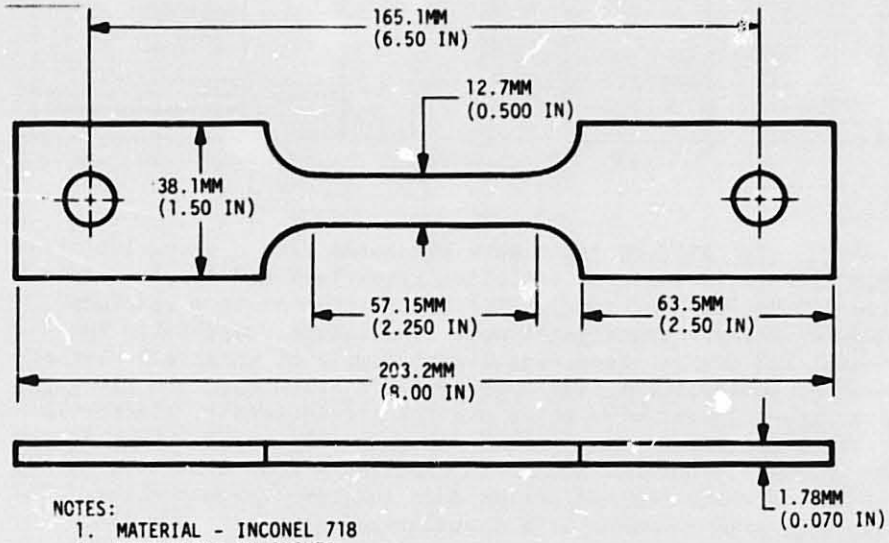

NOTES:
1. MATERIAL - INCONEL 718
2. DIMENSIONS IN INCHES.
3. DO NOT OVERHEAT DURING MACHINING - 322°K (120°F) MAXIMUM. THIS WILL BE CHECKED METALLURGICALLY. OVERHEATING WILL CAUSE ERRONEOUS RESULTS.
4. THE MARKED IDENTITY MUST BE RETAINED ON EACH SPECIMEN.
5. AFTER MACHINING HEAT TREAT:
   992±8°K (1325°F ±15°F) - HOLD FOR 8 HRS
   FURNACE COOL TO
   894±8°K (1150°F ±15°F) - HOLD FOR 8 HRS
   AIR COOL

Fig. 1-Typical test specimen

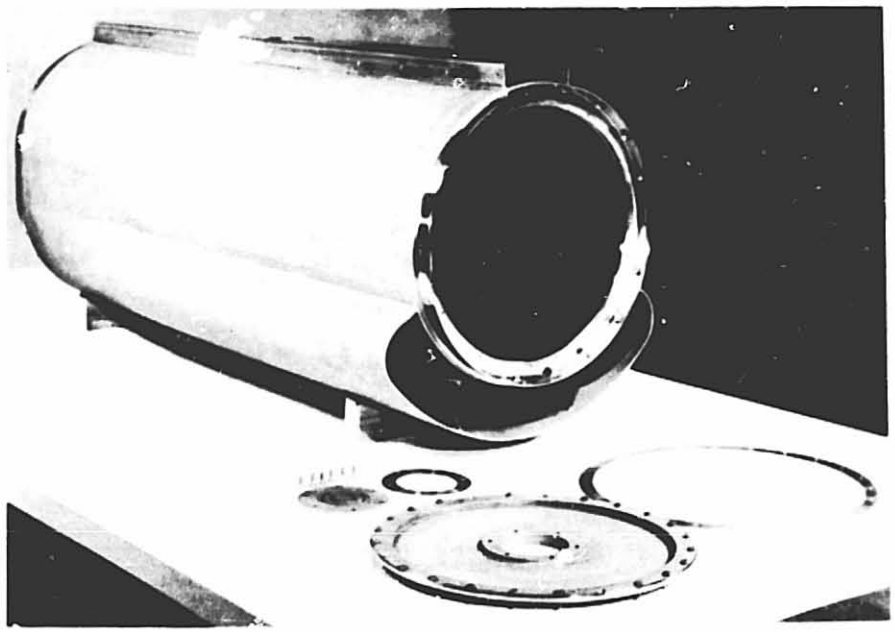

Fig. 2-Missile test section

C. Gage Installation

Figures 3, 4, and 5 show photographs of installed AILTECH, Bean, and BLH gages, respectively. One AILTECH gage was applied to each side of the specimen. The AILTECH gage was spot welded along its flange as per the instructions in Reference 4.

Four chromel alumel thermocouples (28 gage, two on each side of the specimen coupon) were installed on the specimen next to each AILTECH gage. Figure 3 shows gage and thermocouple installations along with auto collimator target tips. Each of the AILTECH gages was designed to read separately in a full bridge circuit.

Both the Bean and BLH filament gages were applied with the Rokide flame spray process which is well detailed in the literature. One Bean gage was applied to each side of the specimen (Figure 4). Again, four chromel alumel theromcouples, two on each side of the specimen, were installed. Each of these gages was wired to read separately in a full bridge circuit similar to that used with the AILTECH gage.

Two BLH gages were applied on each side of the specimen (Figure 5). Each of the two gages was applied in a Poisson bridge installation and also wired in a full bridge circuit.

Fig. 3-Test specimen with AILTECH gage, dual center thermo-couples, and collimator target tips

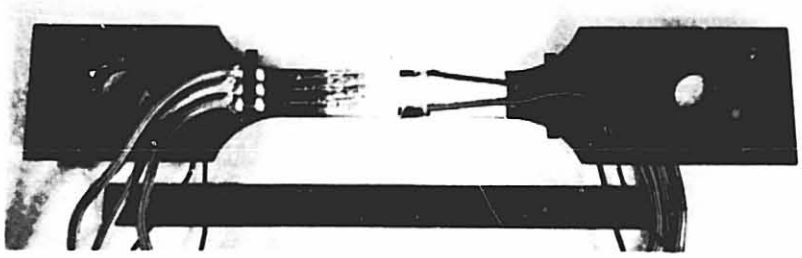

Fig. 4-Bean strain gage installation

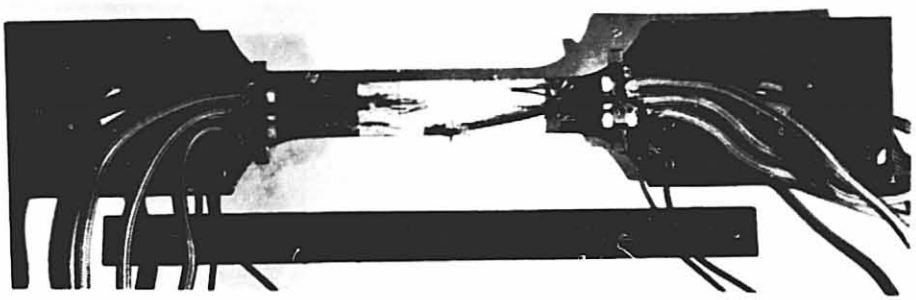

Fig. 5-BLH strain gage installation

D. Test Equipment/Instrumentation

The primary items of equipment in the test setup (Figure 6) consisted of the following:

1 Research Incorporated one channel temperature programmer and power regulator, Model 5052S (3KVA). The regulator delivers power to two quartz lampbanks. Each lampbank houses eight 2000 watt quartz lamps. One feedback thermocouple (which is one of four attached to specimen) completes the closed loop null balance system.

2 Instron Universal Testing Machine Model PTD, 9072 kg (20,000 pound) maximum capacity. The 2268 kg (5000 pound) range has an accuracy of ±1 percent of full scale, i.e., 22.7 kg (50 pounds).

3 BLH Digital Indicator Model 902 used in conjunction with a strain gage conditioning unit model 130. The indicator could be read to 10 microstrain. Its accuracy was approximately ±1 percent of full scale.

4 CEC Oscillograph Recorder Model 5-124 with 7-[illegible] galvanometers for temperature reading.

5 Plotomatic X-Y Plotter Model 690 with an accuracy of ±1 to 2 percent of full scale.

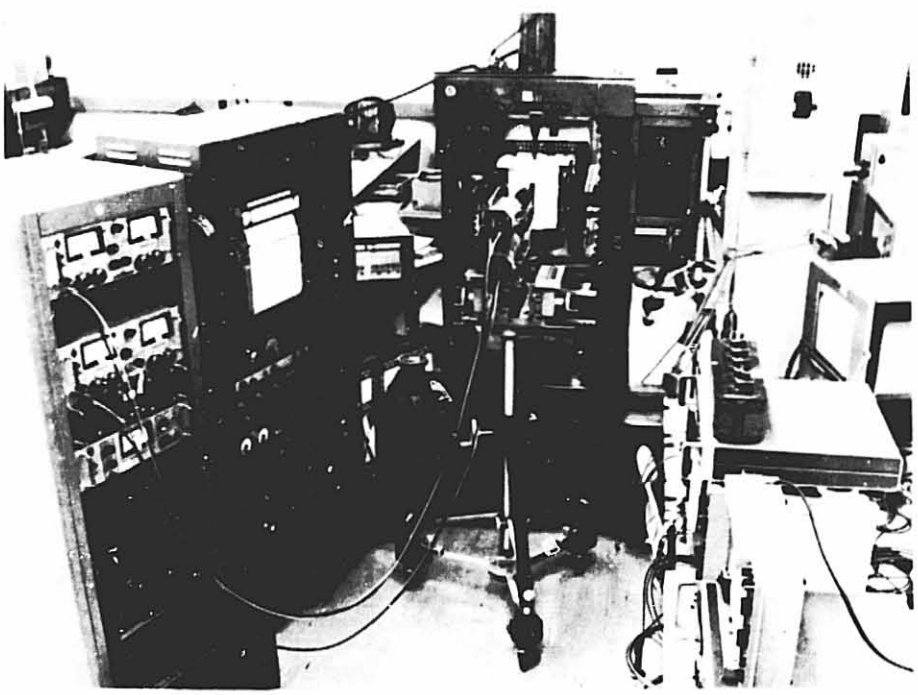

Fig. 6-Overall view of test equipment and instrumentation

Other ancillary test equipment used included an Electro Scientific Resistance Bridge (Model 231), Westronics four channel continuous temperature recorder (Model DD 11E), PhysiTech Electro Optical Auto Collimator (Model 440), and Satec elevated temperature extensometer (Figure 7).

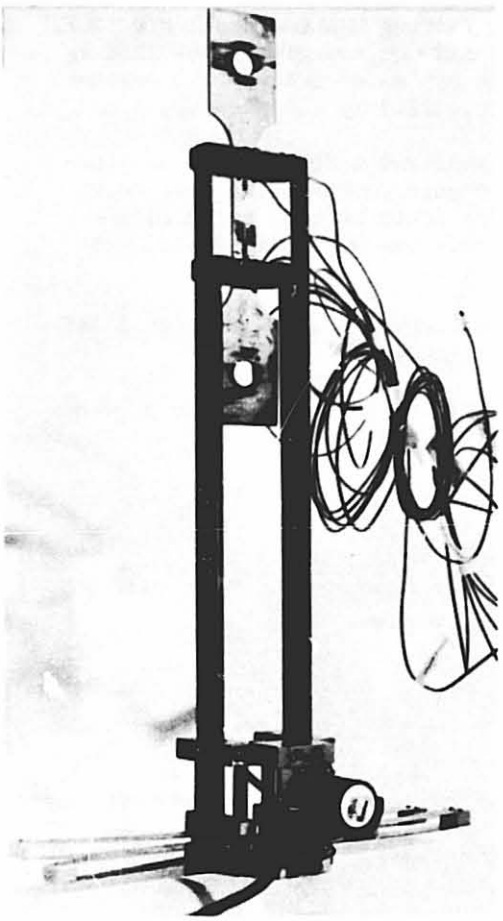

Fig. 7-Instrumented test specimen installed in Sates extensometer

E. Test Setup/Procedure

The test procedure for all candidate gages consisted essentially of the same steps. After mounting specimen with gages in the Instron, dummy (balance) resistors were sized and wired into the complete circuit. The complete circuitry included the initial high temperature leadwire plus vinyl extensions required to reach the common junction chassis box. Additional setup included the sizing and wiring of a shunt resistance (R_{CAL}) for calibrating the strain indicators.

1. AILTECH

Two problems were encountered with the AILTECH gages that required above average attention. One was the mechanics of leadwire attachment and the other, the moisture absorption in the gage/leadwire that reduced the insulation resistance (IR) or resistance to ground.

During the initial test phase we found that the three-wire leads (this system was used to minimize leadwire error) at the end of the stainless steel sheath were very fragile and could not sustain normal flexing or handling. These leads had to be potted against a support backing that prevented their being flexed or pulled apart. Subsequent to the above, the vendor advised that the leadwire could be provided with potting boots and vinyl extensions as an integral feature. From this point on tests were conducted on gages with an integral potting boot that had a 3.18 mm (1/8-inch) diameter (OD).

Moisture absorption with the above (initial) exposed three-wire leads was a major area of concern and required special attention. Although the vendor provided all gages with sealed ends and IR on the order of 1000 megohms, moisture absorption was experienced. We determined that with normal storage and handling the IR dropped from 1000 to 3 megohms in a 3-month period. Attempts were made to drive the moisture out (as per instructions in Reference 4) by heating the last 152.4 mm (6 inches) of leadwire with a heat gun. Since this proved too time consuming, our procedure was changed to storing gages in a 333°K (140°F) oven. One overnight stay in the oven increased the IR from 3 to 150 megohms. The impact of initial IR values on indicated strain readings can be significant. For example, assuming a straight resistance to ground, strain versus IR is as follows:

Indicated Strain μ mm/mm	Insulation Resistance (IR) Megohms
3.2	10
32	1

Although the installation of potting boots minimized moisture absorption, our test procedure required the storage of gages in either a 333°K (140°F) oven or a dry nitrogen environment.

2. Bean and BLH Gages

Moisture absorption is also a problem with these type gages. The moisture problem is not with the leadwire sealant (as with the AILTECH) but instead with the alumina (flame spray) rod and the foil itself. Both of these type gages have a moisture sealant coating applied as an end item. This coating cooks off at 700°K (800°F) and needs to be reapplied if continued moisture sealant is required. It is apparent that in view of our missile section test requirements this is a decided disadvantage.

F. Calibration Techniques

Various calibration techniques were considered to support these tests. Calibration candidates included extensometer, auto collimator, cantilevered beam and analyses.

1. Extensometer

Extensometers considered were the Instron strain gage (room temperature type) and the Satec (elevated temperature). The Instron type is capable of room temperature (RT) readings only. Besides temperature, other limitations included the fact that the gage span was 50.8 mm (2 inches) (this presented a problem in installing strain gages between knife edges) and also with a full scale of 5.1 mm (0.20 inch) and an accuracy of at best 0.1 percent the reading would be ±200 microstrain (0.0002 mm/mm).

The Satec (Figure 7) and similar elevated temperature extensometers also have the above gage span problem. The elevated temperature capability is solely at steady state and only for mechanical loads. Once a steady state temperature is achieved, mechanical load is applied and data read. Thus, for any mechanical load and steady state temperature, only the strain due to load can be read.

Since the calibration standard must have the capability of operating during transient temperature conditions (rates as high as 8°K/sec), consideration was given to insulating the extensometer linkage. This, however, was not considered practical. Based on the above, the use of the extensometer as a standard was abandoned.

2. Auto Collimator

The PhysiTech Model 440 Electro Optical Auto Collimator (Figure 6) is designed to measure angular motion simultaneously in two mutually perpendicular axes. The system is completely self-contained and requires only a mirrored or reflective surface as a position transmitter. Relative position and linear displacement can be obtained with the auto collimator.

From the standpoint of measuring strain due to temperature alone, the collimator performs with an accuracy on the order of ±0.0005 mm/mm. The strain data read compared favorably with available test data.

With mechanical load alone, the minimum test strain is on the order of 0.0005 to 0.001 mm/mm. This small value of elongation, ΔL of about 0.025-0.051 mm (0.001 to 0.002 inch), together with the fact that both target tips move over a large distance, about 1.02 mm (0.040 inch), created a problem with the use

of the collimator. Since the lens heads must track both targets, then large amplifier full scale settings are required. Thus, a full scale sensitivity problem exists due to test facility, wherein the movement between target tips on a specimen is small but yet individually the tips can have a large movement. This dual requirement makes the use of the collimator unfeasible.

3. Cantilever Beam

Use of the cantilever beam approach was not considered feasible because of the inability to handle high transient heating rates.

4. Summary

In view of the above, analytical techniques based on experimentally generated modulus of elasticity and linear coefficient of expansion were used as the calibration standard.

G. Test Results

All candidate gages were subjected to two tests, the first (Test 1) generated strain as a function of load (at RT) and the second (Test 2) apparent strain as a function of temperature. In Test 1 the load was varied from 0 to 1134 kg (0 to 2500 pounds) in 113 kg (250 pound) increments. Test 2 determined the strain as a function of temperature, while the load was kept constant at 0 kg. These are the data which are used to generate apparent strain curves. Based on the results of Tests 1 and 2 the best gage was selected for further tests.

1. Strain as a Function of Load (at RT)

Figure 8 shows a compilation of strain at RT data for candidate gages. The (R.S.) and (L.S.) for both Bean and BLH refers to gages on the right and left side of the test specimen. All data are for the second cycle where repeatability was achieved. The Bean data are very close to the analytical strain uncorrected for the effect of gage installation (X). The BLH (R.S.) and AILTECH gage numbers 4660-5 and -7 are slightly low. The analytical strain corrected for the effect of AILTECH gage installation is noted (θ). The low readings on AILTECH -4 and BLH (L.S.) may be due to installation procedure.

2. Apparent Strain as a Function of Temperature

Measured apparent strain as a function of temperature is shown in Figure 9 for the AILTECH and Bean gages. Compression is noted as (+) and tension as (-). Data on BLH gages (where each of two gages was applied in a poisson bridge and also wired in a full bridge circuit) were not plotted since they were very erratic. Note that the figure shows the data scatter

(vertical bars) for each type gage. The AILTECH data are for an average of three gages and include both first and second cycle results. The AILTECH with its temperature compensation has been designed to go through 0 microstrain at both RT and 922°K (1200°F). Note that the shift at 0 is about 50 microstrain while at 922°K (1200°F) it is larger, 120 microstrain. The average maximum bow in apparent strain specified by the vendor is 318 microstrain at 260°K (500°F).

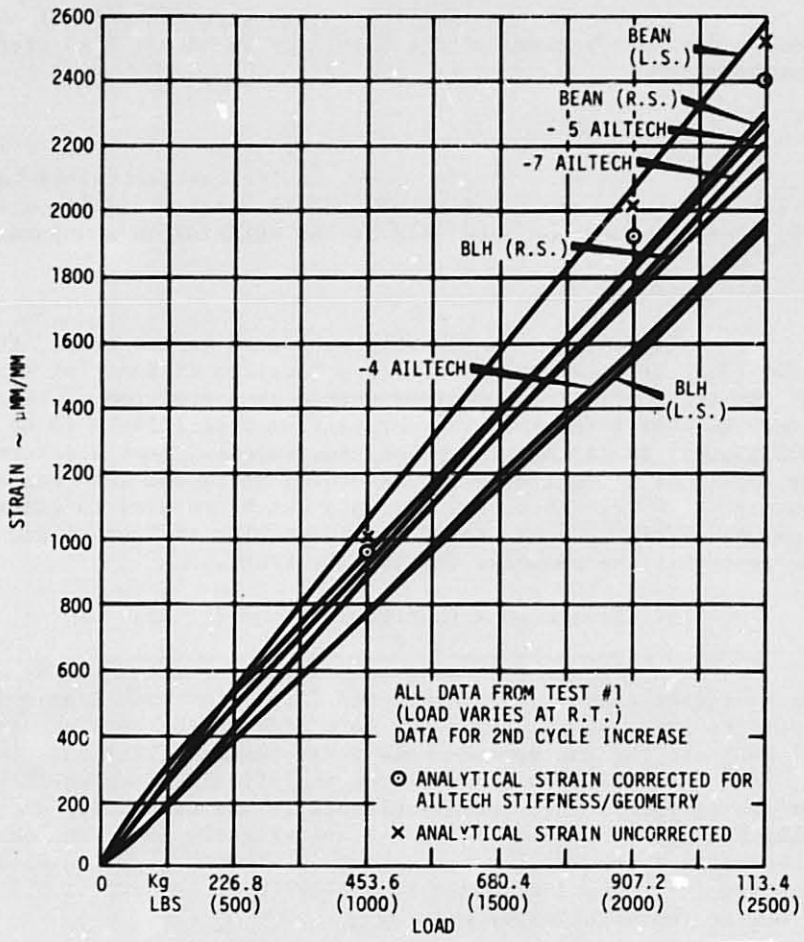

Fig. 8-Strain versus load for candidate gages

The Bean with its temperature compensation is designed to read 0 microstrain at RT and 811°K (1000°F). The shift in the RT reading is quite large. If first cycle results were included, scatter could be as much as 800 to 1000 microstrain.

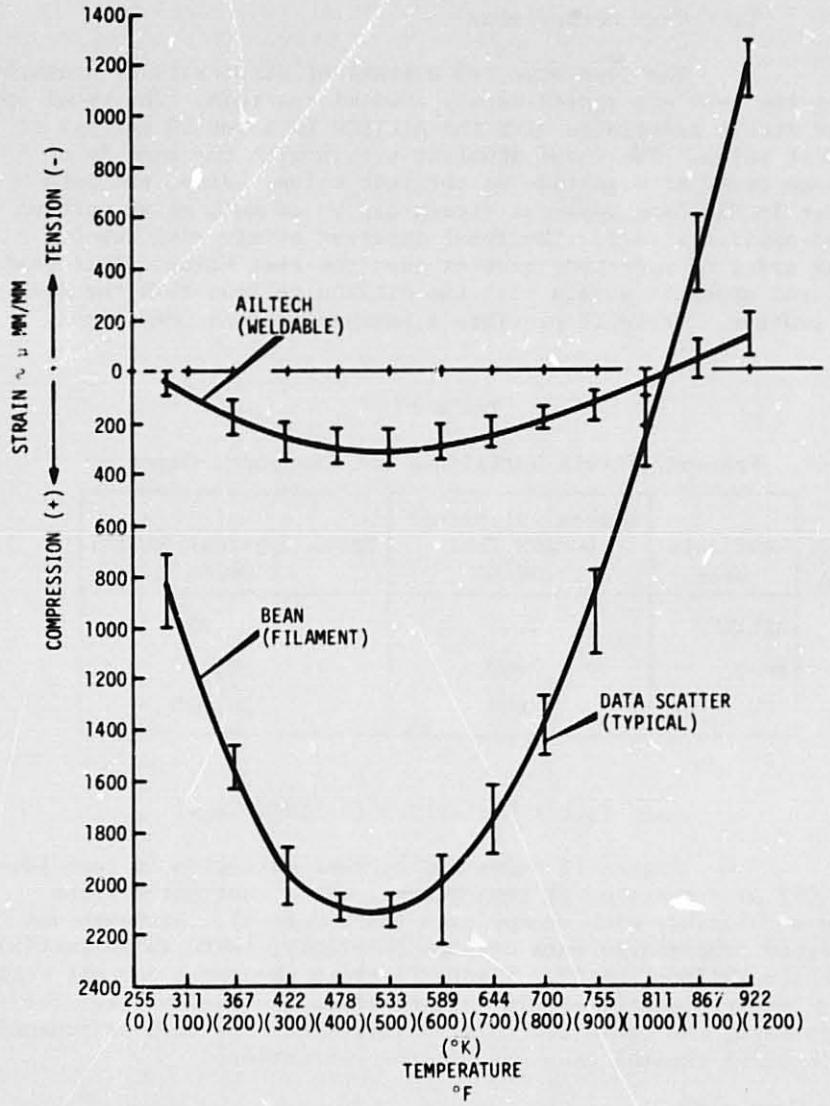

Fig. 9-Apparent strain versus temperature

The erratic data of the BLH were attributed to moisture absorption. Another important point regarding the BLH is that it lacks temperature compensation. Its apparent strain is on the order of 18 microstrain per 0.5°K (1°F). This means that we could be reading strains on the order of 18,000 microstrains at 811°K (1000°F) on our test section.

3. Gage Comparisons

The peak expected mechanical strains to be measured during the test are approximately 2000 microstrain. The total apparent strain associated with the AILTECH is about 10 percent of the test value. The total apparent strain with the Bean is of the same order of magnitude as the test value. Also, the data scatter in the Bean apparent strain can be as much as 40 percent of the applied strain. The total apparent strain with the BLH is one order of magnitude greater than the test value. Note that the total apparent strain with the AILTECH is less than the Bean data scatter. Table II provides a summary of this comparison.

TABLE II

Apparent Strain Variations for Candidate Gages

Candidate Gage	Mechanical Strain During Test μ mm/mm	Total Apparent Strain μ mm/mm
AILTECH	2000	320
Bean	2000	2,100
BLH	2000	20,000

4. Gage Factor Evaluation (AILTECH Gage)

Figure 10 shows the percent variation in gage factor (GF) as a function of temperature. Note that our results compare favorably with vendor data (Reference 1). Although our GF versus temperature data compare favorably, there is an initial variation (offset) at RT. Figure 11 shows the total percent variation in experimental strain as a function of temperature. For the present, the cause for this variation has not been determined and is being treated as a gage factor correction.

III. CONCLUSIONS

Based on results of evaluation, the AILTECH (weldable) gage was selected for application on the missile section tests. Reasons for choice were:

1 Total apparent strain resulting with AILTECH is about 10 percent of test strain while that of next best gage is of the same order of magnitude as test strain. In addition, the total apparent strain resulting with the AILTECH is less than the data scatter of the next best gage.

2 Moisture sealant on filament gages requires refurbishing after being subjected to temperature on the order of 700°K (800°F).

3 The AILTECH is comparatively simpler to install. This feature has allowed gages to be located in areas that would normally be inaccessible to flame spray apparatus.

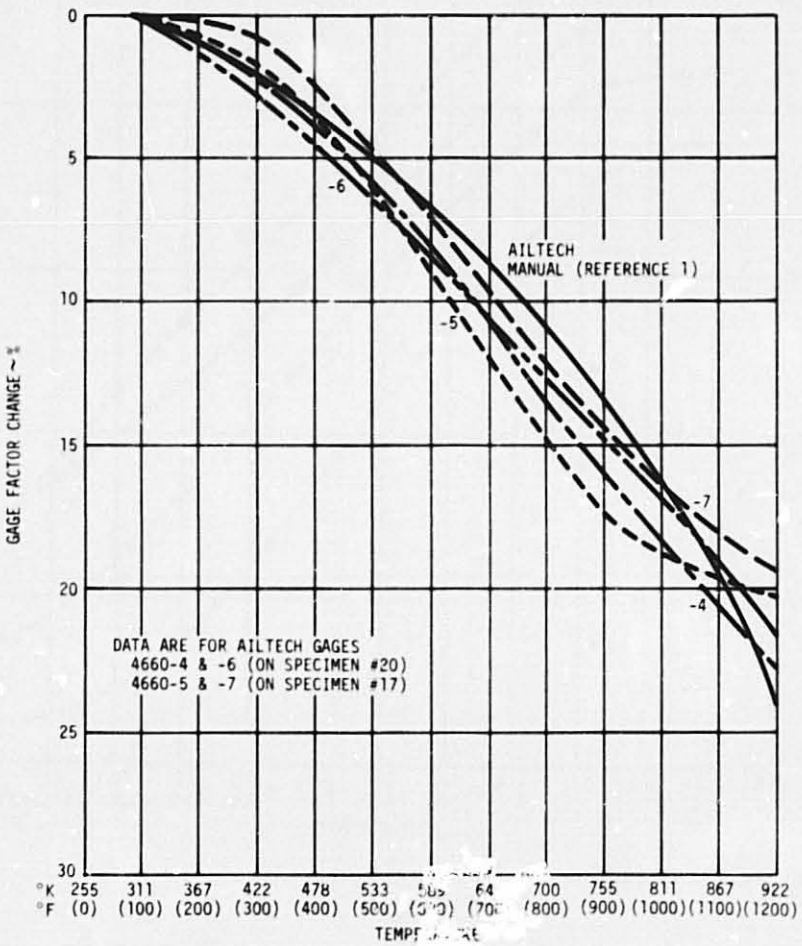

Fig. 10-Gage factor change as a function of temperature

Work presented in this paper was sponsored by the United States Air Force, Air Force Systems Command, Aeronautical Systems Division (YMK), Wright-Patterson AFB, Ohio.

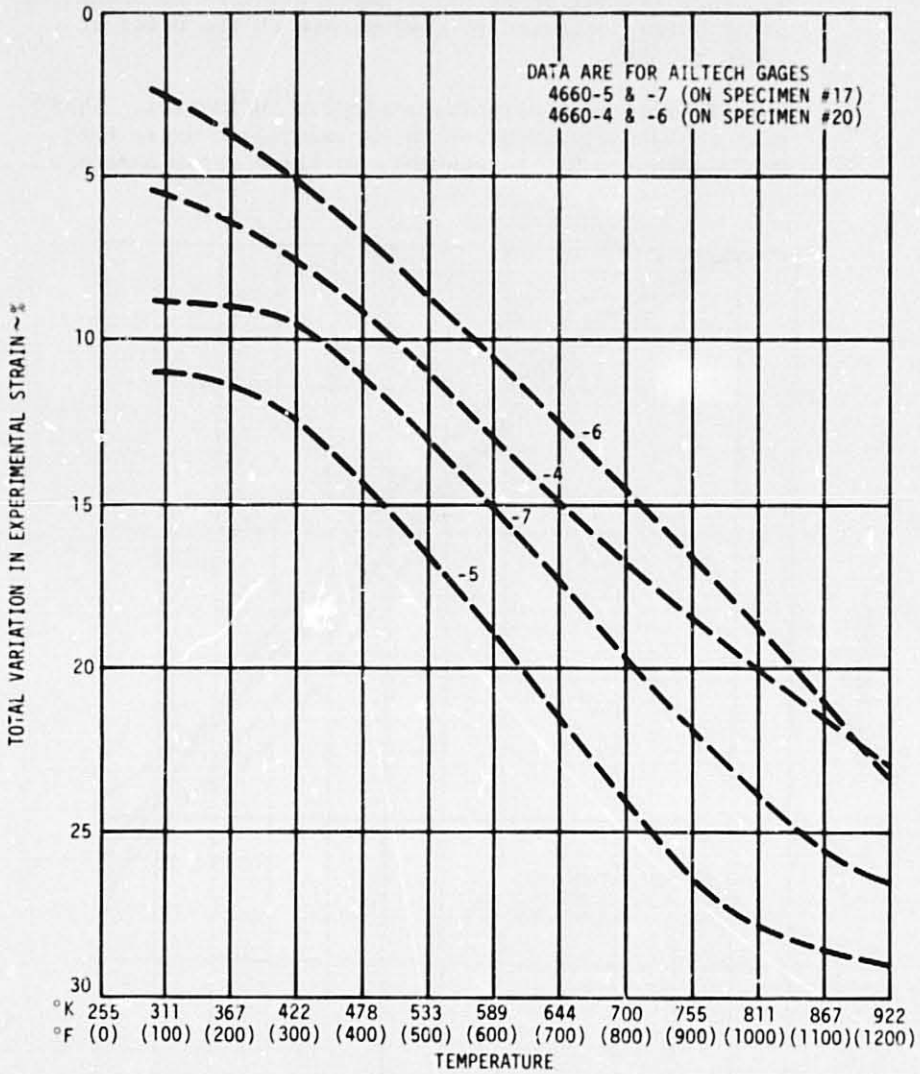

Fig. 11-Total variation in experimental strain as a function of temperature

IV. REFERENCES

1. "Strain Gage Products," Bulletin SGB 101-673, AILTECH, a Cutler-Hammer Company

2. "Foil Wire Strain Gages," Bulletin 100/101-1, Effective March 1970, BLH Electronics, Inc.

3. "Bean Strain Gages - Type WB - Wire/Dual Filament," Bulletins 8-69 and 300/11-69, William T. Bean, Inc.

4. "Weldable Strain Gage Manual," AILTECH, a Cutler-Hammer Company.

D29

Paper No. 34

THERMAL VACUUM TESTING TECHNIQUES FOR SPACECRAFT

S. A. Nichols, *Naval Research Laboratory, Washington, D.C.*

ABSTRACT

Cesium frequency standards are to be flown on the NTS-2 satellite which is part of a program conducted at the Naval Research Laboratory (NRL) to develop technology and time standards for NAVSTAR Global Positioning System (GPS). Mission requirements for the thermal design of this frequency standard called for a low nominal temperature (15°C) and the removal of most of the heat generated by the standard from the spacecraft. This paper describes the test program run at NRL to determine the thermal properties of the frequency standard. Since it was necessary to run tests before delivery, a simulator was constructed for these tests. Special mathematical analysis techniques were developed to obtain the thermal coefficients required for the spacecraft thermal analysis. These coefficients are then used to predict the thermal environment for different orbital conditions. Thermal vacuum tests of the flight frequency standard and the integrated spacecraft demonstrated the validity of this technique.

INTRODUCTION

A Cesium Beam Frequency Standard is being flown on the Naval Research Laboratory developed Navigation Technology Satellite Two (NTS-2)[1] as part of the NAVSTAR Global Positioning System (GPS).[1] This standard was developed especially for NTS-2 and, as a part of that program, a thermal analysis was made of the standard. This paper will present the test techniques, data analysis methods and results of the thermal characteristics of the standard.

Frequency Standard Testing

Due to time constraints, the flight qualification model of the frequency standard was not available for

testing when data was required to complete the satellite thermal design, therfore a simulator was constructed and tested first.

The complete testing program, which was conducted at NRL, consisted of testing the simulator, testing the effects of changes on a simulator (different thermal coatings and conductivity paths) and testing flight qualification models. Tests were also run by another group at NRL on a mockup of the satellite and on the flight model satellite.

The frequency standard as seen in Fig. 1, is a box, 25 cm x 41 cm x 20 cm high, weighing 13 kg and

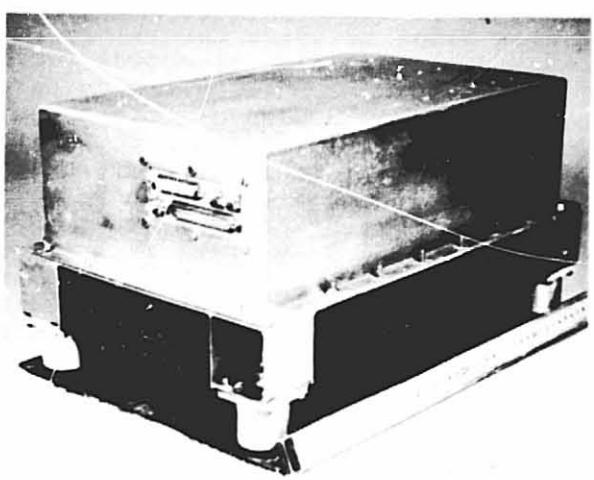

Fig. 1 - Flight Frequency Standard

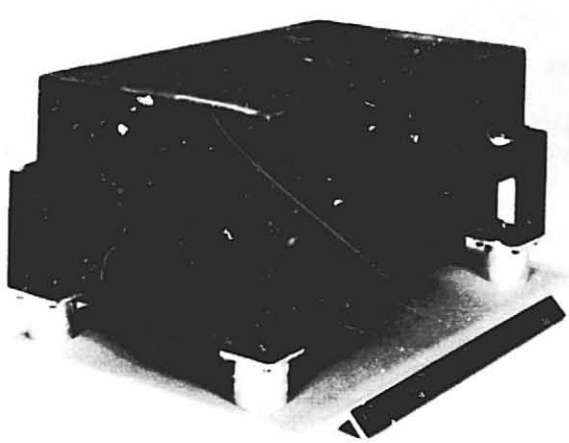

Fig. 2 - NRL Simulator

dissipating approximately 23 watts of DC power. The simulator as seen in Fig. 2, was constructed to have as nearly as possible, the same size, weight, and DC power. Most of the weight was simulated by a one inch thick aluminum plate. Boxes were added top and bottom to simulate the size and the mounting brackets were constructed in a shape similar to the standard. A large electric heating blanket simulated the DC load. It is to be noted that the standard design allowed the use of vibration isolators. Early tests on both the simulator and the standard were made with the vibration isolators, but in the spring of 1976 the isolators were replaced with solid aluminum blocks and another set of test data was taken on both the simulator and the flight model frequency standard.

Frequency standard and simulator thermal vacuum tests were run at NRL in a chamber which has a 17 inch diameter cylinder, 21 inches deep, with a temperature controlled plate. A vacuum pressure of 1×10^{-5} torr and lower was achieved with the use of a diffusion pump. Temperature control was achieved with a recirculating bath which was proportionally controlled. The capacity of the heating and cooling equipment allowed a rapid change of the temperature controlled plate (less than an hour) and temperature stability was better than $\pm .1^{o}C$. The temperature range of the chamber is $-15^{o}C$. to $+50^{o}C$. The walls of the chamber were lined with aluminized mylar early in the test series, and were changed to polished stainless steel late in the test series, due to maintenance problems of the aluminized mylar.

The test procedure consisted of placing the object in the chamber; setting the temperature controlled plate, and the DC power load; and allowing the object to stabilize. Normally four temperature sensors were used. Fig. 3 shows typical locations of the temperature sensors. Temperature stabilization was monitored by observing the rate of change of the sensor mounted on the object under test. A complete test series consisted of three different temperatures with three different DC power settings at each temperature, but due to time limitations, it wasn't possible to obtain a complete data set for each series.

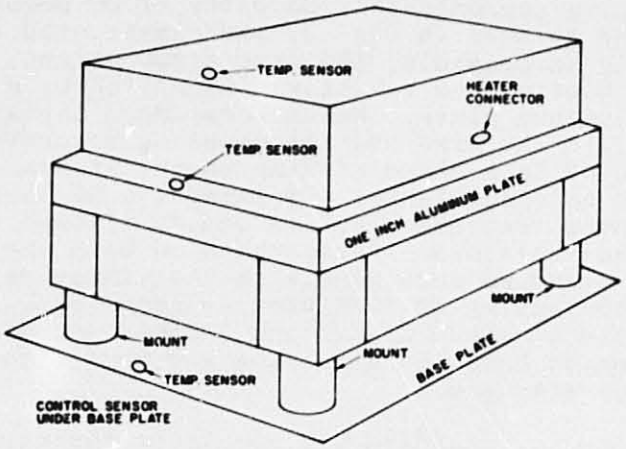

Fig. 3 - Sensor Locations on Standard

Data Analysis

At the equilibrium temperature, the DC power is dissipated by radiation and conduction to the controlled plate and the chamber walls.[2] The energy balance equation is

$$P = A_1(\sigma Ts^4 - JTp^4) + C_1\ (Ts-Tp) + C_a\ (Ts-Ta)$$

where

P = DC power (watts)

A_1 = Effective radiating area (cm^2)

σ = Stefan - Boltzmann constant ($w/cm^2\ {}^oK^4$)

C_1 = Conductivity between the unit under test and temperature controlled plate ($w/{}^oc$)

Ca = Coupling to the ambient room temperature

Ts = Temperature of unit under test (^oK)

Tp = temperature controlled plate temperature (^oK)

Ta = Ambient temperature (^oK)

The purpose of this test program was to determine the parameters A and C_1. By changing the terms T and Tp, it was possible to generate a data set that could be used to calculate A and C_1. The coupling coefficient must be determined and includes the effects of

instrumentation wiring and radiation to the wall which is assumed to be approximately linear.

The problem in data analysis is to separate the radiated and conducted coefficients. A plot of the plate temperature vs. the temperature of the unit under test is nearly linear. An inspection of the methods of solving simultaneous equations shows that small temperature variations cause large coefficient variations.

To illustrate the problem[3], a group of three data sets were chosen which were characteristic of conduction coupling to the baseplate and to ambient. Conduction and radiation parameters were then derived from these data sets assuming no conduction to ambient. Then the frequency standard temperature in the middle data set was incremented by plus and minus one degree and the effect of the increment on the parameter solution was determined. The results are plotted in Fig. 4. The small temperature increment on one data point produced widely varying solutions.

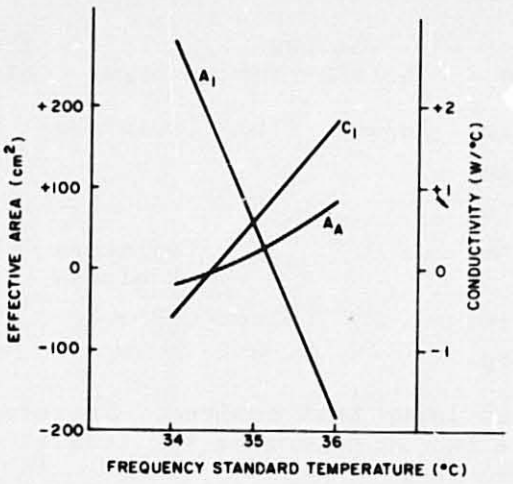

Fig. 4 - Simulated Parameter Solution

A combination of test and analytical techniques yielded a consistent set of coefficients. Since the standard was mounted on four legs, it was possible to run tests using two and then four legs. The energy balance formula is then used to calculate the conductivity coefficient. Once the conductivity coefficient is known, the other coefficients may be calculated from the data set. A complete test run consists of nine lines of data (3 temperatures with 3 DC power levels at

each temperature) the resulting nine energy balance formulas were then analyzed on a desk top calculator using a multiple linear regression technique.[4] It was noted that varying the temperature and not the power yielded a data set, that did not give consistent results using the multiple linear regression.

Test Results

Six major tests were run between October 1975 and July 1976. Table I lists the characteristics of the six units tested. The manufacturer made available for a short time a thermal simulator which used many of the frame components of the flight standard. When that simulator was returned, another simulator was constructed at NRL of approximately the same size and weight of the flight standard. Initial tests indicated that the thermal coupling between the standard and the

Table I

Characteristics of Units Tested

Unit Tested	Coating Bottom	Coating Top	Legs	Thermal Straps
MFG Sim.	Black	Alum	Isolators	No
NRL Sim.	"	"	"	Yes
FLT Std.	"	"	"	Yes
NRL Sim.	"	"	Isolators & Blocks	Yes
NRL Sim.	"	Black	Blocks	No
FLT Std.	"	"	"	No

base plate was lower than desired. Therefore a series of tests were run to determine the feasibility of adding flexible copper braided straps. The formula used to estimate the conductivity coefficient is $C = W/PL^2/K$ where W = weight (2.6 gms/in), L = length, P = density (.22 lb/in^3 for copper), K = conductivity (9.7W/oC - in for copper). Test results gave a coefficient half that of the calculated value, probably due to the difficulty of bonding the braid to the aluminum box.

In the spring of 1976, as the result of the analysis of vibration tests, it was decided to replace the vibration isolation mounts with aluminum blocks to lower the gradient between the frequency standard and the base

and to provide a number for the satellite thermal system design. The value listed in Table II is the 10% to 90% response to a step change in temperature.

The thermal coefficients generated in Table II can now be used to predict operating temperatures in the satellite. The temperature of the baseplate is controlled by the area of the optical surface reflectors on the outer surface of the baseplate panel. Fig. 5 shows expected temperature performance for four different cases, three with the simulator and one with the flight standard, assuming no coupling with the inside of the spacecraft. The temperature difference between the standard and the baseplate was 28°C with a baseplate temperature of 0°C in the original design. The straps reduced the differential by 5.4 °C, and the switch to solid blocks reduced the temperature difference to 14.6°C. The flight standard agreed with the simulator within less than one degree. This error could be attributed to differences in the quality of the black paint of the radiated area.

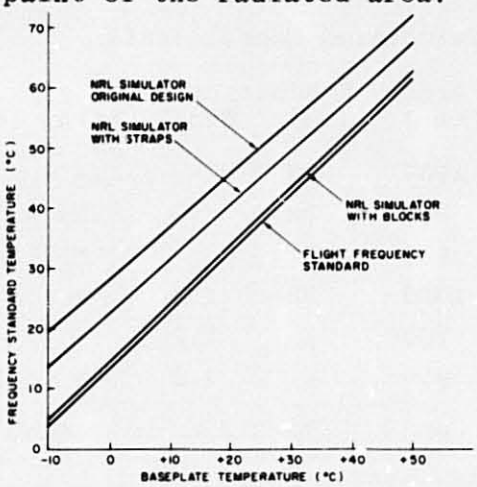

Fig. 5 - Temperature Performance of Simulators and Standard

Conclusion

This testing program was successful in generating a set of thermal coefficients for use in the spacecraft thermal system design, before the flight frequency standard was delivered to NRL. The NRL - conducted simulator was shown to be an accurate model of the flight standard and the technique chosen to separate the conducted and radiated terms produced coefficients which were used to predict performance of the flight standard.

References

1. D. L. Smith, G. W. Criss, GPS NAVSTAR Global Positioning System, Astronautics and Aeronautics, Vol. 14, No. 4, April 1976.

2. R. L. Easton, C. A. Bartholomew, The Thermal Design of the TIMATION I Satellite, NRL Report 6782, Jan. 16, 1969.

3. K. M. Uglow, Thermal Characteristics of NTS-2 Satellite, Final Report for Contract N00173-C0369, Jan. 1976.

4. Model 10 Hewlett Packard Calculator Model 9810A Stat Pac

Paper No. 35

EVALUATION OF THERMAL SOAK TIMES

G. P. Mulholland, *New Mexico State University, Las Cruces, New Mexico*
H. P. Huddleston, Jr., *White Sands Missile Range, New Mexico*

ABSTRACT

A mathematical model for the heat transfer within the electronics package of a Chaparral missile has been performed. The Grashof number for this configuration was less than 2000 which indicated that the primary mode of heat transfer was conduction. The Vodicka theory for heat conduction in laminated composite media was utilized to obtain the solution for the model.

INTRODUCTION

Modern missiles and various items of equipment required to support them are composed of many complex electrical and electronic systems. Many of these systems, if improperly insulated, can malfunction if exposed to excessively high or low temperatures. The thermal performance of these systems must many times be predicted by a mathematical model.

The purpose of the present investigation is to construct a mathematical model for the heat transfer within the electronics package of a Chaparral missile. For this particular configuration, the Grashof number was less than 2000 which indicated that the heat transfer is essentially all conduction. To model this system, the Vodicka theory for the heat conduction in laminated composite media was utilized. This method enables one to predict both the temperature of and the heat flux through the electronics package of the missile given either the surface temperature of the missile or the environmental temperature.

To check the validity of the theory an experimental test was conducted in which the electronics section of a Chaparral missile was placed in the thermal chamber at White Sands Missile Range. The electronics package was instrumented with thermocouples and temperatures were recorded as the chamber temperature was varied. The experimental results show good agreement with the mathematical model indicating that the original assumptions are valid for this situation. This agreement between the experimental results and the theory enables one not only to predict potentially harmful situations to the electronics package due to fluctuations in environmental temperature but to also

design thermal tests of reasonable duration.

SYMBOLS

A_{in}, B_{in}, A_i, B_i	constant
C_{pi}	specific heat at constant pressure in the i^{th} section
D_i^2	thermal diffusivity in the i^{th} section
J_o	zero order Bessel function of the first kind
K_i	thermal conductivity in the i^{th} section
$L(r)$	function of r defined by Eq. (8)
ℓ_{ml}, N_m	constants defined by Eqs (5) and (6)
r	spatial coordinate
$T_i(r,t)$	temperature in the i^{th} section
$T_A(t)$	surface temperature
t	time
V	initial temperature distribution
$X_{in}(r)$	eigenfunction
Y_o	zero order Bessel function of the second kind
γ_n	eigenvalue
ρ_i	density in the i^{th} section

ANALYSIS

Experimental evidence [1,2] indicates that the heat transfer in enclosed air spaces is primarily due to conduction if the Grashof number is less than 2000 for vertical plates and less than 1700 for horizontal plates. The particular problem modeled in this paper is this type of situation where free convection is retarded and the heat transfer through the region can be simulated by the heat transfer through a laminated composite.

The heat conduction equation without heat generation for the i^{th} section of k solidly joined cylinders is

$$\frac{1}{D_i^2}\frac{\partial T_i}{\partial t}(r,t) = \frac{1}{r}\frac{\partial}{\partial r}\left(r\frac{\partial T}{\partial r}(r,t)\right) \qquad (1)$$

The boundary, internal and initial conditions for the composite are taken to be

a) $\frac{\partial T_1}{\partial r}(r_1,t) = 0$

b) $T_k(V_{k+1}, t) = T_A(t)$

c) $T_i(r,o) = V,\ r_i \le r \le r_{i+1},\ i = 1, 2,\ldots,k$ (2)

d) $T_i(r_{i+1},t) - T_{i+1}(r_{i+1},t)$

e) $K_i \frac{\partial T_i}{\partial r}(r_{i+1},t) = K_{i+1}\frac{\partial T_{i+1}}{\partial r}(r_{i+1},t)$

Boundary condition (2b) assumes the wall temperature is known while (2a) assumes layer 1 is solid. For the actual situation, the first layer is hollow; but for practical applications there is no convenient method for monitoring the temperature at this point so (2a) was deemed a reasonable alternative.

The solution to Eq's (1) and (2) has been obtained [3] previously and is given by

$$T_i(r,t) = \sum_{n=1}^{\infty}\left\{g_n \exp(-\gamma_n^2 t) - \ell_{n1}\int_0^t \frac{dT_A(\tau)}{d\tau}\exp[-\gamma_n^2(t-\tau)]d\tau\right\} X_{in}(r) + L_i(r)\,T_A(t);\ r_i \le r \le r_{i+1},$$

$$i = 1, 2, \ldots, k \qquad (3)$$

where

$$g_n = \frac{1}{N_n}\sum_{i=1}^{k}\rho_i C_{pi}\int_{r_i}^{r_{i+1}} rVX_{in}(r)dr - \ell_{n1}T_A(0),\ n = 1, 2, 3, \ldots \qquad (4)$$

$$\ell_{n1} = \frac{1}{N_n}\sum_{i=1}^{k}\rho_i C_{pi}\int_{r_i}^{r_{i+1}} r\,L_i(r)X_{in}(r)dr,\ n = 1, 2, 3, \ldots \qquad (5)$$

$$N_n = \sum_{i=1}^{k} \rho_i C_{pi} \int_{r_i}^{r_{i+1}} r[X_{in}(r)]^2 dr, \quad n = 1, 2, 3, \ldots \tag{6}$$

$$X_{in}(r) = A_{in} J_o\left(\frac{\gamma_n}{D_i} r\right) + B_{in} Y_o\left(\frac{\gamma_n}{D_i} r\right), \quad \begin{matrix} n = 1, 2, 3, \ldots \\ i = 1, 2, \ldots, k \end{matrix} \tag{7}$$

$$L_i(r) = A_i \ell_n r + B_i \tag{8}$$

The coefficients A_{in}, B_{in} for i = 1, 2, ..., k, n = 1, 2, ... the coefficients A_i and B_i for i - 1, 2, ..., k and the eigenvalues γ_n, n = 1, 2, 3, ... are obtained in a straightforward manner by applying the boundary and internal conditions to the assumed solution. Details are given in [3].

MISSILE SYSTEM

The electronics system of a Chaparral missile can be simulated as a five layer composite. Layer one and layer five are strainless steel, layers two and four are air and layer three is the electronics package. The physical dimensions and thermal properties were taken as

Layer					
K(w/m-°K)	16.264	0.0271	9.08×10^{-3}	0.0271	16.264
ρ(gm/cm^3)	7.824	0.00114	0.0818	0.00114	7.824
C_p(cal/gm-°K)	0.11	0.24	0.45	0.24	0.11

$r_1 = 0$, $r_2 = 1.111$ cm, $r_3 = 2.85$ cm, $r_4 = 3.85$ cm, $r_5 = 5.97$ cm, $r_6 = 6.35$ cm

Proceeding in the same manner as outlined previously, we obtain the solution as

$$T_i(r,t) \sum_{m=1}^{\infty} \left\{ \ddot{v}\ell_m \exp(-\gamma_m^2 t) - \ell_m T_A(t) + \gamma_m^2 \ell_m T_A(t) * \exp(-\gamma_m^2 t) \right\} X_{im}(r) + T_A(t) \tag{9}$$

where

$$\ell_m = -\frac{K_5 r_6}{\gamma_m^2 N_m} \frac{dX_{5m}(r_6)}{dr} \tag{10}$$

REFERENCES

1. M. Jakob, "Free Convection Through Enclosed Plane Gas Layers," Trans. ASME, Vol. 68, p. 189 (1946).

2. M. Jakob, Heat Transfer, Vol. 1, John Wiley & Sons, Inc., New York (1949).

3. G. P. Mulholland and M. H. Cobble, "Diffusion Through Composite Media," Int. J. Heat Mass Transfer, Vol. 15, pp. 147-159 (1972).

APPENDIX A

The eigenvalues for the electronics section of the missile configuration described previously are found by solving the matrix equation

$$\begin{bmatrix} M_{01}(r_2)-M_{02}(r_2) & -N_{02}(r_2) & & & & & \\ A_1M_{11}(r_2)-M_{12}(r_2) & -N_{12}(r_2) & & & & & \\ 0 & M_{02}(r_3) & N_{02}(r_3)-M_{03}(r_3) & -N_{03}(r_3) & & & \\ 0 & 0 & 0 & -M_{03}(r_4)-N_{13}(r_3) & & & \\ 0 & 0 & 0 & M_{03}(r_4) & N_{03}(r_4) & & \\ 0 & 0 & 0 & A_3M_{13}(r_4) & A_3N_{13}(r_4)-M_{14}(r_4) & -N_{04}(r_4) & 0 \\ 0 & 0 & 0 & 0 & 0 & M_{04}(r_5) & N_{04}(r_5)P_o \\ 0 & 0 & 0 & 0 & 0 & A_4M_{14}(r_5) & A_4N_{14}(r_5)P_1 \end{bmatrix} = 0$$

where

$$M_{ij}(r) = J_i\left(\frac{\gamma_m}{D_j} r\right)$$

$$N_{ij}(r) = Y_i\left(\frac{\gamma_m}{D_j} r\right)$$

$$A_i = \frac{K_i}{K_{i+1}} \quad \frac{D_{i+1}}{D_i}$$

$$P_i = \frac{-M_{i5}(r_5)N_{05}(r_6) + M_{05}(r_6)N_{i5}(r_5)}{N_{05}(r_6)}$$

$$N_m = \sum_{\ell=1}^{4} \frac{r_{\ell+1}^2}{2} \left\{ (\rho_\ell C_{p\ell} - \rho_{\ell+1} C_{p\ell+1}) X_{\ell m}^2 (r_{\ell+1}) + \frac{1}{\gamma_m^2} \left(\frac{K_\ell K_{\ell+1} - K_\ell^2}{K_{\ell+1}} \right) \left(\frac{dX_{\ell m}}{dr} (r_{\ell+1}) \right)^2 \right\}$$

$$+ \frac{r_6^2}{2} \frac{K_5}{\gamma_m^2} \left(\frac{dX_{5m}}{dr} (r_6) \right)^2$$

and where the ℓ_m are the roots of the eigenvalue equation given in Appendix A.

Figure 1 is a comparison between the experimentally and anlytically obtained temperatures of the outside surface of the electronics package during a test conducted in the thermal chamber at White Sands Missile Range. The differences between the two curves for t > 50 minutes is most likely due to the inexact values of density, specific hear and thermal conductivity used in the model. The package was assumed to be cork at 68°F.

Since the package consists of numerous electronic items of different materials, the true evaluation of these properties would have to be made in a separate test.

The encouraging portion of this figure is for t > 50 minutes. In this region where the effects of density and specific heat are less important, the two curves converge. Since the purpose of the study was to evaluate the time necessary for the electronics package to reach a steady-state operating condition, it is felt that this model will accomplish that function. Better temperature profiles can be obtained if more accurate values for the density and specific heat of the electronics package are utilized.

CONCLUSIONS

A mathematical model for the temperature distribution and heat flux across the electronics package of a Chaparral missile has been obtained. This model can be utilized in situations where natural convection currents are suppressed and the heat transfer can be simulated by conduction through laminate composites.

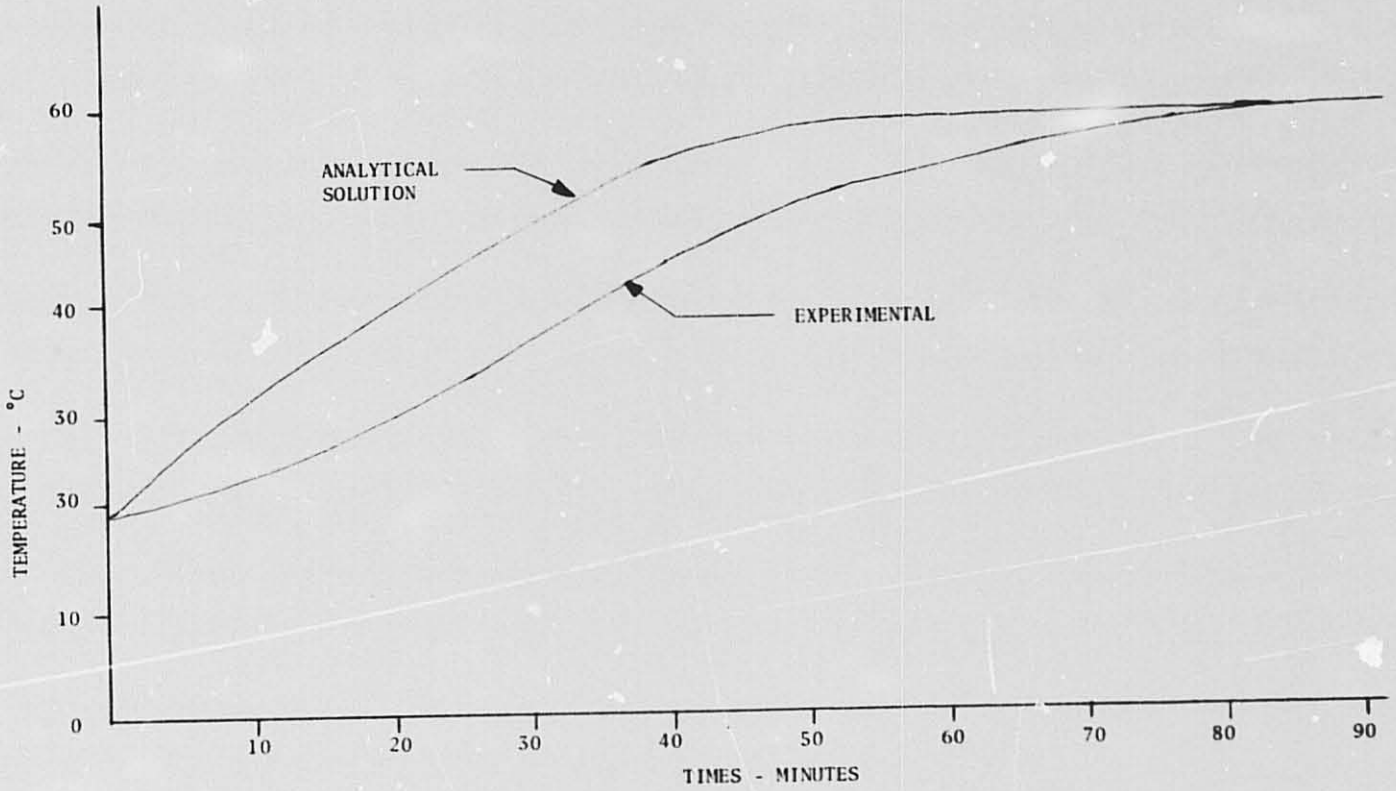

FIGURE 1. TEMPERATURE-TIME HISTORY OF ELECTRONICS PACKAGE

D31

N79-19044

Paper No. 36

AN EFFICIENT NUMERICAL TECHNIQUE FOR CALCULATING THERMAL SPREADING RESISTANCE*

E. H. Gale, Jr., *General Electric Company, Aircraft Equipment Division, Utica, New York*

ABSTRACT

An efficient numerical technique for solving the equations resulting from finite difference analyses of fields governed by Poisson's equation is presented. The method is direct (noniterative) and the computer work required varies with the square of the order of the coefficient matrix. The computational work required varies with the cube of this order for standard inversion techniques, e.g., Gaussian elimination, Jordan, Doolittle, etc.

INTRODUCTION AND BACKGROUND

General

"Thermal spreading resistance" is defined as the conductive thermal resistance between a source region and a sink region in a solid where the geometry is such as to preclude one dimensional heat flow. Knowledge of thermal spreading resistance is needed in two aerospace engineering areas. These are the thermal design of electronic components or equipments and in the prediction and control of thermal contact resistance.

Importance to the Design of Electronic Components and Equipments- The thermal analysis of a power semiconductor or integrated circuit can be reduced to the problem of determining the appropriate spreading and bonding thermal resistances. As an example, the problem of calculating the junction-to-case thermal resistance of a semiconductor bonded to a substrate which is bonded in a metal case will be considered. Figure 1 illustrates this problem.

Heat is generated in a region of known size, the junction region of the semiconductor. The first, and most significant,

*The work reported in this paper was done under National Aeronautics and Space Administration contract NAS8-28616.

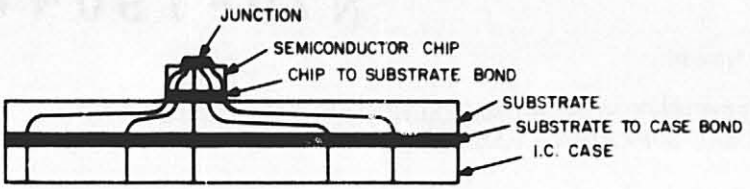

Fig. 1 Semiconductor in an Integrated Circuit

spreading resistance of interest occurs between the junction and the opposite face of the silicon chip. The next thermal resistance of interest is that across the bond between chip and substrate. It is of significance that these thermal resistances are not independent. The thermal conductance of the bond proper can vary several thousandfold depending on the use of a metallic or nonmetallic bonding material. The resistance to heat flow between the semiconductor chip bond region and the rear of the substrate represents a second spreading resistance. In a typical integrated circuit package, the entire bottom region of the substrate would not be available as a sink for a single semiconductor chip due to the presence of other heat dissipating chips. It is usually possible to estimate the size of the effective sink region on the rear of the substrate from considerations of symmetry or because it exceeds dimensions which appreciably affect the thermal spreading resistance. In those few cases where interactions must be considered, the key analytical tool is superposition. Green's function approach may be employed to advantage. For example, see reference 1.

The importance of being able to predict thermal spreading resistances in single and multilayered material in the evaluation of the thermal design of semiconductor or integrated circuits has been shown. Spreading thermal resistances are important in other electrical devices such as phased array antenna elements, Peltier coolers, Seebeck generators, and most devices which utilize conductive heat transfer.

Prediction and Control of Thermal Contact Resistance

The resistance to heat flow between two mating (touching, as in a joint) pieces of metal is called thermal contact resistance. When the actual microscopic regions of contact between two mating surfaces are examined, it is found that metal-to-metal contact occurs in small discrete regions where the asperities or microscopic protuberances make contact. References 2 and 3 describe this model of contact in great detail. Figure 2 illustrates this contact model.

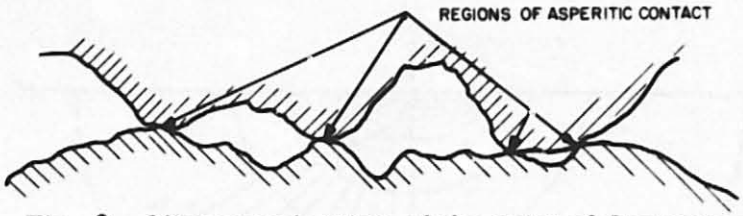

Fig. 2. Microscopic View of the Joint of Contacting Pieces of Metal

The heat flow to and from a region of asperitic contact is seen to be of the "spreading" type. In fact, the effective thermal contact resistance of any contact may be considered as the sum of the parallel microscopic spreading resistances in the contacts themselves. References 2 and 3 deal largely with isotropic contacts in which the thermal conductivity within the bodies of both contacts is uniform.

Analysis has shown that the bulk of the spreading resistance occurs close to the region of actual asperitic contact and that the spreading resistance in any region varies inversely with the thermal conductivity of the material. Figures 3 and 4 illustrate the first of these points. Figure 3, drawn to scale, shows the equipotential lines about a circular contact region eachdrawn to show one-tenth of the total spreading resistance between the circular contact region and a body of semi-infinite extent. It is seen that half of this total resistance occurs within one contact radius from the circular contact or source region and 80 percent occurs within three contact radii. Figure 4 illustrates these relationships. Figures 3 and 4 are taken from reference 4.

The thermal conductivity of the contact material close to the contact region is of such importance that even a thin 45 Angstrom thick layer of oxide on an aluminum contact can contribute measurably to the thermal contact resistance. This has been shown by actual measurement; see reference 4.

Mikic and Carnasciali, reference 5, have utilized the above facts to enhance thermal contact conductance by plating materials of higher conductivity on the contacting faces of a metallic joint. They present an approximate analysis of spreading resistance from a circular contact into a contact region composed of two layers of materials with different conductivities. An exact boundary value solution of this basic problem has proven impossible as no mathematical function has been found which will satisfy all the boundary conditions between the plating and the body materials.

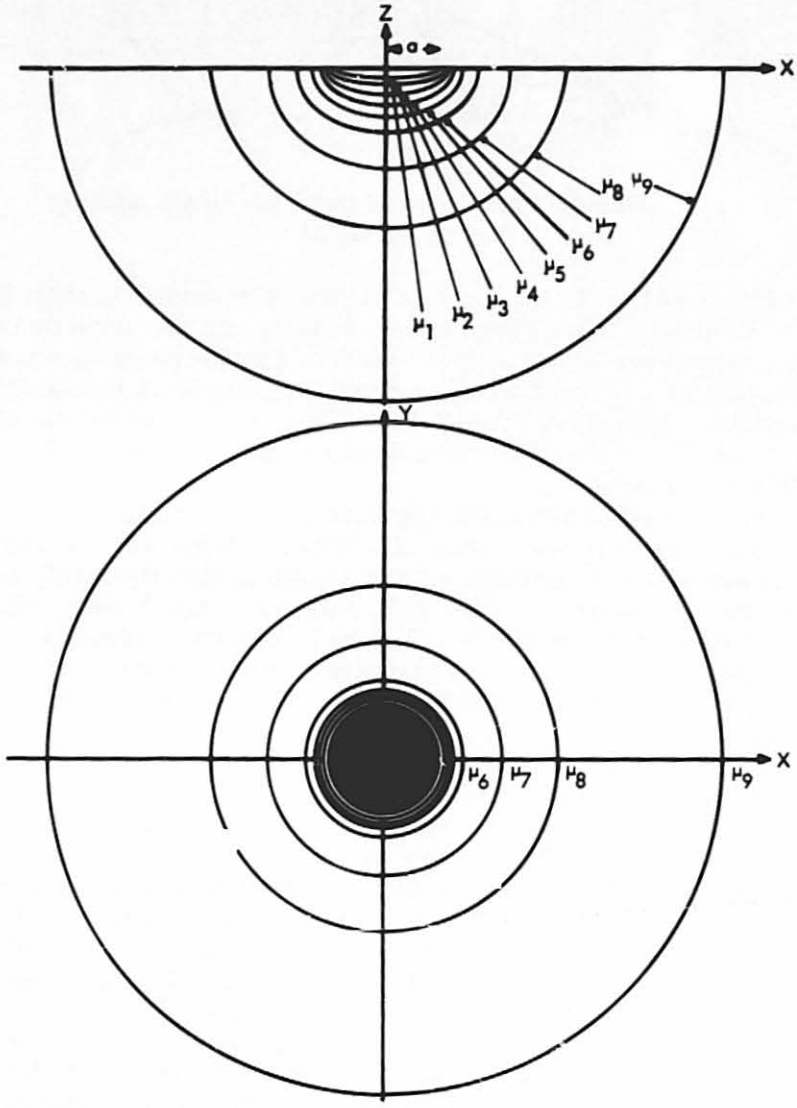

Fig. 3. Temperature Profiles Described by Holm's Equation for Isothermal Circular Source on a Semi-Infinite Slab

Professor C.J. Moore, Jr.,* in his discussion at the end of reference 5, felt this two layered spreading resistance problem

*Associate Professor of Mechanical and Aerospace Engineering, North Carolina State University, Raleigh, N.C.

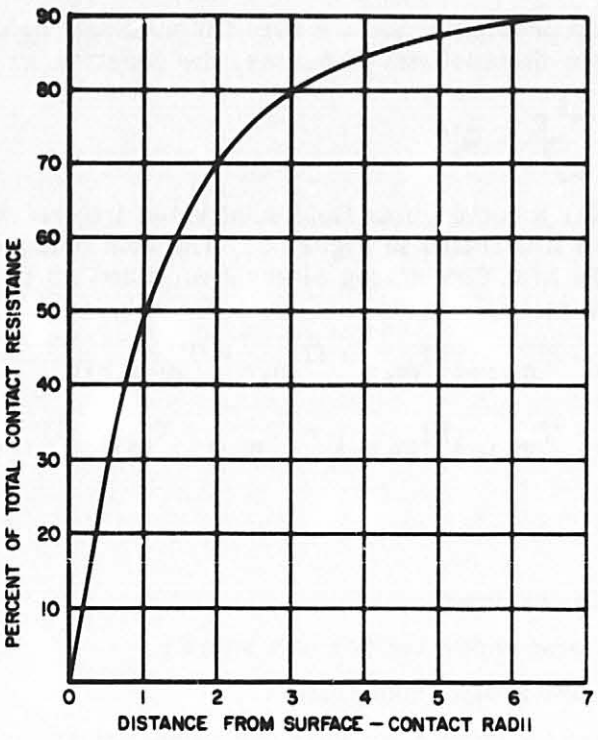

Fig. 4. Percent of Total Constriction Resistance for a Single Isothermal Circular Source on a Semi-Infinite Slab as a Function of Distance into Body of Contact

could best be handled by a "well-conditioned finite difference computer code." Mikic and Carnasciali then question the economic feasibility of such calculations.

Attempts by the author of this study to solve the two layer thermal spreading resistance problem using a finite difference approach utilizing Gauss-Seidel iteration have shown the cost of digital computer calculation to be excessive for large nodal systems.

METHOD

General

The governing differential equation for the thermal spreading resistance problem is Poisson's equation. For those spread-

ing resistance problems that are two-dimensional* or may be reduced to two-dimensional problems, the equation is:

$$\frac{\partial^2 T}{\partial x^2} + \frac{\partial^2 T}{\partial y^2} = Q'''_t \qquad (1)$$

Consider a rectangular field subdivided into rectangular subregions as illustrated in Figure 5. The heat balance equation describing the heat flow among element m, n and its four principal neighbors is:

$$(T_{m,n} - T_{m,n+1})H_{m,n} + (T_{m,n} - T_{m-1,n})V_{m,n} + (T_{m,n} - T_{m,n-1})H_{m,n-1} + (T_{m,n} - T_{m+1,n})V_{m+1,n} = Q_{m,n} \qquad (2)$$

where

T is temperature

Q''' is heat generated per unit volume

x, y, z are spatial coordinates

H, V are horizontal and vertical conductances, respectively

m is row index

n is column index

$Q_{m,n}$ is heat generated in node m, n

The convention for the horizontal and vertical conductances used is shown in Figure 6.

Each of the following observations will be helpful in understanding the discussion which follows:

(1) When any temperature $T_{m,n}$ is known (e.g., as a boundary condition), it will affect equation m, n by yielding a virtual heat generation term $Q'_{m,n}$ which is subtracted from the right-hand side of equation (2) where $Q'_{m,n}$ is:

$$Q'_{m,n} = T_{m,n}(H_{m,n} + V_{m,n} + H_{m,n-1} + V_{m+1,n}) \qquad (3)$$

*The method developed is applicable to three-dimensional problems as discussed in this last part of this section.

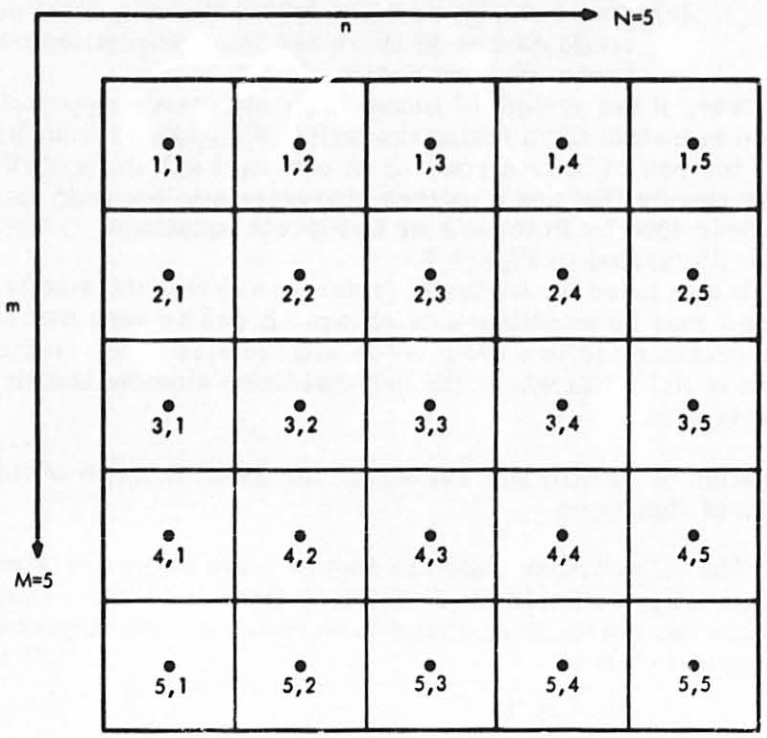

Figure 5. Rectangular Field Divided into 25 Finite Elements

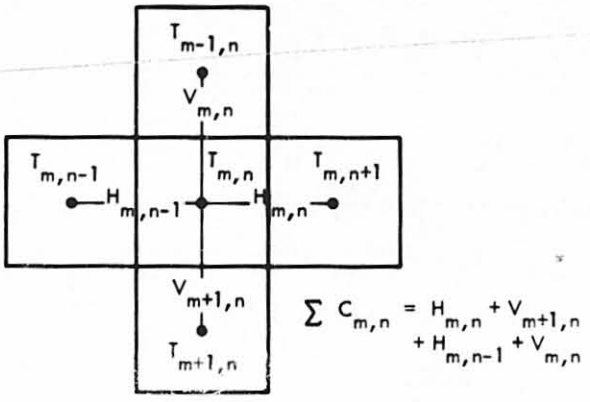

Figure 6. Nomenclature for Nodal Interconductances

(2) If the original physical field is divided into nodes of M rows and N columns, then:
   (a) There will be N*M linear equations.
   (b) There will be not more than N*M unknowns (fewer if some temperatures are initially prescribed).

(c) There can be as many different and distinct nodal conductances as there are interconnections between adjacent nodes.

Now, if the system of linear finite difference equations is written in matrix form (using the nodes of Figure 5) from left to right, top row to bottom row, as in reading English, a coefficient matrix results that has a pattern characteristic for field problems described by Poisson's or LaPlace's equations. This pattern is illustrated in Figure 7.

It was noted by Karlqvist (reference 6) that the matrix in Figure 7 may be partitioned as shown. It can be seen that each of the submatrices is $\sqrt{NM}$ x $\sqrt{NM}$ and the size of the coefficient matrix is NM x NM where the original finite element matrix was N x M in size.

Derivation of an Efficient Technique for Exact Solution of this System of Equations

The submatrices shown in Figure 7 are defined in Figure 8. Expanding the partitioned matrices (Figure 8) into a system of equations, having normalized each equation with respect to the diagonal element:

$$\begin{aligned}
T_1 - A_1T_2 &= C_1 \\
-B_2T_1 + T_2 - A_2T_3 &= C_2 \\
-B_3T_2 + T_3 - A_3T_4 &= C_3 \\
\vdots \quad \vdots \quad & \quad \vdots \\
-B_nT + T_n &= C_n
\end{aligned}$$

the general equation has the form:

$$-B_iT_{i-1} + T_i - A_iT_{i+1} = C_i \tag{4}$$

The first equation can be solved for T_i:

$$T_1 = C_1 + A_1T_2 \tag{5}$$

and the i-th for T_i:

$$T_i = C_i + A_iT_{i+1} + B_iT_{i-1} \tag{6}$$

The goal is to find a recursion relationship built upon successive substitutions, which provides a solution for the i-th

Fig. 7. System of Equations in Matrix Notation

$$\begin{bmatrix} a_{11} & a_{12} & 0 & 0 & 0 \\ a_{21} & a_{22} & a_{23} & 0 & 0 \\ 0 & a_{32} & a_{33} & a_{34} & 0 \\ 0 & 0 & a_{43} & a_{44} & a_{45} \\ 0 & 0 & 0 & a_{54} & a_{55} \end{bmatrix} \quad \begin{bmatrix} T_1 \\ T_2 \\ T_3 \\ T_4 \\ T_5 \end{bmatrix} = \begin{bmatrix} Q_1 \\ Q_2 \\ Q_3 \\ Q_4 \\ Q_5 \end{bmatrix}$$

Fig. 8. System of Submatrices in Matrix Notation

unknown in terms of the (i+1)-th. That is:

$$T_i = A'_i T_{i+1} + B'_i \tag{7}$$

Examining equation (5) for T_1 above, it can be seen that:

$$A'_1 = A_1 \quad \text{and} \quad B'_1 = C_1$$

The equation for T_2 is:

$$T_2 = C_2 + A_2 T_3 + B_2 T_1 \tag{8}$$

which, when written in terms of the equation for T_1, becomes:

$$T_2 = \left[I - B_2 A'_1\right]^{-1} A_2 T_3 + \left[I - B_2 A'_1\right]^{-1} \left[C_2 + B_2 B'_1\right] \tag{9}$$

where I is the unit matrix.

The general coefficients found in this manner become:

$$A'_i = \left[I - B_i A'_{i-1}\right]^{-1} A_i \qquad \text{(a square matrix)}$$

and

$$B'_i = \left[I - B_i A'_{i-1}\right]^{-1} \left[B_i B'_{i-1} + C_i\right] \qquad \text{(a column matrix)}$$

Therefore:

$$T_i = A'_i T_{i+1} + B'_i \tag{10}$$

The temperature matrices (columns) are found starting at the $\sqrt{NM}$ row (or 5th row of Figure 8).

$$T_{\sqrt{MN}} = B'_{\sqrt{MN}} \quad \text{as} \quad A'_{\sqrt{MN}} = 0 \tag{11}$$

Defining O as the order of the coefficient matrix (e.g., square matrix of Figure 7), the system of equations has been solved by operating on $3\sqrt{O} - 2$ submatrices, each of which is the square root of the size of the original NM x NM coefficient

matrix. Three $\sqrt{O}$ inversions of these submatrices are required. The total number of multiplications - a good measure of the computer effort required during solution - is:

$$\text{No. of Multiplications} = 3O^2 + O^{3/2} - O + O^{1/2} \qquad (12)$$

This may be compared against other direct methods (see ref. 7):

Method	Number of Multiplications Required during Solution
Gaussian Elimination	$\frac{1}{3}O^3 + O^2 - \frac{1}{3}O$
Jordan	$\frac{1}{2}O^3 + O^2 - \frac{1}{2}O$
Doolittle	$\frac{1}{3}O^3 + O^2 - \frac{1}{3}O$
Cholesky	$\frac{1}{6}O^3 + \frac{3}{2}O^2 + \frac{1}{3}O$

Cornock's method (ref. 8), a triangulation type, also makes use of the characteristic pattern of submatrices which results during a finite difference solution for fields described by Poisson's equation. When the field properties are homogeneous and isotropic, Cornock's method is very powerful since only one of the above submatrices of order $\sqrt{O}$ need be inverted. However, for the general solution of the nonhomogeneous field, the number of multiplications required is:

$$\frac{13}{2}O^2 - \frac{3}{2}O^{3/2} - 2O - 5 \qquad (13)$$

Cornock's method does not lend itself to ready general programming for matrices of variable size as does the method described in this paper.

That equation (12) is indicative of the computer effort required for solution has been substantiated in practice. Figure 9 shows the variation is cost realized in the solution of very large matrices using the method developed in this paper. The measured slope of the line in Figure 9 is very close to 2.

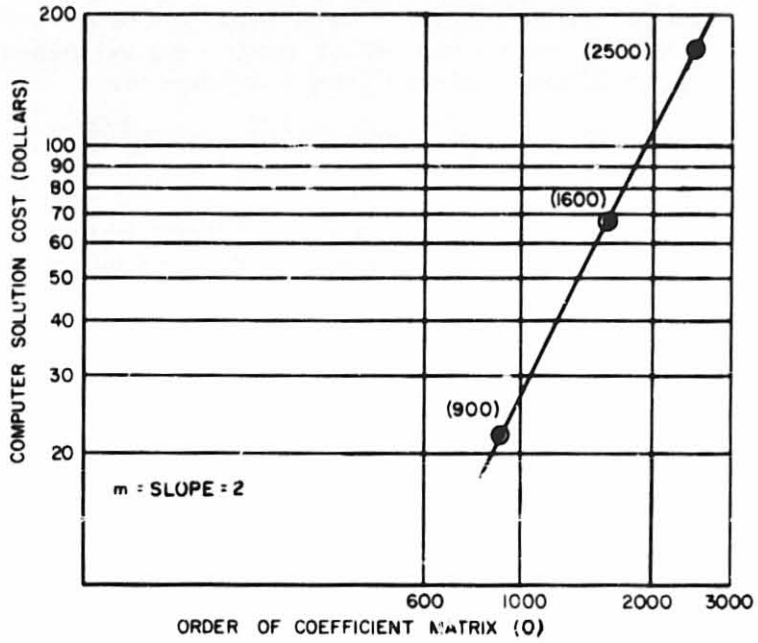

Figure 9. Cost of Computation versus Size of Coefficient Matrix

Applicability of Technique to Three-Dimensional Problems

The technique discussed above is suited to the solution of field problems having three or more dimensions. Figure 10 illustrates the characteristic pattern of the coefficient matrix for a three-dimensional finite element array. It is seen that the submatrices are $\sqrt[3]{O} \times \sqrt[3]{O}$ in size for an O x O coefficient matrix. The same block tridiagonal pattern of submatrices is seen to occur as in the two-dimensional case so the derivation above for the technique of solution for two-dimensional matrices is still applicable. Since the submatrices are $\sqrt[3]{O} \times \sqrt[3]{O}$ rather than $\sqrt[2]{O} \times \sqrt[2]{O}$ in size, the technique is even more powerful for three-dimensional problems. The number of multiplications required for solution of the three-dimensional problem is a function of $O^{4/3}$ as opposed to O^2 for the two-dimensional array where O is the order of the coefficient matrix.

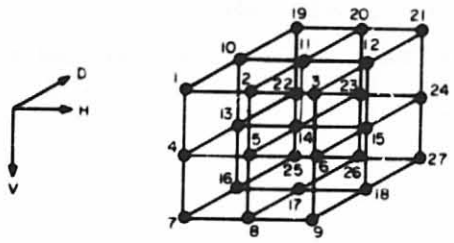

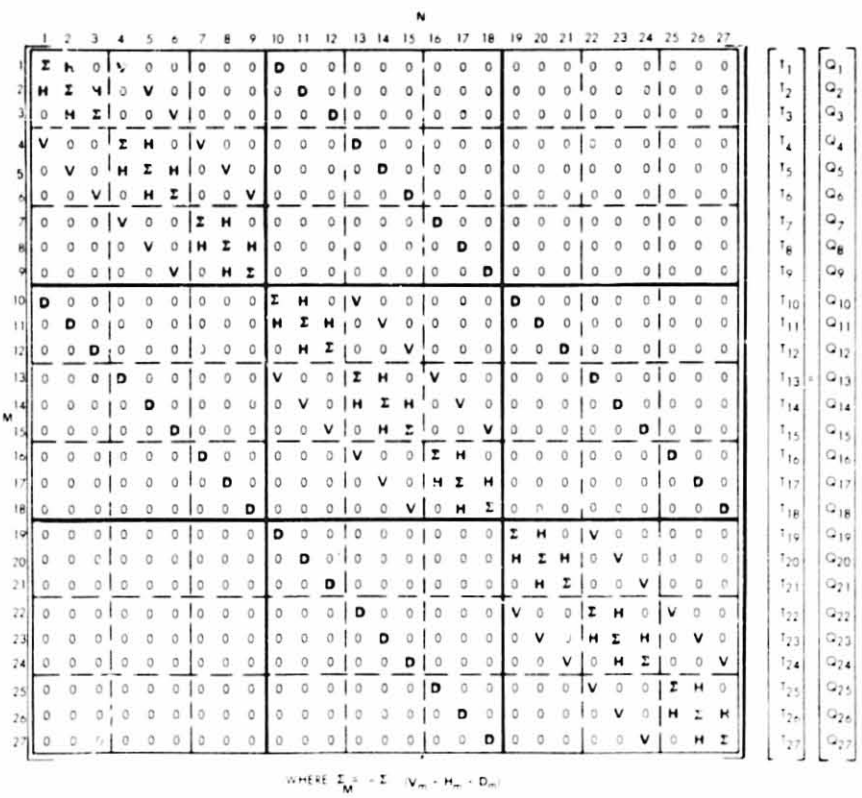

Fig. 10 Matrix Representation of System of Equations Describing Three-Dimensional Field Showing Pattern Established by Submatrices of Coefficient Matrix

REFERENCES

1. Hein, V.L., "Convection and Conduction Cooling of Substrates Containing Multiple Heat Sources," The Bell System Technical Journal, XLVI, No. 8, Oct. 1967.
2. Clausing, A.M., and Chao, B.T., "Thermal Contact Resistance in a Vacuum Environment," University of Illinois, PhD Dissertation, 1963.
3. Tenech, H., and Rohsenow, W.M., "Reduction of Thermal Conductance of Metallic Surfaces in Contact," ASME Paper No. 62-HT-32, 1962.
4. Gale, E.H., "Effects of Thin Surface Films on the Thermal Contact Resistance of Microscopically Sized Contacts," Syracuse University, PhD Dissertation, 1970.
5. Mikic, B., and Carnasciali, G., "The Effect of Thermal Conductivity of Plating Material on Thermal Contact Resistance," ASME Journal of Heat Transfer, Aug. 1970.
6. Kalqvist, O., Tellus, 4, 1952, p. 374.
7. Westlake, Joan R., A Handbook of Numerical Matrix Inversion and Solution of Linear Equations, New York: John Wiley and Sons, 1968, p. 99.
8. Cornock, A.V., "The Numerical Solution of Poisson's and the Biharmonic Equations by Matrices," Proc. Cambridge Philosophical Society, Book 50, 1954, p. 524.